

NASA TM X-53711

# SPECIALIST CONFERENCE



# ON MOLECULAR RADIATION

# AND ITS APPLICATION TO DIAGNOSTIC TECHNIQUES



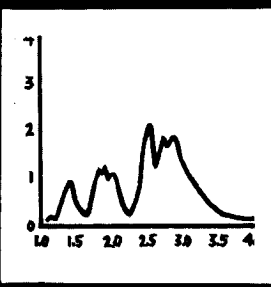
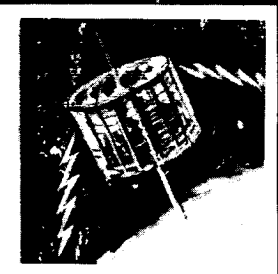
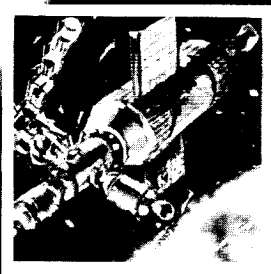
N 68-18082 N 68-18114

FACILITY FORM 602

ACCESSION NUMBER 779 (THRU) 7

(PAGES) TMX-53711 (CODE) 23

(NASA CR OR TMX OR AD NUMBER) (CATEGORY)



MARSHALL SPACE FLIGHT CENTER  
HUNTSVILLE, ALABAMA

October 5-6, 1967

MOLECULAR RADIATION AND ITS APPLICATION  
TO DIAGNOSTIC TECHNIQUES

Proceedings of a Specialists Conference  
Held at the Marshall Space Flight Center  
Huntsville, Alabama  
on October 5-6, 1967

Chairmen: W. K. Dahm and R. Goulard

Editor: R. Goulard  
Purdue University



## FOREWORD AND ACKNOWLEDGEMENTS

The "Specialist Conference on Molecular Radiation and Its Application to Diagnostic Techniques" was attended by 120 engineers and scientists who met for two days in the Morris Auditorium of the Marshall Space Flight Center. In his opening address, Dr. Geissler outlined the intended purpose of this interdisciplinary meeting, which was to review the current work in molecular radiation and to evaluate the different possibilities of new research. To achieve as complete an exchange of ideas as possible, the afternoon of the second day was devoted to an open technical forum which has been entirely transcribed in these proceedings.

The task to assemble speakers and participants from the various research groups interested in molecular radiation (rocketry, meteorology, astrophysics, etc. . . .) fell on the following planning committee:

W. K. Dahm	NASA/MSFC
R. Goulard	Purdue University
R. M. Huffaker	NASA/MSFC
J. I. F. King	Geophysics Corporation of America
J. A. L. Thomson	Institute for Defense Analyses

The organization of the meeting itself was efficiently handled by the staff of the Aerophysics Division of the Aero-Astroynamics Laboratory.

These proceedings were transcribed, edited and prepared for publication in great part through the dedication and skill of Mrs. R. J. Low (JILA - University of Colorado), Mrs. Sarah S. Hightower (NASA/MSFC), and Mrs. T. Williamson (Purdue University). A special word of thanks goes to Mr. R. M. Huffaker who diligently insured the continuity of this effort from beginning to end.

R. Goulard, Editor  
January 8, 1968

# TABLE OF CONTENTS

	Page
WELCOME ADDRESS	
Ernst D. Geissler . . . . .	1
INTRODUCTION TO THE PROBLEM OF ROCKET BASE HEATING, AND TO THE BEHAVIOR OF LIQUID PROPELLANT ROCKET JET PLUMES	
W. K. Dahm . . . . .	4 ✓
SESSION I LABORATORY STUDIES J. A. L. Thomson, Chairman	
BAND MODEL REPRESENTATIONS FOR HIGH TEMPERATURE WATER VAPOR AND CARBON DIOXIDE	
C. B. Ludwig and W. Malkmus . . . . .	19 ✓
METHODS OF CALCULATING ATMOSPHERIC TRANSMISSION FUNCTIONS	
S. R. Drayson . . . . .	36 ✓
INFRARED OPACITY OF HOT WATER VAPOR	
J. Auman, Jr. . . . .	50 ✓
THE SURFACE PRESSURE OF VENUS	
L. D. Gray and A. T. Young . . . . .	68 ✓
INFERENCE OF BAND STRUCTURES FROM LABORATORY DATA	
T. L. Altshuler and J. I. F. King . . . . .	96 ✓
APPLICATION OF BAND MODELS TO INHOMOGENEOUS GASES	
F. S. Simmons . . . . .	113 ✓

# TABLE OF CONTENTS (Continued)

Page

## SESSION II APPLICATIONS OF RADIATIVE HEAT TRANSFER CALCULATIONS R. M. Huffaker, Chairman

RADIATION MODEL FOR NONSCATTERING ROCKET EXHAUST GASES	
J. A. L. Thomson . . . . .	137 ✓
REVIEW OF EXPERIMENTAL VERIFICATION OF THE CURTIS-GODSON APPROXIMATION FOR INFRARED SPECTRAL RADIATION FROM HIGH TEMPERATURE GASES	
B. Krakow and H. Babrov . . . . .	164 ✓
RADIATIVE HEAT TRANSFER CALCULATIONS FOR SATURN EXHAUST PLUMES	
J. E. Reardon and R. M. Huffaker . . . . .	184 ✓
EMITTANCE AND RADIANCE CALCULATIONS FOR SOLID PROPELLANT ROCKET EXHAUSTS	
D. J. Carlson and A. D. Laderman . . . . .	219 ✓
THE STATUS OF OPTICAL DIAGNOSTICS ON WAKES BEHIND HYPERSONIC VEHICLES	
J. C. Burns and T. R. Riethof . . . . .	237 ✓

## SESSION III INVERSION TECHNIQUES AND REMOTE SENSING J. I. F. King, Chairman

REMOTE SENSING AND INVERSION TECHNIQUES: STATE OF THE ART	
J. I. F. King . . . . .	253 ✓

## TABLE OF CONTENTS (Continued)

	Page
<b>STATISTICAL INVERSION METHOD FOR THE SOLUTION OF INTEGRAL EQUATIONS OF THE FIRST KIND</b>	
E. R. Westwater and O. N. Strand . . . . .	269 ✓
<b>REMOTE SENSING OF ATMOSPHERIC WATER VAPOR AND OZONE USING INTERFEROMETRY</b>	
Barney J. Conrath . . . . .	277L
<b>REMOTE DETECTION OF LOCAL TEMPERATURES AND LOCAL PARTIAL PRESSURES WITH CROSSED-BEAM SPECTROSCOPY</b>	
F. R. Krause and J. B. Stephens . . . . .	297 ✓
<b>APPLICATION OF LASER DOPPLER TECHNIQUES TO TURBULENT VELOCITY MEASUREMENT</b>	
R. M. Huffaker, E. Rolfe, and A. V. Jelalian . . . . .	328
<b>TEMPERATURE AND CONCENTRATION MEASUREMENTS IN MODEL EXHAUST PLUMES USING INVERSION TECHNIQUES</b>	
W. Herget . . . . .	359 ✓
<b>THE INVERSION PROBLEM IN STELLAR ATMOSPHERES</b>	
Oran R. White . . . . .	380 ✓

### SESSION IV SHORT COMMUNICATIONS

<b>SOME THEORETICAL FREQUENCY AVERAGES FOR THE EMITTANCE OF A HOMOGENEOUS GAS-PARTICLE CLOUD</b>	
Charlotte Decker Bartky . . . . .	397 ✓

# TABLE OF CONTENTS (Continued)

	Page
<p>DETERMINATION OF ATMOSPHERIC TEMPERATURE PROFILES FROM SATELLITE RADIANCE MEASUREMENTS AT THE LIMB OF THE EARTH</p> <p style="padding-left: 40px;">J. W. Burn. . . . .</p>	407 ✓
<p>ESTIMATING DIURNAL TEMPERATURE VARIATION AT THE STRATOPAUSE FROM HORIZON RADIANCE MEASUREMENTS</p> <p style="padding-left: 40px;">John C. Gille . . . . .</p>	412 ✓
<p>MOLECULAR TEMPERATURE DETERMINATIONS IN FLOW FIELDS OF RE-ENTERING BODIES</p> <p style="padding-left: 40px;">W. G. Planet, R. Watson, and C. C. Pitts . . . . .</p>	416 ✓
<p>THE RELEVANCE OF FREQUENCY-AVERAGED PROPERTIES</p> <p style="padding-left: 40px;">S. C. Traugott . . . . .</p>	428 ✓
<p>GAS EMISSIVITY MODEL FOR RADIATIVE TRANSFER CALCULATIONS</p> <p style="padding-left: 40px;">A. F. Sarofim. . . . .</p>	432 ✓
<p>THE DOPPLER ANALOG OF AN ELSASSER BAND MODEL</p> <p style="padding-left: 40px;">S. A. Golden. . . . .</p>	436 ✓
<p>TEMPERATURE SOUNDING WITH THE 4.3 MICRON CO<sub>2</sub> BAND</p> <p style="padding-left: 40px;">R. A. McClatchey . . . . .</p>	439 ✓
<p>NUMERICAL STUDY OF NONLINEAR INVERSION</p> <p style="padding-left: 40px;">E. T. Florance . . . . .</p>	443 ✓

# TABLE OF CONTENTS (Concluded)

	Page	
FORUM		
R. Goulard, Chairman		
QUESTION I. HEAT TRANSFER AND FLOW FIELD SOLUTIONS		
Introductory Remarks: R. M. Huffaker. . . . .	451 ✓	
QUESTION II: REQUIREMENTS, POSSIBILITIES AND PROMISES OF INVERSION TECHNIQUES FOR ROCKET EXHAUST PLUME TECHNOLOGY		
Introductory Remarks: J. I. F. King . . . . .	454 ✓	
QUESTION III. RELEVANCE OF LABORATORY EXPERIMENTS TO ACTUAL RADIATING FLOWS		
Introductory Remarks: W. K. Dahm. . . . .	459 ✓	
QUESTION IV. BAND MODELS AND NON-MODELS		
Introductory Remarks: J. A. L. Thomson. . . . .	477 ✓	
ATTENDEES AT RADIATION CONFERENCE		481

## WELCOME ADDRESS

By

Ernst D. Geissler  
Director Aero-Astrodynamic Laboratory  
MSFC, Huntsville, Alabama

The overall purpose of this conference is to review and discuss our present knowledge of molecular radiation and its utilization by covering three areas, namely, (1) spectral-line studies in the laboratory; (2) application to practical heat transfer calculations of radiative transfer models, as derived with the help of these studies; and (3) use of measured radiation properties of gases not only for comparison with the predictions, but also to gain knowledge, in a diagnostic way, of certain other properties of flowing or stagnant gas masses from remote locations. We would like to present some applications and developments of current interest, and to critically discuss value and limitations of our present approaches. Finally, it is our purpose to provide an opportunity for cross-feed between adjacent areas of the discipline by presentations and by free discussion. We hope that by highlighting the degree of sophistication which these subjects have attained, and by identifying the remaining weak areas and potential alternatives to the approaches we are taking now, we can obtain a somewhat clearer picture for the direction of future experimentation as well as other related research.

The interest of MSFC in the study of molecular radiation properties and radiative transfer dates back to the early days of launch vehicle development, primarily in connection with the problem of base heating. The heating of the rocket aft section by the engine exhaust is, of course, a combination of convection and radiation effects. For single-engine vehicles, such as the Jupiter and Redstone, the plume radiation decreases from their sea level peak to near zero at high altitudes. For the Saturn vehicles with clustered engine configurations, although the radiation component is less at higher altitudes than at sea level, the impinging regions of the intersecting plumes at higher altitudes keep the radiative heat component of the vehicle well from approaching zero. Our current upper stages are powered by LOX/hydrogen engines, which have relatively little radiation, but accurate knowledge of the radiative input due to the engine exhausts is still needed.

We think that the work of the last few years has gone a long way toward establishing useful tools for predicting radiation from nonhomogeneous flame regions with reasonable accuracy, usable both in jet plumes and in such mundane applications as industrial furnaces. In our support of work on jet plume radiation, we at MSFC have deliberately restricted ourselves to predominantly support studies concerned with liquid propellants. We have done this not out of lack of interest in solid propellant engines, but rather in order to attack our immediate problem first, and in order to keep our program in line with the resources of manpower and money. We have, therefore, supported solid propellant studies only to a limited extent.

What about our future work in molecular radiation? As far as the radiation properties of liquid propellant exhaust products are concerned, we feel that we have reached a satisfactory understanding, though there is, of course, always room for improvement. Our most urgent problems are now on the fluid dynamics side of the jet plume problem. As far as the solid rockets are concerned, they offer — as you may know — a feasible method of improving the weight-lifting capability of our Saturn vehicles — the Advanced Saturn I and the Saturn V — by serving as strap-on units of various sizes. When and if our national space program is ready to go to these uprated launch vehicles, there is no doubt in my mind that we will have to intensify our interest in radiation phenomena from solid propellant flames. We will certainly be able to benefit from the amount of data generated empirically by the Titan IIC and other current programs, but it is obvious that a rational prediction of solid propellant jet radiation will not be possible without considerable additional research.

In recent years we have also developed an interest in the diagnostic use of radiation, aimed at measuring flow and turbulence characteristics in wind tunnels and similar facilities, as well as measuring atmospheric winds and other properties in support of our launch operations. Our pertinent studies will be discussed in the third session of this conference.

As background information for the reader, Figure 1 shows the organizational structure of MSFC, and Figure 2 the organization chart of the sponsoring Laboratory.



# GEORGE C. MARSHALL SPACE FLIGHT CENTER

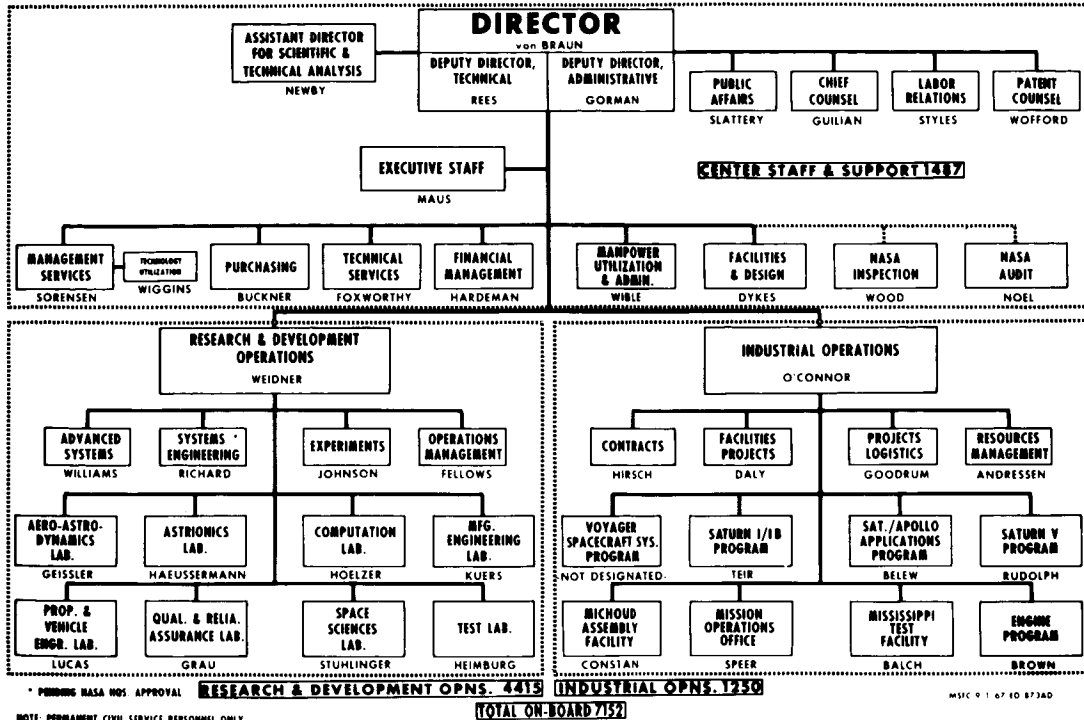


FIGURE 1

## AERO-ASTRODYNAMICS LABORATORY

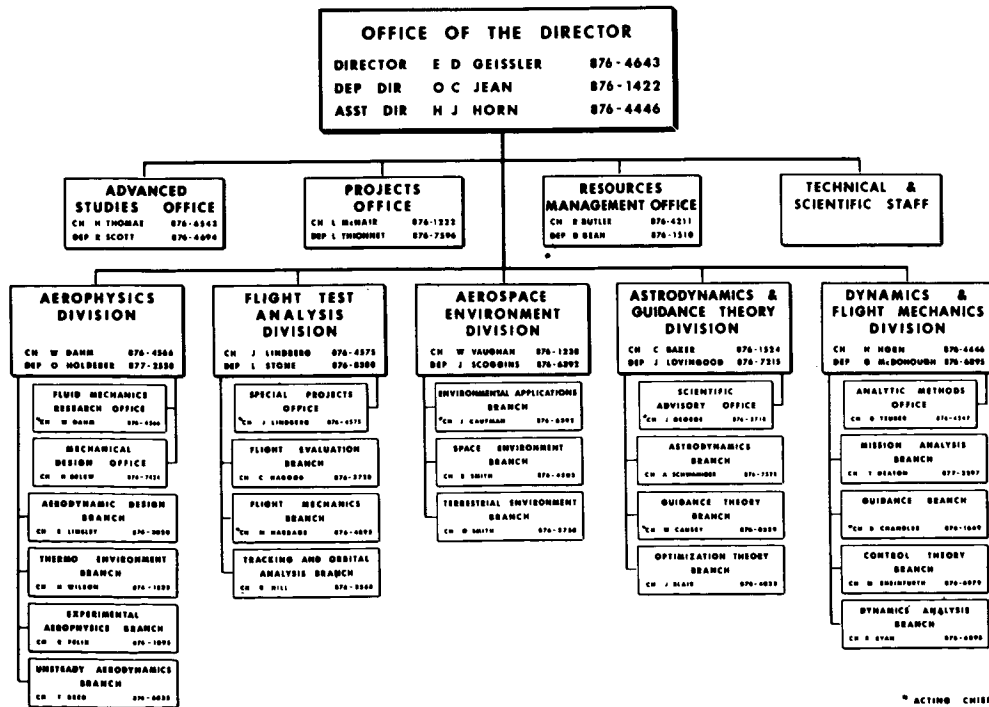


FIGURE 2

# INTRODUCTION TO THE PROBLEM OF ROCKET BASE HEATING, AND TO THE BEHAVIOR OF LIQUID PROPELLANT ROCKET JET PLUMES

By

N 68-18083

Werner K. Dahm

Chief Aerophysics Division  
Aero-Astrodynamics Laboratory  
MSFC, Huntsville, Alabama

As Dr. Geissler indicated, this Center's interest in molecular radiation stemmed originally from the problem of rocket base heating. In fact, most of the Marshall-sponsored work that will be reported at this conference is centered on this problem. The behavior of rocket jets and the problem of base heating are probably outside of the range of experience of the majority of the readers. This chapter will therefore briefly dwell on these subjects with main emphasis on the radiation phenomenon.

In the old times, the heat protection for the rear end of a rocket was empirically developed by a cut-and-try method. The rocket was run in a static test stand, and if the rear-end structure became too hot, additional steel-asbestos sandwiching was added to lower the temperatures. One assumed that, if the design was sufficient for a full-time static test, it was also sufficient for full-time flight. The result was not an optimum design, but it was one that happened to work. It happened to work until about the mid-1950's, that is. At that time a technology switch was made in our engines. We stepped from alcohol to kerosene as fuel, and we replaced the former hydrogen peroxide turbines of our propellant pumps with gas turbines that used the rocket's primary fuel. The kerosene gave us a bright, luminescent flame which radiated much more intensely than the previous transparent flames. However, the real trap turned out to be the gas turbine. Its highly fuel-rich exhaust, piped through the base of the rocket, behaved nicely on the test stand. However, once the rocket lifted off, the air flow trapped this exhaust in the base recirculation zone, turned the missile's base into a flame holder, and literally burned up the base regions of some expensive rockets before we learned to handle this pesty exhaust. Since then, base heating has been treated with much more respect, and scale model experiments with hot jets have, for instance, become a standard practice, though scaling of such models results in a tough question, especially with respect to radiative heat transfer.

There was also another factor which made us press for a much closer analysis of our heat transfer. It was the step from the old single engine rocket configuration to multi-engine clusters, which introduced a variety of possible engine arrangement patterns and engine space parameters, from which a reasonable optimum had to be selected. This selection had to be made on the basis of some analytical models. Under sea level conditions we used (and largely still use) rough shell models for our jets, which assume in essence that the jets consist of hot solid cylinders, whose surface temperature distribution is estimated on the basis of emission measurements of full scale rocket jets, like the well known measurements of DeBell and Simmons (e. g. , references [ 1] through [ 3]). We used also extrapolations of the homogeneous slab emission data of Eckert and Hottel (see [ 4] through [ 7] ), though our jets are never homogeneous gas masses. These approaches could only be stop-gap measures, and we began to attack the non-homogeneous flame problems when the start of the Saturn project made the financial means available.

When we attempt to predict the radiation coming from a rocket jet configuration, we actually have to solve two complex problems. The first one is the fluid dynamics problem of describing the shape and thermodynamic state of the jet or jet cluster at the various altitudes. It involves frequently the description of flows with chemical reactions. The second one is the problem of describing the radiation of an inhomogeneous gas mass of given thermodynamic state, i. e. , one of the topics of this conference. In the range of temperatures with which we are concerned, we can fortunately treat these two as uncoupled problems. As you will see later, we have made fair progress with respect to this radiation problem. On the fluid dynamics side we are not as far along yet, and considerable work remains to be done.

Let us now discuss the jet plumes of some typical liquid propellant rockets. Figure 1 shows a Redstone-Mercury rocket immediately after lift-off. The jet plume of its liquid oxygen (LOX)-alcohol engine is transparent, and is in fact nearly invisible. It is obviously a weak radiation source. The four brightly glowing graphite jet vanes used for the control of the rocket can clearly be seen at the very end of the vehicle, and part of the observable jet luminescence is likely to be caused by solid carbon eroded from these vanes. The Redstone booster was designed in the early 1950's. The heat shield of its base was still developed by the old cut-and-try method mentioned before. The vehicle may be considered as typical for the liquid propellant rockets built up to that time. However, a group of modern rockets, e. g. , the Titan II with its  $H_2O_4$ -Aerzine 50 propellants, also have similarly transparent jets.

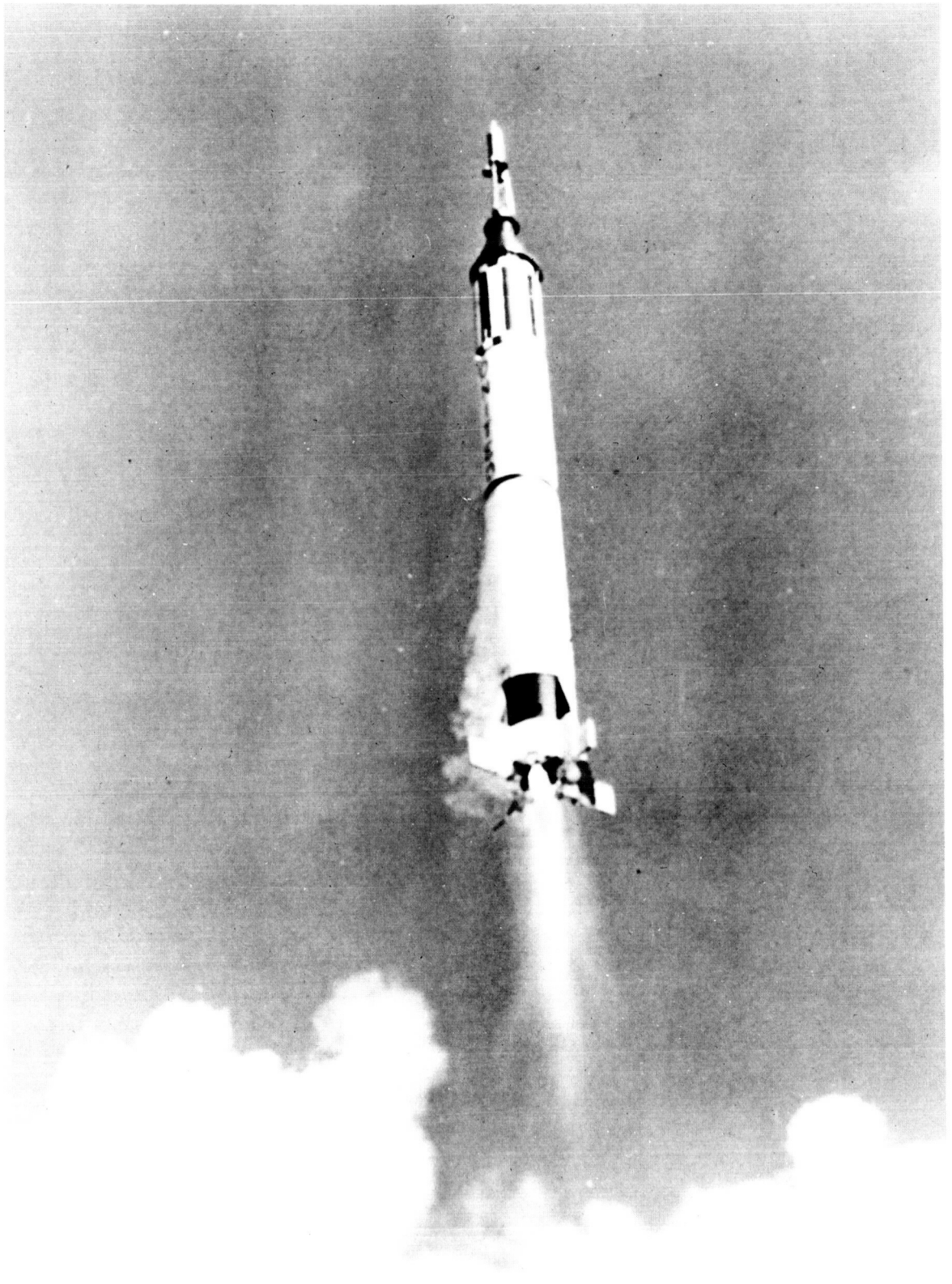


FIGURE 1. REDSTONE MERCURY ROCKET RIGHT AFTER LIFT-OFF

In stark contrast to the transparent jet plume of the Redstone, the three LOX-kerosene jets of the Atlas rocket shown in Figure 2 are optically dense and brilliantly bright. The optical denseness of these jets is caused by minute soot particles that form in the combustion chamber. Their number density and continuum spectrum render jets of this diameter optically dense in both the infrared and the visible parts of the spectrum. The brightness of the jets is caused by the combination of this soot with a secondary combustion process of the jet exhaust and atmospheric oxygen. For maximum performance the engines must burn fuel-rich. Therefore, the exhaust jet reignites when it comes into contact with the atmosphere, and surrounds itself with a flame front that gradually eats its way to the center of the jet. Temperature increases of the order of  $500^{\circ}\text{K}$  and more are observed in this combustion zone, with effective temperatures rising to the order of  $2000^{\circ}\text{K}$  to  $2500^{\circ}\text{K}$ . The continued turbulent mixing with cool air drops the temperature rapidly downstream of this flame front. The radiation from this hot, burning zone furnishes the dominant mode of base heating of a well-designed LOX-kerosene rocket in the lower reaches of the atmosphere.

Close study of Figure 2 reveals that the secondary burning of the jet plume does not start immediately at the nozzle lip, but rather a short distance downstream, i. e. , with an ignition delay. A turbulent-mixing layer is wedged between ambient air and jet exhaust, which begins at the nozzle lip and grows approximately linearly with distance downstream until it fills the whole jet. Secondary combustion takes place in this mixing layer, and the layer must have grown to a certain thickness before it can support a flame. This minimum thickness reflects effects of diffusion of heat and species, as well as the reaction rate constants of the chemical chain reactions of the combustion process. It is influenced by chemical composition, temperature, and pressure, and increases with decreasing pressure and temperature.

Figure 3 shows a modified version of the 1.5 million-pound thrust Rocketdyne F-1 engine, which also uses LOX and kerosene as propellants. In contrast to the flight version of this engine, the lower part of the nozzle has been removed, and the turbine exhaust is discharged directly from the thick stack to the left of the engine. Figure 3 is enclosed because it shows so clearly the secondary combustion and the ignition delay discussed above. The turbulent nature of the process is also evident. Figure 4 shows the same engine in its flight version with the nozzle skirt added and the turbine exhaust discharged into the nozzle. The temperature and composition changes in the outer layers of the jet have moved the onset of the secondary combustion noticeably downstream. The start of the flame front is barely visible above the platform of the test stand. Five of these engines power the first stage of the Saturn V moon rocket.

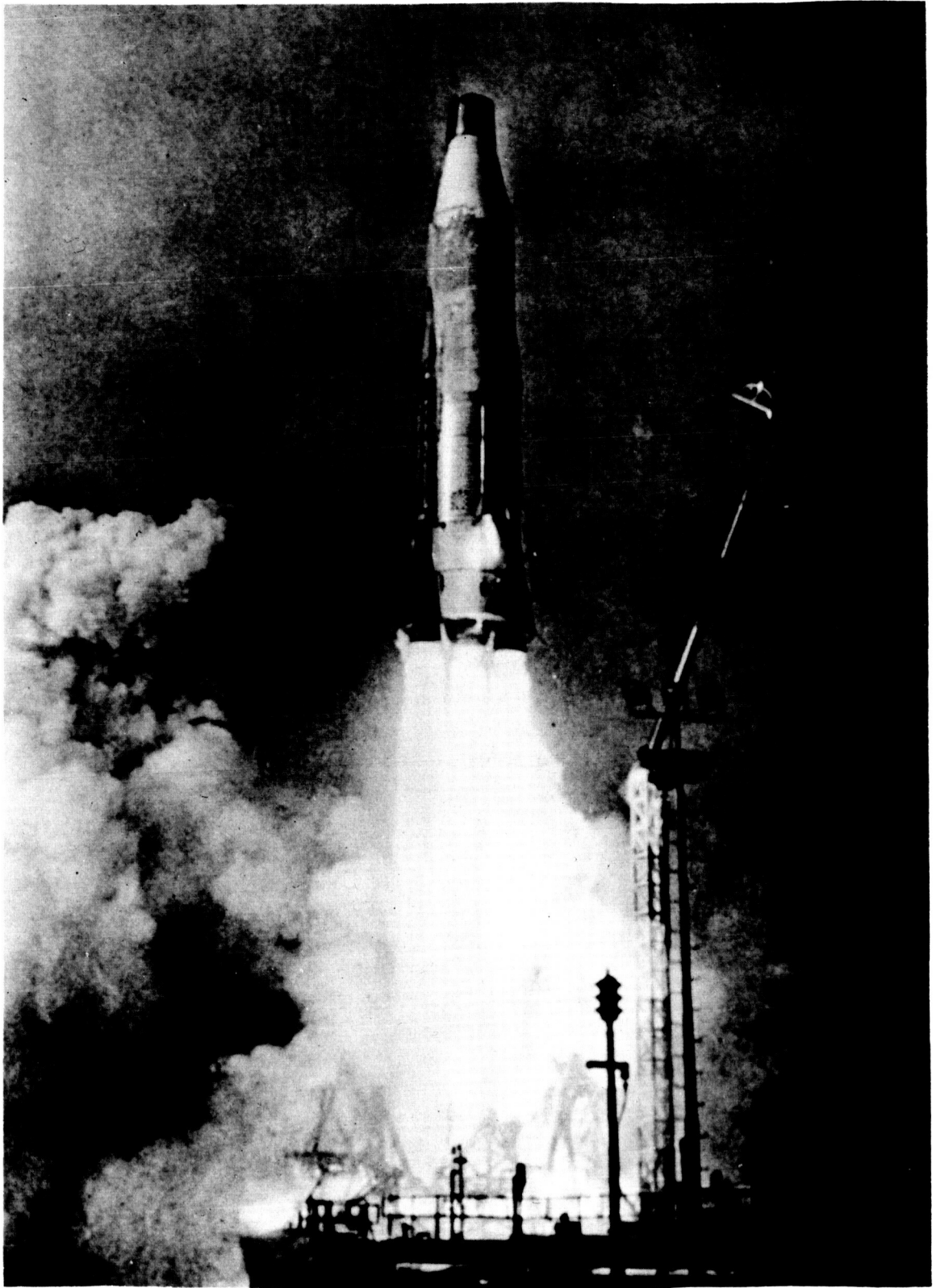


FIGURE 2. ATLAS ICBM LIFTING OFF THE PAD



FIGURE 3. SECONDARY COMBUSTION AND IGNITION DELAY  
IN THE EXHAUST OF A MODIFIED ROCKETDYNE F-1 ENGINE

The second stage of the Saturn V rocket is powered by five Rocketdyne J-2 engines, which burn liquid oxygen and liquid hydrogen (LOX-LH<sub>2</sub>). Figure 5 shows the five jets of this S-II stage on a ground test stand. The rims of the five nozzles are visible in the upper part of the photograph. The jets are essentially invisible except for a bluish tinge in the zones of higher pressure, which is typical of the LOX-LH<sub>2</sub> jets.\* As compared with the LOX-kerosene jets, these LOX-LH<sub>2</sub> jets are weak radiators. They yield only a minor contribution to the base heating of our multi-engined upper stages, which is rather

---

\* The whitish streaks at the nozzle rims on Fig. 5 are caused by water-cooled compressor rings inserted into the nozzle exits during sea-level testing, which bleed cooling water into the jet flow. The J-2 engine is designed for operation in near-vacuum, and the compressor is needed during sea level testing to produce controlled flow separation in the nozzle. The recompression causes a normal shock wave that can clearly be seen in the jet. It is absent under the pressure conditions of actual flight



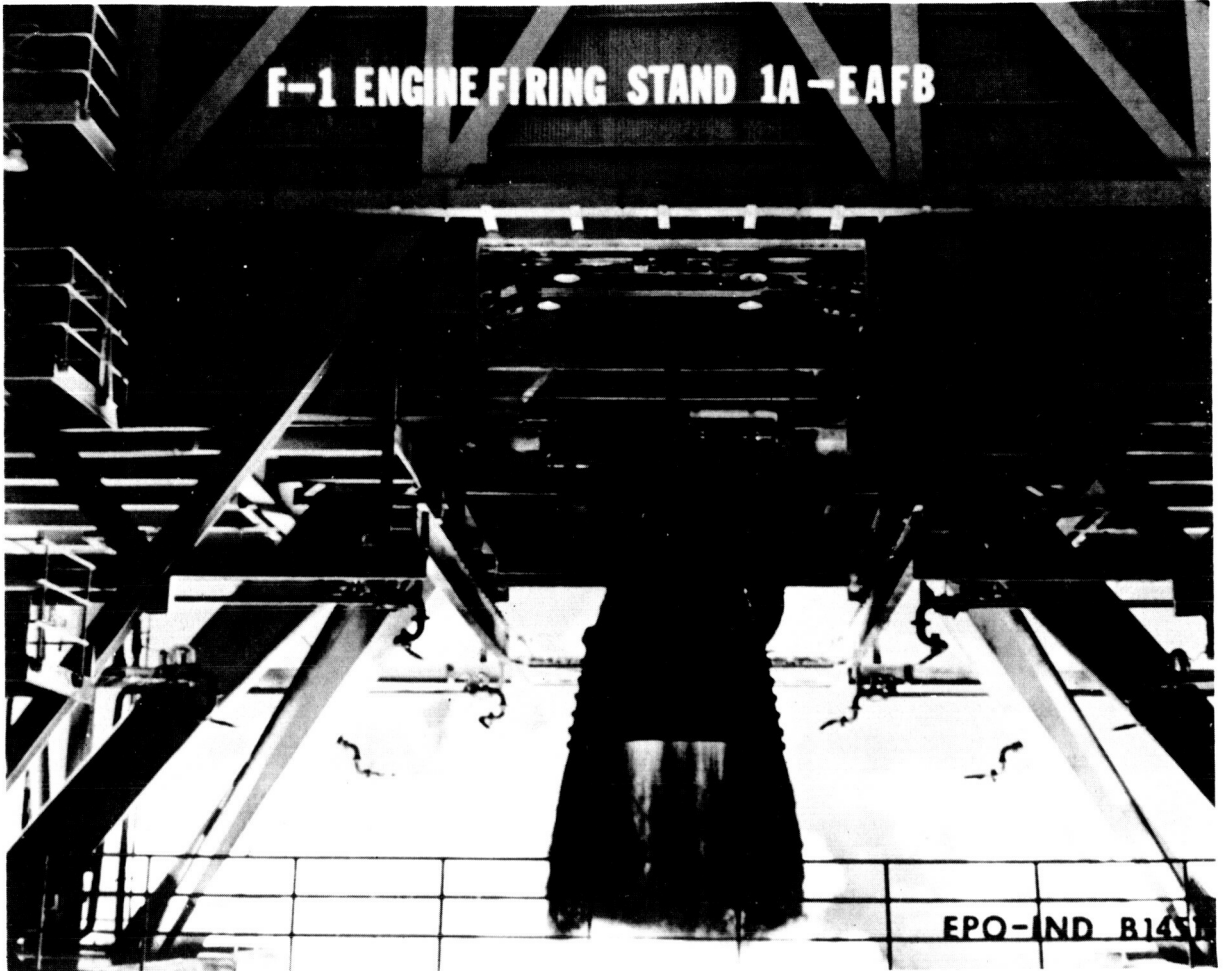


FIGURE 4. FLIGHT VERSION OF ROCKETDYNE F-1 ENGINE

dominated by a convective heat transfer caused by a hot backslash from the colliding jets. Nevertheless, a reasonably accurate description of the radiative component is necessary.

The previous figures had shown some rocket jet plumes under sea level conditions. Altitude has a profound effect on the appearance of the jet plumes, as the subsequent figures will demonstrate. Figure 6 shows the Saturn I vehicle at lift-off. Its first stage is powered by eight LOX-kerosene engines. Three of the four turbine exhaust plumes can be seen as somewhat lumpy clouds streaming from the overboard ducts near the rear end of the vehicle. The plumes are sucked into the main jets somewhat farther downstream. The jets of the individual engines are not completely merged, and the luminescent part of the jet plume is relatively short, being of about the same length as the vehicle. The radiative heat flux to the base of the vehicle is about 60 to 70 kcal/m<sup>2</sup>sec at this instant. Figure 7 shows an essentially identical vehicle, the Saturn IB,





FIGURE 5. JETS OF THE SECOND STAGE OF THE SATURN V VEHICLE ON A GROUND TEST STAND

at an altitude of about 14 km. The luminescent trail has grown to several times the vehicle length, though the heat flux radiated to the base had dropped to about  $20 \text{ kcal/m}^2\text{sec}$ . The burning turbine exhaust floats past the main jet, and an increase of the ignition delay of the secondary burning can be recognized. Figure 8 shows the Saturn I at an altitude of about 30 km. The jet plume has become wide and tenuous, has increased in length, and a striking shock diamond has made its appearance. The radiative heat flux has dropped to about 10 to  $15 \text{ kcal/m}^2\text{sec}$ . Figure 9 shows the Saturn I at an altitude of about 50 km, not far from first stage cut-off. The jet plume has grown to a very wide, smoky trail, and has lost its heat and luminescence except for a small volume right downstream of the vehicle's base. This volume of residual radiation is a characteristic property of multi-engine clusters at high altitudes, and is caused by interference between the jets of the individual engines. The ballooning jets collide with each other, giving rise to intricate shock patterns, and creating shock-heated gas volumes of relatively high temperature and density between

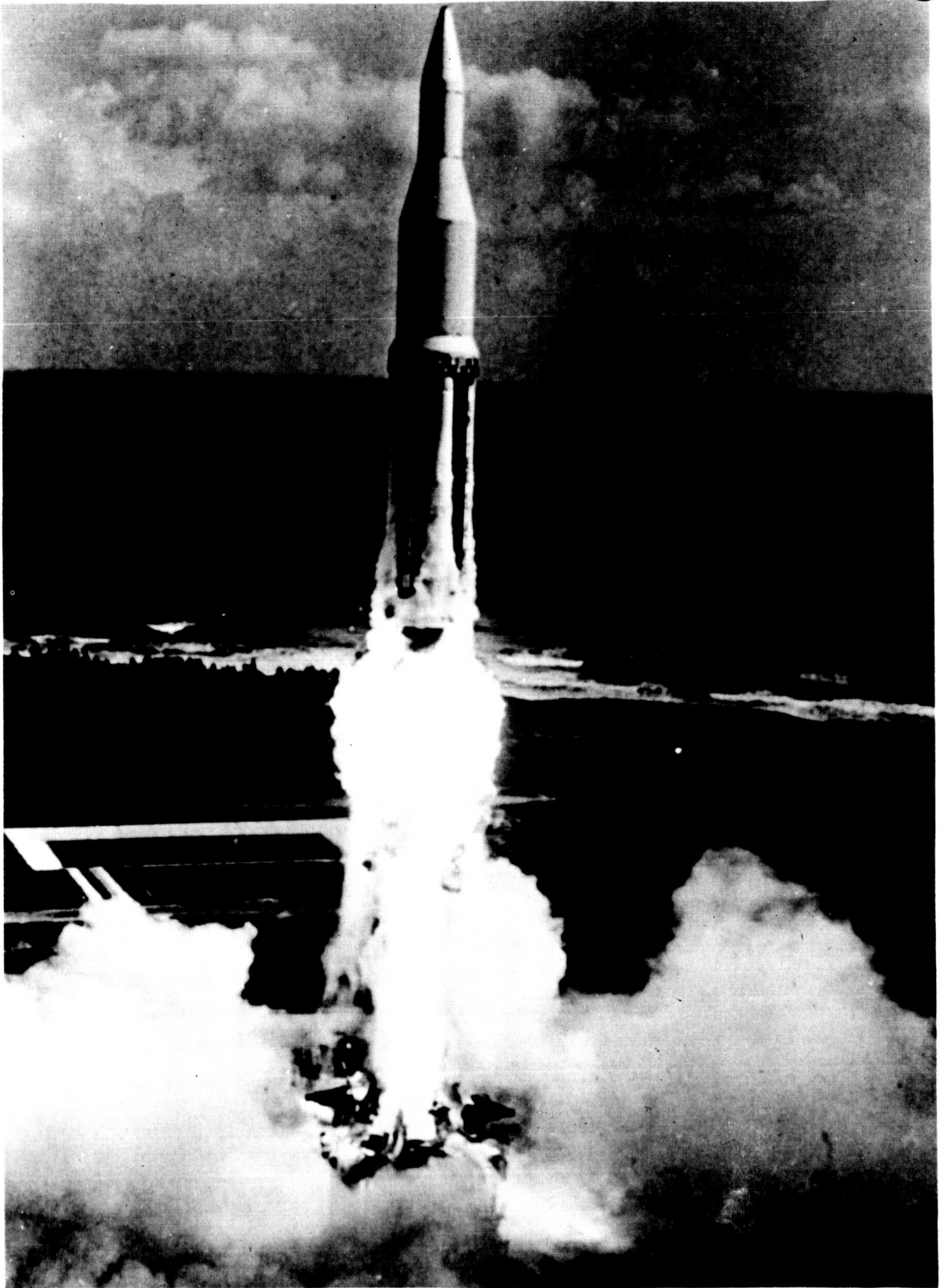


FIGURE 6. SATURN I AT LIFT-OFF

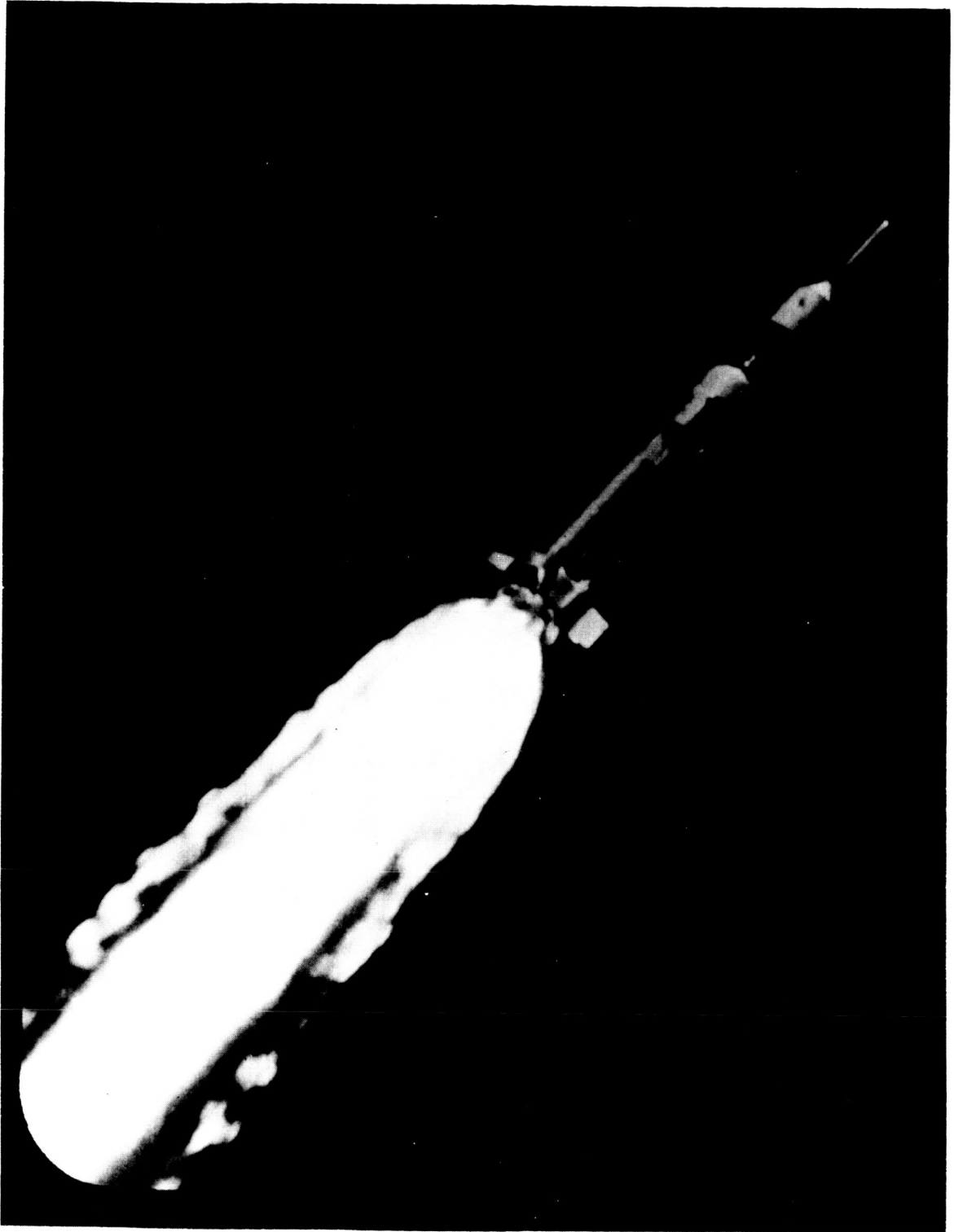


FIGURE 7. SATURN IB AT 14 km ALTITUDE

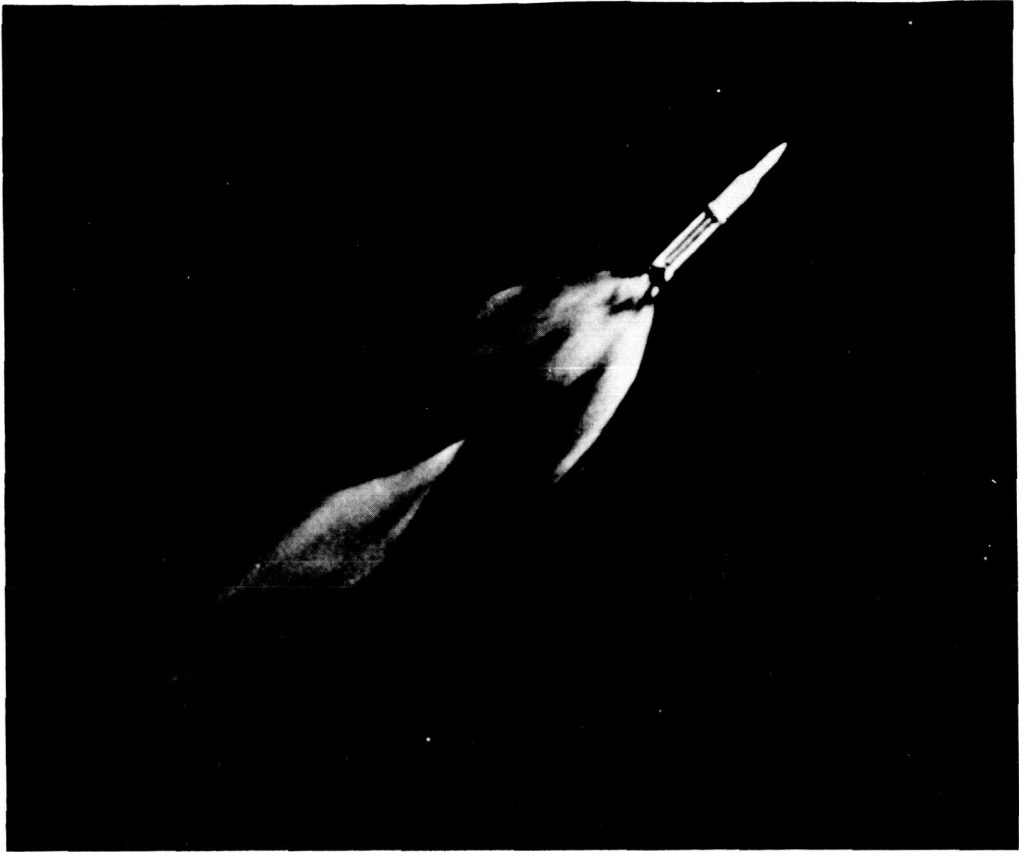


FIGURE 8. SATURN I AT 30 km ALTITUDE

the nozzles, in full view of the vehicle base. This effect keeps the radiative heat flux to the base at a finite level until cut-off; in the case of Saturn I, this level is about  $12 \text{ kcal/m}^2\text{sec}$ . In contrast, the base of a single-engine vehicle sees essentially no radiative heat flux at high altitudes, and it is not possible to recognize cut-off from the heat shield temperature traces. Figure 10 offers a vivid demonstration of this interference effect for the relatively simple case of a twin-engine configuration. The model test was performed in a vacuum chamber, using a short duration testing technique described elsewhere in these proceedings.\*

---

\* A short motion picture of a Saturn I flight was shown at the end of this introduction. The picture showed a view underneath the first stage during ignition and lift-off; a view from the umbilical tower down past the vehicle on the launch platform as it was blasted by the jet; a view of the first stage jet plume as the vehicle rose from lift-off to first stage cut-off; the short blast of the solid propellant retrorocket and ullage rockets of the first and second stages as they pushed the two stages apart at separation; and the ignition of the six LOX-LH<sub>2</sub> engines of the old S-IV stage.



FIGURE 9. SATURN I AT 50 km ALTITUDE

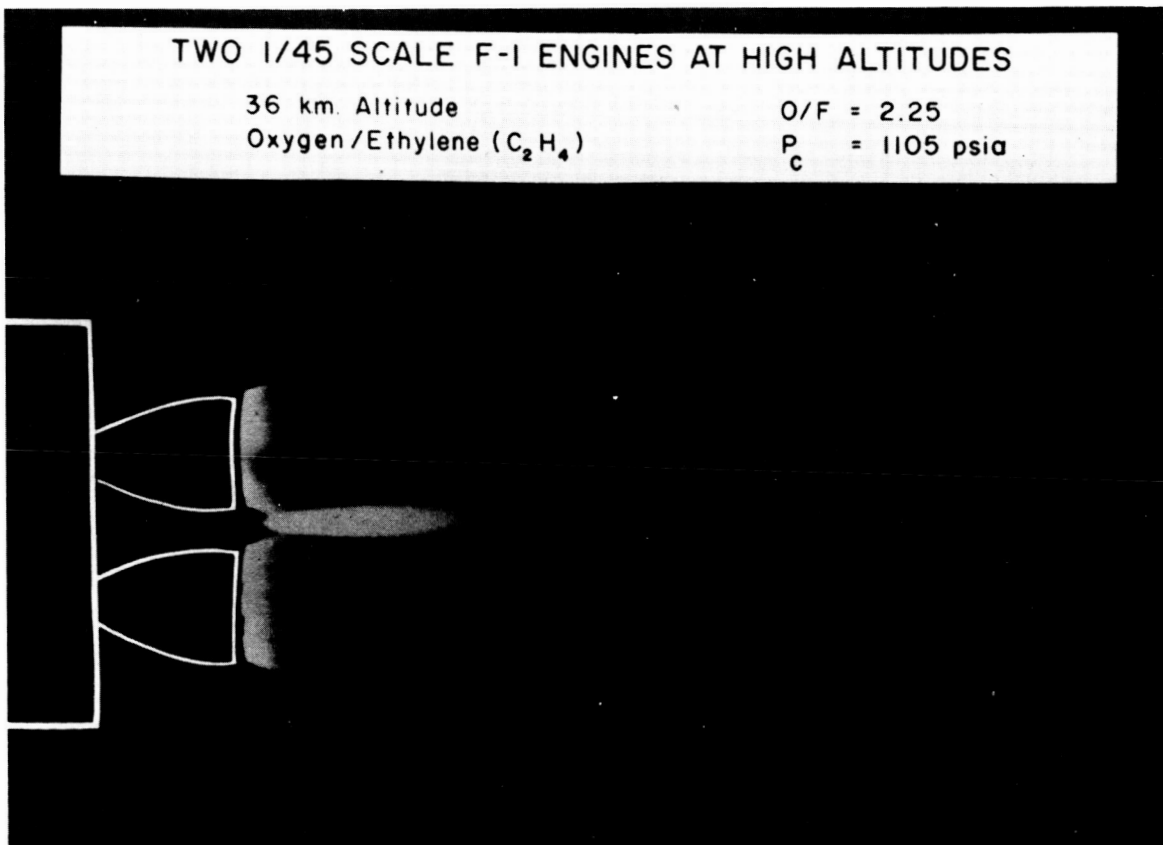


FIGURE 10. TWO 1/45 SCALE F-1 ENGINES AT HIGH ALTITUDES

## REFERENCES

1. DeBell; and Speiser: Infrared Spectral Radiance of Large Liquid Propellant Rocket Engine Exhaust Plumes. Rocketdyne Report R-2019, 1960.
2. Simmons: The Spectral Emittance of the Exhaust Jets from Rocket Engines Using LOX and RP-1 as Propellants. Rocketdyne Res. Rep. 58-36, 1958.
3. DeBell; and Simmons: Radiation Studies of Atlas Engine Exhaust Jets at the Rocketdyne Propulsion Field Laboratory. Rocketdyne Rep. R-1107, 1958.
4. Eckert, E. R. G.: Introduction to the Transfer of Heat and Mass. McGraw-Hill Book Co., Inc., New York, 1950.
5. Hottel, H. C.; and Mangelsdorf, H. G.: Trans. Am. Inst. Chem. Engrs., vol. 31, 1935, pp. 517-549.
6. Eckert, E. R. G.: VDI-Forschungscheft 387, 1937.
7. Eckert, E. R. G.; and Schmidt, E.: Forsch. Gebiete d. Ingenieurwes. vol. 8, 1937, p. 87.

SESSION I  
LABORATORY STUDIES

Chairman: J. A. L. Thompson,  
General Dynamics/Convair

BAND MODEL REPRESENTATIONS FOR HIGH  
TEMPERATURE WATER VAPOR AND CARBON DIOXIDE

By

C. B. Ludwig and W. Malkmus

General Dynamics/Convair  
Space Science Laboratory  
San Diego, California 92112

---

ABSTRACT

The properties of symmetric and asymmetric top molecules relevant to the structure of the vibration-rotation band systems are briefly discussed. The derivation of analytic expressions for the local line intensities and spacings of symmetric top molecules as functions of frequency is described. Further approximations necessary to apply this procedure to asymmetric top molecules are described, and results are shown for H<sub>2</sub>O. The relationships of the calculated parameters to particular band models and the properties of these band models are discussed. The long-burner program for measurement of emissivities of gases at high temperatures and long path lengths is described and compared with other experimental work. New results for twenty-foot path lengths are discussed. Inhomogeneous path measurements are described and comparisons with calculated spectra are shown.

---

We will review briefly the calculations which we have made relative to the emissivities of homogeneous gases, with passing reference to their extension to inhomogeneous gases. This topic will be covered in detail by a later paper [1]. "Emissivity" here refers to the mean local spectral emissivity as would be observed in low resolution.

For a symmetric top molecule, explicit algebraic expressions exist for the rotational energy levels as functions of the rotational constants and quantum numbers. Thus, the frequencies of the transitions, as well as the



line intensities and line spacings, can be expressed as simple functions of quantum number. By inverting the expression  $\omega(J)$ , we can then obtain expressions for the local line intensities and line spacings as functions of  $\omega$ , for each vibrational transition [2-4].

The curve of growth can be determined from the previous expressions by calculating the curves of growth for the separate bands and summing over all vibrational transitions. Notice that these results are exact, to the extent that the molecular parameters, line shapes, etc., have been accurately represented and the assumptions regarding randomness of the bands are valid.

However, it may be quite inconvenient to store such parameters for each of what may be a very large number of vibrational transitions. In this event, the parameters  $S_i/d_i$  and  $S_i^{1/2} \alpha_i^{1/2}/d_i$  may be summed over all vibrational transitions, and the sums designated  $\langle S/d \rangle$  and  $\langle S^{1/2} \alpha^{1/2}/d \rangle$ . A great many parameters have thus been reduced to a single pair. Although these two parameters yield the correct results asymptotically in the weak-line and strong-line regions in performing the summation, the detailed information regarding the local intensities in each band has been lost. First, the two asymptotic regions both provide upper limits to the curve of growth (in the absence of significant Doppler broadening). Simply using the lower of the two upper limits may provide sufficiently accurate results for certain applications.

To reproduce the transitional region of the curve of growth, a band model may be used. This is an idealized representation of the band structure, defined by some simplified description of the intensities of the lines and their locations. For example, the low-temperature spectrum of a linear molecule may be very well represented locally by the Elsasser model: an infinite sequence of equally intense, equally spaced lines of Lorentz shape. Conversely, the spectrum of an asymmetric rotor molecule which possesses no seeming regularities of intensity or spacing may be more plausibly represented by a model in which the positions of the lines are assumed to be uncorrelated.

It is always possible to find examples where the error in using a band model may approach infinity. For example, in any real spectrum, over any finite interval, there is some minimum value of the (monochromatic) absorption coefficient. This minimum will dominate the behavior at very large optical depths, and the curve of growth sufficiently far out will become linear. However, a random line model presupposes the existence of indefinitely small (monochromatic) absorption coefficients, although with increasingly small probability, and

the curve of growth for a random Lorentz model shows an asymptotic square-root behavior. Thus, such a model becomes increasingly unreasonable at large optical depths. However, it is possible that the absorptivity is so close to unity that a large error in the exponent is of no consequence in the particular application.

A compromise can be made in the interests of improving accuracy. Suppose that, in the process of calculating  $S_i/d_i$  for each band, these parameters are sorted out on the basis of the value of the energy level of the lower state  $E_\ell$ . Suppose that intervals  $\Delta E$  (say,  $1000 \text{ cm}^{-1}$ ) are marked off on  $E_\ell$ , and that  $N$  separate subsums are made according as  $0 \leq E_\ell < \Delta E$ ,  $\Delta E \leq E_\ell < 2\Delta E$ , ..., or  $(N-1)\Delta E \leq E_\ell < N\Delta E$ .

Within each group the relative intensities of the lines do not change significantly with  $T$ , if  $\Delta E$  is sufficiently small, although absolute intensities may be quite strongly dependent on  $T$ . Also, the locations of lines in different groups may reasonably be considered to be uncorrelated with one another. A Curtis-Godson type approximation may then be applied to each of the line groupings separately [1].

The case of an asymmetric molecule, such as  $\text{H}_2\text{O}$ , is greatly complicated by the fact that no explicit expressions exist for the energy levels, matrix elements, etc. An approximate approach can be taken by noting that summation rules do exist for matrix elements and energy levels, and thus average values can be expressed for these quantities [5]. The mean frequencies for given  $J$  can be handled analogously. Figure 1 shows the frequencies of the (intense)  $|\Delta\tau| = 1$  transitions for the P- and R- branches of the  $\nu_3$  fundamental. It is seen that the mean values designated by crosses are represented quite well by an expression similar to that for a linear molecule. Similar relations can be found for the  $\nu_1$  fundamental, and for the Q-branches. There is more spread of frequencies for a given  $J$  in these cases than is shown here for the  $\nu_3$  P- and R- branches, but most of the intensity is concentrated in the latter.

With these (primary) assumptions and some further simplifications as described in Reference 5 we can proceed as before to make spectral emissivity calculations. A sample comparison with experiment at  $1200^\circ \text{K}$  is shown in Figure 2. Oppenheim and Goldman's [6] results show the effects of moderate spectral resolution; comparison should be made with a mean curve through their data.

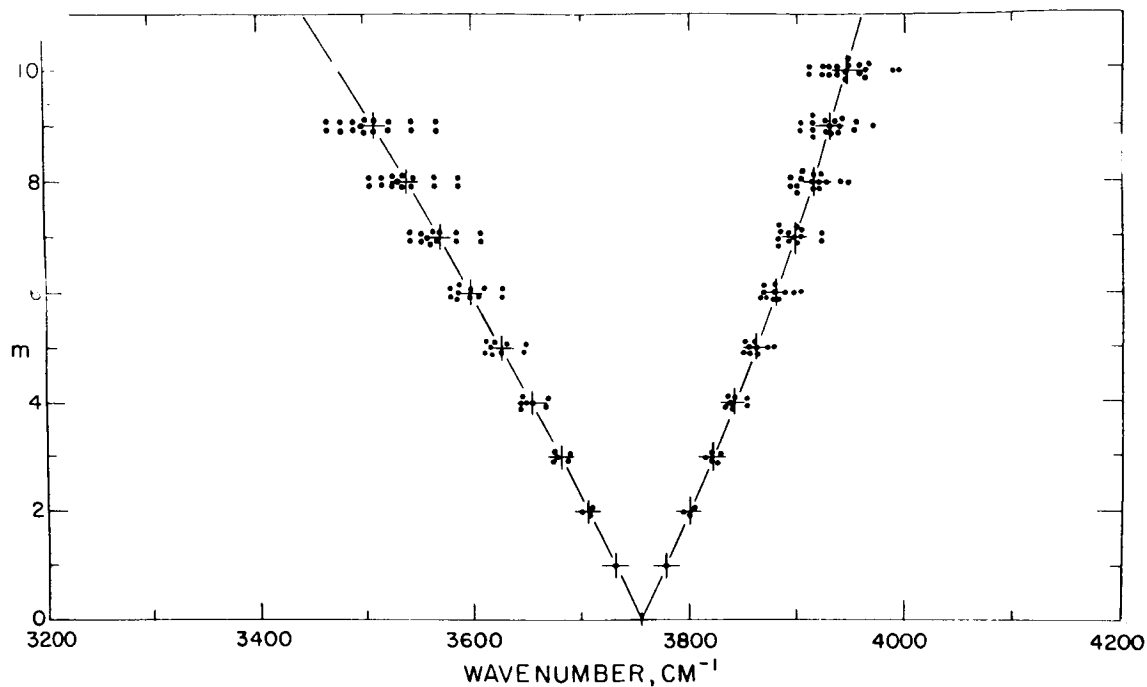


FIGURE 1. FREQUENCIES OF  $|\Delta\tau| = 1$  TRANSITIONS FOR 000-001 BAND OF  $H_2O$

Another phase of our research has been to make measurements (particularly of  $H_2O$ ) over wide ranges of path length and to determine the parameters of a band model which will fit the experimental data. In describing the spectrum of  $H_2O$ , we have thus far used a random band model with an exponential line intensity distribution. This particular model has been used for several reasons.

First, the model has a simple algebraic formulation, viz.,

$$-\ell nt = \frac{ku}{\sqrt{1 + \frac{ku}{4a}}}, \quad (1)$$

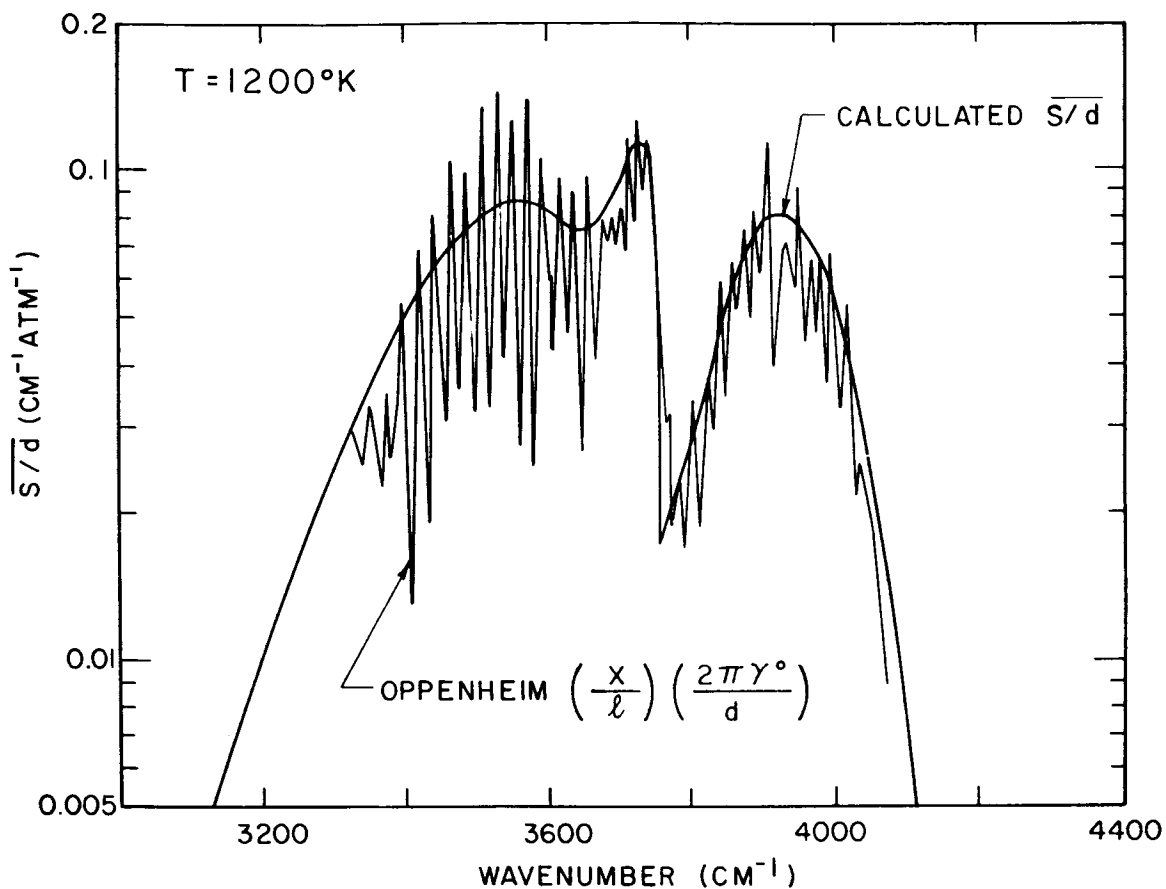


FIGURE 2. COMPARISON OF THEORETICALLY CALCULATED ABSORPTION COEFFICIENT [ 5 ] FOR H<sub>2</sub>O WITH OPPENHEIM AND GOLDMAN'S [ 6 ] MEASUREMENTS AT 1200°K

where the symbols  $t$ ,  $u$ ,  $k$ , and  $a$  have their usual meanings [ 7 ]. Also, a transformation can be made so that a function of  $t$  and  $u$  has a linear dependence on  $u$ :

$$\left[ \frac{\ell n t}{u} \right]^{-2} = \frac{1}{k^2} + \frac{1}{4ak} u \quad (2)$$

Thus, the intercept of this function determines  $k$ , and the slope, the product  $ka$ .

Secondly, this model appears to represent the data with sufficient accuracy. In other words, the extent and accuracy of the data are insufficient to detect any shortcomings of the model.

As an example, Figure 3 shows a set of measurements made on  $\text{CO}_2$  at a reasonably high temperature by a number of observers. This is an example of about the best (most accurate and most extensive) set of measurements made to date. The dashed curve is the curve of growth for a random line model composed of lines all of the same intensity; the solid curve is for a random model with lines having an exponential-tailed  $S^{-1}$  intensity probability distribution.

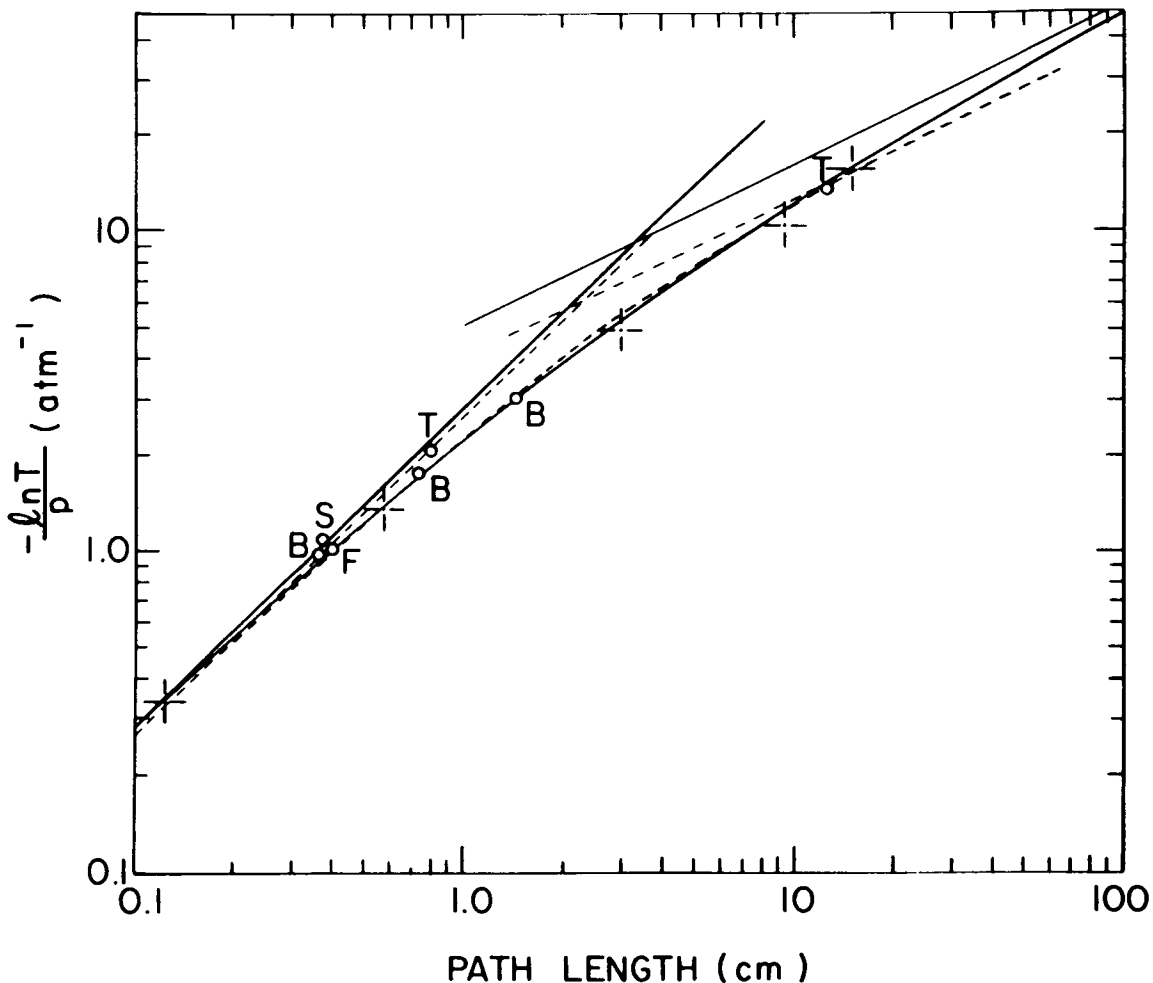


FIGURE 3. EXPERIMENTALLY MEASURED VALUES OF  $-\ln T/p$  FOR  $\text{CO}_2$  AT  $\omega = 2273 \text{ cm}^{-1}$  AND  $T = 1200^\circ \text{K}$  [8-9]

Now certainly it will be agreed that the assumption that every line in a high-temperature spectrum is of equal intensity is most unreasonable. Possibly a convincing argument can be made that an intensity distribution having a dominating  $S^{-1}$  behavior would be more reasonable. But the point is that the data simply cannot discriminate between one (certainly unreasonable) intensity distribution and another, very different, one.

We may note, in passing, that the model we are using is a curve intermediate between these two curves of growth. It is possible that sufficiently extensive data exist for  $H_2O$  to discriminate between the fits to different models. To date, we have not attempted such a comparison.

Our measurements were conducted in a specially designed 20-foot long burner, which has been previously described in detail [8]. The results of these studies for the 10-foot path length have already been published in the form of tables of  $k$  and  $a$  at  $25\text{ cm}^{-1}$  intervals for temperatures up to  $3000^\circ\text{K}$ . We have recently made measurements using the full 20-foot length of the burner.

A plot of  $k$  versus  $\omega$  is shown in Figure 4, for which  $T = 2000^\circ\text{K}$ . The solid line is plotted from the previously published tabulated values, which were based on measurements at path lengths up to 10 feet. The asterisks represent revised values which include the latest measurements at 20 foot path lengths. In general, there are no major changes in the absorption coefficients, which were fairly accurately determined previously.

A more dramatic change is noted in the parameter  $a$  (Fig. 5). This is not surprising, since the 20-foot measurements improve the determination of the square-root region, which was previously well-defined only for the regions having the largest values of  $k$ . There is little change near the center of the  $2.7\text{-}\mu$  band. We note also that there is a tendency for the values of  $a$  to approach a more uniform value (except in the band troughs, where  $a$  is still not well-determined). This is more nearly what one might expect, since the line densities in the various bands should be comparable.

Figure 6 shows the rms scatter (denoted by  $\sigma$ ) in the fit of the experimental points to Equation (2). This is not readily interpreted in terms of accuracy of  $k$  and  $a$ . If the measurements are primarily near the linear region of the curve of growth (Equation (1)), the points in the transformed equation (Equation (2)) have nearly equal ordinates. Thus,  $k$  is well-determined, with experimental accuracy of about  $\frac{1}{2}\sigma$ . The slope of Equation (2) may be poorly determined, and the error in  $a$  may be large. If the measurements are

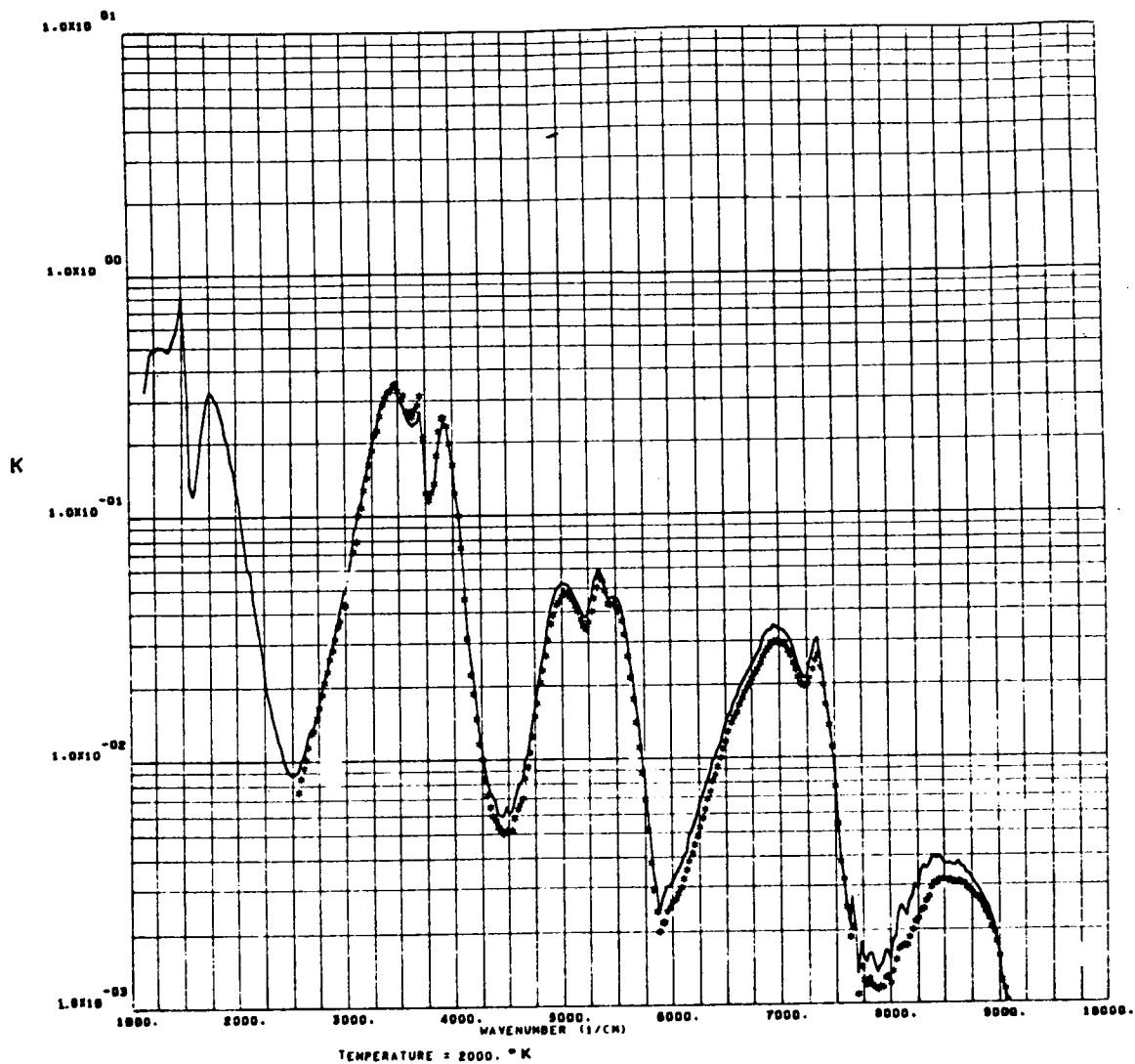


FIGURE 4.  $k$  VERSUS  $\omega$  FOR  $H_2O$  AT  $2000^\circ K$ . (SOLID LINE - PREVIOUS RESULTS [7] BASED ON MEASUREMENTS UP TO 10 FEET IN PATH LENGTH. STARS - NEW RESULTS BASED ON MEASUREMENTS UP TO 20 FEET IN PATH LENGTH)

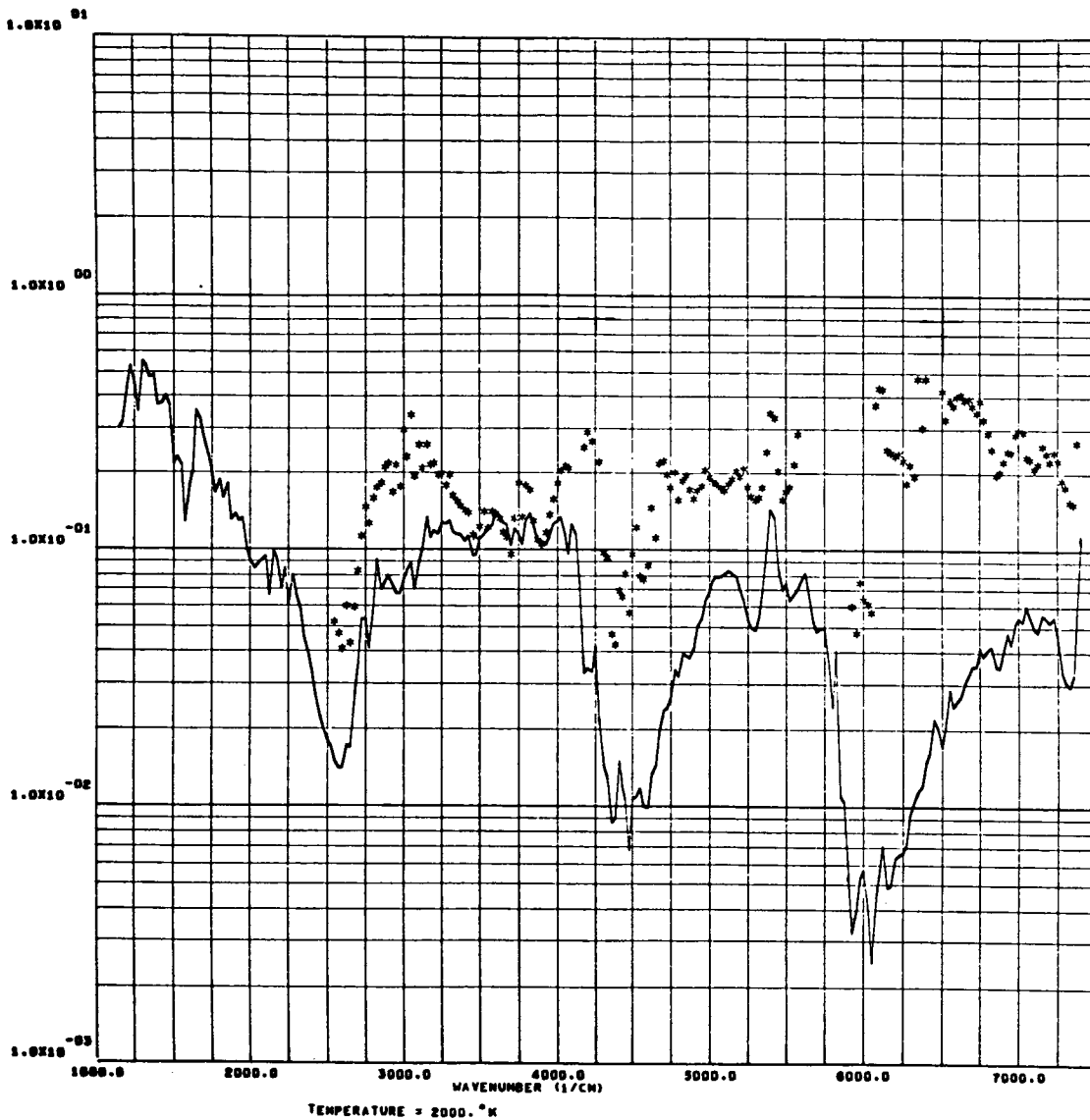


FIGURE 5.  $\alpha$  VERSUS  $\omega$  FOR  $H_2O$  AT  $2000^\circ K$ . (SOLID LINE - PREVIOUS RESULTS [7] BASED ON MEASUREMENTS UP TO 10 FEET IN PATH LENGTH. STARS - NEW RESULTS BASED ON MEASUREMENTS UP TO 20 FEET IN PATH LENGTH)



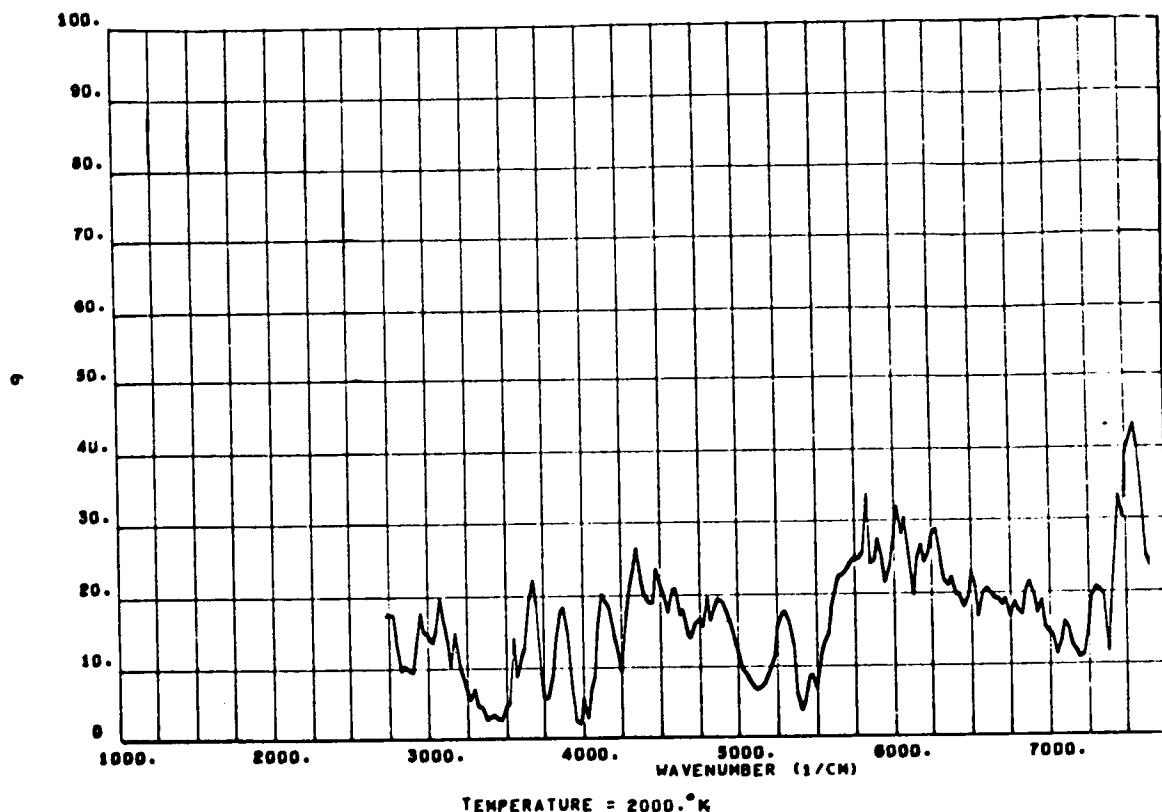


FIGURE 6.  $\sigma$  (rms DERIVATION IN FIT TO EQUATION (2)) VERSUS  $\omega$  FOR  $H_2O$  AT  $2000^\circ K$ , FOR NEW DATA INDICATED AS STARS ON FIGURES 3 AND 4

primarily near the square root region of Equation (1), the slope of Equation (2) may be well-determined, but not the intercept. Thus, the product  $ka$  is known, but  $k$  (and hence,  $a$ ) may not be known separately with any accuracy. If the measurements are located primarily along the transitional region of the curve of growth,  $k$  and  $a$  may both be known with comparable accuracy, but with error greater than  $\frac{1}{2}\sigma$ . Only if the measurements extend well into both the linear and square root regions (so that  $\sigma$  represents the uncertainty in  $k^2$  as well as in the slope  $ka$ ) will both  $k$  and  $a$  be determined with an accuracy of about  $\frac{1}{2}\sigma$  and  $\sigma$ , respectively.

Figure 7 shows a comparison of the experimentally determined values of  $k$  for  $H_2O$  at  $2000^\circ K$  with the calculated values previously described. Two sets

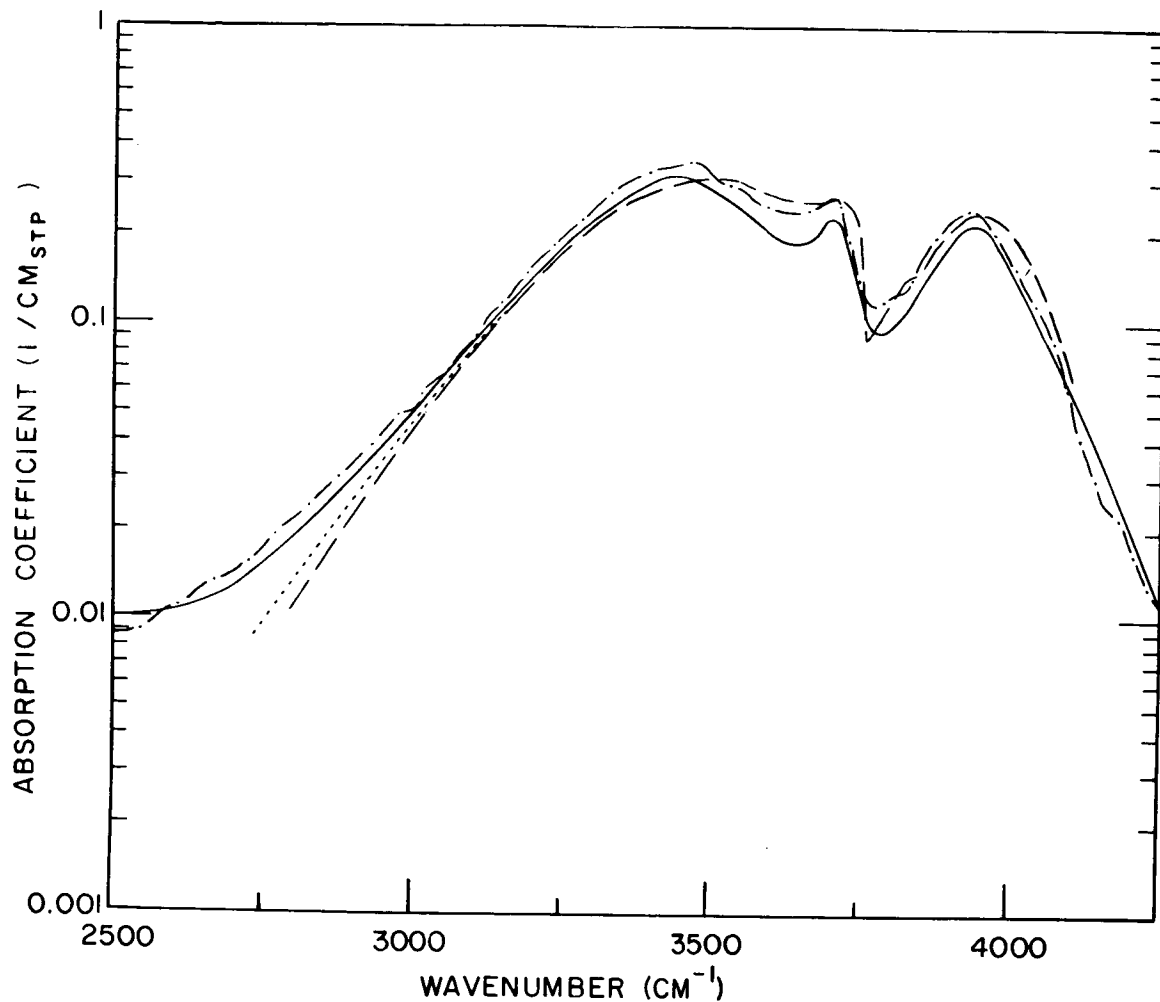


FIGURE 7. COMPARISON OF THEORETICALLY CALCULATED ABSORPTION COEFFICIENT VERSUS EXPERIMENTALLY DETERMINED  $k$  FOR  $H_2O$  AT  $2000^\circ K$ . (SOLID LINE - EXPERIMENTAL  $k$  [6]. DASHED-DOTTED LINE - NEWER EXPERIMENTAL  $k$  [7]. DASHED LINE - CALCULATED ABSORPTION COEFFICIENT [5]. DOTTED LINE - APPROXIMATE CORRECTION TO CALCULATED ABSORPTION COEFFICIENT FOR PRESENCE OF  $2\nu_2$  BAND SYSTEM.)

of experimental values are shown: an earlier set [7] (solid line) and a later set [8] (dashed-dotted line). The dashed line represents the theoretical absorption coefficient [5]. At the lower frequencies, a dotted curve shows an approximate correction for the weak  $2\nu_2$  band system which was ignored in the original calculations.

Figure 8 presents a comparison of recent cell measurements made at Rocketdyne [9] at 578°K (X's) with calculated values using  $k$  from Reference 6 and a band-averaged value of  $a$ .

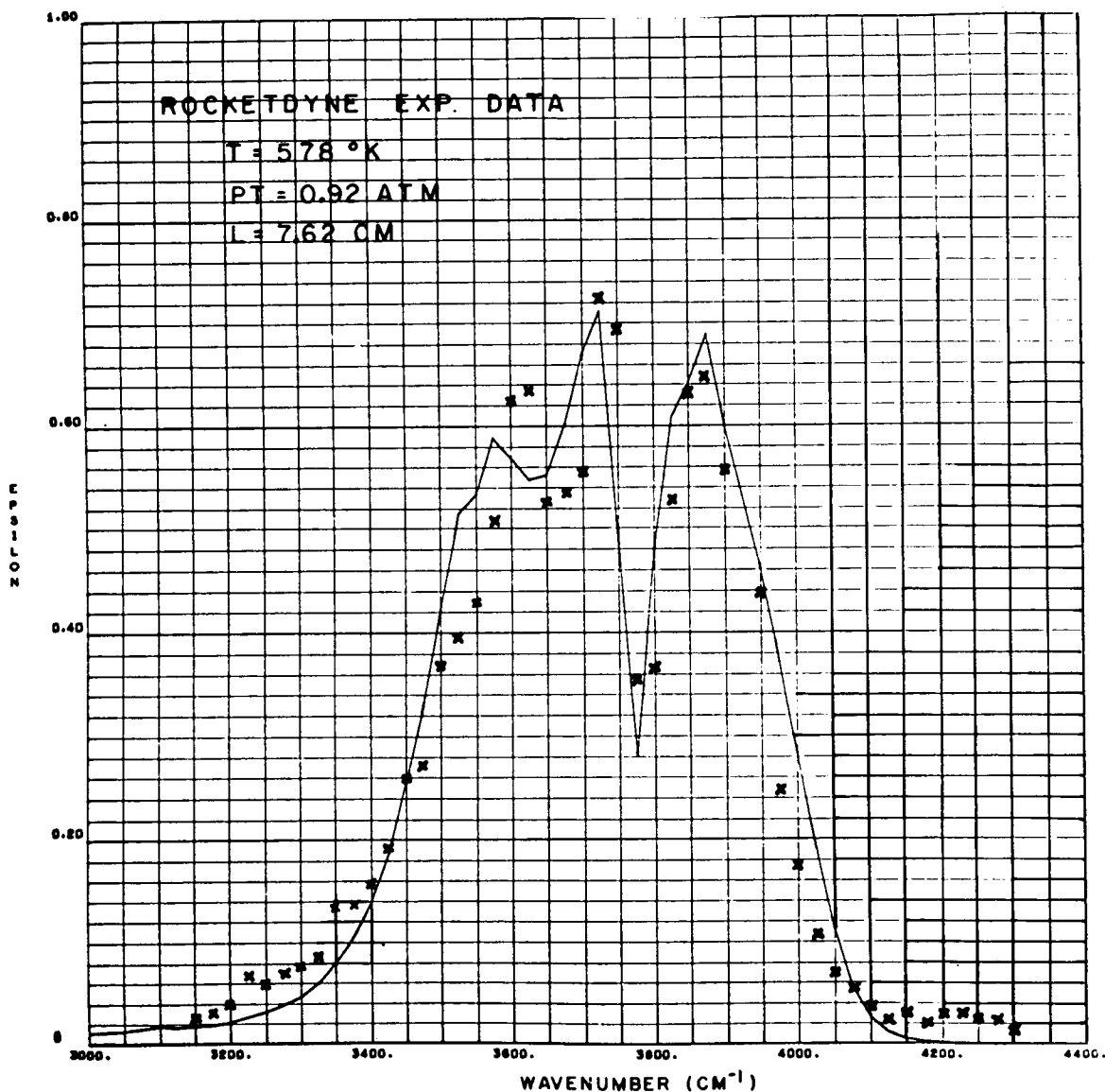


FIGURE 8. COMPARISON OF EMISSIVITY RECENTLY MEASURED BY ROCKETDYNE FOR  $H_2O$  AT 578°K WITH CALCULATED EMISSIVITY BASED ON  $k$  IN [7] AND BAND-AVERAGED  $a$

Figure 9 shows the results of an inhomogeneous burner measurement (solid line) in which the rear 5-foot section was at 2550°K and the front section

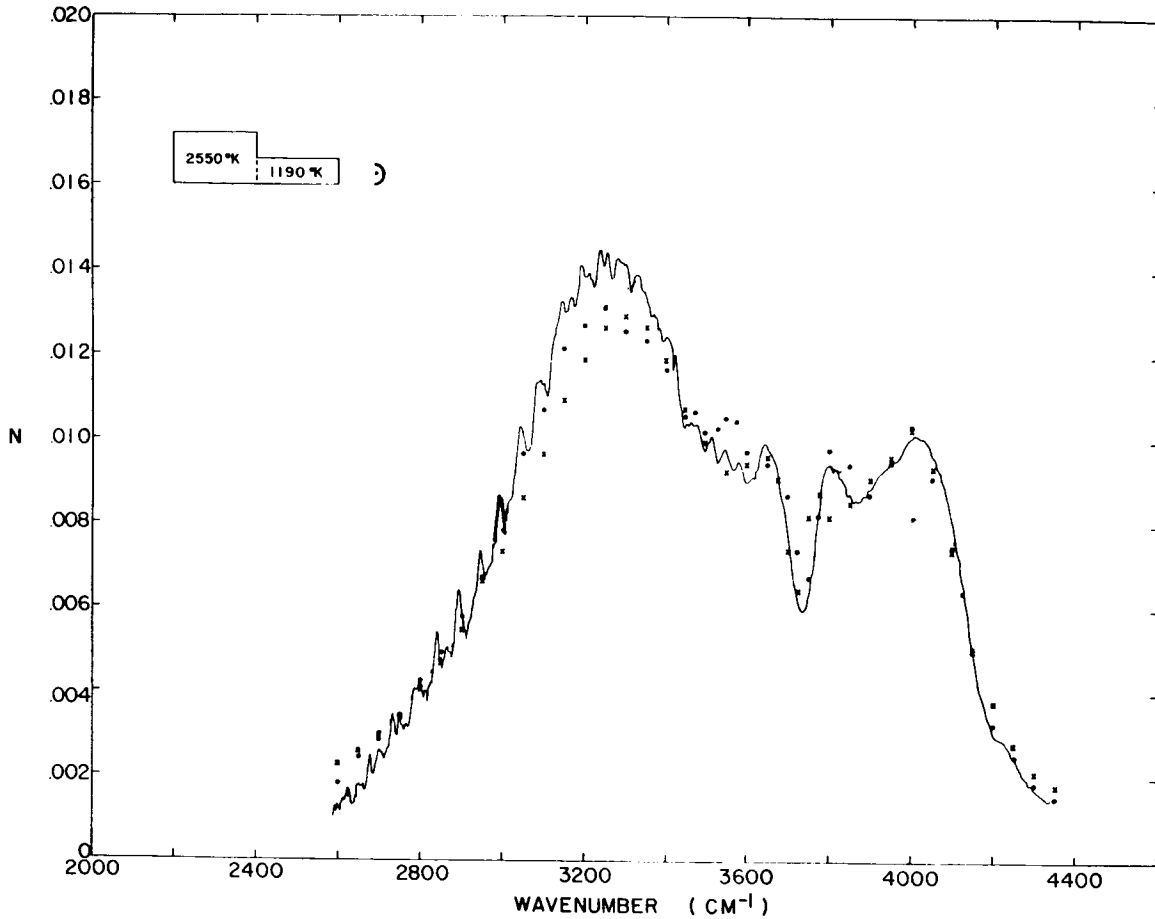


FIGURE 9. COMPARISON OF MEASUREMENT OF WATER-VAPOR RADIANCE USING TWO 5-FOOT SECTIONS OF BURNER ( $T_{\text{front}} = 1190^{\circ}\text{K}$ ,  $T_{\text{rear}} = 2550^{\circ}\text{K}$ ) WITH OUTPUT OF RADIANCE PROGRAM USING  $k$  FROM [7] AND (X's) BAND-AVERAGED VALUE OF  $a$ , AND (DOTS) LOCAL  $a$  AS FUNCTION OF  $\omega$  FROM [7]

at 1190°K. The X's and dots are the outputs of our radiance program using a band-averaged value of  $a$  and the local  $a$  (as a function of  $\omega$ ), respectively.

Figure 10 shows a comparison of an inhomogeneous measurement in the 2.7- $\mu$  region of CO<sub>2</sub> made by Simmons [10] (solid line) and a calculation by our radiance program using the calculated band-model parameters [2-4] for CO<sub>2</sub> (dots). The profile used in the calculations was substantially the same as, but not identical to, the experimentally measured profile. The general features of the spectrum are quite well reproduced. The underestimation of the radiance in the low-frequency wing appears to be a result of the calculated absorption coefficients being too low in this region as a result of the simplifying approximations involved in the calculations.

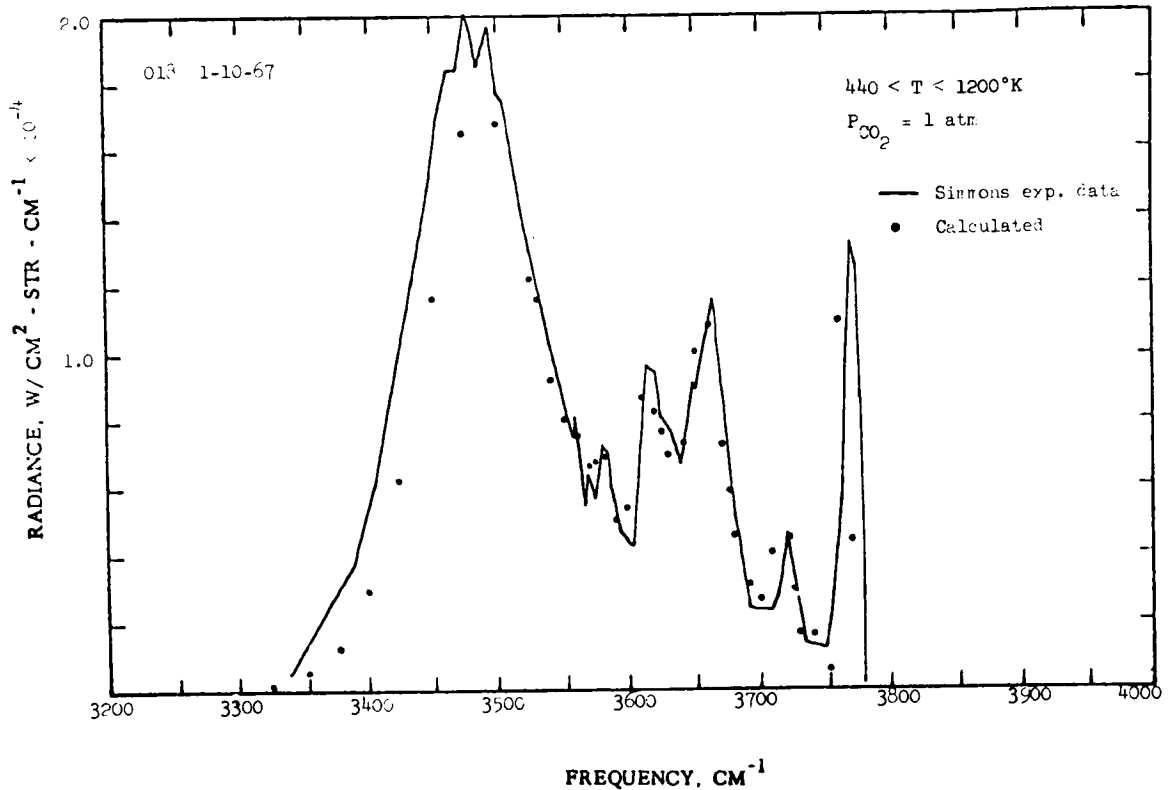


FIGURE 10. COMPARISON OF MEASUREMENTS BY SIMMONS (PRIVATE COMMUNICATION) ON CO<sub>2</sub> WITH  $T_{\text{rear}}/T_{\text{front}} \approx 3$  (440-1200°K) WITH OUTPUT OF RADIANCE PROGRAM FOR SIMILAR PROFILE, USING  $k$  FROM [7] AND BAND-AVERAGED  $a$

## REFERENCES

1. Thomson, J. A. L.: Paper No. II-1, this conference.
2. Malkmus, W.; and Thomson, A.: J. Quant. Spectry. Radiative Transfer, vol. 2, 1962, p. 17.
3. Malkmus, W.: J. Opt. Soc. Am., vol. 53, 1963, p. 951.
4. Malkmus, W.: J. Opt. Soc. Am., vol. 54, 1964, p. 751.
5. Malkmus, W.: General Dynamics Convair, Space Science Laboratory Report, to be published.
6. Goldman, A.; and Oppenheim, U. P.: J. Opt. Soc. Am., vol. 55, 1965, p. 794.
7. Ferriso, C. C.; Ludwig, C. B.; and Thomson, A. L.: J. Quant. Spectry. Radiative Transfer, vol. 6, 1966, p. 241.
8. Oppenheim, U. P.; and Ben-Aryeh, Y.: Statistical Model Applied to the Region of the  $\nu_3$  Fundamental of  $\text{CO}_2$  at  $1200^\circ\text{K}$ . J. Opt. Soc. Am., vol. 53, no. 344, 1963.
9. Malkmus, W.: Random Lorentz Band Model with Exponential-Tailed  $S^{-1}$  Line Intensity Distribution Function. J. Opt. Soc. Am., vol. 57, 1967, p. 323.
10. Study of Exhaust Plume Radiation Predictions. Final Report, Report No. GDC-DBE66-017, General Dynamics Convair, Space Science Laboratory, San Diego, California, December 1966.
11. Herget, W. F.: Private communication.
12. Simmons, F. S.: Private communication.

## DISCUSSION

S. A. Golden, Rocketdyne: In the usual Goody formulation, the frequency averaged absorption coefficient  $k_{\Delta} \equiv \frac{\ell n t}{-u}$  is expressed as

$$k_{\Delta} = \bar{k} \left[ 1 + \frac{\bar{k}u}{4a} \right]^{-\frac{1}{2}}$$

and for the purposes of analysis, this may be written as

$$\left( \frac{1}{k_{\Delta}} \right)^2 = \left( \frac{1}{\bar{k}} \right)^2 + \frac{u}{4\bar{k}a} \quad . \quad (\text{Equation 2 of the paper})$$

For a pure gas, both  $u$  and  $a$  are proportional to the pressure, while  $\bar{k}$  is independent of the pressure. Consequently, for a pure gas the model predicts that the observed absorption coefficient,  $k_{\Delta}$ , should be independent of pressure. However, the high resolution measurements we have been making on pure water seem to indicate that this independence of pressure is not true. Is this an indication of a defect of the approximation?

W. Malkmus: I do not think so. There is not enough consistency in the experimental data I have seen (above 0.1 atmosphere) to infer any failure of the model. Admittedly, the model will certainly break down somewhere; but I doubt that the current data are sufficient to make such a statement.

C. Ludwig, General Dynamics/Convair: I have a comment on Dr. Golden's remark. The applicability of the statistical model (Equation 2 of the paper) can be proved by showing that the log of the transmission  $t$  for fixed path lengths  $L$  is linear in pressure  $p$  (since  $u \equiv \rho L a p L$ ). Careful measurements were made some years ago by Dr. Burch between 900°K and 1500°K for pure water vapor between 0.1 atmosphere and one atmosphere. Plotting these data as  $\frac{-\ell n t}{L}$  versus  $p$  does not show any deviation from a straight line.

J. C. Gille, Florida State University: If one takes the data for the 15  $\mu$  band of carbon dioxide calculated by Yamamoto and Sasamori (later extended by Yamamoto), and plots  $\frac{-\ln t}{p}$  against  $\frac{u}{p}$ , as Dr. Malkmus has done with his data, one finds that over spectral intervals only 25  $\text{cm}^{-1}$  wide, there is good agreement with the random exponential band model. This agreement holds for nine orders of magnitude of absorber amount and three orders of magnitude of pressure.

However, there is lack of agreement and a large pressure effect in the interval containing the Q branch at 667  $\text{cm}^{-1}$ . Could features like this be the source of your pressure effects? Would the product of two random bands, one having a large and the other a small value for the mean line intensity, fit the data better? Murgatroyd and Goody [Q. J. Roy. Meteor. Soc., vol. 84, p. 225, 1958] follow this procedure for the complete 15  $\mu$  band.

H. Babrov, Warner and Swasey: When you set up the burners so that you had non-isothermal flames, what was done at the boundary between flames so as to reduce or minimize the boundary effects?

C. Ludwig: There is no provision made to reduce the transition zone from one section to the next in our non-isothermal measurements. It is assumed in the data reduction that there is a step function which is, I think, a good approximation, since the length of each isothermal section (5 feet) is large in comparison to the transition region.

A. Thomson: Is there any need to include Doppler broadening in your calculation for low pressure flames?

W. Malkmus: The measurements that have been made at Rocketdyne at approximately 0.01 atmosphere show a significant effect of Doppler broadening. Our calculations predict an increase of about 50 percent due to Doppler broadening at these conditions. In the case of  $\text{CO}_2$ , however, the number of lines increases so rapidly with temperature that the effect of the actual line shape becomes almost insignificant in emissivity calculations at temperatures much above 1000° K or 1500° K. But this statement is not true for  $\text{H}_2\text{O}$ , at least up to above 3000° K.

---



# METHODS OF CALCULATING ATMOSPHERIC TRANSMISSION FUNCTIONS

N68-18085

By

S. Roland Drayson\*

High Altitude Engineering Laboratory  
University of Michigan

---

## ABSTRACT

Recent advances in the field of atmospheric radiation have resulted in the need for accurate methods for the calculation of molecular absorption along slant paths in the atmosphere. This problem is of interest to those who study the atmosphere itself, as well as those who wish to look through it at a distant source. Direct application of empirical data may be successful under conditions which can be closely simulated in the laboratory. Band models, when carefully employed, can be used for a wide variety of physical conditions. The development of high speed electronic computers has made attractive a third method, that of direct integration with respect to frequency, which is considerably more flexible, especially when used for nonhomogeneous absorption paths. Some advantages of this method will be discussed and some examples of applications will be given. It demands a rather intimate knowledge of band structure and line shapes and further careful experiments are needed to determine these.

---

\* The theoretical calculations of absorption spectra were made with S. Y. Li and C. Young, and were developed under contracts with NASA and ESSA.

In recent years there has been a renewed interest in atmospheric radiative properties. For some applications the atmosphere is merely a nuisance, obscuring the target which is the object of study. These include the tracking of rockets from their thermal emission and the remote sensing of surface temperatures. Other applications depend on the radiative properties of the atmosphere, including the remote sensing of the atmospheric temperature field as a function of pressure, and the determination of cloud top heights. For the observer of the planets, the terrestrial atmosphere is an obscuring factor, while the planetary atmosphere is often the object of his study. In addition, the gross temperature structure of the terrestrial and planetary atmospheres is determined by radiative transfer processes. For a detailed knowledge of these, it is important to be able to accurately calculate molecular absorption of radiation along an atmospheric slant path.

Ultimately, the accuracy of all calculations of atmospheric absorption depends on laboratory data. Sometimes empirical data can be applied directly to atmospheric problems when the atmospheric conditions can be closely simulated in the laboratory. In general, however, along an atmospheric slant path, the temperature, pressure and concentration of the absorbing gas will all change simultaneously so that interpolation of laboratory data is not sufficient, and considerable extrapolation also must be used. Problems arise if data of higher spectral resolution are required.

Typically, molecular absorption bands contain many thousands of individual absorption lines made up of a mixture of strong and weak lines belonging to both abundant and rare isotopic molecules. Experimental studies are needed to determine the constants required to calculate line positions, and also the band intensities and line half-widths. Generally, line positions present no problems since they can be accurately observed, but line intensities and half-widths are difficult to measure precisely, partly because overlapping lines make it impossible to separate completely the effect of individual lines, even with high spectral resolution.

Suppose now that all the parameters are known for every line in an absorption band. In theory it is easy to calculate the absorption with any desired accuracy. In practice it is a rather difficult problem. The absorption coefficient  $k_\nu$  at a frequency  $\nu$  contains a contribution from each absorption line  $i$ .

$$k_\nu = \sum_i k_\nu(i)$$

and the transmissivity  $\gamma_\nu$  is given by

$$\gamma_\nu = \exp \left( - \int_{\mathbf{u}} k_\nu d_{\mathbf{u}} \right),$$

where the integral is taken along the absorption path. For a homogeneous absorption path, this reduces to

$$\gamma_\nu = \exp \left( - k_\nu u \right).$$

Generally, in radiative transfer problems we must know the average absorption  $\bar{\gamma}_{\Delta\nu}$  over a finite frequency interval  $\Delta\nu$ :

$$\bar{\gamma}_{\Delta\nu} = \int_{\Delta\nu} \exp \left( -k_\nu u \right) d\nu. \quad (1)$$

The integral in Equation (1) can be evaluated simply for certain special distributions of line parameters (positions, intensities, etc.), and this has given rise to band models. Most of these fall into two main groups:

- (a) Regular or Elsasser bands.
- (b) Statistical or random bands.

Some bands contain characteristics from both groups (e.g., random Elsasser model), and many variations for line shapes and special limiting cases are available. (For further details, see any standard text, e.g., Goody, 1964 [1].) Band models approximate the line positions, intensities, etc., by distributions for which a simple solution for average transmissivity exists. There are, however, important limitations:

- (a) The spectral resolution of most band models is limited. For example, in the Elsasser model  $\Delta\nu$  must be multiple of the line spacing.
- (b) Many band models do not allow for contributions from the wings of lines lying outside the spectral region under consideration.
- (c) The actual distribution of lines is difficult to approximate by band models, in some spectral regions.

The quasi-random model has removed many of these objections and, when properly used, is capable of a high degree of accuracy. However, even when models permit accurate calculation of the absorption of a real band, the complexity and length of calculation are considerable, especially for some of the more difficult line shapes (e. g. , the mixed Doppler-Lorentz line shape). Generally, they cannot be carried out by hand, and the aid of computers is enlisted. Modern computing techniques have made attractive an alternative to band models, the method of direct integration involving nothing more than the evaluation of Equation (1) by numerical quadrature. The following are some advantages of this method.

(1) The actual line parameters are used, not approximate ones. The numerical accuracy can be made arbitrarily high, and the absolute accuracy is limited only by our knowledge of the band parameters.

(2) The average transmissivity can be weighted by an instrument response function to compare with experimental data.

(3) The resolution is not limited.

(4) The method is more flexible than models when applied to slant path calculations.

The disadvantages of the method are as follows:

(1) It requires an intimate knowledge of the band structure and parameters of the individual lines, which is lacking for many absorption bands. However, the method can be of considerable assistance in determining some of these parameters.

(2) The computation time required is sometimes long. Suitable programming techniques can reduce time without loss of accuracy. Faster computers are rapidly being developed, so that this problem should become less in the future.

Transmissivity for atmospheric slant paths is usually obtained by reducing the absorption path to some "equivalent" homogeneous absorption path, by use of the Curtis-Godson approximation or some other scaling approximation. In practice, this procedure usually works remarkably well. If greater accuracy is required, the direct integration method allows approximations of this nature to be made over a number of horizontal layers; i. e. , the inhomogeneous slant path is approximated by not one, but a series of homogeneous absorption paths.

Direct integration also has advantages in computing flux divergences, so that more accurate heating and cooling rates can be computed.

Direct integration methods are being used by a number of groups in this country and abroad. I would now like to illustrate some applications of the method.

The first application is the reproduction of laboratory spectra. It is important to be able to do this to verify that values of band parameters are known correctly.

Figure 1 shows the oxygen "A" band near 7600 Å. These spectra were plotted directly from computer output to reproduce spectra of Burch et al. [2] and Burch and Gryvnak [3]. Resolutions of 1.2 and 0.6 cm<sup>-1</sup> and a triangular response function were assumed. Values of Lorentz half-width and band intensity deduced by Burch and Gryvnak [3] were used. The agreement with the original experimental spectra is so good that the two can scarcely be distinguished.

The rotational water vapor band is an important atmospheric absorption band. The calculations of line positions, intensities and half-widths made by Benedict and Kaplan [4] were used to compare with spectra of Palmer [5] between 250 and 500 cm<sup>-1</sup>, and Stauffer and Walsh [6] between 500 and 700 cm<sup>-1</sup>. By using the Van Vleck-Weisskopf line shape, good agreement was obtained between 250 and 500 cm<sup>-1</sup>, but problems remain between 500 and 700 cm<sup>-1</sup>. Representative spectra are illustrated in Figure 2.

Direct integration methods have also been applied to atmospheric slant path calculations. In Figure 3 we see a spectrum which was taken with a Michelson interferometer from a balloon at Palestine, Texas, in May, 1966, by the High Altitude Engineering Laboratory of the University of Michigan (see Chaney [7]). The balloon floated at 7 mb. for most of the day, so that it was above most of the earth's atmosphere. The rotational and 6.3μ bands of water vapor, the 9.6μ bands of ozone and the 15μ bands of carbon dioxide are prominent features. Previous carbon dioxide absorption calculations for homogeneous paths in the 15μ region have shown good agreement with laboratory spectra, and the band parameters used for these calculations were used to deduce atmospheric slant path transmission functions, and hence radiances for the spectral region between 600 and 750 cm<sup>-1</sup>. The theoretical and experimental spectra are compared in Figure 4, where the agreement is remarkably good. An instrumental resonance is responsible for the disagreement near 740 cm<sup>-1</sup>. At the low frequency end, the effect of the rotational water vapor band (not considered in the theoretical calculations) is becoming important. The 14μ

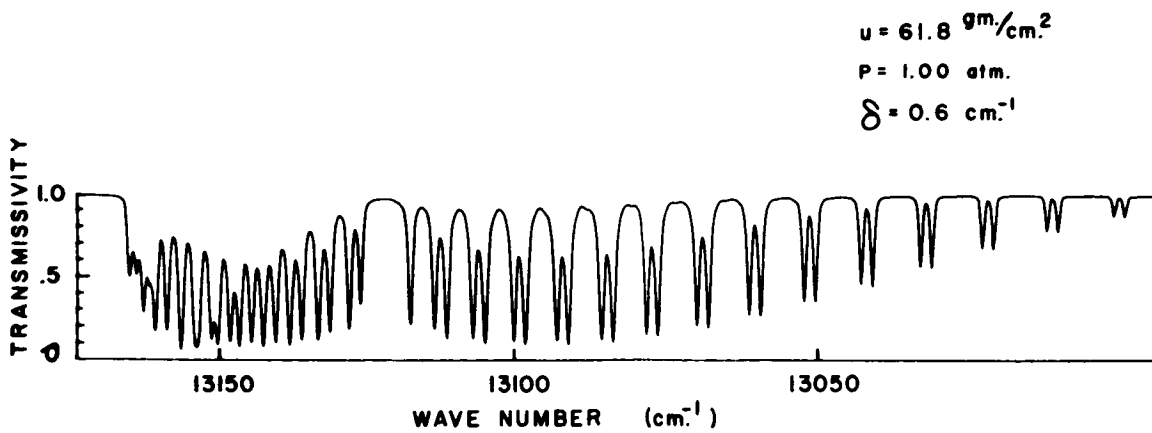
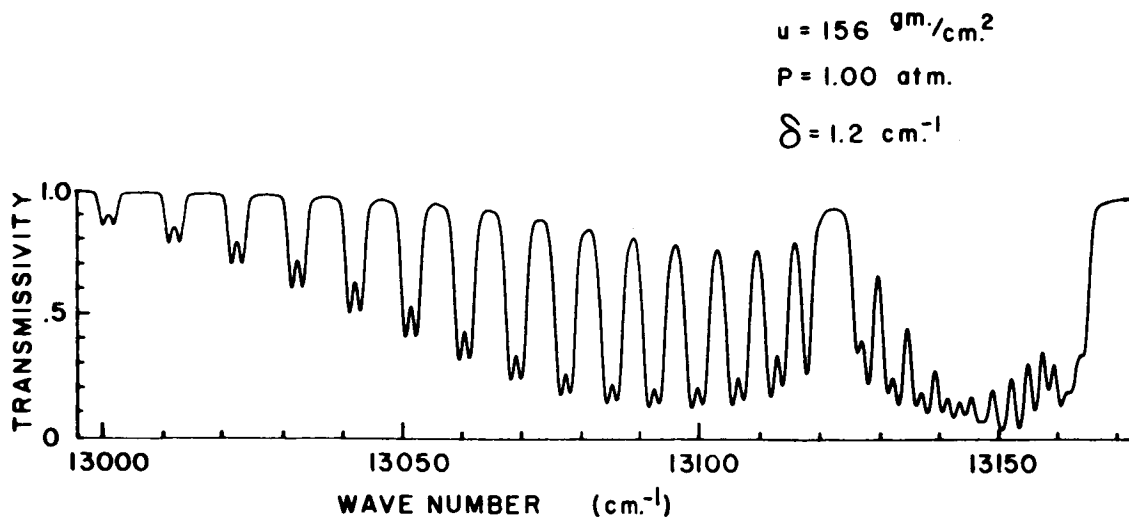
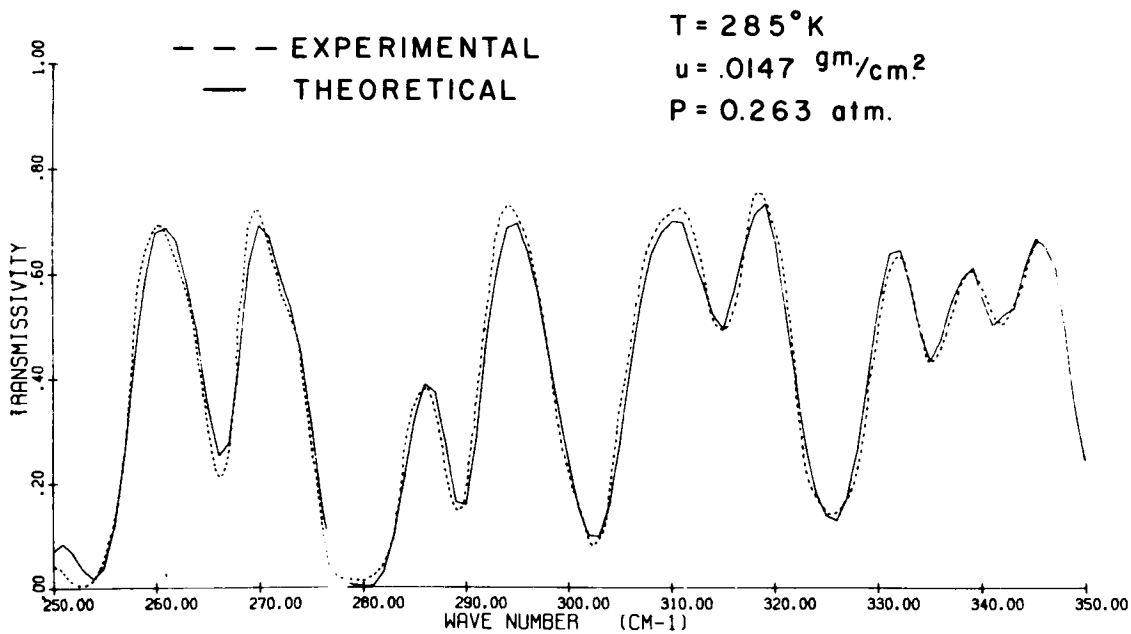
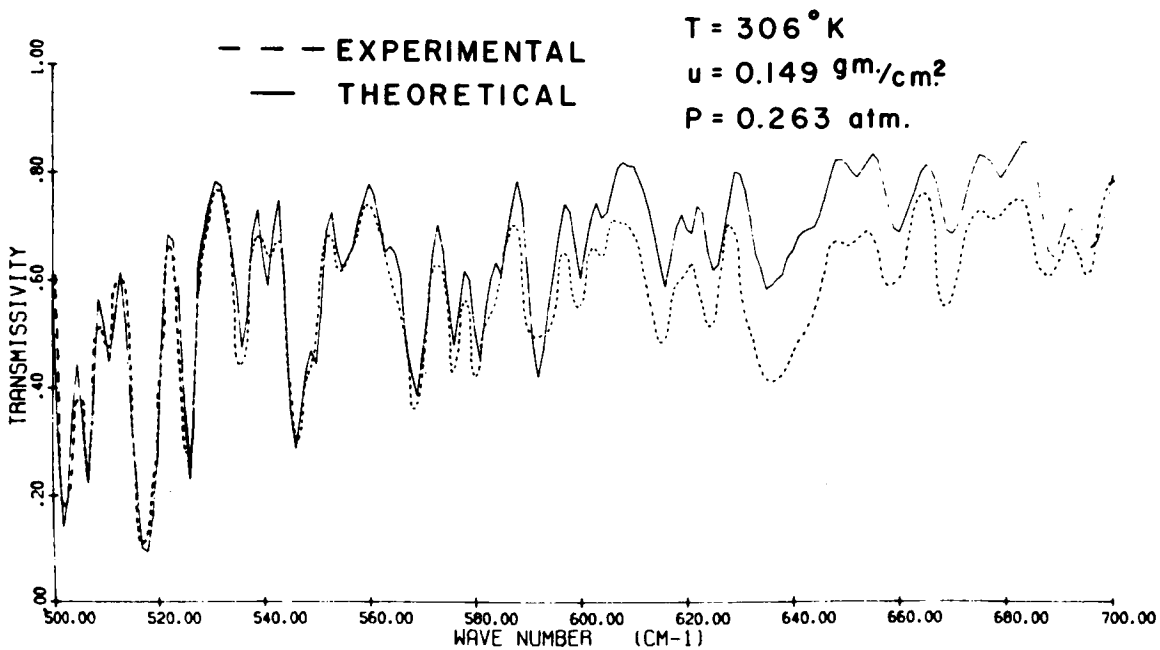


FIGURE 1. THEORETICAL SPECTRUM OF THE OXYGEN "A" BAND



Experimental Data of Palmer (1960)



Experimental Data of Stauffer and Walsh (1966)

FIGURE 2. COMPARISON OF THEORETICAL SPECTRUM

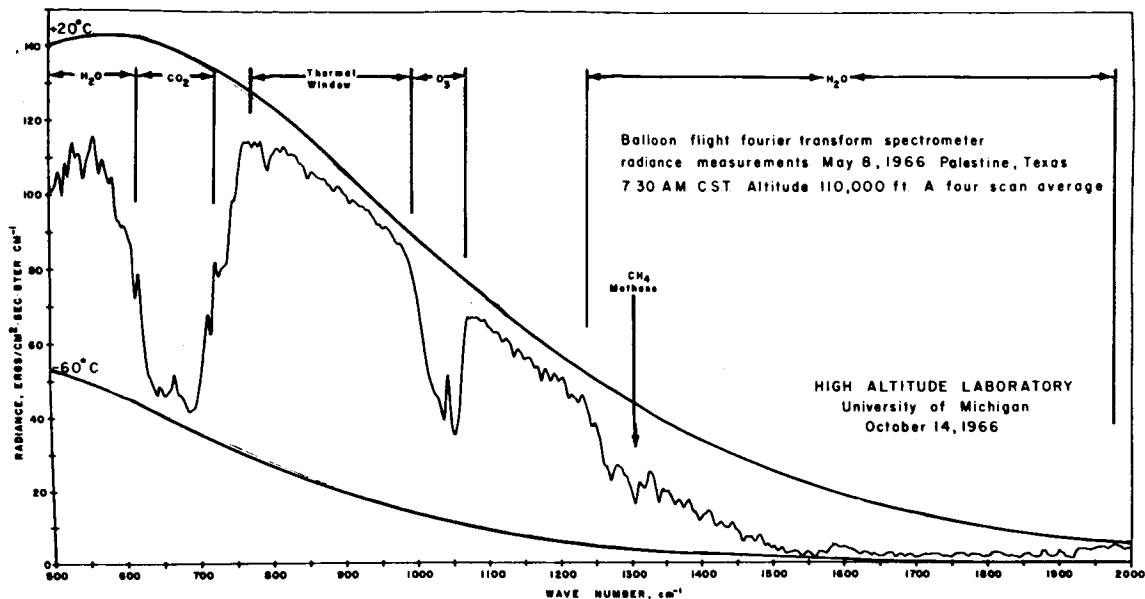


FIGURE 3. BALLOON FLIGHT RADIANCES

band of ozone was also neglected and small differences near  $680$  and  $720\text{ cm}^{-1}$  may be due to this weak absorption band. It is important to note that neither the theoretical absorption data nor the calibration of the experimental spectra was in any way adjusted to produce the agreement. They are completely independent processes.

Such spectra are suitable for the remote sensing of temperature in the atmosphere. Much more information is available on ozone and water vapor, but agreement between theoretical and experimental spectra has not yet been obtained.

These few examples have been designed to show the accuracy and versatility of the direct integration method and to demonstrate the need for a detailed knowledge of the absorption bands. We definitely need more careful experimental studies, particularly at high resolution.

In conclusion, we should examine the question of practical methods of calculating absorption along an atmospheric slant path. First, direct integration is a practical method provided that the line parameters are accurately known; if this is not the case, then calculations with band models will also fail to give accurate results. Second, the method chosen will depend on the accuracy



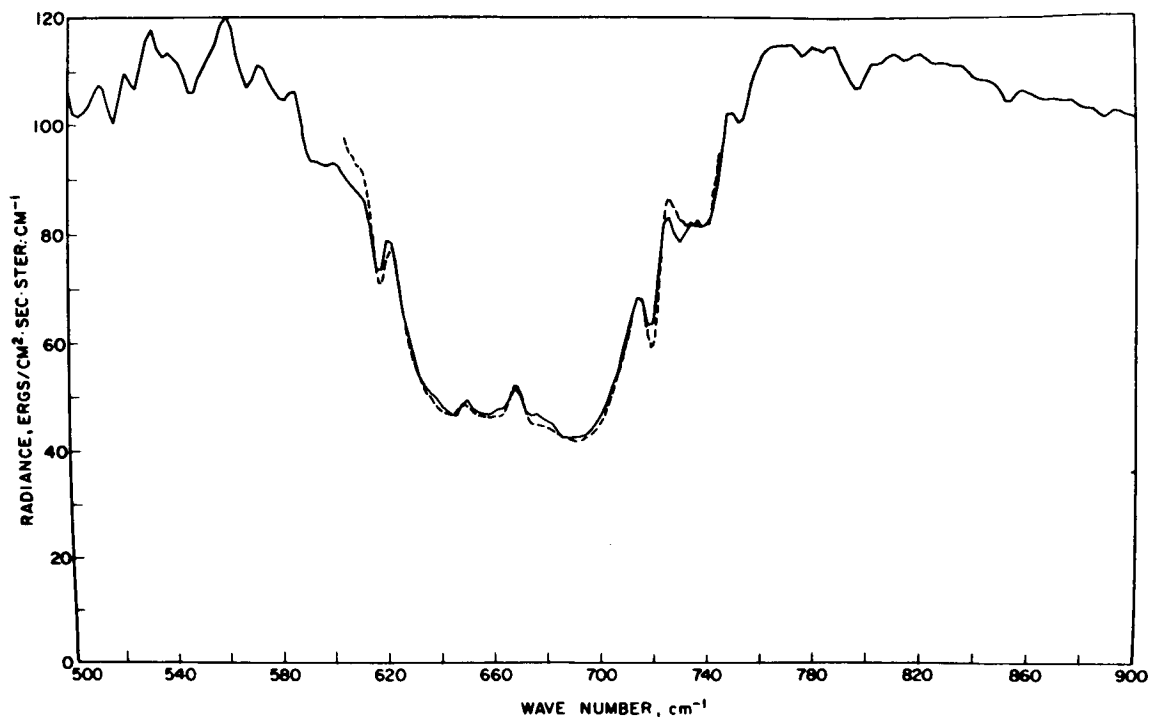


FIGURE 4. COMPARISON OF OBSERVED RADIANCES (SOLID CURVE) WITH THEORETICAL VALUES

and spectral resolution required. Applications such as remote sensing of the atmospheric temperature profile require high accuracy, but other applications may not be so demanding. Third, direct integration requires extensive computing facilities, whereas the simplest band models may require only a desk calculator and a set of tables. The potential user must decide for himself the method best suited to his needs.

## REFERENCES

1. Goody, R. M.: Atmospheric Radiation. Oxford University Press, 436 pp.
2. Burch, D. E.; Gryvnak, D. A.; and Patty, R. R.: Absorption by the 7620 Angstrom Oxygen Band. Aeronutronics Report No U-2908, 1964.
3. Burch, D. E.; and Gryvnak, D. A.: Strength, Widths and Shapes of The Oxygen Lines Near 7600 Angstroms. Aeronutronics Report No. U-4076, 1967.
4. Benedict, W. S.; and Kaplan, L. D.: Listing of Rotational Water Vapor Line Positions, Intensities and Half-Widths. Unpublished.
5. Palmer, C. H. Jr.: Experimental Transmission Functions for the Pure Rotational Band of Water Vapor. J. Opt. Soc. Am., vol. 50, 1960, p. 1232.
6. Stauffer, F. R.; and Walsh, T. E.: Transmittance of Water Vapor - 14 to 20 Microns. J. Opt. Soc. Am., vol. 56, 1966, p. 401.
7. Chaney, L. W.; Drayson, S. R.; and Young, C.: Fourier Transform Spectrometer - Radiative Measurements and Temperature Inversion. Applied Optics, vol. 6, 1967, p. 247.

---

## DISCUSSION

V. Falcone, Jr., AFCRL: You commented that the Van Vleck-Weisskopf form factor agreed with your data. We at AFCRL have made simultaneous measurements of atmospheric emission and absorption and have shown that the Lorentz form factor gave better correlation between measured and calculated values of optical depth.

R. Drayson: Is this a rotational water vapor band?

V. Falcone: Yes, from 15 to 60 GHz ( $0.5$  to  $2$   $\text{cm}^{-1}$ ).

R. Drayson: It seems that different line shapes give better results in different parts of bands. In the microwave regions you might expect quite a different result because of the different kind of processes which influence the line shapes. This should not really surprise us. We have no atmospheric data to compare against, but such a comparison certainly would be very interesting. We have problems where the far wings of lines are important. Almost certainly the Van Vleck-Weisskopf line shape is not the complete answer; but in the region between  $20$  and  $40$   $\mu$  (i. e.,  $250$  to  $500$  wave numbers) it seems to give fairly satisfactory agreement with the experimental data.

R. F. Calfee, ESSA: Barney Farmer has just published as an EMI report (No. DMP2780) a comparison between the Lorentz and the Van Vleck-Weisskopf equations across almost this entire rotational band. He shows that in some areas you must use the Van Vleck-Weisskopf equation, while in other areas the Lorentz equation works quite well.

R. Drayson: The choice of equations does not make very much difference near the center of the line; it is for the fairly distant wings of lines that the question becomes important.

R. F. Calfee: I have made, along with Dr. Benedict, quite an extensive listing of lines for water vapor and for carbon dioxide. These are now available for water vapor in the  $2.7$   $\mu$

region, and in the 1.9 and the 6.3  $\mu$  bands. The 2.7  $\mu$  band for carbon dioxide is also listed. Within this next year, we hope to have the listing completed for the 1.4, the 1.1, the 0.93, and the 0.83  $\mu$  water vapor bands and for a large number of bands in the short wavelength for carbon dioxide.

S. A. Golden, Rocketdyne: Mr. Drayson, will you amplify your statement that the resolution of a regular array is limited to the line spacing?

R. Drayson: Yes, the resolution of the Elsasser band is limited to the line spacing. For instance, you cannot calculate the average absorption of  $3/4$  line spacing.

S. A. Golden: That statement is not true, because you can obtain a closed form expression for the monochromatic absorption coefficient for any of the regular arrays.

R. Drayson: But you are not using the band model as such in this case. You can assume this distribution of lines and calculate the absorption at any monochromatic point, but the whole object of the band model is to obtain the average transmission over a finite frequency interval. Is that not correct?

S. A. Golden: If you wish to use it in that restricted sense, yes. As long as I have a spectral expression, however, why can I not integrate over any frequency interval I wish?

R. Drayson: In that case you will have to use the direct integration method and to calculate the contribution of all the lines.

S. A. Golden: No, that statement is not true, because I am still including in a closed form expression the contributions from all the other lines.

W. Malkmus, General Dynamics/Convair: Mr. Drayson was talking about existing models or what is commonly called the Elsasser model. I also have a point regarding models that might have been misinterpreted. Both the random models and the Elsasser models account for the wings of lines which exist outside the region, but the assumption is that the properties of the lines outside are the same as those of the lines inside the region.

R. Drayson: I agree with you. The models do not accurately account for the wings of the lines centered outside the interval, since the Elsasser function itself will change outside the interval.

W. Malkmus: Therefore, the amount is precise, but it may not precisely represent what you want it to!

D. E. Burch, Philco/Ford: I want to make a few more comments about the line shapes. We have made some measurements in the so-called window at  $350 \mu$ , or approximately 30 wave numbers. It appears there that none of these line shapes are very good. The simple Lorentz expression used in the near infrared (which does not have the  $\frac{\nu}{\nu_0}$  coefficient because it is always about one anyway), predicts fairly well the attenuation you get in this window. I do not think, however, that we should infer from this situation that this is the proper line shape. It simply gives enough extra absorption to some of the lines to make up for the absorption it does not give to others.

I should also say that in the far infrared, there is evidence that the shapes of self-broadened lines are quite different from the shapes of nitrogen-broadened lines. Therefore, we should not really regard any of these line shapes as sacred, because they are all based on a theory that a self-broadened line has the same shape as a foreign-broadened line, or at least ignores the difference. The self-broadened lines are generally stronger in the wings than are the nitrogen-broadened lines, a difference that is apparently even more true when one reaches higher wave numbers, or shorter wavelengths (approximately  $10 \mu$ ). I think that in this case you will find that because of the  $\left(\frac{\nu}{\nu_0}\right)^2$  coefficient, the Van Vleck-Weisskopf shape gives too much weight to the lines that occur around 200 wave numbers. It tends to diverge, as Goody pointed out in his book, because you cannot expect the Van Vleck-Weisskopf shape to hold that far on the high wave number side of a line.

R. Drayson: I believe that our comparisons show a difference for wave lengths of the order of  $18 \mu$  (555 wave numbers).

D. E. Burch: I think that if you reach  $10 \mu$ , the divergence will be even more. Also, the self-broadening versus nitrogen-broadening ratio becomes very large; i. e., nitrogen-broadening becomes so small that it is very difficult to measure. There is probably a factor of 200 between self-broadening and the nitrogen-broadening. The Van Vleck-Weisskopf shape overestimates; but then, the other line shapes that can be found in the literature do not seem to be correct either.

---

# THE INFRARED OPACITY OF HOT WATER VAPOR

N 68 - 18086 By

J. R. Auman, Jr.

Princeton University Observatory  
Princeton, New Jersey

---

## ABSTRACT

As a step in the analysis of the infrared observations of cool stars made from above the atmosphere using a balloon-borne telescope, the opacity due to water vapor has been calculated in the spectral region between  $0.8 \mu$  and  $12.5 \mu$  and for temperatures of  $1680^\circ\text{K}$ ,  $2016^\circ\text{K}$ ,  $2520^\circ\text{K}$ , and  $3360^\circ\text{K}$ . Since the atmospheres are very tenuous in the stars being analyzed, the  $\text{H}_2\text{O}$  spectral lines have been assumed to be broadened only by the Doppler motions, and pressure broadening has been neglected completely. It is known that the envelopes of stars with low surface temperatures are in convective equilibrium and that the spectral lines are not only broadened by the thermal motions of the atoms but also by the random macroscopic velocities of the convective elements. Therefore, the spectral lines have been assumed to be not only broadened by the atomic thermal motions but also by the assumed rms turbulent motions of 2, 4, and 8 kilometers per second. The positions and the strengths of the total of approximately  $2.3 \times 10^6$  spectral lines were calculated, and the water vapor spectrum was reconstructed by summing the contributions of these lines. From the reconstructed spectrum the harmonic mean opacity was calculated in intervals of  $100 \text{ cm}^{-1}$ . The opacity due to  $\text{H}_2\text{O}$  was compared to the continuous opacity assuming that the abundance of the elements was similar to the abundance found in the sun. With this assumption it was found that the  $\text{H}_2\text{O}$  opacity was important at  $T = 3360^\circ\text{K}$  and was the dominant opacity for  $T \leq 2520^\circ\text{K}$ .

---

This paper is concerned with the outgrowth of some observations made from above the atmosphere by Stratoscope II, a balloon-borne telescope. On November 26, 1963, a flight was made which obtained low dispersion spectra of several cool stars in the spectral region between  $0.8 \mu$  and  $3.1 \mu$  [1 and 2]. The observations were made at a high enough altitude that the telluric bands in the infrared were no longer visible. The stars which were observed had effective temperatures between  $2000^{\circ}\text{K}$  and  $4000^{\circ}\text{K}$ . A major discovery of these observations was the great strength of the  $\text{H}_2\text{O}$  features in the infrared spectra of the coolest stars that were observed. Figure 1 gives the infrared spectra

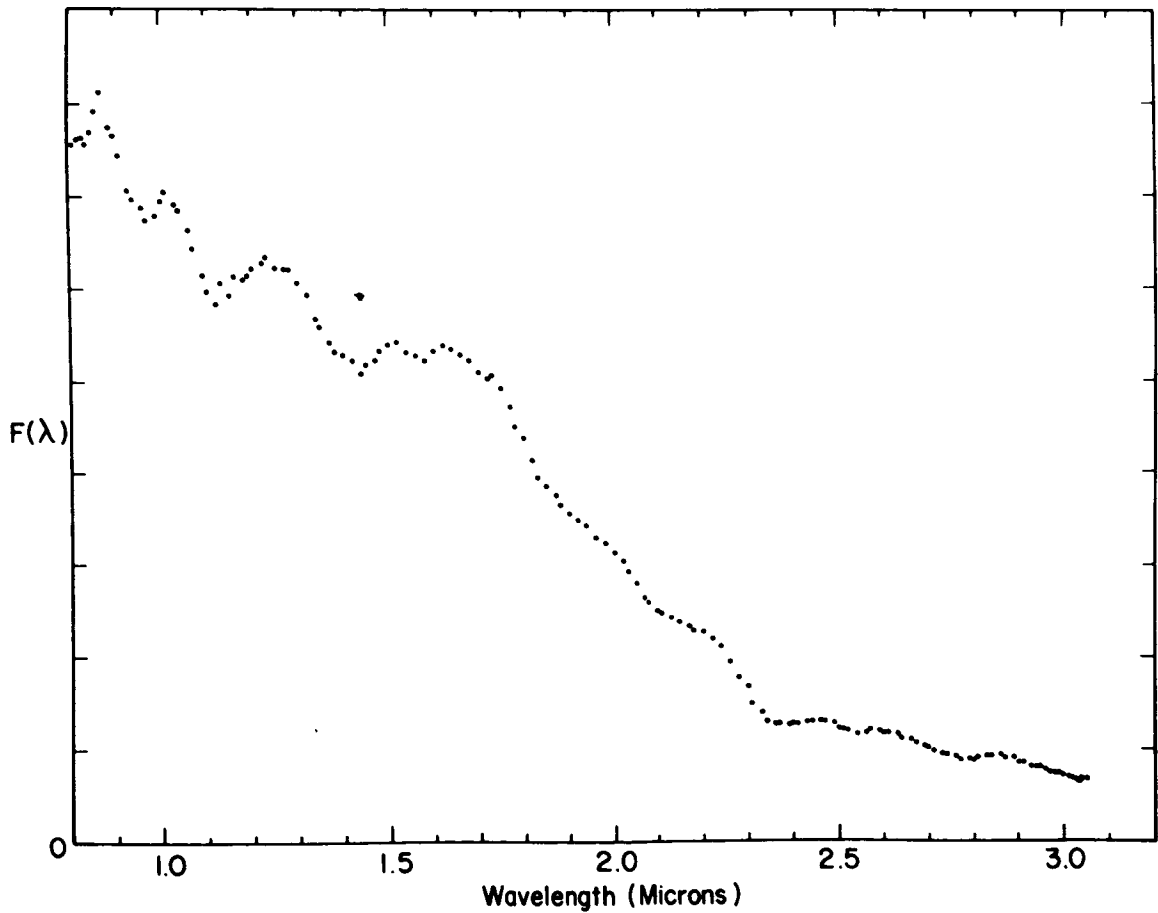


FIGURE 1. INFRARED SPECTRUM OF  $\alpha$  ORIONIS



that was obtained of  $\alpha$  Orionis, a supergiant with an effective temperature of approximately 3500°K. In this spectrum can be seen the features due to H<sub>2</sub>O at 0.9  $\mu$ , 1.1  $\mu$ , 1.4  $\mu$ , and a broad feature between 1.7  $\mu$  and 3  $\mu$  which is composed of a combination of the 1.9  $\mu$  and 2.7  $\mu$  bands of water and the 2.35  $\mu$  band of CO. Figure 2 gives the infrared spectra of  $\theta$  Ceti, a supergiant star with an effective temperature of approximately 2000°K. The features due to H<sub>2</sub>O are much greater in this star than they were in  $\alpha$  Orionis. There are very strong features due to H<sub>2</sub>O at 1.4  $\mu$  and 1.9  $\mu$  in addition to the feature due to the combination of the CO band at 2.35  $\mu$  and the H<sub>2</sub>O band at 2.7  $\mu$ . The water vapor

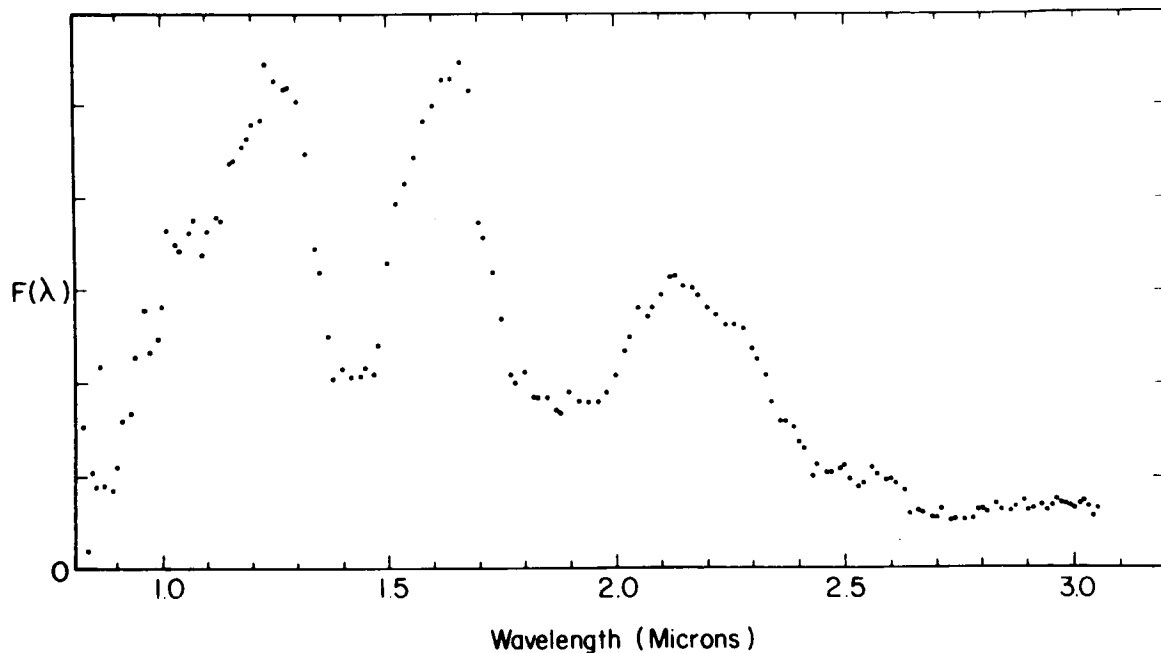


FIGURE 2. INFRARED SPECTRUM OF  $\theta$  CETI

feature at 1.1  $\mu$  can also be seen. Because of the many different vibrational transitions which can occur, the H<sub>2</sub>O bands act to block out a considerable percentage of the total flux being emitted by the star. From these spectra and the others obtained by Stratoscope II, it could easily be seen that the opacity due to hot water vapor should be included when constructing theoretical models of the atmospheres of cool stars. The calculations described below were undertaken, to try to determine the H<sub>2</sub>O opacity in stars.

All of the stars which were observed by Stratoscope have radii which are between 50 and 500 times the radius of the sun. The gas pressures which exist in the regions of these stars where the water is present are less than 0.01 the sea level pressures on earth. In addition, it is well known that the envelopes of these stars are in convective equilibrium. On the basis of the study of the strength of spectral lines in the spectra of these stars, it is known that the outermost parts of the atmospheres of the cool stars have turbulent motions with rms velocities of 2 to 10 km/sec over distance scales of the order of or less than the mean free path of the photon in these atmospheres. The rms velocities of the macroscopic motions in these atmospheres must be added to the thermal motions of the molecules themselves. Since the pressures in these atmospheres are very low and the Doppler motions are very large, the approximation was made to neglect the pressure broadening of the spectral lines relative to the Doppler broadening and to assume that the lines were broadened only by their Doppler motions.

When constructing model atmospheres of stars, what is generally needed to be known is not the opacity alone but the product of the monochromatic opacity times some monochromatic variable describing the radiation field such as  $I_\nu$ ,  $J_\nu$ , or  $F_\nu$ . Since the  $H_2O$  opacity is composed solely of the sum of the contributions of individual spectral lines, the frequency dependence of the  $H_2O$  opacity and the radiation field will vary over wide ranges with a scale comparable to the widths of spectral lines. Because of limitations in the computer, it is not possible to treat this opacity and radiation field in all of its detail. It is necessary to define the opacity and the variables describing the radiation field over intervals which are large compared to the width of a spectral line. The quantities describing the radiation field will vary inversely to the opacity in the optically thin region of the atmosphere, which is the region we are interested in. In order that the integrals over the interval of the product of  $\kappa_\nu$  and  $I_\nu$ ,  $J_\nu$ , or  $F_\nu$  be given correctly, it is necessary that the opacity be described by a weighted mean where the weighting factor is given by the opacity dependence of  $I_\nu$ ,  $J_\nu$ , or  $F_\nu$ . In general, the opacity dependence of these quantities will depend upon which radiation variable is being considered, the frequency, the effective temperature of the atmosphere, and the depth in the atmosphere at which quantities are being determined. For a preliminary analysis of the spectrum, the assumption was made that the  $I_\nu$ ,  $J_\nu$ , and  $F_\nu$  all varied according to  $\kappa_\nu^{-1}$  so that the weighted mean of the  $H_2O$  opacity needed to be calculated with a weighting factor of  $\kappa_\nu^{-1}$ . A weighted mean with this weighting factor is a harmonic mean opacity.

The harmonic mean opacity is considerably harder to calculate than the straight mean would be. Since the opacities are being weighted by  $\kappa_{\nu}^{-1}$ , the frequencies at which the opacity is small are relatively more important than the frequencies at which the opacity is high. The shapes of the spectral lines with pure Doppler broadening are given by the formula

$$I_{\nu} d\nu = \frac{I_0}{\Delta\nu\sqrt{\pi}} e^{-\left(\frac{\nu - \nu_0}{\Delta\nu}\right)^2} d\nu, \quad (1)$$

where  $\Delta\nu$  is given by the formula

$$\Delta\nu = \frac{\nu}{c} \sqrt{\xi_t^2 + \frac{2kT}{M}}. \quad (2)$$

Since the opacity in a line falls off as  $e^{-\left(\frac{\nu - \nu_0}{\Delta\nu}\right)^2}$ , a given spectral line can contribute to the opacity only in an interval of the order of  $\Delta\nu$  on each side of the center of the line. Therefore, a given spectral line, no matter how strong it is, is limited in the amount that it can contribute to the harmonic mean. Care has to be taken to include the contributions of the weak spectral lines since these lines will determine the opacity in the frequency intervals between the strong lines. Enough spectral lines have to be included until either the lines completely cover all the frequencies and no holes are left in the spectrum or until the strengths in the centers of the weakest lines are small compared to the continuous opacity from the other sources of opacity.

The procedures used to calculate the harmonic mean opacity of water are described in Auman [3]. The water molecule is an asymmetric molecule. There are  $2J + 1$  rotational levels for each value  $J$  of the total angular momentum specified by the notation  $J_{\tau}$ , where  $\tau$  is an index,  $-J \leq \tau \leq J$ , which orders the states having the same total angular momentum according to their energies. The  $2J + 1$  levels having the same total angular momentum  $J$  can be divided into sequences of  $J$  and  $J + 1$  levels one with even  $\tau$  and the other with odd  $\tau$ . The levels at the upper and lower ends of the sequences tend to pair up with each other and have equal energies, while in the middle of the sequences the lines are

paired. The quantum number  $J$  denoting the total angular momentum is a good quantum number; and, as a result,  $\Delta J$  is equal to 0,  $\pm 1$  in all radiative transitions. The parameter  $\tau$ , which denotes the orientation of the water molecule about its axis of rotation, is not a good quantum number. As a result, radiative transitions can occur when  $|\Delta\tau|$  is greater than 1 although the transitions become weaker as  $|\Delta\tau|$  becomes larger. In addition, symmetry rules reduced the values of  $\Delta\tau$  for which the radiative transitions can occur by roughly a factor of 2. The water molecule has three normal modes of vibration:  $\nu_1$  3657  $\text{cm}^{-1}$ ,  $\nu_2$  1595  $\text{cm}^{-1}$ , and  $\nu_3$  3756  $\text{cm}^{-1}$ . The overtone and combination bands occur as well as the fundamental vibrational bands although these bands are weaker than the fundamental. Because of the transitions with  $|\Delta\tau| > 1$  and the large number of overtone and combinational vibrational transitions, the  $\text{H}_2\text{O}$  spectrum has many more weak lines than is the case for the diatomic molecules.

The first step in the calculation of the  $\text{H}_2\text{O}$  opacity was to calculate the positions and the strengths of the individual water vapor lines. The lines were assumed to have a rectangular profile with a width of  $2\Delta\nu$  where  $\Delta\nu$  is given

by Equation (2). Because of the  $e^{-\left(\frac{\nu - \nu_0}{\Delta\nu}\right)^2}$  dependence of the line profiles with pure Doppler broadening, the rectangular profile should be a reasonably good approximation. A total of  $2.3 \times 10^6$  spectral lines were included in reconstructing the  $\text{H}_2\text{O}$  spectrum from 800  $\text{cm}^{-1}$  to 12500  $\text{cm}^{-1}$ . The spectrum was reconstructed using a grid in frequency space whose intervals were small compared to the widths of the lines. From the reconstructed spectrum, the distribution of opacity in an interval could be calculated as well as the mean opacity. A total of 40 hours of computer time on an IBM 7094 computer was required to make the calculation, including the writing and debugging of the necessary programs.

The position of a line is given by the

$$\nu = G_V(v_1', v_2', v_3') - G_V(v_1'', v_2'', v_3'') + F'(J', T') - F''(J'', T''). \quad (3)$$

$G_V(v_1', v_2', v_3')$  and  $G_V(v_1'', v_2'', v_3'')$  are the vibrational term values of the upper and lower states while  $F'(J', T')$  and  $F''(J'', T'')$  are the rotational term values. The difference in the vibrational term values gives the origin of the band, while the difference in the rotational term values gives the position of the lines relative to the band origin. The difference in the rotational curve values has been approximated by the formula

$$F'(J', T') - F''(J'', T'') = F_0(J', T') - F_0(J'', T'') + \alpha\Delta A + \beta\Delta B + \gamma\Delta C, \quad (4)$$

where  $F_0(J, T)$  are the rotational term values in the ground vibrational study.  $\Delta A$ ,  $\Delta B$ , and  $\Delta C$  are the changes in  $A$ ,  $B$ , and  $C$  during the transition due to the change in the vibrational state of the molecule; and  $\alpha$ ,  $\beta$ , and  $\gamma$  are, respectively, the partial derivatives of the rotational term values of the ground vibrational state with respect to  $A$ ,  $B$ , and  $C$ . The values of  $\alpha(J, T)$ ,  $\beta(J, T)$ , and  $\gamma(J, T)$  were calculated using the rigid rotor approximation [4]. To be able to specify the position of a line, the vibrational term values and the ground state rotational term values had to be specified. Wherever known, the experimental values of these term values were used. If not known, the values were obtained by extrapolation from the experimentally known values. The extrapolation of empirical data is always extremely dangerous. The calculated energy levels using the rigid rotor approximation cannot be used since the deviations from this approximation are very large in the highly excited states. The details of the extrapolation procedure are given in Auman [3]. The accuracy with which the positions of the spectral lines can be specified will be limited because of the errors in the extrapolation. The size of the errors is important since this determines how finely the frequency dependence on the opacity can be determined. The total error in the calculated position of a line varies from a fraction of  $\text{cm}^{-1}$  for lines coming from transitions between low well-observed states to several hundred  $\text{cm}^{-1}$  for some of the weak lines coming from transitions between highly excited states. The mean error is probably between 25 and 50  $\text{cm}^{-1}$ .

Neglecting the interaction between vibration and rotation and including stimulated emission, we obtain the intensity of a line by the formula

$$I = \frac{S_v L \nu g e^{-E''hc/kT} (1 - e^{-h\nu/kT})}{\nu_0 Q} \quad (5)$$

$L$  gives the rotational line strengths, which have been calculated by Wacker and Pratto [5] for various values of the asymmetry parameter in the rigid rotor approximation. They were kind enough to send the author a copy of the program used to make the calculations. This program was used to generate the values of  $L$  for all values of  $J \leq 40$ .

●  $S_v$ , which is the strength of the vibrational transition, has been determined in the following manner. The values of  $S_v$  for the ground vibrational states are experimentally known. The values of  $S_v$  for the cases where the lower vibrational state is not the ground state were determined relative to the ground state band strength using the harmonic oscillator approximation [6]. The values of  $S_v$  for the ground vibrational state, as well as the values of  $\Delta A$ ,  $\Delta B$ , and  $\Delta C$  and the vibrational rotational term values, were obtained from Dr. W. S. Benedict at Johns Hopkins University.

After a theoretical spectrum had been calculated, the distribution of the opacities within each interval of  $100 \text{ cm}^{-1}$  was obtained. Figure 3 gives the distributions of the opacity for a series of frequency intervals at various positions around the water vapor band at  $1.4 \mu$ . This vibrational band has a band head at  $7500 \text{ cm}^{-1}$  which degrades to the red. The first frequency interval, which is centered at  $7750 \text{ cm}^{-1}$ , is located beyond this band head and, as a result, has very few strong lines in it. The next interval, centered at  $7450 \text{ cm}^{-1}$ , is located in the center of this band head. This interval has the highest density of strong lines of all the intervals in the  $1.4 \mu$  band. However, while there are more strong lines located in this frequency interval, there are fewer weak lines than in the intervals at lower frequencies within the band. The maximum harmonic mean opacity occurs approximately in the interval centered around  $7050 \text{ cm}^{-1}$ . As can be seen, this interval has fewer strong lines than the interval centered around  $7450 \text{ cm}^{-1}$ . However, the opacity between the strong lines is higher than in the interval at  $7450 \text{ cm}^{-1}$ , and the harmonic mean opacity is higher as a result. The next frequency interval considered in Figure 3 is centered around  $6750 \text{ cm}^{-1}$ . This frequency interval has the greatest number of lines of all the frequency intervals in the  $1.4 \mu$  band. The strongest lines in this interval are much weaker than the strongest lines in the previous two intervals. However, the opacities at the points where the opacity is at its minimum are approximately the same as in the interval centered around  $7050 \text{ cm}^{-1}$  and higher than the frequency interval centered around  $7450 \text{ cm}^{-1}$ . Therefore, the harmonic mean opacity at this point is only slightly less than in the interval centered around  $7050 \text{ cm}^{-1}$  and is quite a bit greater than the opacity in the interval centered around  $7450 \text{ cm}^{-1}$ . Because this frequency interval is composed of many weak lines, the dispersion in the opacity in this interval is much less than it is on the high frequency side of the band. The same point should be noticed concerning the band located at  $6450 \text{ cm}^{-1}$ . Here the opacities are, in general, weaker than in the band at  $6750 \text{ cm}^{-1}$  because this interval is farther away from the band origin. However, as in the previous interval, the

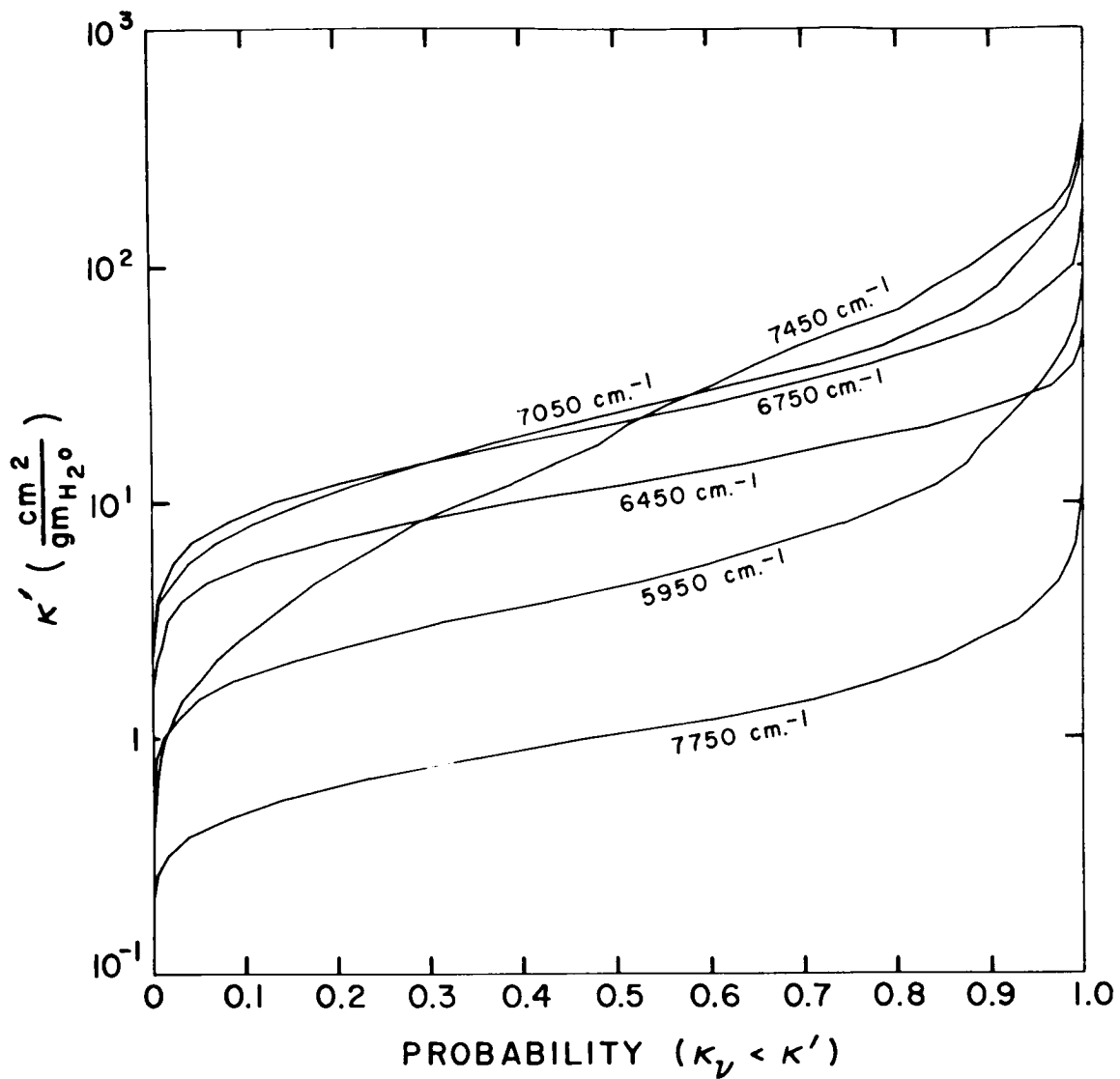


FIGURE 3. THE DISTRIBUTION OF OPACITIES IN INTERVALS OF  $100 \text{ cm}^{-1}$  IN THE INTERVAL BETWEEN  $5950$  AND  $7750 \text{ cm}^{-1}$  FOR A TEMPERATURE OF  $2520^\circ \text{K}$  FOR ASSUMED rms TURBULENT VELOCITIES OF  $4 \text{ km/sec}$

Dispersion in the opacities is relatively small. The final frequency interval considered is at  $5950 \text{ cm}^{-1}$ , at which point the harmonic mean opacity is at a minimum between the  $1.4$  and  $1.9 \mu$  bands. As would be expected since this interval is farther from the band origin, the opacities are smaller than in the previous two intervals. However, it should be noticed that there are some lines in this interval from the  $1.9 \mu$  band; thus, the maximum opacity is higher than in the previous interval.

Figure 4 gives the harmonic mean of the  $\text{H}_2\text{O}$  opacity plus the continuous opacity assuming 2, 4, and 8 kilometers per second rms turbulent velocities for  $T = 1680^\circ \text{K}$  and  $\log P_e = -4$ . The opacities have been calculated assuming solar abundances. As can be seen in Figure 4, the opacity due to water is

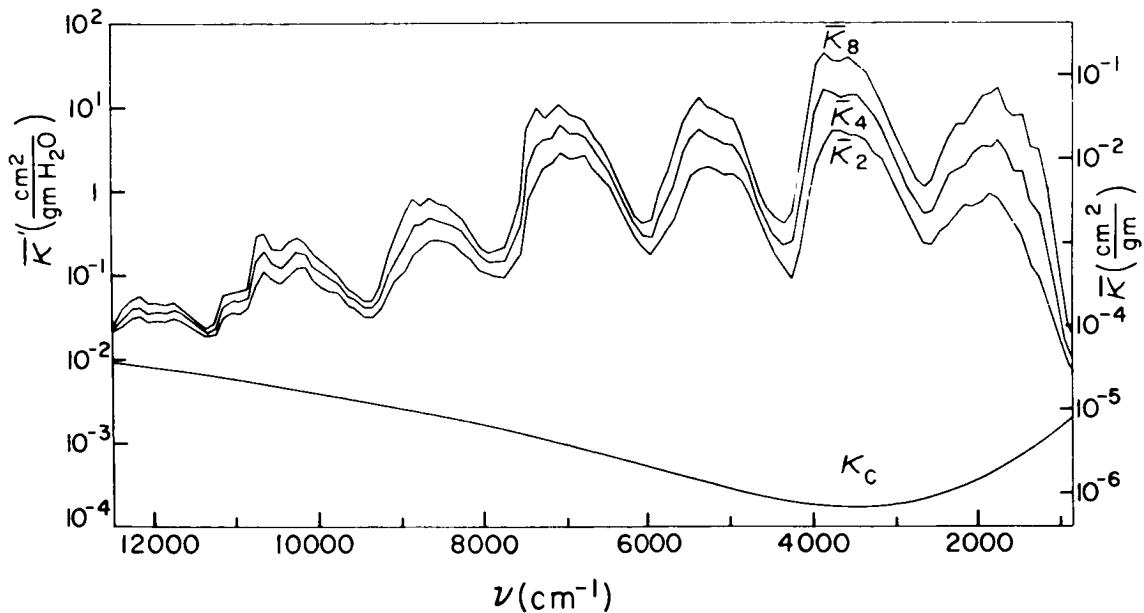


FIGURE 4. HARMONIC MEAN OPACITIES INCLUDING WATER VAPOR FOR  $T = 1680^\circ \text{K}$  AND  $\log P_e = -4.0$  ( $\bar{\kappa}_2$ ,  $\bar{\kappa}_4$ , AND  $\bar{\kappa}_8$  ARE, RESPECTIVELY, THE OPACITIES ASSUMING rms TURBULENT VELOCITIES OF 2, 4, AND 8 km/sec.  $\kappa_c$  IS THE OPACITY NEGLECTING THE CONTRIBUTIONS OF WATER VAPOR)



larger than the continuous opacity by several orders of magnitude. The effect the widths of the lines on the harmonic mean opacity can be seen by comparing the opacities corresponding to different turbulent velocities. The thermal velocities of the water molecule at these temperatures is approximately 1 km/sec. To a reasonably good approximation the increase by a factor of 2 in the rms turbulent velocities represents an equivalent increase in the widths of the lines. As can be seen in Figure 4, changes of a factor of 2 in the widths of the lines make roughly equal percentage changes in the harmonic mean opacity. Figure 5 gives the harmonic mean opacities for the rms turbulent velocities for 2 km/sec and 8 km/sec for  $T = 2016^\circ\text{K}$ ,  $\log P_e = -3.0$ . Although the  $\text{H}_2\text{O}$

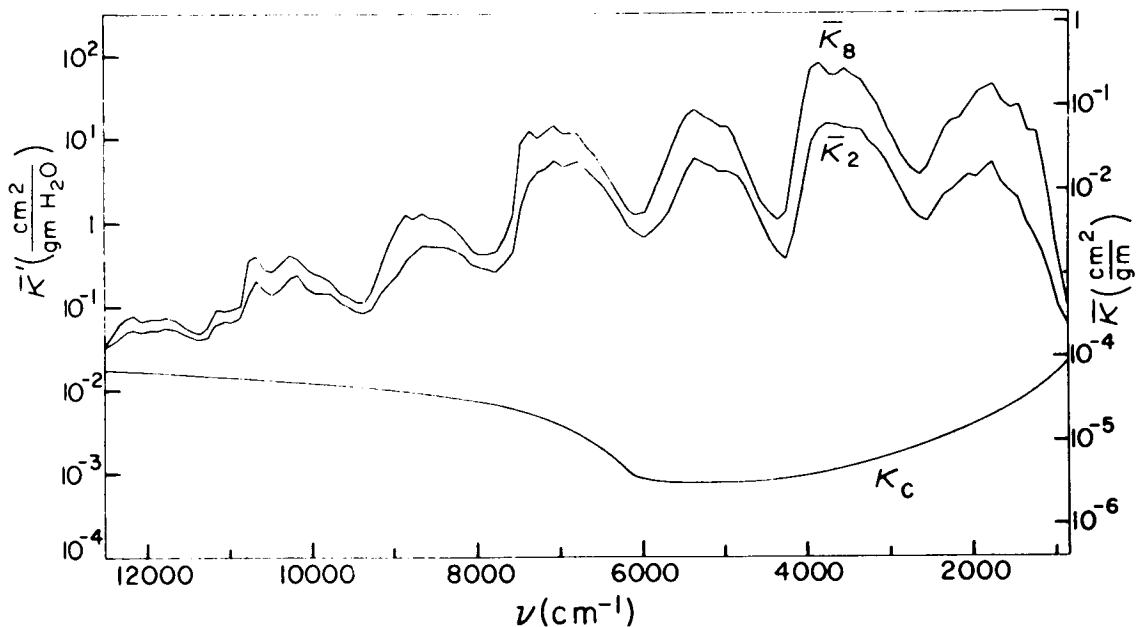


FIGURE 5. HARMONIC MEAN OPACITIES INCLUDING WATER VAPOR FOR  $T = 2016^\circ\text{K}$  AND  $\log P_e = -3.0$ . (THE DEFINITIONS OF  $\bar{\kappa}_2$ ,  $\bar{\kappa}_8$ , AND  $\bar{\kappa}_c$  ARE THE SAME AS IN FIGURE 3.)

opacity is not so large relative to the continuous opacity as in the case with  $T = 1680^\circ\text{K}$ , the water is still by far the dominant source of opacity. Figure 6 gives the same opacities for the case  $T = 2520^\circ\text{K}$  and  $\log P_e = -2.0$ . As can be seen in this figure, the opacity due to water is still the dominant source of opacity.

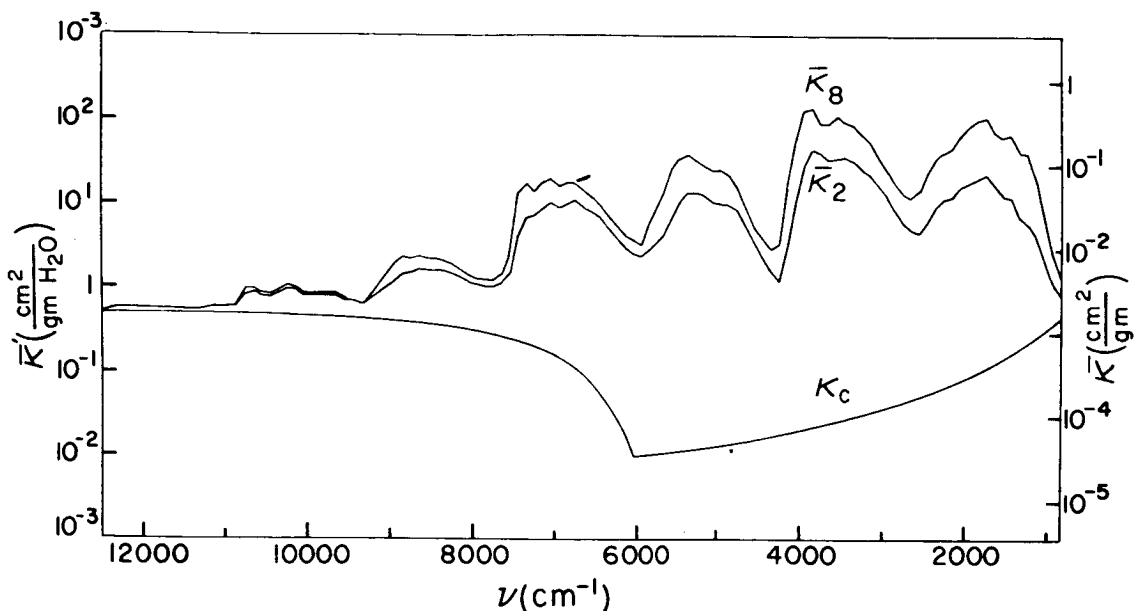


FIGURE 6. HARMONIC MEAN OPACITIES INCLUDING WATER VAPOR FOR  $T = 2520^{\circ}\text{K}$  AND  $\log P_e = -2.0$ . (THE DEFINITIONS OF  $\bar{\kappa}_2$ ,  $\bar{\kappa}_8$ , AND  $\kappa_c$  ARE THE SAME AS IN FIGURE 3.)

Figure 7 gives the opacity for  $T = 3360^{\circ}\text{K}$  and  $\log P = -1.0$ . Here the opacity is no longer the dominant source of opacity but is still an important source of opacity for frequencies less than approximately  $7000\text{ cm}^{-1}$ .

It should be emphasized that the opacities in the past figures were calculated for solar abundances. If a different set of abundances were assumed, the importance of the opacity due to water relative to the other opacities might be quite different. The opacities for frequencies less than  $2500\text{ cm}^{-1}$  may be increased somewhat by a more complete inclusion of the water vapor lines. This would be particularly true below  $1500\text{ cm}^{-1}$  since pure rotational lines will become important at this point. In addition, the pressure broadening becomes important at low frequencies. Since Doppler broadening is proportional to the frequency while pressure broadening is constant with frequency, there will be some frequency below which pressure broadening will become significant. The

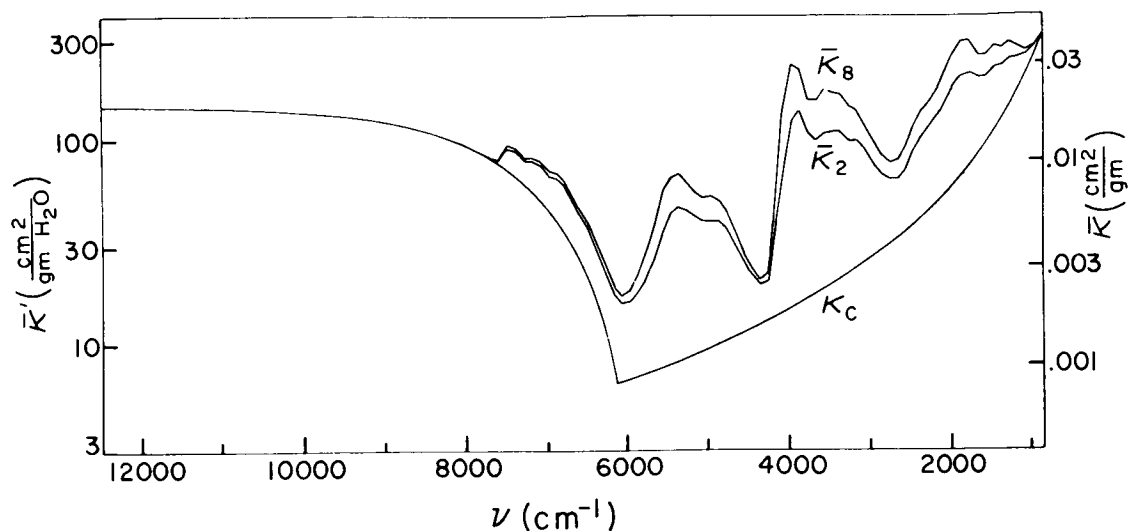


FIGURE 7. HARMONIC MEAN OPACITIES INCLUDING WATER VAPOR FOR  $T = 3360^{\circ}\text{K}$  AND  $\log P_e = -2.0$ . (THE DEFINITIONS OF  $\bar{\kappa}_2$ ,  $\bar{\kappa}_8$ , AND  $\kappa_c$  ARE THE SAME AS IN FIGURE 3.)

exact point will depend upon the degree of turbulent broadening, as well as the pressure of the gas. Since pressure broadening has been completely neglected, any pressure broadening which does occur will tend to raise the opacity.

No studies have been made of the  $\text{H}_2\text{O}$  opacity when the lines are pressure broadened. In such a situation, the importance of the strong lines relative to the weak lines will be increased due to the broad wings which the strong lines will have. This will mean that the shapes of the bands will change so that the maximum opacity will more nearly occur at the frequencies where the greatest number of strong lines appear.

## ACKNOWLEDGMENT

The author gratefully acknowledges the many helpful conversations with Mr. Schwarzschild, who suggested this problem. The author would also like to

knowledge his great debt to W. S. Benedict, who spent a considerable amount of time with the author explaining how to calculate the positions and intensities of the lines and supplied the molecular constants necessary to make the calculations.

This work supported by Project Stratoscope of Princeton University, Princeton, New Jersey, was sponsored by NSF, ONR, and NASA, and made use of computer facilities supported in part by the NSF Grant NSF-GP579.

## REFERENCES

1. Woolf, N. J.; Schwarzschild, M.; and Rose, W. K.: *Ap. J.*, vol. 140, p. 833, 1964.
2. Danielson, R. E.; Woolf, N. J.; and Gaustad, J. E.: *Ap. J.*, vol. 141, p. 116, 1965.
3. Auman, J. R.: *Ap. J.*, Supplements, vol. 14, p. 171, 1967.
4. Allen, H. C.; and Cross, P. C.: *Molecular Vib-Rotors*. New York, John Wiley & Son, 1963.
5. Wachter, P. F.; and Pratto, M. R.: *N.B.S. Monog.* 70, vol. 2, 1964.
6. Penner, S.: *Quantitative Molecular Spectroscopy and Gas Emissivities*. Reading, Mass.: Addison-Wesley Publishing Co., 1959.

---

## DISCUSSION

A. Thomson: Dr. Auman's work represents the first attempt I know of to treat a spectrum as complicated as that of water vapor at high temperature and low pressure by a direct line-by-line calculation. Dr. Auman, how many lines were included and how much computing time was involved?

J. Auman: It took a total of 40 hours on an IBM 7094 computer. A total of 2.3 million lines were included in the calculation.

E. French, North American Rockwell: Dr. Auman, could you comment on how the continuum base level was established?

J. Auman: The continuous opacity was calculated for the temperature and assumed electron pressure at which the H<sub>2</sub>O opacity was being calculated. The opacity at the upper temperatures is primarily due to the bound-free and free-free transitions of H<sub>2</sub>. At the lower temperatures, the opacity is primarily due to the free-free transitions of the H<sub>2</sub> molecule and Rayleigh scattering by molecular hydrogen.

R. Drayson, University of Michigan: I would like to ask Dr. Auman a question about the step functions used for the line shape. Did you make any tests to see how well this method worked, particularly in view of your statement that what is important is the region between the strongly absorbing lines? What is the contribution of the wings of the lines?

J. Auman: I have made no tests. My own feeling is that it will have very little effect as long as the broadening of the spectral lines is due only to Doppler effects. Figure 3 shows that the opacity in the intervals between strong lines is very seldom smaller than a hundredth of the opacity in the strong lines and is quite often about a tenth of it. On the other hand, the opacity at a distance  $2\text{\AA}$  from the center of a line is only two percent of its value at the center of the line. Therefore, the opacity in the intervals between the strong lines will be determined by the opacity in the centers of the weak lines rather than by the wings of strong

lines. For this reason, I believe that the rectangular line profile will give a good representation of the spectra. Of course, if pressure broadening is important and the strong lines have wings, the rectangular profiles will not be a good approximation.

R. Goulard, Purdue University: In your averaging calculations, you have assumed a certain value of intensity. Does it correspond to a constant temperature case?

J. Auman: When the opacity was calculated for a given temperature and electron pressure, all of the quantities which depend upon the temperature were calculated with that temperature.

C. Ludwig, General Dynamics/Convair: One might ask about the relevance of this isothermal case to the problem here at NASA, where radiative heat fluxes must be calculated for many inhomogeneous paths through the rocket plume; this distinction between the two problems bears on the need there is to use band models in the inhomogeneous case. I think that a major conclusion one can draw from Dr. Auman's paper is that it would not be easily feasible to make the same kind of calculations for the problem of rocket plume radiation transfer.

J. Auman: I would like to make two points. The first is that, for the case of radiative transfer in a rocket plume, one has roughly atmospheric pressures. This means that the spectral lines will have wings and that the total number of lines which will have to be considered will be considerably smaller than in the case where there are no wings. The second point is that it should be possible to make a calculation for a molecule, such as I have made for  $H_2O$ , in order to determine the distribution of the opacities, as shown in Figure 3. Once these distributions as functions of temperature and pressure are determined, they can be used to calculate the radiative transfer for the particular cases in which one is interested. If one has several temperatures, the distribution of opacities at each temperature could be obtained by interpolation, using a grid of distributions at different temperatures. If the opacity is due to the absorption of several molecules, the distribution of the opacities at each temperature and pressure could be constructed for the molecules together from the distributions of opacities computed for the individual molecules.

J. C. Gille, Florida State University: Is it necessary to consider departures from local thermodynamic equilibrium?

J. Auman: I have assumed that the H<sub>2</sub>O molecules are in local thermodynamic equilibrium. There is some reason to hope that this is a good approximation, since the energy differences between the rotational levels is small compared to kT, so that inelastic collisions should occur very easily. At the same time, the radiative transitions will not occur as rapidly in the infrared, because of their frequency dependence. Therefore, the H<sub>2</sub>O molecules should be well coupled to the thermal velocities in the gas. Of course, if you go to densities which are low enough, this will break down. However, H<sub>2</sub>O may be dissociated in this case.

J. C. Gille: You spoke of the surface layer of the star, but used a  $\frac{1}{\kappa}$  dependence which suggests a photon diffusion process, as does the Eddington approximation. I would expect this would be applicable in a stellar interior, but that a  $\kappa$  dependence would be more appropriate near the surface. Does the use of  $\frac{1}{\kappa}$  indicate an optically deep surface layer? Finally, the use of  $\frac{1}{\kappa}$  and harmonic means suggest a Rosseland mean absorption coefficient. Would that be a useful approximation to your calculations?

J. Auman: As for the question of what mean of the opacity should be used, I have calculated some model atmospheres of stars with effective temperature between 2000° K and 4000° K. By comparing  $F_{\nu}$  and  $J_{\nu}$  at adjacent frequency points which have different opacities, I can determine the rough opacity dependence of these quantities. If we assume that  $F_{\nu}$  and  $J_{\nu}$  vary as  $\kappa^{-\alpha}$ , the values of  $\alpha$  at the surface varies from approximately 0.2 in a giant with  $T_e = 3500^{\circ}$  K to approximately 0.8 in a giant with  $T_e = 2000^{\circ}$  K. In the deeper layers of the atmosphere,  $J_{\nu}$  will become independent of the opacity, while  $F_{\nu}$  will approach  $\kappa^{-1}$ . Therefore, the best mean will probably be one which is somewhere between the straight mean and the harmonic mean.

One point that I would like to make is that ultimately the fact that the opacity is due to lines will have to be treated explicitly in solving the equation of radiative transfer. Comparisons between grey atmospheres and non-grey atmospheres show that there is no mean by which you could reduce a non-grey atmosphere to a grey atmosphere. The same thing probably applies here. There is no mean by which one can represent the molecular opacity within an interval. The fact that the opacity varies considerably within each interval will also have to be taken into account.

---



## THE SURFACE PRESSURE OF VENUS

By

L. D. Gray\* and A. T. Young\*\*

Department of Astronomy  
University of Texas  
Austin, Texas

---

### ABSTRACT

An upper limit to the Venus surface pressure of 25 bars is obtained by combining a mechanical model of the atmosphere with an atmospheric model that reproduces the observed microwave brightness temperature of the planet. It is also shown that carbon dioxide is not a minor constituent of the Cytherean atmosphere.

---

### INTRODUCTION

A great deal of information about the nature of a planetary atmosphere can be obtained from the radiation received from it. From the ultraviolet to the near-infrared part of the spectrum, an observer on earth sees solar radiation reflected and/or scattered by the atmosphere of the planet. Gases present in the atmosphere give rise to absorption bands, and the amount of these gases in the absorption path can be determined. In the far-infrared and microwave portions of the spectra, the radiation is due to thermal emission from the atmosphere, the clouds, and the surface of the planet.

---

\* On leave of absence from JPL. Present address: Jet Propulsion Laboratory, Pasadena, California.

\*\* Present address: Aerospace Corporation, El Segundo, California.

Visual observations of Venus indicate that the surface of the planet is obscured by an almost uniform cloud cover, and it is not possible to "see" the surface at any wavelength less than 3 cm (in the microwave region of the spectrum). The composition of these clouds is not known, but two explanations have been proposed. These are discussed briefly in Appendix A. Our upper limit for the surface pressure on Venus remains valid regardless of the nature of the clouds, because the inclusion of any additional source of microwave opacity will only reduce this upper limit.

## MECHANICAL MODEL ATMOSPHERES

In the past, a major difficulty in constructing model atmospheres of Venus has been that the distance from the planet's surface to any observable region of its atmosphere was unknown. The recent radar measurement of the surface radius by Ash, Shapiro, and Smith [1] solves this problem, because it can be combined with the radius and pressure at the occulting layer, derived by Menzel and de Vaucouleurs [2], to give the surface pressure for any given composition and temperature distribution.

Since the radar radius is  $6056 \pm 1$  (m.e.) km and the radius of the occulting layer [2] is  $6169 \pm 5$  (m.e.) km, the height of the occulting layer is  $113 \pm 5$  km. At this height, the pressure is about  $(2.55 \pm 0.2 \text{ (m.e.)} \times 10^{-6} \text{ bars})$ , which is only very weakly dependent on the assumed composition. Since the height of this layer is now known, we can extrapolate this pressure to the surface if the composition and temperature distribution are specified. A simple but reasonable temperature model consists of an adiabatic troposphere matching the high microwave surface temperature, and an isothermal stratosphere at about  $240^\circ \text{ K}$  to match the infrared bolometric and  $\text{CO}_2$ -rotational temperatures.

To calculate a mechanical model atmosphere, we adopt a stratospheric temperature  $T_c$  and a surface temperature  $T_s$ . The mean molecular weight

$$\mu = \sum f_i \mu_i \quad (1)$$

where  $f_i$  and  $\mu_i$  are the mole fraction and molecular weight of the  $i$ th constituent.

Similarly, the mean ratio of specific heats is

$$\gamma = \sum f_i \gamma_i \quad (2)$$

where we adopt  $\gamma_{\text{CO}_2} = 1.30$ ,  $\gamma_{\text{N}_2} = 1.40$ , and  $\gamma_{\text{Ne}} = 1.64$  as average values for the lower atmosphere of Venus.

The height of the tropopause is then

$$z_c = \left( \frac{\gamma}{\gamma - 1} \right) \frac{k (T_s - T_c)}{mg}, \quad (3)$$

where  $k$  is Boltzmann's constant,  $m = \mu \times 1.66 \times 10^{-24}$  g, and  $g = 870$  cm/sec<sup>2</sup>. The surface pressure follows from the occultation height  $z_*$  and pressure  $P_*$ :

$$P_s = P_* \left( \frac{T_s}{T_c} \right)^{\frac{\gamma}{\gamma - 1}} \exp [(z_* - z_c)/H_i], \quad (4)$$

where the scale height in the isothermal region is

$$H_i = kT_c/mg. \quad (5)$$

Finally, the tropopause pressure is

$$P_c = P_s \left( \frac{T_c}{T_s} \right)^{\frac{\gamma}{\gamma - 1}}. \quad (6)$$

We have calculated such models for several values of  $T_s$  and  $T_c$ , the values of  $z_*$  and  $P_*$  quoted from Menzel and de Vaucouleurs [2], and composition ranging from pure  $\text{N}_2$  or  $\text{Ne}$  to pure  $\text{CO}_2$ .

If a predominantly  $\text{N}_2$  or  $\text{Ne}$  atmosphere is assumed, the isothermal scale height  $H_i$  is large and the extrapolated surface pressure  $P_s$  is very small; if  $\text{CO}_2$  dominates, the mean molecular weight is large,  $H_i$  is small, and  $P_s$  is large. We shall show that setting the height of the occulting layer at 113 km forces  $\text{CO}_2$  to be a major atmospheric constituent if the mechanical model is to agree with observations of infrared spectra.

Absolute lower limits to the surface pressure and CO<sub>2</sub> abundance follow from the observation by Connes [3] that effective pressure of the reflecting layer is  $80 \pm \frac{100}{40}$  mb, in good agreement with the cloud-top pressure of 90 mb [4] obtained polarimetrically. Obviously the surface pressure cannot be less than 80 mb. If we adopt the Connes [3] value for the temperature of the tropopause (or "cloud top")  $T_c = 240^\circ \text{K}$  and assume  $T_s = 700^\circ \text{K}$ , we find  $P_s = 80$  mb for pure N<sub>2</sub> or for an atmosphere of 24 percent CO<sub>2</sub> and 76 percent Ne. If we assume that the effective pressure of the cloud tops is half of the pressure at the cloud tops (as is true of a purely absorbing atmosphere), then we could obtain  $P_s = 160$  mb for either (3 percent CO<sub>2</sub> + 97 percent N<sub>2</sub>) or (30 percent CO<sub>2</sub> + 70 percent Ne). This is illustrated in Figure 1.

If we assume a colder atmosphere, pure N<sub>2</sub> gives 160 mb or more pressure at the surface; but, if neon dominates, at least 16 percent CO<sub>2</sub> is needed to give  $P_s = 80$  mb even with  $T_c = 220^\circ$  and  $T_s = 675^\circ \text{K}$ . Higher temperatures and pressures require more CO<sub>2</sub>. If we require that the surface pressure exceed 1.0 bar, we need at least 28 percent CO<sub>2</sub> with N<sub>2</sub>, or 47 percent CO<sub>2</sub> with Ne, assuming the (240°, 700°) temperature model. We conclude that CO<sub>2</sub> is a major constituent of the atmosphere, in agreement with reference 3.

Now suppose that we identify the tropopause pressure with the cloud-top pressure of 80 mb derived by reference 3. Figures 2 and 3 show the cloud-top pressure as a function of the molar fraction of CO<sub>2</sub> for Ne and N<sub>2</sub> atmospheres. For the (240°, 700°) temperature model,  $P_c = 80$  mb corresponds to  $P_s = 5.0$  bars and  $f_{\text{CO}_2} = 50$  percent if the remainder is N<sub>2</sub>, or 2.5 bars and 56 percent CO<sub>2</sub> if the rest is neon. Increasing the pressure at the tropopause (or the surface) by a factor of two results in only a 10 percent increase in the CO<sub>2</sub> abundance; increasing the cloud-top temperature by 20° increases the CO<sub>2</sub> abundance by 15 percent and decreases the surface pressure by 12 percent. It therefore seems likely that half or more of the atmosphere of Venus is CO<sub>2</sub>.

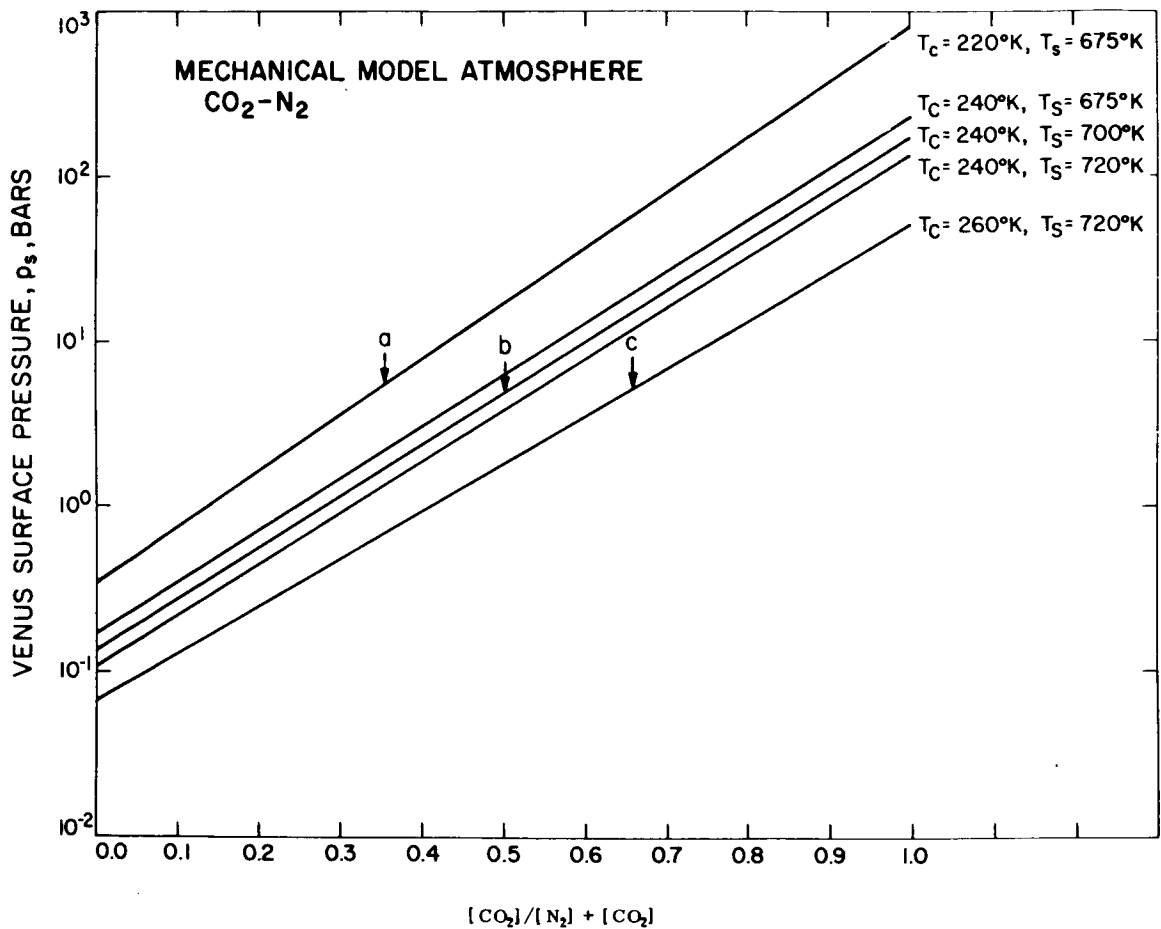


FIGURE 1. THE SURFACE PRESSURE OF VENUS FOR A DRY ATMOSPHERE OF CARBON DIOXIDE AND NITROGEN AS A FUNCTION OF CO<sub>2</sub> CONCENTRATION. (THE CURVES (T<sub>c</sub> = 220° K, T<sub>s</sub> = 675° K) AND (T<sub>c</sub> = 260° K, T<sub>s</sub> = 720° K) ARE FOR THE EXTREMES OF TEMPERATURE CONSIDERED IN THE MECHANICAL MODELS. THE POINTS LABELED a, b, AND c CORRESPOND TO THOSE OF FIGURE 2.)

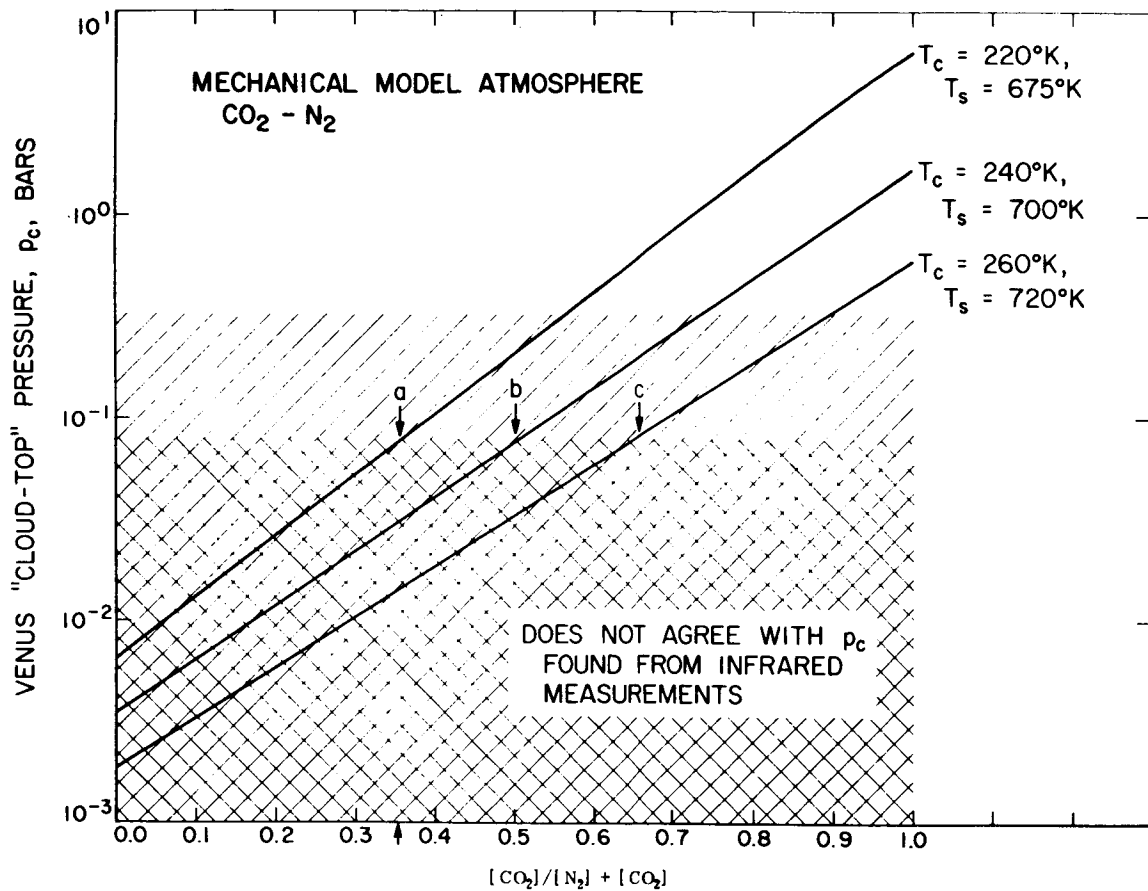


FIGURE 2. THE CLOUD-TOP PRESSURE OF VENUS FOR A DRY ATMOSPHERE OF CARBON DIOXIDE AND NITROGEN AS A FUNCTION OF CO<sub>2</sub> CONCENTRATION. (THE POINTS LABELED a, b, AND c CORRESPOND TO P<sub>c</sub> = 80 mb, AND THE ARROW INDICATES THE ABSOLUTE MINIMUM CONCENTRATION OF CO<sub>2</sub> FOR THE TEMPERATURES USED IN THE MECHANICAL MODELS.)

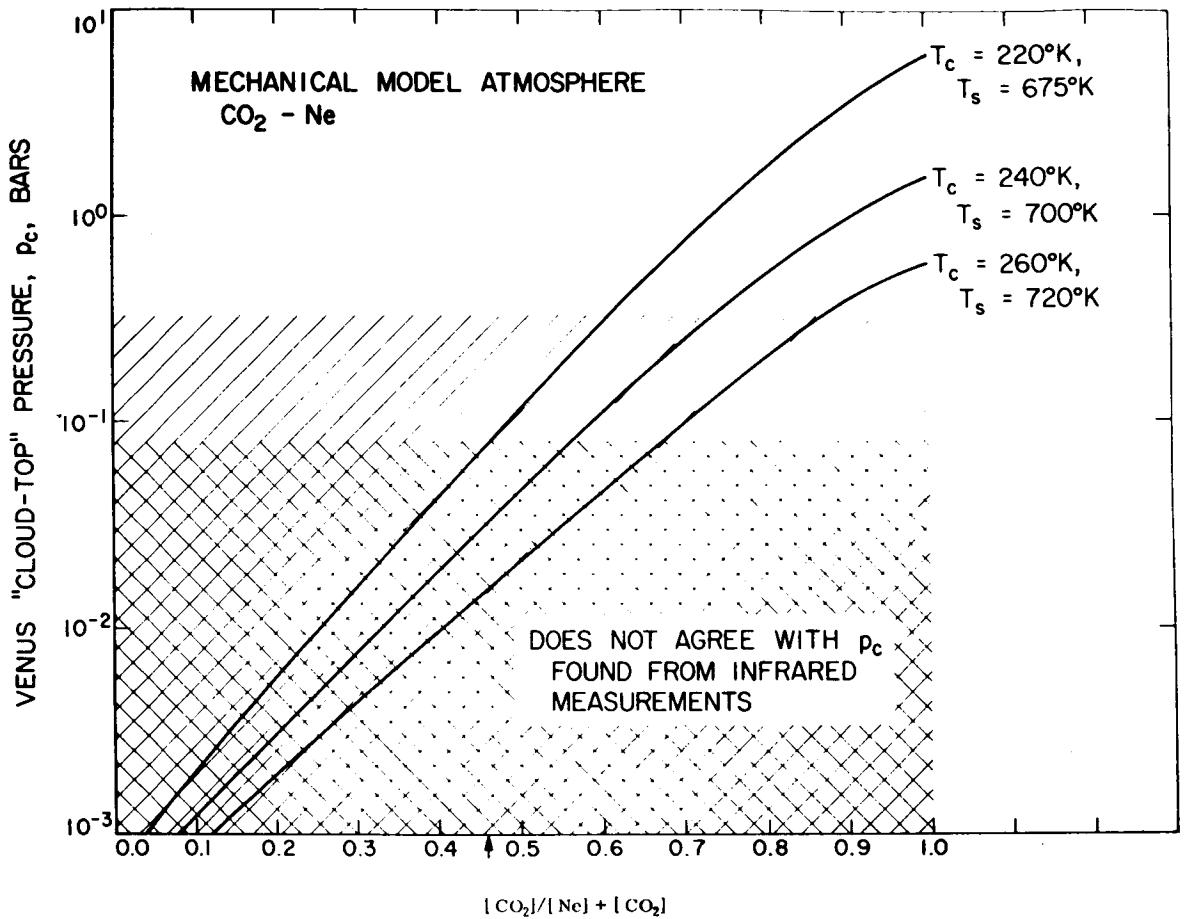


FIGURE 3. THE CLOUD-TOP PRESSURE OF VENUS FOR A DRY ATMOSPHERE OF CARBON DIOXIDE AND NEON AS A FUNCTION OF CO<sub>2</sub> CONCENTRATION. (THE DOUBLY CROSSHATCHED REGION IS IN DEFINITE DISAGREEMENT WITH THE INFRARED OBSERVATIONS OF  $P_c = 80$  mb, WHILE THE SINGLY CROSSHATCHED REGION COULD DISAGREE WITH THE UPPER LIMIT TO THE CLOUD-TOP PRESSURE OF  $P_c \leq 320$  mb. )

# MICROWAVE MODEL ATMOSPHERES

## Pressure-Induced Absorption

Ho, Kaufman and Thaddeus [5] made laboratory measurements of the absorption coefficient for pressure induced absorption of CO<sub>2</sub> over temperature and pressure range that is consistent with the lower atmosphere of Venus. They obtained the following expression:

$$\alpha = p^2 \omega^2 (273/T)^5 (15.7 f_{\text{CO}_2}^2 + 3.90 f_{\text{CO}_2} f_{\text{N}_2} + 2.64 f_{\text{CO}_2} f_{\text{Ar}} + 0.085 f_{\text{N}_2}^2 + 1330 f_{\text{H}_2\text{O}}) \times 10^{-8} \text{ cm}^{-1}, \quad (7)$$

where  $p$  is the pressure in bars,  $\omega$  is the frequency in  $\text{cm}^{-1}$ ,  $T$  is the temperature in  $^\circ\text{K}$ , and  $f_{\text{CO}_2}$ , etc., are the various molar fractions. Ho, Kaufman and

Thaddeus then used this expression to calculate the brightness temperature as a function of wavelength for Venus and obtained a satisfactory fit to the observed microwave spectrum (see Fig. 4). Ho, Kaufman and Thaddeus assumed an isothermal stratosphere with  $T_c = 250^\circ\text{K}$  and an adiabatic lower atmosphere with

$T_s = 675^\circ\text{K}$ . The other atmospheric parameters were identical with those of our mechanical model. Ho, Kaufman and Thaddeus conclude that "water vapor can account for the microwave spectrum only if water is several orders of magnitude more abundant than the infrared studies suggest, "i. e., that some other molecular absorber is required in order to fit the microwave spectra and that pressure induced absorption of carbon dioxide is a likely explanation.

We can combine the results of our mechanical model atmosphere with the results of Ho, Kaufman and Thaddeus. This is shown in Figure 5 where we have used Equation (17) of Ho, Kaufman and Thaddeus which relates the surface pressure to the atmospheric composition. For the dry CO<sub>2</sub> - N<sub>2</sub> model atmosphere, these two models can be satisfied simultaneously only if the atmosphere contains 74 percent CO<sub>2</sub> and has a surface pressure of 25 bars. For the dry CO<sub>2</sub> - Ne atmosphere, we find 78 percent CO<sub>2</sub> and a surface pressure of 25 bars. If any other molecules are present in the Cytherean atmosphere that can absorb in the microwave region, then the above results represent an absolute upper limit to the surface pressure.



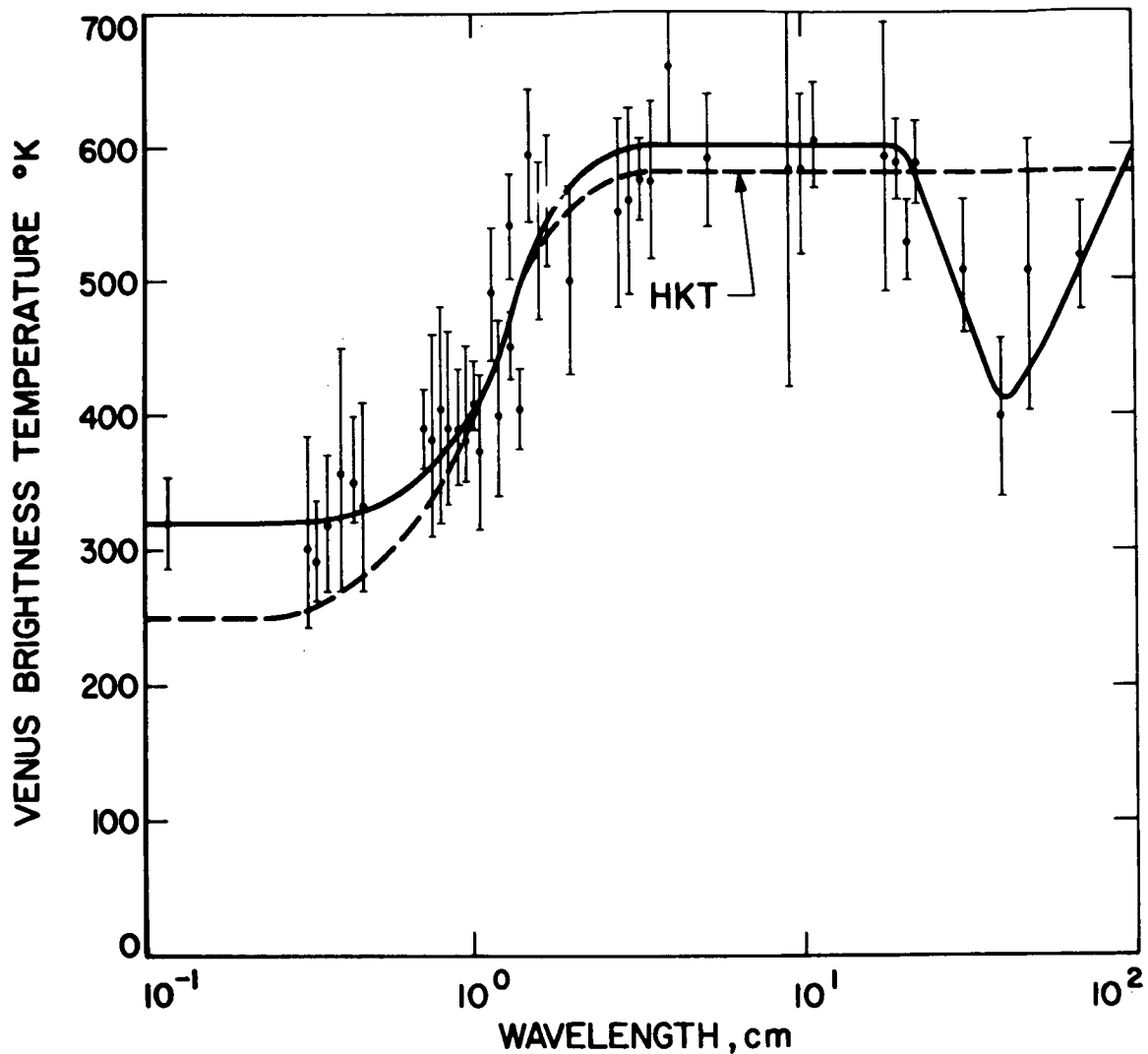


FIGURE 4. THE OBSERVED MICROWAVE BRIGHTNESS TEMPERATURE OF VENUS, SHOWN APPROXIMATELY BY THE SOLID CURVE, AND THE MICROWAVE BRIGHTNESS TEMPERATURE COMPUTED FOR PRESSURE-INDUCED ABSORPTION (DASHED CURVE LABELED HKT). (BECAUSE OF THE CONSIDERABLE UNCERTAINTIES OF THE MICROWAVE DATA, THE AGREEMENT BETWEEN THE SOLID AND DASHED CURVES IS CONSIDERED TO BE SATISFACTORY.)

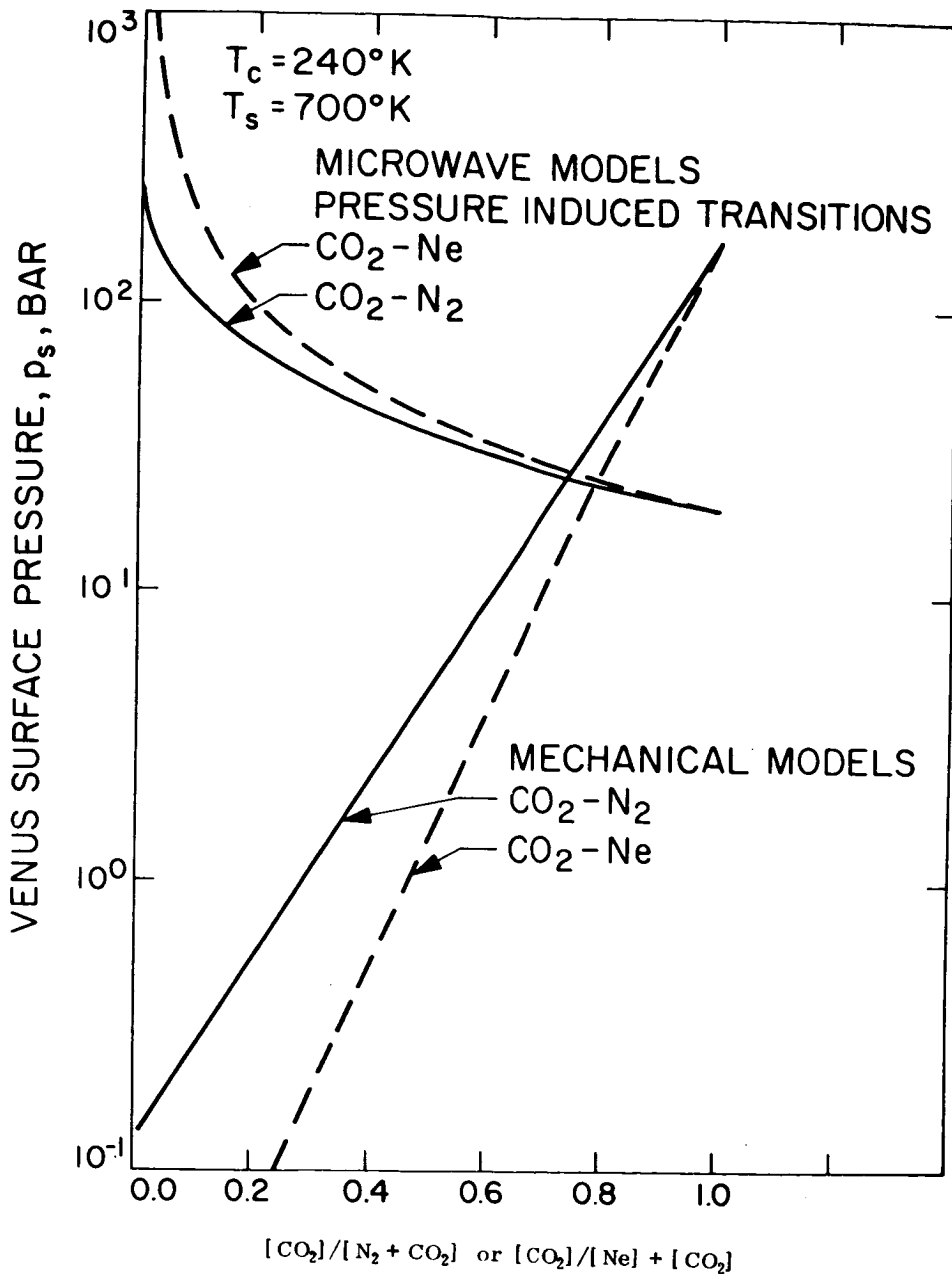


FIGURE 5. THE SURFACE PRESSURE OF VENUS AS A FUNCTION OF CARBON DIOXIDE CONCENTRATION AS GIVEN BY MECHANICAL MODELS AND BY THE MICROWAVE MODEL FOR PRESSURE-INDUCED ABSORPTION. (FOR EITHER CO<sub>2</sub>+N<sub>2</sub> (SOLID CURVES) OR CO<sub>2</sub>+Ne (DASHED CURVES) ATMOSPHERES, THE RESULTS AGREE ONLY FOR  $P_s \approx 25$  BARS.)

The recent discovery of HCl, and HF by Connes [3], and the presence of CO in the Connes near-infrared Venus spectra suggested the possibility that the microwave spectrum of Venus could be accounted for by the pure rotation spectrum of these trace constituents.

## Pure Rotation Spectra

The pure rotation spectrum of HCl<sup>35</sup>, HF and CO was calculated by the method described in Appendix B, and the contribution to the total opacity was compared with that due to the pressure induced absorption of carbon dioxide.

Figure 6 shows the diffuse transmission  $T_{s \rightarrow c}$  computed for the highest allowable value of the surface pressure,  $P_s = 25$  bar,  $T_s = 700^\circ$  K,  $P_c = 0.1$  bar and  $T_c = 240^\circ$  K. The diffuse transmission is given by

$$\tau_{s \rightarrow c}(\omega) \equiv 2 E_3 (\tau_{s \rightarrow c}(\omega)). \quad (8)$$

Here,  $\tau_{s \rightarrow c}(\omega)$  is the total optical depth:

$$\tau_{s \rightarrow c}(\omega) \equiv \sum_k \sum_J \int_s^c S_{J,k} \gamma_k dm_k \cdot f(\omega - \omega_J) / \bar{\gamma}_k, \quad (9)$$

where the contributions of all lines (J) of all species (k) are summed for each wave number. The dashed curve was drawn in between the computed points to indicate the general variation of this transmission with wavelength.

Figure 7 illustrates how the transmission from a particular level in the atmosphere to the "cloud-top" varies throughout the atmosphere and also shows the brightness temperature corresponding to each level in the atmosphere. This is shown for  $\lambda = 1$  mm ( $\omega = 10$  cm<sup>-1</sup>) and the model atmosphere used in Figure 6. Figure 8 shows the Venus brightness temperature  $T_{Br}$  computed for the same model with the additional assumptions that the reflectivity  $\rho_s$  of the planet surface is 0.1 and the line wing absorption is 10 percent greater than that predicted by the VanVleck - Weisskopf theory:

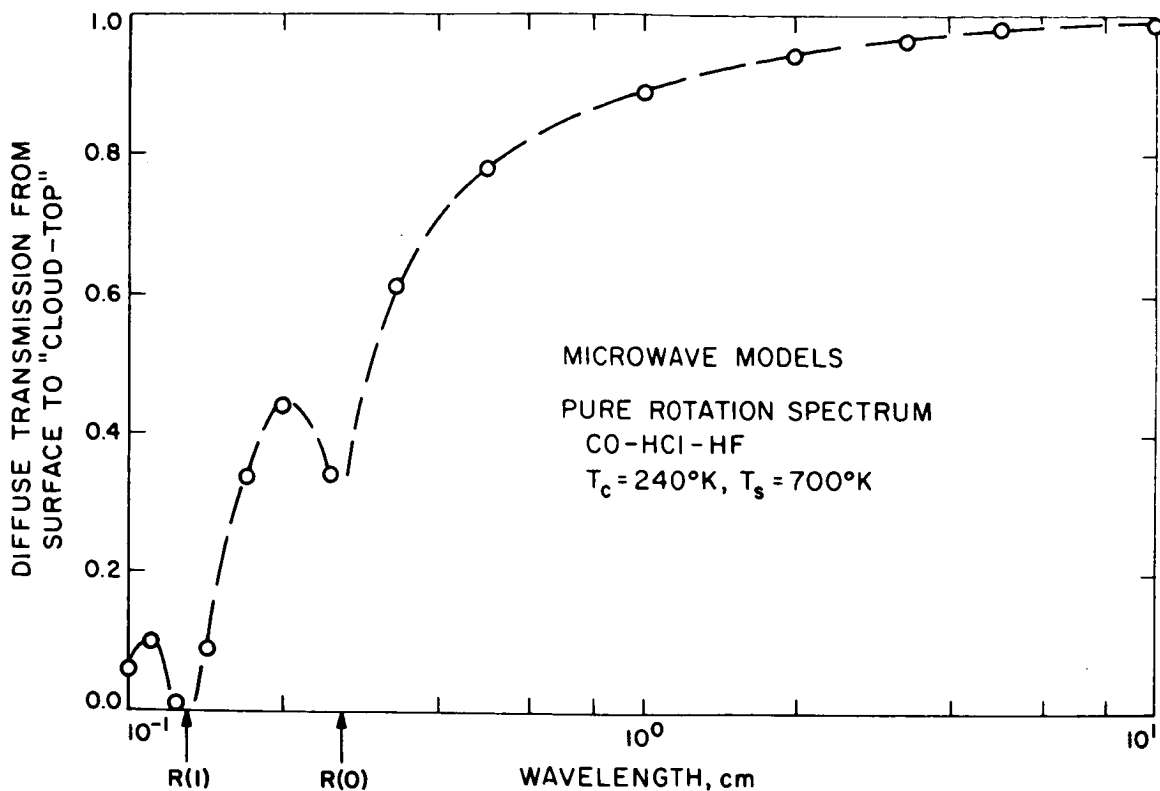


FIGURE 6. DIFFUSE TRANSMISSION FROM THE SURFACE OF THE PLANET TO THE CLOUD TOPS DUE TO THE PURE ROTATION SPECTRA OF CO, HCl<sup>35</sup> AND HF. (COMPUTED FOR THE UPPER LIMIT TO THE SURFACE PRESSURE OF 25 BARS AND A CLOUD-TOP PRESSURE OF 100 mb.)

$$T_{\text{Br}} = T_s \rho_s T_{s \rightarrow c} + \sum_L \epsilon_L T(L) T_{L \rightarrow c} + \rho_s T_{s \rightarrow c} \sum_L \epsilon_L T(L) T_{L \rightarrow s}, \quad (10)$$

where  $\epsilon_L$  is the emissivity of the level due to all lines of species and  $T(L)$  is the temperature of the level. It is apparent that the pure rotation spectrum of these trace species alone does not give a large contribution to the opacity at 1 cm. When the brightness temperature is computed for a model atmosphere which includes both the pressure induced absorption of CO<sub>2</sub> and the pure rotation spectrum of the minor constituents of the atmosphere, we must conclude that pressure-induced absorption of CO<sub>2</sub> is the main source of the microwave opacity of the Venus atmosphere for wavelengths longer than 5 mm.

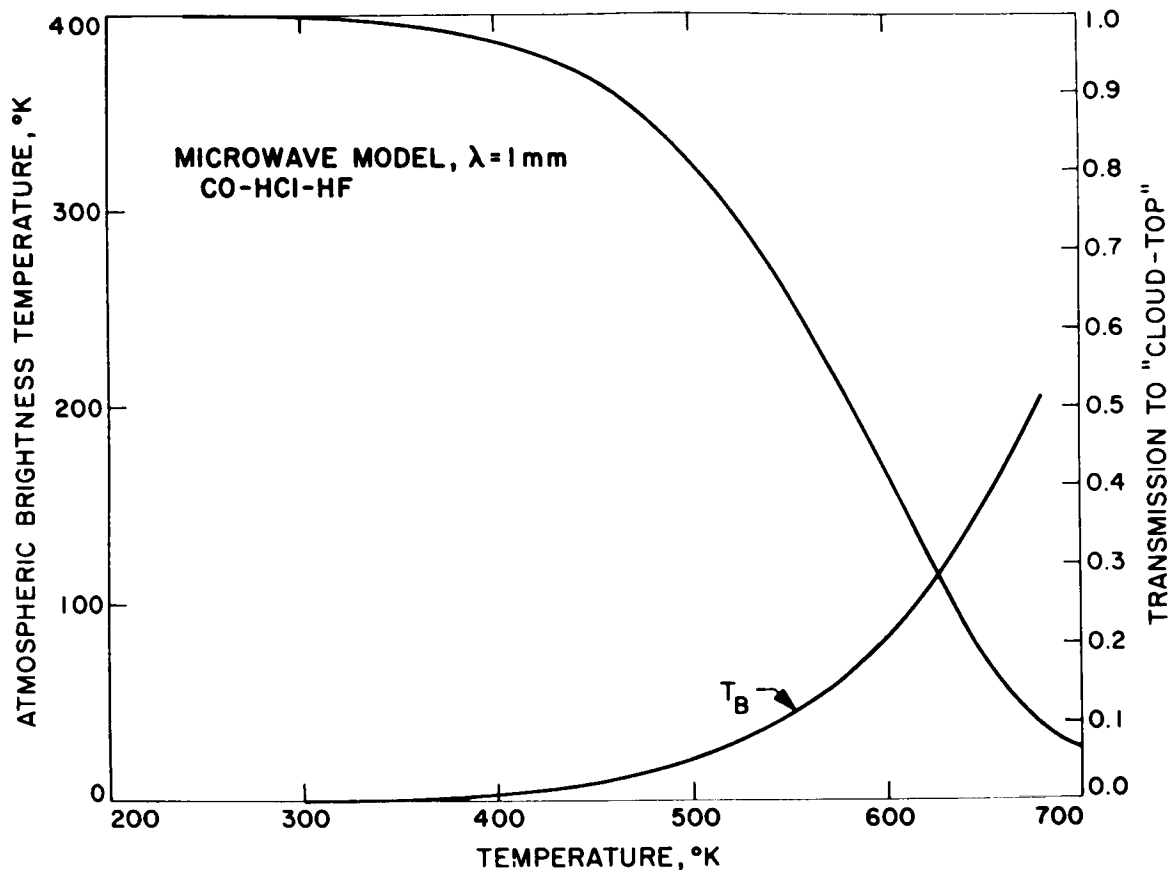


FIGURE 7. TRANSMISSION FOR LAYERS IN THE VENUS ATMOSPHERE TO THE CLOUD TOP, AND THE BRIGHTNESS TEMPERATURE OF EACH LAYER, AS A FUNCTION OF THE TEMPERATURE OF THE ATMOSPHERIC LAYERS. (COMPUTED FOR  $T_s = 700^\circ\text{K}$ ,

$$P_s = 25 \text{ BAR}, T_c = 240^\circ\text{K}, P_c = 100 \text{ mb.})$$

## DISCUSSION

It is apparent that only a limited range of models is capable of satisfying simultaneously the optical, infrared, radio and radar data. Certainly the surface pressure must be less than 25 bars, and  $\text{CO}_2$  must make up about one-half or two-thirds of the atmosphere. Since we have considered the microwave opacity due to only a limited number of lines of CO, HCl, HF and  $\text{CO}_2$ , the actual total absorption coefficient must be somewhat higher, and the true surface

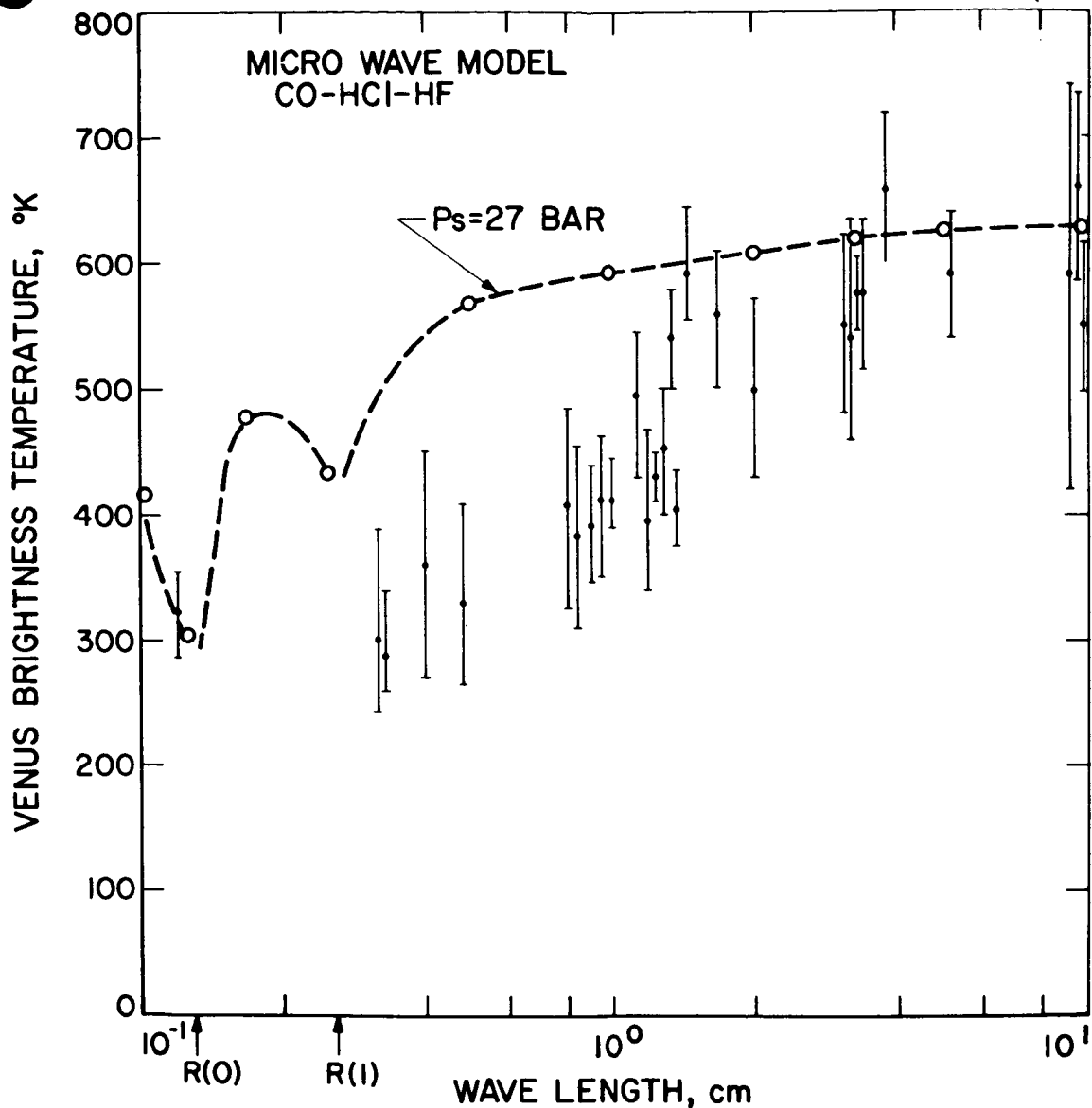


FIGURE 8. BRIGHTNESS TEMPERATURE OF THE VENUS ATMOSPHERE DUE TO TRACE CONSTITUENTS ALONE. (THIS WAS COMPUTED FOR A SURFACE PRESSURE SLIGHTLY HIGHER THAN THE UPPER LIMIT OF  $P_s = 25$  BAR BECAUSE THE LINE WING ABSORPTION HAS BEEN OBSERVED TO BE HIGHER THAN THAT PREDICTED THEORETICALLY. ALSO SHOWN IS THE OBSERVED MICROWAVE BRIGHTNESS TEMPERATURE.)

pressure must be appreciably lower than 25 bars. We emphasize that any additional microwave opacity due, for example, to water vapor or cloud particles must force the surface pressure downward in the microwave models. A subadiabatic temperature gradient in the tropopause has a similar effect on the mechanical models.

At the same time, the cloud-top pressures derived from the Connes spectra and from optical polarimetry set lower limits on the surface pressure. If we are not to have a cloud-top pressure less than 80 mb, our mechanical models require surface pressures of at least 5 bars if  $N_2$  is the remaining major constituent, or about 2.5 bars if neon is the remainder; in no case can  $CO_2$  be less than about 44 percent of the total. Thus, there is a limit to the amount of additional microwave opacity that can be present. However, since our microwave models give rather high cloud-top pressures, a small amount of additional opacity probably exists. It seems likely, therefore, that the true surface pressure lies in the range of 10-20 bars, and that  $CO_2$  is about 45-65 percent of the atmosphere. We cannot say whether the rest is mostly nitrogen or neon.

We have said nothing so far about the greenhouse effect which presumably is responsible for the high surface temperature. Historically, this was one reason for introducing very high ( $> 100$  bars) surface pressures, since an enormous amount of pressure broadening was required to produce the necessary infrared opacity from  $CO_2$ , alone or with water. We do not believe that large amounts of water are present. However, the recently discovered minor constituents HCl, HF, and CO will produce considerable infrared opacity, some  $H_2O$  may be present, and there may be more such components to be discovered. One should remember that the greenhouse opacity in the earth's atmosphere is almost entirely due to trace constituents:  $CO_2$  ( $\sim 10^{-4}$ ),  $H_2O$  ( $\sim 10^{-3}$ ), and even  $O_3$  ( $\sim 10^{-6}$ ) are the major contributors, but even rarer constituents make a significant contribution. Since Venus has a surface pressure an order of magnitude higher than ours, gases with fractional abundances ten to a hundred times lower may make substantial contributions to the Venus greenhouse effect. Since we do not claim to know all gases on Venus with fractional abundances  $\geq 10^{-8}$ , we feel it would be premature to say that our surface pressures are inadequate to provide the necessary infrared opacity.

Leaving the greenhouse problem open, we believe our models satisfy all the observational data and are probably close to actual conditions on Venus. We wish to emphasize that our main results are based on direct, reliable data. The occultation radius is based on timings at many observatories. Similarly, the radio spectrum is based on many different observations. The radar radius

ould have to contain a large systematic error to affect our conclusions. We have used the spectroscopic and polarimetric cloud-top data only as a check on the consistency of our models; thus, our upper limit on  $P_s$  does not depend on these data, on assumptions about the actual level at which reflection or absorption occurs in the clouds, or on the nature of the cloud particles.

## ACKNOWLEDGMENTS

Dr. Eugene E. Epstein kindly supplied us with data for the most recent measurements of Venus brightness temperature obtained in the microwave region. We would particularly like to thank Dr. Lewis D. Kaplan for his help with the model atmosphere radiative transfer program. Dr. Robert H. Norton wrote the subroutine we used to calculate the generalized exponential integral for non-integer orders, and a discussion with Dr. George Birnbaum on absorption in the microwave region was most enlightening.



## APPENDIX A. THE CLOUDS OF VENUS

## Clouds of Ice Crystals or Water Vapor

Bottema, Plummer, Strong and Zander [6] and Strong [7] used a balloon-borne telescope to obtain a low resolution spectrum of Venus in the 1.7-3.4  $\mu$  region. They compared this spectrum with a laboratory spectrum of ice crystals and concluded that the spectra were in good agreement. They also found an upper limit to the amount of water vapor present in the atmosphere of 52 to 222  $\mu$  precipitable water. On the other hand, Moroz [8-11] took many low resolution spectra of Venus and concluded that the clouds could not be composed of ice particles because "ice bands at 1.5  $\mu$  and 2  $\mu$  did not appear in the Venus spectra" and these bands show up clearly in the spectrum of terrestrial cirrus clouds. Kuipers [12] obtained Venus spectra from 1 to 2.5  $\mu$ , and made laboratory measurements on the reflection spectrum of small H<sub>2</sub>O crystals. He found that "the Venus spectra were incompatible with ice clouds." Deirmendjian [13] computed the microwave extinction for ice particles and water droplets and compared his calculations with the observed microwave extinction of Venus. Because of the low extinction cross sections for the ice particles, he found that such a cloud must have a depth of greater than 300 km if it alone was the cause of the microwave extinction.\* If the clouds are composed of water droplets, Deirmendjian estimated their content to be 10<sup>5</sup>  $\mu$  precipitable water and that the surface pressure of the sustaining atmosphere might be as low as 3 bars. Sagan and Pollack [14] found they could reproduce the observed albedo of Venus in the visible and near-infrared with ice crystals of 7.5  $\mu$  diameter and with water droplets only if the cloud temperatures were  $T_c < 280^\circ \text{K}$ . In order to provide sufficient greenhouse effect to maintain surface temperatures  $\sim 700^\circ \text{K}$ , assuming water vapor clouds, Sagan and Pollack [14] found 10 cm precipitable water was needed.

The recent discovery [3] of HCl and HF in the Cytherean atmosphere led Welch and Rea [15] to investigate the effect of these trace constituents dissolved in water on the radar measurements of Venus. It is known that long-wavelength radar signals reach the surface of that planet, and Welch and Rea [15] found that

---

\* Our mechanical models have 40 - 55 km of clouds.

HCl dissolved in water gave essentially the same results as have been obtained for liquid water cloud models [13 and 16]. Approximately 10 cm precipitable water are needed in the Venus atmosphere to account for the microwave spectrum.

Recent spectroscopic studies have given the following upper limits to the amount of precipitable water present in the total absorption path in the Venus atmosphere:  $240 \mu$  (Spinrad, 1962),  $317 \mu$  [17],  $20 \mu$  [3], and  $< 10 \mu$  [12]. We feel that these observations and the water vapor cloud model are not necessarily incompatible.

## Dust Clouds

Dust clouds could be composed of hygroscopic particles which, R. Gallet has pointed out, would have the desirable property of removing water vapor from the Venus atmosphere. Sagan and Pollack [14] considered several model atmospheres for Venus in an attempt to fit the limb-darkening in the 8-13 micron region, observed during the Mariner fly-by. They found that the observations could be fitted either by a model which considered only molecular absorption above the clouds or by a model which considered multiple scattering by the cloud particles. For values of the albedo for single scattering  $0 < \tilde{\omega} < 0.95$ , a good fit was obtained if a distance of 3.3 km was used for the optical depth in the clouds to become equal to 1, i. e., if the clouds are very thin compared to terrestrial clouds, where this distance is typically 50 m. Only if  $\tilde{\omega} \gg 0.99$  did the distance for unit optical depth in the Venus atmosphere become less than 1 km. A very high value of  $\tilde{\omega}$  is not consistent with the observed color of the planet (see below), which indicates appreciable absorption. On the other hand, smaller values of  $\tilde{\omega}$  and large distances for unit optical depth are characteristic of dusty conditions in dry areas on earth.

The yellow color of Venus compared to the sun ( $\Delta (B-V) \sim 0.2$ ) is a strong argument in favor of dust clouds, which are yellowish because of the strong blue and violet absorptions of many common minerals. The ultra-violet reflectivity of Venus is only 2/3 that in the visible [18], and a considerable part of this ultraviolet must be due to Rayleigh scattering from the gas above the clouds if the cloud-top pressure of  $\sim 80$  mb [3] is correct. This pressure is similar to the value of 90 mb deduced from polarimetric data alone [4]. Finally, the polarimetric data for Venus require nearly transparent particles with smaller diameters than are usually found in water clouds on earth.

## APPENDIX B. PURE ROTATION SPECTRUM OF DIATOMIC MOLECULES

For diatomic and linear polyatomic molecules, the rotational line intensity  $S_J$  is given by

$$S_J = L \omega_J (J+1) (2hcB/kT) \exp [-J (J+1) (hcB/kT)] \\ \times [1 - \exp (-hc\omega_J/kT)], \quad (B-1)$$

where  $L \equiv 11.1908 \mu^2$  has units of  $(\text{cm atm})^{-1}$  for the dipole moment  $\mu$  in Debyes. Here  $h$  is Planck's constant,  $c$  is the velocity of light,  $k$  is Boltzmann's constant,  $B$  is the rotational constant of the molecule,  $T$  is the temperature in  $^\circ\text{K}$  and  $\omega_J$  is the position of the  $J$ -th rotational line, in  $\text{cm}^{-1}$ , given by

$$\omega_J = 2B(J+1) - 4D(J+1)^3. \quad (B-2)$$

When the spectrum of the molecules had been studied in the microwave region, we used the observed line positions in our calculations, but when it had not been measured, we computed it from Equation (B-2) and the constants given in Table B-I. The pure rotational spectrum of HF was measured by Rothschild [19]. He found a larger value of the apparent halfwidth than that given in Table B-I, but we have used the latter value in our calculations. Palik and Rao [20] have measured CO and Jones and Gordy [21] have measured both CO and HCl.

TABLE B-I. SPECTROSCOPIC CONSTANTS

molecule	$\mu$ Debyes	$B$ $\text{cm}^{-1}$	$D$ $\text{cm}^{-1}$	$\gamma^\circ$ $\text{cm}^{-1}/\text{Bar}$	$\left(\frac{dm}{dp}\right)^\circ_j$ $\text{cm atm}/\text{Bar}$
CO	$0.12^a$	$1.922521^b$ $1.921199^d$	$-6.1193 \times 10^{-6}^b$	$.0965^c$ $.0581^e$	340
HCl <sup>35</sup>	$1.085^a$	$10.43304^f$	$-5.2828 \times 10^{-4}^g$	$.090^h$	2
HF	$.1.736^a$	$20.5534^i$	$2.114 \times 10^{-3}^i$	$.480^a$	0.02

- <sup>a</sup>Benedict and Herman [ 22]
- <sup>b</sup>Rank, St. Pierre and Wiggins [ 23]
- <sup>c</sup>Dowling and Hall [ 24]
- <sup>d</sup>Jones and Gordy [ 25]
- <sup>e</sup>Benedict, Herman, Moore and Silverman [ 26]
- <sup>f</sup>Jones and Gordy [ 25]
- <sup>g</sup>Rank, Rao and Wiggins [ 27]
- <sup>h</sup>Benedict, Herman, Moore and Silverman [ 28]
- <sup>i</sup>Kuipers, Smith and Nielsen [ 12]

<sup>j</sup>The mixing ratios were obtained from [ 3] and the Connes spectra. Because of the uncertain path length in the Venus atmosphere, these numbers are probably not accurate in absolute value to more than an order of magnitude. But the relative concentrations are correct.

Assuming that the centrifugal stretching term, D, is small enough that the line positions are given by the first term of Equation (B-2), we can rewrite Equation (B-1) as

$$S_J \approx L \omega_J^2 (hc/kT) \exp(-hc\omega_J J/2kT) \left[ 1 - \exp\left(\frac{-hc\omega_J J}{kT}\right) \right] \quad (\text{B-3})$$

For a constant lapse rate in the atmosphere, we can relate the temperature and pressure in the atmosphere by

$$p = p_s \left( \frac{T}{T_s} \right)^\kappa, \quad (\text{B-4})$$

where  $\kappa = \gamma/(\gamma-1)$  for an adiabatic lapse rate and  $\gamma = C_p/C_v$  is the ratio of specific heats. If a constant mixing ratio is assumed for the atmosphere, we can write

$$dm = \left( \frac{dm}{dp} \right)_o dp \quad . \quad (B-5)$$

We further assume that the variation of half-width  $\gamma$  with pressure and temperature is given by the kinetic theory:

$$\gamma = \gamma^o (p/p_o) (T_o/T)^{1/2} \quad , \quad (B-6)$$

where  $p_o = 1$  Bar and  $T_o = 300^\circ K$ . Kaplan [29] has shown that if  $T$  is chosen as the variable of integration, the following equations result:

$$\int_{m_1}^{m_2} S dm = A_1 \left\{ \left( \frac{T_2}{T_o} \right)^{\kappa-1} [ E_{\kappa-1} (hc\omega_J J/2kT_2) - E_{\kappa-1} (hc\omega_J (J+2)/2kT_2) ] \right. \\ \left. - \left( \frac{T_1}{T_o} \right)^{\kappa-1} ( E_{\kappa-1} (hc\omega_J J/2kT_1) - E_{\kappa-1} (hc\omega_J (J+2)/2kT_1) ) \right\} \quad (B-7)$$

and

$$\int_{m_1}^{m_2} S \gamma dm = A_2 \left\{ \left( \frac{T_2}{T_o} \right)^{\frac{4\kappa-1}{2}} [ E_{\frac{4\kappa-1}{2}} (hc\omega_J J/2kT_2) - E_{\frac{4\kappa-1}{2}} (hc\omega_J (J+2)/2kT_2) ] \right. \\ \left. - \left( \frac{T_1}{T_o} \right)^{\frac{4\kappa-1}{2}} [ E_{\frac{4\kappa-1}{2}} (hc\omega_J J/2kT_1) - E_{\frac{4\kappa-1}{2}} (hc\omega_J (J+2)/2kT_1) ] \right\} \quad (B-8)$$

where the  $E_\nu$  function is the generalized exponential integral.

The constants  $A_1$  and  $A_2$  are given by

$$A_1 = (L \omega_J^2 hc/k) \left( \frac{dm}{dp} \right)_o (P_s/kT_s) \quad (B-9)$$

$$A_2 = A_1 \gamma_o (P_s/P_o) (T_o/T_s)^{1/2} \quad (B-10)$$

Thus, we can obtain the value of the mean half-width appropriate for computing the emissivity of any level of the atmosphere and the half-width to be used in computing the transmission between various levels in the atmosphere, etc., from

$$\bar{\gamma} = \int S \gamma \, dm / \int S \, dm. \quad (\text{B-11})$$

We assume that the lines have a Van Vleck-Weisskopf [30] line shape factor

$$f(\omega - \omega_J) = \frac{\omega \bar{\gamma}}{\pi \omega_J} \left[ \frac{1}{(\omega - \omega_J)^2 + \gamma^2} + \frac{1}{(\omega + \omega_J)^2 + \bar{\gamma}^2} \right] \quad (\text{B-12})$$

and this expression may give too low a value for the absorption coefficient in the line wings of all three molecules. Maryott and Birnbaum [31] have recently found that for HCl the observed absorption is two to eight times greater than predicted by Van Vleck-Weisskopf [30] in the line wings.

## REFERENCES

1. Ash, M. E.; Schapiro, I. I.; Smith, W. B.: Astronomical Constants and Planetary Ephemerides Deduced from Radar and Optical Observations. *Astron. J.*, vol. 72, 1967, pp. 338-350.
2. Menzel, D. H. and de Vaucouleurs, G.: Final Report on the Occultation of Regulus by Venus, July 7, 1959. Scientific Report No. 1, ARDC Contract AF 19 (604)-7461, Jan 10, 1961 (AFCRL-227).
3. Connes, P.; Connes, J.; Benedict, W. S.; and Kaplan, L. D.: Traces of HCl and HF in the Atmosphere of Venus. *Astrophys. J.*, vol. 147, 1967, pp. 1230-1237.
4. Dollfus, A.: Chapter 9 of Planets and Satellites, ed. G Kuiper, Univ. of Chicago Press, 1961, pp. 343-399.
5. Ho, W.; Kaufman, I. A.; and Thaddeus, P.: Laboratory Measurement of Microwave Absorption in Models of the Atmosphere of Venus. *J. Geophys. Res.*, vol. 71, 1966, pp. 5091-5108.
6. Bottema, M.; Plummer, W.; Strong, J.; and Zander, R.: *Astrophys. J.*, vol. 140, 1964, p. 1640.
7. Strong, J.: Balloon Telescope Studies of Venus. Proceedings of the Caltech-JPL Lunar and Planetary Conference, 15 Jun 1966, pp. 147-149.
8. Moroz, V. I.: Recent Observations of Infrared Spectra of Planets (Venus 1-4 $\mu$ , Mars 1-4 $\mu$ , and Jupiter 1-6 $\mu$ ). *Mem. Soc. R. Sci. Liege*, vol. 9, 1964, p. 520.
9. Moroz, V. I.: Infrared Spectra and the Problem of Physical Conditions on the Surface of Venus. Proceedings of the XIIIth International Astronautical Congress, Varna 1962, Springer Verlag Wien, 1964.
10. Moroz, V. I.: New Observations of Infrared Spectrum of Venus. *Astr. Cirk.*, Moscow, no. 262, 1963, p. 6.

## REFERENCES (Continued)

11. Moroz, V. I.: New Observations of Infrared Spectrum of Venus (1.2-3.8 $\mu$ ). *Astr. Zu.*, vol. 41, 1964, p. 711.
12. Kuipers, G. A.; Smith, D. F.; and Nielsen, A. H.: Infrared Spectrum of Hydrogen Fluoride. *J. Chem. Phys.*, vol. 25, 1956, p. 275.
13. Deirmendjian, D.: A Water Cloud Interpretation of Venus' Microwave Continuum. *Icarus*, vol. 3, 1964, pp. 109-120.
14. Sagan, C.; and Pollack, J. B.: On the Nature of the Clouds and the Origin of the Surface Temperature of Venus. *Astron. J.*, vol. 71, 1966, p. 178.
15. Welch, W. J.; and Rea, D. G.: Upper Limits on Liquid Water in the Venus Atmosphere. *Astrophys. J.*, vol. 148, 1967, pp. 151-153.
16. Griffith, P. H.; Thornton, D. D.; and Welch, W. J.: The Microwave Spectrum of Venus in the Frequency Range 18-36 Gc/Sec. *Icarus*, vol. 6, 1967, pp. 175-188.
17. Belton, M. J. S.; and Hunten, D. M.: Water Vapor in the Atmosphere of Venus. *Ap. J.*, vol. 146, 1966, pp. 307-308.
18. Harris, D. L.: Chapter 8 of *Planets and Satellites*, ed. G. Kuiper. Univ. of Chicago Press, 1961, pp. 272-342.
19. Rothschild, W. G.: Pure Rotational Absorption Spectrum of Hydrogen Fluoride Vapor between 22 and 250 $\mu$ . *J. Opt. Soc. Amer.*, vol. 54, 1964, pp. 20-22.
20. Palik, E. D.; and Rao, K. N.: Pure Rotational Spectra of CO, NO, and N<sub>2</sub>O between 100 and 600 Microns. *J. Chem. Phys.*, vol. 25, 1956, pp. 1174-1175.
21. Jones, G.; and Gordy, W.: Extension of Submillimeter Wave Spectra of HCl and HBr. *Phys. Rev.*, vol. 136, 1964, pp. 1229-1232.



## REFERENCES (Concluded)

22. Benedict, W. S.; and Herman, R.: The Calculation of Self-Broadened Line Widths in Linear Molecules. *J. Quant. Spectry. Radiat. Transfer*, vol. 3, 1963, pp. 265-278.
23. Rank, D. H.; St. Pierre, A. G.; and Wiggins, T. A.: Rotational and Vibrational Constants of CO. *J. Mol. Spectry.*, vol. 18, 1965, pp. 418-427.
24. Dowling, J. M.; and Hall, R. T.: Far Infrared Interferometry: Upper Limit for Line Widths for the Pure Rotational Band of Carbon Monoxide. *J. Mole. Spectry.*, vol. 19, 1966, pp. 108-111.
25. Jones, G.; and Gordy, W.: Extension of Submillimeter Wave Spectros — copy below a Half Millimeter Wavelength. *Phys. Rev.*, vol. 135, 1964, pp. 295-298.
26. Benedict, W. S.; Herman, R.; Moore, G. E.; and Silverman, S.: The Strengths, Widths and Shapes of Lines in the Vibration-Rotation Bands of CO. *Astrophys. J.*, vol. 135, 1962, pp. 277-297.
27. Rank, D. H.; Rao, B. S.; and Wiggins, T. A.: Molecular Constants of HCl<sup>35</sup>. *J. Mol. Spectry.*, vol. 17, 1965, pp. 122-130.
28. Benedict, W. S.; Herman, R.; Moore, G. E.; and Silverman, S.: The Strengths, Widths, and Shapes of Infrared Lines. II. The HCl Fundamental. *Canad. J. Phys.*, vol. 34, 1956, p. 850.
29. Kaplan, L. D.: A Method for Calculation of Infrared Flux for Use in Numerical Models of Atmospheric Motion. The Rossby Memorial Volume, The Rockefeller Institute Press, New York, 1959.
30. Van Vleck, J. H.; and Weisskopf, V. F.: On the Shape of Collision-Broadened Lines. *Rev. Mod. Phys.*, vol. 17, 1945, p. 227.
31. Maryott, A. A.; and Birnbaum, G.: Line Shape and Collision Effects in the Microwave Wing of Far Infrared Rotational Lines. *J. Chem. Phys.* (in press), 1967.

## BIBLIOGRAPHY

- Bottema, M. ; Plummer, W. ; and Strong, J. : *Astrophys. J.*, vol. 139, 1964, p. 1021.
- Bottema, M. ; Plummer, W. ; and Strong, J. : *Ann. Astrophys.*, vol. 28, 1965, p. 225.
- Jesipov, V. F. ; and Moroz, V. I. : *Experiment of Spectrophotometry of Venus and Mars in the Interval 7000-10,000 A.* *Astr. Cirk.*, Moscow, No. 262, 1963, p. 1.

---

## DISCUSSION

A. Thomson: What frequencies are involved in the microwave measurements?

L. D. Gray: Our calculations were made from 0.1 wave number to 10 wave numbers.

A. Thomson: Can anyone comment on the potential of using such microwave measurements, for determining pressure in gas systems in which CO and H<sub>2</sub>O are both present (e. g. , in a flame), when one must view it through an atmospheric path? Is it possible to measure separately the constituents which would be characteristic of the flame but not characteristics of the atmosphere, for example, CO?

S. A. Golden: The biggest problem of microwave measurements in flames would be the presence of electrons in the flames. At these frequencies, the absorption of radiation by the free electrons would dominate molecular absorption.

---

# INFERENCE OF BAND STRUCTURES FROM LABORATORY DATA\*

N 68 - 18088

By

Thomas L. Altshuler  
NASA/Electronics Research Center

and

J. I. F. King  
GCA

---

## ABSTRACT

The probability distribution function (probability distribution of the ratio of absorption coefficients and harmonic absorption coefficient) for carbon dioxide in the 4.3 micron band was inferred from the data of Howard, Burch, and Williams [1]. First, the transmission versus optical thickness was determined by methods described by Altshuler [2]. The transmission data were then inverted by using Prony's algorithm in a manner similar to King [3]. This resulted in a series of multi-ramp profiles which were combined to yield a probability distribution function.

Both the Elsasser and Goody models were inverted to yield probability distribution functions. These were compared to the CO<sub>2</sub> function. From this, one can infer that some spectral line clustering exists in CO<sub>2</sub>. Furthermore, there is a finite probability that the absorption coefficient is zero for the CO<sub>2</sub> band and the Goody Model.

---

\* This work was done by both authors during the employment of Dr. Altshuler at Geophysics Corporation of America (GCA). The work was done for Air Force Cambridge Research Center under Contract No. AF 19(628)-5738.

## INTRODUCTION

A great deal of work has been done to devise spectral line models that approximate the behavior of real atmospheric gases. This approach has encountered several difficulties. First, because models do not completely describe the characteristics of real gas spectra, much information is lost. Second, these models are verified by superimposing laboratory data upon them. Since most of these data do not contain a sufficiently large range of optical thicknesses to directly verify the correctness of a model, serious errors may arise. These errors are most apparent for large optical thicknesses.

This paper describes gas spectra in terms of a probability distribution of absorption coefficients (probability distribution function), using laboratory data to determine this function. Furthermore, comparisons are made between the 4.3 micron band of carbon dioxide and the Elsasser and Goody Models.

## DESCRIPTION OF THE PROBABILITY DISTRIBUTION FUNCTION

Figure 1a shows a typical spectral line distribution of a real gas, where  $\kappa$  is the absorption coefficient and  $\nu$  is the frequency. Within a spectral region  $\Delta\nu$ , one can find a probability  $p$  in which  $\kappa$  is greater than a given value. This is plotted in Figure 1c, and is known as a probability distribution curve. A curve such as the one shown in Figure 1b also has the same probability distribution function as in Figure 1a. Because the curve in Figure 1b and its mirror image can be repeated without changing its probability distribution function, it is known as an equivalent repeatable line. Therefore, Figures 1b and 1c should have identical shapes. Also, in the case of the Elsasser Model (regular spectral line spacing), Figures 1a, 1b and 1c should have identical shapes provided that  $\Delta\nu$  is equal to half the distance between spectral lines. In other cases,  $\Delta\nu$  must be large enough to contain a representative distribution of  $\kappa$  versus  $\nu$  for the spectral band being considered. In practice,  $\Delta\nu$  should contain at least ten spectral lines.

Beer's law states that

$$\tau(Lu) = \int_{\Delta\nu} e^{-\kappa u} d\left(\frac{\nu}{\Delta\nu}\right) \quad (1)$$

for the region  $\Delta\nu$  in Figure 1a. Here,  $\tau$  is the transmission,  $L$  is a constant, and  $u$  is the optical thickness of the gas in question. If  $p \propto \frac{\nu}{\Delta\nu}$ , as justified in Figure 1, then equation (1) becomes

$$\tau(Lu) = \int_0^1 \left[ \exp - \left( \frac{\kappa}{L} \right) (Lu) \right] dp . \quad (2)$$

By knowing how  $\tau$  varies with  $Lu$ , the expression in equation (2) can be inverted to yield values of  $\frac{\kappa}{L}$  as a function of  $p$ . A series of ramps can be obtained through inversion by using Prony's algorithm, as shown by King [3]. To make this inversion, the transmission must be found for values of

$$Lu = r(\ell + q) , \quad (3)$$

where

$$\ell = 0, 1, 2, \dots, 2n - 1$$

$n$  = number of joints in the ramp function resulting from inversion

$q$  = constant, unity in this case

$r$  = ratio, arbitrarily chosen.

Here,

$$L = \frac{\pi S \alpha}{d^2} , \quad (4)$$

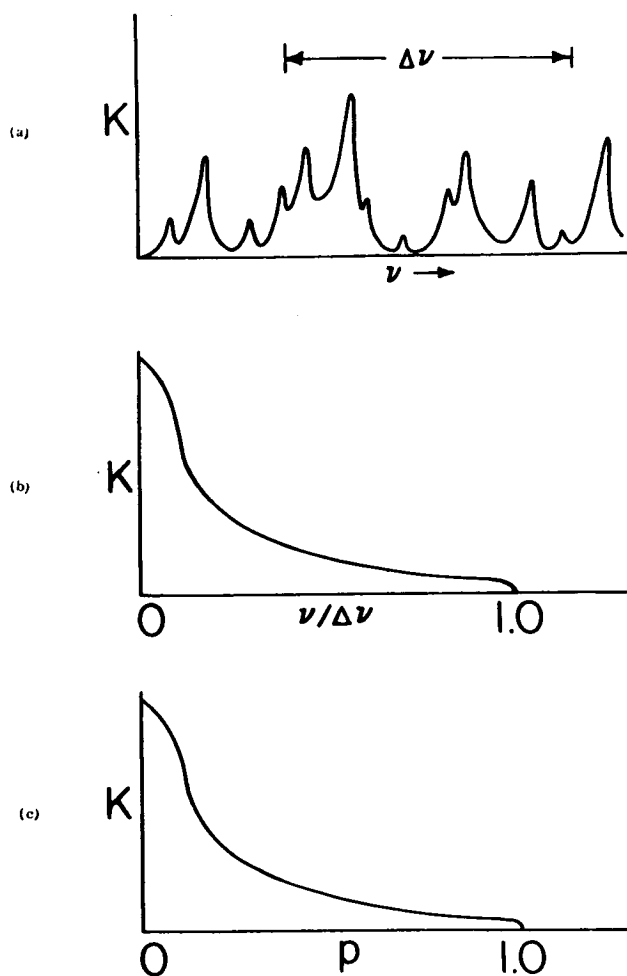


FIGURE 1

where

$S$  = average line intensity

$\alpha$  = average line half width

$d$  = average line spacing .

Figure 2 shows a series of ramp functions resulting from inversion of laboratory data of the 4.3 micron  $\text{CO}_2$  band by Howard, Burch and Williams [1].

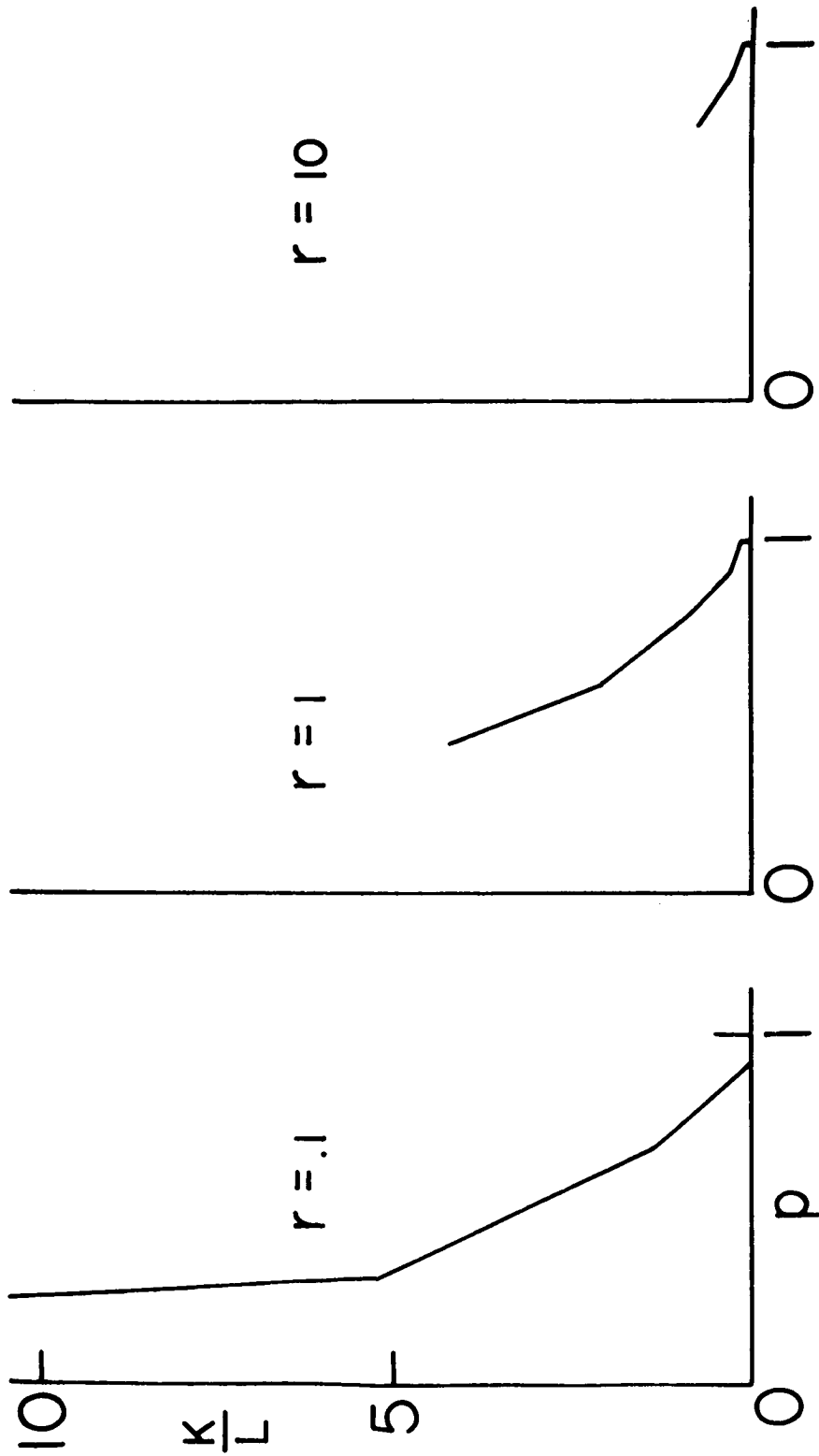


FIGURE 2



By varying  $r$ , we can change the distance between joints (see Figure 2). Variation in  $q$  will shift the position of the group of joints, thus permitting analysis of different regions. The ordinate is  $\frac{\kappa}{L}$  instead of  $\kappa$  so that all inversions resulting from the transmission at different wave number regions will describe a common curve.

Combining the ramp functions of Figure 2 will result in Figure 3. If many such combinations are made, a "best" smooth curve can be drawn in Figure 4. This curve does indeed describe the  $\frac{\kappa}{L}$  versus  $p$  function, as seen from Figure 5 for the Elsasser case. Here, two ramp models are combined. A comparison with the Elsasser model curve, which is known, shows a remarkably good fit. A combination of five ramp models would fit even better.

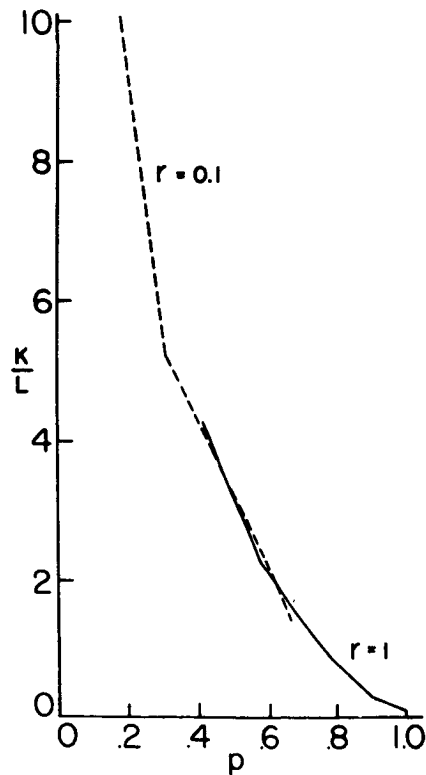


FIGURE 3

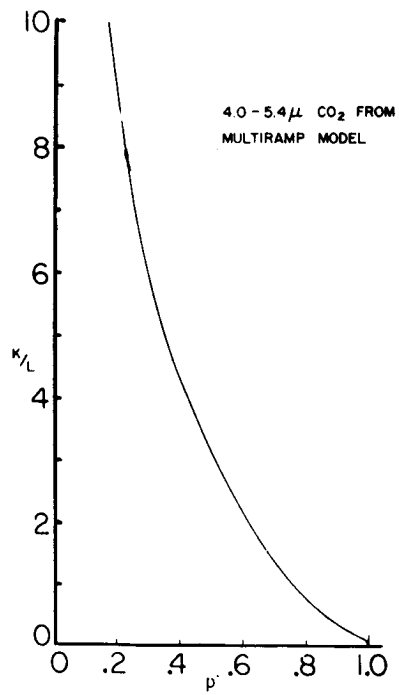


FIGURE 4

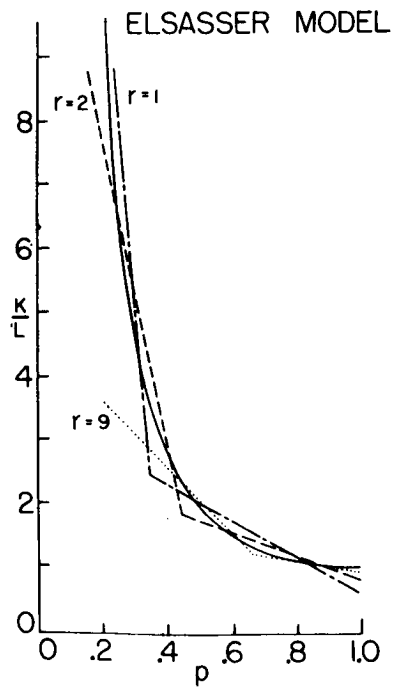


FIGURE 5

## COMPARISON BETWEEN THE 4.3 MICRON CARBON DIOXIDE BAND AND THE ELSASSER AND GOODY MODELS

Comparison can be readily made for the  $\frac{\kappa}{L}$  versus  $p$  curves for the Elsasser and Goody models. However, difficulties arise when comparisons are made using experimental data because  $L$  is unknown. An alternative is to compare curves of  $\frac{\kappa}{\kappa_h}$  versus  $p$ , where  $\kappa_h$ , the harmonic absorption coefficient, is defined by

$$\frac{1}{\kappa_h} = \int_{\Delta\nu} \frac{d(\nu/\Delta\nu)}{\kappa} \quad . \quad (5)$$

Let

$$y = \int_0^{\infty} \tau d(Lu) \quad . \quad (6)$$

A combination of Equations (1), (5), and (6) results in

$$\frac{L}{\kappa_h} = \int_0^{\infty} \tau d(Lu) \quad . \quad (7)$$

Therefore,  $\frac{\kappa}{\kappa_h} = \left(\frac{\kappa}{L}\right) \left(\frac{L}{\kappa_h}\right)$  can be found regardless of the value of  $(L)$ .

The ratios  $\frac{L}{\kappa_h}$  for various models are as follows:

$$\text{Elsasser Model, } \frac{L}{\kappa_h} = 0.5$$

$$\text{Goody Model, } \frac{L}{\kappa_H} = 2.0$$

$$\text{Experimental Data, } \frac{L}{\kappa_h} = 1.07.$$

The experimental data were obtained for the 4.3 micron band of CO<sub>2</sub> by Howard, Burch, and Williams [1]. When all  $\frac{\kappa}{L}$  curves are reduced to  $\frac{\kappa}{\kappa_h}$  versus  $p$  curves, Figure 6 results.

It is apparent from Figure 6 that the experimental curve and the Goody model (random line spacing) have  $\frac{\kappa}{\kappa_h}$  approach zero as  $p$  approaches unity and  $p' \rightarrow 0$ . This is true for all cases, as will be shown later. When  $p > 0.9$ , the values of  $\frac{\kappa}{\kappa_h}$  decrease from the Elsasser to the Goody to the experimental curve. It is believed that this region describes the effect of the line wings. Since  $\frac{\kappa}{\kappa_h}$  is smallest for the experimental curve, we can infer the greatest spectral line clustering. Thus, there would be regions where the line spacing is great with low absorption of infrared.

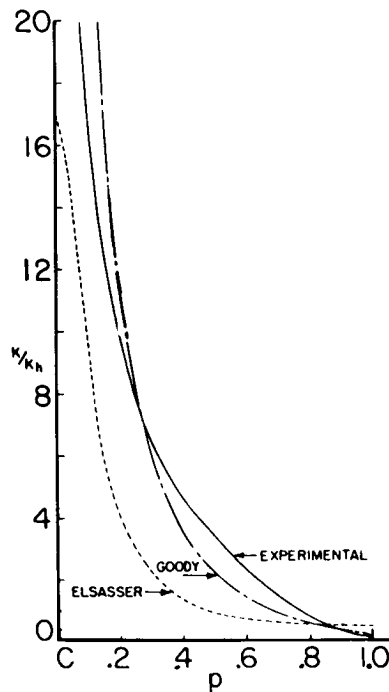


FIGURE 6

## METHODS USED TO OBTAIN THE PROBABILITY DISTRIBUTION FUNCTION

Experimental data for the 4.3 micron band of CO<sub>2</sub> were obtained from Howard, Burch and Williams [1]. The absorption of such data for  $\Delta\nu$  at various frequencies is given for a number of values of  $u$ , and can be plotted (Altshuler [2], Figure 7). The limiting bounds on either side of the absorption curve represent the region that contains 95 percent of the data points. The data were permitted to determine the shape of the curve rather than fitting a curve of known shape to the data. This results in less data scatter (Altshuler [2]). Figure 8 compares this curve with the Elsasser model.

Values of  $\tau$  versus  $Lu$  were taken from the experimental curve and inverted to obtain  $\frac{\kappa}{\kappa_h}$  versus  $p$  ramps (Fig. 9). To write Equation (2) in a form that can be evaluated by Prony's algorithm, let

$$p' = \frac{dp}{d\left(\frac{\kappa}{L}\right)} \quad (8)$$

Substituting into Equation (2) yields

$$\tau(Lu) = \int_0^\infty p' \left[ \exp - \left(\frac{\kappa}{L}\right)(Lu) \right] d\left(\frac{\kappa}{L}\right). \quad (9)$$

Let

$$p' = \sum_{j=1}^n \Delta p'_j s(p' - p'_j) + p'_0, \quad (10)$$

where

$s$  = step function

$$p'_0 = p' \text{ at the origin } \left(\frac{\kappa}{L} = 0\right).$$

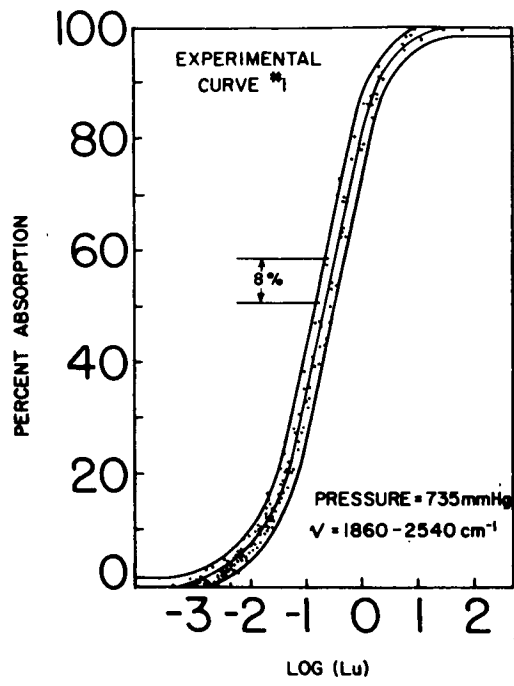


FIGURE 7

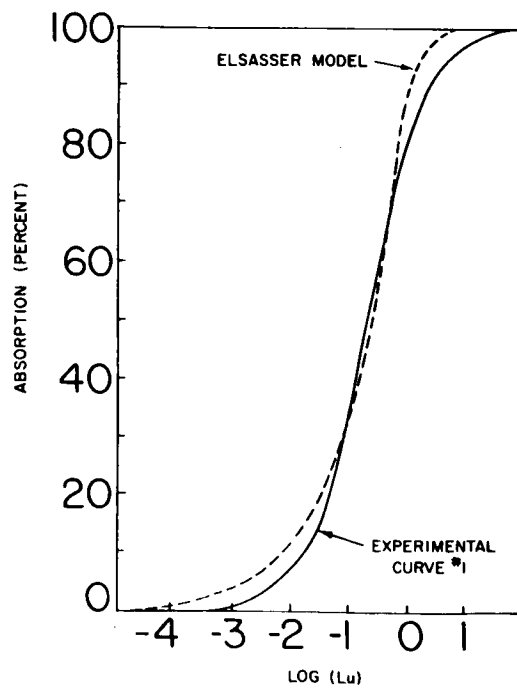


FIGURE 8

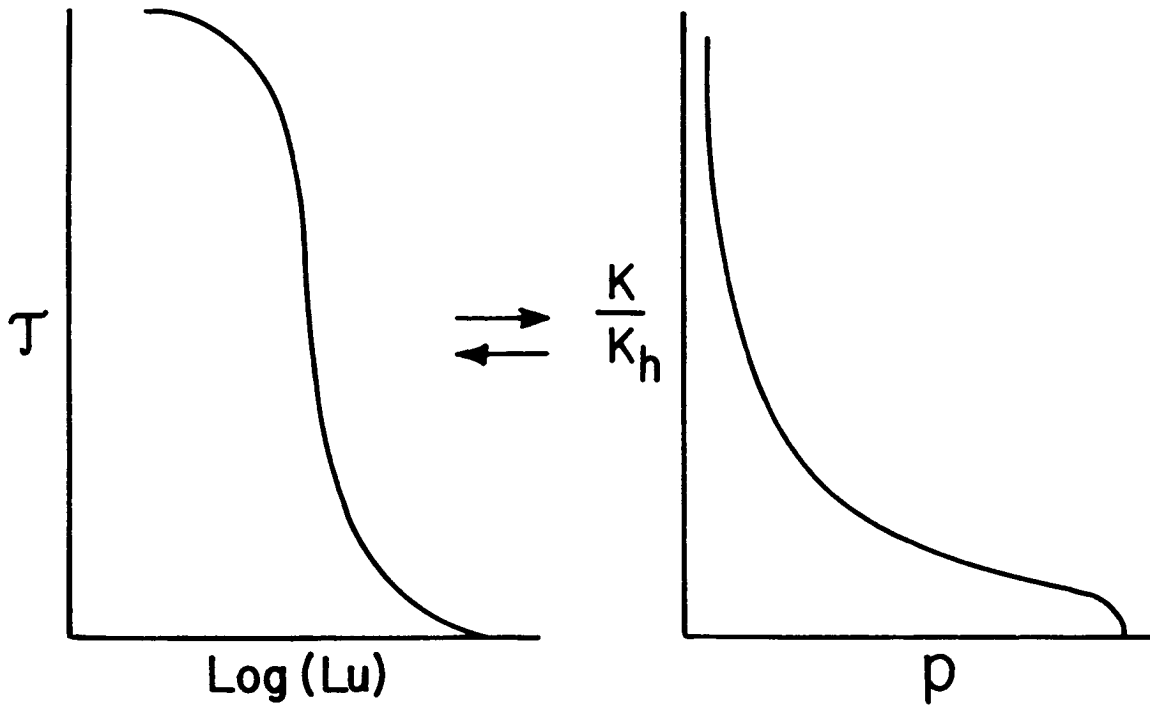


FIGURE 9

Substituting Equation (10) into Equation (9), we get

$$(Lu) \tau (Lu) = \sum_{j=1}^n \Delta p'_j \exp \left[ - \left( \frac{\kappa_j}{L} \right) (Lu) \right] + p'_0 . \quad (11)$$

From Equation (2), we see that

$$(Lu) \tau (Lu) = (Lu) \int_0^1 \left[ \exp - \left( \frac{\kappa}{L} \right) (Lu) \right] dp. \quad (12)$$

When we let  $u \rightarrow \infty$ , then  $(Lu)\tau \rightarrow 0$  from Equation (12). Also,

$$\sum_{j=1}^n \Delta p'_j \exp \left[ - \left( \frac{\kappa_j}{L} \right) (Lu) \right] \rightarrow 0 \text{ (see Equation (11)).}$$

Therefore,  $p'_0 = 0$ , and Equation (11) becomes

$$(Lu)\tau(Lu) = \sum_{j=1}^n \Delta p'_j \exp \left[ - \left( \frac{\kappa_j}{L} \right) (Lu) \right]. \quad (13)$$

Equation (13) can now be inverted using Prony's algorithm, where  $Lu$  is assigned values according to Equation (3) and  $\tau$  is determined for those values of  $Lu$ .

When the curve in Figure 7 was read directly, only several ramp functions could be obtained. This was due to the lack of precision in reading the curve. To eliminate this problem, a function was generated that would deviate less than one percent from the drawn curve. This function,

$$\tau = \exp \left[ - \exp (a_0 + a_1 x + \dots + a_6 x^6) \right] \quad (14)$$

$$x = \text{Log} (Lu) , \quad (15)$$

was used for inversion resulting in several five-ramp functions. There was excellent agreement between the  $\frac{\kappa}{\kappa_h}$  versus  $p$  curve derived from these ramps and the two ramp functions previously described.

Table I compares the actual transmission,  $\tau(\text{actual})$ , with the function transmission  $\tau(\text{function})$ , obtained by Equations (14) and (15). This was done for various values of  $Lu$ . Furthermore, the transmission was calculated from



the  $\frac{\kappa}{\kappa_h}$  versus  $p$  curve using Equation (2). The results, shown as  $\tau$  (calculated) in Table I, give confidence in the inversion process. It is interesting to note that the line centers have little effect upon the total transmission, except for very small values of  $(u)$ .

TABLE I

$\tau$ (actual)	0.020	0.205	0.662
$\tau$ (calculated)	0.017	0.218	0.660
$\tau$ (function)	0.015	0.213	0.660

### SUMMARY

A number of multi-ramp functions were developed using Prony's algorithm and inverting laboratory data for the 4.3 micron band of  $\text{CO}_2$ . These multi-ramp functions were superimposed. A smooth curve was then faired through these ramps, resulting in Figure 6. Inspection of these curves reveals the following:

1.  $\frac{dp}{d\left(\frac{\kappa}{\kappa_h}\right)} \rightarrow 0$  as  $p \rightarrow 1.0$
2. The real gas has line clustering to a greater extent than the Goody case.
3. The causes of variations in the probability distribution function for various real gases are not clearly understood at this time. However, it is expected that further study of these functions will yield fruitful results.

## REFERENCES

1. Howard, J. N.; Burch, D. E.; and Williams, D.: Near-Infrared Transmission through Synthetic Atmospheres. Geophys. Res. Paper No. 40, AFCRC: November, 1955.
2. Altshuler, T. L.: Infrared Transmission and Background Radiation by Clear Atmospheres. General Electric Document No. 61SD 199, December, 1961.
3. King, J. I. F.: J. Atm. Sci., vol. 21, no. 3, 1964, p. 324.

---

## DISCUSSION

W. Malkmus, General Dynamics/Convair: What you say casts some suspicion on the Elsasser model. Actually, what you would most expect to represent the spectrum would be a random Elsasser model.

T. L. Altshuler: I would rather not have any model represent the spectrum. What is the purpose of using models? They do not describe properties of the real data. If you can describe the real data in terms of a probability distribution function, you know something about the real data. Furthermore, models do not give correct curves of growth. I think we can represent the curve of growth with greater accuracy using a polynomial expression, as in Equations (14) and (15). In fact, one can obtain reasonable accuracy by using the first three terms of the series in Equation (14).

J. Auman, Jr., Princeton: The experimental data, of course, have experimental errors associated with them, and these experimental errors will limit the accuracy to which you can determine the experimental curves which you calculate. Do you have any idea of the degree of the uncertainty which is introduced by the experimental errors?

T. L. Altshuler: There are two types of errors to be considered, systematic errors and random errors. Systematic errors will, indeed, create errors in inversion. Since we let the data determine the curve of growth, rather than the other way around, we believe that the systematic errors were greatly reduced. Comparison between the Elsasser model and experimental curve in Figure 6 shows the large effect of systematic errors.

Random errors, on the other hand, are removed during the inversion process. Since the data must be self consistent, noise in the data is filtered out when using Prony's algorithm. What, in fact, happens is that the number of ramps that can be obtained from a given number of data points is reduced. Inversion of erroneous data results in imaginary joints for ramps with zero weight.

In conclusion, I believe that if someone else obtained a different experimental curve derived from the same data of Howard, et al. , [1] that experimental curve would be close to the one I obtained. The inversion of that curve would also be close to the one we obtained.

---

# APPLICATION OF BAND MODELS TO INHOMOGENEOUS GASES\*

By

F. S. Simmons

N 68-18089

Willow Run Laboratories  
Institute of Science and Technology  
The University of Michigan

---

## ABSTRACT

The formulation of a band model expression for the calculation of spectral radiances from an inhomogeneous radiating body of gas is reviewed. By the method described, relations for the total radiances and equivalent widths of isolated Lorentzian lines along non-isothermal paths can be used to obtain expressions for average radiances and absorptances in spectral intervals that contain many lines but are small compared with the extent of the band. These expressions are based on a random-line band model with a nearly constant line strength distribution; the procedures for extracting the band model parameters from experimental absorptance data are outlined. The physical implications of the resultant relations are discussed along with various aspects of the applications.

Comparisons are made of the predictions of this model with observed spectra in the  $2.7 \mu$  bands of water vapor along a 60 cm path upon which various known temperature gradients were imposed.

The inverse problem of deducing unknown temperature profiles from observed spectra and the application of band models for this purpose are briefly reviewed.

---

\* This research was conducted for the Advanced Research Projects Agency under contract DAHC15 67 C 0062, with the U. S. Army Defense Supply Service-Washington, as a part of Project DEFENDER.

# INTRODUCTION

Molecular band models were originally introduced for the treatment of atmospheric transmission problems a number of years before high speed computers were available. The complex structure of polyatomic atmospheric species such as H<sub>2</sub>O and CO<sub>2</sub> gives rise to a multiplicity of vibration-rotation bands, frequently superimposed or overlapping, each of which exhibited a large number of lines. Consequently, the representation of an individual or composite band by a simple model, e. g., lines of equal intensity regularly spaced or randomly spaced lines with a constant or a probability distribution of intensities, simplified the analysis, i. e., afforded analytical solutions of the Lambert-Beer absorption equation. The development and utility of band models for such purposes is well documented in the literature; a comprehensive review of the subject has recently appeared as an IRIA state-of-the-art report [ 1 ].

In recent years, another application for band models has emerged: the calculation of thermal radiation from hot gases of moderate optical depths and nonuniform temperatures and concentrations. Although modern computers can handle line-by-line calculations of atmospheric absorption [ 2 ], high temperatures populate many more vibrational and rotational states so that numbers of lines increase enormously. Hence, line-by-line calculations for the case of radiating gases would still be a formidable task, even if the necessary data on line strengths and widths were available.

As opposed to transmission problems which can be treated by a relatively simple exponential relation, the application of band models to the nonisothermal emission-absorption problem requires a solution of the radiative transfer equation, which for the case of local thermodynamic equilibrium can be written as

$$N_{\nu} = \int_0^{X_L} N_{\nu}^*(X) k(\nu, X) \exp \left[ - \int_0^X k(\nu, X') dX' \right] dX \quad (1)$$

with the definition

$$\bar{N}_{\nu} = \frac{1}{\delta \nu} \int_0^{\infty} g(\nu) N_{\nu} d\nu \quad (2)$$

where  $\bar{N}_\nu$  is the average spectral radiance in the interval  $\delta\nu$  as defined by the function  $g(\nu)$ ;  $N_\nu^*(X)$  is the Planck function of the local temperature  $T = T(X)$ ;  $k(\nu, X)$  is the local value of the temperature dependent absorption coefficient; and  $X$  and  $X_L$  are, respectively, the local and total optical depths. The averaging interval  $\delta\nu$  is usually taken to be large compared with the mean line spacing but small compared with the extent of the total band. Under these conditions, which experimentally correspond to spectral measurements at a slit wide enough to smear out the rotational detail but narrow enough to observe the gross branch structure of the band, the average radiances are relatively insensitive to the value of the interval  $\delta\nu$ . That this is only approximately so is one of the factors limiting the utility of band models.

The solution of Equations (1) and (2) by direct application of a band model is itself a most difficult task because of the dependency of the spectral absorption coefficient on both temperature and frequency. (The interval  $\delta\nu$  is assumed to be small enough that the Planck function can be taken to be constant with frequency.) Furthermore, because band models themselves are intrinsically nothing more than mathematical artifices contrived to permit approximate solutions of generally intractable expressions, there is little point in maintaining an extreme dedication to rigor in such analyses. Band model expressions are empiricisms that have value only to an extent established by experiment.

Accordingly, simpler approaches have been used for the application of band models to the radiating gas problem. One approach makes use of the fact that Equation (1) can be written in the form

$$N_\nu = \int_1^{\tau(\nu, X_L)} N_\nu^*(\tau) d\tau, \quad (3)$$

where the transmittance  $\tau(\nu, X)$  is defined by

$$\tau(\nu, X) = \exp\left[-\int_0^X k(\nu, X') dX'\right]. \quad (4)$$

The assumption is made that Equation (3), which strictly is valid only for a differential interval in wavelength, is also operative in terms of an average transmittance  $\bar{\tau}(\nu, X)$  in a finite interval  $\delta\nu$ . Thus, an average radiance in this interval can be calculated by

$$\bar{N}_\nu = \int_1^{\bar{\tau}(\nu, X_L)} N_\nu^*(\tau) d\bar{\tau}, \quad (5)$$

where  $\bar{\tau}(\nu, X)$  is obtained using band model relations expressed in terms of equivalent homogeneous paths, e. g., by use of the Curtis-Godson approximation [3,4]. At first glance such an assumption would appear to be difficult to justify. The rationale of the justification and the associated physical implications will be discussed presently.

An alternative but essentially comparable approach involves the direct application of Equations (1) and (2) to isolated spectral lines to obtain expressions for the total radiances and equivalent widths, which can then be extended to groups of partially overlapping lines. This is the approach taken at the Willow Run Laboratories in studies of absorption and emission along nonisothermal paths in water vapor and other gases [5,6]. This report is a review of that work in particular, and such applications of band models in general.

## A BAND MODEL FORMULATION

Equation (1) can be applied to a single isolated line and integrated over all frequencies to obtain an expression for the total radiance of the line:

$$N = \int_0^\infty \int_0^{X_L} N_\nu^*(X) k(\nu, X) \exp\left[-\int_0^X k(\nu, X') dX'\right] dX d\nu. \quad (6)$$

The solution of Equation (6) requires a separation of the expression of the absorption coefficient into a space dependent and a frequency dependent part. For the case of a Lorentz line, this was done by use of an effective value of the line half width,

$$k(\nu, X) \approx \frac{S(X)}{\pi} \frac{\gamma_e}{\gamma_e^2 + (\Delta\nu)^2} F(X). \quad (7)$$



For weak lines it can be shown that  $F(X) \equiv 1$  and for strong lines  $F(X) \equiv \gamma(X)/\gamma_e$ . The use of these values for lines of intermediate strengths and an effective half-width representing a mass-weighted average along the entire path constitute the "nearly weak" and "nearly strong" line approximations [7]. The use of a mass-weighted value for  $\gamma_e$  and for unity for  $F(X)$ , i. e., the nearly weak approximation, is equivalent to Curtis' approximation for the treatment of transmission along an inhomogeneous path in the atmosphere [8].

The use of Equation (7) and a transformation of variables then permits the integration over frequency, leading to the expression [7]

$$N = 2\pi\gamma_e \int_0^{f(x_L)} N_\nu^*(f) df, \quad (8)$$

where  $f = f(x) = xe^{-x} [J_0(ix) - iJ_1(ix)]$  is the Ladenburg-Reiche function of the dimensionless optical depth,  $x$ , defined for the inhomogeneous path by

$$x = (2\pi\gamma_e)^{-1} \int_0^X S(X') F(X') dX', \quad (9)$$

where  $S(X)$  is the temperature dependent line strength.

A similar procedure leads to a corresponding expression for the equivalent width

$$W = 2\pi\gamma_e f(x_L). \quad (10)$$

Equations (8) and (10) combine to yield the apparent blackbody radiance of an inhomogeneous source:

$$N_\nu^*(T^*) = \frac{N}{W} = \frac{1}{f(x_L)} \int_0^{f(x_L)} N_\nu^*(f) df. \quad (11)$$

The utility of the nearly weak and nearly strong line approximations is illustrated in Figure 1, a plot of the apparent temperature  $T^*$  as a function of optical depth for the R(0,9) line of a hypothetical hydrogen-fluorine flame [7]. Since it can be shown that, in the weak and strong line limits, the apparent blockbody radiances are independent of scale, the corresponding apparent temperatures are also constant. Clearly these approximations provide a pair of limiting values which bracket much more closely the actual values in the intermediate regions; a simple interpolation procedure in the numerical computations can then provide a single relation appropriate for the entire range of optical depths. The small bump in the nearly weak approximation is considered to be anomalous; its location is very close to the optical depth for which Drayson found maximum error in his comparison of exact calculation and Curtis-Godson approximations for the equivalent widths of  $\text{CO}_2$  lines [9].

Analytical expressions similar to Equations (8) and (10) have been obtained for Doppler lines by Yamada [10]; the empirical use of similar equations in numerical calculations for Voigt lines by using values for a growth function extracted from curves of growth obtained for the isothermal case [11] has also been suggested and is presently being investigated [12].

For vibration-rotation band radiation at ordinary pressures, collision broadening is dominant, and an assumption of Lorentz profiles is reasonable. The extension of Equation (8) to a band of randomly spaced nonoverlapping spectral lines of nearly equal intensities is straightforward and leads to the expression [6]

$$\bar{N}_\nu = \beta_e \int_0^{f(\bar{x}_L)} N_\nu^* (\bar{f}) \bar{d}f, \quad (12)$$

where  $\bar{f} = f(\bar{x})$ , the argument  $\bar{x}$ , an average value for the interval  $\delta\nu$ , being defined by

$$\bar{x} = \frac{1}{\beta_e} \int_0^X \bar{k}(X') F(X') dX'. \quad (13)$$

The parameter  $\bar{k}(X) = \bar{S}/\bar{d}$  is an average absorption coefficient, and  $\beta(X) = 2\pi\bar{\gamma}/\bar{d}$  is essentially a ratio of mean line width to mean line spacing. The function  $F(X)$  in this case is either unity or  $\beta(X)/\beta_e$ , where  $\beta_e$  is a mass weighted average, corresponding, respectively, to a nearly weak and nearly strong line approximation in this case also.

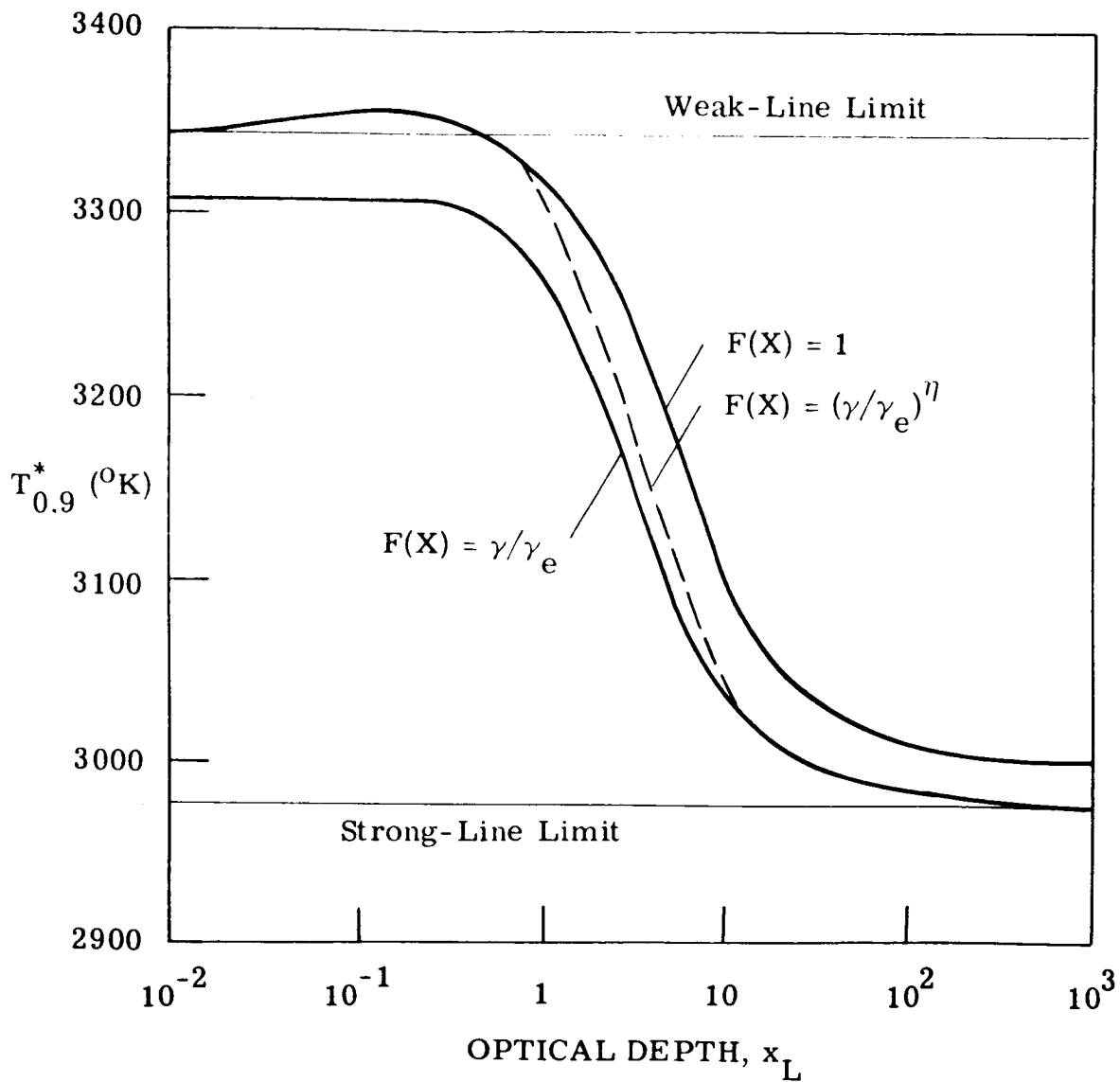


FIGURE 1. VARIATION OF APPARENT TEMPERATURE WITH OPTICAL DEPTH FOR THE R(0,9) OF HF IN A HYPOTHETICAL  $H_2-F_2$  FLAME

By means of an inductive line of reasoning, Equation (12) can be further extended to handle partial overlapping of lines [6]; the resultant expression is

$$\bar{N}_\nu = \beta_e \int_0^{f(\bar{x}_L)} N_\nu^* (\bar{f}) e^{-\beta_e \bar{f}} d\bar{f}. \quad (14)$$

The corresponding expression for the average spectral absorptance is

$$\bar{\alpha}(\nu) = 1 - \exp \left[ -\beta_e f(\bar{x}_L) \right]. \quad (15)$$

Since an average transmittance is defined as  $1 - \bar{\alpha}(\nu)$ , Equation (14) reduces to the form of Equation (5). The value of the present procedure, aside from providing more credence to the use of Equation (5), lies in suggesting the use of the nearly weak and nearly strong approximations for band-model calculations as well as for isolated lines. In essence, it is equivalent to the application of the Curtis-Godson approximation in a band model for absorbing-emitting gases.

The physical implications of the use of Equation (14), or equivalently, Equation (5), might bear some discussion. In a given spectral interval,  $\delta\nu$ , in general there would be lines both increasing and decreasing in strength as the temperature varied along the path. Therefore, generally, the temperature derivative of the average transmittance cannot be simply related to the derivative of the exact transmittance for an infinitesimal spectral interval. However, two special cases can be specified. If the lines in the interval  $\delta\nu$  all exhibit similar temperature derivatives of the line strengths,  $dS/dT$ , the average would be related to the derivative  $d\bar{\tau}/dx$ . This is more likely to be realistic in the extreme wings of a molecular band where absorption and emission are dominated by lines originating from energy levels representing higher rotational states. The other special case is where there are equal numbers of lines of positive and negative  $dS/dT$  so that the net result is  $d\bar{\tau}/dT \approx 0$ , corresponding in effect to a grey gas in the interval  $\delta\nu$ . This situation is more likely to be encountered near the band center where the lower rotational lines of a number of vibrational transitions are encountered.

In other regions of the band where neither of these two conditions clearly prevail, it is to be expected that the band model would be less applicable. The degree to which applicability can be substantiated on the above basis ought to correlate with the degree to which unambiguous values of the band-model parameters can be specified from absorption measurements. This remains, of course, to be established by experiment for each molecule considered.

## EVALUATION OF BAND MODEL PARAMETERS

The band model represented by Equations (14) and (15) is expressed in terms of two parameters:  $\bar{k}(\nu, T)$ , the average absorption coefficient; and  $\beta(\nu, T)$ , the line overlap factor. The evaluation of these parameters from low-resolution experimental absorptance measurements obtained under isothermal conditions requires combinations of path lengths and pressures such that both linear and square root growth can be observed. (The alternative task of examining a complex molecular band under sufficiently high resolution that actual line strengths and shapes could be measured is itself nearly as formidable as treating the entire radiative transfer calculation on such a detailed basis.)

The mean spectral absorption coefficient,  $\bar{k} = \langle S(\nu, T/d) \rangle$ , is obtained from measurements in the linear region in which all lines are weak. Thus,

$$\bar{k}(\nu, T) = \frac{\bar{\alpha}(\nu, T)}{PL}, \quad \alpha(\nu, T) \ll 1, \quad (16)$$

where  $P$  is the partial pressure of the absorbing species in atmospheres and  $L$  is the geometrical path length in centimeters. Note that the required condition for linear growth is that the true absorptance is much less than unity throughout. A low-resolution observation  $\bar{\alpha}(\nu, T) \ll 1$  is not sufficient to apply Equation (16) for determining  $\bar{k}(\nu, T)$ . Also, note that the temperature dependence of the density of the absorbing gas is incorporated into the absorption coefficient as defined above. Frequently, therefore, experimental data are normalized by a factor of  $(273/T)$ , for presentation in terms of reciprocal centimeters at standard temperature and pressure.

The line overlap factor,  $\beta$ , can be evaluated directly by measurements in the square-root region of growth. This is a more difficult task for two reasons: For path lengths accommodated in ordinary spectroscopic apparatus, the pressure required for a sufficient number of absorbers will produce overlapping of lines before a sufficient fraction of the lines becomes strong. A more fundamental difficulty is that a condition of all strong lines can never be attained even locally in a complex molecular band at high temperatures as higher rotational and vibrational states become populated. In other words, no combination of pressures and path lengths will eliminate the presence of some weak lines. However, presumably, a pressure and length can be chosen to produce a preponderance of strong nonoverlapping lines exhibiting a nearly square-root growth. Under these conditions, a strong-line parameter [5],  $Q$ , can be evaluated by

$$Q(\nu, T) = \langle \{ [\bar{S}/\bar{d}] (\bar{\gamma}/\bar{d}) \}^{\frac{1}{2}} \rangle = \frac{\bar{\alpha}(\nu, T)}{2X^{\frac{1}{2}}}, \quad \alpha(\nu, T) \sim 1. \quad (17)$$

If it assumed that the ratios of mean line strength to spacing  $\langle \bar{S}/\bar{d} \rangle$  and mean line half-width to spacing  $\langle \bar{\gamma}/\bar{d} \rangle$  are uncorrelated, it can be shown that the strong-line parameter can be separated into two components:

$$Q \approx \langle \bar{S}/\bar{d} \rangle^{\frac{1}{2}} \langle \bar{\gamma}/\bar{d} \rangle^{\frac{1}{2}}. \quad (18)$$

Thus,

$$\beta = 2\pi Q^2/k. \quad (19)$$

If neither the linear nor square root regions can easily be attained in the experiment,  $\bar{k}(T)$  and  $\beta(T)$  can nevertheless be evaluated in the process of fitting the absorptance data with Equation (15). The graphical method for this purpose as developed by Oppenheim and Ben-Aryeh [13] involves a plot of  $\ln \tau(\nu)/P_e$  versus path length, where  $P_e$  is the effective broadening pressure. This method requires the use of a wide range of path lengths so that the full curve of growth can be observed and asymptotes drawn. In principle, however, only two measurements at a particular frequency and temperature would be required to determine the values of the band-model parameters  $\beta(\nu, T)$  and  $\bar{k}(\nu, T)$ . A procedure for doing this, based on the nearly weak and nearly strong line version of the band model, requires two measurements of spectral absorptance  $\bar{\alpha}(\nu, L_1)$  and  $\bar{\alpha}(\nu, L_2)$ , representative of path lengths  $L_1$  and  $L_2$  corresponding, respectively, to a nearly weak and a nearly strong line region of growth. Writing Equation (15) for each case, one simply solves for the band-model parameters  $\beta$  and  $\bar{k}$  by an iterative calculation. For the first attempt, a pair of values can be obtained through use of the asymptotic limits  $f(x) = x$  and  $f(x) \approx \sqrt{2x/\pi}$ , representing, respectively, the weak-line and strong-line extremes. The rate at which convergence occurs should depend upon how close to the weak-line and strong-line limits the two lengths  $L_1$  and  $L_2$  are taken. This procedure can be generalized to take advantage of additional data; a computer program for accomplishing this is now being prepared at the Willow Run Laboratories.

A method by which variable pressure broadening is taken into account must be included in the application of these models. In general, Lorentz profiles result from collisions of like or unlike molecules which can be respectively characterized as self and foreign gas broadening. A single expression embodying both effects is

$$\gamma = P_e \left[ aT + bT^{\frac{1}{2}} \right], \quad (20)$$

where  $P_e$  is an effective broadening pressure. Varying the resonance half-width directly with temperature reflects the dependence on gas density; the half-power variation for foreign-gas broadening effect reflects the dependence on the collision frequency. The coefficients  $a$  and  $b$  can be calculated from theory [14], but are more reliably determined by fitting Equation (20) to experimental data when available. The effective broadening pressure  $P_e$  is calculated from  $P_e = \sum P_i \alpha_i$ , where  $\alpha_i$  are experimentally determined coefficients characterizing the relative broadening effectiveness of the  $i$ th species on the active species  $i = 0$  for which  $\alpha_0 = 1$  by definition. An alternate but essentially equivalent expression of Equation (20) is the empirical relation

$$\gamma = \gamma_0 \frac{P_e}{P_0} \left( \frac{T_0}{T} \right)^n \quad (21)$$

where  $\gamma_0$  is the half-width at reference pressure  $P_0$  and temperature  $T_0$ , and the experimentally evaluated exponent  $n$  will lie between  $\frac{1}{2}$  and 1. For example, Benedict arrived at a value  $n = 0.62$  for  $H_2O$  broadened by nitrogen [15]. The usual assumption, however, is that nonresonant broadening dominates and the value  $n = \frac{1}{2}$  is appropriate. This value was used and the assumption was made that Equation (21) also applies in terms of the local average  $\bar{\gamma}$  in the calculations described below.

The present band model was formulated on the basis of an array of randomly located lines of nearly equal intensities. This intensity distribution is not the most reasonable; a modified probability distribution [16] is undoubtedly closer to reality. However, the resultant curves of growth do not differ greatly. Therefore, in view of the uncertainties in temperatures and concentrations in practical problems, such refinement of the model was not considered necessary.

## COMPARISON WITH EXPERIMENT

An experimental study was undertaken at the Willow Run Laboratories specifically to test such band model formulations as applied to the infrared vibration-rotation bands of typical combustion products. The experimental apparatus and procedures are described in detail elsewhere [5]. Figure 2 is a schematic illustration of the setup. Particular attention was devoted to the  $2.7 \mu$  bands of  $H_2O$ . For these measurements, the path length was 60 cm; the evacuated cell was loaded by connection to a flask containing distilled water whose temperature was carefully monitored. Most of the measurements were for pure water vapor; a few were made to illustrate the slight effect of nitrogen broadening under the conditions at hand. Typical results of these measurements, which have been reported previously [17], are shown as the solid lines in Figures 3 and 4. The corresponding temperature profiles, shown in Figures 5 and 6 were selected to represent a substantial range of conditions for which the average temperatures remained approximately constant, for a given amount of water in the cell. The isothermal conditions at the maximum and minimum temperatures were included for reference. To be noted is the similarity of the intermediate curves representing the nonisothermal paths.

Equation (14) was programmed using trapezoidal approximations to the integrals, and values of  $\bar{N}_\nu$  were computed at intervals of  $25 \text{ cm}^{-1}$  from 2800 to  $4200 \text{ cm}^{-1}$ . The mean absorption coefficients were taken from the tables given by Ferriso et al. [18], the values of the line overlap factor from the work of Oppenheim and Goldman [19] (see [18]). The calculations were performed using an incremental length of 1 cm, and interpolations between the nearly weak and nearly strong line approximations were made by use of an empirically derived relation [7].

Spectral radiances so calculated are shown in Figures 3 and 4 by the dashed lines. The agreement between the predicted and observed spectra is generally satisfactory in view of the probable errors in the radiance measurements, the uncertainty in the band model parameters, especially the line overlap factor, and the difference between the degree of smoothing of the data shown in these figures and the original data from which the band model parameters were extracted.





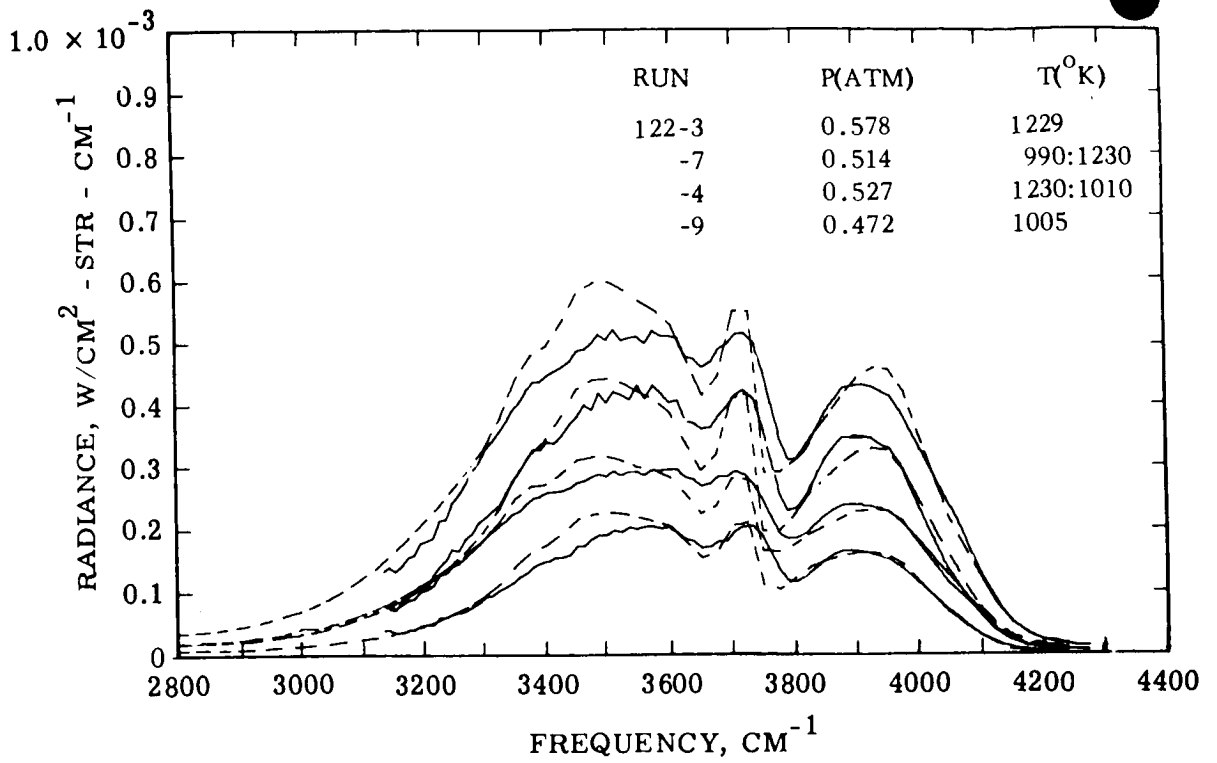


FIGURE 3. BAND MODEL PREDICTIONS AND OBSERVED SPECTRA, RUNS 122-3, -4, -7, -9

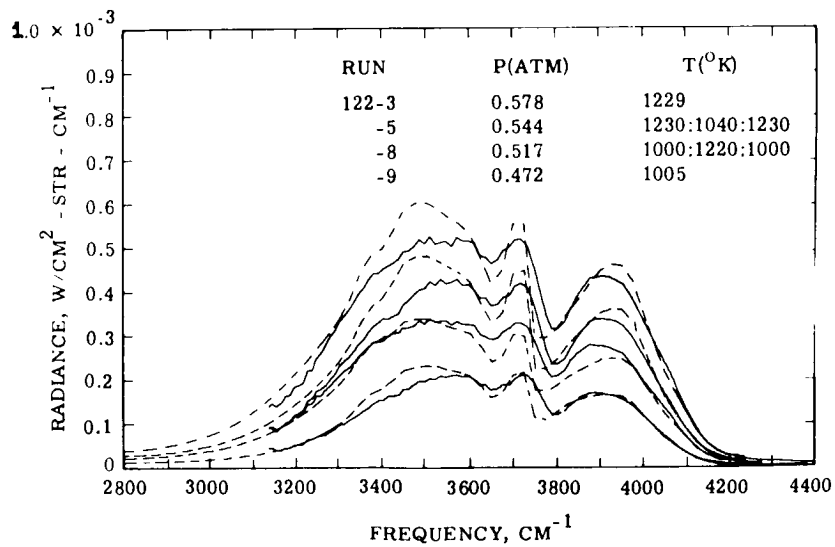


FIGURE 4. BAND MODEL PREDICTIONS AND OBSERVED SPECTRA, RUNS 122-3, -5, -8, -9

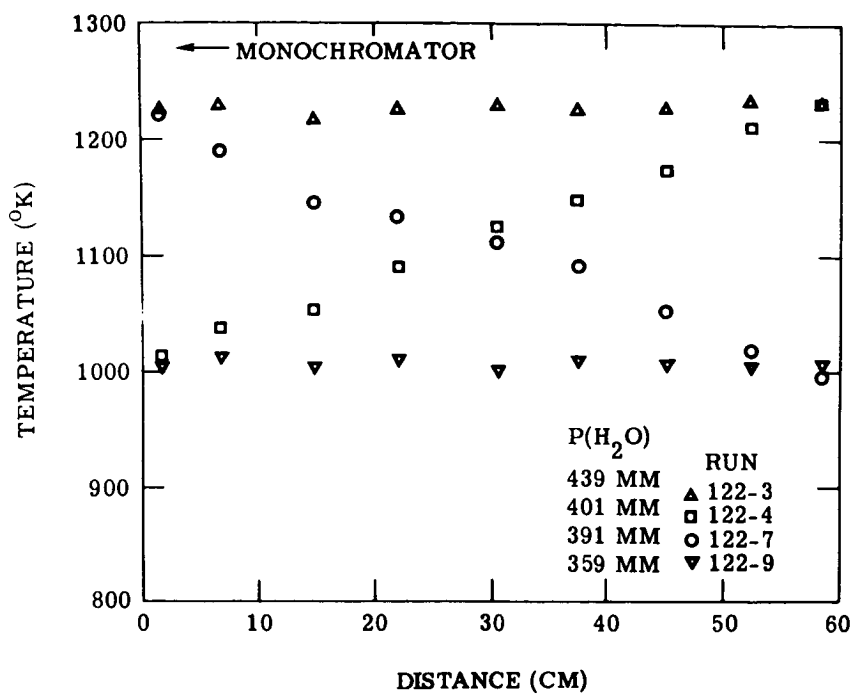


FIGURE 5. TEMPERATURE PROFILES, RUNS 122-3, -4, -7, -9

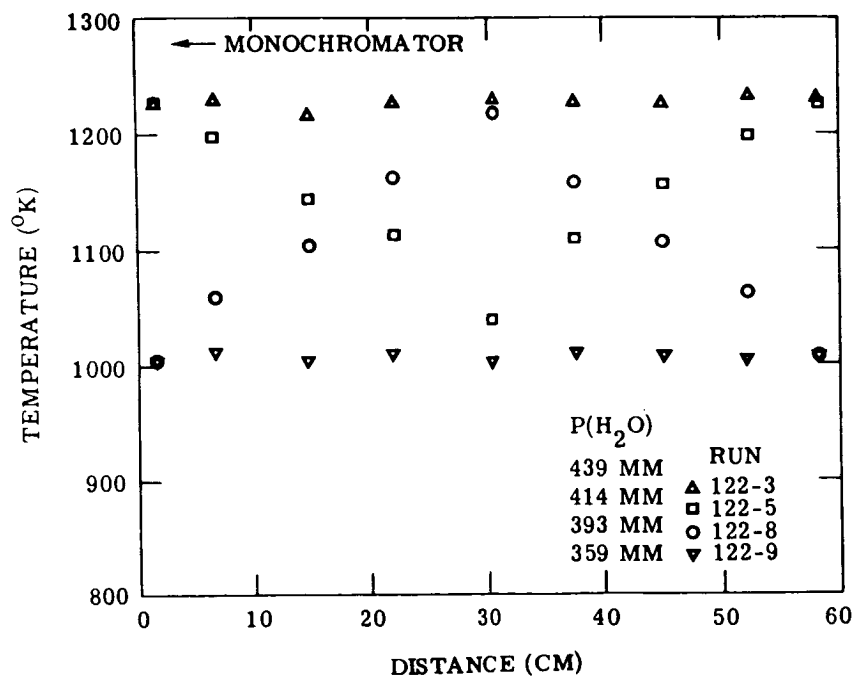


FIGURE 6. TEMPERATURE PROFILES, RUNS 122-3, -5, -8, -9

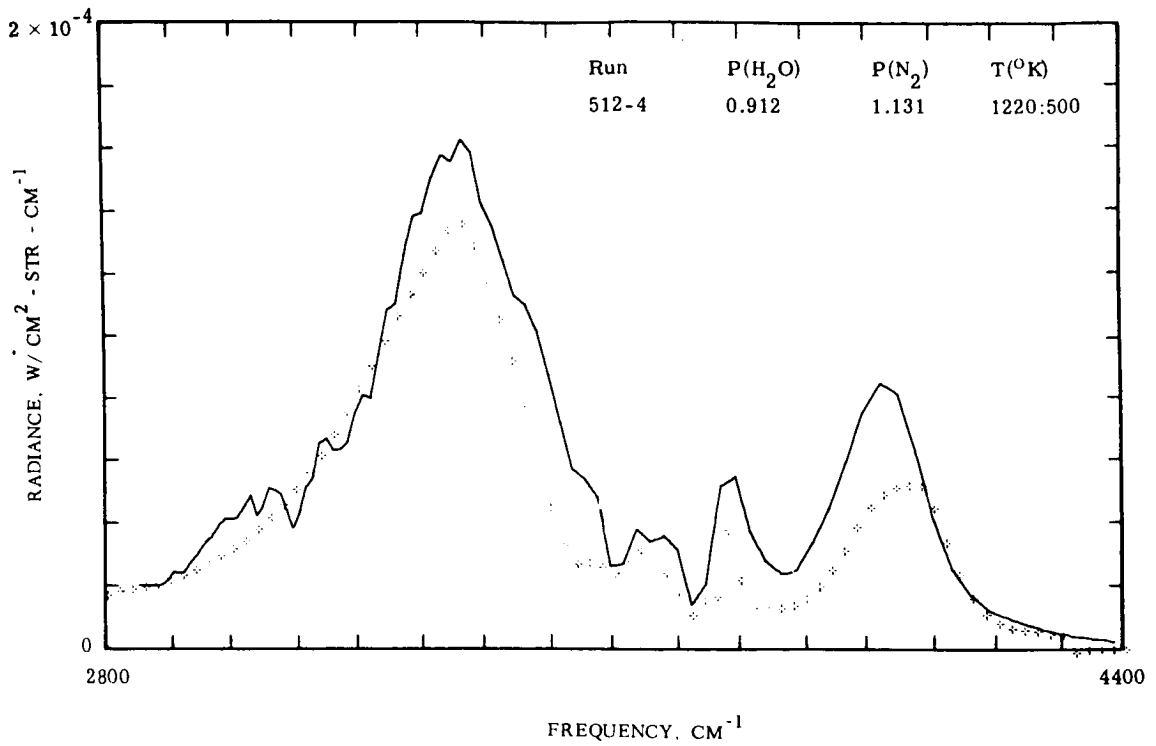


FIGURE 7. BAND MODEL PREDICTIONS AND OBSERVED SPECTRA, RUN 512-4

## TEMPERATURE PROFILE DETERMINATIONS

The prior discussions have been concerned with the straightforward problem of determining the net spectral radiance distribution for an inhomogeneous gas with a specified temperature profile. The inverse problem of deducing a temperature profile from observed spectra is a much more difficult one. There is a great deal of literature on this subject, mostly concerned with the inversion of the line spectra or continua from axisymmetric systems. However, it is only recently that band models such as that described herein have been applied to the determination of the temperature profiles in hot gases from observations of their infrared spectra. The main difficulty is one of non-uniqueness; in other words, more than one profile can yield a particular spectral distribution within the accuracy of measurements. That this is so can be inferred from the similarities in the nonisothermal spectra of Figures 3 and 5.

A more practical approach relies on prior knowledge or a reasonable assumption of the general shape of the temperature profile which can thus be specified in terms of a very few parameters. Band model calculations can then be performed adjusting these parameters until the best fit is obtained with the experimental spectra. A comparable approach was taken in a recent study of the infrared spectra from hydrogen fluorine flames [21]; in that case, the spectral lines were well resolved so that the calculations could be performed in terms of total radiances and equivalent widths of individual lines. Figure 8 shows the forms of the assumed temperature and concentration profiles which could be characterized by two parameters: the temperature and radius of the isothermal core of the flame. The values of these parameters in calculations using Equation (11) were adjusted to obtain agreement with observed values for two selected lines. Figures 9 and 10 show the predictions of Equation (11) based on this profile in comparison with the observed transverse profiles for the two lines and with values for other lines in the  $0 \rightleftharpoons 1$  and  $1 \rightleftharpoons 2$  bands. The agreement is satisfactory except for the discrepancies at low rotational numbers which were due to additional absorption by HF recirculating around the flame.

A current study at this laboratory, under NASA support, is concerned with the extension of this approach to more complex molecular bands by use of band model relations such as Equations (14) and (15). The objective of this work will be to assess the utility of infrared spectroscopy as a diagnostic tool for experimental studies of advanced air-breathing engines.

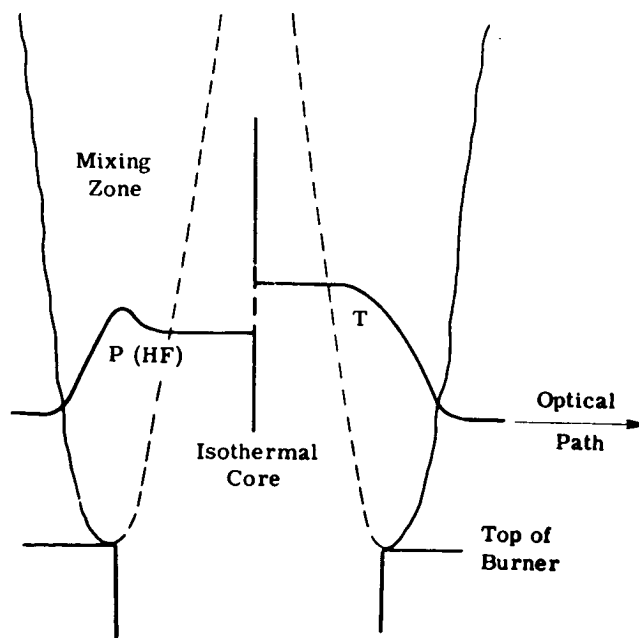


FIGURE 8. TEMPERATURE AND CONCENTRATION PROFILES ASSUMED IN  $H_2-F_2$  FLAME

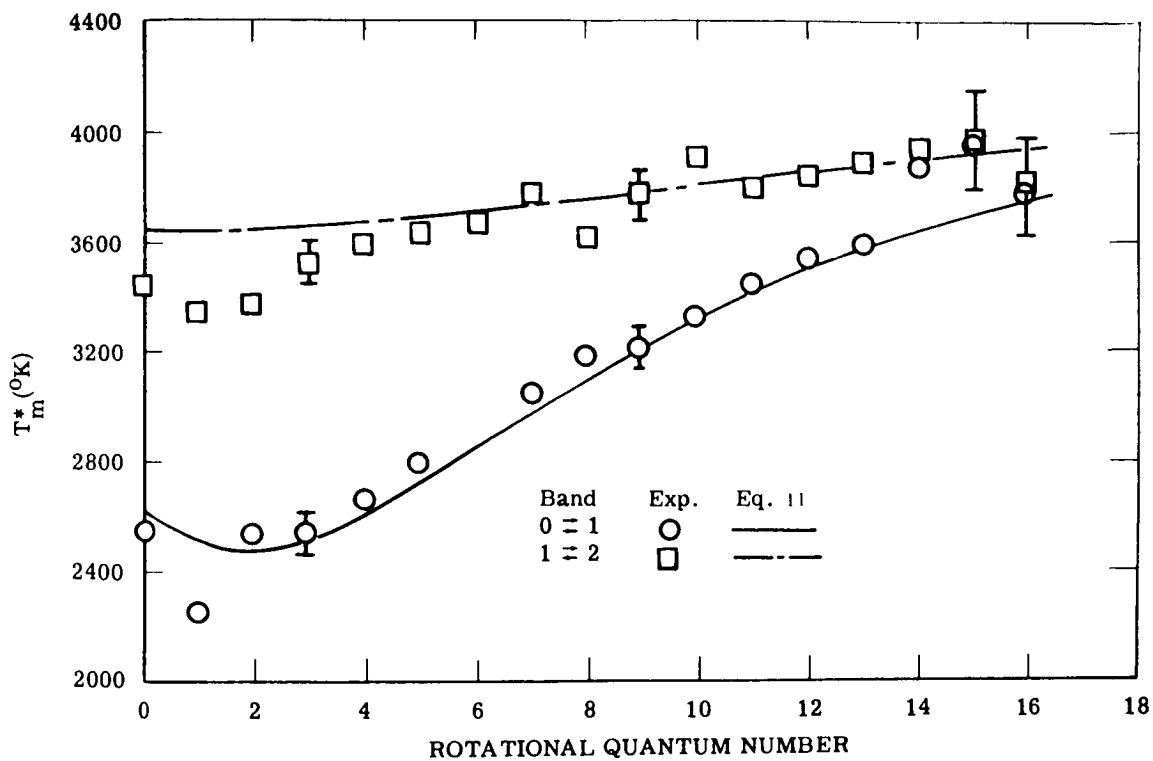


FIGURE 9. SPECTRAL VARIATION OF APPARENT TEMPERATURES IN  $H_2-F_2$  FLAME

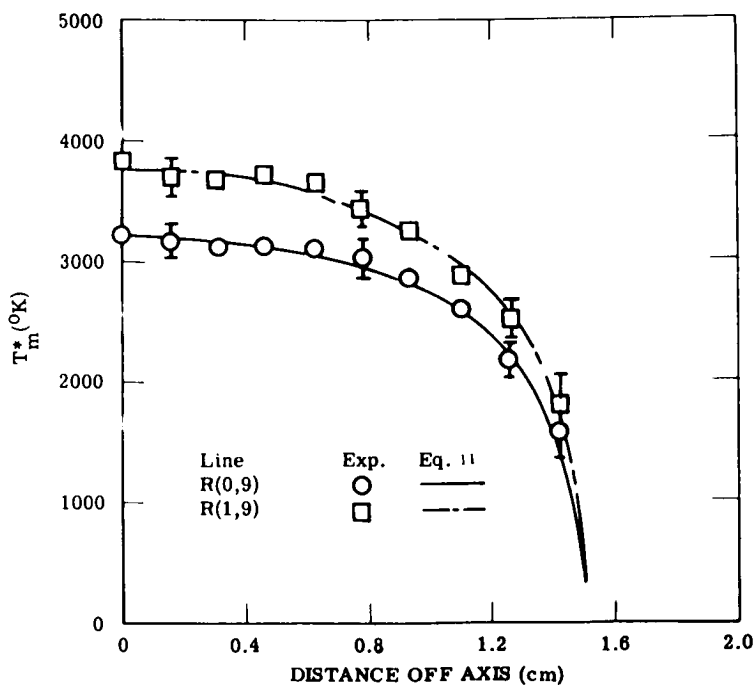


FIGURE 10. SPATIAL VARIATION OF APPARENT TEMPERATURE IN  $H_2-F_2$  FLAME

## REFERENCES

1. Anding, D.: Band-Model Methods for Computing Atmospheric Slant-Path Molecular Absorption. Willow Run Laboratories, Report No. NAVSO P-2499-1, The University of Michigan, Feb. 1967.
2. Gates, D. M.; Calfee, R. F.; Hansen, D. W.; and Benedict, W. S.: Line Parameters and Computed Spectra for Water Vapor Bands at  $2.7 \mu$ . NBS Monograph 71, 1964.
3. Ludwig, C. B., et al.: Study on Exhaust Plume Predictions. General Dynamics/Convair Report No. DBE66-017, Dec. 1966.
4. Krakow, B., et al.: Use of the Curtis-Godson Approximation in Calculations of Radiant Heating by Inhomogeneous Hot Gases. *Appl. Optics*, vol. 5, 1966, p. 1791.
5. Simmons, F.; Arnold, C.; Smith, D.; and Kent, N.: Studies of Infrared Radiative Transfer in Hot Gases. Reports 4613-91T, 92T, 93T. Institute of Science and Technology, University of Michigan, 1965.
6. Simmons, F.; and Yamada, H.: Relations for Molecular Radiative Transfer Based on a Random-Line Band Model. Willow Run Laboratories, Report No. 4613-150T, The University of Michigan, 1967.
7. Simmons, F.: Radiances and Equivalent Widths of Lorentz Lines for Nonisothermal Paths. *J. Q. S. R. T.*, vol 7, 1967, p. 111.
8. Curtis, A. R.: Discussion of a paper by R. M. Goody, Q. J. Roy. *Meteor. Soc.*, vol. 78, 1952, p. 638.
9. Drayson, S. R.: Atmospheric Transmission in the  $\text{CO}_2$  Bands Between  $12 \mu$  and  $18 \mu$ . *Appl. Optics*, vol. 5, 1966, p. 385.
10. Yamada, H.: Total Radiances and Equivalent Widths of Doppler Lines for Nonisothermal Paths. *J. Q. S. R. T.*, in press.

## REFERENCES (Concluded)

11. Penner, S. S.: Quantitative Molecular Spectroscopy and Gas Emissivities. Addison-Wesley, 1959.
12. Yamada, H.: Private Communication, Willow Run Laboratories, The University of Michigan.
13. Oppenheim, U. P.; and Ben-Aryeh, Y.: A General Method for the Use of Band Models with Applications to Infrared Atmospheric Absorption. J. Q. S. R. T., vol. 4, 1964, p. 559.
14. Benedict, W. S., et al.: The Strengths, Widths, and Shapes of Spectral Lines. Can J. Phys., vol. 34, 1956, p. 830,
15. Benedict, W. S.; and Kaplan, L. D.: Calculation of Line Widths in H<sub>2</sub>O-N<sub>2</sub> Collisions. J. Chem. Phys., vol. 30, 1959, p. 388.
16. Malkmus, W.: Random Lorentz Band Model with Exponential-Tailed S<sup>-1</sup> Line Intensity Distribution Function. General Dynamics/Convair Report No. DBE65-020 Nov. 1965.
17. Simmons, F.: Band Models for Nonisothermal Radiating Gases. Appl. Optics, vol. 5, 1966, p. 1801, vol. 6, 1967, p. 1423.
18. Ferriso, C. C.; Ludwig, C. B.; and Thomson, A. L.: Empirical Infrared Absorption Coefficients of H<sub>2</sub>O from 300 to 3000° K. General Dynamics/Convair Report DBE-65-028 Dec. 1965.
19. Oppenheim, U. P.; and Goldman, A.: Spectral Emissivity of Water Vapor at 1200° K. Tenth Symposium on Combustion. The Combustion Institute 1965, p. 185.
20. Arnold, C. B.: Willow Run Laboratories. The University of Michigan, work in progress.
21. Simmons, F.: Infrared Spectroscopic Study of Hydrogen Fluorine Flames, AIAA J. vol. 5, 1967, p. 778.



---

## DISCUSSION

S. A. Golden, Rocketdyne: It seems to me that at any optical depth the absolute upper limit for the equivalent blackbody radiance is given by the transparent gas expression

$$N_{\text{eq}}^{\circ} = \frac{\int_0^L N_{\omega_0}^{\circ}(s) S(s) p(s) ds}{\int_0^L S(s)p(s) ds}$$

Despite this, in Dr. Simmons' first figure, the results for the weak line curve are larger than this transparent gas limit for intermediate optical depths. How do you explain these results?

F. S. Simmons: I am not certain that it is true, a priori, that the weak line limit gives a maximum value for the ratio of the total radiance to equivalent width. It does, of course, give a maximum value for the radiance. On the other hand, you may be correct. I feel that the bump above the weak line limit on Figure 1, although exaggerated by the artist, is anomalous. It so happens that it occurs at an optical depth at which a maximum error was noted between a direct integration and a Curtis-Godson approximation, as performed by Dr. Drayson recently for CO<sub>2</sub> lines.

S. T. Wu, University of Alabama: Dr. Simmons, have you tried to pin down the conditions of non-LTE or LTE in your work?

F. S. Simmons: No, we have not. In the furnace work, of course, I think we are very safe in assuming LTE. In the case of the flames, an estimate of the relative value of the radiative lifetime and the collision mean free time was such that we thought the assumption of LTE was a good one. Nothing we saw in the data suggested that this was not the case.

---

PRECEDING PAGE BLANK NOT FILMED.

SESSION II  
APPLICATIONS OF RADIATIVE HEAT TRANSFER CALCULATIONS

Chairman: R. M. Huffaker,  
NASA, Marshall Space Flight Center

# RADIATION MODEL FOR NONSCATTERING ROCKET EXHAUST GASES\*

By

J. A. L. Thomson

N 68-18090

General Dynamics/Convair\*

---

## ABSTRACT

A model for calculating the spectral distribution of the heat transfer from an inhomogeneous volume of high temperature water vapor, carbon dioxide, and carbon monoxide is described. The method uses the statistical band model to evaluate the mean transmission over relatively broad spectral intervals and a modification of the Curtis-Godson approximation to account for the gas inhomogeneity along the line of sight. The effects of both collision and Doppler broadening are included. Emphasis is placed on introducing approximation techniques to reduce computation times. The sensitivity of the predicted radiance both to the approximations inherent in the model and to the present uncertainties in the values of the various model parameters is evaluated for a wide variety of conditions.

---

---

\* Present address: Institute for Defense Analyses, 400 Army-Navy Drive, Arlington, Virginia 22202.

## INTRODUCTION

Current design of various aerospace systems often requires the evaluation of the radiant heat transfer from moderately thick volumes of gas at sub-atmospheric pressure. Of particular interest to vehicle booster designers are techniques for evaluating the radiant heating of a large space vehicle by the exhaust gases from the rocket engines. A useful technique for calculating the heat transfer must satisfy two rather contradictory requirements. First, the method must be reasonably precise in order to be useful in establishing the thermal environment criteria for the vehicle base structure. Second, the method cannot be so complicated that it is economically not feasible to be applied to the rather complex exhaust flow distributions characteristic of current large multiengine boosters. This latter requirement is so stringent for a vehicle such as the Saturn that the sophistication of the techniques that can be incorporated into normal engineering design is severely limited.

In the present paper we will examine some of the techniques for evaluating the thermal emission from an inhomogeneous gas volume when the thickness is large enough and the pressure low enough that both self-absorption and rotational fine structure effects are important. These techniques typically involve "band model approximations" of the type studied extensively in the context of radiative transfer within planetary atmospheres (see, for example, Goody [1] and Plass [2]). We will be particularly concerned with evaluating the sensitivity of the computed radiance to the approximations involved in formulating a computatively feasible model.

For temperature characteristic of combustion processes ( $1000^{\circ}$  -  $3000^{\circ}$  K), the molecular emission is predominantly in the infrared ( $\lambda > 0.7 \mu$ ), and the important transitions are those between various vibrational levels in the ground electronic state.

For the purposes of the present discussion, we assume that a local equilibrium condition applies to the molecular excited states, that the species concentration and temperature distributions have been determined, and that the line strengths, positions, and shapes are known. The evaluation of the radiant heat transfer requires an integration over distance along the line of sight and over wave number. Even for a homogeneous gas, the integration over wave number can present formidable difficulties when molecular spectra are involved. The difficulty stems from the very large number of individual lines that must be

included in the calculation even at moderately low temperatures. Molecules having low moments of inertia and high vibrational frequencies (such as HF) give rise to relatively few lines and in this case it is feasible to consider the direct evaluation of the monochromatic absorption coefficient by summing over individual lines, followed by a detailed integration over space and frequency to obtain the heat transfer. However, for the more important triatomic molecules, such as CO<sub>2</sub> and H<sub>2</sub>O, the number of lines that must be included become so large that such direct evaluation of the total radiant heat transfer from an inhomogeneous gas can become exceedingly expensive when many lines of sight must be considered.

The spectral radiance due to the gas lying between  $s = 0$  (the observer) and  $s = S$  may be written in the general form

$$I = \int I_{\omega} d_{\omega} = \int_0^{\infty} \int_0^S B^0(\omega, T(s)) \frac{d}{ds} (t(\omega, s)) ds d\omega. \quad (1)$$

Here  $B^0(\omega, T)$  is the black-body function at the wave number  $\omega$  and at the local temperature  $T$ , and  $t(\omega, s)$  is the transmission at  $\omega$  to the depth  $s$ . The major difficulty in the computation of  $I$  arises in the integration over wave number. The widths of the individual spectral lines are usually very small compared to the total effective integration interval. The transmission  $t(\omega, s)$  often fluctuates so rapidly with  $\omega$  that the wave number integration is exceedingly lengthy. The purpose of the band model approximations techniques commonly invoked in molecular radiative transfer problems is to enable part of this integration to be carried out analytically. Before discussing these techniques, we will consider certain limiting cases where a direct integration is practical.

## The Overlapping Line Limit

When the width of the individual rotational lines is sufficiently large compared to the average line separations that the rotational fine structure is smeared out, the absorption coefficient becomes a relatively smoothly varying function of frequency. When the line widths are not too large (compared to the vibrational band widths), the absorption coefficient is insensitive to the form of the shape of individual lines and is directly proportional to the total line strength (or  $f$  number) in a unit wave number — a quantity which is fairly easily evaluated. In general this weak line or just overlapping line approximation tends to be useful only at fairly high pressures. However, at extremely

high pressures, or long pathlengths, the absorption coefficient may again become line-shape dependent in the "windows" of the spectrum where absorption by the far wings of intense lines becomes appreciable.

In practice, reasonable representations of the individual vibration-rotation bands can usually be obtained in this case with fewer than 20 or 30 spectral intervals per band. When the temperature is uniform, the overlapping line approximation always overestimates the emissivity subject only to the restriction that the Planck black-body function varies negligibly across each interval, and thus would be quite useful for obtaining a conservative estimate of the heat transfer. However, when the gas is inhomogeneous, it neither provides an upper nor a lower limit. A true upper limit can always be obtained by neglecting the self-absorption entirely, but this is not very useful for large gas volumes (i. e., under conditions where the heat transfer is important). A more useful upper limit can always be obtained by assigning to the black-body function a constant value equal to the peak value along the line of sight. This latter limit is particularly useful in situations where the gas temperature does not vary greatly through the gas volume.

## The Nonoverlapping Line Approximation

When the line spacing is large compared to the line width, the overlapping line approximation fails for optically thick gases. When the lines are sufficiently separated to absorb independently, the so-called nonoverlapping line approximation is applicable. Here, the frequency integration may be expressed as an arithmetic sum of contributions from each line:

$$J = \sum_n \int_0^S B_\nu^0(\nu_n) \left( \int_0^\infty \frac{d}{ds} \left[ e^{-\tau_{\nu_n}} \right] d\nu \right) ds.$$

Since approximate techniques are available for obtaining an evaluation of the line equivalent width, this can provide a useful simplification. However, the requirement for validity of the nonoverlapping line approximation is that the net emissivity in the "windows" between adjacent spectral lines be small compared to unity. Since this condition is usually associated with quite low average emissivities, this approximation is not usually valid in situations where the radiative heat transfer is important.

## The Band Model Approximations

When the widths of the individual lines are neither sufficiently large to justify the just overlapping line approximation nor sufficiently narrow to justify the nonoverlapping approximation, it is usually necessary to resort to one of the so-called band model approximations in order to obtain a practical procedure for evaluating the curve of growth. In the band model approach, relatively simple representations of the distribution of line intensities and/or line positions in the spectral interval under consideration are used so that part of the integration over wave number in Equation (1) may be carried out analytically. These techniques have been discussed extensively by Goody and Plass ([1] and [2]), among others, and only a brief summary of the procedure will be given here.

The purpose of a band model approximation is to obtain a relatively simple representation of the mean value of the spectral transmission ( $\bar{t}$ ) in a wave number interval  $\Delta\omega$  large enough to include several spectral lines. For this purpose approximate representations of the correlation between the locations of the centers of neighboring lines are introduced. Commonly used models are the Elsasser or regular model in which the lines are assumed to be equidistant and equally intense, the Goddy-Mayer or random model in which the line positions are completely uncorrelated and the quasi-random model in which the correlation between line positions is partially accounted for. For Lorentz line shapes, the regular model yields a mean transmission given by

$$t = \frac{1}{\pi} \int_0^{\pi} \exp \left\{ - \left( \frac{\beta x \sinh \beta}{\cosh \beta - \cos z} \right) \right\} dz,$$

where  $x = \bar{k}l/\beta$  and  $\beta = 2\pi\gamma/d$ . Here  $\bar{k}$  is the mean absorption coefficient and  $\gamma/d$  the ratio of line width to line spacing.

In the random model for arbitrary line shapes, the mean transmission may be written in the form

$$\bar{t} = \exp \left( - \sum_{n=1}^N \frac{W_n}{d} \right),$$

where  $W_n$  is the equivalent width of the  $n$ th line and  $d$  the mean line spacing ( $d = \frac{\Delta\omega}{N}$  where  $N$  is the total number of lines in the interval  $\Delta\omega$ ). In other words, the mean absorptivity  $\alpha$  for partially overlapping randomly distributed lines is related to the mean absorptivity  $\bar{\alpha}'$  calculated neglecting the overlap, according to

$$\bar{\alpha} = 1 - \exp(-\bar{\alpha}')$$

The difference between the regular and random models becomes large at long path lengths where the value of the transmission is determined principally by the gaps in the spectrum. However, the two models yield emissivities which differ by less than 20 percent throughout the entire range of optical depth.

Plass considers also an intermediate model: a random superposition of  $N$  regular Elsasser bands. Here, the mean transmission may be expressed as a product of the transmissions of the individual bands  $\left( \prod_{n=1}^N \bar{t}_n \right)$ . For similar bands, each having a line spacing equal to  $Nd$ , the net mean transmission may be written in the form

$$\bar{t} = \left( 1 - \frac{\bar{W}}{Nd} \right)^N,$$

where  $\bar{W}$  is the equivalent width of a single Elsasser band. For large  $N$ , this random-regular model reduces to the completely random model:

$$\bar{t} \approx \exp\left(-\frac{\bar{W}}{d}\right).$$

Wyatt, Stull and Plass [3] have developed a more sophisticated version of the random model which is capable of producing a fairly accurate representation of molecular spectra with a reasonable amount of computation. In this quasi-random model the wave number scale is divided into intervals small compared to the spectral resolution desired and the lines within interval assumed to be randomly distributed. The contribution of the wings of lines centered in other intervals and the effects of the finite width of the interval are properly



accounted for. When detailed information concerning the line strengths, widths, and positions are available, the quasi-random model is probably the most efficient method of computing the transmission. For large spectral intervals it reduces to the completely random model. As the spectral cell size is made successively smaller, the precision improves, approaching the exact result when the cell size becomes small compared to the line width. Although no attempt appears to have been made to develop suitable methods for interpreting experimental data directly in terms of the quasi-random model, this would seem to be quite feasible when the experimental data are sufficiently accurate.

## The Statistical Model for High Temperature Exhaust Gases

In the remainder of this paper, we will examine the validity of the random or statistical model for evaluating the radiant heat transfer from a gas volume containing several molecular species, specifically,  $H_2O$ ,  $CO_2$ , and  $CO$ . The transmission at the wave number  $\omega$  is due to the  $j$ th species may be written in the form

$$t_j(\omega, s) = \exp \left[ -\frac{1}{\Delta\omega} \sum_i \int_0^s S_{ij} g_{ij}(\omega - \omega_{ij}, \gamma) \rho_j ds' \right],$$

where  $S_{ij}$  is the strength,  $\omega_{ij}$  the center,  $g(\omega - \omega_{ij}, \gamma)$  the shape of the  $i$ th line (of width  $\gamma$ ) of the spectrum of the  $j$ th species and  $\rho_j$  its density. The summation extends over all lines in the interval  $\Delta\omega$ .

In general, the line shape is a function of both wave number and, through its dependence on line width, position. To obtain a representation of the mean value of the transmission averaged over a moderately large spectral interval, the Curtis-Godson approximation (see, for example, Goody [1]) is commonly introduced at this point. Here, it is assumed that the line shape function  $g(\omega - \omega_{ij}, \gamma(s'))$  may be evaluated for some suitable average line width  $\bar{\gamma}_{ij}(s)$  and thus depends only on the value of the end point  $s$ . This approximation permits the integration over  $s'$  and the averaging over  $\omega$  to be carried out independently.

In the random band model approximation, the spectral radiance, averaged over a moderate sized wave number interval  $\Delta\omega$ , may thus be approximated by the expression

$$J(\omega) \approx - \int_0^{\infty} B^0(\omega, T) \frac{d}{ds} \left( \Pi_j \overline{t_j(\omega, s)} \right) ds ,$$

where the mean transmission of the  $j$ th species has the form

$$\overline{t_j(\omega, s)} = \exp \left[ - \frac{1}{\Delta\omega} \sum_i W_{ij} \left( \bar{\gamma}_{ij}(s), \tau_{ij}(s) \right) \right] .$$

Here 
$$\tau_{ij}(s) = \int_0^s S_{ij} \rho_j ds' ,$$

$W_{ij}$  is the equivalent width of the  $i$ th line in the spectrum of the  $j$ th species, and the summation extends over all lines in the interval  $\Delta\omega$ . To further reduce the amount of computation required, it is desirable to separate the lines of a particular species into the minimum number of groups and assign a uniform line intensity, shape, and width to all lines in one group. This grouping is best done on the basis of the value of the energy of the lower state of the transition so that all the lines belonging to one group have a similar dependence on temperature. With these approximations, the mean transmission may be determined from the relation

$$- \ln \overline{t_j(\omega, s)} = \sum_n \left( \frac{W_n}{d_n} \right) ,$$

where the summed term is the ratio of the equivalent width to mean line spacing for the  $n$ th group.

In general it will be found that, when the lines are divided into a relatively small number of groups, the temperature dependence of all the lines will not be the same and the effective spectral density of lines of one group will vary with temperature (and thus with position). Thus, it is natural to consider a modification of the Curtis-Godson approximation which will account for this variation. Here, we attempt to approximate the inhomogeneous gas transmission function by the corresponding homogeneous function evaluated in an appropriate average value for the ratio of line width to line spacing (rather than just of the line width itself). In this case we may express the value of  $(W/d)_n$  for the inhomogeneous path in terms of the curve of growth for an equivalent homogeneous path:

$$\frac{W}{d}_n = F\left(\tau_n^*, \bar{a}_{C,n}, \bar{a}_{D,n}\right),$$

where  $\tau_n^*$  is the optical depth for the nth group in the just overlapping line approximation:

$$\tau_n^* = \int_0^s k_n ds,$$

and  $\bar{a}_{C,n}$  and  $\bar{a}_{D,n}$  are mean values for the fine structure parameters:

$$\bar{a}_{C,n} = \frac{1}{\tau_n^*} \int_0^s \frac{\gamma_{C,n}}{d_n} k_n ds,$$

$$\bar{a}_{D,n} = \frac{1}{\tau_n^*} \int_0^s \frac{\gamma_D}{d_n} k_n ds.$$

Here  $\gamma_{C,n}$  and  $\gamma_D$  are values for the collision-broadened and Doppler-broadened half-widths, respectively, and  $d_n$  is the mean line spacing for the nth group.

The absorption coefficient for the nth group is evaluated from

$$k_n = \bar{k}(T) f_n e^{-n\Delta E/kT} / \left[ \sum_{n=0}^{\infty} f_n e^{-n\Delta E/kT} \right],$$

and the line density from  $1/d_n$  from

$$\frac{1}{d_n} = g_n / d_o(T) .$$

Here  $\bar{k}(T)$  is the mean absorption coefficient in the interval  $\Delta \omega$

$$\left( \bar{k}(T) = \sum_i S_{ij} / \Delta \omega \right), f_n \text{ and } g_n \text{ temperature independent parameters, and}$$

$\Delta E$  is the line grouping parameter.

For approximate calculations a considerable saving in computation time can be achieved by utilizing simple analytic representations of the appropriate curves of growth  $F(\tau^*, \bar{a}_C, \bar{a}_D)$ . Some useful formulas are tabulated in the appendix.

## SENSITIVITY ANALYSIS

In many cases, particularly for water vapor, it has been necessary to derive the appropriate band model parameters directly from experimental data. Generally, it has not been possible to take high temperature data with sufficiently high resolution to separate individual lines in order to measure their strengths and widths. Even if this were possible, the cost of the experiment would be considerable. More commonly, curves of growth are measured at fairly low spectral resolution. From these latter data, absorption coefficients and fine structure parameters may be deduced. However, since such fine structure parameters really have no physical meaning and represent some sort of effective or "average" quantities; it can be dangerous to use these data to extrapolate to field conditions which may be considerably different in terms of pressure, relative concentrations, and degree of inhomogeneity. This is especially true when the model formalism being used is not obviously reliable or is clearly oversimplified. Nevertheless, this is essentially what has to be done in practice. Thus, it is important to establish, for a given formalism,

What sort of errors may be involved. We have carried out a number of parametric sensitivity analyses to determine the type of errors that might be expected under various conditions using the simple formalism described in the previous section. These have included "numerical" tests of the statistical approximation, the Curtis-Godson approximation, the assumptions involved in the choice of the line widths, the effects of including or not including "hot" lines and the effects of choosing different curve-of-growth functions.

## Errors Due to the Curtis-Godson Approximation

To obtain an estimate of the error associated with the modified Curtis-Godson approximation, we treat a simple two-slab distribution. We first consider the effect of the variation of the line density. Here the front layer, which is assumed to have a low temperature, is assumed to have only one spectral line in the interval under consideration; whereas, in the rear high temperature section of the gas, the oscillator strength of this line is presumed to be divided among  $n$  equally intense lines, one of which coincides with the original line. The remaining ones are new and displaced "hot" lines. Since we are primarily interested in the effects of the variable line spacing term, we assume the line width to be the same in both sections.

In Figures 1a and 1b we compare the Curtis-Godson estimate with the exact value of the emission from the rear layer as a function both of the depth and the rear layer and of the thickness of the front layer. Reference to these figures shows that the line density variations are reasonably accounted for by this modified Curtis-Godson approximation so long as the mass in the rear layer is not too small. The error does not appear to be strongly dependent on how many new lines appear as long as there is at least one. The fact that the errors become large when the mass of the emitting layer becomes small compared to that of the absorbing layer is characteristic of the Curtis-Godson approximation and is associated with the fact that the line widths and line spacing ratios are mass-averaged.

The effects of varying line width are shown in Figures 2 and 3. In Figure 2 the Curtis-Godson approximations for the total equivalent width of a two-slab volume are shown for Lorentz and Doppler lines. It is apparent that the Curtis-Godson approximation yields reasonably accurate estimates so long as the variation in line width is not excessive (<500 percent for a Lorentz line and <50 percent for a Doppler line). The emission from a hot region located behind

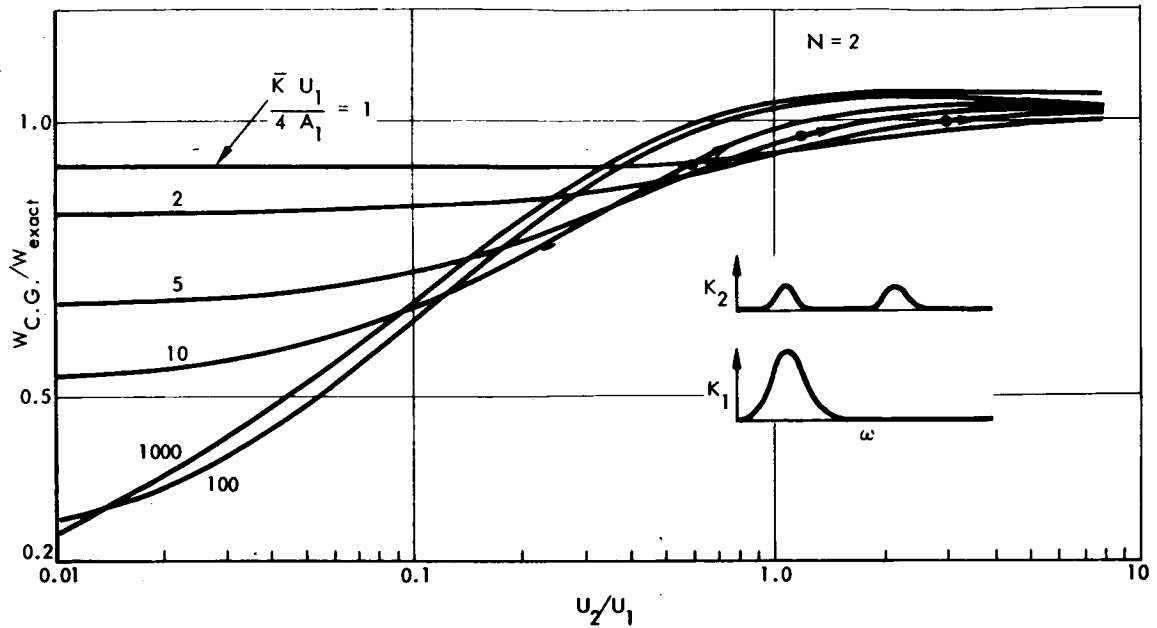


FIGURE 1a. EFFECT OF HOT LINES ON THE EMISSION FROM HIGH TEMPERATURE GAS VIEWED THROUGH A COOL ABSORBING LAYER.

(The ordinate is the ratio of the radiance of a two temperature slab computed in the modified Curtis-Godson approximation to the exact value. The abscissa is the ratio of the mass of the high temperature rear slab to that of the low temperature front slab. In the rear slab two equally intense lines are excited; whereas in the front slab, all the line strength is concentrated in only one of the lines.)

a cool absorbing layer is more sensitive to differences between the line widths in the two slabs (Fig. 3). The worst case occurs when the emission width is small and the absorption path is large. In this case, for Lorentz lines, errors greater than a factor of two can occur. Again, however, the errors are relatively small when the thickness of absorber is not too large compared to that of the emitter.

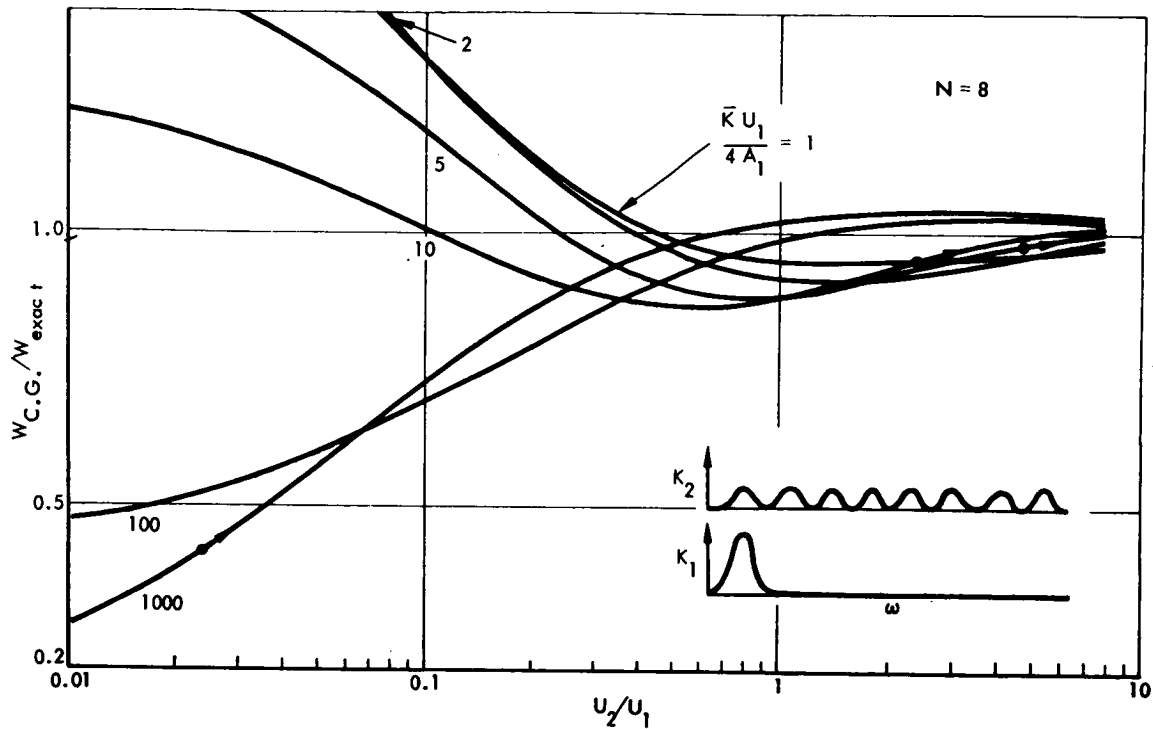


FIGURE 1b. EFFECT OF HOT LINES ON THE EMISSION FROM A HIGH TEMPERATURE GAS VIEWED THROUGH A COOL ABSORBING LAYER.

(This figure is the same as Figure 1a except that the single line in the cool section is divided into eight equally intense lines in the hot section, one of which is the original line.)

### Errors Due to the Use of the Random Model and Simplified Curves of Growth

The validity of the random band model is fairly easily tested experimentally. It is well known that, for Lorentz lines, the random model predicts that the logarithm of the low resolution transmission of a cell of absorber should be exactly linear in the pressure so long as the cell length, temperature, and mole fractions of the various species are held constant. This is not true of other models. For example, an Elsasser model predicts a linear dependence at high transmission changing over to a quadratic dependence at low transmission. Examination of data taken by Burch [4] and by Simmons [5] indicates that, for temperatures above 600° K, the random model is consistent with the data within experimental scatter. However, since these measurements cover a

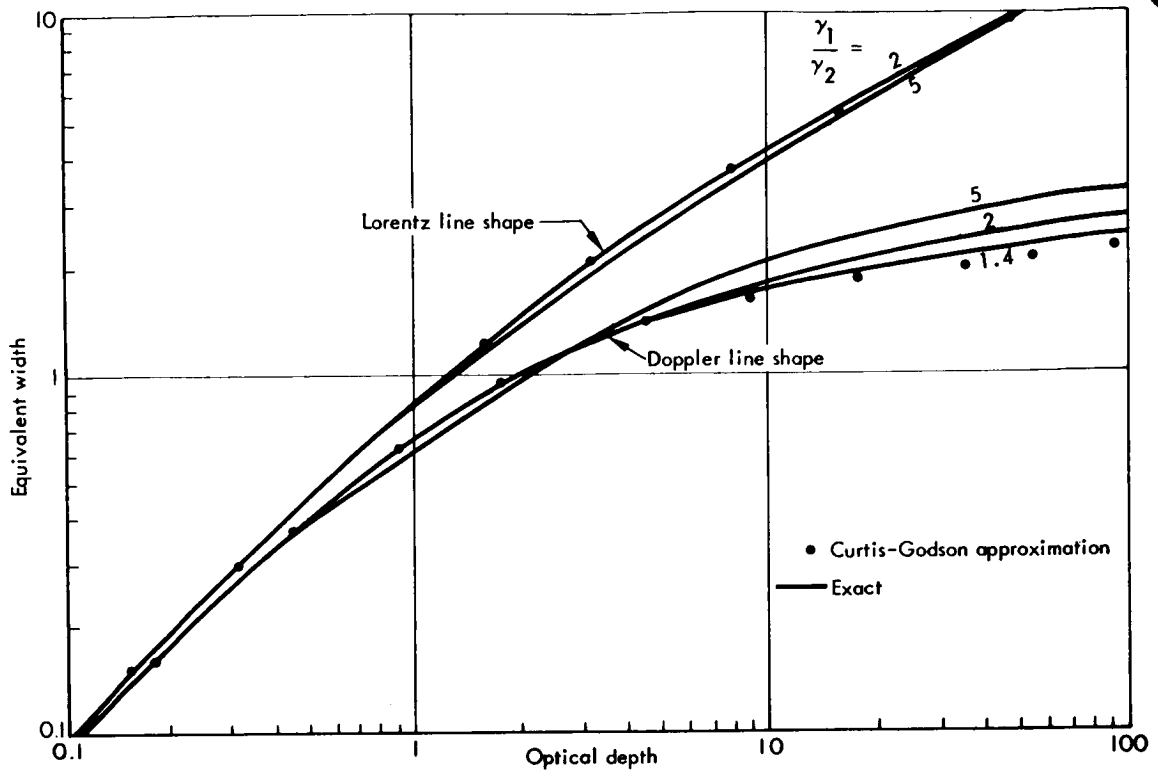


FIGURE 2. ACCURACY OF THE CURTIS-GODSON APPROXIMATION FOR EVALUATING TOTAL EQUIVALENT ABSORPTION WIDTHS FOR A TWO SLAB GAS. (The solid lines represent the exact values and the points the values given by the Curtis-Godson approximation. The two slabs have the same masses but different line half widths.)

limited range of path lengths and pressures, it is desirable to obtain additional confirmation. To accomplish this and also to test the whole procedure used at General Dynamics/Convair for interpreting the laboratory data for long homogeneous path measurements at one atmosphere pressure to derive appropriate band model parameters for the inhomogeneous radiance calculation, we have carried out the following numerical "experiment." The lines strengths and widths for water vapor tabulated by Gates et al. [6] were used to carry out detailed calculations of the spectrum in the region near  $3950\text{ cm}^{-1}$ . Although it is known that this tabulation does not include many of the "hot" lines important at high temperature and also does not take into account the vibration-rotation interaction effects, it was assumed to describe a "pseudo" molecule



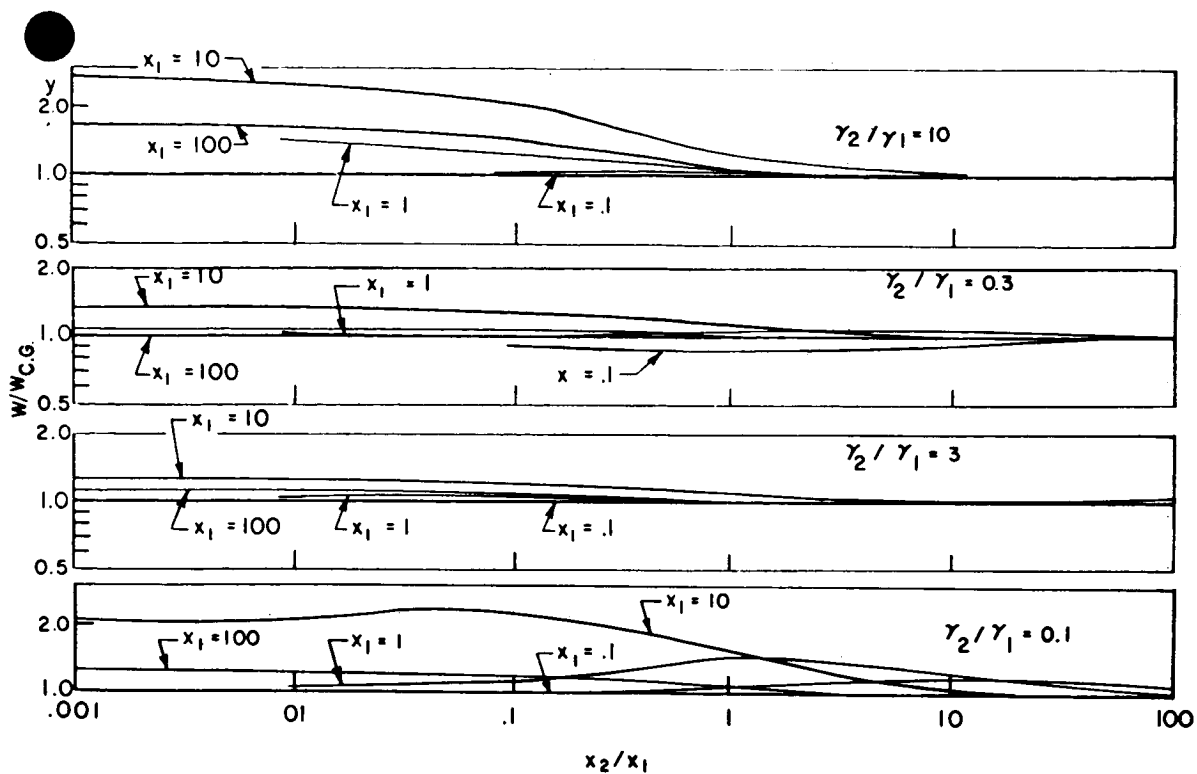


FIGURE 3. ACCURACY OF THE CURTIS-GODSON APPROXIMATION FOR EVALUATING THE EQUIVALENT EMISSION WIDTH OF A LORENTZ LINE FOR A TWO SLAB GAS WHEN ONLY THE REAR SLAB RADIATES. (The abscissa is the ratio at the line center of the optical depth of the rear slab to that of the front slab.)

similar to water vapor. The quasi-random band model procedure with a  $1 \text{ cm}^{-1}$  cell size was used to calculate the transmission of various path lengths between 0 and 10 meters of "water vapor" at one atmosphere pressure and at various temperatures. (The conditions covered the same range as the General Dynamics/Convair long path measurements.) These data were then degraded spectrally with a triangular slit function of  $25 \text{ cm}^{-1}$  half width. These resulting low resolution data were then "reduced" by the same procedure used in the General dynamics/Convair experiments (Ludwig et al [7]) to obtain values for the mean absorption coefficient and the fine structure parameter ( $a = \gamma/d_{LR}$ ), that is, by fitting the experimental curves of growth with a Ladenburg-Reiche function.

To test the inhomogeneous formalism, two sets of calculations were carried out. The radiances of various two-slab volumes were calculated with the low resolution model described previously in this report (The Band Model Approximations), using these "experimentally" derived band model parameters. In Figures 4 and 5, these data are compared to the values obtained from a direct quasi-random band model calculation of the inhomogeneous path (using the normal Curtis-Godson approximation to evaluate the effective half-widths). The calculations were carried out for a range of slab thickness between 0 and 10 meters and pressures between 0.1 to 1 atmosphere. Figure 4 shows that, when the temperature varies by less than a factor or two, the two calculations agree quite well — even when all the lines are assigned a uniform average intensity ( $\Delta E = \infty$ ). The data in Figure 5 indicate, however, that when the front layer is at a very low temperature, sizable errors may be incurred when the cold layer is appreciably absorbing if "hot" lines are not considered.

### Choice of the Curve Growth

It is well known that, for a homogeneous volume of gas, the curves of growth for collision-broadened lines are not very sensitive to the distribution of line intensities. This is demonstrated in Figure 6 where the curves of growth for a delta function distribution, an  $S^{-1}$  distribution and that deduced from detailed calculations of water vapor by Malkmus [8] are compared. The curve of growth based on Malkmus' calculations was evaluated by taking all the lines for which the energy of the lower state was less than  $15,000 \text{ cm}^{-1}$  above the ground state and dividing these into ten groups ( $\Delta E = 1500 \text{ cm}^{-1}$ ). A mean absorption coefficient and a mean line density were evaluated for each group, the mean line density being defined according to

$$1/d_n = \left[ \sum (S^{1/2}/d)_i \right]^2 / \sum (S/d)_i ,$$

where the summation extends over all branches (i) belonging to the nth interval. The fact that this curve of growth is flatter than that for a  $S^{-1}$  distribution indicates that "hot" lines may be fairly important for high temperature water vapors.

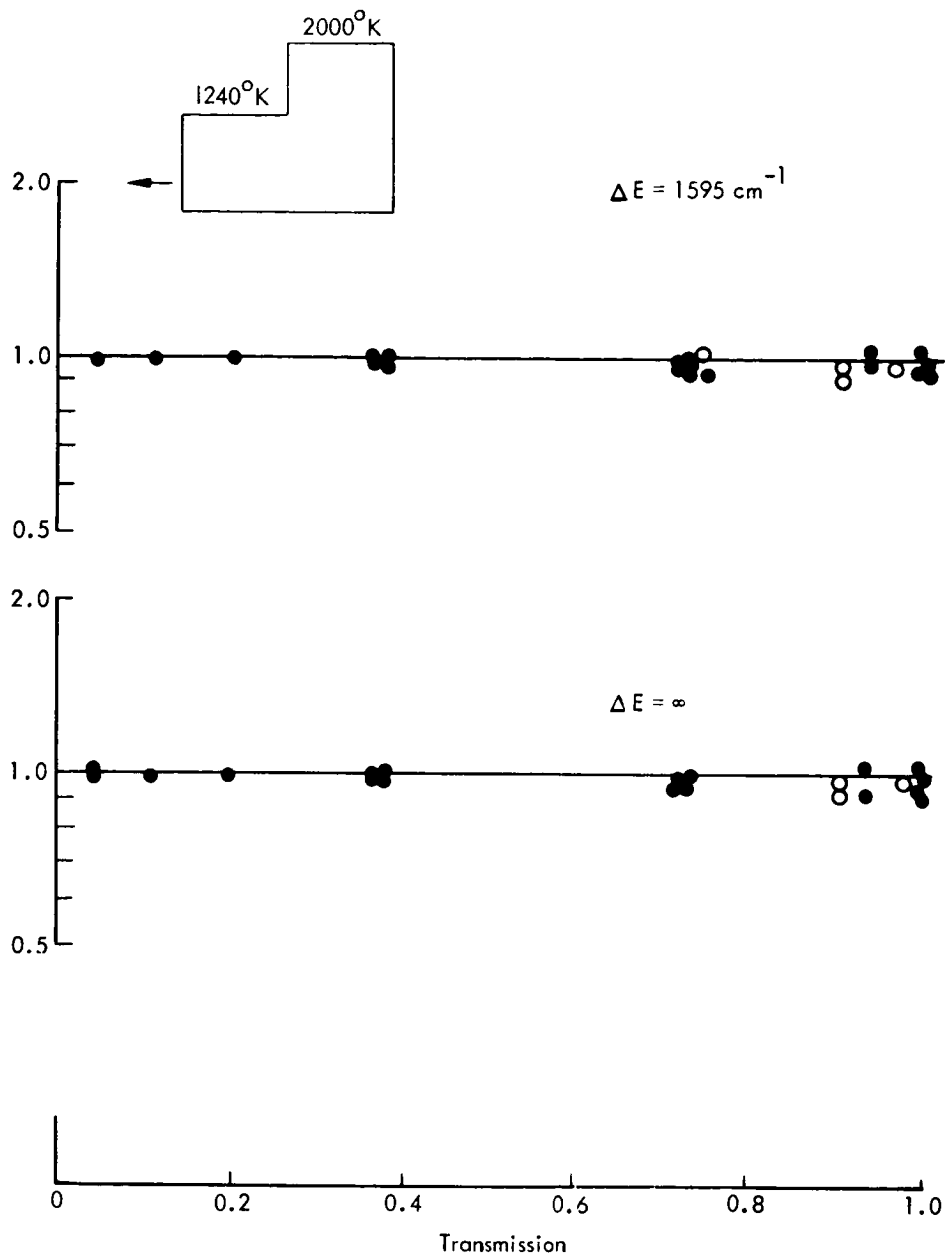


FIGURE 4. EFFECT OF THE CHOICE OF THE LINE GROUPING PARAMETER  $\Delta E$  ON THE CALCULATED EMISSION OF A TWO SLAB GAS WHEN THE TEMPERATURE VARIATIONS ARE MODERATE.

(The points represent the ratios of the predicted low resolution radiance to the "exact" values for various combinations of pressures and slab thicknesses. The pressures varied from 0.1 to 1 atmosphere and the slab thicknesses from 0 to 10 meters. The abscissa is the transmission of the front slab for grey radiation.)

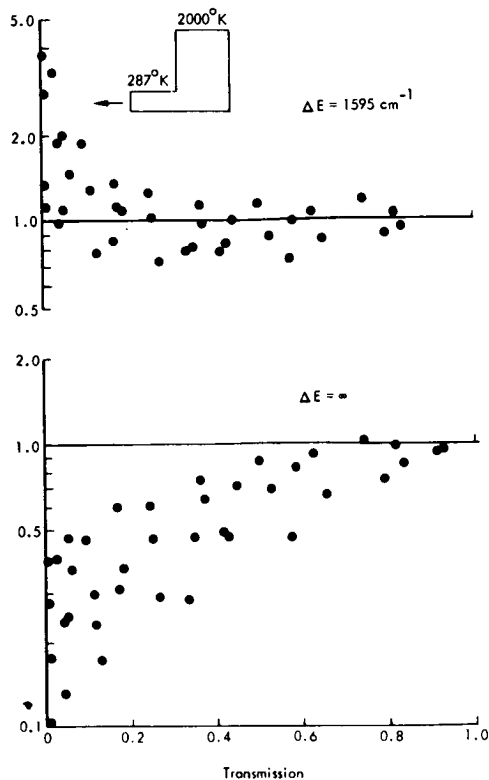


FIGURE 5. EFFECT OF THE CHOICE OF THE LINE GROUPING PARAMETER ON THE CALCULATED EMISSION OF A TWO SLAB GAS WHEN THE FRONT SLAB HAS A LOW TEMPERATURE. (Here the abscissa is the transmission of the front slab for the radiation emitted by the rear slab.)

To study the effect of "hot" lines in a more reasonable inhomogeneous flow field, some calculations were carried out for a temperature and concentration distribution characteristic of a constant pressure turbulent flame. Here the temperature distribution was assumed to be bell-shaped and the water vapor mole fraction to be similarly bell-shaped or to be uniform (Fig. 7). In Figure 8 we compare the calculated radiance for three models. In the first ( $g_n = f_n = \delta_{n1}$ ), all the lines are assigned a uniform average intensity; the second ( $g_n = f_n = 1$ ) roughly corresponds to a  $S^{-1}$  distribution, and the third ( $f_n, g_n$  variable) is that deduced from Malkmus' calculations. In all cases the line density and the mean absorption coefficients were normalized so that each model gave the same answer for a homogeneous path in the optically thin limit and in the square root limit.

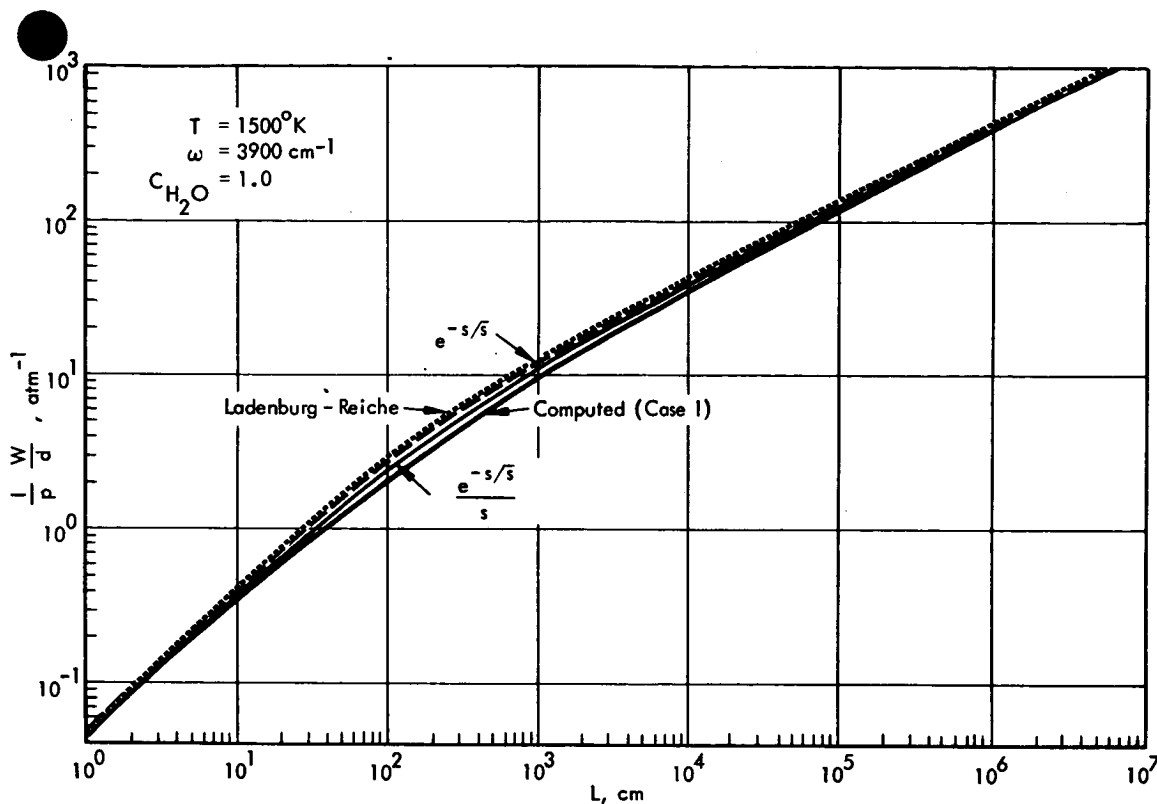


FIGURE 6. COMPARISON OF VARIOUS CURVES OF GROWTH.  
 (The lowest curve was deduced from detailed calculations by Malkmus for water vapor at  $3950 \text{ cm}^{-1}$ .)

The characteristic widths of the temperature profile varied from 1 to 10 meters at 1 atmosphere pressure to 10 to 100 meters at 0.01 atmospheres. Two peak temperatures were considered:  $1900^{\circ}\text{K}$  and  $1000^{\circ}\text{K}$ . Figure 8 shows that the computed radiances for the second and third case do not differ by more than 30 percent except at the lowest pressure (where Doppler broadening is important) or when the gas is highly opaque. However, considerable error can occur when the first (and simplest) model is used.

There is little information available for individual collision line widths at high temperature. However, the calculations do not appear very sensitive to variations in the widths of the hot lines so long as the low resolution curves of growth can be measured for homogeneous paths. A decrease of a factor of two in the width of the "hot" lines caused the computed radiances for these particular inhomogeneous paths to change by less than 11 percent.

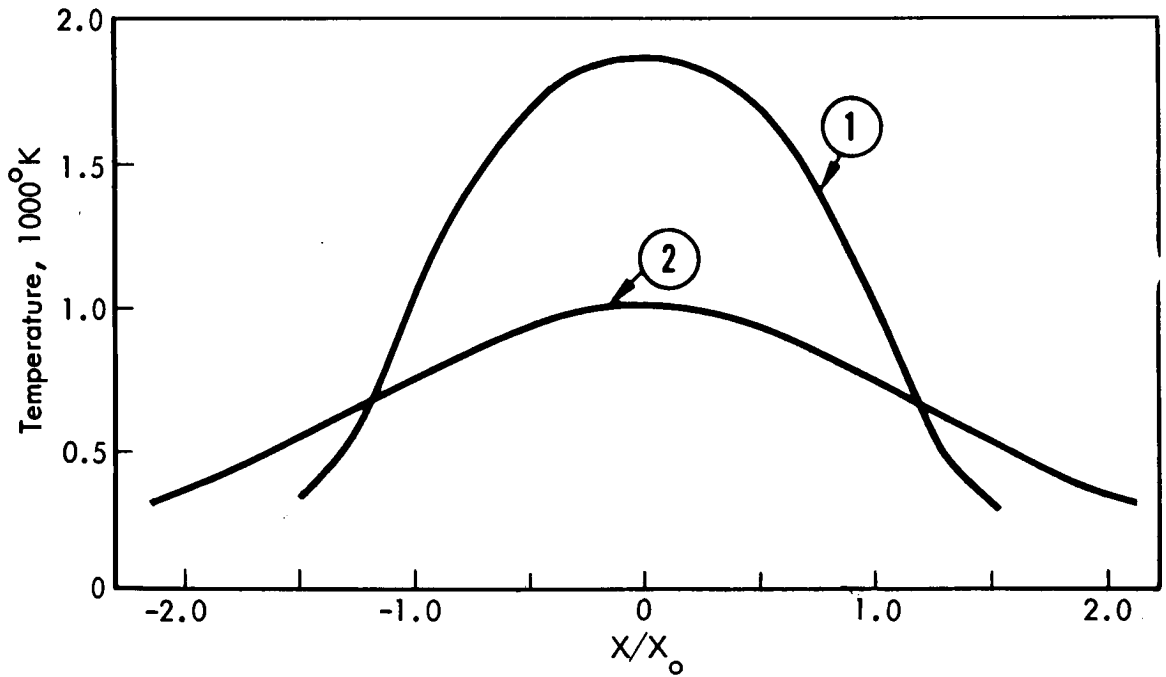
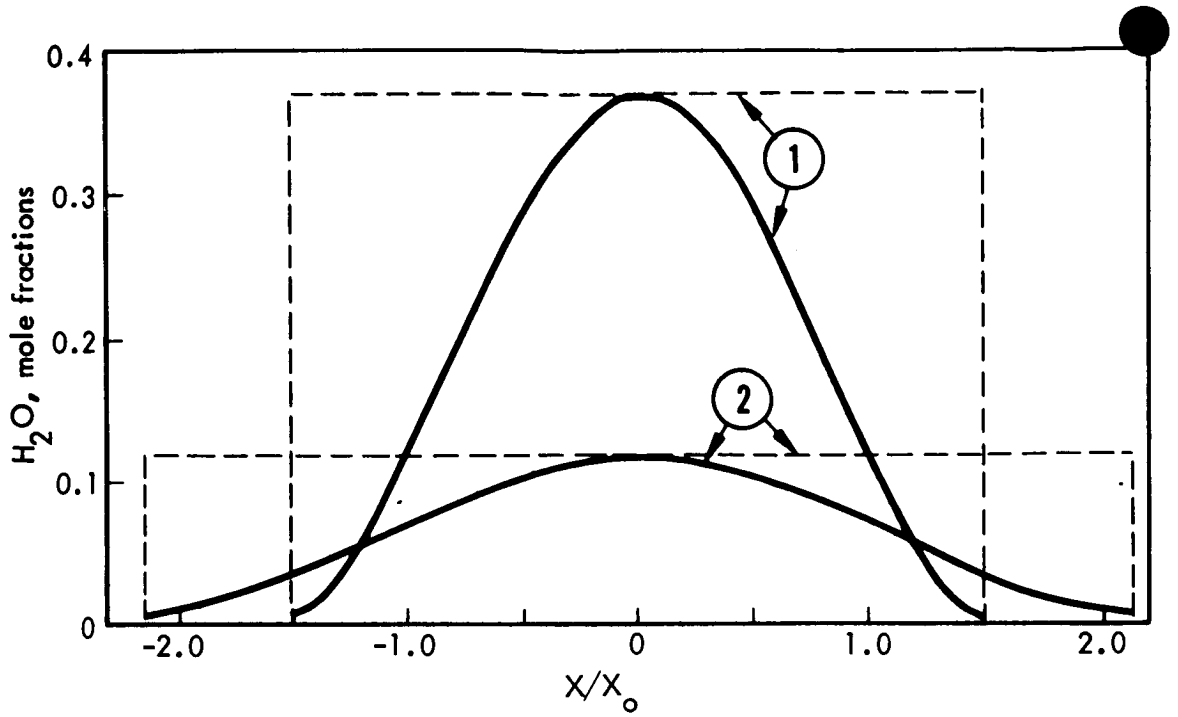


FIGURE 7. TEMPERATURE AND CONCENTRATION PROFILES USED TO COMPARE VARIOUS RADIANCE MODELS (See Fig. 8)

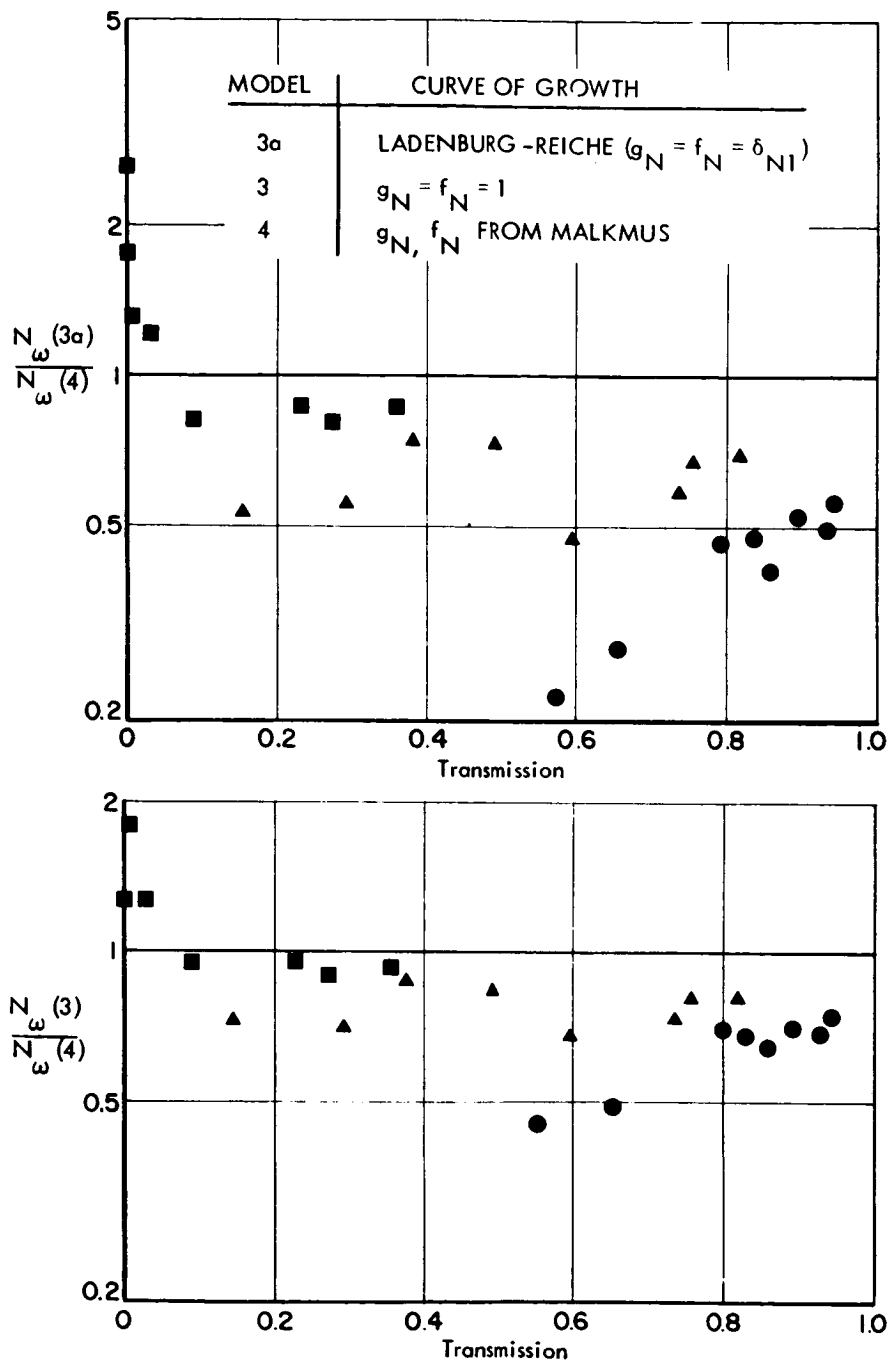


FIGURE 8. EFFECT OF MODEL COMPLEXITY ON THE COMPUTED RADIANCE FOR THE GAS PROFILES SHOWN IN FIGURE 7. (The squares, triangles and circles correspond to pressures of 1, 0.1 and 0.01 atmospheres, respectively. The abscissa is the transmission of the entire volume for grey radiation.)

## SUMMARY

The present sensitivity analyses have given some indication of the absolute accuracy that may be expected in evaluating the infrared radiant heat transfer from fairly large inhomogeneous volumes of gases characteristic of typical nonscattering rocket exhaust gases. Although it was found that the use of somewhat different curves of growth, and the use of the Curtis-Godson approximation could result in errors of more than a factor of two in some cases, these large errors occur only in rather unique situations, such as a short hot volume transmitting through a long cool absorber. The larger errors for inhomogeneous paths tended to occur at very low pressures and/or when the total transmission along the line of sight was small. For more moderate conditions, the errors tended to be less than about 30 percent. This is comparable to our present uncertainty in the absolute value of water vapor absorption coefficients.

A set of numerical values for the absorption coefficients, line density functions, recommended line widths and the parameters  $f_n$  and  $g_n$  for  $H_2O$ ,  $CO_2$  and  $CO$ , tabulated at  $25\text{ cm}^{-1}$  intervals between 1000 and  $9000\text{ cm}^{-1}$  and temperatures between  $300^\circ$  and  $3000^\circ\text{ K}$ , may be found in reference 7. A revised set is currently being prepared. These data have been incorporated into a numerical computer program for axisymmetric flow fields which may be obtained from NASA-MSFC.



## APPENDIX. USEFUL APPROXIMATION FORMULA FOR CURVES OF GROWTH

In carrying out numerical calculations of radiant heat transfer, the computation time may often be considerably reduced if simple analytic expressions for the curves of growth can be used. We have found the following expressions to be useful.

### 1. Single Lorentz line

$$f_{LR}(x) = x e^{-x} [J_0(ix) - iJ_1(ix)] \quad : \quad \text{exact (Ladenburg-Reiche)}$$

$$f_1(x) = x / \sqrt{1 + \pi x / 2} \quad : \quad \text{within 8 percent}$$

$$f_2(x) = \frac{x}{\sqrt{1 + \pi x / 2}} + \frac{0.07x^{3/2}}{1+x^{2/2}} \quad : \quad \text{within 0.5 percent}$$

### 2. Equally intense, randomly spaced Lorentz lines

$$\ell n t \approx \bar{\tau} / \sqrt{1 + \bar{\tau} / 4a_c} \quad : \quad \text{within 8 percent}$$

Here,  $\bar{\tau}$  is the mean opacity in the weak line approximation ( $\bar{\tau} = \bar{S}\ell/d$ ) and  $a_c$  is the value of the ratio of the (intensity weighted) mean line width to the mean line spacing ( $\gamma/d$ ).

### 3. Superposition of groups of equally intense, randomly spaced Lorentz lines of geometrically decaying line strength

$$(\tau_n = (1-\beta) \beta^n \bar{\tau}) :$$

$$\ln t \approx \frac{\bar{\tau} (1-\beta)}{\sqrt{1 + \bar{\tau} (1-\beta) 4a_c}} + \frac{8a_c}{1-\beta} \left[ \sqrt{1 + \left( \beta (1-\beta) \bar{\tau} / 4a_c \right)} - 1 \right].$$

For  $\beta$  close to unity (slowly decaying intensities), this expression reduces to that for the intensity probability distribution function  $S^{-1} e^{-S/\bar{S}}$ :

$$\ln t \rightarrow 2a'_c \left[ \sqrt{1 + \bar{\tau} / a'_c} - 1 \right]$$

where  $a'_c = 4a_c / (1-\beta)$ .

4. Equally intense, randomly spaced Doppler lines:

$$\ln t \approx \sqrt{2/\ell n 2} a_D \sqrt{\ell n \left( 1 + \frac{\ell n 2}{2} (\bar{\tau} / a_D)^2 \right)} \quad : \quad \text{within 9 percent}$$

5. Superposition of groups of equally intense, randomly spaced Doppler lines of geometrically decaying strengths:

$$\ln t \approx \sqrt{2/\ell n 2} a_D \sqrt{\ell n \left( 1 + \frac{\ell n 2}{2} \left( \frac{\bar{\tau} (1-\beta)}{a_D} \right)^2 \right)} + \sqrt{\frac{6}{\ell n 2}} \frac{a_D}{1-\beta} \left\{ \ell n \left[ 1 + \left( \sqrt{\frac{\ell n 2}{6}} \frac{\bar{\tau} \beta (1-\beta)}{a_D} \right)^{2/3} \right] \right\}^{3/2}.$$

For  $\beta$  close to unity, this reduces to an approximate expression for the  $S^{-1} e^{S/\bar{S}}$  intensity distribution:

$$\ln t \approx \sqrt{\frac{3}{2\ell n 2}} a'_D \left\{ \ell n \left[ 1 + \left( \sqrt{\frac{2\ell n 2}{3}} \frac{\bar{\tau}}{a'_D} \right)^{2/3} \right] \right\}^{3/2}$$

where  $a'_D = 2a_D / (1-\beta)$ .

## 6. Voigt line shape

If  $W_C$  and  $W_D$  are the equivalent widths for the pure Lorentz line shape and the pure Doppler line shape, respectively, (either exact expressions or one of the approximate expressions given above), and approximate expression for the equivalent width of a line having combined Lorentz and Doppler broadening is given by

$$W_V = W^* \sqrt{1 - y^{-\frac{1}{2}}}$$

$$\text{where } y = \left[ 1 - (W_C/W^*)^2 \right]^{-2} + \left[ 1 - (W_D/W^*)^2 \right]^{-2} - 1.$$

Here  $W^*$  is the equivalent width in the optically thin approximation ( $W^* = S\ell$ ).

The equivalent width calculated according to this expression is compared to the exact values by van der Held in Figure 9.

## REFERENCES

1. Goody, R. M.: Atmospheric Radiation I: Theoretical Basis. Oxford Clarendon Press, 1964.
2. Plass, G. N.: J.O.S.A., vol. 50, 1960, p. 868.
3. Wyatt, P. J.; Stull, V. R.; and Plass, G. N.: J.O.S.A., vol. 52, 1962, p. 1209.
4. Burch, D. E.; and Gryvnak, D. A.: Report U-1929, Ford Motor Co., 1962; Burch, D. E.; France, W. L.; and Williams, D.: Appl. Optics, vol. 2, 1963, p. 585.
5. Simmons, F. S.; Arnold, C. B.; and Smith, D. H.: Studies of Infrared Radiative Transfer in Hot Gases, I: Spectral Absorptance Measurements in the  $2.7\mu$   $H_2O$  Bands. BAMIRAC Report 4613-91-T, Infrared Physics Laboratory, Willow Run Laboratories, University of Michigan, Aug. 1965.
6. Gates, D. M.; Calfee, R. F.; Hansen, D. W.; and Benedict, W. S.: NBS Monograph 71, 1964.
7. Ludwig, C. B., et al.: Study on Exhaust Plume Radiation Predictions, Final Report. General Dynamics/Convair Report No. GDC-DBE 66-017, Dec. 1966.
8. Malkmus, W.: Private communication.

---

## DISCUSSION

J. H. Clarke, Brown University: Is the intent of these detailed calculations to find only the heating at the base of rockets, or are they also applicable to plume discrimination and diagnostic problems?

A. Thomson: The intention of the work we have done for NASA was primarily to evolve techniques for evaluating radiant heat transfer to the vehicle base. The diagnostic problem was of secondary interest. The accuracy requirements in the two cases are quite different. If the models are sufficiently accurate, then perhaps they can be used for the inverse problem; but our primary concern was heat transfer.

J. H. Clarke: From the perspective of a fluid mechanist, I infer that the influence of the radiation on the flow is negligible.

A. Thomson: Yes, mostly because the temperatures are low, 2000° to 3000°K. At low pressures there can be significant radiative cooling of particulate matter in the flow, if the particles are strong radiators, such as carbon particles; but the net heat losses are still relatively small compared to the energy stored in the gas. On the other hand, if you follow the hot gas far enough down in the trail, you may lose eventually significant amounts of energy by radiation; but that loss does not affect the heat transfer to the vehicle.

---

# REVIEW OF EXPERIMENTAL VERIFICATION OF THE CURTIS-GODSON APPROXIMATION FOR INFRARED SPECTRAL RADIATION FROM HIGH TEMPERATURE GASES

By

N 68-18091

B. Krakow and H. J. Babrov

---

## ABSTRACT

Calculations of radiant heating for inhomogeneous hot gases require knowledge of spectral transmittances of inhomogeneous optical paths. Determination of these transmittances is a difficult problem that can be attacked by means of the Curtis-Godson approximation. This method replaces each inhomogeneous optical path with a hypothetical homogeneous path that has the same transmittance. The formulae depend on the parameter  $x = S^* p l / 2 \pi \gamma$ , where  $S^*$  is the mean line strength,  $p$  the partial pressure of absorber,  $l$  the path length, and  $\gamma$  the mean line half-width for the spectral interval considered. Any inhomogeneous path may be treated as a series of imaginary zones that are small enough to be considered homogeneous.

The Curtis-Godson approximation has been tested experimentally at the Warner & Swasey Company, at General Dynamics/Convair, and at the University of Michigan.

At the Warner & Swasey Company infrared spectral transmittances of inhomogeneous hot samples of  $H_2O$  and  $CO_2$  were measured. Each inhomogeneous hot gas specimen actually consisted of two or three homogeneous zones in series. The transmittance of each zone was measured, as was the transmittance of the entire multi-zone assembly. The measured transmittance of each inhomogeneous path was compared with a transmittance calculated from the homogeneous zonal transmittance, using the Curtis-Godson approximation in conjunction with a random band model. The measured and calculated inhomogeneous transmittances concurred to within about 0.02. The error appeared to be due more to the band model theory than to the Curtis-Godson approximation.

The General Dynamics workers correlated measured radiances of combustion products above the flames from an array of burners with calculated values obtained using the Curtis-Godson approximation and previously measured band model parameters.

At the University of Michigan radiances of samples with continuous temperature distribution were studied in both flames and furnace-heated gas cells. The data were compared with predictions based on a semi-empirical expression that has been shown by D. K. Edwards to be a limiting form of the Curtis-Godson approximation.

---

## INTRODUCTION

Fundamental data on transmittances of gases are usually measured and reported for homogeneous gases. In most practical problems, however, the specimens have gradients of temperature, pressure, and/or concentration, and the transmittances of these inhomogeneous gases are needed for the calculation of the radiant heat transfer.

Homogeneous gases are often treated successfully by band model methods. Since these methods are the subject of other papers at this meeting, we will not delve into band models in this paper.

A method that meteorologists have found useful for calculating transmittances of inhomogeneous atmospheric paths is the Curtis-Godson approximation. Since the theoretical basis for this approximation is discussed in other papers at this meeting, we will discuss experimental verification of the method for conditions typical of combustion gases. The experiments discussed here were carried out at the Warner & Swasey Company Control Instrument Division [1], at General Dynamics/Convair [2], and at the University of Michigan, Willow Run Laboratories [3, 4, and 5]. Before we proceed to a description of the experiments, we wish to clarify one point regarding the Curtis-Godson method. The Curtis-Godson approximation is separate and distinct from band model approximations, and can be used for a single line, whereas band models are useful for an ensemble of lines over a given spectral interval. Thus, either theoretical method (band model or Curtis-Godson) can be validated independently of the other.

## WARNER AND SWASEY MEASUREMENTS

At the Warner & Swasey Company the accuracy of the Curtis-Godson approximation has been tested experimentally with measurements of the absorptance of hot water vapor and carbon dioxide. To simplify the problem of predicting the transmittance through an inhomogeneous gas and to permit easy comparison of theoretical and experimental transmittances, we used inhomogeneous paths that were composed of series of smaller homogeneous paths.

Measurements were made at a variety of temperatures, pressures, and path lengths. Figure 1 shows a schematic diagram of the optical system used for the longest optical paths. With this system, the chopped signal from a globar makes three passes through each of two furnaces and then enters a small grating monochromator with which spectral measurements are made. Each furnace contained an 8-inch gas cell thereby providing two individually isothermal zones in series with a 24-inch optical path per zone. The temperatures and pressures of the two zones were independently variable.

In order to make measurements with shorter optical paths, we could, by changing the mirrors of the fore optics, pass the globar signal through each furnace only once. We used this single pass mode of operation with a 1.5 inch cell to study short optical paths and with an 8-inch cell for intermediate paths. A description of the experiment procedure is presented in the following paragraphs.

The first cell was filled and its transmittance measured with the second cell evacuated. Then, the second cell was filled and the transmittance of the entire two-zone assembly was measured. Finally, the first cell was evacuated, and the transmittance of the second cell was measured.

After making these measurements, the two-zone transmittance was calculated from the transmittances of the two individual zones using the Curtis-Godson approximation. The calculated value was then compared with the measured two-zone transmittance.

The furnace-heated gas cells just described were used to study water vapor at temperatures up to 1273° K. Carbon dioxide samples, produced by flat flame burners, were studied at higher temperatures. Figure 2 shows a three-zone burner assembly. Each zone consisted of a 2-inch-square main burner flanked by a pair of 0.5 inch by 2 inch burners. Hot CO<sub>2</sub> was generated



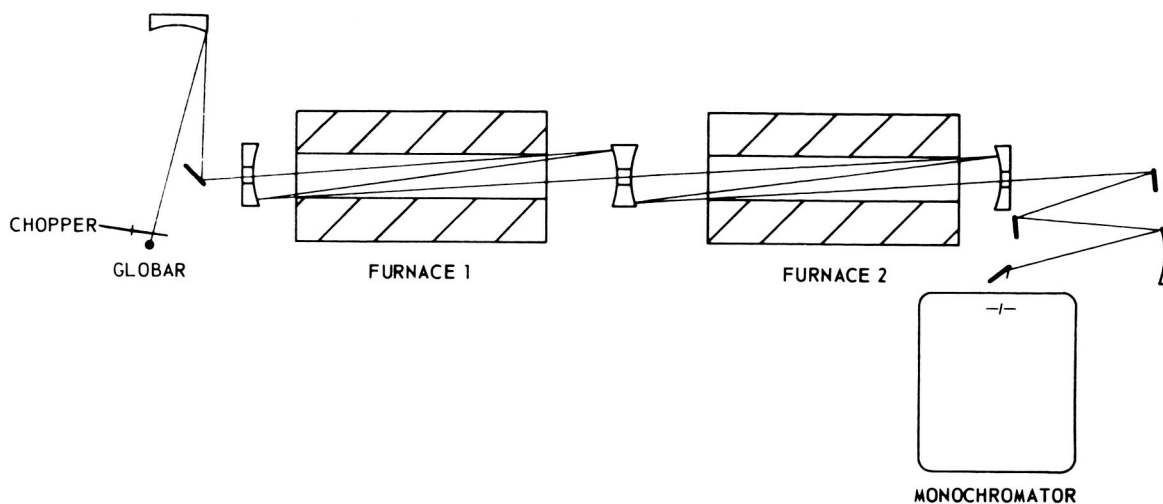


FIGURE 1. TWO FURNACE TRIPLE-PASS OPTICAL SYSTEM

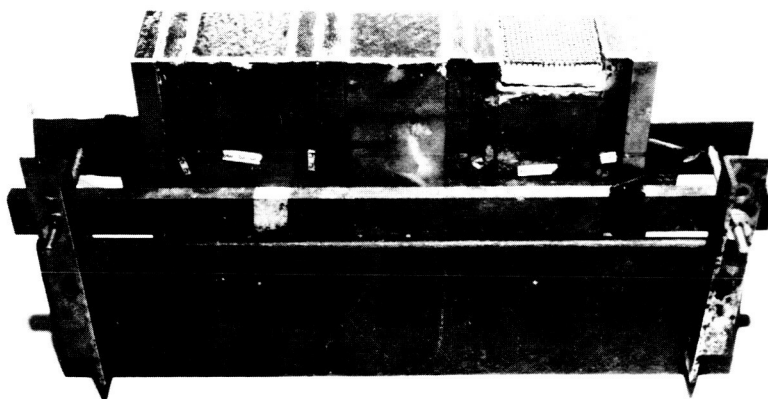


FIGURE 2. THREE-ZONE FLAT-FLAME BURNER ASSEMBLY

by burning carbon monoxide with oxygen on the 2-inch-square burner and adding a controlled amount of cold  $\text{CO}_2$  to each burning mixture to regulate the flame temperature. Guard flames on the 0.5-inch by 2-inch burners produced combustion products that had the same temperature as the  $\text{CO}_2$  but were all transparent at the wavelengths studied. Therefore, each zone was simply an isothermal specimen of  $\text{CO}_2$  as far as the spectroscopic observations were

concerned. Measurements were made on individual zones to obtain their transmittances and temperature, as well as on two zones in series to test methods of calculating temperature profiles from spectroscopic data.

The zone on the right side of Figure 2 was used for the lowest temperatures. It had a stainless steel gauze filter above the main burner to help cool the combustion product. At each end of the assembly was a 0.5 inch x 2 inch sparger by means of which the optical path between the flames and the spectrometer housing was flushed with nitrogen to eliminate interference by atmospheric CO<sub>2</sub>.

As with furnace-heated water vapor, a comparison was made between measured transmittances of inhomogeneous CO<sub>2</sub> samples and those calculated, using the Curtis-Godson approximation, from measured transmittances of its component zones.

In making these calculations, the band model used was the random model with constant line widths. Two line strength distributions which were tried, the exponential distribution and delta function distribution, showed virtually no difference in accuracy. The formulae depend on the parameter

$$x = [ (S/d) \ell ] / [ 2\pi (\gamma/d) ],$$

where  $\ell$  is the path length and the parameters  $S/d$  and  $\gamma/d$  (usually called band model parameters) are the effective line strength and effective line width per unit frequency interval. Using the Curtis-Godson approximation, the transmittance of an inhomogeneous sample can be expressed in terms of the transmittances and  $x$ -values of its component zones.

Generally, transmittances calculated with this expression are not very sensitive to errors in zonal  $x$ 's as long as the determination of zonal transmittances are independent of them. Therefore, with moderately accurate values of zonal  $x$ 's, the accuracy with which the transmittance of an inhomogeneous sample can be calculated should be limited by the accuracy of our transmittance measurements and the suitability of the theory. This is particularly true at the high and low  $x$ -values where the equation reduces to forms in which the transmittance of the whole is independent of the zonal  $x$ 's to a good approximation.

Simmons has used the high- $x$  approximation extensively, and we have found it to be quite good.

Measurements of hot water vapor transmittances were made at two frequencies,  $3990\text{ cm}^{-1}$  and  $3505\text{ cm}^{-1}$ . These were convenient frequencies at which to work because, at these frequencies, the absorptance of hot water vapor is substantial, while absorptance by atmospheric water vapor is much weaker, and it is easy to eliminate the absorptance due to atmospheric water vapor by flushing the optical train with dry nitrogen. On the other hand, we believe that these are representative frequencies in the water vapor spectrum, and the observations made should be typical of what may be expected at other frequencies.

Data reduction was carried out in two ways to get results corresponding to two different-sized spectral intervals. First the transmittance at a point in the spectral traces was studied. This transmittance was an average (weighted by the slit function) over the spectral slit width of the spectrometer (about  $2\text{ cm}^{-1}$ ). Second, the area under the spectral trace of an interval of about  $10\text{ cm}^{-1}$  was studied to get transmittance values averaged over this larger spectral interval. The area measurements are insensitive to the instrumental slit function. Calculations made with the area measurements appeared to be a trifle more accurate than those using single points, but the differences were very small. Results involving area measurements were published in Reference 1. At this time we will only present single point data.

Table I compares measured and calculated transmittances at  $3990\text{ cm}^{-1}$  for two zones for both of which the parameter,  $x$ , was high. Properties of zone 1 are labeled with the subscript 1, and properties of zone 2 are labeled with the subscript 2. Zone 1 had a temperature of  $1273^\circ\text{K}$  and the temperature of zone 2 was  $637^\circ\text{K}$ . The pressures of water vapor in the two zones are given in columns 1 and 2. Columns 3 and 4 give the measured transmittance of each zone. Column 5 gives the measured transmittance of the two-zone assembly. Column 6 gives the two-zone transmittance calculated by the Curtis-Godson approximation using the explicit values for  $x_1$  and  $x_2$  given in the heading. Column 7 gives the two-zone transmittance calculated with the high- $x$  approximation to the Curtis-Godson approximation (in which the  $x$  values do not occur explicitly). The calculated two-zone transmittance in column 6 is always higher than the measured transmittance by approximately 0.01 to 0.02.

TABLE I. TWO-ZONE WATER VAPOR TRANSMITTANCE AT  $3990 \text{ cm}^{-1}$

Optical Path: 24 inches per zone  
 $T_1 = 1273^\circ \text{ K}$        $T_2 = 637^\circ \text{ K}$   
 $x_1 = 3.49$        $x_2 = 2.53$

$p_1$ (mm)	$p_2$ (mm)	Measured Transmittance			Calculated $\bar{\tau}$	
		$\tau_1$	$\tau_2$	$\bar{\tau}$	Using $x_1$ And $x_2$	Using High-x Limit
49	53	0.745	0.711	0.622	0.630	0.638
100	104	0.597	0.503	0.399	0.414	0.424
151	151	0.443	0.358	0.247	0.260	0.270
101	51	0.573	0.722	0.501	0.518	0.525
148	52	0.452	0.710	0.402	0.415	0.421

Table II gives similar data for measurements made with both cells at the same temperature. Here the only inhomogeneities are due to pressure differences. The discrepancies between measured and calculated two-zone transmittances are about the same as before. Note that when the pressures, as well as the temperatures in the two cells, are essentially the same, this discrepancy is not generally any smaller. In this case, where the inhomogeneity is negligible, the discrepancy cannot be due to the Curtis-Godson approximation. Therefore, the Curtis-Godson approximation may not be the major source of error in any case. The discrepancy may be primarily due to the error in the band model representation of the real spectrum.

Table III gives the results of medium  $x$ -measurements. This is the case we were most worried about because it is the case in which the transmittances are most sensitive to errors in  $x$  and the case where the Curtis-Godson approximation is expected to be least accurate. However, unless these errors compensated for each other, they appear to be small.

TABLE II. TWO-ZONE WATER VAPOR TRANSMITTANCE AT 3990 cm<sup>-1</sup>

Optical Path: 24 inches per zone  
 $T_1 = T_2 = 1273^\circ \text{K}$   
 $x_1 = x_2 = 3.49$

p <sub>1</sub> (mm)	p <sub>2</sub> (mm)	Measured Transmittance			Calculated $\bar{\tau}$	
		$\tau_1$	$\tau_2$	$\bar{\tau}$	Using x <sub>1</sub> And x <sub>2</sub>	Using High-x Limit
53	53	0.720	0.729	0.621	0.628	0.634
102	105	0.571	0.566	0.425	0.443	0.450
150	153	0.438	0.443	0.284	0.306	0.314
51	104	0.743	0.571	0.515	0.524	0.530
56	146	0.724	0.464	0.419	0.428	0.435

TABLE III. TWO-ZONE WATER VAPOR TRANSMITTANCE AT 3990 cm<sup>-1</sup>

Optical Path: 8 inches per zone  
 $T_1 = 1273^\circ \text{K}$        $T_2 = 637^\circ \text{K}$   
 $x_1 = 1.16$        $x_2 = 0.84$

p <sub>1</sub> (mm)	p <sub>2</sub> (mm)	Measured Transmittance			Calculated $\bar{\tau}$		
		$\tau_1$	$\tau_2$	$\bar{\tau}$	Using x <sub>1</sub> And x <sub>2</sub>	Using High-x Limit	Using Low-x Limit
50	50	0.846	0.849	0.771	0.772	0.791	0.718
100	100	0.744	0.728	0.617	0.619	0.648	0.542
150	150	0.655	0.625	0.496	0.496	0.530	0.409

Table IV is concerned with measurements in which one zone was in the medium-x range and the other had a low-x. Transmittance of the two zones in series is not much lower than the transmittance of the 8-inch zone alone. Since the transmittance of the 8-inch zone was part of the input in our calculations, these calculations were not likely to be very wrong, and they are not. Table IV demonstrates the difficulty of trying to test the Curtis-Godson approximation in the low-x region with water vapor. When x is low, water vapor just does not provide enough absorption.

TABLE IV. TWO-ZONE WATER VAPOR TRANSMITTANCE AT  $3990 \text{ cm}^{-1}$

$$T_1 = 1273^\circ \text{K}$$

$$T_2 = 637^\circ \text{K}$$

$$l_1 = 8 \text{ inches}$$

$$l_2 = 1.5 \text{ inches}$$

$$x_1 = 1.16$$

$$x_2 = 0.16$$

$p_1$ (mm)	$p_2$ (mm)	Measured Transmittance			Calculated $\bar{\tau}$	
		$\tau_1$	$\tau_2$	$\bar{\tau}$	Using $x_1$ And $x_2$	Using Low-x Limit
50	50	0.853	0.960	0.840	0.836	0.819
100	100	0.751	0.923	0.723	0.720	0.693
150	150	0.650	0.882	0.612	0.607	0.573

High absorptance with low x-values can be observed in the spectrum of hot carbon dioxide where many overlapping hot bands make the average line spacing very small. Table V shows the results of three-zone measurements of hot  $\text{CO}_2$ . The temperatures in these experiments were too high for the use of furnace heated gas cells. The specimens were the streams of combustion products above  $\text{CO-O}_2$  flames. A regulated amount of cold carbon dioxide was added to one of the burning mixtures to lower the temperature of the specimen. Differences between measured values and those calculated with the low x approximation were well within the experimental error.

TABLE V. THREE-ZONE CO<sub>2</sub> TRANSMITTANCES

Optical Path: 2 inches per zone

Atmospheric Pressure

T<sub>1</sub> = 1460° K; T<sub>2</sub> = 2170° K; T<sub>3</sub> = 2760° K

Wavelength (microns)	Measured Transmittances				Using Low-x Limit
	$\tau_1$	$\tau_2$	$\tau_3$	$\tau_{total}$	
4.555	0.068	0.014	0.098	0.000	0.000
4.696	0.745	0.252	0.290	0.049	0.055
4.865	0.952	0.734	0.601	0.414	0.415

We have now tested the Curtis-Godson approximation through the gamut from high-x calculations through medium to low-x calculations. It was mentioned earlier that we also made measurements of hot water vapor at 3503 cm<sup>-1</sup>. These data are not shown because they were so much like the results at 3990 cm<sup>-1</sup> that they would lead to the same conclusions. This similarity corroborates what was said earlier about the likelihood that the behavior at these two frequencies would be typical of the water vapor spectrum.

This study indicates that the accuracy of the Curtis-Godson approximation is at least comparable to that of the band model theory we used. Consequently, it should be possible to calculate transmittances of inhomogeneous and homogeneous specimens with similar accuracy, whenever the band model parameters are available.

## GENERAL DYNAMICS/CONVAIR MEASUREMENTS

Radiance measurements of inhomogeneous samples of water vapor with higher temperatures and longer path lengths than those shown in our previous slides were made at General Dynamics/Convair [2]. A sketch of the optical system is shown in Figure 3. The burner has a slotted tube design and is

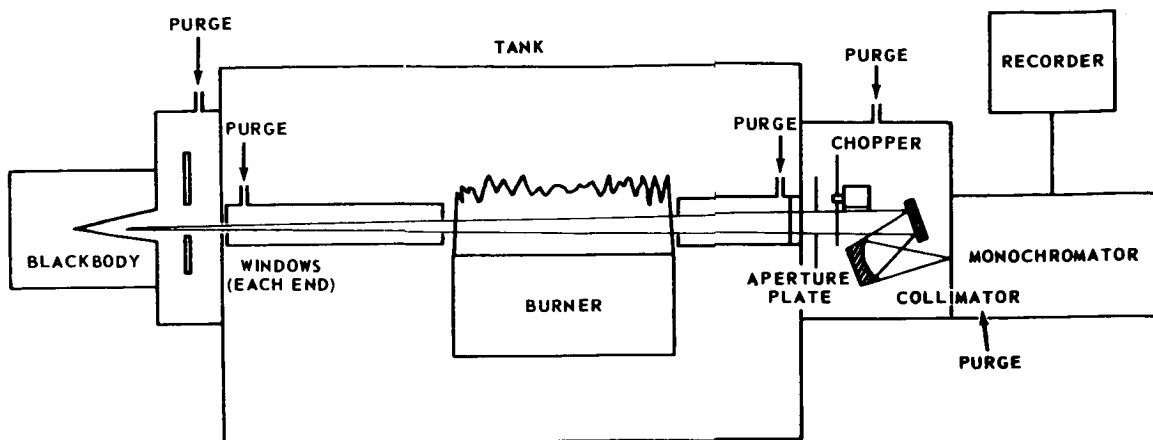


FIGURE 3. SCHEMATIC DIAGRAM LONG BURNER OPTICAL SYSTEM

composed of an array of 5-foot sections placed end to end. It is installed in a 30 ft. x 6 ft. cylindrical tank. Inhomogeneous samples were produced by operating two 5-foot sections at different temperatures. The observed radiance of such a sample in the  $2.7\mu$  band is shown as a solid line in Figure 4. The radiance of this sample, calculated at a number of frequencies with the Curtis-Godson approximation and previously determined band model parameters, is shown as circles in this figure. The agreement between theory and experiment is good.

## UNIVERSITY OF MICHIGAN MEASUREMENTS

The third study of spectra of inhomogeneous hot gases that we would like to discuss is that of F. S. Simmons at the University of Michigan, Willow Run Laboratories, who investigated samples of hot water vapor [3 and 4] and hot hydrogen fluoride [5] with continuous temperature distributions.

The water vapor samples were contained in a 60 cm cell contained in a segmented combustion tube furnace which permitted the imposition upon the sample of various controlled temperature profiles. The segmented nature of the furnace is illustrated in Figure 5.



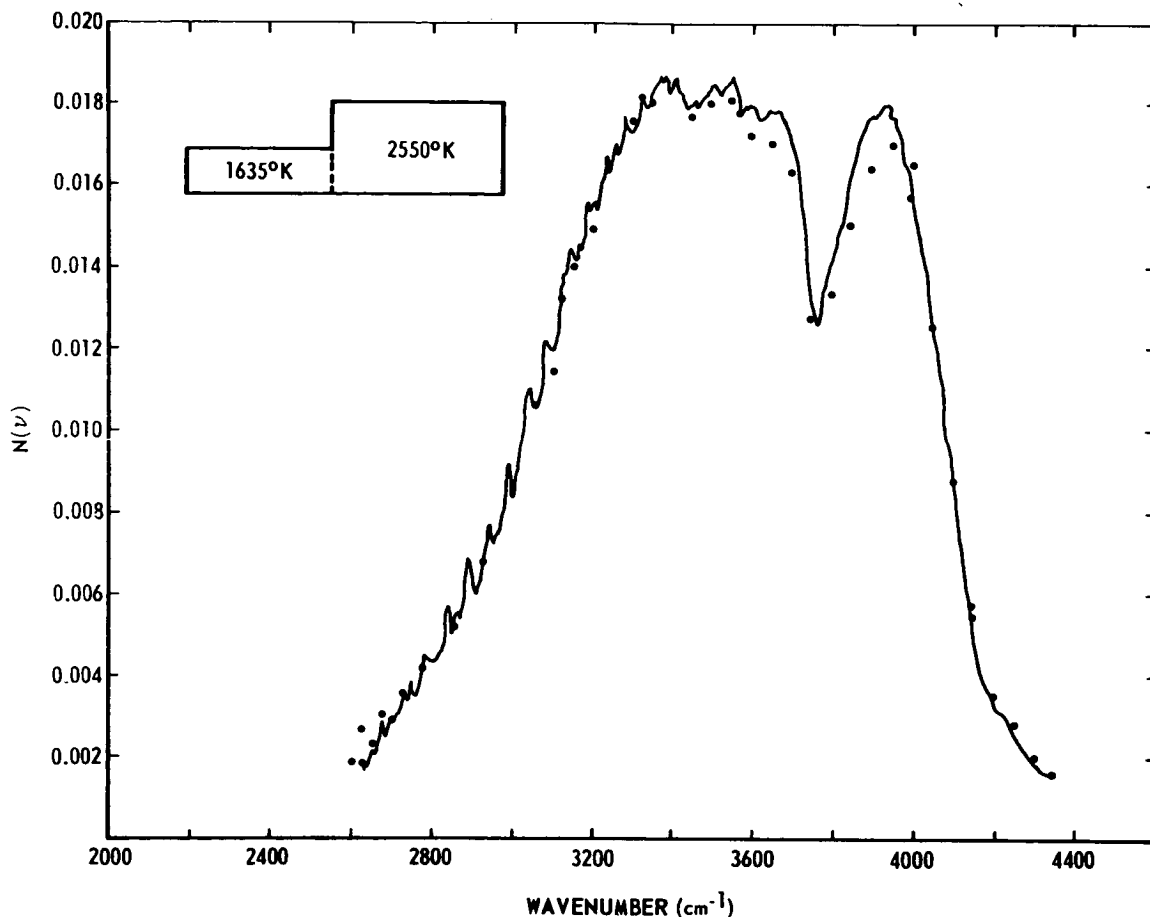


FIGURE 4. TWO-ZONE EXPERIMENTAL SPECTRAL RADIANCE USING 5-FT SLOT BURNERS AND SPECTRAL RADIANCE CALCULATED BY THE CURTIS-GODSON METHOD. (The Solid Line is from the Experimental Data.)

Simmons developed an equation for describing the radiances of his inhomogeneous samples which was based on the strong line approximation and arrived at by an inductive rather than deductive line of reasoning. However, D. K. Edwards of U. C. L. A. has shown that this formula is a limiting form of the Curtis-Godson approximation. It is gratifying to see inductive and deductive approaches lead to such common ground. Sample comparisons between calculated and observed radiances are shown in Table VI. In Simmons' words, "The results certainly indicate the utility of a nonisothermal band model, and suggest that this strong line model can be used to predict the spectral emission of hot water in the  $2.7\mu$  region, with an accuracy sufficient for many purposes."

TABLE VI. EXPERIMENTAL SPECTRAL RADIANCE USING THE SEGMENTED FURNACE AND CALCULATED RADIANCE USING THE STRONG LINE APPROXIMATION

Run	$\lambda$ ( $\mu$ )	$Q(T_o)$ ( $\text{cm}^{-1/2}$ )	$k(T_o)$ ( $\text{cm}^{-1}$ )	$\bar{N}_\lambda$ (Eq. 1) ( $\text{w-cm}^{-2}\text{-sr}^{-1}\text{-}\mu^{-1}$ )	$\bar{N}_\lambda$ (exp) ( $\text{w-cm}^{-2}\text{-sr}^{-1}\text{-}\mu^{-1}$ )
122-3	$T_o = 1229^\circ \text{K};$		$P_o = 439 \text{ mm};$	$(\Delta Y)_o = 0.175 \text{ cm};$	$T = 1229^\circ \text{K}$
	2.465	0.117	0.053	0.298	0.372
	2.562	0.250	0.100	0.528	0.667
	2.635	0.129	0.051	0.316	0.456
	2.685	0.300	0.130	0.582	0.713
	2.728	0.272	0.106	0.541	0.640
	2.805	0.296	0.127	0.560	0.654
	2.927	0.256	0.107	0.492	0.537
	3.122	0.101	0.037	0.222	0.192
122-4	$T_o = 1019^\circ \text{K};$		$P_o = 401 \text{ mm};$	$(\Delta Y)_o = 0.193 \text{ cm}$	
	2.465	0.093	0.041	0.139	0.201
	2.562	0.250	0.100	0.281	0.375
	2.635	0.141	0.055	0.185	0.274
	2.685	0.300	0.130	0.319	0.400
	2.728	0.247	0.095	0.290	0.378
	2.805	0.296	0.127	0.319	0.378
	2.927	0.209	0.088	0.270	0.309
	3.122	0.065	0.023	0.113	0.112
122-5	$T_o = 1223^\circ \text{K};$		$P_o = 414 \text{ mm};$	$(\Delta Y)_o = 0.156 \text{ cm}$	
	2.465	0.116	0.052	0.224	0.260
	2.562	0.250	0.100	0.415	0.518
	2.635	0.130	0.052	0.249	0.343
	2.685	0.300	0.130	0.460	0.578
	2.728	0.271	0.106	0.423	0.504
	2.805	0.296	0.127	0.443	0.542
	3.122	0.100	0.036	0.163	0.126

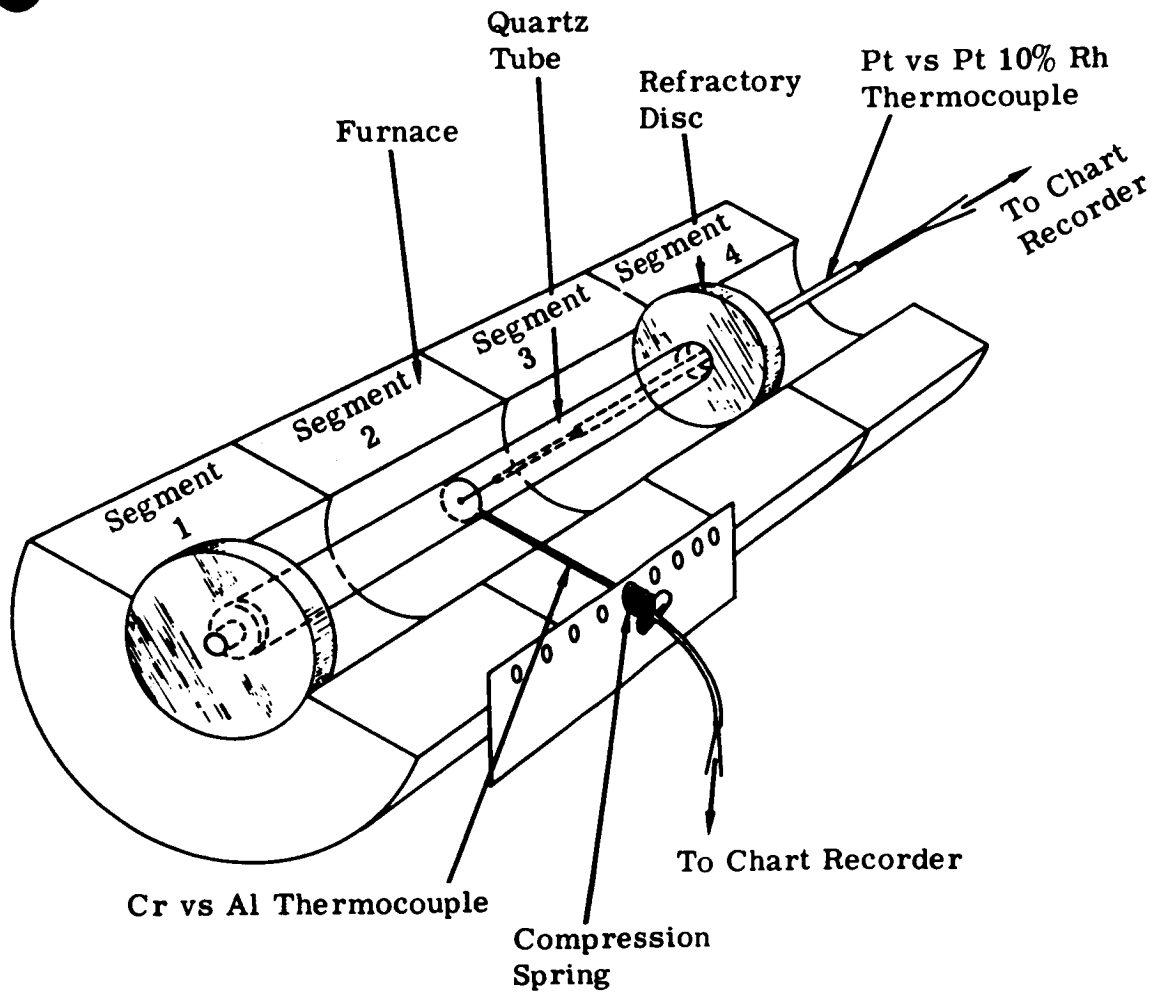


FIGURE 5. CUTAWAY ILLUSTRATION OF SEGMENTED FURNACE USED TO GET CONTROLLED TEMPERATURE PROFILES

Simmons also fitted his measured water vapor radiances to calculations involving a more general empirical expression with interpolation between a nearly weak and nearly strong line approximation. The results of these calculations are compared with experimental values in Figures 6 and 7. In these figures the specified temperatures identify the type of profile: a single value signifies an approximately isothermal path; two values represent more or less linear profiles (e.g., 1230:1010 indicates hotter gas viewed through cooler); three values indicate a nearly triangular profile. The solid lines are the observed spectra; the dashed lines are the predictions of the more general band model. The agreement between the predicted and the observed spectra is

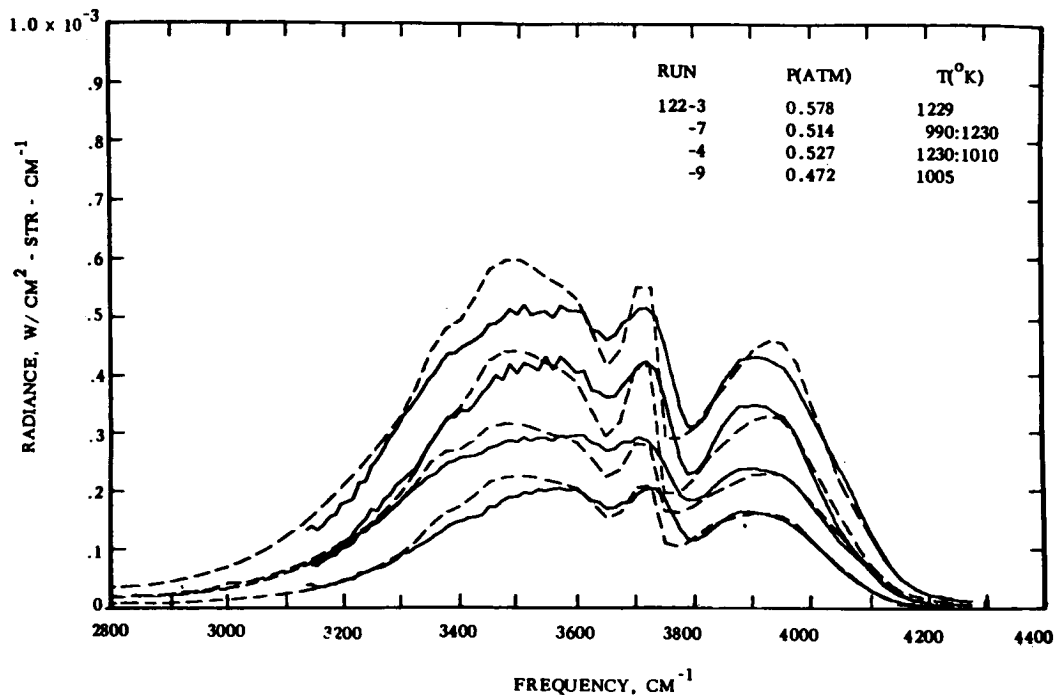


FIGURE 6. CALCULATED AND EXPERIMENTAL SPECTRAL RADIANCE FROM NONISOTHERMAL GASES. (The solid lines are the experimental data from  $H_2O$  in the segmented furnace.)

generally better than that obtained with the strong line models, and is quite satisfactory in view of the probable error in the radiance measurements and the uncertainty in the band model parameters.

Simmons also applied his limiting case formulae to inhomogeneous samples of hot hydrogen fluoride. These calculations were compared with measurements made on hot hydrogen fluoride samples produced by hydrogen-fluorine flames burning on a multiple diffusion burner, a diagram of which is shown on Figure 8. The hydrogen is introduced in the lower manifold and passes through the tubes; the fluorine enters the upper manifold and passes between the tubes. The two gases mix and burn at the surface.

Table VII gives the experimentally determined values of rotational line radiances and equivalent widths in the 1-0 and 2-1 vibrational bands compared with values calculated from the nearly weak or nearly strong line approximation, as appropriate. Agreement is good for the higher J values. The larger discrepancies observed with low J values may be attributed to a small concentration of HF in the optical path outside the confines of the hot sample. This HF gas would accumulate in the ambient gas surrounding the flame by recirculation.

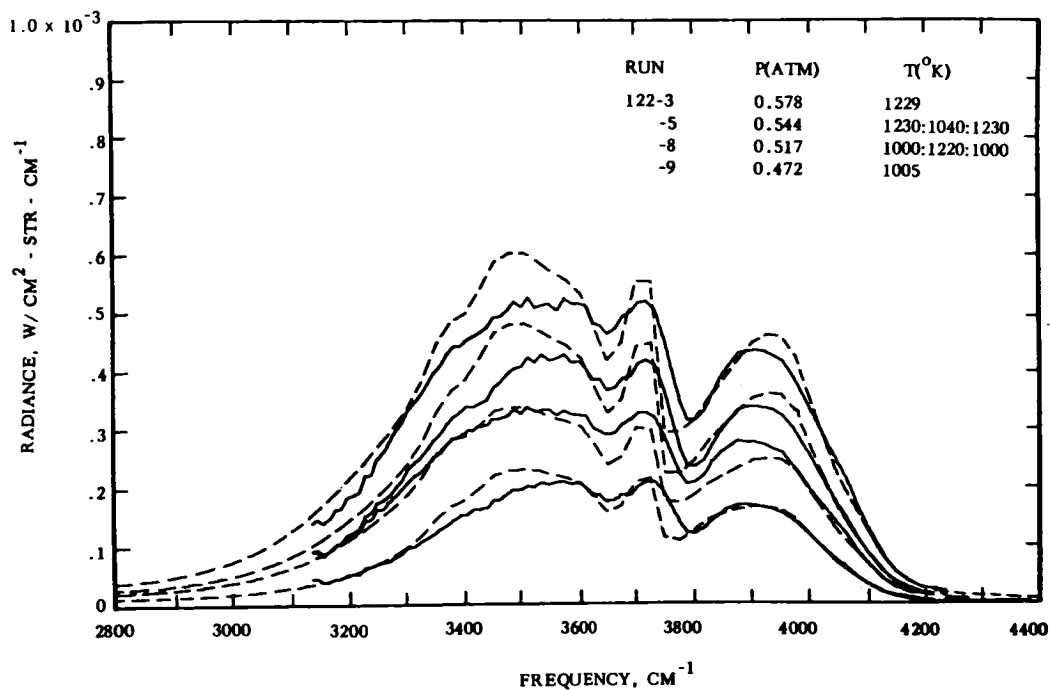


FIGURE 7. CALCULATED AND EXPERIMENTAL SPECTRAL RADIANCE FROM NONISOTHERMAL GASES. (The solid lines are experimental data from H<sub>2</sub>O in the segmented furnace.)

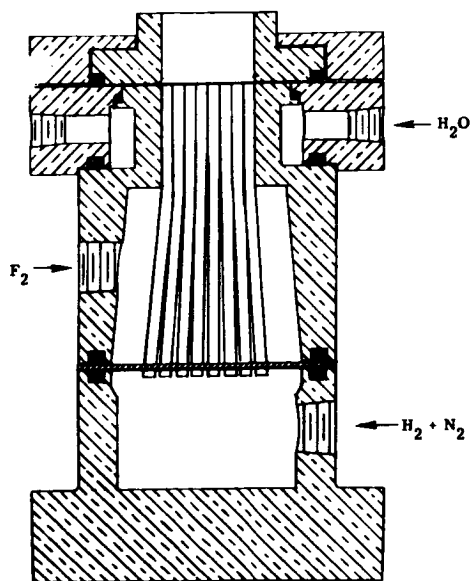


FIGURE 8. MULTIPLE DIFFUSION BURNER

TABLE VII. COMPARISON OF THEORETICAL AND EXPERIMENTAL RADIANCES AND EQUIVALENT WIDTHS

J	N ( $w\text{-cm}^2\text{-sr}^{-1}$ )		W ( $\text{cm}^{-1}$ )	
	Exp.	Theor.	Exp.	Theor.
(A) $v = 0 \rightleftharpoons 1$ Band, R-Branch				
0		0.00171		0.183
1	0.00264	0.00221	0.413	0.269
2	0.00350	0.00260	0.402	0.312
3	0.00424	0.00299	0.422	0.343
4	0.00444	0.00339	0.466	0.355
5	0.00469	0.00375	0.414	0.352
6		0.00406		0.340
7	0.00544	0.00431	0.384	0.324
8	0.00528	0.00440	0.337	0.300
9	0.00492	0.00451	0.310	0.280
10	0.00484	0.00436	0.277	0.253
11	0.00438	0.00421	0.233	0.228
12	0.00397	0.00399	0.200	0.204
13	0.00363	0.00371	0.174	0.181
14	0.00325	0.00336	0.140	0.156
15	0.00278	0.00300	0.180	0.134
(B) $v = 1 \rightleftharpoons 2$ Band, R-Branch				
0	0.00172	0.00136	0.102	0.072
1	0.00250	0.00230	0.156	0.120
2	0.00312	0.00300	0.189	0.156
3	0.00351	0.00354	0.190	0.181
4	0.00373	0.00393	0.194	0.199
5	0.00445	0.00419	0.226	0.208
6	0.00417	0.00431	0.206	0.210
7	0.00394	0.00431	0.182	0.206
8	0.00396	0.00421	0.198	0.207
9	0.00361	0.00403	0.164	0.185
10	0.00332	0.00378	0.140	0.170
11	0.00298	0.00345	0.133	0.153
12	0.00263	0.00310	0.114	0.135
13	0.00233	0.00273	0.097	0.117
14	0.00202	0.00236	0.082	0.100
15	0.00160	0.00200	0.075	0.083

## SUMMARY

We have described experimental investigations of inhomogeneous hot gases made at three different laboratories. Most of the work involved water vapor since the virtual omnipresence of this molecule makes it very important and the complexity of its spectrum makes it tiresome. Work was also done on hydrogen fluoride and carbon dioxide. In all cases Curtis-Godson and band model techniques for calculating transmittances and radiances of inhomogeneous hot gases appeared to have sufficient accuracy for most purposes. In fact, the errors in currently available parameters which go into the calculation (band model and thermodynamic parameters) seemed to introduce much larger errors than either the Curtis-Godson approximation or the band model theory.

## REFERENCES

1. Krakow, B.; Babrov, H. J.; Maclay, G. J.; and Shabott, A. L.: Use of the Curtis-Godson Approximation in Calculations of Radiant Heating by Inhomogeneous Hot Gases. *Appl. Optics*, vol. 5, 1966, p. 1791.
2. Study on Exhaust Plume Radiation Predictions. Interim Progress Report, General Dynamics/Convair TR GD/C-DBE-66-001, (Contract NAS 8-11363), 1966.
3. Simmons, F. S.: Band Models for Nonisothermal Radiating Gases. *Appl. Optics*, vol. 5, 1966, p. 1801.
4. Simmons, F. S.: Further Notes on Band Models for Nonisothermal Radiating Gases. *Appl. Optics*, vol. 6, 1967, p. 1423.
5. Simmons, F. S.: Some Measurements of the Infrared Spectral Radiances and Emissivities of Hydrogen Fluoride in Combustion Gases at 1000° C. *J. Quant. Spectry. Radiative Transfer*, vol. 4, 1964, p. 95.

---

## DISCUSSION

R. Goulard, Purdue University: Is the transmission of hot line radiation through the cooler layers due to the thicker wings of their profiles?

H. Babrov: No. These contributions are not due to the broadening of the same lines which exist at low temperatures. Rather, they are contributed by the lines whose excited states are populated at high temperature but are not populated at a low temperature, so that they are emitting without being absorbed.

R. Goulard: Have you observed this effect in your experiment?

H. Babrov: Yes, we had hot lines in our experiments which involved temperature variations as high as two to one. But, as Dr. Thomson showed earlier, one would have to go to larger ratios before this phenomenon becomes important. For temperature ratios of two to one, both Curtis-Godson calculations gave the same results as the exact calculation; i. e., all three sets of points clustered together.

Our maximum temperature variation was two to one, i. e., either 1270° K and 637° K or 2800° K and 1400° K. A temperature of 2800° K is almost the highest obtainable. A 1400° K combustion flame was the lowest temperature we could get in our flames.

A difficult case would be that of a long path of air at essentially atmospheric temperature (approximately 290° K) and a hot flame behind it. The hot-line problem would be very real, but it is more relevant to the task of trying to detect incoming missiles, rather than to the base heating problem.

R. Goulard: In the case of a flame where the ratio of extreme temperature is at most one to three, one could then safely say that the Curtis-Godson approximation is adequate?

A. Thomson: I would agree with that statement except, perhaps, at the lowest pressure where Doppler broadening becomes important.



H. Babrov: Yes, at extremely low pressures you could get into trouble, too. Luckily with water vapor the collision broadening predominates even for extremely low pressure.

I do not pretend, incidentally, that the Curtis-Godson approximation is a cure-all. Plass has written a paper in Applied Optics in which he gives an example of a case where the Curtis-Godson approximation would give ridiculous results: in the case of several layers at different pressures but same temperature, the combined equivalent width would be higher than the sum of the separate equivalent widths. I made once a high resolution measurement with a  $1 \mu$  Hg background pressure and a long path length spectrometer; I also used a short cell, 1.5 inches long at perhaps on third of an atmosphere pressure. The Curtis-Godson approximation just would not work in this case. These conditions can be found in the laboratory.

V. R. Stull, General Research Corporation: In an early figure, Dr. Babrov compared calculations with measurements for two cells, and obtained differences of approximately 0.01. Did such differences persist when the transmittance was 98 or 99 percent?

H. Babrov: We tried to work in the area where the transmittance was between 80 and 20 percent. When working in the very opaque region, it is very difficult to make accurate measurements; and when there is very nearly total transmittance, it is also difficult to make accurate measurements. Some of the CO<sub>2</sub> cases were quite opaque; in the water cases, I think we had no bad experiments. I think the worse difficulties lie where there is high optical density; there may not be too many in the low absorption case.

V. R. Stull: I think there is a practical interest in these low emissivity cases. Although it may be an easy problem, analytically, I wonder whether experimental data would not be of practical value here.

---

# RADIATIVE HEAT TRANSFER CALCULATIONS FOR SATURN EXHAUST PLUMES

By

N 68-18092

J. E. Reardon  
Hayes International Corporation

and

R. M. Huffaker  
NASA/Marshall Space Flight Center

---

## ABSTRACT

The basic methods developed to predict the radiative heat transfer from the exhaust plumes of Saturn vehicles are described, and typical results are presented to assist in evaluating the applicability of the methods used. In addition, the development of computer programs presently used is briefly reviewed; and the capabilities of the latest program are described.

Early prediction methods used equivalent black-body temperature models of the engine exhaust plumes with appropriate form factors between the plumes and locations in the base region of the vehicles. The temperature models were derived from engine static tests at sea level and used an empirical decay of radiance with altitude based on previous flight experience. This method was adequate for the vehicle first stage, since the primary heating load occurs at low altitude so that errors in the extrapolation to higher altitudes are not too serious. However, this method is not adequate for the predictions of heat flux on upper stages.

To provide a more accurate prediction method, NASA/MSFC sponsored research for inhomogeneous radiance calculations using band model representations for the radiating species of interest in the Saturn vehicles. These methods have been used to predict the radiative transfer for the upper stages of the Saturn vehicle.

Several experimental measurements of full scale and model rocket engines have been made under simulated altitude conditions, but it is not yet possible to fully evaluate the accuracy of radiance calculations because of the uncertainties in the predicted plume gas properties.

Two computer programs are presently available at MSFC for radiation calculations using the band models. One of these is for axisymmetric exhaust plumes with four radiating species; the other is for three-dimensional exhaust plumes with a single radiating species. Each of these programs was developed for limited applications and contains certain undesirable limitations. Therefore, a general program is being prepared with increased flexibility, which will handle either axisymmetric or three-dimensional plumes and will provide radiation calculations using band models with up to ten line groups. To provide for future growth, storage will be provided in the program for up to six constituents even though band model data are presently available for only water vapor, carbon dioxide, carbon monoxide, and carbon particles.

---

## INTRODUCTION

The significance of exhaust plume radiation in the thermal environment of rocket vehicles, and the problems involved in the accurate prediction of this radiation vary with each application. Although the most important factors in these variations are the propellants used and the altitude range to be considered, other factors, such as engine arrangement, engine chamber pressure, nozzle area ratio, and the method of exhausting fuel rich turbo-pump exhaust gases, can also have a significant influence on the problem.

The propellants used fix the radiating constituents which must be considered. In the first stage of both the Saturn I and the Saturn V vehicles, kerosene/oxygen propellants are used. In this case, the dominant radiating species is carbon particles, although significant concentrations of water vapor, carbon dioxide and carbon monoxide are also present. Since the upper stages of the Saturn vehicles use hydrogen/oxygen propellants, the only significant radiating constituent for these stages is water vapor.

The primary radiation source at low altitudes (below 10 km) is the mixing layer where air combines with the fuel-rich exhaust plume to produce a high temperature afterburning mantle. As altitude increases, the reduction in atmospheric pressure eliminates the combustion on the exterior of the plume. With the elimination of plume afterburning, the most significant radiation sources become the high temperature regions formed by the shock waves surrounding the impingement planes between the plumes of clustered engines

Because of the intense radiation in the exhaust of the first stage vehicles, the radiation prediction for these stages has been a significant design problem since the first kerosene burning vehicles were developed. Therefore, the first radiation prediction methods centered around the prediction of the radiation environment for first stage vehicles. Since the initial methods depended upon a prior knowledge of certain empirical data, a more fundamental approach was sought. The ensuing research programs led to the development of a calculation method using band models with a modified Curtis-Godson approximation to account for inhomogeneous gas properties.

In this paper, the early prediction methods will be briefly reviewed followed by a description of the band model prediction method including the characteristics of the computer program used, a typical application to the Saturn S-II stage, and comparisons with various experimental measurements.

## FLAME MODEL PREDICTION METHODS

Two characteristics of the radiation from exhaust plumes of first-stage vehicles were used in the development of the preliminary prediction techniques. The first important characteristic is that the afterburning around the exhaust plume is most intense at low altitudes, and the second characteristic is the effect of the carbon particles in the exhaust gas. The carbon particles provide continuum radiation and greatly increase the optical thickness of the gases, so that radiation can be approximated by assuming a continuum radiation emanating from the outer layers of gases. This approximation, combined with empirical measurements of the equivalent black-body temperature of the exhaust plume, provides a flame model consisting of cylindrical sections with a temperature assigned to each section. This model can be used with appropriate form factors to predict the radiation environment in the base region for sea level conditions. The decrease in the radiant heating with increasing altitudes, which is

estimated from previous flight data, is applied to the predicted sea level heating rates to estimate the variation in radiant heat load throughout the flight. A typical flame model and altitude decay curve are shown in Figure 1.

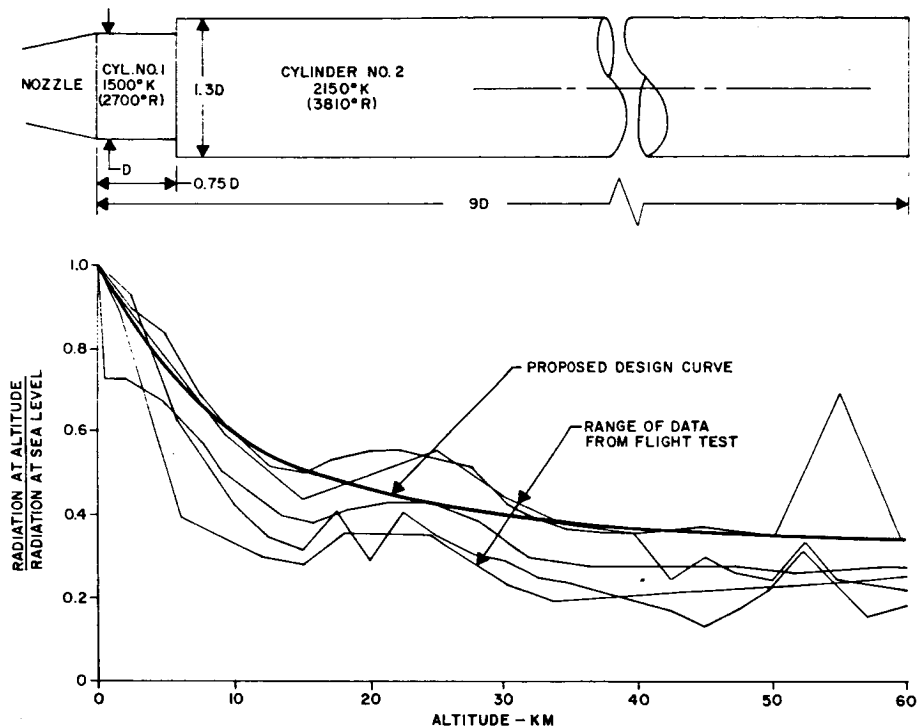


FIGURE 1. TYPICAL FLAME PATTERN AND ALTITUDE DECAY DATA

Although this method of prediction cannot be depended upon to accurately predict the heating rates at high altitude, it has been adequate for the thermal design of first-stage vehicles. Because of the low initial acceleration of the first stage, a significant portion of the flight is at low altitudes where the flame model provides a more realistic representation of the heating problem and the heating loads are the highest.

It was obvious that this prediction method would not be satisfactory for upper stage vehicles. In the case of the upper stages, no representative measure of the plume radiance could be obtained before flight; therefore, the method to be used under these conditions had to be based on a more fundamental approach. The MSFC-sponsored research on this problem led to the development of prediction methods using theoretical and/or empirical band model data.

## BAND MODEL PREDICTION METHOD

The general method of analysis, referred to here as the band model prediction method, uses absorption coefficients corresponding to the thin-gas values. These absorption coefficients are used with a random or statistical band-model representation of the curve of growth in which the effective fine structure parameters for both Doppler and collision-broadening are evaluated using a modified Curtis-Godson approximation. In this section, the equations used will be presented with a brief summary of the sources of the data which are used for water vapor, carbon dioxide, carbon monoxide, and carbon particles.

The coordinate system used for the heat transfer calculations is shown in Figure 2. The exhaust plume properties are specified in a Cartesian coordinate system, which normally has its origin at the center of the nozzle exit plane. Spatial relationship of the point of interest to the exhaust plume is specified by relating the U, V, W axes at the point of interest to the plume coordinate system. This is done in the general case by specifying the coordinates of the point and the nine direction cosines which fix the U, V, and W axes with respect to the X, Y, and Z axes.

The radiant flux is calculated using a spherical coordinate system centered at the point of interest. In this system, the inclination of a line of sight,  $s$ , to the surface normal,  $W$ , is the angle,  $\theta$ , while the angle between the projection of  $s$  in the U-V plane and the U axis is  $\phi$ .

The heat transfer equation used to predict the radiation from a spherical segment over a spectral region between wave numbers  $\nu_i$  and  $\nu_f$  is

$$\dot{q}/A = \int_{\theta_i}^{\theta_f} \int_{\phi_i}^{\phi_f} \int_{\nu_i}^{\nu_f} \int_0^{S_{\max}} -I_{b\nu} \left( \frac{dG}{dS} \right) dS d\nu d\phi \cos \theta \sin \theta d\theta, \quad (1)$$

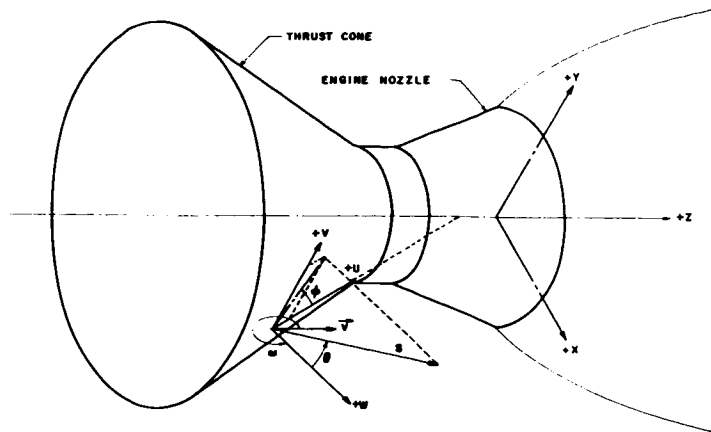


FIGURE 2. ILLUSTRATION OF COMPUTER PROGRAM GEOMETRY

where  $G$  is the transmissivity of the gas and  $I_{b\nu}$  is Planck's function.

When this equation is put in numerical form, it becomes

$$\dot{q}/A = \sum_{\theta_i}^{\theta_f} \sum_{\phi_i}^{\phi_f} \sum_{\nu_i}^{\nu_f} \sum_0^{S_{\max}} -I_{b\nu} [\bar{G}(S, \nu) - \bar{G}(S - \Delta S, \nu)] \cos \theta \sin \theta \Delta \theta \Delta \phi \Delta \nu. \quad (2)$$

This is evaluated using the average transmission over a spectral interval  $\Delta \nu$ .

$$\bar{G}(S, \nu) = \exp [ -\bar{D}(S, \nu) ] \quad (3)$$

where the optical depth  $\bar{D}(s, \nu)$  is summed over the  $i$  radiating species

$$\bar{D}(S, \nu) = \sum_i \bar{D}(S, \nu, i). \quad (4)$$

The details of the evaluation of the optical depth vary depending upon the radiating species considered, and will be described below. In the following description, the functional notation for position,  $s$ , wave number,  $\nu$ , and species,  $i$ , will be omitted except where required for clarity.

The carbon particles in the rocket exhaust are treated as a gas since they have been shown to be so small that scattering can be neglected without appreciable error for a total radiation calculation (References 1 and 2). Optical depth for carbon particles is simply

$$\bar{D} = \int_0^S \bar{k}(T) \rho ds, \quad (5)$$

where  $\bar{k}(T)$  is the absorption coefficient per unit density and path length, and  $\rho$  is the local carbon density.

The absorption coefficients for carbon particles were determined by a combined analytical and experimental technique described in reference 1. This determination provided data over the ranges of 1 to 4  $\mu$  in wavelength and 300° K to 2600° K in temperature. Since an appreciable amount of heat transfer could occur outside of the 1 to 4  $\mu$  spectral range, the data was extended as described in reference 3. The extension used a combination of the analytical data of reference 1 for short wavelengths ( $< 1 \mu$ ) and lower temperatures ( $< 1600^\circ \text{K}$ ) and at extrapolation for the longer wavelengths ( $> 4 \mu$ ) at temperatures above 1600° K. With this extension, carbon absorption coefficients are available over a range of wave numbers from  $10^3 \text{ cm}^{-1}$  to  $2 \times 10^4 \text{ cm}^{-1}$ . Since the carbon absorption coefficients are continuous over the spectrum, they are represented for computational purposes by fourth order polynomials in wave number for seven different temperatures. The coefficient for any particular spectral interval is then taken to be the coefficient at the center of the wave number interval.

The optical depth for each of the gaseous constituents is a function of the analytical model chosen. In the development of the analysis of the gaseous radiators ([4] through [6]), two analytical models were recommended. The more exact method, Model 3, uses a number of line groups for each species to account for "hot lines" from high temperature regions which are not significantly attenuated when passing through lower temperature regions. From this model, a simplified model was developed in which all the lines for each species are grouped together. This is termed Model 3A. A comparison of the equations used in determining the optical depth for Model 3 and Model 3A is presented in Table I. Although Model 3 is shown analytically as an infinite sum of line groups, only four or five groups need be considered in most applications.



TABLE I. COMPARISON OF MODELS 3 AND 3A

PARAMETER	MODEL 3	MODEL 3A
OPTICAL DEPTH	$D = \sum_{n=0}^{\infty} D_n$	$D = \sqrt{1-\bar{Y}^{1/2}} D^*$
OPTICAL DEPTH OF THE $n^{\text{th}}$ LINE GROUP	$D_n = \sqrt{1-\bar{Y}_n^{1/2}} D_n^*$	NOT APPLICABLE
COMBINED COLLISION AND DOPPLER OPTICAL DEPTHS	$Y_n = \left[ 1 - \left( \frac{D_{cn}}{D_n^*} \right)^2 \right]^{-2} + \left[ 1 - \left( \frac{D_{0n}}{D_n^*} \right)^2 \right]^{-2} - 1$	$Y = \left[ 1 - \left( \frac{D_c}{D^*} \right)^2 \right]^{-2} + \left[ 1 - \left( \frac{D_0}{D^*} \right)^2 \right]^{-2} - 1$
OPTICAL DEPTH FOR THE JUST OVERLAPPING LINE APPROXIMATION	$D_n^* = \int_0^S \bar{k}_n ds$	$D^* = \int_0^S \bar{k}(p_i, \tau) ds$
OPTICAL DEPTH FOR A PURE COLLISION CURVE OF GROWTH	$D_{cn} = D_n^* (1 + D_n^* / 4\bar{a}c_n)^{-1/2}$	$D_c = D^* (1 + D^* / 4\bar{a}c)^{-1/2}$
OPTICAL DEPTH FOR A PURE DOPPLER CURVE OF GROWTH	$D_{0n} = 1.7\bar{a}_0 \int_0^S \sqrt{1 + \left( \frac{0.589 D_n^*}{\bar{a}_{0n}} \right)^2} ]$	$D_0 = 1.7\bar{a}_0 \int_0^S \sqrt{1 + \left( \frac{0.589 D^*}{\bar{a}_0} \right)^2} ]$

TABLE I. COMPARISON OF MODELS 3 AND 3A (Continued)

PARAMETER	MODEL 3	MODEL 3A												
COLLISION BROADENED FINE STRUCTURE PARAMETER	$\bar{\alpha}_{cn} = \frac{1}{D_n^*} \int_0^s \frac{\chi c}{dn} \bar{k}_n ds$	$\bar{\alpha}_c = \frac{1}{D^*} \int_0^s \frac{\chi c}{d} \bar{k}(p_i, T) ds$												
DOPPLER BROADENED FINE STRUCTURE PARAMETER	$\bar{\alpha}_{Dn} = \frac{1}{D_n^*} \int_0^s \frac{\chi D}{dn} \bar{k}_n ds$	$\bar{\alpha}_D = \frac{1}{D^*} \int_0^s \frac{\chi D}{d} \bar{k}(p_i, T) ds$												
ABSORPTION COEFFICIENT FOR THE $n$ th LINE GROUP	$\bar{k}_n = \bar{k}(p_i, T) \frac{f_n \exp(-\theta_n/T)}{\sum_{n=0}^{\infty} f_n \exp(-\theta_n/T)}$ <table data-bbox="877 727 1003 1120"> <tr> <td></td> <td><math>f_n</math></td> <td><math>\theta</math> (°K)</td> </tr> <tr> <td>H<sub>2</sub>O</td> <td>1.0</td> <td>2300</td> </tr> <tr> <td>CO<sub>2</sub></td> <td>1.0</td> <td>960</td> </tr> <tr> <td>CO</td> <td>1+n</td> <td>3123</td> </tr> </table>		$f_n$	$\theta$ (°K)	H <sub>2</sub> O	1.0	2300	CO <sub>2</sub>	1.0	960	CO	1+n	3123	NOT APPLICABLE
	$f_n$	$\theta$ (°K)												
H <sub>2</sub> O	1.0	2300												
CO <sub>2</sub>	1.0	960												
CO	1+n	3123												
BAND AVERAGED ABSORPTION COEFFICIENT (CM). THE COEFFICIENT AT STANDARD TEMP. AND PRESS. $\bar{k}$ (STP), IS TABULATED AS A FUNCTION OF WAVENUMBER AND TEMPERATURE.	$\bar{k}(p_i, T) = \bar{k}(\text{STP}) (p_i / 1 \text{ atm.}) (273/T)$													

TABLE I. COMPARISON OF MODELS 3 AND 3A (Continued)

PARAMETER		BOTH MODELS 3 AND 3A				
COLLISION HALF-WIDTH (CM <sup>-1</sup> ) FOR THE <i>i</i> th SPECIES. BROADENING SPECIES NOTED BY <i>j</i> . PARTIAL PRESSURES <i>p<sub>i</sub></i> and <i>p<sub>j</sub></i> ARE IN ATMOSPHERES, AND THE TEMPERATURE <i>T</i> IS IN °K.		$\gamma_{ci} = \sum_j \left[ (\gamma_{i,j})_{STP} p_j \left( \frac{273}{T} \right)^{\eta_{i,j}} \right] + (\gamma_{ii})_{STP} p_i \left( \frac{273}{T} \right)^{\eta_{ii}}$				
<i>i</i>	<i>j</i>	( <i>γ<sub>ij</sub></i> ) STP	<i>η<sub>ij</sub></i>	( <i>γ<sub>ii</sub></i> ) STP	<i>η<sub>ii</sub></i>	
H <sub>2</sub> O	H <sub>2</sub> O	(0.09)	0.5	0.44	1.0	
	N <sub>2</sub>	0.09				
	O <sub>2</sub>	0.04				
	H <sub>2</sub>	0.05				
	CO <sub>2</sub>	0.12				
CO <sub>2</sub>	CO	0.10				
	CO <sub>2</sub>	0.09				
	H <sub>2</sub> O	0.07				
	N <sub>2</sub>	0.07				
	O <sub>2</sub>	0.06				
CO	H <sub>2</sub>	0.08				
	CO	0.06				
	CO	0.05				
	H <sub>2</sub> O	0.05				
	CO <sub>2</sub>	0.05				
	H <sub>2</sub>	0.05				
	N <sub>2</sub>	0.05				
	O <sub>2</sub>	0.05	0.5			

$$\gamma_{D_i} = (5.94 \times 10^{-6}) \frac{\nu}{m_i^{1/2}} \left( \frac{T}{273} \right)^{1/2}$$

WHERE *m<sub>i</sub>* = MOLECULAR WT. OF THE *i*th SPECIES

DOPPLER HALF-WIDTH (CM<sup>-1</sup>)

TABLE I. COMPARISON OF MODELS 3 AND 3A (Concluded)

<u>PARAMETER</u>	<u>MODEL 3</u>	<u>MODEL 3A</u>
LINE DENSITY ( $\text{CM}^{-1}$ )	$1/d_n = g_n/d_0$	<u>FOR H<sub>2</sub>O</u> $1/d = a^* / \gamma^*$
<u>SPECIES</u>	<u>g<sub>n</sub></u>	<u>WHERE:</u>
H <sub>2</sub> O	1	$a^* = 10 (b\nu + c\nu T)$
CO <sub>2</sub>	$(1 + \epsilon n)^2$	$b\nu$ AND $c\nu$ ARE CONSTANT OVER SPECTRAL REGIONS
CO	1	$\gamma^* = [0.44 (T_0/T) + 0.09 (T_0/T)^{1/2}] C^*$ $+ 0.044 (T_0/T)^{1/2} (1 - C^*)$
<u>FOR H<sub>2</sub>O</u>	<u>1/d<sub>0</sub></u>	$C^* = -0.1002 + 0.2802 \times 10^{-3} T - 0.1089 \times 10^{-6} T^2 + 0.0291 \times 10^{-9} T^3$
	$1/d_0 = 1/d \frac{(1 - \text{EXP}(-\theta/2T))}{(1 + \text{EXP}(-\theta/2T))}$	<u>FOR CO<sub>2</sub></u>
	WHERE 1/d IS DETERMINED AS IN MODEL 3A	1/d IS TABULATED AS A FUNCTION OF $\nu$ AND T.
		<u>FOR CO</u>
		$1/d = 1/d_0 \frac{(1 + \text{EXP}(-\theta/2T))}{(1 - \text{EXP}(-\theta/2T))} 1.75$

The effect of inhomogeneous gas properties on the fine structure parameters ( $\bar{a}_C$  and  $\bar{a}_D$ ) is accounted for by the use of a Curtis-Godson approximation. In this application, the approximation is modified in the sense that it is applied to a spectral interval rather than a single spectral line. Experimental evidence of the validity of this modification of the Curtis-Godson approximation has been presented in references 6 and 7.

The band model parameters used in the radiation models have been obtained from both experimental and analytical studies. In general, the collision-broadened line half-widths,  $\gamma_C$ , have been approximated by simplified analytical expressions with coefficients based on experimental or theoretical data in most cases (reference 5). However, where no data were available, estimates have been made to complete the necessary data until better information becomes available. The expression for evaluating the Doppler-broadened line half-width,  $\gamma_D$ , was derived theoretically.

Using the expressions for  $\gamma_C$  and  $\gamma_D$ , the absorption coefficient  $\bar{k}$  (stp), and the line density,  $1/d$ , can be determined from a complete set of either experimental or theoretical data, using Model 3A. However, if Model 3 is used, values must also be assigned for  $\theta$ ,  $f_n$ , and  $g_n$ . The value of  $\theta$  should be chosen as large as possible, and a convenient choice is the value corresponding to the least energetic vibrational mode [5].

For  $H_2O$ , the values of  $\bar{k}$  (stp) and  $1/d$  were calculated from experimental data as described in reference 6. The values of  $f_n$  and  $g_n$  for water vapor have been assumed to be 1 for Model 3 (reference 5). Further theoretical studies [6] have indicated that both  $g_n$  and  $f_n$  tend to increase with  $n$ , but no revised expressions have been recommended at this time.

For  $CO_2$  and  $CO$ , the values of  $\bar{k}$  (stp),  $1/d$ ,  $f_n$ , and  $g_n$  were evaluated from theoretical calculations by Malkmus and Thomson ([8] through [10]). In the case of  $CO_2$ , many of these theoretical calculations have been verified by experiments so that they are believed to give an adequate representation of the spectral properties of the gases.

# COMPUTER PROGRAMS USING BAND MODELS

At present, two computer programs are in use at MSFC, both of which use the Model 3A calculation method. One of the programs provides for the calculation of radiation from an axisymmetric multi-constituent exhaust plume [11]; the other computes the radiance from three-dimensional exhaust plumes in which water vapor is the only radiating species [12]. Because of the limitations of these programs in flow field geometry, constituent storage, calculation methods, and input flexibility, a general program is being developed to avoid many of the modifications necessary for special applications. To acquaint the reader with this new program, its capabilities will be summarized.

To provide sufficient computer storage, the program is divided into five overlay subroutines as shown in Figure 3. The first two subroutines (Parts 1 and 2) interpolate in the input flow field properties and generate a tape with the properties on each line of sight stored in the proper order. The next two subroutines (Parts 3 and 4) calculate the radiation heat transfer with either Model 3 or Model 3A. The final subroutine (Part 5) generates a tape

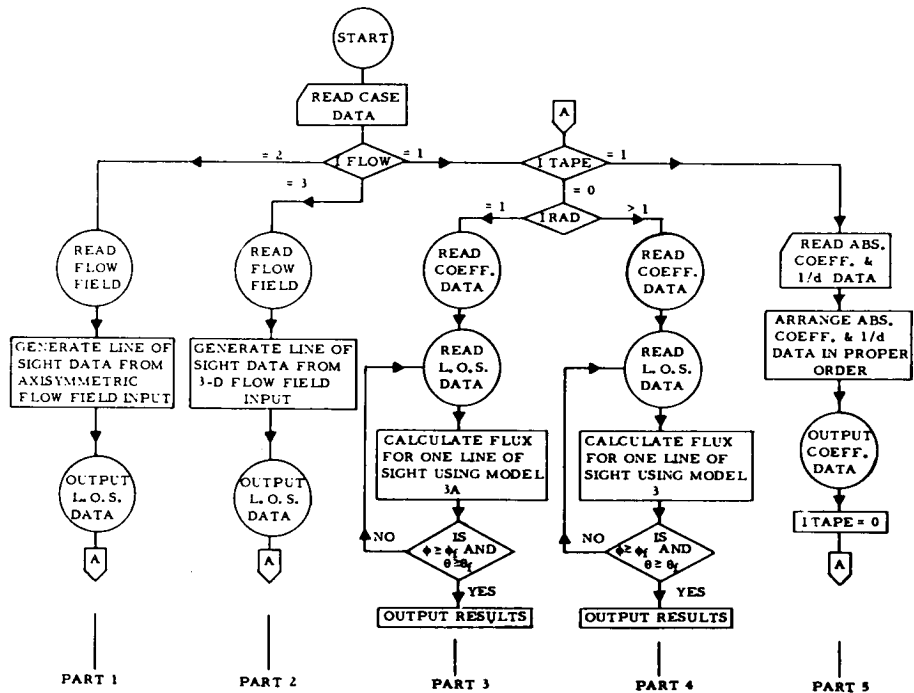


FIGURE 3. ARRANGEMENT OF THE RADIATION COMPUTER PROGRAM

containing the absorption coefficients (and line density, if required) as functions of temperature and wave number. It will only be necessary to use this part when a change is required in the input data. Otherwise, the tape with the coefficient data on it could be saved and reused.

The flow field is described using either of the coordinate systems shown in Figure 4. In the axisymmetric case, the properties are specified as a function of radius in planes parallel to the X-Y plane. A similar method is used for the three-dimensional case except that the additional dimension  $\eta$  is added, and the flow field is specified about the centerline of an outboard engine. The outboard engine was used to take advantage of symmetry between the outboard and center engines to reduce the amount of data required. Although the illustration shows a five-engine configuration, the method used will be applicable to any multi-engine configuration in which the outboard engines are spaced at equal angles around the cluster.

At each point in the flow field, the temperature, pressure, and constituent mole fractions must be specified. The program will allow for storage of up to six constituent mole fractions, although only four radiating species are presently being considered. The additional storage can be used at the present time to specify nonradiating gases so that the collision-broadened half-width,  $\gamma_c$ , can be more accurately defined. However, in future applications additional radiating gases may be specified with a slight sacrifice in the accuracy of the collision-broadening terms.

One of the problems in handling the flow fields from kerosene/oxygen rocket engines is that the equilibrium chemical processes assumed do not predict the formation of carbon particles. Therefore, the carbon particles must be artificially inserted in either the flow field prediction or the radiation calculation. To provide for this, the radiation program will accept various forms of carbon particle input. The carbon particle mole fraction may be specified as a constant, as a function of  $R$  and  $\eta$ , or as a function of  $R$ ,  $\eta$  and  $Z$ .

The most significant feature of the radiation heat transfer subroutines in the new program will be the addition of the capability of using the Model 3 calculation procedures. The number of line groups used in Model 3 will be an input variable with a maximum value of 10. Although it will be convenient to

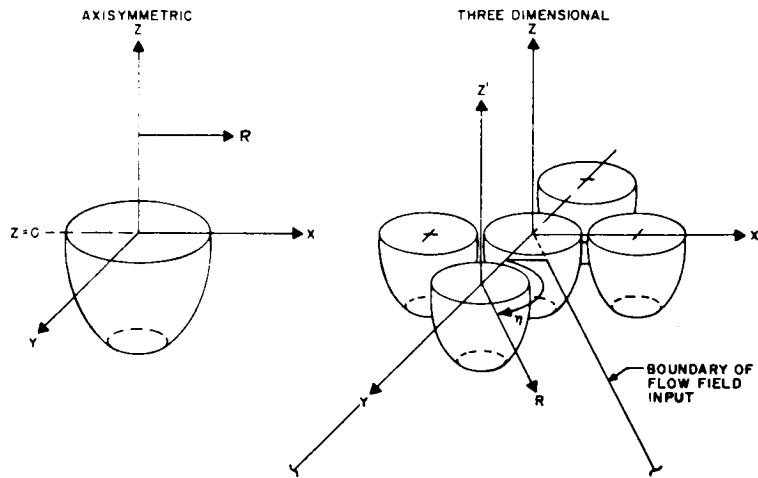


FIGURE 4. FLOW FIELD COORDINATE SYSTEM

make comparisons between Model 3 and 3A for particular problems, it is doubtful that Model 3 will be used extensively for heat flux calculations, since the computer time required will increase roughly in proportion to the number of line groups considered.

## TYPICAL RADIATION PREDICTION

The radiation prediction to be reviewed is that for the S-II, the second stage of the Saturn V vehicle. It will illustrate the problems which must be solved in predicting a three-dimensional exhaust plume and applying the band model prediction method. The S-II stage uses five Rocketdyne J-2 engines



which begin operation at an altitude of approximately 60 km. The engine exit diameter is approximately 70 inches and the thrust is approximately 230,000 pounds for the portion of the flight considered in this analysis. The propellants are oxygen and hydrogen and the mixture ratio at the thrust level considered is 5.5 (wt. of oxygen/wt. of hydrogen). The nozzle stagnation pressure is 715 psia, and the nozzle area ratio is approximately 27. These engine operating conditions produce a water vapor mole fraction of approximately 0.69 in the exhaust plume assuming equilibrium gas properties. The remainder of the gas in the exhaust plume is hydrogen.

The first step in the radiation analysis is the prediction of the exhaust plume properties. Although two methods were being developed to predict properties in three-dimensional exhaust plumes [13], neither one could be applied to this problem because of operational difficulties or incomplete development. Therefore, it was necessary to approximate the exhaust plume properties using an axisymmetric method-of-characteristics program [14]. This program is particularly convenient to use because it contains a subroutine for interpolating in the characteristics output to provide properties in the coordinate system used by the radiation computer program.

The flow field geometry required by the radiation program is shown in Figure 5. Using the symmetry provided by the engine arrangement and impingement planes between the engine plumes, it is only necessary to specify the exhaust plume in a 45° sector. The radiation computer program automatically refers any point in the flow to a similar point in this sector to obtain the necessary gas properties: temperature, pressure, and water vapor mole fraction. The portion of the sector surrounding the center engine (cdbc in Fig. 5) was assumed to be identical to the symmetrical region on the outboard engine (abda). Although this assumption would not be true for a three-dimensional flow field, it was used as an approximation in this case.

Gas properties were to be specified as a function of radius ( $R$ ) at the values of  $\eta$  shown in Figure 5 for planes downstream of the exit plane ( $Z$ ). Because computer storage was limited, only ten values of  $Z$  were allowed so that the flow field extended only 300 inches downstream of the engine exit plane.

The geometry for approximating the plume properties is shown in Figure 6. In this approximation, the gas at the nozzle exit is expanded along a 45° cone and turned into a cylinder. The radius of the cylinder was set equal to the distance of the impingement plane from the nozzle centerline for the particular value of  $\eta$  being estimated.



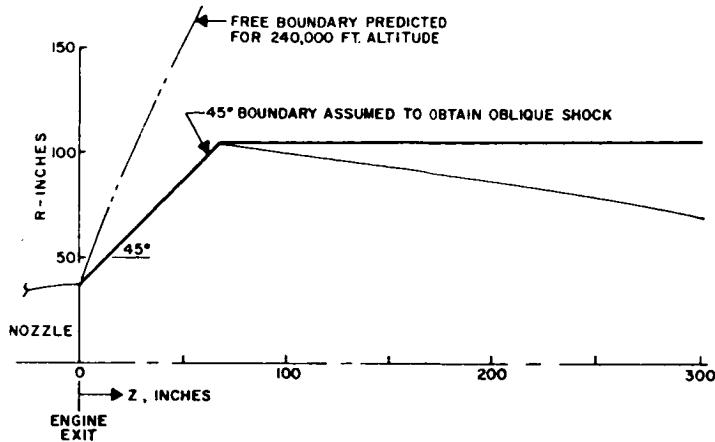


FIGURE 6. TYPICAL AXISYMMETRIC FLOW FIELD GEOMETRY USED TO APPROXIMATE A 3-D FLOW FIELD

The effects of neglecting this high temperature region are offset to some extent by the more conservative temperature predictions caused by the assumption that the flow is turned into a cylinder. In the actual three-dimensional case, the gas could expand laterally in some regions as it proceeds downstream, but the cylindrical boundary causes a constant relatively high temperature along the impingement plane.

Another difficulty encountered with this method of approximating the flow field was its inability to properly account for shock reflections. The representation of the flow field conditions in a plane through the center engine and two outboard engines shown in Figure 8 indicates that the shock from the closest impingement point intersects the engine centerline approximately 200 inches downstream of the engine exit. In the center engine, some types of shock reflection should occur, but since the flow is not axially symmetric, prediction of the reflection was not attempted. In the outboard engines, it is not clear what would occur when the shock reached the engine centerline.

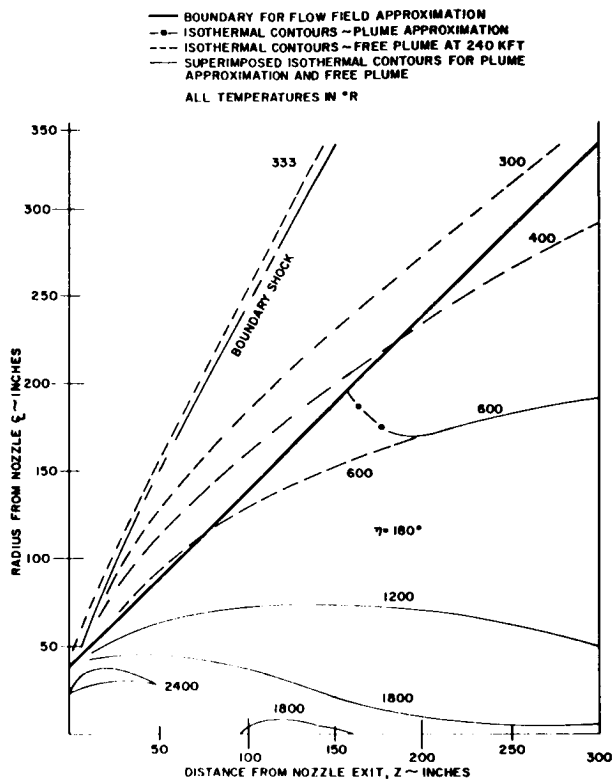


FIGURE 7. COMPARISON OF FREE PLUME TEMPERATURES TO THE S-II FLOW FIELD APPROXIMATION

Because of this difficulty, the gas properties in the cone downstream of the shock impingement were estimated to conform with the surrounding temperatures in the flow field.

Before extensive radiation calculations were made, a study was made of the variables which could be used to reduce computer time so that the resulting accuracy could be evaluated. This study was conducted using the line of sight from the edge of an outboard engine exit shown in Figure 8. The properties and predicted radiance for this line of sight are shown in Figure 9.

The variables in the radiation calculation which were expected to provide the greatest reduction in computation time were the wave number interval,  $\Delta\nu$ , and the spatial step size. To properly account for the relatively narrow impingement regions, reasonably small spatial steps were used ( $\Delta\theta = \Delta\phi = 3^\circ$ ,  $\Delta s = 3$  inches). However, the computer program is arranged so that the radiation equation (2) is not summed at each  $\Delta s$  step. Instead, the flow field is searched

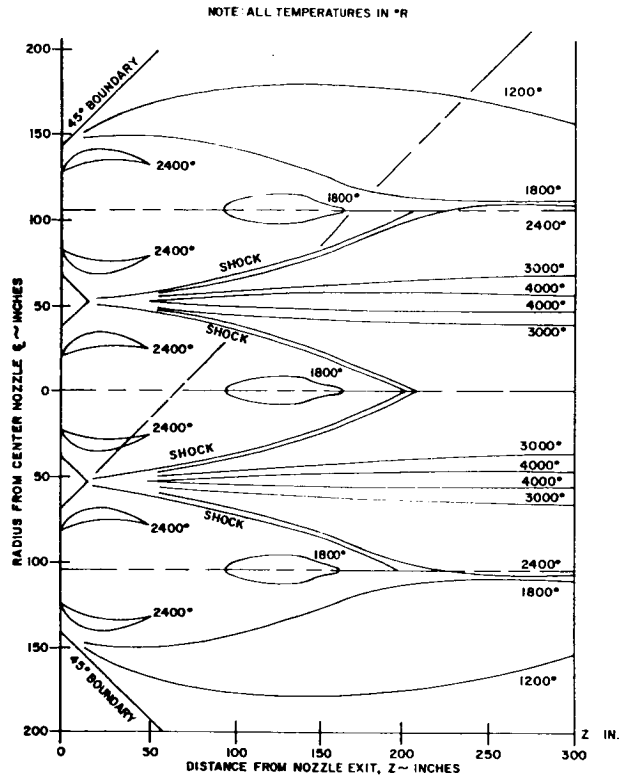


FIGURE 8. ISOTHERMAL CONTOURS FOR THE X-Z PLANE OF THE S-II FLOW FIELD APPROXIMATION

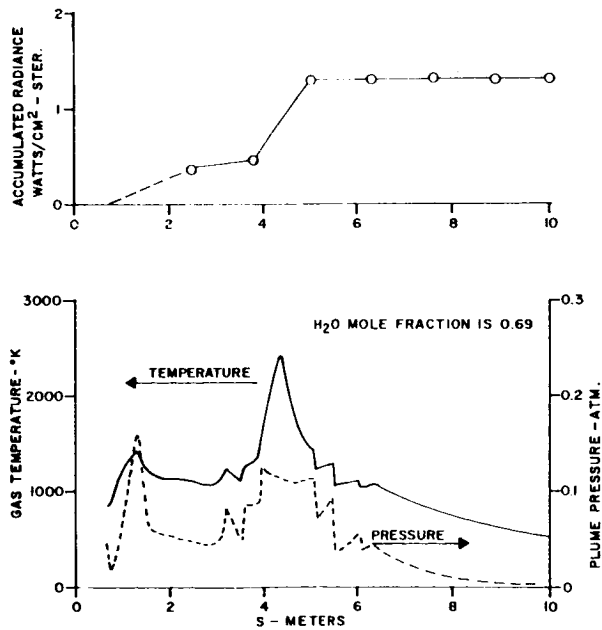


FIGURE 9. TYPICAL LINE OF SIGHT VARIATIONS ON THE SATURN S-II STAGE

at increments corresponding to the input  $\Delta s$  until some desired temperature change has occurred or until the slope of the temperature as a function of  $s$  changes sign. At this point, the average properties over the portion of the line of sight are used with the accumulated length to calculate a term in the summation. This procedure achieves the desired details in regions of rapid temperature change without spending excessive time in computing regions which are at a relatively constant temperature.

A reference flux,  $F_r$ , was computed for the line of sight using  $\Delta \nu = 25 \text{ cm}^{-1}$ , and  $\Delta T = 0$ . (This provides for an integration step each 3 inches.) The time required for this computation was referred to as the reference time,  $\tau_r$ . A comparison of the reduction in computer time and decrease in accuracy using larger values of  $\Delta \nu$  and  $\Delta T$  are shown in Figures 10 and 11.

As a result of these test runs, a temperature increment of  $200^\circ \text{R}$  and a wave number interval of  $100 \text{ cm}^{-1}$  were selected for the remaining calculations. Even though the use of these values indicated a reduction in run time to about 10 percent of what would be required with  $\Delta \nu = 25 \text{ cm}^{-1}$  and  $\Delta T = 0$ , the heat transfer calculations for the points of interest in the base region required in the neighborhood of 1 to 2 hours on an IBM 7094. Time variations between runs are caused by the location of the point of interest and the temperature gradients along the lines of sight. When a line of sight misses the flow field or is blocked by an engine or the heat shield, the time required for processing the line of sight is extremely short.

Heat transfer calculations were made for the eight points shown in Figure 12. The results are presented in Table II.

TABLE II. HEAT TRANSFER CALCULATIONS

Location	Coordinates-inches			Predicted Flux watts/cm <sup>2</sup>
	X	Y	Z	
Heat shield, HS-1	52.5	0	-60	1.1
HS-2	70.7	70.7	-60	1.1
Nozzle Exit, NE-1	66.6	0	0	4.4
NE-2	66.6	0	0	2.0
Thrust Structure,* TS-1	140	140	-212	0.15
TS-2	124.5	124.5	-212	0.047
Interstage, IS-1	140	140	-16	0.79
IS-2	140	140	-16	1.1

\* In the calculations for the thrust structure, the occlusion representing the interstage skirt was not used.

$\tau_r$  = computer run time based on the reference conditions,  
 $H_{min} = 0.000$ ,  $\Delta\nu = 25$ , and  $\Delta T = 0.0$   
 $F_r$  = computed flux for reference conditions

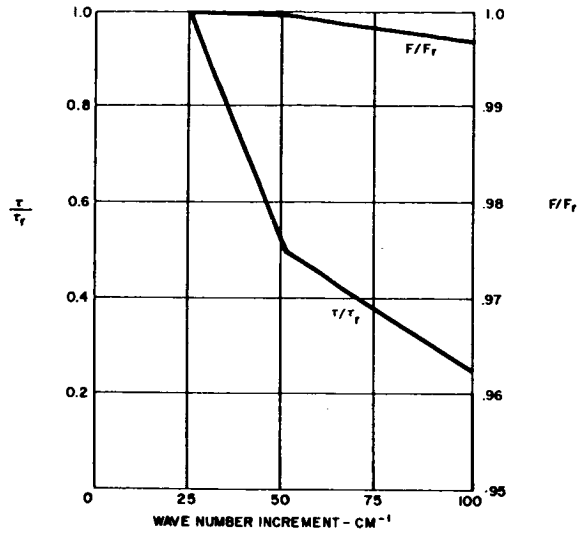


FIGURE 10. EFFECT OF VARYING WAVE NUMBER ON COMPUTER RUNNING TIME AND CALCULATION ACCURACY

$\tau_r$  = computer run time based on the reference conditions,  
 $H_{min} = 0.000$ ,  $\Delta\nu = 25$ , and  $\Delta T = 0.0$   
 $F_r$  = computed flux for reference conditions

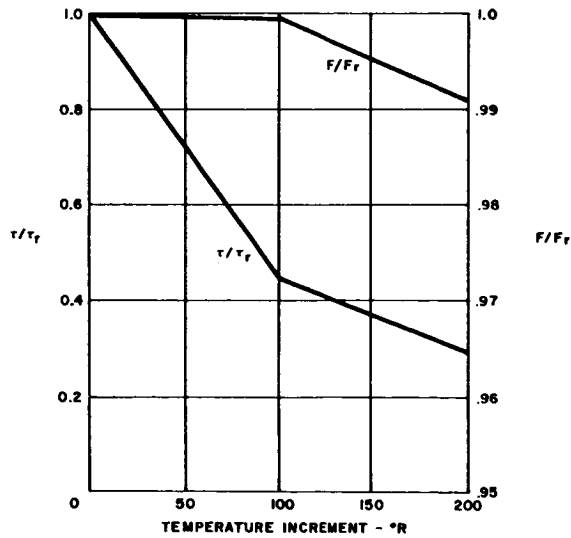


FIGURE 11. EFFECT OF VARYING TEMPERATURE STEP INCREMENT ON COMPUTER RUNNING TIME AND CALCULATION ACCURACY

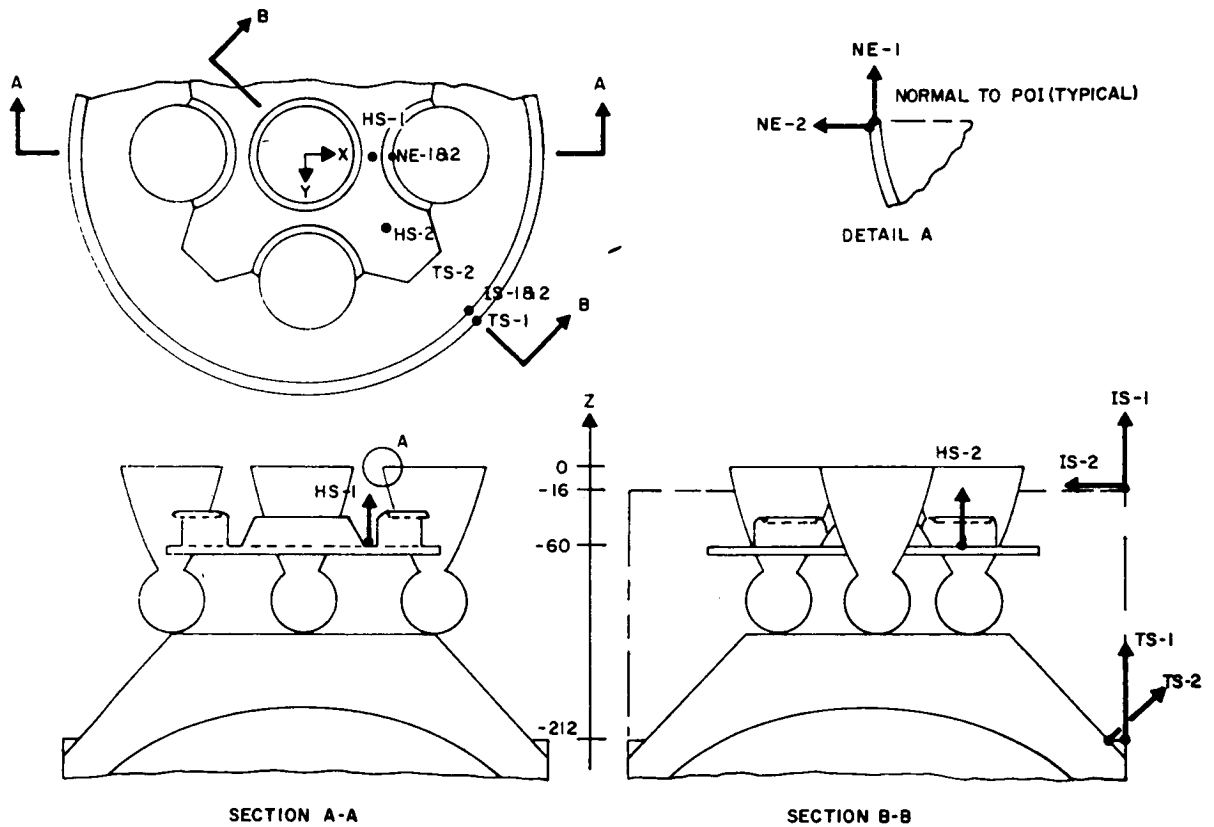


FIGURE 12. LOCATION OF POINTS OF INTEREST

## COMPARISON WITH EXPERIMENTS

Several radiation measurements have been made of engine exhaust plumes to provide a basis for evaluating the flow field and radiation prediction methods which are presently available. Although the evaluation of these measurements is not yet complete, some typical results will be presented to indicate the degree of agreement being obtained between the analytical and experimental results. Typical results from model F-1 engine tests, a sea level static firing of a J-2 engine, and flight measurements on the Saturn 203 will be reviewed.



## Model F-1 Engine Measurements

Tests of 1/45 scale model F-1 engines were conducted at Cornell Aeronautical Laboratory using a short-duration technique which produces a steady gas flow out of the engines for approximately 5 milliseconds. The propellants used were gaseous ethylene and oxygen, and the nozzle stagnation pressure was approximately 1000 psia. Simulated altitude during the short test period was approximately 120,000 feet, and no carbon particles were apparent in the free plume. However, carbon particles were apparently formed in the impingement region between plumes when two engines were fired.

Radiation measurements were made using a Warner and Swasey fast scanning spectrometer, which was set up to scan from 1.6 to 5  $\mu$  in 1 millisecond with a 0.25 millisecond interval between scans. With this timing, 4 scans could be completed during the 5 millisecond test event. Because of timing difficulties, usually only one or two scans were actually made when the rocket operation and altitude simulation were both satisfactory.

The preliminary results of these tests have been reported in References 3, 15, and 16, but no comparisons have yet been made for the impingement region between plumes. Gas property predictions for two locations on the nozzle axis 0.6 and 9.94 inches downstream of the exit are shown in Figures 13 and 14, and the corresponding radiation prediction is compared with measured values in Figures 15 and 16. The levels of the measurements agree well with the predictions, but there appears to be a slight discrepancy in the wavelength. This discrepancy is attributed to uncertainties in the data reduction. It was necessary to assign a wavelength to some spectral feature in the data to obtain absolute wavelength values, and the radiation predictions were not available at the time the data were reduced.

## J-2 Sea Level Measurement

The spectral radiance of a J-2 engine was measured during sea level static firings at MSFC. The measurements were made using a Block Engineering Company BD-1A spectrometer mounted 137.5 inches from the engine centerline and aligned to view normal to the centerline 7.5 inches downstream from the exit.

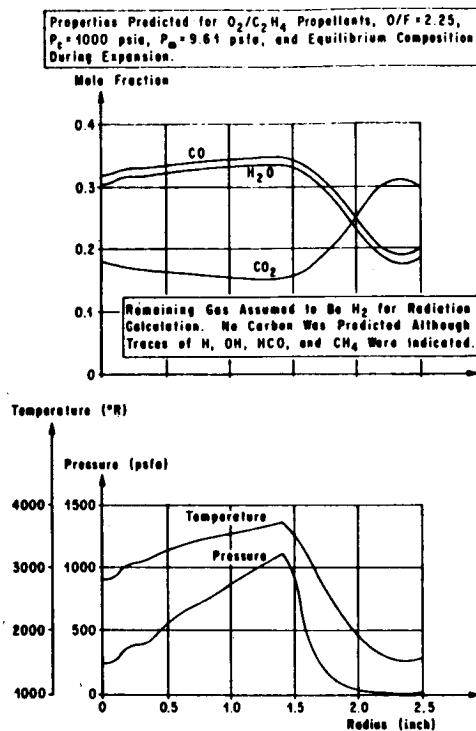


FIGURE 13. PREDICTED PROPERTY VARIATIONS 0.6 INCHES  
 DOWNSTREAM OF A 1/45 SCALE F-1 ENGINE EXIT

For sea level tests, it is necessary to install a short conical diffuser on the J-2 engine to prevent possible flow disturbances in the nozzle. With the diffuser installed, the predicted plume properties along the spectrometer line of sight contain a strong discontinuity because of an oblique shock wave as shown in Figure 17. In making the gas property predictions, the nozzle boundary layer was neglected, since it would be difficult to obtain a reasonable boundary layer prediction for this case. This is due to the rapid pressure rise caused by the shock which should cause flow separation.

A comparison of measured and predicted radiation (Fig. 18) shows that the predicted radiance is somewhat lower than the measured values. However, the agreement is considered to be reasonable when possible gas property and measurement errors are considered. It was predicted that 84 percent of the radiation is emitted by the high temperature layers surrounding the plume with 55 percent originating in the near side and 29 percent from the far side. Therefore, small errors in predicting the shock position could lead to appreciable errors in the predicted flux.

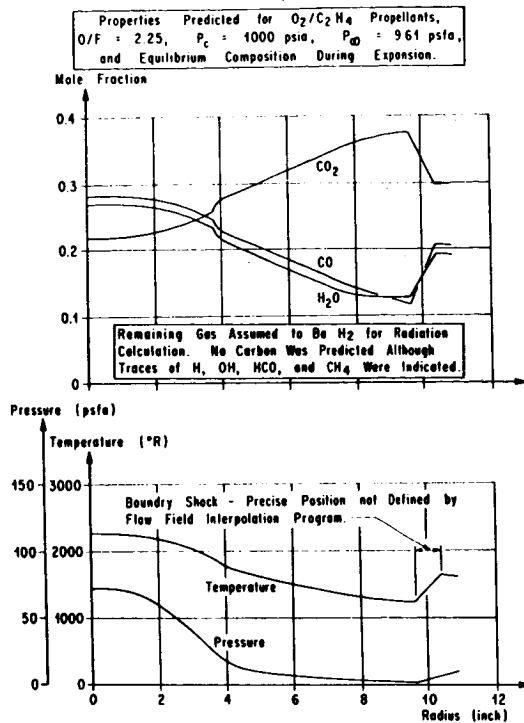


FIGURE 14. PREDICTED PROPERTY VARIATIONS 9.94 INCHES  
 DOWNSTREAM OF A 1/45 SCALE F-1 ENGINE EXIT

## Saturn 203 Flight Measurement

Detailed spectral measurements of the engine exhaust plumes were made on the Saturn 203 vehicle using a Block E8G spectrometer mounted in the heat shield of the S-IB first stage [ 17 ], which has eight Rocketdyne H-1 engines. The spectrometer was mounted between an inboard and outboard engine as shown in Figure 19. The spectrometer scanned three spatial positions in sequence and then recorded a reference level from an internal calibration lamp. Scanning time was approximately one second per position.

Although the spectrometer functioned and returned data through the entire flight, the sensitivity of the long wavelength channel apparently decreased by about a factor of 2 around 75 seconds after launch. Corrections for the apparent sensitivity changes were made using correction factors which would give constant levels of reduced data for the scans of the calibration source within the instrument. To evaluate the probable validity of this compensation

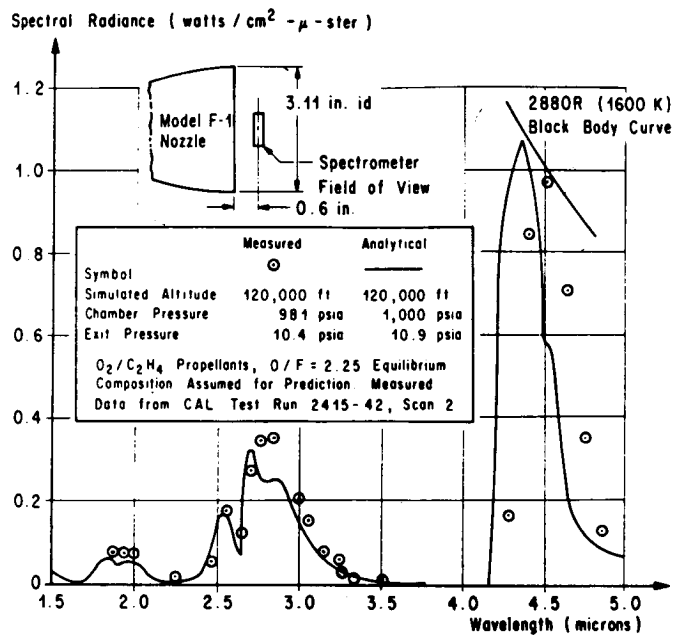


FIGURE 15. COMPARISON OF MEASURED AND PREDICTED RADIATION NEAR THE EXIT OF A 1/45 SCALE F-1 ENGINE

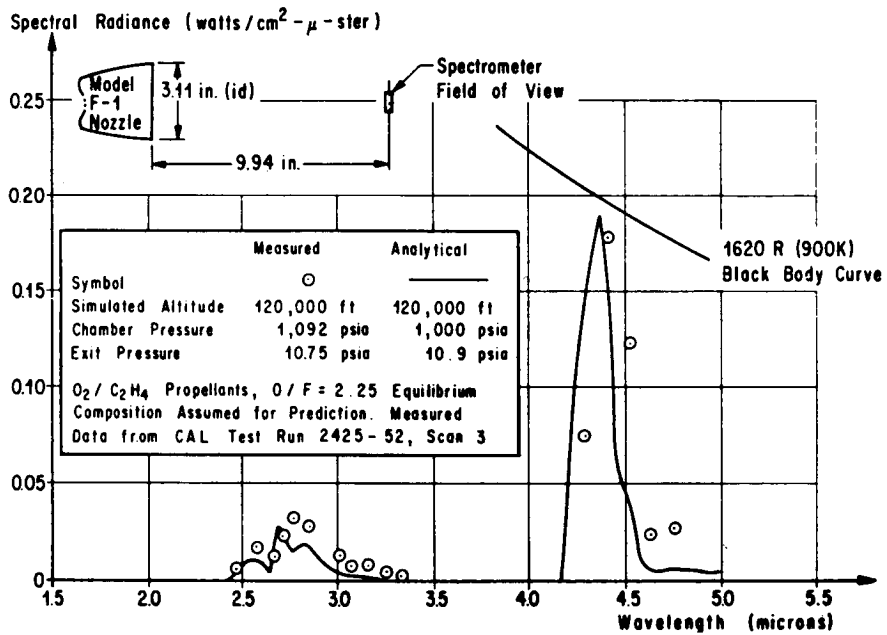


FIGURE 16. COMPARISON OF MEASURED AND PREDICTED RADIATION 9.94 INCHES AFT OF THE EXIT OF A 1/45 SCALE F-1 ENGINE

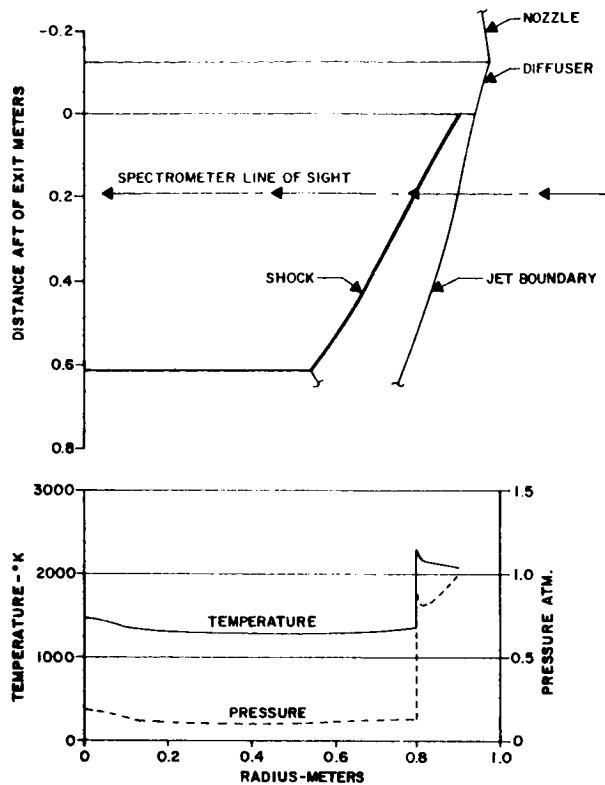


FIGURE 17. FLOW FIELD PREDICTIONS FOR THE J-2  
SEA-LEVEL STATIC TESTS

method, the brightness temperatures were compared at 1.6 and 3.9  $\mu$  after the correction was made. This essentially compares the effective carbon particle temperature from each of the two channels. The temperatures were practically identical on the  $-4.5^\circ$  scan position after 70 seconds, but on the other scans, and at earlier times on the  $-4.5^\circ$  scan, the short wavelength channel was apparently saturated.

The  $+4.1^\circ$  view angle looks between the plumes early in flight and then into the intersection region between plumes at higher altitude. The brightness temperature at this position is compared in Figure 20 with that for the  $-4.5^\circ$  position, which appears to look into the undisturbed plume. The trends in the temperature are reasonable considering the plume regions being viewed, but the temperatures are somewhat higher than have been predicted thus far in the analysis.

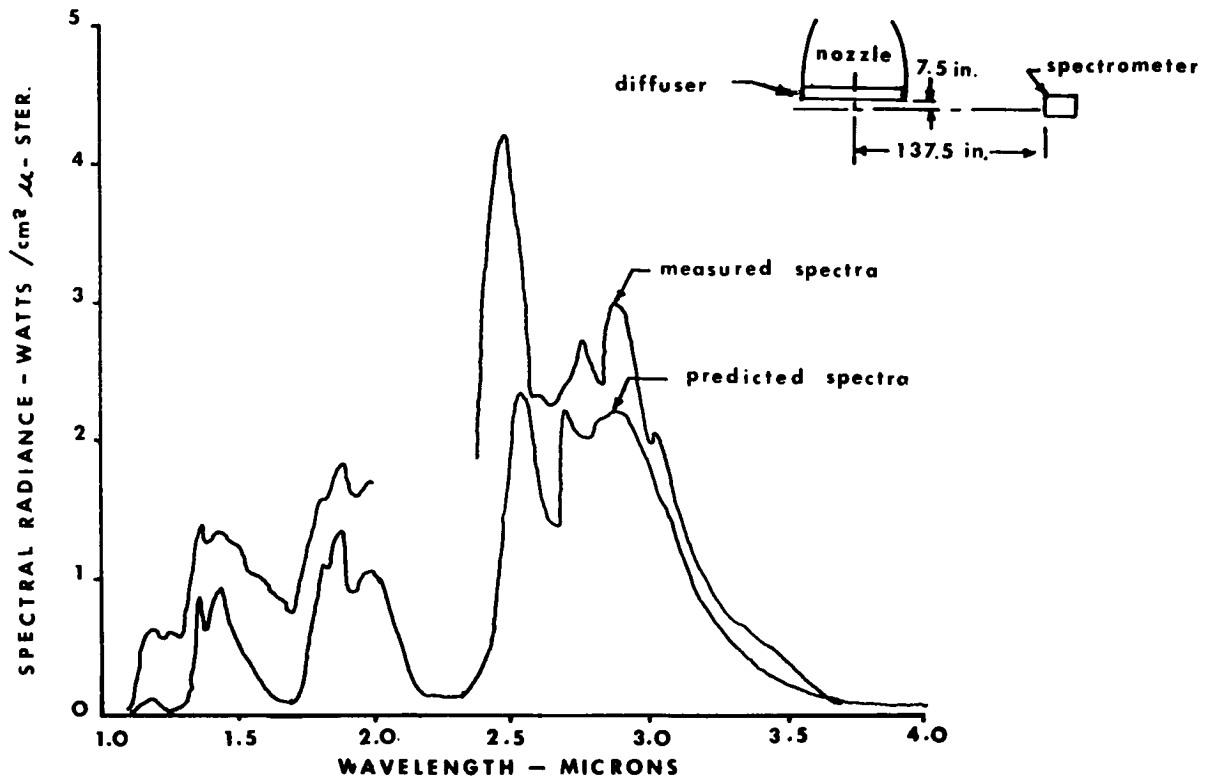


FIGURE 18. COMPARISON OF MEASURED AND PREDICTED RADIATION ON A J-2 ENGINE SEA LEVEL STATIC FIRING

Indicated temperatures for the  $-4.5^\circ$  position approach the predicted combustion chamber stagnation temperature of approximately  $3500^\circ\text{K}$ . This high temperature is apparently caused by afterburning. As the flow begins to reverse in the base region to exclude the ambient flow, the afterburning appears to decrease until a stable radiation level is reached at about 20 km.

The temperatures indicated early in flight for the  $+4.1^\circ$  view position are slightly lower than the  $-4.5^\circ$  position since the view is farther downstream between the jets. The indicated temperatures at higher altitudes for the  $+4.1^\circ$  position are higher, as expected, since it views the impingement zone between engines.

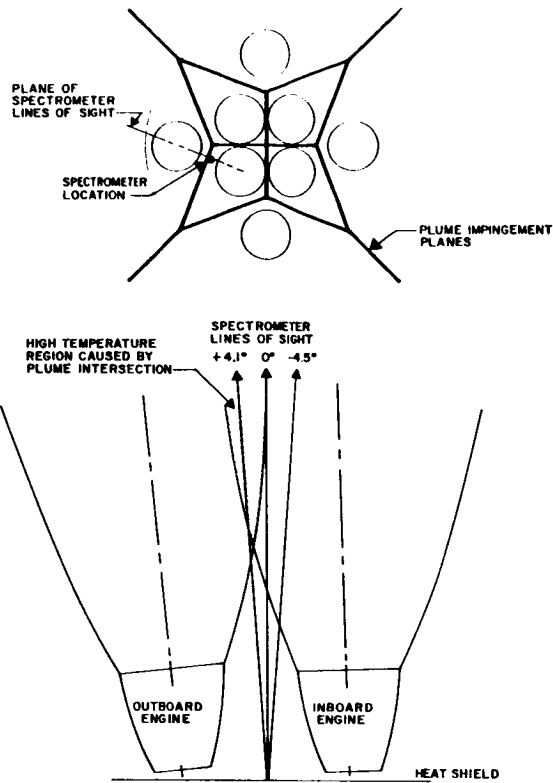


FIGURE 19. SPECTROMETER ORIENTATION ON SATURN 203

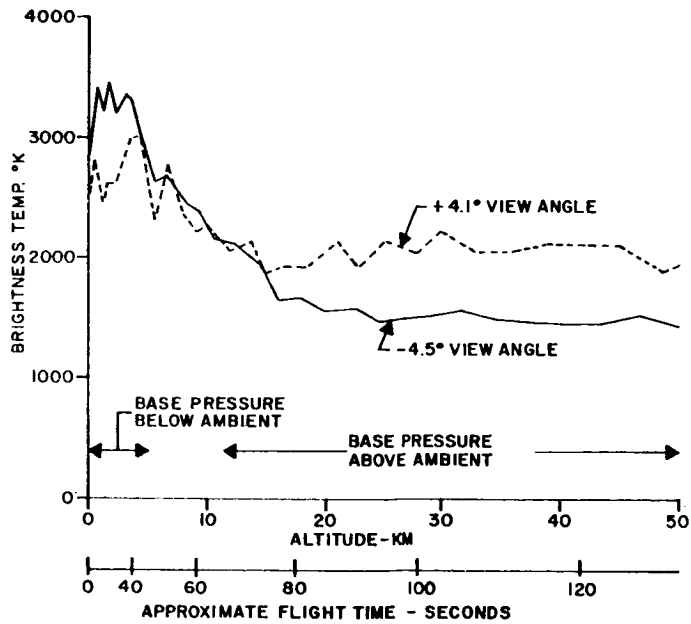


FIGURE 20. BRIGHTNESS TEMPERATURE AT  $3.9\mu$  FROM SATURN FLT. 203 SPECTROMETER DATA

Preliminary attempts to make theoretical predictions to compare with the measurements have not been very successful since the flow models used have not predicted temperatures as high as those which have been indicated.

A comparison was made for the early portion of the flight using afterburning plume properties furnished by Chrysler Corporation Space Division. The maximum temperature predicted in the mixing layer along the spectrometer line of sight was about 2700° K. Assuming a 5 percent weight fraction of carbon particles, the predicted effective temperature is approximately 2100° K as shown in Figure 21. As the percentage of carbon particles is varied, the apparent temperature would vary, but there is no way to achieve the indicated 3400° K brightness temperatures using the plume properties predicted.

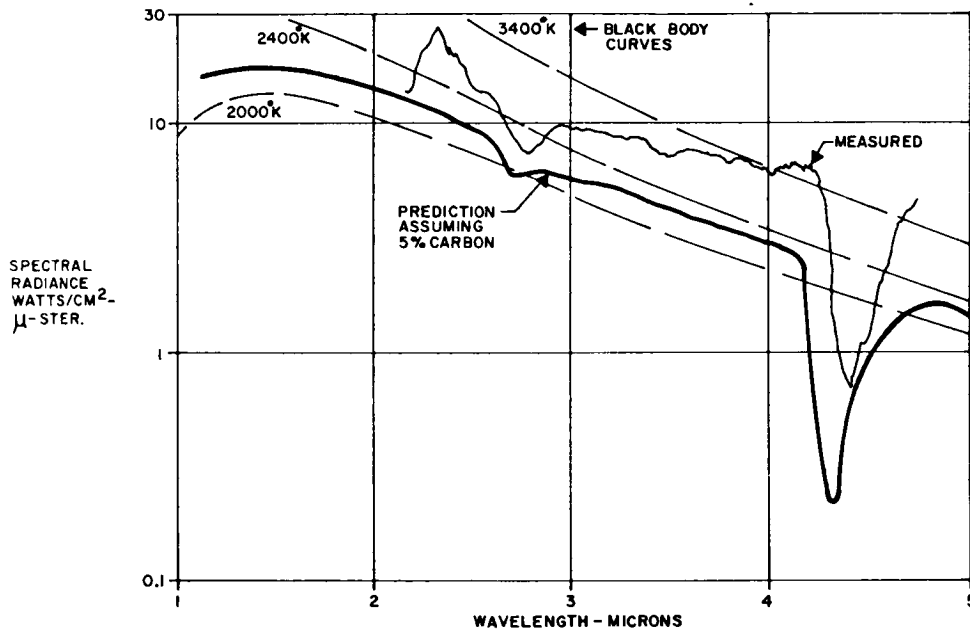


FIGURE 21. SATURN 203 SPECTRUM FOR THE -5° VIEW POSITION AT A FLIGHT TIME OF 28 SECONDS

A comparison at a high altitude condition without afterburning is presented in Figure 22. Here again, the measured data appear to come from a higher temperature gas than has been predicted by the axisymmetric method of characteristics program. No predictions have yet been made of the extent of the plume impingement regions, but when these predictions are made, they may indicate that the -4.5° line of sight intersects one of the impingement regions surrounding the inboard engines.



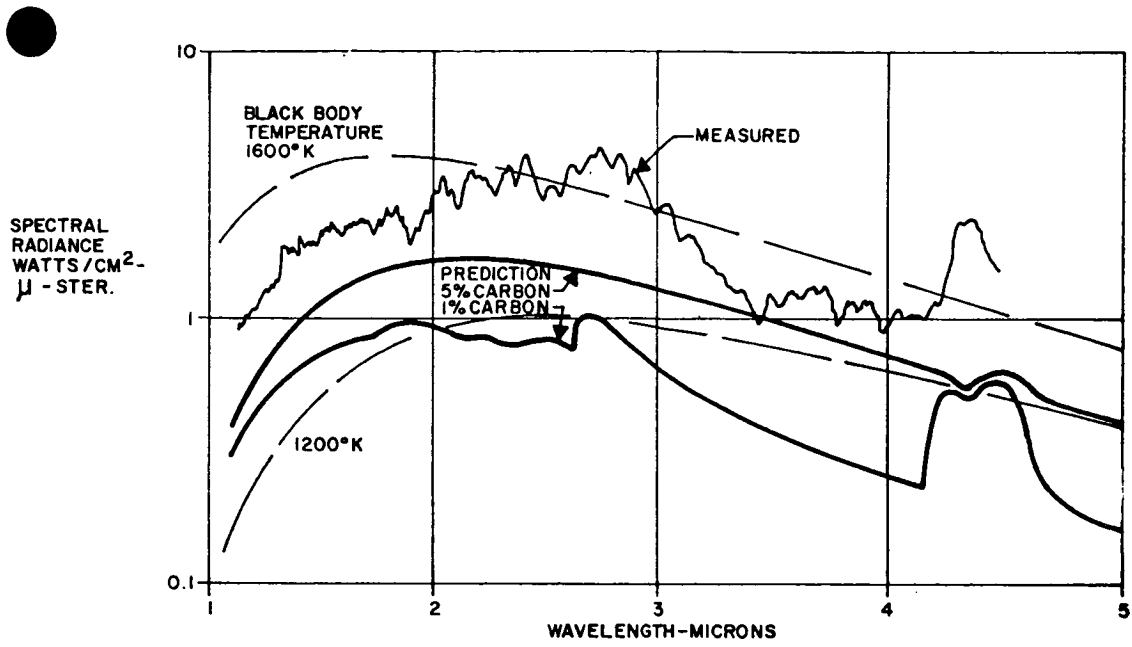


FIGURE 22. SATURN 203 SPECTRUM FOR THE -5% VIEW POSITION AT A FLIGHT TIME OF 114 SECONDS

### CONCLUSIONS

Effective methods have been developed for predicting the radiation heat transfer from rocket exhaust plumes containing water vapor, carbon dioxide, carbon monoxide, and carbon particles. These methods are now being refined, and are being compared with experimental measurements. The accuracy of the radiation predictions is considered to be reasonably good for the intended use in predicting the thermal environment of the rocket vehicle. However, it has become apparent that satisfactory methods are not available for predicting the gas properties in the exhaust plumes for many of the complex flow problems encountered.

## REFERENCES

1. Study on the Spectral Emissivity of Carbon Particles Produced by a Rocket Motor. Final Report on Contract NAS8-11455, General Dynamics Corp., Convair Division, GD/C-DBE 66-006, May 1966.
2. Thomson, J. D.: A Study of Radiative Properties and Composition of the Turbine Exhaust Products in the F-1 Engine. Rocketdyne Division of NAA, R-6743, Sept. 1966.
3. Study of the Radiation and Convection Environment of the Saturn V. Summary Report on Contract NAS8-11350, Hayes International Corp., ER 1333, October 1966.
4. Study on Exhaust Plume Radiation Predictions - Interim Progress Report. Contract NAS8-11363, General Dynamics Corp., Convair Division, GDC-DBE-66-001, January 1966.
5. Study on Exhaust Plume Radiation Predictions - Interim Progress Report. Contract NAS8-11363, General Dynamics Corp., Convair Division, GDC-DBE-66-001a, February 1966.
6. Study on Exhaust Plume Radiation Predictions. Final Report on Contract NAS8-11363, General Dynamics Corp., Convair Division, GDC-DBE-66-017, December 1966.
7. Krakow, B.; Babrov, H. J.; Maclay, G. J.; and Shabott, A. L.: Use of the Curtis-Godson Approximation in Calculations of Radiant Heating by Inhomogeneous Hot Gases. NASA TM X-53411, March 1966.
8. Malkmus, W.: J. Opt. Soc. Am., vol. 53, 1963, p. 951.
9. Malkmus, W.: J. Opt. Soc. Am., vol. 54, 1964, p. 751.
10. Malkmus, W.; and Thomson, A.: J. Quant Spectrosc. Rad. Transfer, vol. 2, 1962, p. 17.

## REFERENCES (Concluded)

11. Huffaker, R. M.; and Dash, M.: A General Program for the Calculation of Radiation from an In-Homogeneous, Non-Isobaric, Non-Isothermal Rocket Exhaust Plume. NASA TMX 53-622, June 1967.
12. Delwadia, M.; Reardon, J. E.; and White, S. A.: A Three-Dimensional Radiation Program for the Saturn S-II Stage. Hayes International Corp., ER 1470, August 1967.
13. Chu, C. W.; Niemann, A. F.; Powers, S. A.; D'Attorre, L.; Nowak, G.; and Thommen, H. U.: An Inviscid Analysis of the Plume Created by Multiple Rocket Engines and a Comparison with Available Schlieren Data. AIAA Paper 66-651, Presented at the Second Propulsion Joint Specialist Conference, June 1966.
14. Prozan, R. J.: Development of a Method of Characteristics Solution for Supersonic Flow of an Ideal, Frozen, or Equilibrium Reacting Gas Mixture. Lockheed Missiles and Space Co., Huntsville Research and Eng. Center, LMSC/HREC A782535, April 1966.
15. Klein, L.; and Penzias, G. J.: AIAA Jour., vol. 5, 1967, p. 9.
16. Huffaker, R. M.: Inhomogeneous Radiant Heat Transfer from Saturn Rocket Exhaust Plumes. NACA TM X-53630, June 1967.
17. Thibodeaux, D.: Infrared Spectra of the Saturn IB, SA-203 Rocket Exhaust Plumes Measured During Flight. Chrysler Corp. Space Division TN-AP-67-161, February 1967.

---

## DISCUSSION

G. H. Kelley, Grumman Aircraft: Does the program also yield heat fluxes to other surfaces than the base of the rocket, on the structure of the launch pad, for instance?

J. E. Reardon: Yes, you can use it that way. The geometry is fairly flexible, the only restriction being that the normal to the surface must be in the  $xz$  plane of the flow field (Fig. 4). This is the major restriction on our program. In addition, of course, computer storage capacity limits the extent of the flow field which we can calculate.

G. H. Kelley: How detailed a plume structure is required to get a reasonably accurate radiation calculation?

J. E. Reardon: That is still to be found out. Until now, we have calculated as many points as we had storage for. In our new program we hope to be able to handle a much larger flow field by doing it a piece at a time.

---

# EMITTANCE AND RADIANCE CALCULATIONS FOR SOLID PROPELLANT ROCKET EXHAUSTS

N 68-18093

By

D. J. Carlson and A. J. Laderman

Philco-Ford Corporation  
Aeronutronics Division  
Newport Beach, California

---

## ABSTRACT

The phenomenology of solid propellant plumes is reviewed with emphasis on prediction of spectral radiancy. Sample calculations are presented and compared with experimental values, and important uncertainties noted.

---

## INTRODUCTION

Several papers have been presented at this conference which are concerned with the calculation of radiation from the gaseous constituents of rocket exhaust plumes. In the case of aluminized solid propellant rockets, however, a significant fraction of the exhaust products may be present in the form of condensed-phase micron-size particles which can strongly influence the radiative behavior of the plume. The objective of this paper is to review briefly the current status of our capability to calculate particle cloud radiation, to highlight the major uncertainties which still exist, and to illustrate the effects of these uncertainties on practical calculations using the results of a recent NASA/Huntsville-sponsored study [ 1 ] of the Saturn II ullage motor.

## DEFINITION OF THE PROBLEM

Since we are concerned specifically with particle radiation, the discussion which follows is restricted to those cases where gas phase radiation can be neglected (e. g. , at high altitudes where afterburning of the fuel-rich exhaust gas ceases) or where the radiation from the gaseous and condensed phase emitters can be treated independently (e. g. , when the plume is optically thin). The optically thick gas-particle cloud, where the presence of one phase alters the emission from the other phase, will be discussed separately by Bartky [ 2 ] .

Since our purpose here is to concentrate on the radiative properties of the particulate emitters, it is further assumed that the structure (i. e. , the local pressure, temperature, and concentrations of gaseous and particle constituents of the plume) can be determined. Calculation of the entire plume structure is itself a difficult problem, and the effect of coupling between gas and particle flows in a heterogeneous plume introduces an added complication. A detailed phenomenological description of the gas dynamics of two-phase plumes presented recently by Carlson [ 3 ] in a comprehensive review of the subject indicates that the particle plume can be defined to the same extent as the gas plume. Carlson points out that, for most conventional solid propellant rockets, the gas and particle flows are weakly coupled. Thus, a practical method for computing the particle plume, which is used in the calculational scheme described later, is to determine first the gas plume structure, and, for a given initial size distribution, trace the particle trajectories through the known gas flow field.

Within this framework, it is appropriate now to examine the nature of the important phenomena involved in calculation of particle radiation. First the particles, which in the case of aluminized propellants are aluminum oxide, are of micron size. For a particular motor, however, the size of the particles present in the plume varies over at least an order of magnitude. Second, while the chamber temperature is generally in excess of the melting point of alumina, the particles may appear in the plume in either the liquid or solid state. Third, in spite of the small size of the particles, inertia effects can be significant. Consequently, the velocity and temperature of the particles may lag appreciably those of the gas and, in addition, the particles tend to classify according to size. The latter effect is illustrated in Figure 1, which shows limiting particle streamlines in the near field of the vacuum plume for a typical solid propellant rocket. These streamlines, which originate at the

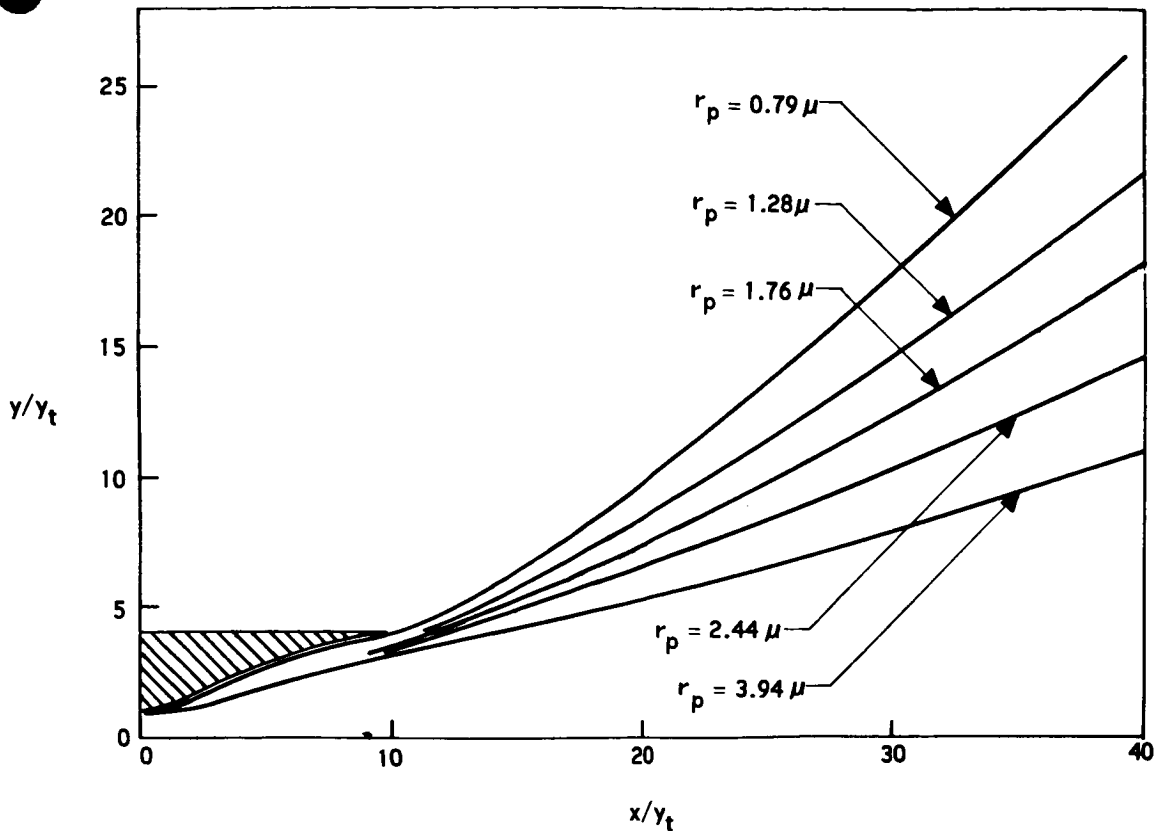


FIGURE 1. LIMITING PARTICLE STREAMLINES IN THE NEAR FIELD

wall of the nozzle inlet, represent a limiting conical boundary within which all particles of a given size are contained. The temperature histories associated with the various size particle limiting streamlines are shown in Figure 2. The plateau which comprises a segment of each temperature profile represents solidification of the particles during which the temperature remains constant as the particle releases its heat of fusion.

In addition to the above, it should be recognized that, unlike the gas, the particles are continuum emitters. Also, the particles act as effective scattering centers, which can serve to reduce the apparent emittance of the plume in the optically thick limit. Finally, in addition to thermal emission from the particles, the plume radiancy can be enhanced by the so-called "searchlight effect," where radiation originating within the rocket nozzle or chamber is scattered into other directions.

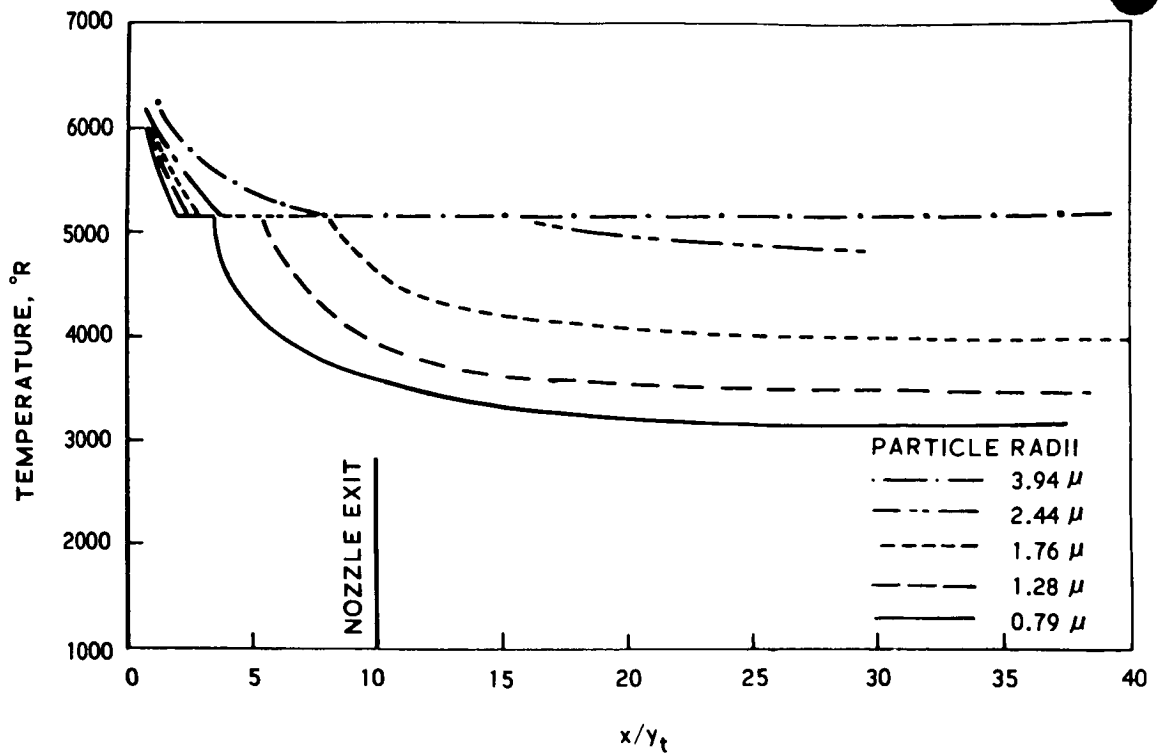


FIGURE 2. NEAR FIELD TEMPERATURE OF LIMITING STREAMLINE PARTICLES

### GENERAL CALCULATION SCHEME

In general, a method for calculation of plume radiation will require the elements shown in Figure 3, where the circled quantities represent input parameters and the boxed items denote calculation routines. Thus, a thermochemical calculation is needed to specify the chamber temperature and species concentrations and the variation of these parameters throughout the nozzle and plume expansion. These results, together with the nozzle geometry, are used to determine the gas flow field in some manner, e.g., by the method of characteristics. Specification of the initial size distribution then allows calculation of the particle plume, consisting of the local particle temperature, velocity, number density, and size distribution. With index of refraction data, the Mie theory is used to find the absorption and scattering cross sections,  $\sigma_a$  and  $\sigma_s$ , as a function of particle size. Knowing the plume structure, we can calculate



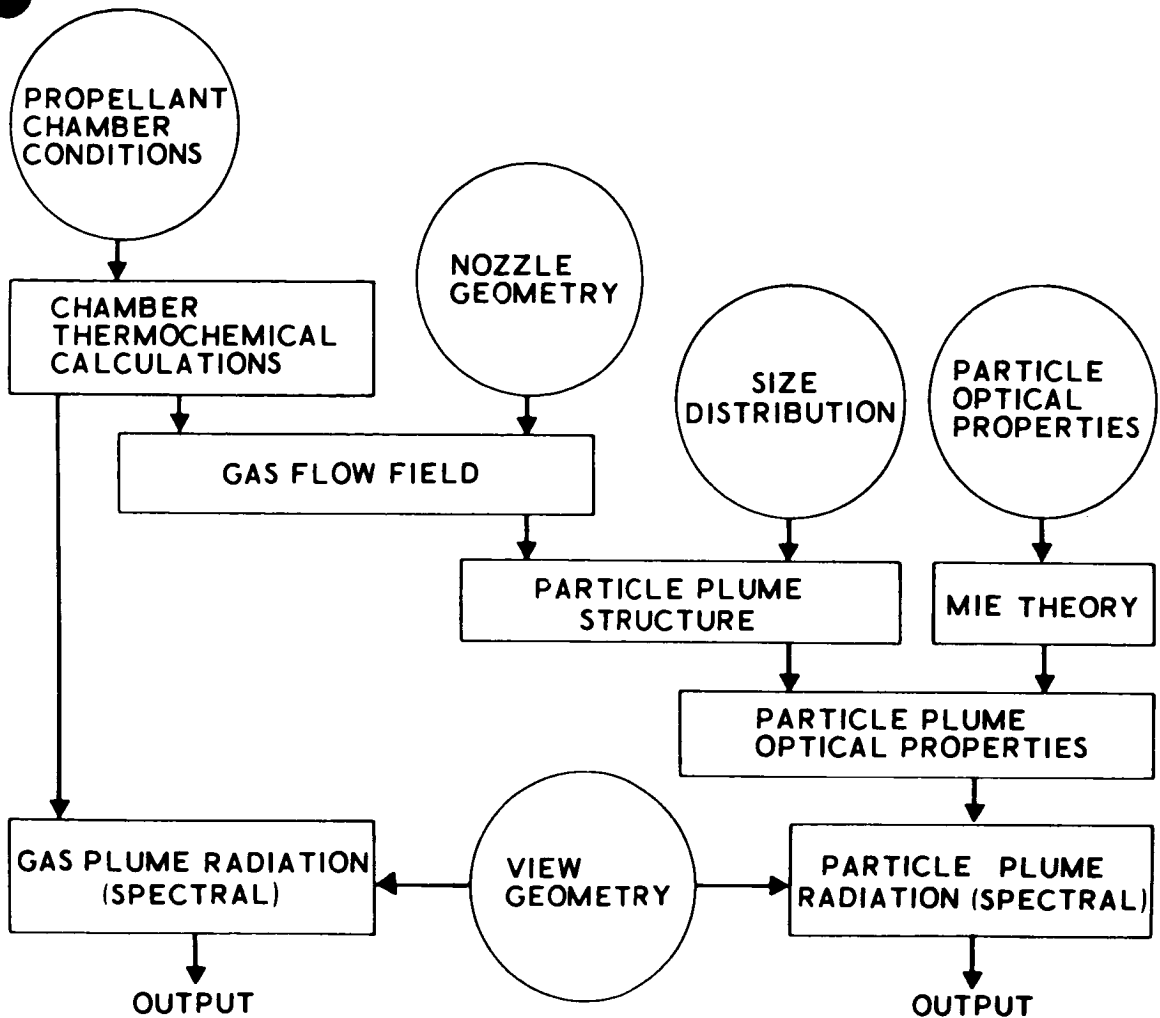


FIGURE 3. FLOW CHART FOR PLUME RADIATION CALCULATIONS

the local values, averaged over particle size, of  $\langle \sigma_a \rangle$ ,  $\langle \sigma_s \rangle$ , and  $\langle R^* \rangle$  where  $R^*$  is the blackbody function. The plume is then divided into slabs normal to the line of sight, where each slab assumes the values of  $\langle \sigma_a \rangle$ ,  $\langle \sigma_s \rangle$ , and  $\langle R^* \rangle$  at its midpoint, and the radiative equation of transfer, simplified by the one-dimensional beam approximation, is applied to each slab. Solving the resulting set of simultaneous equations yields, finally, the spectral radiance of the plume along the line of sight. Repeating the radiation portion of this procedure for several wavelengths and applying the appropriate view factor allow the determination of the heat flux to a given target. Complete details of the method are given in [1].

The flow chart of Figure 3 also includes a loop for calculating gas radiation. As shown in the diagram, it implies that the two radiation contributions can be computed independently, consistent with our earlier restrictions. In the example discussed later, the plume was optically thin so that this procedure could be followed, and both contributions have been included here since the gas phase radiation was shown to be important.

## MAJOR UNCERTAINTIES

Although the calculation scheme described above involves numerous approximations, each of which contributes to inaccuracies in the final answer, the major uncertainties are associated with inadequate or insufficient input data, supercooling of the particles, and identification of significant continuum emitters.

a. Optical Properties. As mentioned earlier the absorption and scattering cross sections can be determined from the Mie theory if the imaginary index of refraction  $m = n_1 - n_2i$  and the particle size are known. Data on the real part of the refractive index,  $n_1$ , for the solid have been reported by Bartky and Bauer [4]. For the liquid,  $n_1$  data can be deduced from the reflectivity measurements of Diamond and Drago [5] and Eisner et al. [6].

The imaginary part of the refractive index,  $n_2$ , for solid alumina at elevated temperatures has been determined from the experiments of Grynak and Burch [7] over the wavelength interval from 0.5 to 6 microns. Mergerian's [8] emissivity measurements of alumina slabs provide  $n_2$  data in the interval from 11 to 13 microns, although his maximum temperature was 1000° C. For liquid alumina,  $n_2$  has been determined from the measurements of Carlson [9] (from 2320° K to 3000° K) and Adams [10] (from 2470° K to 2900° K). However, Carlson's data are restricted to the range from 0.58 to 2.3 microns, while Adams' data were taken only at 0.58 microns. The results of these several investigations are shown in Figure 4. Since it was necessary to extend the calculations for the S-II ullage motor to at least 10 microns, two extrapolations of the liquid  $n_2$  are presented. The first reflects the data of Carlson in the near IR, while beyond 3 microns the liquid  $n_2$  curves have been drawn parallel to those of the solid. The second extrapolation is compatible with Adams' results at low wavelengths (which was roughly a factor of ten greater than Carlson's data) and approaches the solid  $n_2$  curves at long wavelengths following with the "squeezing together" trend observed for the solid by Grynak and Burch.

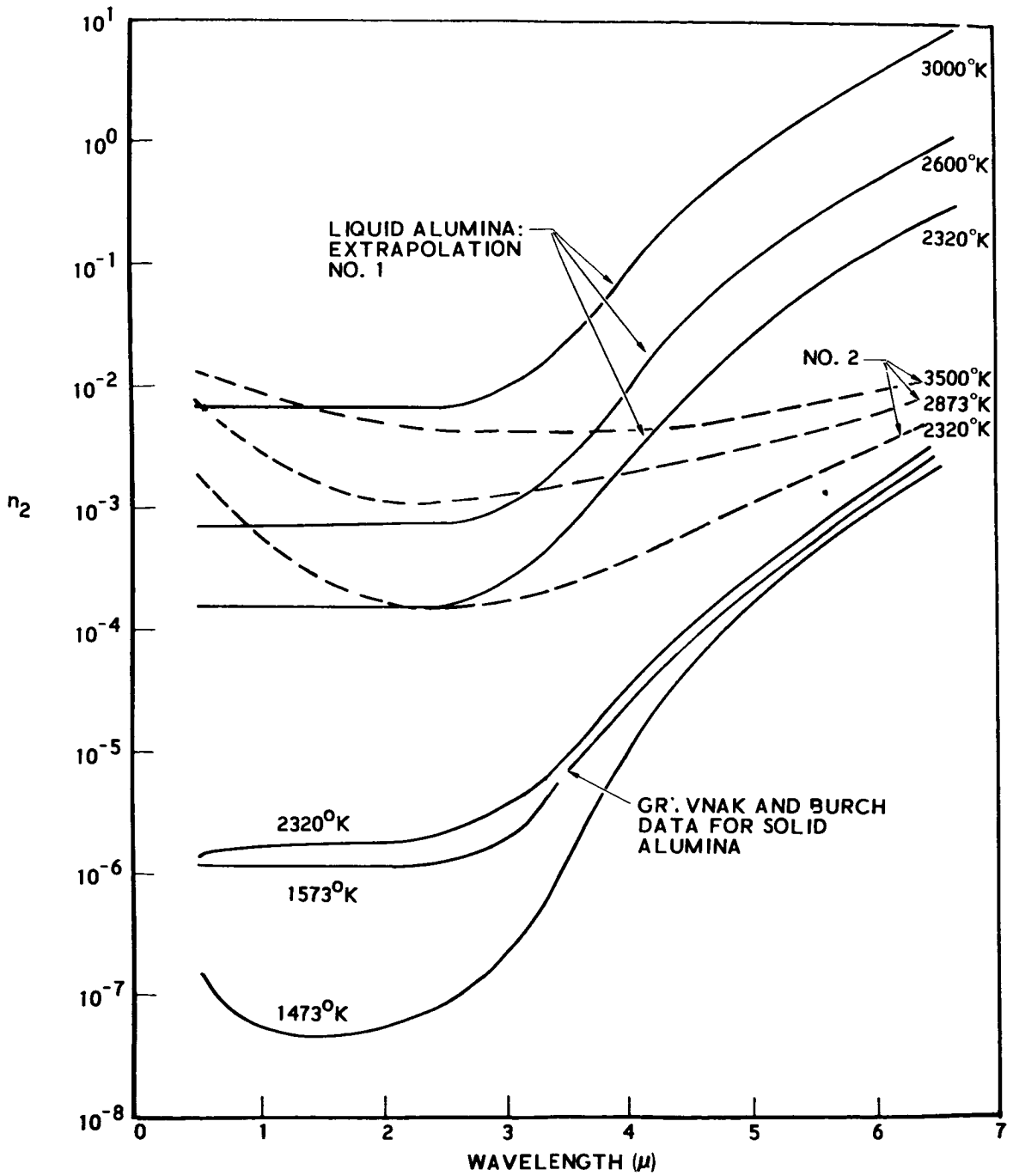


FIGURE 4. EXTRAPOLATIONS OF IMAGINARY PART OF REFRACTIVE INDEX  $n_2$ , FOR LIQUID ALUMINA

The consequences of the two extrapolations for the liquid  $n_2$  will be discussed later. However, for the particle size distribution used in the S-II ullage motor calculations, the particle emissivity becomes unity when  $n_2$  exceed  $\sim 2 \times 10^{-2}$ .

b. Particle Size Distribution. Data on particle sizes typical of solid propellant formulations have been reported by numerous investigators, employing a variety of experimental techniques and sampling methods. A detailed review of this subject can be found in [3]. Selected results for alumina are compared in Figure 5, which provides an indication of the existing conflict concerning the influence of chamber pressure, residence time, and nozzle size and demonstrates that the uncertainty in particle size is as large as a factor of 3 or 4.

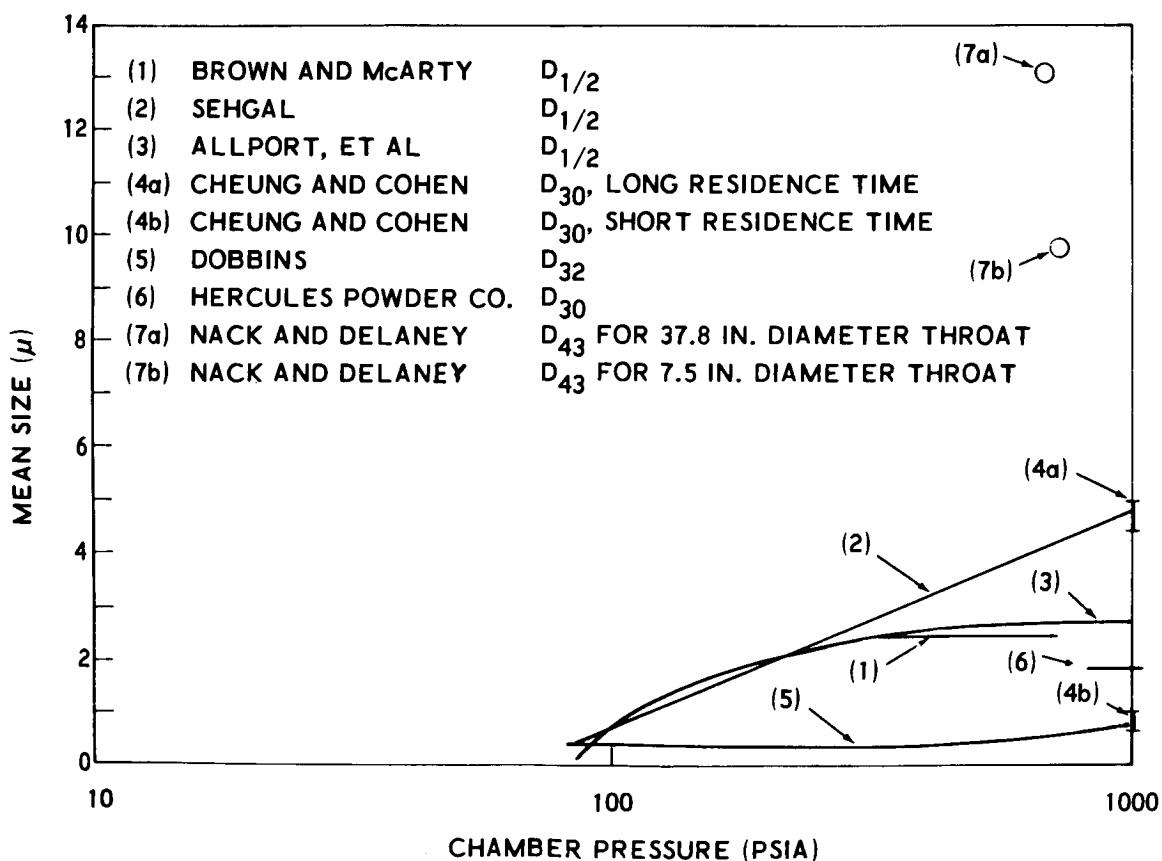


FIGURE 5.  $Al_2O_3$  PARTICLE SIZES DETERMINED FROM DIFFERENT STUDIES

Interpretation of experimental results is complicated by the different definitions of "mean" or "average size" used by various investigators and the fact that the several "means" are frequently compared ignoring their possible differences. In addition, information on the distribution of sizes is often omitted although such data are equally important in the calculation of particle radiation.

c. Supercooling. If supercooling occurs, the particles pass through the melting point without giving up their heat of fusion, and the constant temperature plateaus of Figure 2 no longer exist. Furthermore, the particles probably retain a liquid-like emissivity which, in the near IR, is several orders of magnitude greater than that of solid alumina. Although the larger particles, which comprise a large portion of the total particle mass and consequently contribute a significant portion of the plume radiancy, frequently remain above the melting point until well out into the plume, supercooling should lead to enhanced radiation, particularly at low wavelengths. While there is no conclusive evidence that supercooling occurs, Brown [11] has reported that examination of a collection of solid particles which were liquid in the chamber revealed an amorphous, rather than crystalline, structure, which is characteristic of the liquid phase.

d. Other Continuum Emitters. For some time it has been felt that alumina is the dominant continuum emitter in aluminized solid propellant exhausts. Based on the results of [1], it appears that this may not generally be true. Other metallic oxides are frequently present in quantity in many propellant formulations as a burn rate controller. The S-II ullage motor, for example, contains almost 2 percent ferric oxide, which should be condensed in the plume. The exact radiative contributions of these materials cannot be evaluated since high temperature optical data are generally lacking. However, the existing ferric oxide data indicates that the value of  $n_2$  at one micron at room temperature is about 15 times the value for liquid alumina at its melting point and more than 7 orders of magnitude larger than the room temperature value for solid alumina. If the value of  $n_2$  for ferric oxide increases with temperature as does the alumina value, its importance is obvious.

In addition to the metal oxide content of the propellant, the possibility of the non-equilibrium formation of carbon particles cannot be overlooked even in solid-fueled rockets. For example, the report [12] on the experimental measurements of radiation from the S-II ullage motor plume notes the presence, at the end of the test, of soot on a probe located in the plume. It is not known whether this carbon particulate matter is present only on start-up or shut-down (which would not affect the experiment) or both, or is present during the steady state burn. It was also noted that part of the ablative nozzle was lost during the test. This nozzle ablation could have possibly introduced

solid carbon into the plume mixing region. Unfortunately, much of the available carbon data are qualitative because of difficulties in measuring the extremely small particle sizes (50-500 Angstroms) and determining the relative amount present in the plume. While the importance of carbon radiation cannot be quantitatively evaluated, solid carbon is known to be an efficient emitter, and its contribution must be considered.

## NUMERICAL RESULTS: COMPARISON BETWEEN THEORY AND EXPERIMENT

To illustrate the magnitude of the uncertainties discussed above, we can examine some recent calculations [ 1] of the S-II ullage rocket at an altitude of 120 000 feet. There exist several experimental measurements of the plume radiation, which will be discussed first.

At AEDC [ 12] a Hayes FF1 narrow view (8 millirad x 8 millirad at 20 ft) detector, located 6 inches downstream of the exit plane and 5 feet from the plume centerline, was used to measure total radiation. The detector response was relatively flat to 15 microns [ 13]. The results of this test indicated an average steady state flux of 6.5 watts/cm<sup>2</sup>-ster.

At OAL [ 14] several spectral measurements were made over the wavelength interval from 0.5 to 3 microns. Results of these tests indicate that (1) on the basis of the AEDC test result, over one half the radiative flux occurs at wavelengths greater than 3 microns and (2) in the observed spectral interval from 1.7 to 3 microns, the gas band radiation is approximately one-third of the particle continuum.

To compute the plume radiation, the following assumptions were made:

(1) The initial particle size distribution was based on existing data for similar sized motors. Thus, the mass mean diameter was 3.24 microns, while the number mean was 1.12 microns, and the distribution was determined from the skew-symmetric formula of Bauer and Carlson [ 15].

(2) In the absence of ferric oxide data, alumina was considered to be the only continuum emitter although the S-II ullage motor contained 2 percent of ferric oxide compared to 8 percent of alumina.

Figure 6 shows the calculated spectral radiancy of the particle continuum obtained for the two  $n_2$  extrapolations shown in Figure 4. The areas under the two curves, which reflect the spectral differences in the  $n_2$  extrapolations, differ by a factor of 3.5 and represent 35 percent and 10 percent of the total measured radiation for extrapolations no. 1 and no. 2, respectively.

To evaluate the gas radiation, calculations were made for the following bands: 1.38, 1.87, 2.7, and 6.3 micron bands of  $H_2O$  and 2.7 and 4.3 micron bands of  $CO_2$ . The 4.5 micron band of  $CO$  was neglected since its contribution to the total gas phase radiation was small [16]. The 3.5 micron band of  $HCl$  was also neglected since calculations based on the work of Stull and Plass [17] indicated a very small contribution. The gas band results, which are in excellent agreement with those obtained using an MSFC gas radiation program [18], represent 23 percent of the total measured radiation.

The combined gas-particle radiation, using  $n_2$  extrapolation no. 2 is shown in Figure 7, which also includes the results of the OAL measurement. The total computed radiation is only 33 percent of the AEDC measurement, and the agreement with the OAL spectra is poor.

Figure 8 shows the theoretical prediction, based on extrapolation no. 1, which includes gas band radiation and the contributions from the searchlight effect and supercooling. Both of the latter effects are significant below 3 microns and account for 15 percent and 20 percent of the total measured radiation. In this case, the total radiancy corresponds to almost 90 percent of the AEDC results, the spectral radiancy is in good agreement with the OAL data, and, more significantly, indicates that over 50 percent of the emission originates beyond 4 microns.

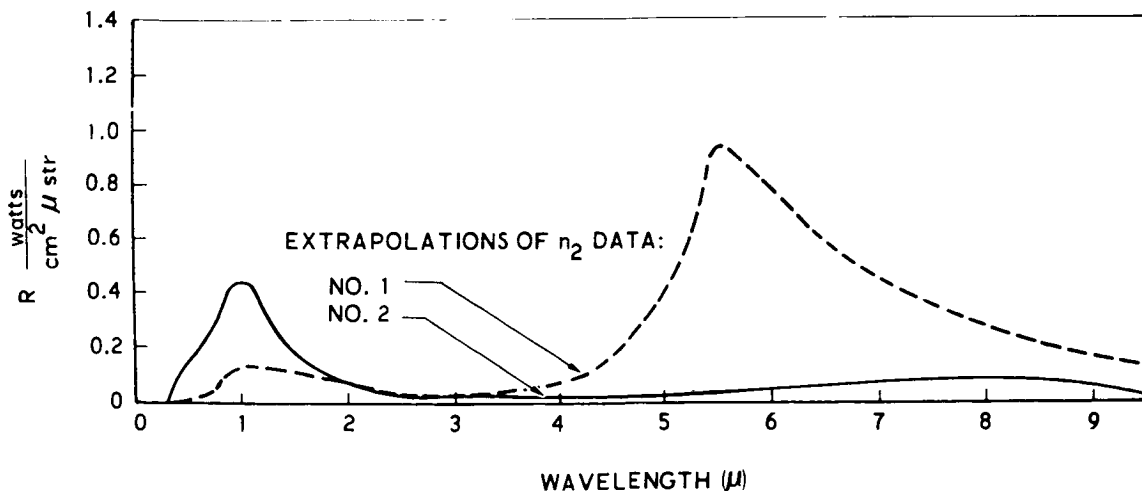


FIGURE 6. EFFECT OF  $n_2$  EXTRAPOLATION ON CALCULATED PARTICLE CONTINUUM

The calculations are summarized in Table I where the magnitude of the uncertainties involved is indicated.

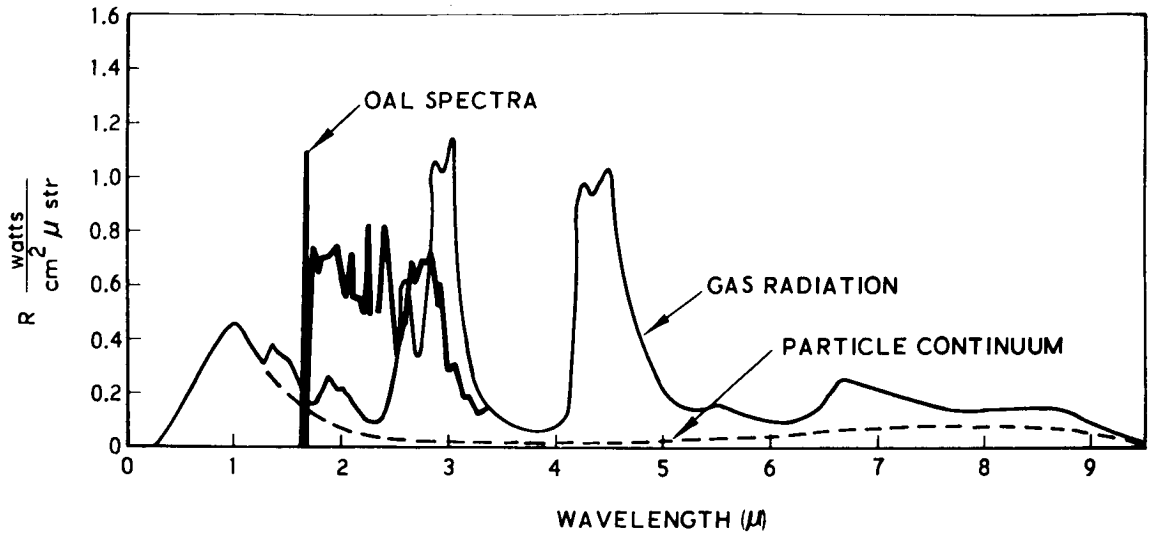


FIGURE 7. THEORETICAL PREDICTION COMPARED WITH OAL EXPERIMENT

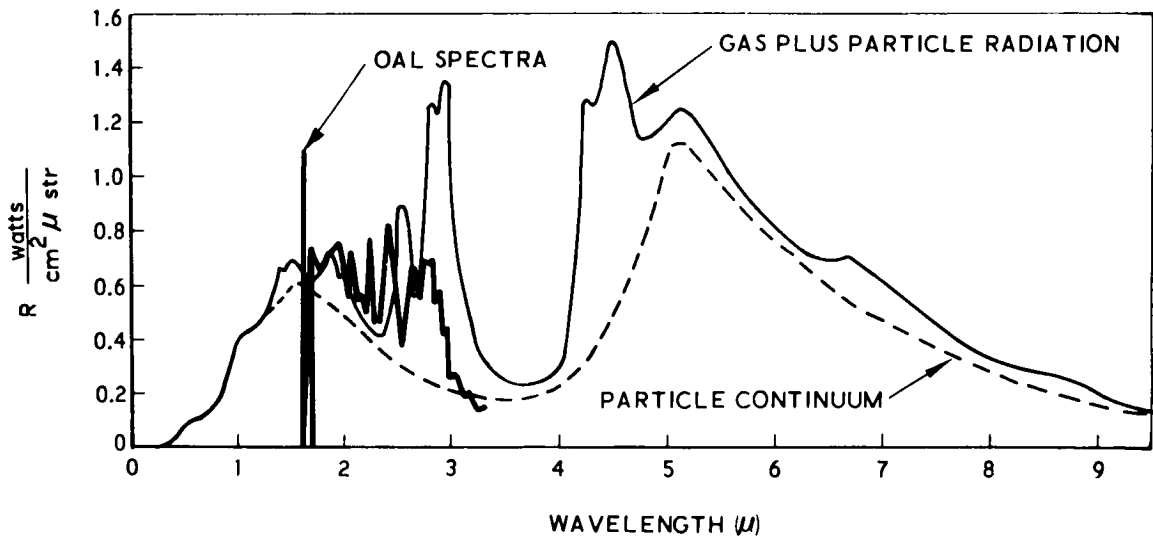


FIGURE 8. THEORETICAL PREDICTION BASED ON EXTRAPOLATION NO. 1 WITH SEARCHLIGHT AND SUPERCOOLING EFFECTS INCLUDED



TABLE I. S-II ULLAGE PLUME RADIATION

	<u>Percent of Experimental Measurement</u>
Nominal calculation of particle radiation	10
Calculated gas radiation	23
Searchlight radiation	<u>15</u>
Total theoretical prediction:	48
Uncertainty in $n_2$ of alumina	25
Supercooling uncertainty	20
Size distribution uncertainty	10

The last entry was obtained by increasing the mass mean diameter to 6.2 microns which doubled the particle radiation based on  $n_2$  extrapolation no. 2. Although this change in size is not unrealistic in view of existing particle size data, because of uncertainties in these data, size effects were not further pursued.

## CONCLUSIONS

While the results of Figure 8 are encouraging, on the basis of the preceding discussion, it is not possible to isolate conclusively the physical mechanisms responsible for particle plume radiation. However, the following conclusions can be made.

Gas phase radiation clearly cannot be ignored without demonstrating that its contribution is negligible. This is particularly true of lightly loaded solid propellant motors such as the S-II ullage motor.

Insufficient alumina optical property data are available for valid predictions of liquid alumina radiation at wavelengths less than 1.5 microns and greater than 3 microns. Furthermore, uncertainties in existing data are sufficient to account for a major portion of the discrepancy between measurement and theoretical calculation.

For the S-II ullage motor, the comparison between experiment and theory is good provided that the  $n_2$  extrapolation no. 1 is used and the effects of gas band radiation, searchlight, and supercooling are included.

Finally, other solids, particularly iron oxide and possibly carbon, are probably important or even dominant contributors to particle radiation. radiation.

## REFERENCES

1. Laderman, A. J.; Kuby, W. C.; Byron, S. R.; Carlson, D. J.; and Bartky, C. D.: Study of Thermal Radiation, Particle Impingement Heating, and Flow Field Analysis of Solid Propellant Rocket Exhausts. Applied Research Laboratories, Philco-Ford Corporation, Aeronutronic Division Publication No. U-4045, April 19, 1967.
2. Bartky, C. D.: Some Theoretical Frequency Averages for the Emittance of a Homogeneous Gas-Particle Cloud. Proceedings of Specialist Conference on Molecular Radiation, Marshall Space Flight Center, Huntsville, Alabama, October 5-6, 1967.
3. Carlson, D. J.: Radiation from Rocket Exhaust Plumes. Part II: Metallized Solid Propellants. Paper No. 66-652, AIAA Second Propulsion Joint Specialist Conference, Colorado Springs, Colorado, June 13-17, 1967.
4. Bartky, C. D.; and Bauer, E.: J. Spacecraft, vol. 3, 1966, p. 1523.
5. Diamond, J. J.; and Drago, A. L.: Rev. Hautes Temper. et. Refract., vol. 3, 1966, p. 273.
6. Eisner, L.; Fisher, D. W.; and Leftwich, R. F.: Spectroradiometric Instruments and Techniques for Use in Imaging Furnaces. Chapter 9 of Thermal Imaging Techniques. Plenum Press, 1964.
7. Grynak, D. A.; and Burch, D. E.: J. Opt. Soc. Am., vol. 55, 1965, p. 625.
8. Mergerian, D.: Proc. IRIS, vol. 4, 1959, p. 193.
9. Carlson, D. J.: Emittance of Condensed Oxides in Solid Propellant Combustion Products. Tenth Symposium (International) on Combustion, The Combustion Institute, Pittsburgh, 1965.

## REFERENCES (Concluded)

10. Adams, J. M.: J. Quant. Spectrosc. Radiat. Transfer, 1967, p. 273.
11. Brown, B.: Private communication.
12. Rochelle, W. C.: Modified S-IC Ordnance Disconnect Heating Analysis and S-II Ullage Motor Test Results. NASA/MSFC Memorandum for File, AT-20-65, November 23, 1965.
13. Reardon, J.: Private communication.
14. Rochelle, W. C.: Private communication.
15. Bauer, E.; and Carlson, D. J.: J. Quant. Spectrosc. Radiat. Transfer, vol. 4, 1964, p. 363.
16. Ferriso, C. C.; and Ludwig, C. B.: Appl. Opt., vol. 3, 1964, p. 1435.
17. Stull, R. V.; and Plass, G. N.: J. Opt. Soc. Am., vol. 50, 1960, p. 1279.
18. Rochelle, W. C.: Private communication.

---

## DISCUSSION

S. A. Golden, General Dynamics/Convair: In reference to your Figure 5 (particle mean size versus chamber pressure), were the measurements all made on the same propellant composition?

A. Laderman: I am not certain. In view of the many investigations, it is probable that the propellants were not the same.

V. R. Stull, Defense Research Corp.: You mentioned that you included scattering in the calculation. How? You must have needed the real part of the index of refraction at some point in the calculations.

A. Laderman: The method accounts for scattering. However, in this particular calculation, the plume was optically thin to scattering.

V. R. Stull: Do you then simply calculate single scattering at approximately  $90^\circ$  for the searchlight effect?

A. Laderman: That is correct. I should point out that, in the case reported, the searchlight calculations indicate this effect to be important only at wavelengths below  $2 \mu$ .

D. P. Thibodeaux, Chrysler Corporation: Could the discrepancies between your calculations and the OAL data be due to uncertainties in the particle size distribution, rather than to differences in the extrapolation of the refractive index?

A. Laderman: The discrepancies could be due to a number of factors. I am not certain how accurate the OAL measurements, or the total radiometer measurements, are. When I discussed these measurements, I implied that they are known with good accuracy; but in all probability there are large uncertainties in these data, as well as in our knowledge of the particle properties.

D. Thibodeaux: Are there no experimental measurements of refractive index for the liquid phase in this longer wavelength region above  $5 \mu$ , where you found a large difference between experiment and theory?

A. Laderman: I know of nothing beyond  $3 \mu$ . The extrapolations used here may be looked upon as upper and lower bounds to the refractive index.

D. J. McCaa, Cornell Aeronautical Laboratory: We have some more data on the S-II ullage engine spectra, obtained with a scale model, which goes out to  $5 \mu$ . Spectral radiance measurements out to  $5 \mu$  give no indication of any continuum such as your extrapolation number 1 on Figure 6 would predict.

A. Laderman: If you recall the last figures, the continuum from  $2$  to  $5 \mu$  was very small in both cases. Not until we reach  $4$  or  $5 \mu$  do contributions from the particle continuum become significant. This is very clear for extrapolation number 2 of Figure 6; but even in the other extrapolation, contributions from the particle continuum did not occur until beyond  $4 \mu$ .

D. J. McCaa: That is correct. We went to almost  $5 \mu$ . Beyond the  $4.3 \mu$   $\text{CO}_2$  band, the radiant intensity fell to zero and did not start increasing before we reached  $5 \mu$ , where the spectral scan stopped.

---

# THE STATUS OF OPTICAL DIAGNOSTICS ON WAKES BEHIND HYPERSONIC VEHICLES

By

J. C. Burns and T. R. Riethof  
Space Sciences Laboratory  
General Electric Company

N 68-18094

---

## ABSTRACT

Measurements of the radiation from the wake left by a body moving through the atmosphere at hypersonic speeds can yield diagnostic information on vehicle performance, on flow field properties and, where the atmosphere is unknown, on the atmosphere itself.

Experimental techniques for making such measurements, including controlled laboratory work in ballistic ranges, vehicle-borne experiments, and remote off-board observations are reviewed, and the scope and limitations of the information which can be derived from the data are discussed.

---

## INTRODUCTION

The wake behind a hypersonic body, in which the gas, having passed through the region immediately surrounding the body, eventually expands and returns to ambient conditions has been the subject of a large body of literature which has recently been reviewed [1 and 2]. Practical motives for continuing interest in this region of the flow are that it is a major source of the observables which characterize re-entry and that it can have significant effects on communication to and from hypersonic vehicles. In what follows, a number of diagnostic applications of measurements of molecular radiation from hypersonic wakes will be reviewed.

There are three major areas of interest here: (1) Vehicle diagnostics in which observations of the wake can yield information on the performance of the vehicle itself, specifically heat shield performance, and vehicle dynamics. (2) Flow field diagnostics in which specific inputs for theoretical models of the wake are derived; i. e. , temperature, species concentrations and flow structure. (3) Atmospheric diagnostics in which one deduces properties of the ambient gas.

There are three basic measurement situations in which wake studies may be made: (1) Free flight or tunnel-type laboratory facilities. (2) Measurements using instruments carried on-board a vehicle in free flight in the atmosphere. (3) Remote observations; e. g. , from the ground or an air-borne platform, of vehicles in free flight.

Each of the basic experiment configurations listed above can accommodate (at least potentially) both active and passive experiments which have the following general characteristics.

a. Active experiments permit measurements of radiation from specific species excited in a known fashion at a given point in the flow, for example, by a beam of electrons or quanta. Thus, local measurements of ground state species concentrations and temperatures become possible. (Absorption experiments using continuum or other sources also fall into this category.)

b. Passive experiments, on the other hand, mean that one measures radiation from whatever excited species exist within the field of the measuring instrument, and that one hence cannot avoid integration at least along the line of sight. Furthermore, any knowledge of ground state species concentrations must be deduced from the measurements using appropriate models for excitation and de-excitation, which unlike the active case, are unlikely to be well enough known, or if known, tractable.

Again, over a wide range of flight conditions, one has a situation where many degrees of freedom may be out of equilibrium so that the appropriate temperatures may not exist or may differ from each other, while much of the observed radiation from re-entry wakes comes from minor species which may never be in equilibrium, in terms of concentration, with the major species.

Thus, the role of passive observation in flow diagnostics is to establish fairly gross features of the wake and to provide data for the comparison of wake models, not to provide measurements of quantities such as temperature or density.



## LABORATORY MEASUREMENTS

The two basic forms of laboratory facility are free flight ballistic ranges and tunnel-type systems. The primary difference between them is that, in the former, observations are made in space-fixed coordinates and, in the latter, in vehicle-fixed coordinates. Some examples of the capabilities and limitations of each type follow.

Free Flight Ballistic Range Measurements. The basic limitations of the ballistic range, in which necessarily small models are accelerated to hypersonic speeds and then fly freely through a controlled atmospheric path at constant pressure and temperature, are those of scaling [3,4], the range of achievable flight conditions [4], the short time scale for making observations, low passive radiation intensities, and the small geometric scale of the flow.

In general, only semi-quantitative spectral measurements of wake radiation have been made. Broad-band radiometer measurements have been made at CARDE on the near wakes of ablating (LEXAN) spheres and 2-color temperatures deduced [5]. The wake radiation was attributed in this case to ablated particles radiating thermally and sufficiently small in size and heat capacity to follow the flow temperature. The use of a highly sensitive image-converter slitless spectrograph to obtain semi-quantitative wake spectra of spheres and cones in a ballistic range has been reported by Liu [6], who discusses, but does not derive, vibrational and rotational temperatures.

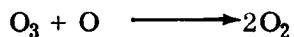
Quantitative sodium line-reversal measurements made on the wakes of spheres and cones have been reported by Rockman [7], who derived effective axial temperature and emissivity profiles integrated along a line of sight normal to the wake axis with a radial resolution of about 0.3 body radii. The results obtained agree reasonably well with the calculations of Lin and Hayes [8]. Young [9] has inferred temperatures in the wake of a small sphere fired into an atmosphere containing 5 percent CO<sub>2</sub> from measurements of the total intensity of the 4.3 micron band of CO<sub>2</sub>.

Bryant and Bradley [10] have recently made quantitative spectral observations of radiation from the turbulent wake of non-ablating spheres fired in clean air at 50 torr pressure. They found the wake to be divided into two distinct regions. In the nearer regions (<300 diameters downstream) the radiation is identified as the Lewis Rayleigh N<sub>2</sub> afterglow and chemi-excited NO band

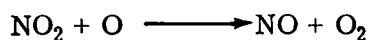
radiation (predominantly the NO  $\beta$  bands). In the far wake ( $\geq 300$  diameters downstream) the radiation is identified as due to the chemi-luminescent reaction



in agreement with the results of Reis [11]. Two extreme mixing models — homogeneous mixing and the "blob" or marble-cake model — were tested in each region, and the not unexpected conclusion reached was that neither would describe all features of the data. Bryant and Bradley also looked for ozone-in absorption in the far wake in order to check on the mode of removal of atomic oxygen in the far wake. For, if the far wake is taken to be homogeneously mixed as it expands, the primary routes for the removal of atomic oxygen will be



together with



Their finding was that the ozone concentration in the far wake appears to be considerably less than that predicted by the above reactions in a homogeneously mixed wake.

Tunnel-Type Facilities. The main advantages of such facilities as shock tunnels lie in the vehicle-fixed geometry and the larger physical scale of model and flow that becomes possible. The major disadvantage is the relatively short time scale of the flow, and the resulting difficulties in dealing with reacting flows. The electron beam excitation technique has been used extensively by

Muntz and his co-workers [12] to make point measurements of density and temperature in the near wake of cones. This technique represents the ultimate in near wake flow diagnostic measurements in that measurements of radiation from molecular nitrogen which has been excited in a known and controlled fashion yield local values of ground state population and temperature without disturbing the flow, and with sufficiently high time resolution to yield quantitative data on turbulent fluctuations. Accuracies of 10 to 15 percent are quoted for temperatures and densities obtained from experiments at Mach numbers between 12 and 18 and Reynolds numbers of  $10^5$  to  $10^6$  per foot, which make the data of real value to flow-field analysts. In particular, values of the neck enthalpy deduced from this work are currently in general use as starting points for wake calculations.

## ON-BOARD MEASUREMENTS

Passive Wake Measurements. The development of radiometric and spectrometric equipment capable of operating in the severe environment of launch and re-entry has meant that passive measurements of radiation from the boundary layer and wake of re-entering vehicles are not too difficult. The real problems in such experiments are the basic ones dictated by the experiment geometry in that instruments mounted in the vehicle base will record irradiance originating anywhere in the field of view and integrated along the line of sight.

However, suitable combinations of wide- and narrow-field instruments and imaging devices can produce data which can be meaningfully compared with the predictions of specific flow models — and on-board measurements of wake radiation must always be designed with a specific critical function in mind.

The major practical limitations on on-board experiments are imposed by telemetry capacity, the relatively short time during which the wake may be considered stationary due to the rate of traversal of the atmosphere ( $\sim 2$  seconds per scale height) and disturbances in the flow due to varying angle of attack.

The basic advantages of on-board re-entry measurements are as follows:

a. We are dealing with the real situation, and thus scaling problems disappear.

b. The geometrical scale is large enough for radial resolution to be readily obtained — at the expense of integration along the axial direction.

c. Proximity to the near wake alleviates problems of instrument sensitivity, so that data can be obtained at much higher altitudes than with off-board observations.

As implied above, on-board optical measurements can be usefully made only if detailed analysis of near wake models shows that a critical measurement exists; this denies us the possibility of making general statements on what diagnostic information can be obtained.

However, some extreme examples can be quoted:

a. Molecular transitions sensitive to temperature can be studied with wide-field spectral or filtered imaging devices to yield gross estimates of (electronic) temperature distribution in the wake neck; e. g., the red and violet electronic transitions of CN provide two systems of the same radiator whose upper states are separated by about almost 2 ev.

b. Vibration-rotation transitions of compounds, e. g., CO<sub>2</sub>, CO and H<sub>2</sub>O, whose intensity is relatively insensitive to temperature, can be observed in the same way to yield estimates of the radial distribution of the species and evidence as to whether chemical equilibrium prevails.

c. Vibrational analysis of electron transitions of molecules known to arise from ablation which display well-developed band sequences at typical near wake temperatures, e. g., BeO, would provide information on the establishment of vibrational equilibrium (i. e., collision frequency) and on the radial distribution of material from the boundary layer.

d. Rotational analysis of the emission spectra of suitable molecules (e. g., CH) can again yield information on collision frequency and rotational temperatures.

Flights of both blunt and sharp slender re-entry vehicles carrying rearward-facing radiometers and spectrometers [13] have already provided a considerable body of diagnostic information on heat shield performance, on flow chemistry, and on conditions in the near wake.

Active Measurements. As discussed above, one way to make point measurements and to obtain estimates of ground state populations by optical means is by creating excited states in a controlled manner and having an experiment geometry capable of yielding local information. The former is possible in the on-board case by using an electron beam or high intensity optical radiation source, while the geometry can be realized by the use of an axial boom or, in a more limited fashion, by the suitable deployment of narrow field instruments in the base of the vehicle.

Absorption measurements, using an external light source on a boom, are another class of active measurements. Again, the results could be compared only with the results of model calculations, but when combined with passive emission measurements would add considerably to our ability to interpret on-board data.

## OFF-BOARD MEASUREMENTS

Remote observation from ground-based or air-borne platforms has been a major source of data on re-entry wakes. Here, we shall be concerned only with passive experiments, except in the sense that one can examine radiation from species deliberately introduced into the flow.

The basic limitations inherent in this type of observation are as follows:

- a. Distances of from 20 to 150 km from the source reduce the irradiance at the instrument.
- b. The presence of the atmosphere gives rise to signal attenuation and to image distortion, limiting the accuracy of intensity measurements and the spatial resolution obtainable.
- c. The experiment geometry is such that integration along the line of sight is unavoidable — usually in the radial direction as opposed to the axial integration in the on-board case.
- d. High resolution measurements at low intensity levels require rapid, smooth tracking of physically large instruments; e. g. , rates of  $10^\circ/\text{sec}$  or more, and sufficiently smooth tracking to freeze an image exposed for up to a few tens of milliseconds to less than 2 seconds of arc.

Measurement Techniques. By definition, some degree of spatial resolution in the axial direction is required for remote observation of wake radiation.

Instruments in use on various observation programs include (1) cine camera with lenses up to 100" focal length, (2) image orthicon cameras, (3) axial scanning radiometers, and (4) long focal length cinespectrographs. With such instruments, a considerable amount of diagnostic information on the vehicle itself (e. g. , heat shield performance, vehicle motion) and on the gross features of the wake can be obtained. High resolution photographic instruments currently in field use obtain a spatial resolution of the order of 0.5 meter at a range of 100 km and a spectral resolution of better than 1 Angstrom, and depending on light-gathering power and siting vis-a-vis the re-entry path, can record data from large blunt targets from altitudes above 200 000 feet down to impact. The optical wakes of sharp slender vehicles are much less intense, and in general are not observed until below boundary layer transition.

Off-Board Diagnostics. While the primary information gathered by on-board observation (passive or active) concerns the near wake, high resolution spectral observations from off-board can, in addition, yield data on the far wake which can be used to check the predictions of far-wake chemistry models.

For example, it can be shown that at altitudes above about 70 000 feet most of the energy in the far wake of any blunted body will be in the form of dissociated oxygen, and that the chemistry of the eventual recombination of this to molecular oxygen plays an important part in the decay of electron density in the far wake, and hence in radar wake behavior, through electron attachment processes and negative ion chemistry [14].

The optical observable in question here is radiation from the reaction



which has been extensively investigated in the laboratory and which has been measured in the wake at hypersonic spheres in a ballistic range by Reis [11] and by Bryant and Bradley [10]. Observation of this radiation as a function of downstream distance provides a test of models of the neutral chemistry of the far wake, which in turn defines the ambient conditions in which the electron chemistry takes place.

In the above example, high spectral resolution is not necessary. However, full advantage can be taken of the 1 Angstrom capability of existing spectrographs in recording the electronic transitions of such molecules as CH, CN and BeO. In the case of the first, its extremely open rotational structure enables one to obtain an idea of how nearly rotational equilibrium is approached throughout the wake under given flight conditions, while vibrational analysis of CN or BeO can yield similar information on vibrational equilibrium. The BeO blue-green system, in particular, displays four or five well developed sequences of bands so that an analysis of self absorption, which should yield information on radial temperature distribution, is possible.

## FURTHER DIAGNOSTIC APPLICATIONS

There are a number of experiments which can now be carried out on full-scale vehicles and in laboratory facilities which would provide important flow field information.

a. The dwell time of gas in the recirculation region immediately aft of the vehicle is an important unknown. This could be determined either in the laboratory or in the field using optical seeding techniques in which a known amount of some identifiable gas is introduced into the boundary layer in a controlled fashion. Either passive emission or emission stimulated by electron or photon beams can be observed as a function of time.

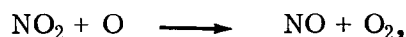
b. Turbulent mixing in the far wake is most important in determining the chemistry of the far wake. Most progress in explaining field data has been made so far with the completely mixed model mentioned above. However, there is some evidence that the two fluids concerned (i. e. , the ambient air and the originally hot, highly dissociated viscous core of the wake) are not at any stage completely mixed on the micro-scale associated with chemical kinetics. It is most important to clarify this point since, for example, reactions involving NO, O and O<sub>2</sub> are clearly important in far wake chemistry. Thus, if the homogeneous far wake is assumed, the major route for the recombination of O atoms will be



While in the other extreme, if the cool ambient air engulfed as the turbulent wake expands is not rapidly mixed with the fluid of the core, the primary mechanisms would be



and



with reactions involving  $\text{O}_2$  only taking place in a relatively small volume of fully mixed material. Turbulent mixing experiments could be done in the laboratory, using streams contained in NO and O as tracers, with the NO + O chemiluminescence indicating the degree and geometry of mixing. Alternatively, sensitive ozone-absorption-imaging experiments on the turbulent wakes of spheres should reveal the space and the time scale of structure in the far wake by detecting the region where atomic and molecular oxygen are reacting together.

c. If a suitable tracer such as BeO or sodium can be introduced in quantity into the turbulent wake of re-entry bodies, high resolution pictures can be used to check the growth law of the turbulent wake, and the position and diameter of the neck.

d. Wake observation made from an orbiter as a clean blunt probe enters a planetary atmosphere could yield important data on the composition of the atmosphere. These would complement observations of high temperature radiation from the stagnation region and would have the advantage that the observation geometry would be easier. Some work has been done on stagnation region simulation for Venus and Mars entries using ballistic ranges [15, 16], but little has been done on studying the sensitivity of the wake signature to composition and pressure in synthetic atmospheres. This would make an attractive experiment for a free flight ballistic range capable of firing reasonably large ( $\geq 2.5$  cm diameter) spheres at realistic entry velocities. This in turn would permit the design of a full scale experiment.



## REFERENCES

1. Lykoudis, Paul S.: A Review of Hypersonic Wake Studies. AIAA J., vol. 4, 1966, p. 577.
2. Zarin, N.: The Flow Fields of Hypersonic Wakes: A Literature Review. BAMIRAC Report 4613-146-T, University of Michigan Institute of Science and Technology, March 1967.
3. Eschenroeder, Alan Q.: Nonequilibrium Scaling of High-Enthalpy Flows. Technical Report TR 64-026, General Motors Defense Res. Labs., June 1964.
4. Eschenroeder, A. Q.; King, N. K.; and Wen, K. S.: Aerophysics Research Based on Free Flight Range Measurements. Tech. Report TR 67-01J, AC Electronics - Defense Res. Labs, General Motors Corp., July 1967.
5. Gallagher, G.; and Lemay, A.: Temperature Measurements of the Near Wake Generated by Hypervelocity Bodies. Technical Report TR 502/64, Canadian Armament Research and Development Establishment, July 1964.
6. Liu, I. D.: Time-Resolved Spectra Associated with High-Speed Projectiles in Rarified Air. Technical Report TR 65-01G, General Motors Defense Research Labs, October 1965.
7. Rockman, C. M.: Line Reversal Measurements of Hypersonic Wake Temperatures. General Motors Defense Research Labs, Technical Report 66-01B, March 1966.
8. Lin, S. C.; and Hayes, J. E.: A Quasi-One-Dimensional Treatment of Chemical Reactions in Turbulent Wakes of Hypersonic Objects. AIAA J., vol. 2, 1964, p. 1214.
9. Young, L. A.: Infra-red Temperature Measurements of the Laminar Wake of a Hypersonic Sphere. AIAA J., vol. 3, 1965, p. 610.
10. Bryant, B. W.; and Bradley, L. C.: Private Communication.
11. Reis, V. H.: Chemiluminescent Radiation from the Far Wake of Hypersonic Spheres. Technical Report TR 66-01, General Motors Defense Research Labs, June 1966.

## REFERENCES (Concluded)

12. Muntz, E. P.; and Softley, E. J.: An Experimental Study of Laminar Near Wakes. AIAA J., vol. 4, 1966, p. 961.
13. Thompson, T. R., ed.: Re-entry Vehicle Instrumentation Program: 2nd Data Workshop. Technical Report BSD-TR-67-46, TRW Systems, February 1967.
14. Sutton, E. A.: The Chemistry of Electrons in Pore Air Hypersonic Wakes. Research Report 266, AVCO-Everett Research Laboratory, July 1967.
15. Arnold, J. O.; Reis, V. H.; and Woodward, H. T.: Theoretical and Experimental Studies of Equilibrium and Non-Equilibrium Radiation to Bodies Entering Postulated Martian and Venusian Atmospheres at High Speeds. AIAA Paper Number 65-116, 2nd AIAA Aerospace Sciences Meeting, January 1965.
16. James, C. S.: Experimental Study of Radiative Transport from Hot Gases Simulating the Atmospheres of Mars and Venus. AIAA J., vol. 2, 1964, p. 470.

## DISCUSSION

R. Goulard, Purdue University: Dr. Riethof, in the present state of the art in reentry studies, do you make any use of the molecular band models that we have discussed today, such as the Curtis-Godson models?

T. R. Riethof: No, our spatial resolution is so poor that we cannot use them. In addition, in most cases our gases are optically thin. We have considered trying to obtain the wake temperature distribution by doing spatial traverses of the wake; but we found it impossible in the field, because we have no spatial resolution in the direction of the steep temperature gradients.

R. Goulard: Have these experiments already been done in the laboratory, or are they only a possibility?

T. R. Riethof: Dr. Willard Pearce of General Electric has done Abel inversions on arc columns. In our tunnels, the only thing we have looked at is the  $N_2$  system. The gas is optically thin, and I think we have not used bad model corrections.

C. Ludwig, General Dynamics/Convair: In answer to Dr. Goulard's question, I know that AVCO used infrared data to determine the reentry temperature from on-board measurements. The  $2.7 \mu$  water band was observed in the infrared, and some temperature determinations were made by the BRT method.

S. A. Golden: Is the Barnes spectrograph stigmatic?

T. R. Riethof: It is a slitless spectrograph, so it is stigmatic in the sense that you have imaging in both dimensions.

S. A. Golden: I do not know about the degree of spatial resolution possible in this case. You could get some inversion properties by using a densitometer to scan vertically along a given frequency.

T. R. Riethof: We do a little of this scanning with a densitometer, but we are talking about a remote measurement with very little spatial resolution. The best we obtained is on the order of two seconds of arc, which corresponds to about a meter or two at our slant ranges. While this resolution is useful for investigations along the wake axis, the entire width is only about a meter, so that no spatial resolution is obtained perpendicularly to the axis.

---

SESSION III  
INVERSION TECHNIQUES AND REMOTE SENSING

Chairman: J. I. F. King,  
Geophysics Corporation of America

# REMOTE SENSING AND INVERSION TECHNIQUES: STATE OF THE ART\*

By

J. I. F. King  
GCA Corporation  
Bedford, Massachusetts

N 68-18095

---

## ABSTRACT

The electromagnetic radiation emitted by a radiating system is a function of the physical state of the emitter. Mathematically, the externally viewed field is an integral transform of a state function such as temperature over depth in the medium. Thus, the internal state is given by the inverse transform of the remotely sensed radiation field.

The problems associated with inversion are (1) non-uniqueness of the inferred profiles, (2) proper choice of representational set for the internal state function, and (3) the noise problem. The attempts to cope with these difficulties in the development of modified linear and nonlinear inversion techniques are reviewed.

Furthermore, we show how the radiative transfer implications of the nonlinear inversion method lead to a formulation of a new wave theory of radiative transfer. Finally, a connection is established between the upwelling intensity and the radiative constraints operative internally to produce the observed pattern.

---

The inversion problem arises in the electromagnetic probing of a remotely viewed radiating system. In the far infrared, the earth and atmosphere form such a system suitable for study. By careful frequency scanning of the upwelling intensity across the infrared bands, we are able to infer vertical structure of the emitting atmosphere. Since the intercepted radiation is a weighted average of

---

\* Research supported by NASA-GSFC under contract NAS5-3352.

the internal field, the transformation from intensity of the electromagnetic signature to the uncovering of vertical atmospheric structure is an inversion operation.

All inversion methods seek to infer the maximum structural information inherent in the observations. Since there are severe limits to this information fixed by data density and accuracy, it is important to determine the validity of the inferences.

After outlining the problem, we discuss linear and nonlinear inversion techniques devised for its solution. A careful study of the nonlinear method has uncovered certain deficiencies of classical radiative transfer theory. The bulk of the paper is devoted to the formulation of a wave theory of radiative transfer free from this incompleteness.

The inversion problem is simply expressed in a model in which the atmosphere is assumed to have a piecewise gray absorption coefficient which scales uniformly with depth. In this event, the upwelling intensity  $I(0, 1/\kappa)$  is proportional to the Laplace transform of the Planck intensity  $B(u)$  considered as an implicit function of depth:

$$I(0, 1/\kappa) = \int_0^{\infty} B(u) e^{-\kappa u} \kappa du = \kappa L[B(u)]. \quad (1)$$

This relation is the upwelling solution of the transfer equation

$$\frac{dI(u, 1/\kappa)}{\kappa du} = I(u, 1/\kappa) - B(u), \quad (2)$$

taken at the top of the atmosphere.

To facilitate comparison between inversion methods, we relate the upwelling intensity to the source function derivative with an integration by parts:

$$I(0, 1/\kappa) - B(0) = \int_0^{\infty} \frac{dB(u)}{du} e^{-\kappa u} du = L \left[ \frac{dB(u)}{du} \right]. \quad (3)$$

In many problems, the intensity is sensed at a fixed number of channels. This requires that the problem be digitized. In linear inversion methods, this is done by expanding the source function derivative in a suitably chosen orthogonal polynomial set:

$$\frac{dB(u)}{du} = \sum_{j=1}^n b_j P_j(u). \quad (4)$$

Substituting this expression into the integral transform leads to

$$\Delta I(0, 1/\kappa_i) = \sum_{j=1}^n b_j p_j(\kappa_i), \quad i = 1, 2, \dots, n, \quad (5)$$

where  $p_j(\kappa) = L[P_j(u)]$ . The specification of the intensity at  $n$  points thus leads to  $n$  linear simultaneous equations whose  $n$  solutions  $b_j$  are the desired weights of the source function polynomial terms.

Although straightforward in principle, unmodified linear techniques are disastrous in application. First consider the non-uniqueness aspect. The data points can all be fit by an arbitrary choice of orthogonal set. The majority of these, however, will lead to highly oscillatory solutions which are ruled out on physical grounds. We have had considerable success, however, in using empirical orthogonal expansions based on climatological sets.

A more difficult and subtle problem arises with noisy data. Again, an indiscriminate application of a linear inversion scheme leads to trouble. Inversion, the counterpart of averaging, tends to amplify rather than suppress inaccuracies. Modified linear methods cope with this problem by smoothing the data, a risky procedure, since subtleties of structure may be lost in the averaging process.

It is possible to cope with these problems of non-uniqueness and noise by refined methods of applied analysis using proper base sets and smoothing criteria.



Perhaps the most successful and sophisticated development of linear inversion methods is that reported on by Westwater in a subsequent paper.

We turn now to the formulation of a nonlinear inversion method which leads to a unique profile inference. In addition, the algorithm appears capable of discriminating between noise and valid information without any requirement for data smoothing.

We begin by representing the desired source function by an array of slabs of varying weight and thickness:

$$B(u) = \sum_{j=1}^n \Delta B_j S(u - u_j) , \quad (6)$$

$$\frac{dB(u)}{du} = \sum_{j=1}^n \Delta B_j \delta(u - u_j) .$$

The nonlinearity arises in that not only are the weights  $\Delta B_j$  to be determined, but also the slab thicknesses  $u_j - u_{j-1}$  are to be uniquely specified.

Substitution of this slab expression for  $B(u)$  into the transform yields the following nonlinear equation set for solution:

$$\Delta I(0, 1/\kappa_i) = \sum_{j=1}^n \Delta B_j e^{-\kappa_i u_j} . \quad (7)$$

By defining  $x_j = \exp(-\kappa_{\min} u_j)$  and  $\alpha_i = \Delta I(0, 1/\kappa)$ , Equation (7) is recognizable in its more familiar form as the moment problem in physics

$$\alpha_i = \sum_{j=1}^n \Delta B_j x_j^{\kappa_i / \kappa_{\min}} . \quad (8)$$

This nonlinear simultaneous equation set can be solved uniquely for  $n$  slab weights and  $n$  slab thicknesses using the Prony algorithm, by specifying that the  $2n$  sensing channels be equally spaced:

$$\frac{\kappa_i}{\kappa_{\min}} = 0, 1, \dots, 2n - 1. \quad (9)$$

The Prony algorithm is a familiar technique in applied analysis for construction of Gaussian-type quadrature formulas. The uniqueness follows in that, for any set of  $2n$  intensity measurements, there is one and only one array of  $n$  slabs which fit the data.

The manner in which the algorithm reacts to noise in the data is its most interesting feature. In the algorithm, the slab boundaries are determined as the roots of an  $n$ th degree polynomial in  $x$ . Thus, for real slabs, since  $\ln(1/x) = \kappa_{\min} u$ , the roots of  $x$  must lie between zero and one. The presence of noise results in one or more of these roots becoming negative. The weights  $\Delta B_j$  associated with these inadmissible roots  $u_j$  are characteristically down some three orders of magnitude from those of the real slabs. Further, the remaining real slabs are relatively unaffected, continuing to reproduce the gross profile configuration. In summary, the nonlinear inversion method responds to noise by the loss of one or more slabs, which corresponds to a poorer resolution of the profile. This inevitable information loss leaves unaffected, however, the valid inferences inherent in the observations.

The upwelling intensity field  $I(0, 1/\kappa)$  is a projection of photon events which occur within the atmosphere. Thus far, we have sidestepped the internal radiation field by considering only the transformation from the upwelling intensity to its Laplace inverse, the source function, with no thought given to why a particular regime is established. In other words, to this point, we have dealt with a problem in applied analysis. We now propose to study radiative transfer theory. Such a corpus of theory exists in the treatise of Chandrasekhar.

The unexpected ease of the nonlinear method in fitting a variety of upwelling data led to a search for its place in radiative theory. More specifically, the relationship between internal source and the upwelling intensity was sought.

The two theories, nonlinear inversion and classical radiative transfer, proved incompatible. Stated explicitly, there is no combination of internal constraints in classical theory which will give rise to a steady-state configuration of slabs for the source function. This incompatibility is compounded by the inadmissible noise solutions of the source functions which have no classical analogue.

The dilemma has been resolved by the construction of a new wave theory of radiative transfer in which slabs appear as a natural consequence and simple expression of certain internal constraints. The new theory is self-consistent and complete in the sense that any source function configuration can be specified to arbitrary accuracy. The cornerstone of radiative transfer, viz., that the upwelling intensity is the Laplace transfer of the source function, is unchanged. Thus the inversion problem, by itself, is noncommittal between the classical and wave theory. The new theory seeks to relate the external manifestation of upwelling radiation to the physics of the internal radiation field.

We begin, in common with classical theory, with the transfer equation:

$$\frac{dI(u, 1/\kappa)}{\kappa du} = I(u, 1/\kappa) - B(u). \quad (10)$$

This equation is satisfied by solutions other than the classical exponential functions. As a matter of fact, the transfer equation possesses the following general wave solution for the internal field:

$$I(u, 1/\kappa) = c \left[ \sum_{j=1}^{\infty} \frac{\kappa}{2i} \left( \frac{b_j e^{iw_j u}}{\kappa - iw_j} + \frac{b_{-j} e^{-iw_j u}}{\kappa + iw_j} \right) + \frac{1}{\kappa} + u + Q \right]. \quad (11)$$

This wave solution may be verified by differentiating and subtracting:

$$\frac{dI(u, 1/\kappa)}{\kappa du} = c \left[ \sum_{j=1}^{\infty} \frac{w_j}{2} \left( \frac{b_j e^{iw_j u}}{\kappa - iw_j} - \frac{b_{-j} e^{-iw_j u}}{\kappa + iw_j} \right) + \frac{1}{\kappa} \right], \quad (12)$$

yielding

$$I(u, 1/\kappa) - \frac{dI(u, 1/\kappa)}{\kappa du} = B(u)$$

$$= c \left[ \sum_{j=1}^{\infty} \frac{1}{2i} \left( b_j e^{iw_j u} + b_{-j} e^{-iw_j u} \right) + u + Q \right]. \quad (13)$$

Thus, the internal wave field, Equation (11), has associated with it a standing wave solution of the source function.

We note, in passing, that the corresponding form of the upwelling intensity is

$$I(0, 1/\kappa) = c \left[ \sum_{j=1}^{\infty} \frac{\kappa}{2i} \left( \frac{b_j}{\kappa - iw_j} + \frac{b_{-j}}{\kappa + iw_j} \right) + \frac{1}{\kappa} + Q \right], \quad (14)$$

and, furthermore, that the source function is the inverse Laplace transform of the upwelling intensity:

$$B(u) = L^{-1} \left[ \frac{I(0, 1/\kappa)}{\kappa} \right] = c \left[ \sum_{j=1}^{\infty} \frac{1}{2i} \left( b_j e^{iw_j u} + b_{-j} e^{-iw_j u} \right) + u + Q \right]. \quad (15)$$

If we specify odd parity for the source function  $B(u)$ , that it can be represented by a sine series, it follows that

$$B(u) + B(-u) = c \left[ \sum_{j=1}^{\infty} \frac{b_j + b_{-j}}{2i} \left( e^{iw_j u} + e^{-iw_j u} \right) + 2Q \right] = 0, \quad (16)$$

requiring that  $b_{-j} = -b_j$ ,  $Q = 0$ .

The source function, internal radiation field, and upwelling intensity then become

$$B(u) = c \left[ \sum_{j=1}^{\infty} b_j \sin w_j u + u \right] \quad (17)$$

$$I(u, 1/\kappa) = c \left[ \sum_{j=1}^{\infty} b_j \frac{\kappa^2 \sin w_j u + \kappa w_j \cos w_j u}{\kappa^2 + w_j^2} + \frac{1}{\kappa} + u \right] \quad (18)$$

$$I(0, 1/\kappa) = c \left[ \sum_{j=1}^{\infty} \frac{b_j \kappa w_j}{\kappa^2 + w_j^2} + \frac{1}{\kappa} \right] = c \frac{\prod_{\ell=1}^{\infty} \left( \frac{\kappa^2}{\kappa_{\ell}^2} + 1 \right)}{\kappa \prod_{j=1}^{\infty} \left( \frac{\kappa^2}{w_j^2} + 1 \right)} \quad (19)$$

The equivalent quotient polynomial form indicates that the upwelling intensity has roots at  $\kappa = \pm i\kappa_{\ell}$  and simple poles at  $\kappa = 0, \pm iw_j$ . Notice that  $I(0, 1/\kappa)$  has odd parity in  $\kappa$ . Thus, parity is conserved in the transformation between  $B(u)$  and  $I(0, 1/\kappa)$ .

The source function  $B(u)$  is capable of fitting, by proper choice of weights  $b_j$  and frequency modes  $w_j$ , any non-pathological internal density profile. The unique configuration realized in a particular situation is governed by the prevailing internal constraints linking  $B(u)$  and  $I(u, 1/\kappa_{\ell})$ . As in the classical case, we assume that the source function is a weighted average of the various modes  $\kappa_{\ell}$  of the internal field; i. e. ,

$$B(u) = \frac{1}{2} \sum_{\ell} a_{\ell} I(u, 1/\kappa_{\ell}) \quad (20)$$

Our central problem, therefore, is to relate the viewed upwelling intensity  $I(0, 1/\kappa)$  to the strengths and frequencies of the internal wave field. This is one step beyond the inversion problem which is content to relate  $I(0, 1/\kappa)$  to a source function, bypassing considerations of how it is brought about.

Applying this constraint to Equations (17) and (19), we find that

$$\sum_{j=1}^{\infty} b_j \sin w_j u + u = \frac{1}{2} \sum_{\ell} a_{\ell} \left[ \sum_{j=1}^{\infty} b_j \frac{\kappa_{\ell}^2 \sin w_j u + \kappa_{\ell} w_j \cos w_j u}{\kappa_{\ell}^2 + w_j^2} + \frac{1}{\kappa_{\ell}} + u \right]. \quad (21)$$

The odd parity terms vanish because of the paired character of  $\kappa = \pm i\kappa_{\ell}$ , leaving, on equating coefficients,

$$1 = \frac{1}{2} \sum_{\ell} a_{\ell} \quad \text{and} \quad 1 = \frac{1}{2} \sum_{\ell} \frac{a_{\ell} \kappa_{\ell}^2}{\kappa_{\ell}^2 + w^2}. \quad (22)$$

Combining these, we obtain the characteristic equation:

$$\sum_{\ell=1}^{\infty} \frac{a_{\ell} w^2}{\kappa_{\ell}^2 + w^2} = 0, \quad (23)$$

which has roots at  $w = \pm iw_j$  and a double root at the origin. We notice that the characteristic function has simple poles at  $w = \pm i\kappa_{\ell}$ . By expressing the characteristic function in quotient polynomial form,

$$T(1/w) = w^2 \frac{\prod_{j=1}^{\infty} \left( \frac{w^2}{w_j^2} + 1 \right)}{\prod_{\ell=1}^{\infty} \left( \frac{w^2}{\kappa_{\ell}^2} + 1 \right)}, \quad (24)$$

we find that the upwelling intensity  $I(0, 1/\kappa)$  is proportional to the reciprocal of the characteristic function:

$$\frac{1}{\kappa} I(0, 1/\kappa) = L[B(u)] = \frac{c}{T(1/\kappa)} \quad (25)$$

This reciprocity between upwelling intensity and characteristic function is the most far-reaching result of our analysis. Since the roots and poles of the characteristic function are directly related to the weights and frequencies of the internal field, from an analysis of the upwelling intensity we can determine the constraints operative in the internal field. Conversely, from internal constraint conditions, we can specify the associated upwelling intensity pattern.

Let us do precisely this for the condition of radiative equilibrium. It is natural to assume in this case that the vibrational modes are of equal weight, i. e.,  $a_\ell = \text{const}$ , and equally distributed in frequency:

$$\frac{\kappa_\ell}{\pi} = \pm 1, \pm 3, \pm 5, \dots \quad (26)$$

This choice of  $\kappa_\ell$  assures that the frequencies are equally-spaced and paired, while avoiding an unphysical  $\kappa = 0$  mode. For these conditions the characteristic function may be written as

$$\sum_{\ell=1}^{\infty} \frac{8w^2}{(2\ell - 1)^2 \pi^2 t w^2} = 2w \tanh \frac{w}{2} = T(1/w), \quad (27)$$

with roots  $(w/\pi) = 0, \pm 2, \pm 4, \dots$

Using the reciprocity relation, Equation (25), it follows that the equilibrium emergent intensity is given by

$$\frac{I(0, 1/\kappa)}{c} = \frac{1}{2} \coth \frac{\kappa}{2} = \frac{1}{e^{\kappa} - 1} + \frac{1}{2} . \quad (28)$$

In Figure 1 the equilibrium upwelling intensities predicted by the classical and wave theories can be compared. The similarities are striking in view

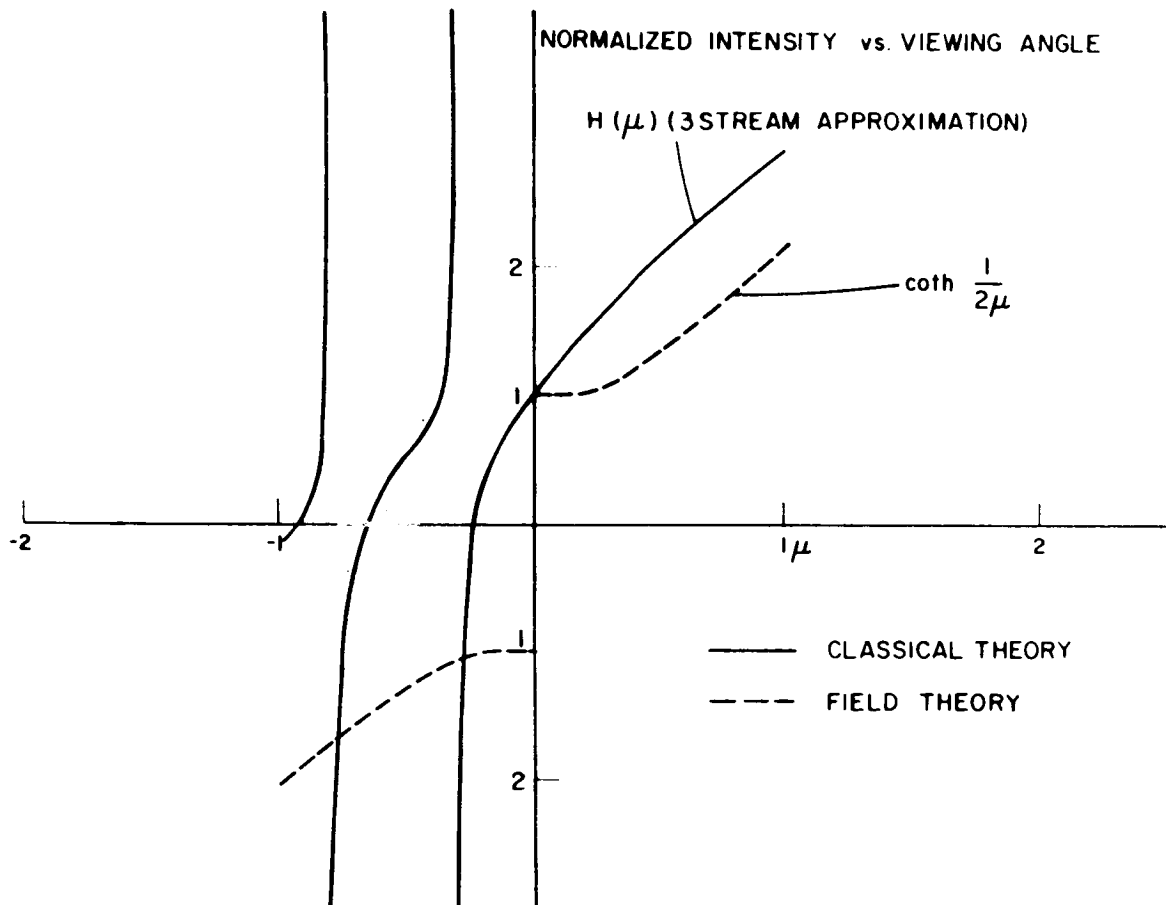


FIGURE 1



of the disparate character of the underlying models. Both predict a minimum but finite intensity for extremal limb-viewing or high-opacity probing. The two curves then increase monotonically, eventually showing linear growth for large values of  $\mu$  or  $1/\kappa$ . The main difference in the curves is in the limb behavior in which the gradient of the classical profile becomes infinite at the limb while that of the wave theory approaches zero.

Figure 2 displays the equilibrium source functions obtained by Laplace inversion from the curves of Figure 1. The slab character of the source function

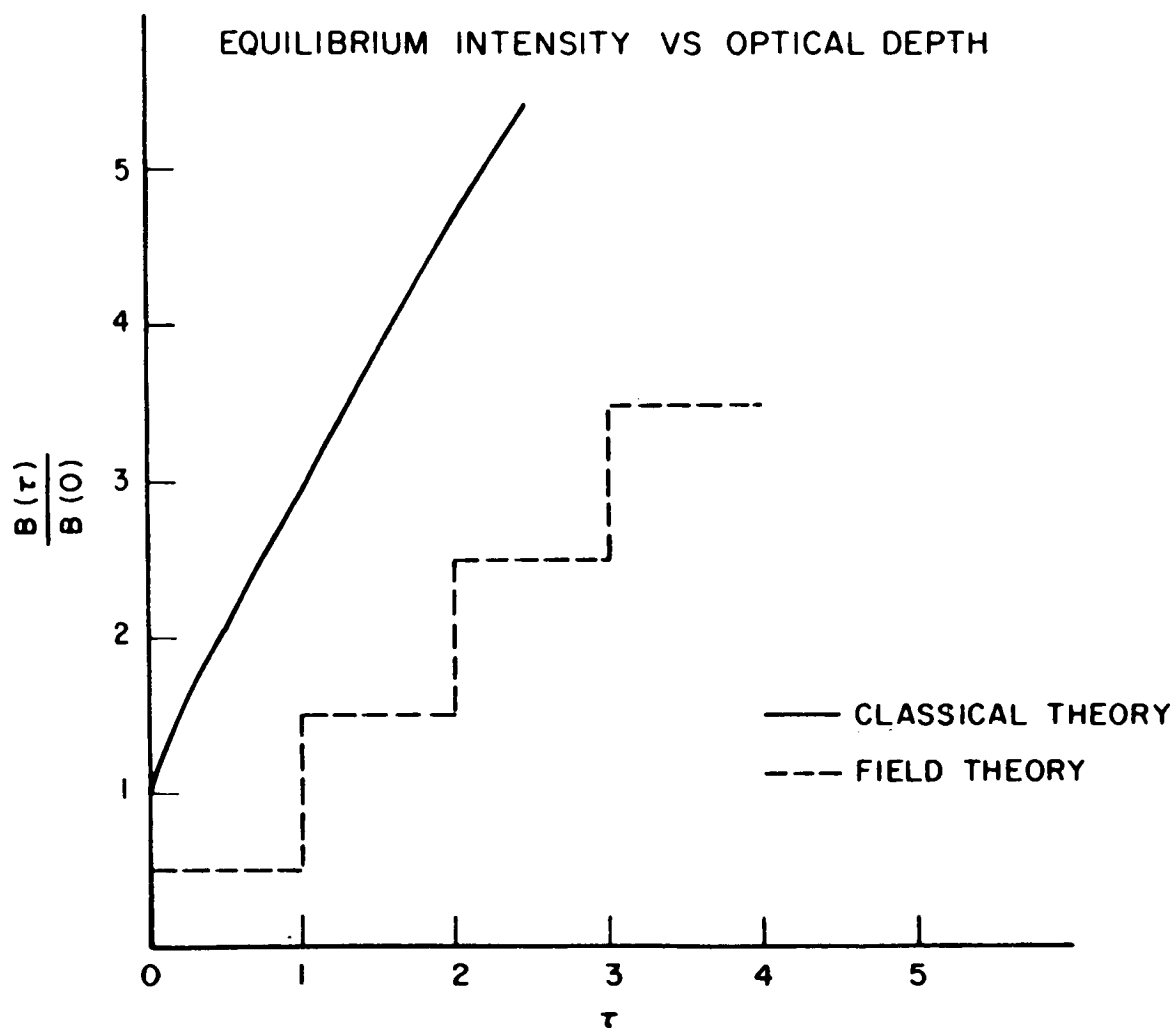


FIGURE 2

inferred from wave theory underscores the incompatibility of nonlinear inversion and classical radiative transfer theory.

Finally, we note the mathematically equivalent form, apart from constants, of the equilibrium emergent intensity, Equation (28), with the Planck intensity:

$$B_{\nu}(T) = \frac{2h\nu^3}{c^2} \frac{1}{e^{h\nu/kT} - 1} \quad (29)$$

This agreement is not fortuitous, but is a reflection of the fact that both functions are external manifestations of internal radiative transfer processes which are essentially wavelike in character.

---

## DISCUSSION

J. H. Clarke, Brown University: One does introduce quantum mechanics in the absorption coefficient and the source function. What occurred to me is this: Suppose one restores the usual small time derivative term or a nonlinear space derivative term in another ray direction (photon-photon interaction) in order to recover the wave propagation properties which are a priori in the electromagnetic equations of radiative transfer. Is there any sort of cure short of a return to the full field theory?

J. I. F. King: I don't think so. Classical radiative transfer theory is inadequate to deal with time-dependent properties. One is forced to insert a time-dependent term through the flux in a quite unsatisfactory manner. The correct way of doing it in a wave theory, of course, is as in quantum mechanics. One represents the energy operator as the time rate of change of the state function. I don't think any rules such as adding a time-dependent term will save the classical equations.

J. H. Clarke: It is always nice to speak of reverting to the Maxwell equations and quantum electrodynamics in principle, but it might be possible to model the effects in some phenomenological way that would not be quite as painful as reverting to the complete formulation.

J. I. F. King: On the contrary, this wave approach simplifies transfer theory. It is much easier to deal with complex wave geometry. Because the photon field is linear, you can superpose solutions. Another drawback of classical theory is the difficulty of dealing with a geometry that is not plane parallel, i. e., a one-dimensional geometry. It is difficult merely to formulate the classical transfer equation for a spherical atmosphere.

S. T. Wu, University of Alabama Research Institute: We know that the radiative transfer equation is also the photon transport equation if we consider photons as particles without mass. This equation can easily be derived from the Boltzmann transport

equation by writing the distribution function in terms of specific intensity and by generalizing the collision integral. We can do this by using the assumption of weak coupling between the translational and internal mode of the particle, so that the collision integral will consist of both elastic and inelastic terms. This is to say we treat the problem semiclassically; in this manner, some of the quantum mechanical features are retained. Therefore, the radiative transfer equation is not a bad model, although it may not be adequate for the problem which interests you.

J. H. Clarke: The approach suggested by Dr. Wu is emphatically the corpuscular approach, whereas in Dr. King's treatment, one presumably wishes to introduce the wave-particle complementarity and so provide for wave propagation by photon-photon interaction.

S. T. Traugott, Cornell University: Usually one thinks of interferences in waves as becoming important when the wavelength gets to be like the size of the medium. In your problem, the height of the atmosphere is a typical length of the medium. One would ordinarily think that you are pretty safe from wave interferences with this kind of ratio of wavelength to scaling length.

J. I. F. King: Well, I did not mention anything about the wavelength of these interfering internal waves. To get a progressive wave, of course, one needs a time-dependent term. This is a steady state configuration, so these waves in the medium are, of course, standing waves; and the time dependence disappears through the interference of the progressive waves. So I really don't know the answer to your question because I have not thought through what the physical interpretation of these waves is. I think that they are obviously carriers of the electromagnetic field. They probably represent photons; and I'm sure this is linked to quantum mechanics, but I haven't got that far yet.

S. A. Golden, Rocketdyne: Aren't the quantum effects of the transfer problem taken into account by the use of the blackbody function?

J. I. F. King: No. The Planck blackbody function is an ad hoc addition to the classical transfer equation. It cannot be derived from classical considerations. The history of quantum mechanics testifies to that.

J. A. L. Thomson, IDA: If you start with Maxwell's equations, you can derive the geometrical optics limit by letting the wavelength go to zero.

J. I. F. King: No, that is not the way it is done. One assumes that the variation of all ties within the medium is small over a wavelength which leads to a WKB-type solution of Maxwell's equations, as Dr. Clarke mentioned earlier.

J. A. L. Thomson: I agree. In that limit you obtain geometric optics and you presumably can then derive the classical transport equation with attenuation effects included. Such a calculation should lead to results that are consistent with Maxwell's equations at zero wavelength. Unless you have actual physical measurements that disagree with these formulae, I do not see how you can draw conclusions about their failure and consequently about the failure of the geometric optics approximation.

R. Goulard, Purdue University: I think that one could also mention the difficulties that are faced when one tries to define radiation transfer properties that are compatible with the corresponding electromagnetic properties. The compatibility of the radiative flux vector and the Poynting vector have been studied in a statistical context by J. W. Sidwell ("The Electromagnetic Basis of the Radiative Transfer Theory" Purdue University, Ph. D. Thesis, June 1965).

---

# STATISTICAL INVERSION METHOD FOR THE SOLUTION OF INTEGRAL EQUATIONS OF THE FIRST KIND

By

N 68-18096

E. R. Westwater and O. N. Strand

Environmental Science Services Administration  
Institute for Telecommunication Sciences and Aeronomy  
Boulder, Colorado

---

## ABSTRACT

The statistical minimum-rms inversion method for solving the integral equation of radiative transfer is summarized and discussed. The accuracy attainable by using this method to infer profiles is shown to be a function of the kernel of the equation, the measurement noise level, and the a priori statistical knowledge of the profile. Examples are given of the application of the method to remote inference of the vertical temperature distribution from microwave measurements of oxygen thermal emission.

---

## DISCUSSION

Various attempts to infer atmospheric profiles from measurements of emitted, absorbed, or scattered radiation are common in both the recent and the older literature. Many of these problems can be reduced to solving an integral equation of the first kind in the presence of error in the measured quantity. Some of the difficulties in solving this type of equation are:

- a. Finite measurements. Only a finite (and usually small) number of measurements can be taken with which to infer an entire profile.
- b. Instability. Direct attempts to solve the equation by standard methods of matrix inversion can yield unstable solutions because of ubiquitous measurement error. By unstable is meant that small errors in the measured quantity can yield large, physically unrealistic estimates of the inferred quantity.

c. Nonuniqueness. In a mathematical sense, the solutions are not unique, since any function that can be integrated to yield the observed value to within the noise level of the sensor is a mathematically (but not necessarily physically) legitimate solution.

d. Ill-Conditioning. Because kernel functions encountered in practical applications are smooth functions of physical parameters, measurements are often dependent, in the sense that certain measurements can be obtained from linear combinations of the others to within the noise level of the observations.

e. As has been shown by Twomey [1], methods which attempt to approximate the profile by approximating its transform are based on the incorrect premise that "nearness" to the transform implies "nearness" to the profile.

Some previous inversion methods [2] have advocated nonlinear techniques to achieve useable results; others, such as that of Twomey [1], have used linear methods incorporating smoothing to reduce the instability. More recent methods [3] have often employed empirical orthogonal functions to maximize the information obtainable from the small number of determinable parameters. The minimum-rms inversion method [4, 5, 6] is linear, achieves smoothing by filtering the signal from the noise in a statistically optimum manner, and estimates the profile from the measurements at hand and the a priori statistical knowledge of both the profile and the noise level of the sensor. The essentials of this method may be described as follows.

The Fredholm integral equation of the first kind is written

$$g_e(x) = g(x) + \epsilon(x) = \int_a^b K(x, y) f(y) dy + \epsilon(x), \quad (1)$$

where  $g_e(x)$  is the measured value and is the sum of the amount contributed by the profile alone,  $g(x)$ , and the instrumental noise  $\epsilon(x)$ ;  $K(x, y)$  is the kernel (assumed to be known); and  $f(y)$  is the unknown. From measurements of  $g_e(x)$  at some set of values of  $x$ , say  $x_i$ ,  $i = 1, 2, \dots, n$ , it is wished to infer  $f(y)$ . Introduction of a suitable quadrature approximation to Equation (1) yields the matrix equation

$$g_e = Af + \epsilon, \quad (2)$$

where

$$g_e = [g_e(x_1), g_e(x_2), \dots, g_e(x_n)]^T,$$

$$(A)_{ij} = K(x_i, y_j) w_j, \quad f = [f(y_1), f(y_2), \dots, f(y_m)]^T,$$

$$\epsilon = [\epsilon(x_1), \epsilon(x_2), \dots, \epsilon(x_n)]^T,$$

$w_j$  is the quadrature weight associated with the point  $y_j$ , and the superscript T means matrix transposition. The minimum-rms inversion method does not attempt to solve Equation (2); rather it attempts to use the data vector,  $g_e$ , to estimate the solution in the mean square sense. Let

$$\eta \equiv f - f_o, \quad (3)$$

where  $f_o$  is the mean of  $f$ , obtained by averaging over a representative ensemble of profiles. If one assumes that the estimate to the profile,  $\hat{\eta}$ , can be expressed as a linear combination of the data,  $g_e$ , then the estimate that minimizes the expected mean-square of  $\hat{\eta} - \eta$  is given by [5]:

$$\hat{\eta} = S_f A^T H^{-1} (g_e - A f_o), \quad (4)$$

where

$$H = S_\epsilon + A S_f A^T,$$

$S_f =$  known covariance matrix of the profile

$$\equiv E\{(f - f_o)(f - f_o)^T\}$$

(E denotes expected value operator),

and

$S_\epsilon =$  known covariance matrix of experimental observations.

In addition, the covariance matrix of the solution,  $S_{\hat{\eta} - \eta}$ , is given by



$$S_{\hat{\eta} - \eta} = X^{-1}, \quad (5)$$

where

$$X = S_f^{-1} + A^T S_\epsilon^{-1} A.$$

The sum of the diagonal elements of  $S_{\hat{\eta} - \eta}$  is  $m$  times the expected mean-square error per quadrature point. The essential properties and requirements of the solution may be summarized as follows:

a. The method requires knowledge of  $S_f$  and  $S_\epsilon$ .  $S_f$  can be estimated from past observations of  $f$  (usually direct observations);  $S_\epsilon$  can be determined experimentally by calibration of the sensor.

b. Data with correlation errors can be treated with the method.

c. The instability problem is completely eliminated: as  $S_\epsilon \rightarrow \infty$ ,  $\hat{\eta} \rightarrow 0$ ; i. e., in this case the best estimate of the profile is its mean.

d. The average error of the solution can be immediately determined from properties of the equation of transfer, the measurement noise level and the a priori information.

e. The introduction of basis vectors to represent the solution is neither necessary nor desirable. A completely adequate representation of the solution is its values at each of the quadrature abscissas.

f. The solution yields the best fit to the profile in the sense of minimum mean square linear unbiased estimation when averaged over the joint probability distribution of  $f$  and  $\epsilon$ , where components of  $f$  are assumed uncorrelated with those of  $\epsilon$ .

g. A criterion for optimum observation ordinates (such as frequency or angle) may be given. From a large set of possible measurement locations, the optimum subset is the set which yields the minimum overall expected mean-square error ( $\text{Tr} S_{\hat{\eta} - \eta} = \text{Tr} X^{-1}$ ). The optimum subset is a function of the kernel, the noise level of observations, the a priori information and the number of elements in the subset [7].

We have applied the minimum-rms method to the problem of inferring the vertical temperature profile from measurements of microwave thermal emission from oxygen [7, 8]. The absorption versus height was determined from the Van Vleck equations and five-year (1951 to 1956) mean temperature and pressure data from Denver, Colorado for February. The covariance matrix,  $S_T$ , was determined from the Denver data for 15 quadrature points covering a height interval from 0 to 10 km. Calculations at five frequencies of 51.2, 53.3, 55.0, 57.3 and 61.2 GHz were performed for three cases of interest: (1) looking upward; (2) looking upward and using surface observations to further constrain the solution; and (3) looking downward from 10 km. The noise levels,  $\sigma_\epsilon$ , of each channel are expressed in units of brightness temperature [ $^\circ\text{K}$ ] and are assumed to be the same for each channel. The extent to which the temperature profile can be recovered, on the average, using the above five channels is shown in Figures 1, 2, and 3 for the three cases. These calculations apply to clear atmosphere conditions and neglect the small contribution of water vapor emission.

## CONCLUSIONS

The inversion method presented in this paper applies to the wide variety of inference problems in which there is a priori statistical knowledge of the profile and of the noise properties of the sensor. The method gives an optimum mean-square fit to the profile in the sense of minimum mean square linear unbiased estimation using the set of radiance measurements as estimators. The estimate of the profile is a function of the a priori covariance matrix of the profile, the covariance matrix of experimental observations, the kernel of the equation of radiative transfer, and the radiance measurements at hand.

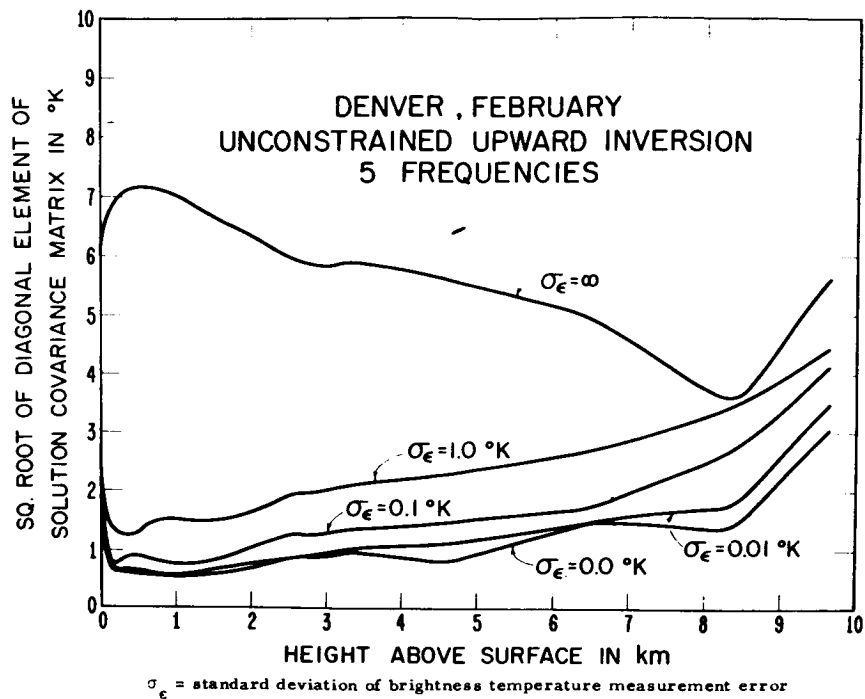


FIGURE 1

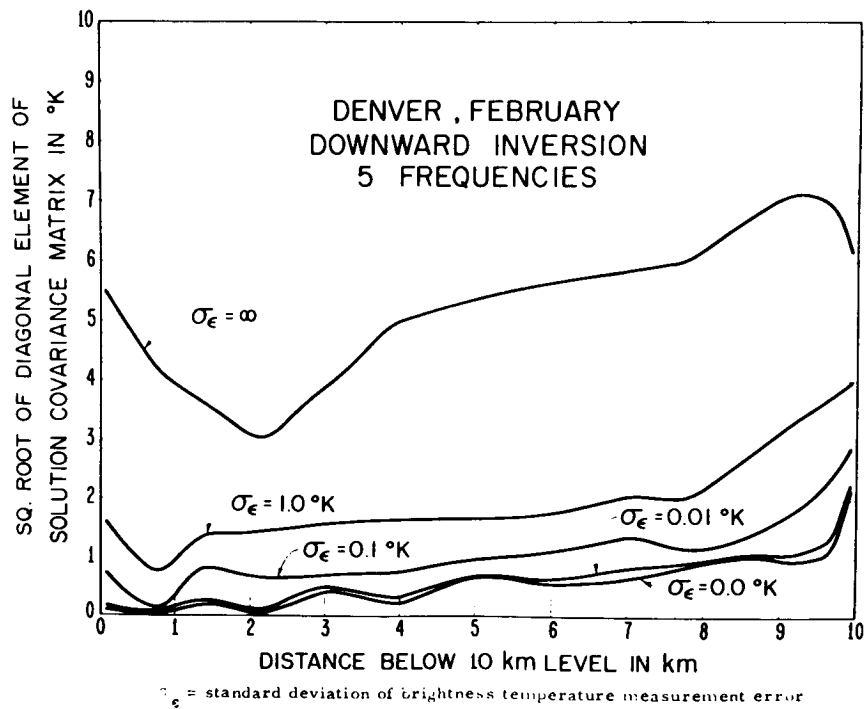


FIGURE 2

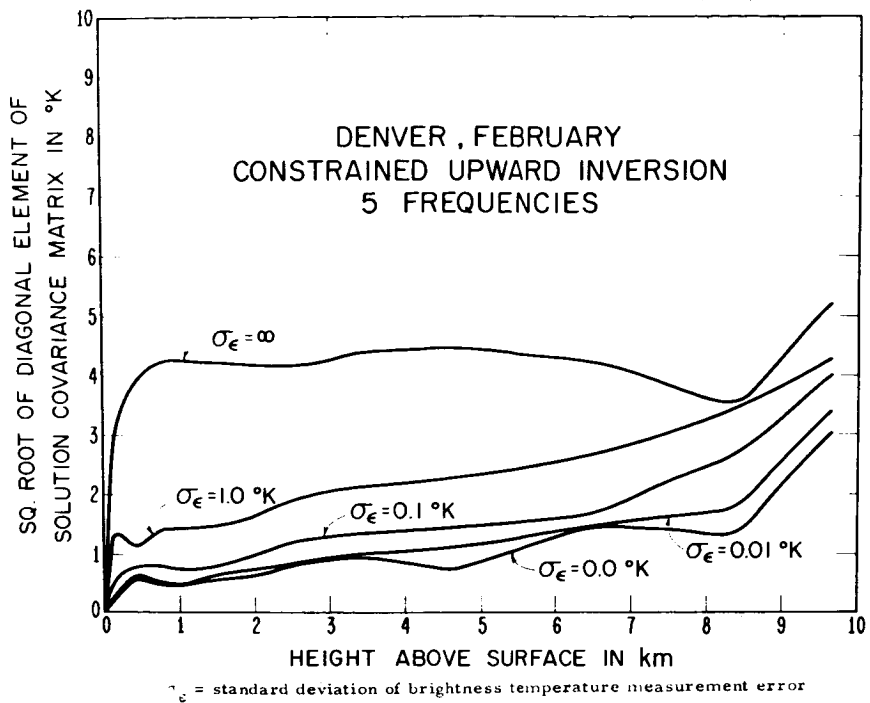


FIGURE 3

## REFERENCES

1. Twomey, S. : The Application of Numerical Filtering to the Solution of Integral Equations Encountered in Indirect Sensing Measurements. *J. Franklin Inst.* vol. 279, no. 2, 1965, pp. 95-109.
2. King, J. I. F. : Inversion by Slabs of Varying Thickness. *J. Atmospheric Sci.*, vol. 21, 1964, pp. 324-326.
3. Alishouse, J. C. : Crone, L. J. ; Fleming, H. E. ; Van Cleef, F. L. ; and Wark, D. Q. : A Discussion of Empirical Orthogonal Functions and Their Application to Vertical Temperature Profiles. *Tellus*, vol. XIX, 1967, pp. 477-481.
4. Strand, O. N. ; and Westwater, E. R. : The Statistical Estimation of the Numerical Solution of a Fredholm Integral Equation of the First Kind. (Accepted for publication by the *J. ACM.*)
5. Strand, O. N. ; and Westwater, E. R. Minimum-rms Estimation of the Numerical Solution of a Fredholm Integral Equation of the First Kind. To be published.
6. Rodgers, C. D. : Private communication.
7. Westwater, E. R. ; and Strand, O. N. : The Statistical Information Content of Radiation Measurements Used in Indirect Sensing. To be published.
8. Westwater, E. R. ; and Strand, O. N. : The Application of Statistical Estimation Techniques to Ground-based Passive Probing of Tropospheric Structure. ESSA Tech. Rept IER 37 -ITSA 37, April 1967.

# REMOTE SENSING OF ATMOSPHERIC WATER VAPOR AND OZONE USING INTERFEROMETRY

By

Barney J. Conrath

N 68-18097

Planetary Radiations Branch  
Goddard Space Flight Center  
Greenbelt, Maryland

---

## ABSTRACT

The problem of obtaining vertical humidity profiles in the earth's troposphere from data obtained with an infrared interferometer spectrometer is examined. Emphasis is placed on the development of techniques which will utilize to the fullest extent the large number of data points obtainable with this type of instrument. One particular inversion technique, involving a linearization of the integral equation of transfer, is considered in some detail. Examples of applications to both synthetic data in the 6.3 micron band from model atmospheres and to real data obtained from a high altitude balloon flight are given, along with an analysis of the propagation of experimental error. Remote sensing of ozone, using data in the 9.6 micron band, is considered briefly.

---

## INTRODUCTION

Several infrared interferometer spectrometer experiments (IRIS) are to be flown on forthcoming Nimbus meteorological satellites. The first of these will cover the spectral range from 5 to 20 microns with a resolution equivalent to about  $5 \text{ cm}^{-1}$ . The instrument, a Michelson interferometer, has been described in detail elsewhere [1]. A spectrum obtained with a breadboard version of this instrument flown in a balloon at the 7 mb level by the High Altitude Engineering Laboratory of the University of Michigan is shown in Figure 1 [2].

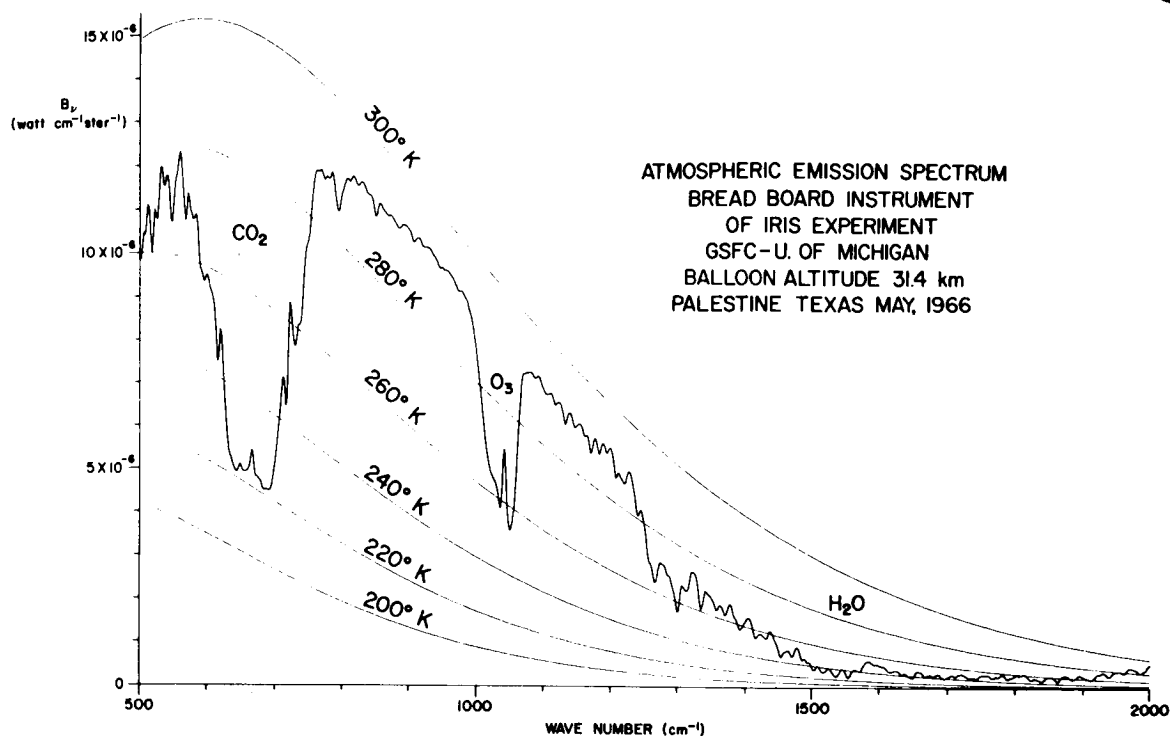


FIGURE 1. ATMOSPHERIC SPECTRUM ACQUIRED WITH A  
 BREADBOARD VERSION OF AN IRIS INSTRUMENT IN A BALLOON  
 FLIGHT 8 MAY 1966 AT PALESTINE, TEXAS

Included in this spectral interval are the water vapor absorption band centered at 6.3 microns, the 9.6 micron ozone band, and the 15 micron carbon dioxide band. Hence, information, on a global basis, on atmospheric water vapor and ozone should be available from these data, as well as vertical temperature structure from the 15 micron band. The problem of obtaining temperature profiles is considered elsewhere in this collection. The present paper considers some theoretical aspects of the problem of obtaining information on the vertical distribution of nonuniformly mixed optically active gases from IRIS data.

One possible formulation of the water vapor inversion problem will be considered in detail. Within the framework of this formulation, the problem of extracting the maximum amount of information from the relatively large number of data points available in the 6.3 micron band from the IRIS experiment will be examined. The propagation of errors in the spectral radiance measurements as well as the influence of uncertainties in the temperature profile employed will be studied.

Finally, some of the difficulties which may be encountered in obtaining information from the relatively weak 9.6 micron ozone band will be considered briefly.

## BASIC FORMULATION

To examine the fundamental principles of the constituent inversion problem, let us consider a highly simplified model. The model (Fig. 2) consists of a semi-infinite column of optically active gas with a discontinuity in temperature at some depth with a total absorber mass  $u_0$  between that depth and the surface of the column. The intensity  $I$  of the thermally emitted radiation emerging from the column at a particular frequency is assumed to be given by

$$I = B(T_2) \tau(u_0) + [1 - \tau(u_0)] B(T_1) \quad (1)$$

where  $B(T)$  is the Planck intensity corresponding to temperature  $T$  and  $\tau(u)$  is the transmissivity of a column of gas with total absorber mass  $u$ . If in some way we have been able to obtain the temperatures  $T_1$  and  $T_2$ , then from Equation (1) we should be able to obtain  $u_0$  from a measurement of  $I$ . From spectral measurements alone, we cannot obtain information on the way in which the gas is distributed within an isothermal layer, but can obtain only the total amount of gas within the layer.

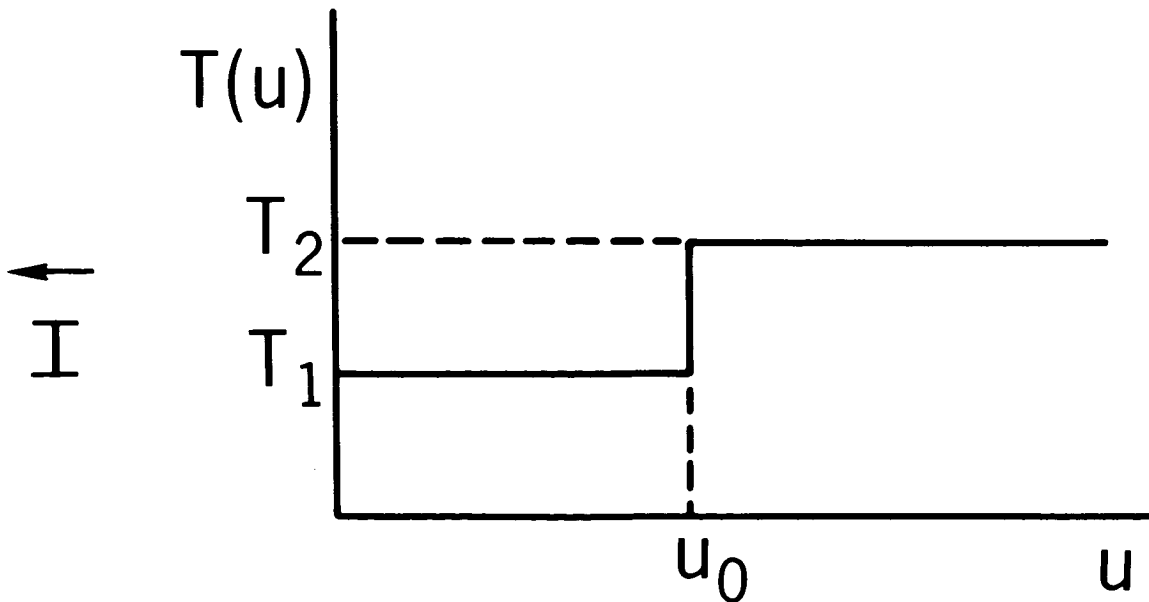


FIGURE 2. SIMPLIFIED MODEL ILLUSTRATING THE PRINCIPLE OF THE CONSTITUENT INVERSION PROBLEM



It is of interest to inquire into the sensitivity of the measured intensity  $I$  to small changes in the absorber mass  $u_0$ . We can do this by differentiating Equation (1) to obtain

$$\Delta I = [B(T_2) - B(T_1)] \frac{d\tau}{d \ln u_0} \frac{\Delta u_0}{u_0}. \quad (2)$$

Thus, in order that the measured intensity  $I$  be as sensitive to  $u_0$  as possible, we would like to choose conditions under which  $\tau$  has a maximum sensitivity to changes in  $u$  and the difference in Planck intensities is as large as possible. However, in the practical situation there will be experimental errors associated without determination of  $I$ ,  $T_1$ , and  $T_2$ , which must be taken into consideration. For example, the choice of a spectral region in which the Planck intensity is strongly dependent on  $T$  may improve the sensitivity of  $I$  to  $u_0$ , but may also permit errors in the temperatures  $T_1$  and  $T_2$  to propagate strongly.

If, instead of the idealized model treated above, we have a more complex temperature profile, we can imagine such a profile approximated by a large number of isothermal slabs. In the limit of an infinite number of slabs we might expect (2) to be replaced by

$$\Delta I \approx \int_{\text{Entire Column}} dT \frac{dB}{dT} \frac{d\tau}{d \ln u} \frac{\Delta u}{u}. \quad (3)$$

In the atmospheric case, the temperature can be expressed as a function of the pressure associated with a given level, and it is convenient to use pressure as the independent variable. In this case, (3) becomes

$$\Delta I(\nu) \approx \int_0^p K(\nu, p) \frac{\Delta u(p)}{u(p)} dp, \quad (4)$$

where

$$K(\nu, p) \equiv \frac{\partial B[\nu, T(p)]}{\partial p} \frac{\partial \tau[\nu, u(p)]}{\partial \ln u}. \quad (5)$$

We have now explicitly displayed the dependence on wave number  $\nu$ .

The above considerations suggest the possibility of obtaining  $u(p)$  from a set of measurements of  $I(\nu)$  by using a "first guess" at  $u(p)$  to calculate  $K(\nu, p)$  and taking  $\Delta I(\nu)$  to be the differences between the measured values of  $I(\nu)$  and those calculated using the first guess. Relation (4) could then be regarded as a linear Fredholm integral equation of the first kind in  $\Delta u(p)$ .

After solving this equation, the resulting  $\Delta u(p)$  could be used as a correction to the first guess. The process could then be iterated until  $\Delta I(\nu)$  becomes less than the experimental error in  $I(\nu)$ , assuming that convergence is obtained. The same formulation can be derived somewhat more formally by starting with the solution to the radiative transfer equation in the integration by parts form, expanding  $\tau(u)$  in a Taylor series about the first guess, and truncating after the linear term [3].

The kernel function  $K(\nu, p)$  can be interpreted physically as a measure of the sensitivity of the outgoing intensity at wave number  $\nu$  to small changes in the total absorber mass above pressure level  $p$ . Thus,  $K(\nu, p)$  can be regarded as a weighting function for this type of formulation.

## APPLICATION TO WATER VAPOR

We shall now pursue the application of the above formulation to the problem of inferring vertical water vapor distribution in the earth's troposphere from IRIS data.

The most directly accessible quantity is the absorber mass or reduced absorber mass, depending on the transmissivity model used. To obtain from a solution  $u(p)$ , a local quantity such as mixing ratio or relative humidity requires, in principle, an additional differentiation. However, in practice, we can assume, for either the mixing ratio or humidity profile, a model with free parameters which we can attempt to evaluate. This is the approach which we shall follow.

Before we can proceed with sample calculations, it is necessary to choose a transmissivity model. For the purpose of the present study, the 6.3 micron water vapor transmissivities given by Möller and Raschke [4] were adopted. The transmissivity is approximated by a formula of the form

$$\tau(\nu, u^*) = \exp \left[ - \frac{1.97 \ell_{\nu} u^*}{(1 + 6.57 \ell_{\nu} u^*)^2} \right], \quad (6)$$

where  $\ell_{\nu}$  is a generalized absorption coefficient and the reduced absorber mass  $u^*$  is given by

$$du^* = \left( \frac{P_0}{P} \right)^{0.72} \sqrt{\frac{T_0}{T}} du \quad . \quad (7)$$

We shall return later to the question of atmospheric transmissivity.

Using Equation (6) and a moderately wet mid-latitude model atmosphere, kernel functions  $K(\nu, p)$  of the form shown in Figure 3 are obtained. The finer structure in these functions reflects the variations in the humidity profile of the model atmosphere employed.

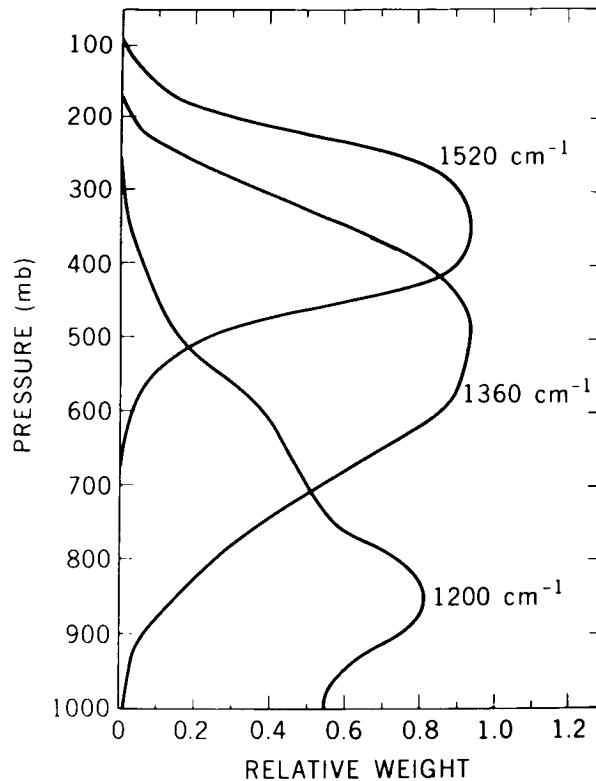


FIGURE 3. KERNEL FUNCTIONS FOR WATER VAPOR INVERSIONS IN THE TROPOSPHERE. A MID-LATITUDE MODEL ATMOSPHERE WAS EMPLOYED IN MAKING THE CALCULATIONS.

The approach described above was first tried using a simple power law model for the mixing ratio

$$\omega = \omega_s \left( \frac{P}{P_s} \right)^k, \quad (8)$$

where  $\omega_s$  is the surface mixing ratio and  $P_s$  is surface pressure which is assumed known. The parameters  $\omega_s$  and  $k$  are to be calculated using the radiance measurements. The same modeling has been employed by Smith [5] in a somewhat different computational scheme.

In order to insure validity of the transmission model used, the data were integrated over  $40 \text{ cm}^{-1}$  intervals or about eight spectral resolution elements of the IRIS data. The inversions were then carried out using data from two such intervals centered at  $1520 \text{ cm}^{-1}$  and  $1200 \text{ cm}^{-1}$ .

Applications were first made to self-consistent synthetic "data" calculated from model atmospheres. It was found that convergence occurred within two or three iterations even when the first guess at the mixing ratio profile was rather bad. Results for a tropical model are shown in Figure 4 and those for a polar winter model in Figure 5. The limitations of the simplified mixing ratio model are apparent, especially in the polar model. Figure 6 shows the results of an inversion of actual IRIS data. The data were taken during the previously mentioned balloon flight on May 8, 1966, at Palestine, Texas. Radiosonde data taken the same day at Shreveport are included in the figure. However, it is felt that these data cannot be taken as in situ measurements since radiosondes obtained at other nearby stations show a large amount of scatter.

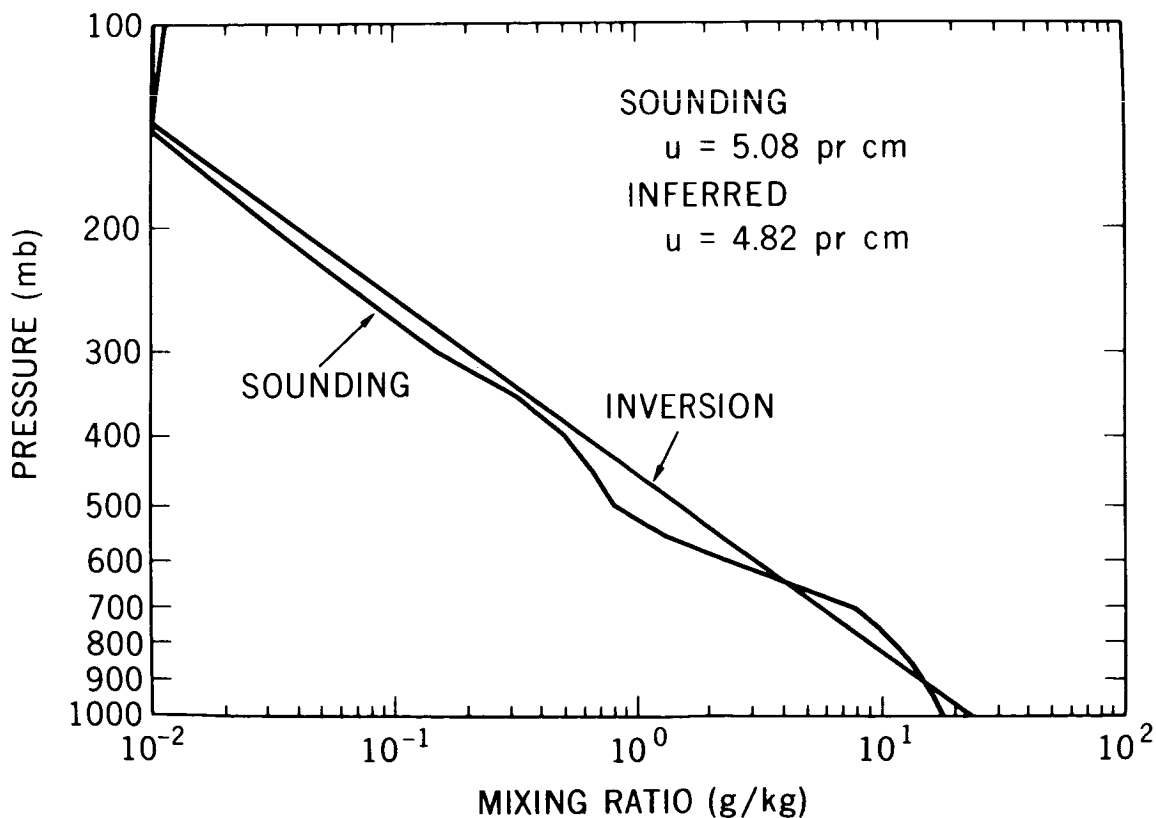


FIGURE 4. EXAMPLE OF A TWO-PARAMETER WATER VAPOR INVERSION APPLIED TO SYNTHETIC DATA FROM A TROPICAL MODEL ATMOSPHERE

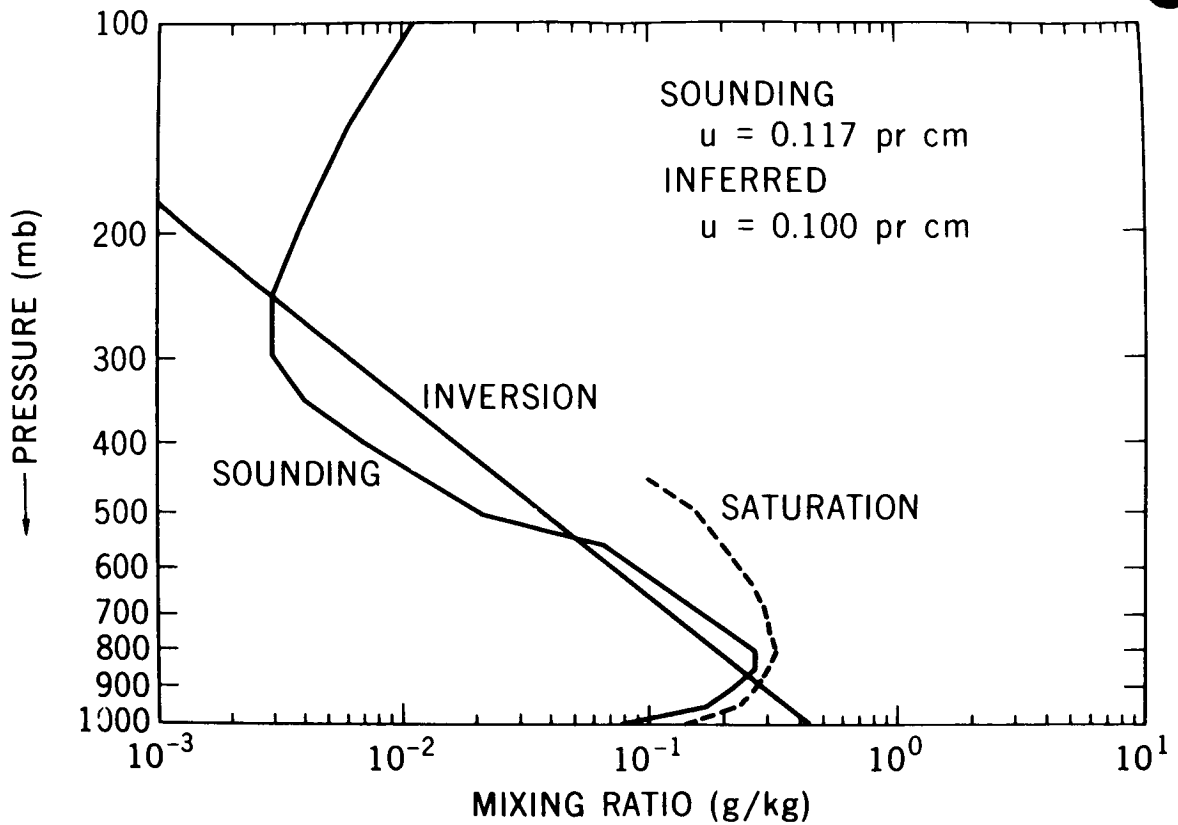


FIGURE 5. EXAMPLE OF A TWO-PARAMETER WATER VAPOR INVERSION APPLIED TO SYNTHETIC DATA FROM A POLAR WINTER MODEL ATMOSPHERE

Disadvantages of attempting to model the mixing ratio profile include the fact that it may vary by several orders of magnitude between the surface and the upper troposphere, and its shape is strongly influenced by the behavior of the temperature profile, as seen in Figure 5, for example. These considerations led to the investigation of the relative humidity profile as a possible quantity for modeling.

The formulation being considered here can easily be adapted to a relative humidity inversion. Let us assume that the relative humidity profile  $f(p)$  can be represented approximately by a linear expansion in some arbitrary function set

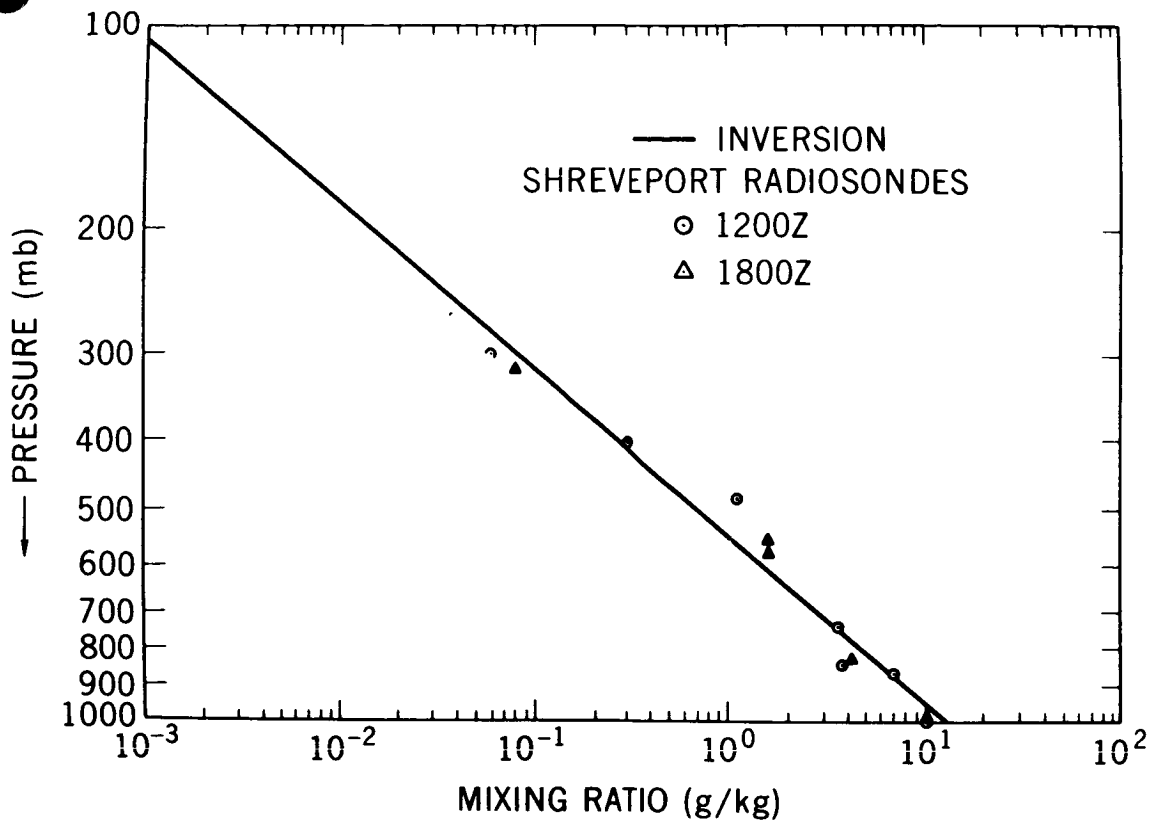


FIGURE 6. APPLICATION OF A TWO-PARAMETER INVERSION OF IRIS BALLOON FLIGHT DATA

$$f(p) \approx \sum_{i=1}^n c_i \phi_i(p), \quad (9)$$

where the  $c_i$ 's are expansion coefficients to be determined. Making use of the well known relationship between mixing ratio and relative humidity,

$$\omega \text{ (g/kg)} = 622 \frac{e}{p} f, \quad (10)$$

and Equation (7), along with the expression for absorber mass,

$$du = \frac{1}{g} \omega dp, \quad (11)$$

we find that Equation (4) can be rewritten in the form

$$\Delta I(\nu) = \sum_{i=1}^n \Delta c_i \int_0^{p_s} \frac{\partial B(\nu, p)}{\partial p} \frac{\partial \tau(\nu, p)}{\partial u^*} \psi_i(p) dp, \quad (12)$$

where

$$\psi_i(p) \equiv \frac{622}{g} \int_0^p \left( \frac{p'}{p_0} \right)^{0.72} \sqrt{\frac{T_0}{T}} \frac{e_s(T)'}{p'} \phi_i(p') dp'. \quad (13)$$

The saturation vapor pressure  $e_s$  is a function of temperature only. If we have measurements of  $I(\nu)$  at  $N$  wavenumbers, then Equation (12) reduces to a set of linear algebraic equations in the  $\Delta c_i$ 's which can be solved provided the equations can be regarded as linearly independent. Thus, a first guess can be made at the expansion coefficients and Equation (12) can be used to calculate the corrections  $\Delta c_i$  to this guess. The process can be iterated as before until the  $\Delta I$ 's are less than the experimental error. This provides a rather versatile formulation for doing the water vapor inversion in terms of the relative humidity profile, provided that convergence can be readily obtained.

The method was tested first on synthetic data calculated using model atmospheres in order to study convergence behavior. The results of one such test are shown in Figure 7. The model atmosphere used in this case had a humidity profile consisting of three layers of constant relative humidity: 85 percent from 100 to 400 mb, 65 percent from 400 to 700 mb, and 50 percent from 700 to 1000 mb. In doing the inversion, a three-term expansion for  $f(p)$  was employed, and the  $\phi_i$ 's in Relation (9) were chosen in such a manner that the expansion coefficients corresponded to relative humidities in the same three atmospheric layers so that it would be possible for an exact solution to be obtained. In the example in Figure 7, the first guess consisted of 100 percent humidity at all levels or a completely saturated atmosphere. The solution for each layer following each iteration is shown in the figure, with convergence to the correct solution occurring fairly rapidly.

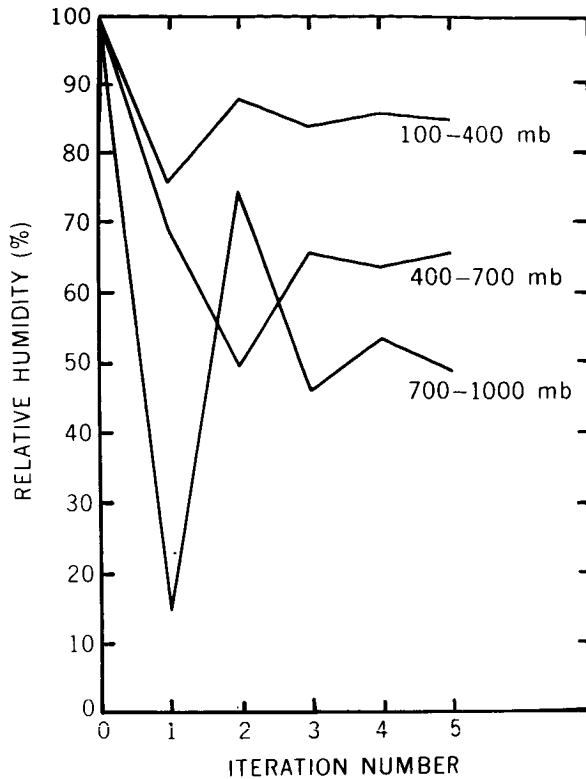


**FIGURE 7. EXAMPLE OF THE CONVERGENCE BEHAVIOR OF A THREE-LAYER INVERSION IN TERMS OF THE RELATIVE HUMIDITY PROFILE**

One characteristic of the convergence behavior found in most models tested was a tendency to initially overshoot the true solution followed by an oscillatory convergence. This behavior resulted in negative relative humidities sometimes being obtained on the first iteration when a very dry layer existed in the model. This difficulty was overcome by making a test for negative humidities in the computer program employed for the calculations. If a negative humidity occurred, the first guess was revised downward by a factor of 2, and the calculation was begun again. This was repeated until all humidities were positive and convergence could proceed.

A three-layer inversion was performed on the IRIS balloon flight data. The results are shown in Figure 8. The Shreveport radiosonde data are included once again. The same inversion, converted to mixing ratio from relative humidity using Equation (10), is shown in Figure 9 for comparison with the previous two-parameter inversion of the same data.



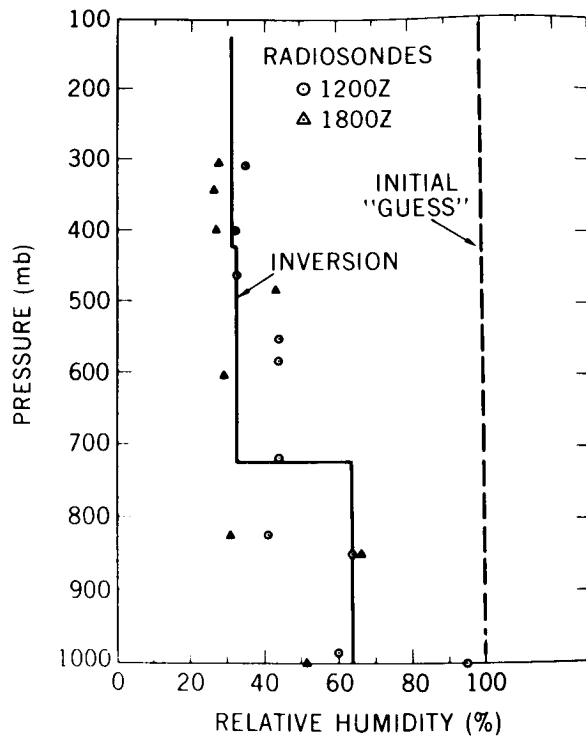


FIGURE 8. THREE-LAYER RELATIVE HUMIDITY INVERSION OF IRIS BALLOON FLIGHT DATA

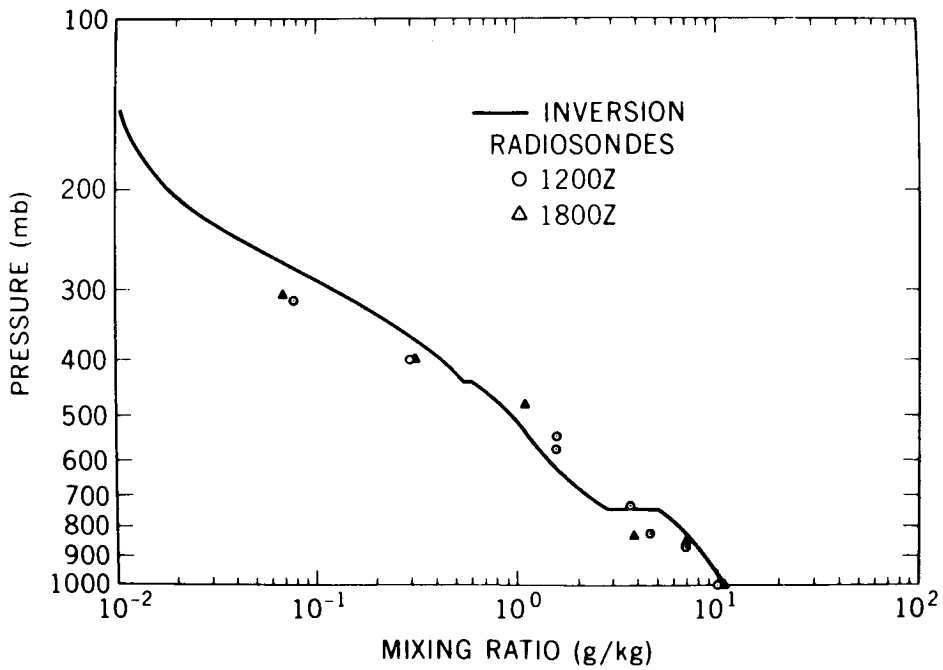


FIGURE 9. THREE-LAYER INVERSION OF IRIS BALLOON FLIGHT DATA EXPRESSED IN TERMS OF MIXING RATIO

## EFFECTS OF OBSERVATIONAL ERROR

As in most inversion problems, the question of the propagation of observational error is a critical one. The degree of ill-conditioning of the linear system obtained from Equation (12) depends on a number of factors including the spectral regions in which the measurements were made, the type of expansion functions used in Relation (9), the number of independent parameters to be determined, and the behavior of the profile sought.

To obtain some idea of the total information content of the IRIS data, synthetic data were calculated using a typical mid-latitude type of model atmosphere, and a three-layer inversion was performed using three of the calculated intensities at  $1200\text{ cm}^{-1}$ ,  $1320\text{ cm}^{-1}$ , and  $1520\text{ cm}^{-1}$ . The humidity profile obtained in the inversion was then used to recalculate all intensities between  $1200\text{ cm}^{-1}$  and  $1520\text{ cm}^{-1}$ . The intensities interpolated in this way between  $1200\text{ cm}^{-1}$  and  $1320\text{ cm}^{-1}$  and between  $1320\text{ cm}^{-1}$  and  $1520\text{ cm}^{-1}$  were found to agree with the intensities calculated from the original profile to more than three significant figures or to well within any realizable experimental error. Thus, we cannot hope to infer additional independent information by adding a fourth measurement to our original three. However, we can use the remaining measurements in a least-squares calculation for three constant humidity layers and thus gain some improvement in effective signal-to-noise ratio.

To obtain some feeling for the sensitivity of the solution to errors in the measured intensities, errors were added to exact synthetic data and inversions were performed. The results are summarized in Table I. The table first shows the results of a three-layer inversion using "exact" data for comparison purposes. Errors of 0.1 c. g. s. unit and 0.2 c. g. s. unit were subtracted and added to alternate pieces of data. "Set 1" and "Set 2" refer to the two possible combinations of alternating errors with constant amplitude. Inversions were performed using only three intensities averaged over  $40\text{ cm}^{-1}$  and also using nine intensities averaged over  $40\text{ cm}^{-1}$  in a least-squares calculation. This is indicated in the column headed "Number of Data Points."

The error from the IRIS experiment is expected to be on the order of 0.5 c. g. s. unit for intensities associated with individual  $5\text{ cm}^{-1}$  resolution elements. This corresponds to approximately a 1 percent error at  $1200\text{ cm}^{-1}$ , but a 15-20 percent error at  $1520\text{ cm}^{-1}$ . After averaging over  $40\text{ cm}^{-1}$  intervals, the effective error should then be  $\sim 0.2$  c. g. s. unit. The table shows that the use of nine averaged intensities in a least-squares calculation results in a significant reduction in errors in the solutions compared to the cases which employed only three intensities.

TABLE I. PROPAGATION OF INTENSITY ERRORS IN THREE-LAYER INVERSION

Intensity Errors (c. g. s. units)	No. of Data Pts.	125 - 425 mb		425 - 725 mb		725 - 1000 mb		Total H <sub>2</sub> O	
		RH (%)	Error	RH (%)	Error	RH (%)	Error	u (pr cm)	Error
Exact	3	29	--	36	--	52	--	2.31	--
0.1 (Set 1)	3	34	+ 5	29	- 7	66	+14	2.71	+ .40
0.1 (Set 2)	3	26	- 3	43	+ 7	39	-13	1.93	- .38
0.2 (Set 1)	3	39	+10	22	-14	82	+30	3.18	+ .87
0.2 (Set 2)	3	22	- 7	50	+14	26	-26	1.57	- .74
0.1 (Set 1)	9	30	+ 1	35	- 1	55	+ 3	2.39	+ .08
0.1 (Set 2)	9	29	0	37	+ 1	49	- 3	2.23	- .08
0.2 (Set 1)	9	31	+ 2	34	- 2	58	+ 6	2.47	+ .16
0.2 (Set 2)	9	28	- 1	38	+ 2	47	- 5	2.16	- .15

The IRIS balloon flight data used in the previous section consisted of three separate spectral scans averaged together. The experimental error for individual scans is estimated at 0.5 c. g. s. unit [6]. Thus, when the three-scan average is integrated over  $40 \text{ cm}^{-1}$ , the error in the resulting intensities should be  $\sim 0.1$  c. g. s. unit. Unfortunately, averaging over successive scans will probably not prove practical for the satellite experiments because of spatial smearing.

Thus far, we have implicitly assumed a precise a priori knowledge of the tropospheric temperature profile in carrying out water vapor inversions. For model atmospheres, we have used the temperature profile of the original model, and in inverting the IRIS data, we have used radiosonde temperature profiles. In the satellite experiment, however, it will be necessary to use tropospheric temperature profiles obtained from inversions performed in the 15-micron carbon dioxide band, which will be subject to errors. A temperature inversion for the troposphere obtained from IRIS Palestine balloon flight data is shown in Figure 9. There is some overlapping water vapor absorption in the 15-micron band which should be taken into account if accurate temperature inversions are to be obtained in the lower troposphere. Thus, the water vapor and temperature inversions are essentially coupled. In practice, we can take advantage of the relatively weak dependence of the temperature inversion on water vapor and use a first guess at the humidity profile to obtain a temperature inversion. The resulting temperature profile can be used to do a water vapor inversion in the 6.3 micron band. The procedure can be iterated as many times as necessary.

Some feeling for the sensitivity of the water vapor inversion method to errors in the temperature profile can be obtained from Figure 10. A two-parameter inversion in terms of mixing ratio was performed, using a temperature profile with a  $-2^\circ \text{K}$  systematic error, giving the rather poor results shown.

When working in terms of relative humidity, it must be borne in mind that temperature errors affect the calculation both through Planck intensity and through the conversion from relative humidity to mixing ratio. Both the Planck function and the saturation vapor pressure are strong functions of temperature for the cases of interest in this problem. The two temperature dependencies appear to be somewhat compensating, at least in the cases considered in this study (see Fig. 11). When the humidity profile is held constant and the temperature profile is allowed to vary, the resulting calculated intensities show considerably less variation than when the mixing ratio profile is fixed with the temperature allowed to vary. Preliminary calculations indicate temperature profile errors may prove to be the limiting factor in the application of this method to IRIS data. A more comprehensive study of this part of the problem is now under way.

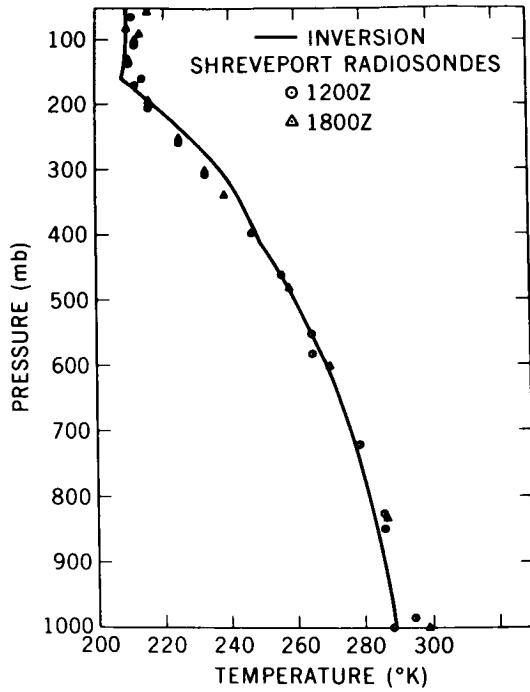


FIGURE 10. TROPOSPHERIC TEMPERATURE INVERSION FROM IRIS BALLOON FLIGHT DATA IN THE 15 MICRON BAND

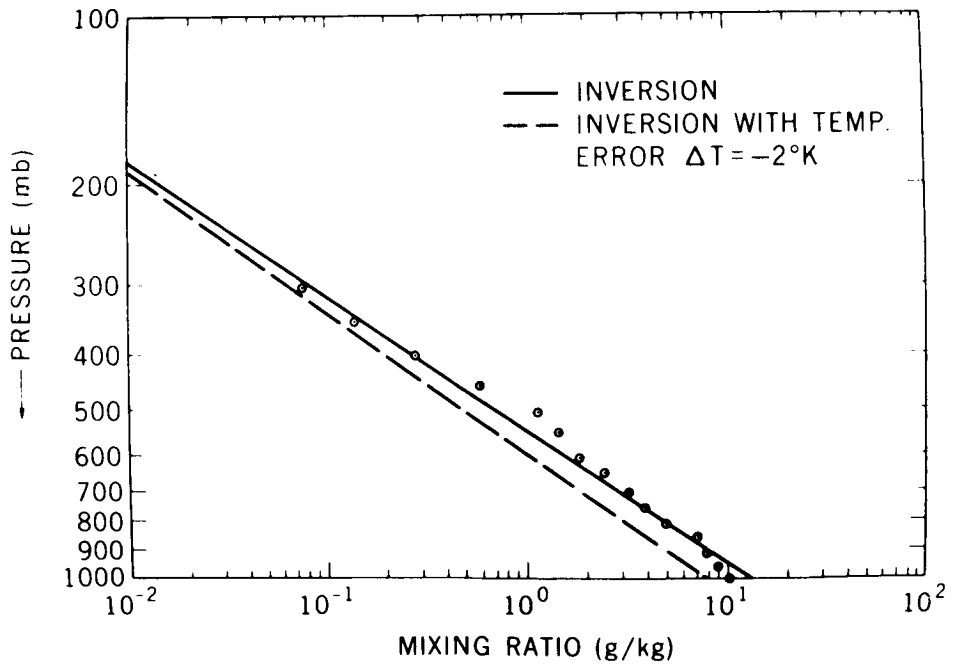


FIGURE 11. TWO-PARAMETER INVERSION OF SYNTHETIC DATA USING A TEMPERATURE PROFILE WITH A  $2^\circ K$  SYSTEMATIC ERROR

## OZONE INVERSION

The problem of obtaining information on the vertical distribution of ozone has not been investigated in detail. In this section we shall merely indicate some of the difficulties encountered in obtaining such information from an IRIS type of experiment.

The 9.6 micron band is relatively weak, and the bulk of the ozone in a typical distribution is located at heights where the pressure broadening of individual lines is low. Weighting functions calculated by Bolle [7] show widths greater than the characteristic heights over which the ozone concentration varies. Thus, it would appear to be difficult to extract information on the vertical ozone distribution in any detail with IRIS data.

Another limitation is imposed by the need to know the temperature profile at heights above those for which information can be reliably obtained from the 15-micron band with a resolution equivalent to  $5 \text{ cm}^{-1}$ .

## SUMMARY AND DISCUSSION

The problem of obtaining information on the vertical distribution of water vapor in the troposphere from data obtained with a satellite-borne interferometer spectrometer has been examined within the framework of one method of solution. For one particular type of model atmosphere, it was found that an inversion in terms of three constant relative humidity layers exhausted the information content of the data in the sense that the inverted profile obtained from three intensities could be used to predict all of the remaining intensities in the 6.3-micron water vapor band to within the experimental error.

Some estimates of the effects of experimental errors on the inversion solutions were obtained by adding errors to "exact data" calculated from model atmospheres. Inversions were performed in terms of three layers of constant relative humidity, using both three intensities and nine intensities in a least-squares solution. The least-squares solution was found to produce a marked improvement over the three-intensity solution. Preliminary estimates of the propagation of errors in the temperature profile indicate that this may be the

limiting factor in the application of the method to IRIS data. In practice, the temperature profile must be obtained in an inversion of data in the 15-micron band, which is overlapped to some extent by water vapor absorption. Hence, the temperature and water vapor inversions are essentially coupled, and any complete formulation must take this aspect into consideration.

The weakness of the 9.6-micron ozone band, along with the fact that most of the ozone is concentrated at altitudes where the pressure is low resulting in narrow spectral lines, makes it seem unlikely that vertical distributions can be determined in any detail from IRIS data. An additional complication is the need to know the temperature profile at altitudes above those from which reliable estimates can be obtained from the 15-micron band, at least with a spectral resolution of  $5 \text{ cm}^{-1}$ .

Throughout this study, we have employed the transmissivities of Möller and Raschke. The method employs a reduced absorber mass, the use of which is strictly valid only when the strong line approximation holds. In addition, it is not possible to employ the full  $5 \text{ cm}^{-1}$  resolution of the instrument using this model. Hence, the possibility of employing other transmission models, such as the random model with a Curtis-Godson approximation, the quasi-random model, and a direct spectral integration, is the subject of current study.

Finally, it should be emphasized that only one method of performing the water vapor inversion has been considered here. It may be possible to adapt other methods for application to inversions of IRIS data such as those of Smith [5] and of King [8], and this possibility should be given consideration in future work.

## REFERENCES

1. Hanel, R. A.; and Chaney, L.: The Infrared Interferometer Spectrometer Experiment (IRIS). Goddard Space Flight Center, Report X-650-65-75, March 1965.
2. Chaney, L. W.; Drayson, S. R.; and Young, C.: Fourier Transform Spectrometer—Radiative Measurements and Temperature Inversion. *Applied Optics*, vol. 6, 1967, pp. 347-349.
3. Conrath, B. J.: On a Mathematical Formulation of the Constituent Inversion Problem for Planetary Atmospheres. Goddard Space Flight Center, Report X-622-66-542, October 1966.
4. Möller, F.; and Raschke, E.: Evaluation of TIROS III Radiation Data, Final Report. NASA Research Grant NsG-305, March 1964.
5. Smith, W. L.: An Iterative Method for Deducing Tropospheric Temperature and Moisture Profiles from Satellite Radiation Measurements. *Monthly Weather Review*, vol. 95, 1967, pp. 363-369.
6. Chaney, L. W.; Loh, L. T.; and Surh, M. T.: A Fourier Transform Spectrometer for the Measurement of Atmospheric Thermal Radiation. University of Michigan High Altitude Engineering Laboratory Technical Report, NASA Contract NASr-54 (03), May 1967.
7. Bolle, H. J.: Infrarotspektroskopie als Hilfsmittel und Gegenstand meteorologischer und planetarischer Forschung. Meteorologisches Institut der Ludwig-Maximilians-Universität München Forschungsbericht W 67-17, July 1967.
8. King, J. I. F.: Meteorological Inferences from Satellite Radiometry. I, *J. Atmos. Sci.*, vol. 20, 1963, pp. 245-250.



---

## DISCUSSION

J. I. F. King, GCA: In the temperature inversion problem, you have the advantage of the amplification due to fourth power dependence of the emission on temperature. Have you anything like this in the constituent inversion, Dr. Conrath?

B. Conrath: No, not really. The kernel functions that we have shown here are essentially a measure of the sensitivity of the outgoing intensity to the absorber mass above the various atmospheric levels, and they depend primarily on the rapidity with which the transmissivity varies with the absorber mass.

R. Drayson, University of Michigan: I would like to comment on Dr. Conrath's statement, made near the end of his presentation, that one of the problems he found is the effect, in the inversion for the temperature profile, of water vapor in the far wings on the  $15 \mu$  band. I think that we really should not try to solve for the temperature structure and water vapor distribution separately, but ought to consider all our information together. Ultimately, we can expect information from the microwave region, the rotational water vapor band, the  $15 \mu$   $\text{CO}_2$  bands, the  $6.3 \mu$  water vapor bands, and perhaps the  $4.3 \mu$   $\text{CO}_2$  bands. We should try to find a way in which we can consider together all the measurements we have available and obtain some optimal solution. Some of the methods for inversion that have been developed rely on rather specialized features of certain absorption bands; for example, in the microwave region, we can make assumptions about the temperature dependence of the Planck function which we cannot make in the infrared region. I think that an overall approach might lead to considerable improvement over solutions from individual absorption regions.

B. Conrath: Yes, I agree that one should attempt to incorporate into the various inversion schemes all the information that is available at any given time. I was concerned primarily with looking at this one particular experiment, since it will be flying soon, and we wanted to see what we could do with data of the type I discussed in the paper. I agree that ultimately we should certainly take into consideration all available data.

---

# REMOTE DETECTION OF LOCAL TEMPERATURES AND LOCAL PARTIAL PRESSURES WITH CROSSED-BEAM SPECTROSCOPY

By

F. R. Krause and J. B. Stephens

N 68-18098

---

## ABSTRACT

The physical interpretation of crossed-beam tests is formulated mathematically for a set of experiments, which differ only by using a different optical wave number for one of the two photometer units.

Crossed-beam methods differ from single path observations in that modulations of radiative power are used instead of mean values. These modulations come from inhomogeneous distributions of radiation sources traversing the detector's narrow field of view. Two passive remote detection systems are employed to select a region from triangulation of the two beams. The beam modulations are multiplied and averaged over time to discriminate against all beam modulations which originate outside the selected region. The measurements of the resulting two-beam product mean value is then repeated by setting one detector at different optical wave lengths to obtain a "crossed-beam spectrum." The physical interpretation of these spectra then allows us to analyze the optical and thermodynamic properties inside a region already selected by triangulation and statistical correlation methods. This general concept of crossed-beam spectroscopy is illustrated for a statistical band model of pressure broadened lines. The analytical formulation indicates that, with the proper choice of only two wavelengths, we may obtain the mean absorption, as well as both the local mean temperature and partial pressure. In addition, these two-line measurements disentangle the space-time covariance of pressure and temperature variations and open direct experimental studies of turbulent heat and mass transfer in inhomogeneous flows.

---

# I. INTRODUCTION

The remote detection of local temperatures and local partial pressures in turbulent flows is theoretically possible by analyzing crossed-beam experiments which have been conducted at different optical wave numbers. The physical interpretation of such experiments is formulated mathematically for a gas which has isolated bands of pressure-broadened weak or strong rotational lines.

The crossed-beam technique has been developed originally to study turbulence in subsonic jets [1], in supersonic jets [2], and in the earth's atmosphere [3]. The review of these studies, which is given in sections III and IV, indicates how crossed-beam arrangements select a local flow region by triangulation and how they isolate the changes of radiative power in the region by statistical cross-correlation. Repeating crossed-beam tests at different optical wave length therefore allows us to spectroscopically analyze a preselected local flow region. The resultant concept of "Crossed-Beam Spectroscopy" was first outlined by Krause, Davies and Cann [4] and is reviewed in detail in section V. The interpretations of spectroscopic crossed-beam experiments will require an a priori knowledge of the molecular constants of the absorbing gas, which is illustrated in section VI. This knowledge requires an application of molecular spectroscopy, which was first outlined by Davies [5]. The derivations in section VI differ, however, from the original treatment by admitting a simultaneous variation of all thermodynamic properties instead of admitting only one thermodynamic variation at a time. This extension was necessary for a consideration of experiments in actual flows, where turbulence will change all thermodynamic properties simultaneously. The concept of crossed-beam spectroscopy has, so far, never been verified experimentally. We do plan, however, to conduct such experiments in the near future.

## II. LIST OF SYMBOLS

Symbol	Definition
B	Rotational constant of the molecule
b	Line half-width
c	Speed of light
d	Spacing of rotational lines
$G(\xi; \dots) = \overline{i_\eta(t) i_\xi(t)}$	Two-beam product mean value
h	Planck's constant
I	Radiative power (watts)
$\Delta I$	Local change of radiative power
$i = I - \bar{I}$	The beam modulations of the radiative power
$K(\ell; \dots) = \frac{I(\ell, \dots) - I(\ell + \Delta\ell, \dots)}{I(\ell, \dots)} = -\frac{1}{I} \frac{\partial I}{\partial \ell}$	The local spectral absorption coefficient
k	Boltzman constant
$\ell$	Path length along the beam
$\Delta\ell$	Local change in path length
P	Static pressure of the gas
p	Partial pressure of the gas
$Q_{\vec{p}} = \overline{\int \int P'(\vec{x}, t) K_2'(\vec{x} + \vec{\xi}, t + \xi, \lambda_2) d_\eta d_\xi}$	Turbulence factor for the static pressure of the gas

## LIST OF SYMBOLS (Continued)

Symbol	Definition
$Q_p^- = \iint \overline{p'(\vec{x}, t) K_2'(\vec{x} + \vec{\xi}, t + \tau, \lambda_2)} d_\eta d_\zeta$	Turbulence factor for partial pressure
$Q_T^- = \iint \overline{T'(\vec{x}, t) K_2'(\vec{x} + \vec{\xi}, t + \tau, \lambda_2)} d_\eta d_\zeta$	Turbulence factor for static temperature
q	Frank Condon factor
$R(\xi, \lambda, \dots) = \frac{G(\xi, \dots)}{\bar{I}_\eta \bar{I}_\zeta} = \frac{\lim_{1 \rightarrow \infty} \frac{i_\eta i_\zeta}{\bar{I}_\eta \bar{I}_\zeta}}{1}$	The normalized two-beam mean value
S	Rotational line strength
T	Integration time
t	Static temperature of the gas
$\xi$	Length coordinate normal to both beams
$\zeta$	Length coordinate following beam B
$\eta$	Length coordinate parallel to beam A
$\Omega(T) = \sqrt{\frac{4k\bar{T}B}{hc}}$	
$\lambda$	Wave length
$\Delta\lambda$	Monochromator's band pass

## LIST OF SYMBOLS (Concluded)

Symbol	Definition
$\omega$	Wave number
$\omega_0$	Wave number at band center
$\bar{\omega}$	Center of experimental band pass in wave number

## Superscripts and Subscripts

Symbol	Definition
d	The detector
o	At standard conditions except for $\omega_0$
S	The source
SL	Strong line approximation
WL	Weak line approximation
$\xi$	Occurs normal to the beam in the $\xi$ -direction
$\eta$	Occurs in beam A in the $\eta$ direction
s	Occurs in the B beam in the $\zeta$ -direction
<>	An experiment average.

### III. SINGLE BEAM SIGNALS

Crossed-beam arrangements employ two single "beams," which are defined by the narrow field of view of two photodetectors. Two beams are needed to select a local flow area by triangulation between two lines of sight. Figure 1 illustrates the arrangements that we have used for turbulence investigations in subsonic [1] and supersonic [2] jets. Light was provided by man-made sources such as lasers, mercury arcs, and ultraviolet discharge lamps (McPherson lamp). The left side of Figure 1 shows a passive system where the light is

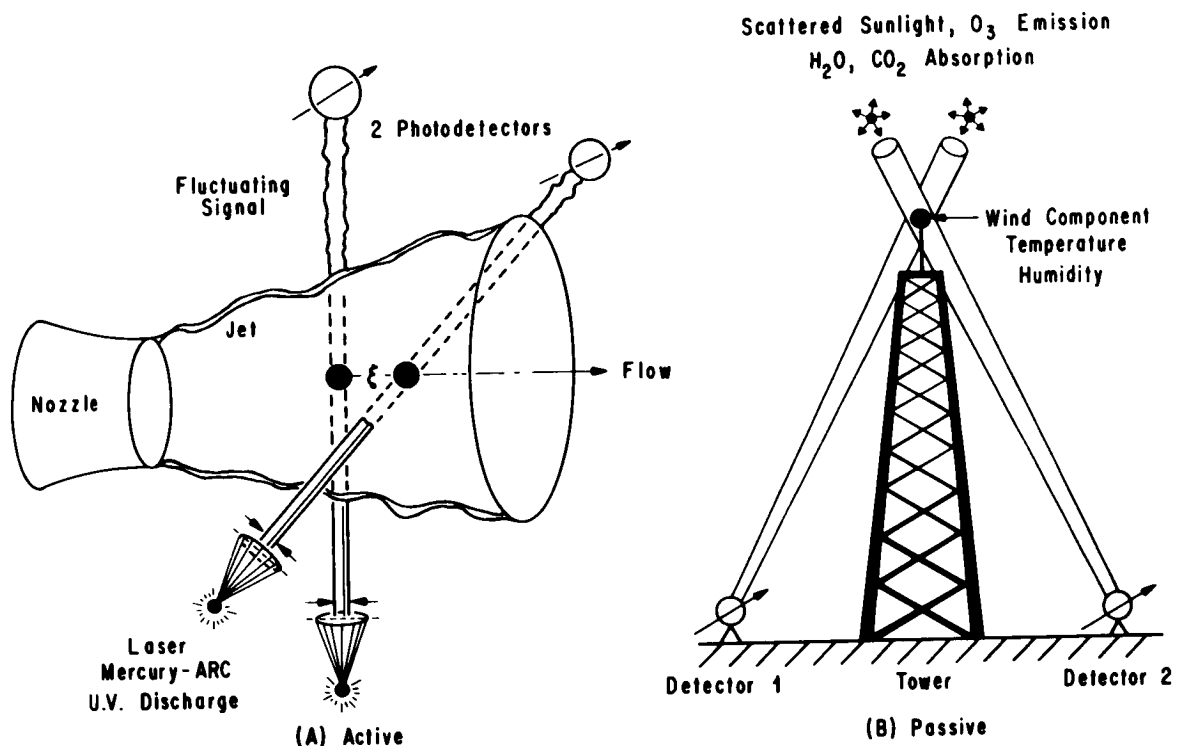


FIGURE 1. GROUND BASED CROSSED-BEAM ARRANGEMENTS

provided by natural radiation backgrounds rather than man-made sources. This passive crossed-beam arrangement is being used in field tests to demonstrate that wind profiles can be determined from fluctuations of scattered sunlight [3]. The individual beam of a crossed-beam arrangement is selected by the same optical systems that have already been developed for inversion techniques [2] as illustrated in Figure 2. The field of view is chosen by the field stop on the

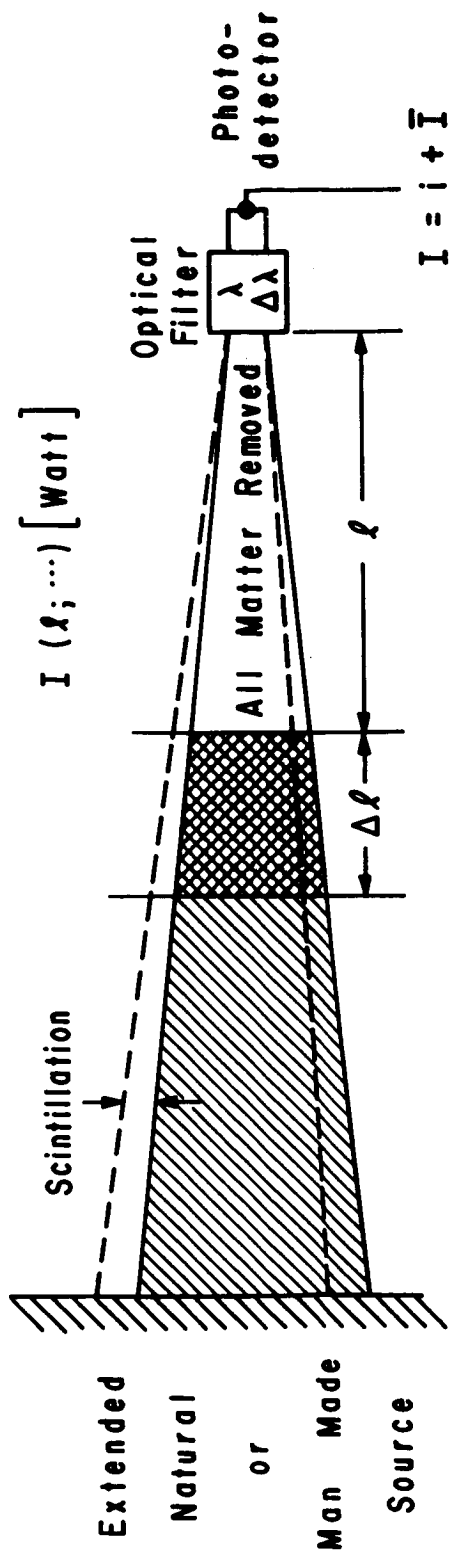


FIGURE 2. INTERPRETATION OF SINGLE-BEAM SIGNAL



collector optics. Optical wave length  $\lambda$  and spectroscopic band pass  $\Delta\lambda$  are set by an optical filter. The filter is followed by a photodetector, the output signal  $I$  of which is directly proportional to the radiative power on the detector's field of view.

An equation of radiative transfer will be needed to relate the observed signal  $I$  to the local radiation phenomena along the line of sight. In setting up these equations, we assume that the distant natural or man-made source is an extended source. The word "extended" means that its radiance is uniform within the range of apparent source image scintillation, which is provided by the local change of refractive index in the beam. These scintillations are usually small. In our wind tunnel experiments, a source may be called extended if it radiates uniformly over an area of 5 mm in diameter. For an extended and uniform source, the radiative power will not be altered by a change of refractive index. The scintillation of the extended source will thus not change the optical signal, except for slightly decreasing the accuracy of triangulation. Equations of radiative transfer thus do not account for schlieren, shadowgraph and interferometer effects. These effects are of no concern when using extended sources.

The optical signal from an extended source accounts only for local changes of radiative power by light emission, absorption and scattering. However, a more restricted equation of radiative transfer, where emission and scattering can be neglected relative to absorption, is chosen for clarity. An extension of crossed-beam spectroscopy to flows with emission and scattering would be straightforward [4].

The restricted equation between the detected signal  $I$  and the local changes of radiative power  $\Delta I(l, \dots)$  along the beam may now be explained by an imaginary experiment. Suppose that one could remove all matter between a beam cross section at position  $l$  and the detector. This cross section will then appear as a radiating surface and the detected signal,  $I(l, \dots)$ , will account for all radiative power which this surface element emits into the detector's narrow field of view. The local absorption effects can then be studied by repeating the imaginary experiment by further removing the matter between positions  $l$  and  $l + \Delta l$ . The difference between the two imaginary observations will account for the absorption inside the beam element  $\Delta l$ . This difference is thus used to define the local absorption coefficient

$$\begin{aligned}
 k(l, \dots) &= \frac{I(l, \dots) - I(l + \Delta l; \dots)}{\Delta l} \\
 &= -\frac{1}{I} \frac{\partial I}{\partial l} \quad . \quad (1)
 \end{aligned}$$

The actual observable signal  $I$  follows by accounting for all imaginary changes of radiation power along the entire line of sight. The integration of equation (1) gives the desired equation of radiative transfer:

$$I_s = I_d \exp \left[ - \int_{\text{detector}}^{\text{source}} k(\ell, \dots) d\ell \right] . \quad (2)$$

This equation is clearly time-dependent since all imaginary experiments refer to an instantaneous observation and could lead to different results the next instant of time. However, in most inversion techniques, the equation is applied to time-averaged values only. The detector output  $I_{\text{detector}}(t, \lambda \dots)$  is replaced with its mean value over a certain period  $T$ .

$$\bar{I} = \frac{1}{T} \int_0^T I(t; \lambda, \dots) dt . \quad (3)$$

This average is then related to the average absorption coefficient along the line of sight:

$$\bar{K} = \frac{1}{T} \int_0^T K(\ell; t; \lambda) dt . \quad (4)$$

Crossed-beam methods differ from inversion methods by using the complete time history of the optical signals rather than the mean values. These fluctuations are calculated by subtracting the mean value from the time history of the signal, as illustrated in Figure 3. The associated "beam modulation"

$$i = I - \bar{I} \quad (5)$$

is related to the local flow modulation of the absorption coefficient,

$$K' = K - \bar{K} , \quad (6)$$

by equation (3). We assume (a) that the optical integral along the line of sight,

$$\int K d\ell ,$$

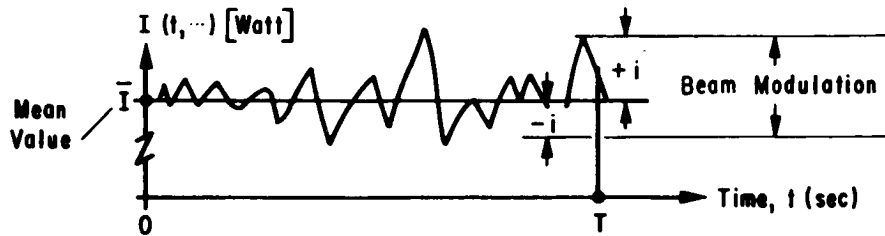
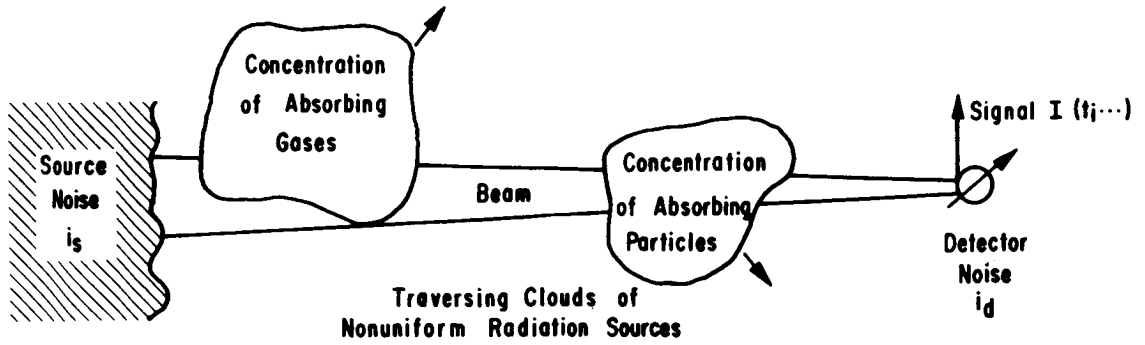


FIGURE 3. BEAM MODULATION

is a small perturbation and (b) that the source fluctuations,  $i_s$ , and the flow modulations,  $K'$ , are uncorrelated. The resulting beam modulation then consists of three parts:

$$i = i_s \frac{\bar{I}_d}{\bar{I}_s} + \bar{I}_d \int_{\text{source}}^{\text{detector}} K'(l, \dots) dl + i_d \quad (7)$$

The first term denotes the fluctuations of the optical background source which have been transmitted to the detector. The second denotes the beam modulations by local flow phenomena, such as passing clouds of absorbing gases or particles. The third term denotes detector noise. The modulation of a single beam thus accounts for any change of radiative power along the entire line of sight. This is not desired. One would like to isolate the local radiation phenomena around the line of minimum beam intersection. Such a retrieval of local information is possible by statistical data reduction method and will be reviewed in the next chapter.

#### IV. REVIEW OF THE CROSSED BEAM CONCEPT

In crossed-beam arrangements, two beams, A and B, are set to choose a local flow region by triangulation. This region extends around the beam normal, that is, around the one which passes the two points of minimum beam separation. Local information from this region will be described by a beam-fixed coordinate system,  $\xi$ ,  $\eta$ ,  $\zeta$ . This system is centered in space at the point of minimum separation on beam B. The  $\xi$  axis follows the beam normal, the  $\zeta$  axis follows beam B, and the  $\eta$  axis is parallel to beam A as shown in Figure 4.

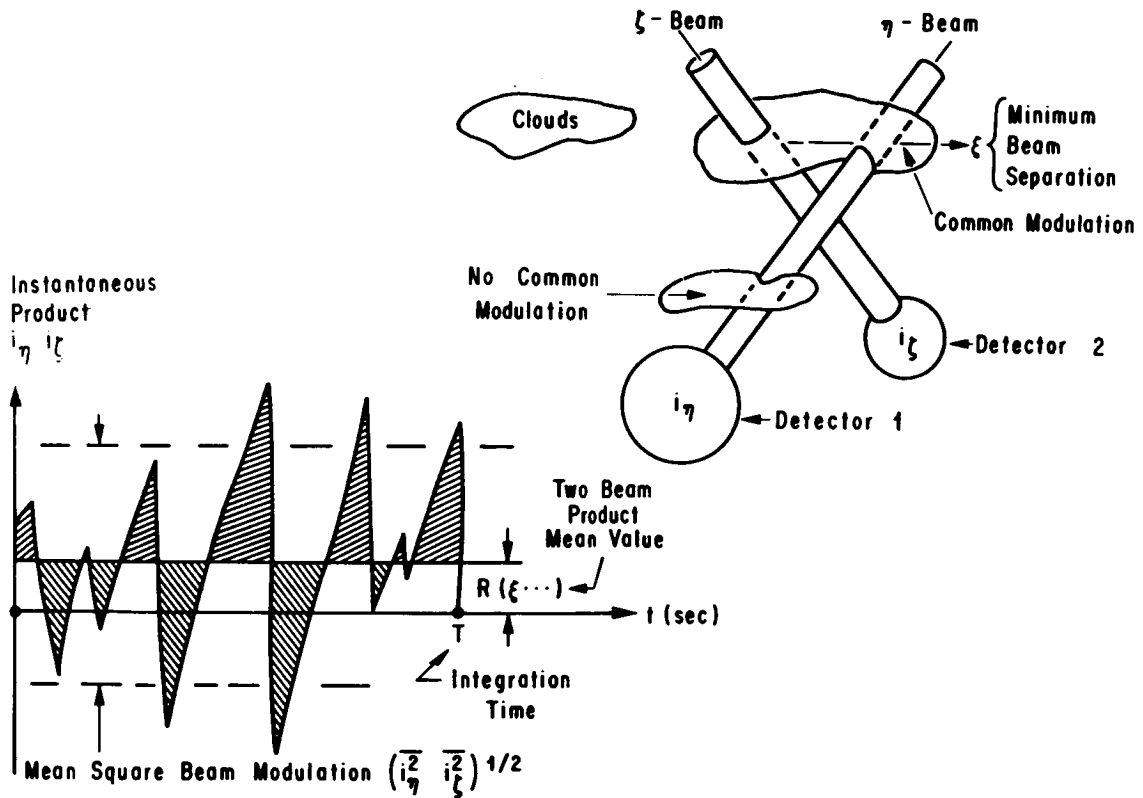


FIGURE 4. RETRIEVAL OF COMMON FLOW MODULATIONS

The beam-fixed coordinates are not necessarily orthogonal since the beams may not intersect at right angles. However, the desired local regions and the wanted optical signals in the local region are most easily expressed in these beam-fixed coordinates, which will be used throughout the paper.

The wanted signals,  $K$ , from the vicinity of the origin  $\vec{\xi} = 0$  contribute to the detected beam modulation,  $i$ , in a way given in equation (7). Replacing the beam coordinate  $\ell$  in equation (7) with either  $\eta$  or  $\zeta$ , we may express the contributions by denoting a beam point,  $\ell = \eta$  or  $\ell = \zeta$ , in an earth-fixed reference frame  $\vec{x}$ . Substituting the associated transformations from beam to earth-fixed frames,  $\vec{x} = \vec{x}(\xi, \eta, \zeta)$ , into equation 7, the beam modulations become:

$$i_{\eta} = i_{\eta N} + i_{\eta M} = i_{\eta N} + \bar{I}_{\eta} \int_{\text{source}}^{\text{detector}} K' \left[ \vec{x}(\xi, \eta, 0); t; \lambda \right] d\eta \quad (8)$$

and

$$i_{\zeta} = i_{\zeta N} + i_{\zeta M} = i_{\zeta N} + \bar{I}_{\zeta} \int_{\text{source}}^{\text{detector}} K' \left[ \vec{x}(0, 0, \zeta); t; \lambda \right] d\zeta . \quad (9)$$

Each beam modulation accounts for radiation sources along the entire line of sight. Local information is then retrieved from these integrated signals by determining statistically which modulations are "common" to both beams. The concept of "common" signals has been developed in the analysis of communication signals and random vibrations [6] and is based on "lagged product calculations." The two modulations,  $i_{\eta}$  and  $i_{\zeta}$ , are analyzed for common signals by multiplying them with each other and by averaging this instantaneous product over time. This gives a "two-beam product mean value":

$$G(\xi, \dots) = \overline{[i_{\eta}(t) i_{\zeta}(t)]}_{\xi} . \quad (10)$$

The instantaneous product oscillates between positive and negative values, and these oscillations will cancel each other, at least partially, when the product is averaged by integrating it over time (see Fig. 4). Two beams are said to have no common modulations if the two-beam product mean value vanishes. This complete cancellation will occur when the increase or decrease of radiative power in one beam is independent of the power changes in the other beam in the sense that the change in the other beam may be positive or negative with equal likelihood. Typical examples for such independent beam modulations are the combined source and detector noise and any cloud which traverses only one beam without hitting the other beam. Conversely, common beam modulations are produced by any physical process which produces power changes in both beams — these have either the same or opposite signs. A typical example for such a common modulation is a cloud which moves through both beams.

Common modulations can be retrieved even if their magnitude is very small relative to the independent beam modulations. Such cases are recognized by the large amplitude of the instantaneous product as illustrated in Figure 4. Suppose that the beam modulation is split into the independent or "noise" component and the common component:

$$i_{\eta} = i_{\eta N} + i_{\eta C}$$

$$i_{\xi} = i_{\xi N} + i_{\xi C} \quad .$$
(11)

The two-beam product mean value may then be written as a sum of the component product mean values:

$$\overline{i_{\eta} i_{\xi}} = \overline{i_{\eta N} i_{\xi N}} + \overline{i_{\eta N} i_{\xi C}} + \overline{i_{\eta C} i_{\xi N}} + \overline{i_{\eta C} i_{\xi C}} \quad .$$
(12)

The first three of these component products have at least one noise component; i. e. , they will cancel each other if one only integrated long enough. In the limit of infinite integration time, the two-beam product mean value will thus be provided by the common modulations even if these modulations are almost infinitesimal:

$$G(\xi; \dots) = \lim_{T \rightarrow \infty} \overline{i_{\eta} i_{\xi}} = \lim_{T \rightarrow \infty} \overline{i_{\eta C} i_{\xi C}} \quad .$$
(13)

The physical interpretation of the above two-beam product mean value,  $G$ , assumes that common modulations  $i_{\eta C}$  and  $i_{\xi C}$  are produced by a concentration of radiation sources which traverses both beams. As discussed in the previous chapter, this light source concentration may be any inhomogeneous distribution of emitting, absorbing, or scattering centers which could have been produced by the transport of passive additives, such as aerosols, by local two-phase flow phenomena, such as evaporation or condensation, and by photochemical processes. The word "cloud" is used from this point onward to describe such an inhomogeneous distribution of radiation sources. Actual clouds do, in fact, provide a very good large-scale picture of a concentration of scattering and absorbing particles. However, in the context of this paper, the word "cloud" is also used to describe a concentration of light "sources" in small scale flows, such as wind tunnel and jet air streams.

The moving cloud which traverses both beams has been introduced as a physical model of common beam modulations. Whenever this model applies, a maximum two-beam product mean value will be produced by a series of clouds which pass through a beam intersection,  $\vec{\xi} = 0$ . If, on the other hand, the beams are separated by more than a cloud diameter, then one cloud cannot be common to both beams, and the two-beam product mean value should vanish. Therefore, "common" beam modulations,  $i_{\zeta C}$  and  $i_{\eta C}$ , defined by the line integrals in equations (8) and (9), can only come from those portions of the line of sight which extend around the beam intersection,  $\vec{\xi} = 0$ , by a typical cloud diameter,  $L$  on the beam direction  $\eta$  or  $\zeta$ :

$$i_{\eta C} = \bar{I}_{\eta} \int_{-L_{\eta}}^{+L_{\eta}} K'[\vec{x}(\xi, \eta, 0); t; \lambda] d\eta \quad (14)$$

and

$$i_{\zeta C} = \bar{I}_{\zeta} \int_{-L_{\zeta}}^{+L_{\zeta}} K'[\vec{x}(0, 0, \zeta); t; \lambda] d\zeta . \quad (15)$$

Substitution of equations (14) and (15) into equation (13) gives a normalized two-beam produce mean value:

$$R(\xi; \lambda) = \frac{G(\xi, \dots)}{\bar{I}_{\eta} \bar{I}_{\zeta}} = \lim_{T \rightarrow \infty} \frac{\overline{i_{\eta} i_{\zeta}}}{\bar{I}_{\eta} \bar{I}_{\zeta}} \quad (16)$$

$$= \int_{-L_{\eta}}^{+L_{\eta}} \int_{-L_{\zeta}}^{+L_{\zeta}} K'[\vec{x}(\xi, \eta, 0); t; \lambda] K'[\vec{x}(0, 0, \zeta); t; \lambda] d\eta d\zeta .$$

The produce of two line integrals in equation (16) has been expressed by an area integral and a "homogeneity" term:

$$R(\xi; \lambda) = \int_{\text{cloud area}} \int K'[\vec{x}(\xi; 0; 0); t; \lambda] K'[\vec{x}(0, -\eta; \xi); t; \lambda] d\xi d\eta + \int_{-L}^{+L} \eta g_{KT} d\eta \quad (17)$$

The second integral is called "homogeneity" term, because the integrand,  $g_{KT}$ , will vanish in statistically homogeneous fields of turbulence [7]. In inhomogeneous fields,  $g_{KT}$  does not vanish. However, the line integral over  $g_{KT}$  will still vanish as long as the change of  $g_{KT}$  is a linear or odd function of the translational distance along the  $\eta$ -beam [3]. Inhomogeneities which deviate from the linear variation with translational distance inside a typical cloud cross section will not be encountered very often. Neglecting this inhomogeneous term, we find that the normalized two-beam product mean value may be expressed by an area integral as illustrated in Figure 5.

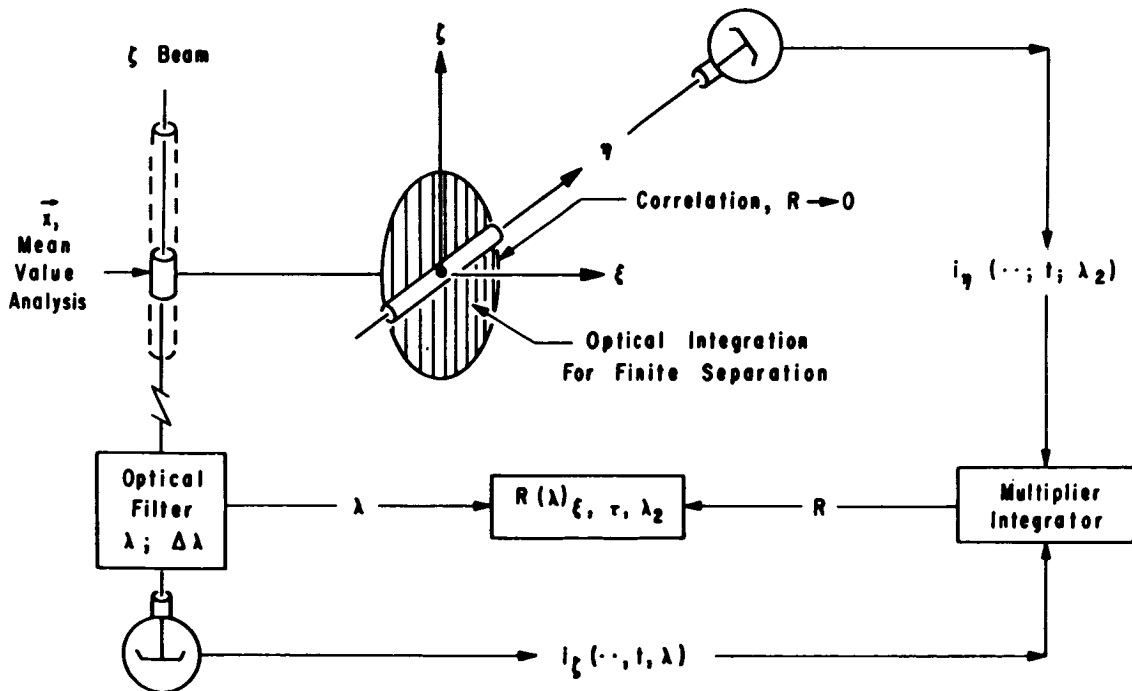


FIGURE 5. CROSSED-BEAM SPECTROSCOPY



$$R(\xi; \lambda; \dots) = \int_{\text{cloud area}} \int K'[\vec{x}(\xi, 0, 0); t; \lambda] K'[x(0, -\eta, \zeta); t; \lambda] d\zeta d\eta. \quad (18)$$

The integrand in equation (18) describes the lagged product mean value between two point observers. The first observer is fixed to the downstream point of minimum beam separation,  $\vec{x}(\xi; 0; 0)$ . The position of the other observer is variable over the "beam front," i. e. , over the plane which is generated by moving the upstream beam parallel to the downstream beam. The integral may thus be described as an area integral over the beam front. Furthermore, the integrand will vanish for those portions of the beam front which are separated from the fixed point by a distance exceeding the diameter of a cloud cross section. The integration limits may thus be reduced to a disc-shaped "cloud area," the radius of which exceeds the largest diameter of all passing cloud cross sections.

The above results indicate that a two-beam correlation compares a cross section with an outside point on the same streamline. Individual streamlines may thus be selected by adjusting the position of this point. This resolution of individual streamlines from a remote distance has been verified by separating two mutual perpendicular beams along streamlines in subsonic and in supersonic jets. These measurements gave convection speed probes within the accuracy of the hotwire points. Crossed-beam methods can thus retrieve individual flow phenomena inside a typical cloud volume [1, 2, 3].

## V. CROSS-BEAM SPECTROSCOPY

The term "cross-beam spectroscopy" has been coined for the interpretation of crossed-beam tests that have been conducted at different optical wave lengths [4]. Such tests contain spectroscopic information about a local flow region which has been selected by triangulation of two beams and which has been isolated by statistical cross-correlation. Although the resolution in space does in general depend on the size of local clouds, the crossed-beam tests will very often isolate local regions in flows with a known direction with a resolution approaching the local beam diameter (see section VI). The objective of crossed-beam spectroscopy is thus to retrieve the thermodynamic state variables and turbulence parameters in a remote or inaccessible area, the size of which is comparable to the beam diameter.

Consider a crossed-beam arrangement where an optical filter has been added to one of the photodetection systems (see Fig. 5). This filter is set at a variable optical wave length,  $\lambda$ , whereas the experimental band pass of the second detector,  $\lambda_2 + \Delta\lambda/2 \leq \lambda \leq \lambda_2 + \Delta\lambda/2$ , remains unchanged. According to equation (18), the results of such crossed-beam tests may be expressed by

$$R(\lambda; \dots) = \frac{\overline{i_{\xi}(\lambda; t) i_{\eta}(\lambda_2; t)}}{\overline{I_{\xi}(\lambda) I_{\eta}(\lambda_2)}} = \int_{\text{cloud area}} \int K'[\vec{x}(\xi; 0; 0); t; \lambda] K'[\vec{x}(0; -\eta; \zeta); t; \lambda_2] d\zeta d\eta .$$

The interpretation of this function in terms of thermodynamic state variable requires relating  $R(\lambda; \dots)$  to these variables. The main difference between conventional spectroscopy and cross-beam spectroscopy is now that we deal with local optical fluctuations,

$$K' = K(p, P, T) - K(\bar{p}, \bar{P}, \bar{T}) , \quad (21)$$

which are caused by the fluctuations of the thermodynamic state variables:

$$\begin{aligned} p'(\vec{x}, t) &= p(\vec{x}, t) - \bar{p}(\vec{x}) \\ P'(\vec{x}, t) &= P(\vec{x}, t) - \bar{P}(\vec{x}) \\ T'(\vec{x}, t) &= T(\vec{x}, t) - \bar{T}(\vec{x}) . \end{aligned} \quad (22)$$

Cross-beam spectroscopy has, thus, to be based on the relation between optical and thermodynamic fluctuations. To this purpose, we replace the average values of the thermodynamic state variables with the instantaneous values at a certain time  $t_0$ , which is chosen so that the instantaneous and the average values are numerically equal.

$$\begin{aligned} K(\vec{x}; t_0) &= K(p = \bar{p}; P = \bar{P}; T = \bar{T}; \lambda) \\ &= \bar{K} = \frac{1}{T} \int_{t=0}^{t=T} K(\vec{x}; t) dt . \end{aligned} \quad (23)$$

The fluctuations of equation (22) could thus be conceived as the result of a Taylor series approximation of  $K[p(\vec{x}, t); P(\vec{x}, t); T(\vec{x}, t); \lambda]$  around the time  $t = t_0$ . Furthermore, this Taylor series provides the desired relation between optical and thermodynamical fluctuations:

$$K'(p, T, P, \lambda) = K'(\vec{x}, t, \lambda) = \left[ p' \frac{\partial}{\partial p} + T' \frac{\partial}{\partial T} + P' \frac{\partial}{\partial P} \right] K(\bar{p}, \bar{T}, \bar{P}, \lambda) \quad (24)$$

$$+ \frac{1}{2} \left[ p' \frac{\partial}{\partial p} + T' \frac{\partial}{\partial T} + P' \frac{\partial}{\partial P} \right]^2 K(p + \theta p', T + \theta T', P + \theta P', \lambda)$$

with  $0 < \theta < 1$ .

Substituting the Taylor series for  $K'(\vec{x}, t)$  into equation (24), we may rewrite the spectral curve as

$$R(\lambda; \dots) = \frac{\partial \bar{K}}{\partial P} \int \int \overline{p'(\vec{x}, t) K'(\vec{x} + \vec{\xi}, t + \tau, \lambda_2)} d\eta d\xi$$

$$+ \frac{\partial \bar{K}}{\partial T} \int \int \overline{T'(\vec{x}, t) K'(\vec{x} + \vec{\xi}, t + \tau, \lambda_2)} d\eta d\xi$$

$$+ \frac{\partial \bar{K}}{\partial P} \int \int \overline{P'(\vec{x}, t) K'(\vec{x} + \vec{\xi}, t + \tau, \lambda_2)} d\eta d\xi$$

$$+ \frac{1}{2} \left\{ \int \int \frac{\partial^2 \bar{K}}{\partial p^2} \overline{p'^2 K'} + \frac{\partial^2 \bar{K}}{\partial P^2} \overline{P'^2 K'} + \frac{\partial^2 \bar{K}}{\partial T^2} \overline{T'^2 K'} \right\} d\eta d\xi$$

$$+ \iint \left\{ \frac{\partial^2 \bar{K}}{\partial p \partial P} \overline{p' P' K'} + \frac{\partial^2 \bar{K}}{\partial p \partial T} \overline{p' T' K'} + \frac{\partial^2 \bar{K}}{\partial T \partial P} \overline{T' P' K'} \right\} d\eta d\xi \quad (25)$$

In this equation, the second order terms of the Taylor series are weighted with triple products. As long as the fluctuations of the thermodynamic state variables are small perturbations, these terms may be neglected. If these fluctuations are large, the second order terms may still be neglected, as long as two of the fluctuations in the triple product are not, or only weakly, correlated. If the fluctuations are both large and correlated, the second order terms may still be

suppressed in special cases where the optical absorption band can be chosen so that the mixed second derivatives of the mean extinction coefficient are small. The pure second derivatives in the fourth row of equation (25) should contribute very little since the associated triple product contains only one oscillating part. For example, these triple products would vanish even if the thermodynamic state variables  $p'$ ,  $P'$ , or  $T'$  and the optical fluctuations  $K'$  are perfectly correlated by the same harmonic wave.

In view of the above considerations, we assume that second order terms of the Taylor series make no contribution in most cases of practical interest. The last relation may then be approximated by

$$R(\lambda; \dots) = [Q_p \frac{\partial}{\partial p} + Q_P \frac{\partial}{\partial P} + Q_T \frac{\partial}{\partial T}] \bar{K}(\bar{p}, \bar{P}, \bar{T}, \lambda_1) \quad (26)$$

In this expression, the "Turbulence Factors"

$$\begin{aligned} Q_p &= \overline{\int \int p'(\vec{x}, t) K_2'(\vec{x} + \vec{\xi}, t, \lambda_1) d\eta d\xi} \\ Q_P &= \overline{\int \int P'(\vec{x}, t) K_2'(\vec{x} + \vec{\xi}, t, \lambda_2) d\eta d\xi} \\ Q_T &= \overline{\int \int T'(\vec{x}, t) K_2'(\vec{x} + \vec{\xi}, t, \lambda_2) d\eta d\xi} \end{aligned} \quad (27)$$

are independent of  $\lambda$ , and may be treated as constants. The spectrum curve  $R(\lambda_1)$  may thus be approximated as a linear superposition of the three mean value derivatives  $\partial \bar{K} / \partial p$ ,  $\partial \bar{K} / \partial P$  and  $\partial \bar{K} / \partial T$ , which may be functions of  $\lambda$ .

Equations (26) and (27) provide the basis for extending spectroscopic methods from stagnant gases to nonuniform gases with time variations. All radiation sources outside the correlation disc are suppressed by the correlation analysis. Furthermore, the optical integration inside the cloud area considers only variable positions of the second observer. The position of the first observer, which was used in the Taylor series (equation (25)), is not subject to integration. In fact, the absorption fluctuation at this position could have been taken out of the area integral of equation (20). Equation (25) may thus be viewed as a system of nonlinear equations between several crossed-beam observations  $R_1(\lambda = \lambda_1; \dots)$ ;  $R_2(\lambda = \lambda_2; \dots)$ ;  $R_3(\lambda = \lambda_3; \dots)$ ; the local thermodynamic state variables at the

outside point and the turbulence factors. This system of equations has six unknowns:  $\bar{p}$ ;  $\bar{P}$ ;  $\bar{T}$ ;  $Q_p$ ;  $Q_P$  and  $Q_T$ . The general application of crossed-beam spectroscopy would therefore require that we repeat the crossed-beam experiments at six different optical wavelengths. The derivation of the next chapter indicates, however, that in many practical cases, two observations will be sufficient.

The concept of crossed-beam spectroscopy may become very important for turbulence investigations since it may provide experimental insight in two problem areas which have so far defied experimental and theoretical solutions. These problems are the relation between mean values and fluctuations and the independent turbulent transport of heat and mass. The relationship between mean values and fluctuations is inherent in equation (26), which relates the time averages, pressures and temperatures to purely fluctuating quantities. The separation of heat and mass transfer becomes possible by a study of the turbulence factors,  $Q_p$ ,  $Q_P$ , and  $Q_T$ , which disentangle partial pressure fluctuations, static pressure fluctuations, and temperature fluctuations. They may thus be used to find (1) which thermodynamic state variable is primarily responsible for the optical fluctuations  $K'$ , and (2) how the space-time correlations of these fluctuations differ. We therefore hope that the general concepts of this chapter may find a wide and challenging range of applications. Simple applications which we will use for future experimental verification of crossed-beam spectroscopy are outlined in the next section.

## VI. APPLICATION OF MOLECULAR SPECTROSCOPY

The measurement of crossed beam spectra alone is not sufficient to obtain the local thermodynamic properties of a local flow region. These properties may, however, be retrieved if the mean absorption or emission spectra, or at least some spectroscopic constants, are known from laboratory studies. The exact amount of such a priori knowledge which is needed in crossed-beam spectroscopy depends on the local absorption or emission characteristics. We will now proceed to outline the necessary a priori knowledge for a special flow where the entire local absorption is provided by molecular absorption bands of pressure-broadened lines. This illustration was suggested and treated by W. O. Davies [5] for a hypothetical flow where only one of the fluctuations  $p'$ ,  $P'$  or  $T'$  existed. The following treatment will consider all three thermodynamic fluctuations simultaneously, since this is what happens in most turbulent flows. However, the relationships for  $K(\lambda, \bar{p}, \bar{P}, \bar{T})$ , which are being used, will be taken from original treatment [4].

The application of molecular spectroscopy to the flow of a weakly or strongly absorbing gas is discussed in terms of two hypothetical experiments outlined schematically in Figure 6. In the first experiment an absorption cell is filled with a stagnant gas of partial pressure  $\bar{p}$ , static pressure  $\bar{P}$ , and static temperature  $\bar{T}$ . The length of cell,  $\ell$ , is adjusted to approximate the diameter of the beam which will be used in the crossed-beam arrangement. A narrow beam of radiation is traversing the cell and the radiative power in this beam is measured with a grating spectrograph, which is set at the optical wave length  $\lambda$  and spectroscopic resolution  $\Delta\lambda$ . The spectrograph measures a mean intensity  $\bar{I}_\zeta$ , which is then used to establish the absorption coefficient  $K$  as a function of wave length  $\lambda$  and the thermodynamic state variables. As a result one obtains the molecular absorption spectrum

$$K(\lambda, \bar{p}, \bar{P}, \bar{T})_{\Delta\lambda} = \bar{K} = \frac{2.303}{\ell} \log_{10} \frac{\bar{I}_\zeta}{\bar{I}_{\text{source}}} \quad (28)$$

In the second experiment the spectrophotometer, which has been used at the gas cell, is transferred to the crossed-beam test site and is employed to record

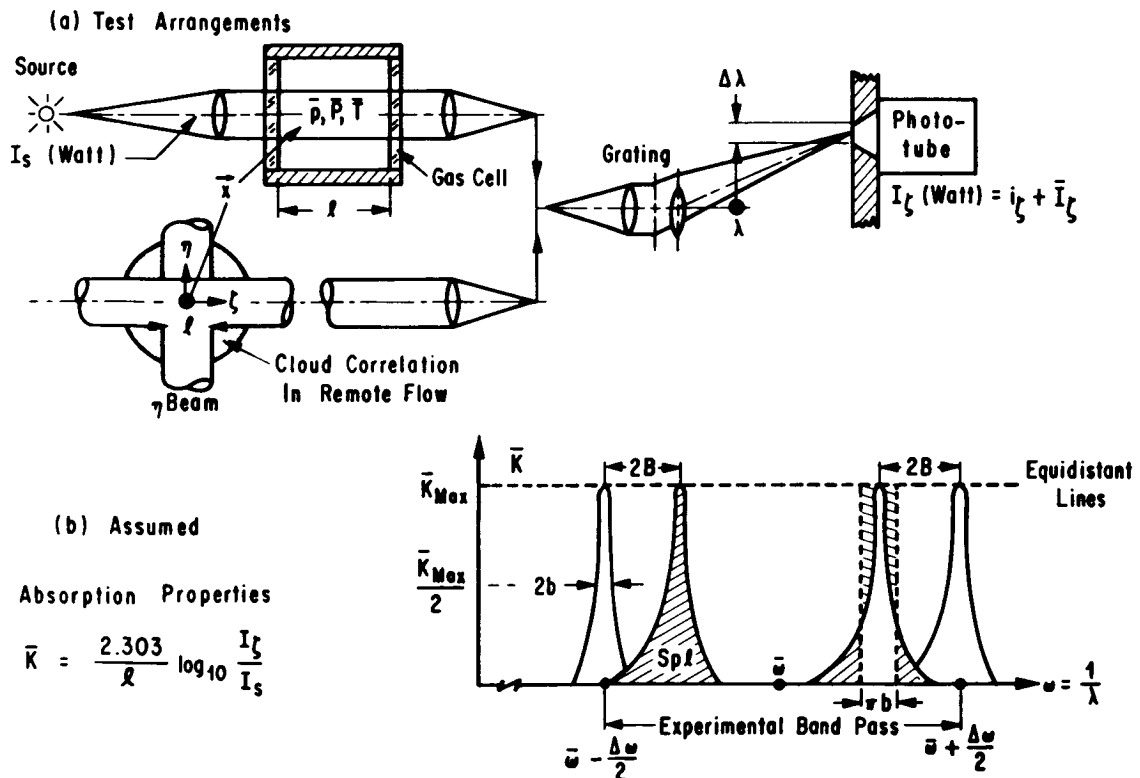


FIGURE 6. APPLICATION OF MOLECULAR SPECTROSCOPY

the time history of the radiative power  $I_\zeta$  in the  $\zeta$ -beam. This record is then used to calculate the crossed-beam spectrum of a remote flow region by adding lagged products.

$$R(\lambda; \Delta\lambda)_{\bar{p}; \bar{P}; \bar{T}, \lambda_2} = - \frac{\overline{i_\zeta(t; \lambda; \Delta\lambda)} \overline{i_\eta(t; \lambda_2; \Delta\lambda_2)}}{\overline{I_\zeta(\lambda, \Delta\lambda)} \overline{I_\eta(\lambda_2; \Delta\lambda_2)}} \quad (29)$$

We now assume that both the cell and the local flow region are transparent except for an isolated band of weak or strong rotational lines. Furthermore, both hypothetical experiments will always use identical settings of the monochromator. The relation between the two spectra is then given by equation (26):

$$R(\lambda; \Delta\lambda) = \left[ Q_p \frac{\partial}{\partial p} + Q_P \frac{\partial}{\partial P} + Q_T \frac{\partial}{\partial T} \right] K(\bar{p}; \bar{P}; \bar{T}; \lambda; \Delta\lambda) .$$

For weak and strong lines the absorption coefficient  $K$  becomes independent from the monochromator band pass  $\Delta\lambda$ , if the band pass is small enough, such that molecular band models apply. This is usually the case if the experimental band pass covers a narrow band portion, which contains, however, still several rotational lines. The weak line approximation of the absorption coefficient is

$$\bar{K}_{WL} = \frac{S\bar{p}}{d} \quad (30)$$

In this expression  $S$  and  $d$  describe the rotational line strength and the line spacing of the lines which appear in the experimental band pass. We have approximated both properties by assuming that the molecule absorbs like a rigid rotator. Replacing the optical wave length  $\lambda$  with the optical wave number,

$$\bar{\omega} = \frac{1}{\lambda} \quad \text{"Center of experimental band pass"} \quad (31)$$

the rigid rotator approximation of the rotational line strength,  $S$ , may be expressed by three molecular constants: The band center  $\omega_0$ , (transition between levels with zero rotation); Frank Condon Factor,  $q$ ; and the rotational constant  $B$ .

$$S(\bar{\omega}, \dots) = \frac{1}{\bar{p} \ell} \int_{\text{single line}} K(\omega; \dots) d\omega .$$

$$\cdot \frac{8\pi^3 \omega_0 q}{3k} \frac{|\omega - \omega_0|^2}{\bar{T}} \exp \left\{ (-) \frac{hc |\omega - \omega_0|^2}{4k T B} \right\} . \quad (32)$$

The rigid rotator approximation of the line spacing is related to the rotational constant B, which in turn follows from the molecules moment of inertia:

$$d = 2B = \frac{3k h}{32\pi^3 \omega_0 q \cdot (\text{molecule moment of inertia})} . \quad (33)$$

The strong line approximation of the absorption coefficient depends on the type of band model used. We choose the statistical band model because this model applies to the infrared absorption of water vapor, which occurs in our jet experiments and field tests. This band model gives

$$\bar{K}_{SL} = \sqrt{\frac{Sb\bar{p}}{B^2 \ell}} \quad (34)$$

where B and S denote the rotational constant and line strength given in equations 33 and 32. The half width b denotes an average line width, as shown in Figure 6, and may be related to the known half width  $b_0$  at standard conditions ( $\bar{p}_0 = 1 \text{ atm}$ ,  $\bar{T}_0 = 273.2^\circ \text{ K}$ ):

$$b = b_0 \frac{\bar{p}}{p_0} \sqrt{T_0 / \bar{T}} . \quad (35)$$

Substituting the expressions for S and b into the weak and strong line approximations, the pressure gradients become

$$(a) \frac{\partial \bar{K}_{WL}}{\partial p} = \frac{\bar{K}_{WL}}{\bar{p}} ; \quad (b) \frac{\partial \bar{K}_{SL}}{\partial \bar{p}} = \frac{\bar{K}_{SL}}{2\bar{p}} ; \quad (c) \frac{\partial \bar{K}_{WL}}{\partial P} = 0;$$

$$(d) \frac{\partial \bar{K}_{SL}}{\partial P} = \frac{\bar{K}_{SL}}{2\bar{P}} . \quad (36)$$



In flows with a frozen composition, the mass concentration  $\bar{p}/\bar{P}$  of the absorber is time invariant. The modulations of the partial and static pressures are then related by

$$p'/\bar{p} = P'/\bar{P} \quad \text{"frozen composition."} \quad (37)$$

Substituting this relation into the definition of the turbulence factors, one finds

$$Q_p/\bar{p} = Q_P/\bar{P} \quad \text{"frozen composition."} \quad (38)$$

The last three relations allow a great simplification of the relation between crossed-beam and mean intensity spectra, equation (26). Both limiting cases of weak lines and strong lines with frozen composition have identical pressure terms. This allows us to cover both cases with the same equation:

$$\frac{R(\bar{\omega})}{\bar{K}(\bar{\omega})} \xi = \frac{Q_p}{\bar{P}} + \frac{1}{\bar{K}} \frac{\partial \bar{K}}{\partial T} \frac{Q_T}{T} \quad (39)$$

The pressure term is independent of the optical wave number  $\bar{\omega}$ . The temperature term depends on  $\bar{\omega}$  only very weakly. Neglecting this wave number dependence, crossed-beam and mean intensity spectra become proportional to each other.

The proportionality between crossed-beam and mean intensity spectrum means that crossed-beam measurements might be treated as ordinary spectra that have been measured in unknown units. Such measurements occur in the spectroscopic analysis of distant stars where the source area and therefore the absolute source intensity are unknown. However, the temperature and composition of such stars have been determined spectroscopically by using band ratio techniques. The same is true for crossed-beam measurements. Although the size of the common clouds is not known at any instant of time, band ratio techniques can be applied to retrieve temperatures and mass concentrations.

Any "ratio" technique requires us to compare two observations, which have been obtained at two different wave numbers. Let us suppose that both hypothetical experiments have been repeated by centering the experimental band pass on the optical wave numbers  $\bar{\omega} = \bar{\omega}_2$ . The measurements at  $\bar{\omega} = \bar{\omega}_1$  and  $\bar{\omega}_2$  then provide a band ratio for both the gas cell and the flow. Furthermore, these ratios are approximately equal, since the spectra are approximately proportional to each other.

$$\frac{R(\bar{\omega}_1; \dots)}{R(\bar{\omega}_2; \dots)} = \frac{K(\bar{\omega}_1; \bar{p}, \bar{P}, \bar{T})}{K(\bar{\omega}_2; \bar{p}, \bar{P}, \bar{T})}$$

The crossed-beam experiment is therefore approximately the ratio of two mean absorption coefficient measurements which in turn is directly related to temperature. A multitude of different temperature relations can be derived by using portions of the same or different bands and one or two molecules. Four important cases are summarized in Table I. These cases have been derived by substituting the weak or strong line approximations, equations (30) and (34), and the rotational line strength, equation (32) into the band ratio, equation (37), and by solving the resultant expression for temperature. The results indicate that time-averaged temperatures can be measured locally in turbulent flows, if molecular spectroscopy provides the following spectroscopic constants for each of the two band regions: the wave number  $\omega_0$  of the band center, the rotational constant B of the molecule, the half width  $b_0$  at standard conditions and the Frank Candon factors, q.

Mean pressures and the associated turbulence factor are more difficult to measure than temperature. A two-line approximation is mathematically possible only if the temperature fluctuation term of equation (39) can be suppressed. This suppression is possible by choosing the center wave number  $\bar{\omega}$  of the experimental band pass in such a way that the temperature gradient  $\partial\bar{K}/\partial T$  vanishes when being integrated over the experimental band pass. Such settings are illustrated in Figure 7, and may be derived by plotting the wave number dependence of  $\partial\bar{K}/\partial T$ . A partial differentiation of the weak line approximation gives

$$\frac{\partial}{\partial T} \bar{K}_{WL}(\omega; \dots) = \frac{\bar{K}_{WL}}{\bar{T}} \left( \frac{hc(\omega - \omega_0)}{4k B T} - 1 \right). \quad (40)$$

The partial differentiation of the strong line approximations leads to

$$\frac{\partial}{\partial T} \bar{K}_{SL}(\omega; \dots) = \frac{K_{SL}}{2\bar{T}} \left( \frac{hc(\omega - \omega_0)^2}{4k B T} - \frac{3}{2} \right). \quad (41)$$

Both relations are plotted in Figure 7. Then plots indicate that the temperature term will vanish with  $\partial\bar{K}/\partial T$  at three different settings. The first is the band center  $\bar{\omega} = \omega_0$ . The other two settings are symmetric from the band center by a distance which depends on temperature. For weak lines, temperature fluctuations will be suppressed if the monochromator is adjusted to

$$\bar{\omega}_{WL} = \omega_0 \pm \Omega(T). \quad (42)$$

TABLE I. TWO-LINE APPROXIMATION OF TIME AVERAGED LOCAL TEMPERATURES

Band Choice	Average Thermodynamic Properties
<p>1. Two Weak Line Regions:</p> <p>A. Different Molecules and Band Systems</p>	$\bar{T} = \frac{\frac{hc}{4k} \left[ \frac{(\omega_1 - \omega_0)^2}{B_1} - \frac{(\omega_2 - \omega_0')^2}{B_2} \right]}{\ln \left[ \frac{R_1 \omega_0' q_2  \omega_2 - \omega_0'  B_1}{R_2 \omega_0 q_1  \omega_1 - \omega_0  B_2} \right]}$
<p>B. Same Molecular Band System</p>	$\bar{T} = \frac{\frac{hc}{4kB} \left[ (\omega_1 - \omega_0)^2 - (\omega_2 - \omega_0')^2 \right]}{\ln \left[ \frac{R_1  \omega_2 - \omega_0' }{R_2  \omega_1 - \omega_0 } \right]}$
<p>2. Two Strong Line Regions:</p> <p>A. Different Molecules and Band Systems</p>	$\bar{T} = \frac{\frac{hc}{8k} \left[ \frac{(\omega_2 - \omega_0')^2}{B_2} - \frac{(\omega_1 - \omega_0)^2}{B_1} \right]}{\ln \left[ \frac{R_1 \left( \omega_0' q_2 (\omega_2 - \omega_0') B_1^2 b_{02} \right)^{1/2}}{R_2 \left( \omega_0 q_1 (\omega_1 - \omega_0) B_2^2 b_{01} \right)} \right]}$
<p>B. Same Molecular Band System</p>	$\bar{T} = \frac{\frac{hc}{8kB} \left[ (\omega_2 - \omega_0')^2 - (\omega_1 - \omega_0)^2 \right]}{\ln \left[ \frac{R_1 \left( \frac{\omega_2 - \omega_0'}{\omega_1 - \omega_0} \right)^{1/2}}{R_2} \right]}$

Suppression of Temperature Fluctuations  
By Special Choice of  $\bar{\omega}$ , Such That

$$\left\langle \frac{\partial \bar{K}}{\partial T} \right\rangle_{\text{exp}} = \frac{1}{\Delta\omega} \int_{\bar{\omega} - \frac{\Delta\omega}{2}}^{\bar{\omega} + \frac{\Delta\omega}{2}} \frac{\partial \bar{K}}{\partial T}(\omega, T) d\omega = 0$$

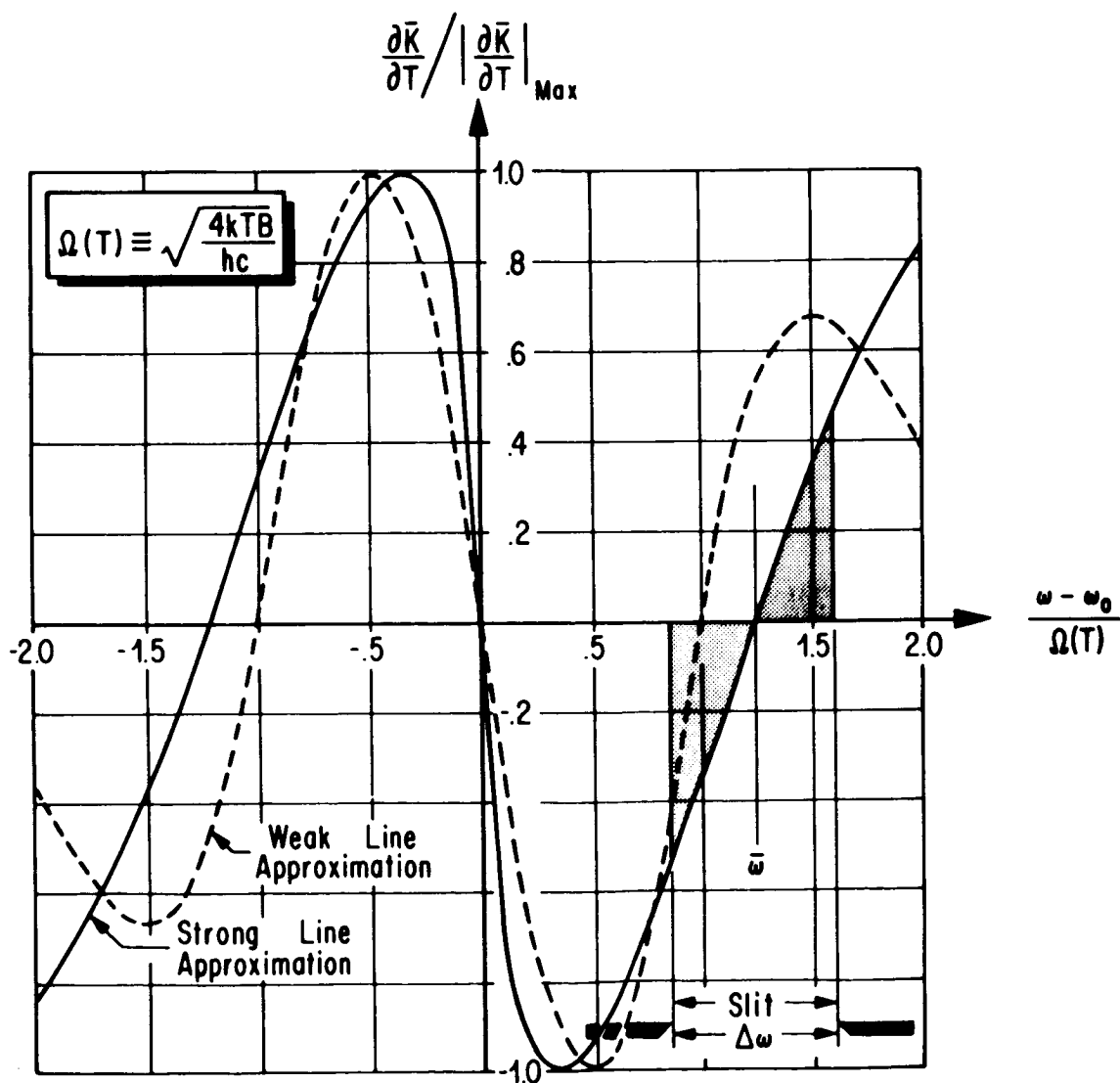


FIGURE 7. SPECTROSCOPIC DISCRIMINATION BY INTEGRATION ACROSS EXPERIMENTAL BANDPASS

Here,  $\Omega(T)$  is given by

$$\Omega(T) = \sqrt{\frac{4k \bar{T} B}{hc}} \quad (43)$$

For strong line, the spectroscopic discrimination against temperature fluctuations requires

$$\omega_{SL} = \omega_o \pm 1.25 \Omega(T) \quad (44)$$

Whenever such a special wave number is chosen, the simplified relation between crossed-beam and mean absorption spectra, equation (28), provides a system of equations that can be solved for mean mass concentrations or the turbulence factors. Moreover, this solution requires only two "lines." The algebra indicates that mean mass concentrations may be obtained from crossed-beam observations at one weak and one strong line.

$$\frac{\bar{p}}{\bar{p}} = 4 \frac{b_o}{\bar{P}_o \ell} (T_o/T)^{\frac{1}{2}} \left\{ \frac{S^{\frac{1}{2}}(\bar{\omega}_{SL}) R(\bar{\omega}_{WL})}{S(\bar{\omega}_{WL}) R(\bar{\omega}_{SL})} \right\}^2 \quad (45)$$

Turbulence factors can be derived in more than one way. Several important combinations of weak or strong lines with or without the suppression of temperature fluctuations are given in Table II. Although mean concentration and turbulence measurements are more complicated than temperature measurements, they do not require more a priori knowledge of the spectroscopic constants.

## VII. SUMMARY

Crossed-beam arrangements employ two narrow-field-of-view photo-detection systems to select a remote or inaccessible flow region by triangulation. Local variations of radiative power in this region are then isolated by retrieving the modulations of the two photodetector outputs which are common to the two lines of sight. This retrieval of common signals has been used earlier in communication and random vibration theory and requires us to add the products of the observed modulations of the photodetector outputs. The resulting "two beam product mean value" may be interpreted as the average modulation from a cloud

TABLE II. TWO-LINE MAPPING OF TURBULENCE PARAMETERS

Spectroscopic Discrimination	Space-Time Covariance Of Thermodynamic State Variations
1. One Weak Line and the Proper Choice of $\bar{u}_{WL}$ and $\Delta u_{WL}$	$Q_{\bar{p}} = \iint \overline{p'(\vec{x}, t) \cdot K_2'(\vec{x} + \vec{\xi}, t + \tau, \lambda_2)} d\eta d\xi = 2R_{WL} \cdot B_{WL} / \bar{S}_{WL}$
2. Two Weak Lines	$Q_{\bar{T}} = \iint \overline{T'(\vec{x}, t) \cdot K_2'(\vec{x} + \vec{\xi}, t + \tau, \lambda_2)} d\eta d\xi$ $= \frac{B_1 \cdot R_1 \cdot \bar{S}_2 - B_2 \cdot R_2 \cdot \bar{S}_1}{B_1 \cdot \bar{S}_2 \cdot \langle \partial \bar{K} / \partial T \rangle_1 - B_2 \cdot \bar{S}_1 \cdot \langle \partial \bar{K} / \partial T \rangle_2}$
3. One Weak Line and One Strong Line with Frozen Composition	$Q_{\bar{T}} = \frac{\frac{B_{WL} \cdot R_{WL}}{\bar{S}_{WL}} - \frac{B_{SL} \cdot R_{SL}}{2} \sqrt{\frac{p_0'}{\bar{S}_{SL}} \cdot (\bar{T}/T_0)^{1/2}}}{\frac{B_{WL}}{\bar{S}_{WL}} \cdot \langle \partial \bar{K} / \partial T \rangle_{WL} - \frac{B_{SL}}{2} \cdot \langle \partial \bar{K} / \partial T \rangle_{SL} \cdot \sqrt{\frac{p_0'}{\bar{S}_{SL}} \cdot (\bar{T}/T_0)^{1/2}}}$
4. One Strong Line, Frozen Composition, the Proper Choice of $\bar{u}_{SL}$ and $\Delta u_{SL}$	$\bar{Q}_{\bar{p}} = R_{SL} \cdot B_{SL} \cdot \sqrt{\frac{p_0'}{\bar{S}_{SL}} \cdot (\bar{T}/T_0)^{1/2}}$
5. Two Strong Lines	$Q_{\bar{T}} = \frac{B_1 \cdot R_1 \cdot \sqrt{\bar{S}_2} - B_2 \cdot R_2 \cdot \sqrt{\bar{S}_2}}{B_1 \cdot \sqrt{\bar{S}_2} \cdot \langle \partial \bar{K} / \partial T \rangle_1 - B_2 \cdot \sqrt{\bar{S}_1} \cdot \langle \partial \bar{K} / \partial T \rangle_2}$

which passed both lines of sight. However, in flows with a known direction, one can also retrieve local information inside a cloud sized volume by separating the beams along a streamline. The two-beam product mean value will then compare a flow cross section (beam front) with an outside point on the same streamline. Individual streamlines may thus be selected by adjusting the position of the outside point. This selection of streamline inside a cloud has been verified experimentally by measuring velocity profiles in subsonic and supersonic jets.

The application of spectroscopy to crossed-beam arrangement is needed for the interpretation of two-beam product mean values which have been measured at different optical wave numbers. Such a "crossed-beam spectrum" does contain spectroscopic information about a local flow region which has been selected by triangulation and which has been isolated by digital cross correlation. The relation between crossed-beam spectra and conventional mean absorption spectra is derived. The inspection of this relation reveals that the mean values of the thermodynamic state variables  $\bar{p}$ ,  $\bar{P}$  and  $\bar{T}$ , as well as certain turbulence factors  $Q_p$ ,  $Q_P$  and  $Q_T$  may be retrieved by repeating crossed-beam experiments at six different optical wave numbers. Such measurements should provide experimental insight in two turbulence problems which have defied experimental and theoretical solutions. These problems are (1) the relation between mean values and fluctuations and (2) the separation of turbulent heat and mass transfer phenomena.

The interpretation of crossed-beam spectra requires an a priori knowledge on the spectroscopic properties of the absorbing flow component. This knowledge may be identified in laboratory experiments or from spectroscopic band models. The use of such laboratory experiments and/or band models is illustrated for a special flow which is transparent except for certain spectroscopic regions, with isolated bands of weak or strong pressure-broadened rotational lines. In this special case, one needs not six but only two wave numbers to retrieve both the mean thermodynamic state variables and the turbulence factors. Furthermore, the a priori knowledge of spectroscopic properties can be identified in terms of the following molecular constants of the absorbing molecule: Band center  $\omega_0$  (transition between rotation free levels), rotational constant  $B$ , half width at standard conditions  $b_0$ , and "Frank Condon Factor"  $q$ .

## REFERENCES

1. Fisher, M. J.; and Krause, F. R.: The Crossed-Beam Correlation Technique. *J. Fluid Mech.*, no. 28, 1967, pp. 705-717.
2. Fisher, M. J.; and Demkevala: Shock Wave Shear Layer Interaction in Clustered Rocket Exhausts. Final Report on Contract NAS8-20408, Oct. 1967.
3. Krause, F. R.: Mapping of Turbulent Fields by Crossing Optical Beams. Invited paper, A. P. S., Division of Fluid Mechanics, Bethlehem, Pa., Nov. 20-22, 1967.
4. Krause, F. R.; Davies, W. O.; and Cann, M. W. P.: The Determination of Thermodynamic Properties with Optical Cross-Correlation Methods. NASA TM X-53647, 1967,
5. Davies, W. O.: Final Report on Contract NAS8-20108, Part II, May 1967.
6. Bendat, J. S.; and Piersol, A. G. P.: Measurement and Analysis of Random Data. John Wiley & Sons, Inc., New York, N. Y., 1966.
7. Krause, F. R.; and Fisher, M. J.: Optical Integration over Correlation Areas in Turbulent Flows. 5th Intern. Congr. Acoustics, paper K65, Liege, Belgium, 1965.



# APPLICATION OF LASER DOPPLER TECHNIQUES TO TURBULENT VELOCITY MEASUREMENT

N 68-18099

By

R. M. Huffaker, E. Rolfe, and  
A. V. Jelalian

## ABSTRACT

---

A laser doppler technique for the measurement of a mean and fluctuating gas velocity has been developed by the Aerophysics Division, Aero-Astrodynamic Laboratory, MSFC. Optical heterodyning of the laser light scattered from the flowing gas with a portion of the incident laser beam split off from a beam splitter will produce a beat signal at the frequency of the Doppler shift due to the motion of the gas. Measurements of the beat signal frequency, together with the geometry of the optical system, determine the flow velocity of the gas. Measurements have been made on wind tunnel and rocket jet type flows over a wide range of velocities and turbulent intensities. These results compare well with other means of instrumentation such as hot wires and Pitot tubes. An outline of the three-dimensional instrument will be given. The parameters that influence the frequency spread and intensity of the heterodyned signal and the effects of aperture size, particle size, particle size distribution, convergence of beams, optics and polarization on the heterodyned signal are discussed.

The potential of this technique for a wind velocity measurement will be given. Coherent versus incoherent detection and the signal-to-noise level equation for atmospheric measurements are presented. Recent experimental results are also included.

---

# PART I. LASER DOPPLER VELOCITY INSTRUMENTATION FOR WIND TUNNEL TURBULENCE AND VELOCITY MEASUREMENTS<sup>ψ</sup>

By

E. Rolfe\* and R. M. Huffaker\*\*

## INTRODUCTION

The objectives of this program were to establish, by analysis and experiment, the basic parameters of the measurement of a laser doppler velocity instrument used for the measurement of turbulence; to design and build an experimental prototype three-dimensional laser Doppler velocity instrument for the measurement of vector velocity; and to make feasibility measurements of subsonic turbulence and supersonic velocities in the NASA-George C. Marshall Space Flight Center facilities. The behavior and performance of such an instrument in measurement of turbulence in the Saturn rocket engine were also to be studied.

The program which began about three years ago has been carried out jointly by the Marshall Space Flight Center, Huntsville, Alabama, and the Raytheon Company, Sudbury, Massachusetts.

The program involved detailed analytical work, together with experimentation to verify the analytical results. It included an experimental comparison of the conventional hot-wire anemometer with a laboratory laser Doppler velocity instrument, when used to measure turbulence and velocity in a subsonic flow.

---

<sup>ψ</sup>Paper presented at the George C. Marshall Space Flight Center Specialist Conference on Molecular Radiation and its Application to Diagnostic Techniques, October 5-6, 1967.

\*Raytheon Company, Sudbury, Massachusetts

\*\*NASA, George C. Marshall Space Flight Center

As a result of this work, the basic design parameters for the laser Doppler velocity instrument have been clearly determined, and forms of the important analytical relationships verified experimentally. An experimental comparison of the hot-wire anemometer with the laser Doppler velocity instrument indicated an impressive correspondence between the two. Measurements of velocity up to approximately Mach 2 were made in the 7-inch wind tunnel at the George C. Marshall Space Flight Center. These compared well with simultaneous velocity measurements using the existing conventional tunnel instrumentation. Measurements were made both with a 50-milliwatt helium-neon laser and with a one-watt argon laser. The three-dimensional vector velocity measuring instrument is in the final stages of construction.

In the laser Doppler velocity instrument, the velocity of the gas is measured by scattering of particles in the gas, i. e. , by Mie scattering, not Rayleigh or Thomson scattering. Either naturally present or artificially injected particles are used. To keep the measured Doppler frequency within the bandwidth of readily available photomultiplier tubes, the laser beam is set up at right angles to the mean flow velocity, and scattering is measured at a small angle  $\theta$ . Under these conditions the gas velocity for a Doppler shift frequency  $\Delta f$  using laser light of wavelength  $\lambda$  is given by

$$U = \frac{\lambda}{\sin \theta} \Delta f. \quad (1)$$

The intensity of scattered light is independent of velocity and frequency and is given by

$$I = \text{const } V_s N \sigma, \quad (2)$$

where  $N$  is the number of scatterers per unit volume,  $\sigma$  is the total scattering cross section per scatterer, and  $V_s$  is the scattering volume.

The scattering volume within which the flow is measured is determined completely by the wavelength of the laser light and by the f-number  $\equiv F$  of the lens which collects the scattered beam. Dimensions of the scattering volume are, when focused optics are used, given by  $d_A \approx 2.44 \lambda F$  transverse to the optical axis, and  $z \approx 4 \lambda F^2$  in the direction of the optical axis. If parallel

beams are used, their volume of intersection is the scattering volume. In general, focused optics are chosen to minimize the power required from the laser beam.

Figure 1 shows a schematic layout of a laser Doppler velocity instrument measuring velocities in one dimension.

Figure 2 is a photograph of the one-dimensional laboratory Doppler velocity instrument set up with  $\alpha = 90^\circ$ , and a scattering angle of  $8^\circ$ . Readily available optical components are used. It was found that stability from day to day with this class of equipment was very good. All of the receiving equipment, including light stops, photomultiplier and pre-amplifiers are assembled in one cylindrical, shielded container seen at the left hand end of the photograph.

The key waveforms of the signals measured at the photomultiplier anode are shown in Figure 3. The first waveform, as displayed on a cathode ray oscilloscope, shows a wave whose frequency and amplitude are both modulated in accordance with the turbulence fluctuations of the gas velocity and density. Since all the information on velocity, both mean and turbulent, is contained in the frequency of the photomultiplier output wave, an amplitude limiter circuit is used in the electronic signal processing apparatus to remove amplitude variations. This is followed by a frequency discriminator circuit whose output amplitude is proportional to input frequency, giving a display of frequency shift,  $\Delta f$ , with respect to time. The important point to note is that this wave contains all the information which is conventionally measured with respect to turbulence; namely, intensity, scale and power spectrum. Also, as compared with the direct output from the photomultiplier, which cannot be recorded because its frequency is too high, the frequency shift versus time display can be recorded directly on magnetic tape. This is because the maximum frequencies contained in it are at the most 200 kHz, even in a turbulent flow stream of Mach number greater than 1.

Finally, this frequency versus time waveform can be spectrum analyzed to give the power spectrum of the turbulence.

In early work on the laser Doppler velocity instrument, it was considered that a good method of signal processing would be to spectrum analyze the signal directly out of the photomultiplier anode. Further study has shown this to be undesirable for the following reasons.

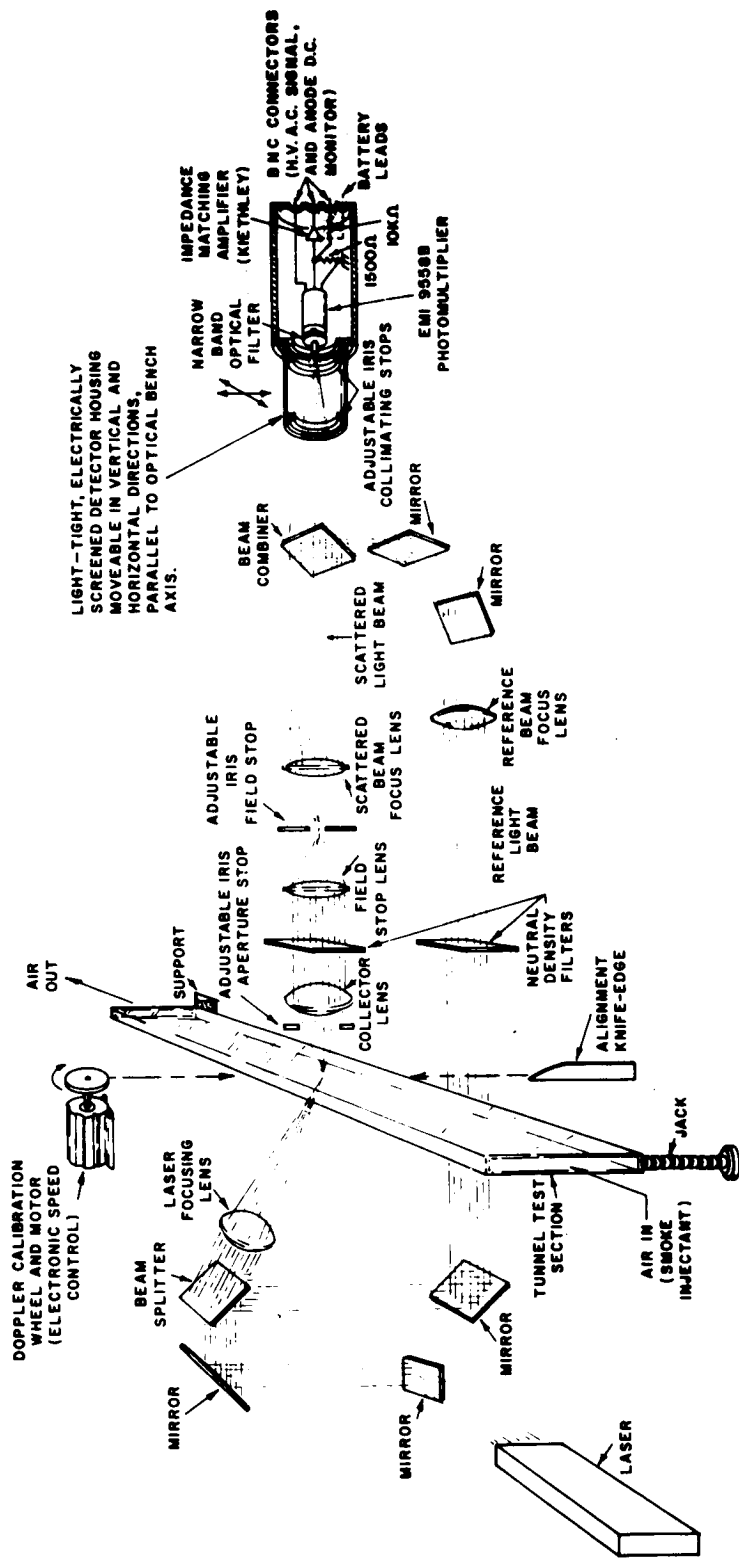


FIGURE 1. LASER DOPPLER VELOCITY INSTRUMENT SCHEMATIC DIAGRAM



As shown on Figure 4, the spectrum of a frequency modulated wave depends considerably on the modulation index, defined as the ratio maximum frequency deviation divided by the rate at which the frequency deviates (the signal frequency). Even in the simple case of a single tone modulated by a

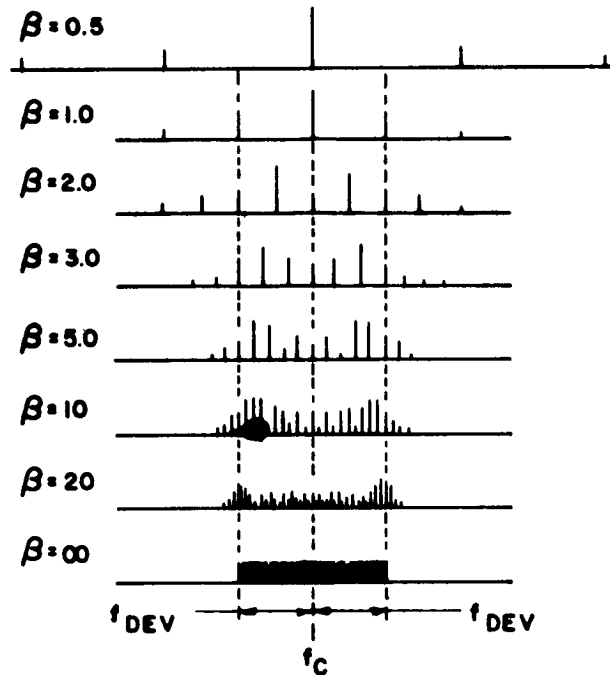


FIGURE 4. FM SPECTRUM OF SINGLE-TONE MODULATION

$$\text{BANDWIDTH VS. MODULATION INDEX } \beta = \frac{f_{\text{DEV}}}{f_s}$$

single frequency (see Fig. 4), the spectrum changes very radically as the modulating frequency (signal frequency) varies. In fact, with a complicated combination of frequencies, it is believed that the information on frequency deviation and signal frequency obtained by inverting the spectrum is not unique. A second reason that a spectrum analyzer used directly is not desirable is that the energy becomes spread out over the total spectrum. Since the noise level remains uniform over the spectrum, the signal seen on the spectrum analyzer becomes indistinguishable from background noise for a highly turbulent signal. Reference 1 examines the point in detail.

Figure 5 shows the basic elements of a superheterodyne receiver. This is important because in fact the photomultiplier tube behaves just like such a receiver. The operation of a photomultiplier as a receiver is quite different from that in the role of a very low level signal detector.

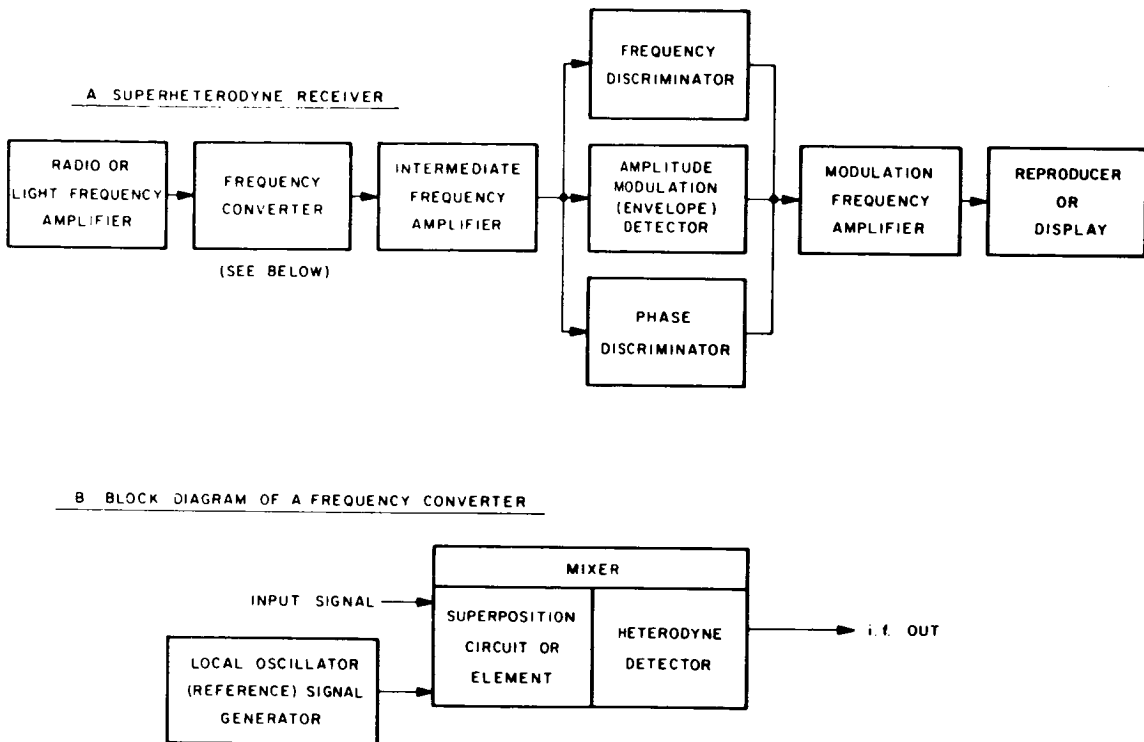


FIGURE 5. BASIC BLOCK DIAGRAMS OF SUPERHETERODYNE RECEIVERS AND ELEMENTS

The first three blocks on the left-hand side of the diagram are all contained in the photomultiplier itself.

Analysis of the mean square signal-to-noise ratio of such a system, measured at the photomultiplier anode, results in the following equation:



$$\left(\frac{S}{N}\right)_{A,MS} = \mu_T \left(\frac{P_s}{\delta f}\right) \left(\frac{S_k}{ek}\right) \left[ \frac{1}{1 + \frac{P_s}{P_{LO}}} \right], \quad (3)$$

where  $\mu_T$  is the heterodyning loss factor,  $S_k$ ,  $e$ ,  $k$  are constants,  $P_s$  and  $P_{LO}$  are the scattered and reference beam average powers, respectively, and  $\delta f$  is the bandwidth of the photomultiplier and its electronic system.

This equation shows that, for low scattered light powers, the power of the local oscillator beam should be as high as possible, up to the limit of the power handling capacity of the photomultiplier. In this situation, the signal-to-noise equation can be rewritten as

$$\left(\frac{S}{N}\right)_{A,MS} = (\text{CONSTANT}) \mu_T \frac{P_s}{\delta f}, \quad \left(\frac{P_s}{P_{LO}} \ll 1\right). \quad (4)$$

Here we see that, in this method of operation (the one normally used in the laser Doppler velocity instrument), the signal-to-noise ratio is no longer affected by local oscillator power, provided this is large (in practice, greater than about five times the scattered beam power). It is, however, directly proportional to scattered light power. Another important point is that the signal-to-noise ratio is inversely proportional to the bandwidth of the electronic system. This means that it is of key importance to use a system which always keeps the bandwidth of the system to an absolute minimum.

Equation (4) was verified experimentally in our laboratory by scattering of light passed through a rotating translucent wheel (see Fig. 6). The measurement is somewhat more elaborate than might be expected. This is because there are, in all, five parameters which have to be measured: the dc level of each of the scattered and local oscillator beams, the noise generated by each of these dc signal levels arriving at the photocathode, and the signal itself. As will be seen in the diagram, by suitable filtering, the dc and ac components are measured independently. The ac component must be measured on a true rms meter and the various noise components derived by difference calculations, measurements being made first, with both beams on together; second, with the local oscillator beam blocked, and third, with the scattered light beam blocked.

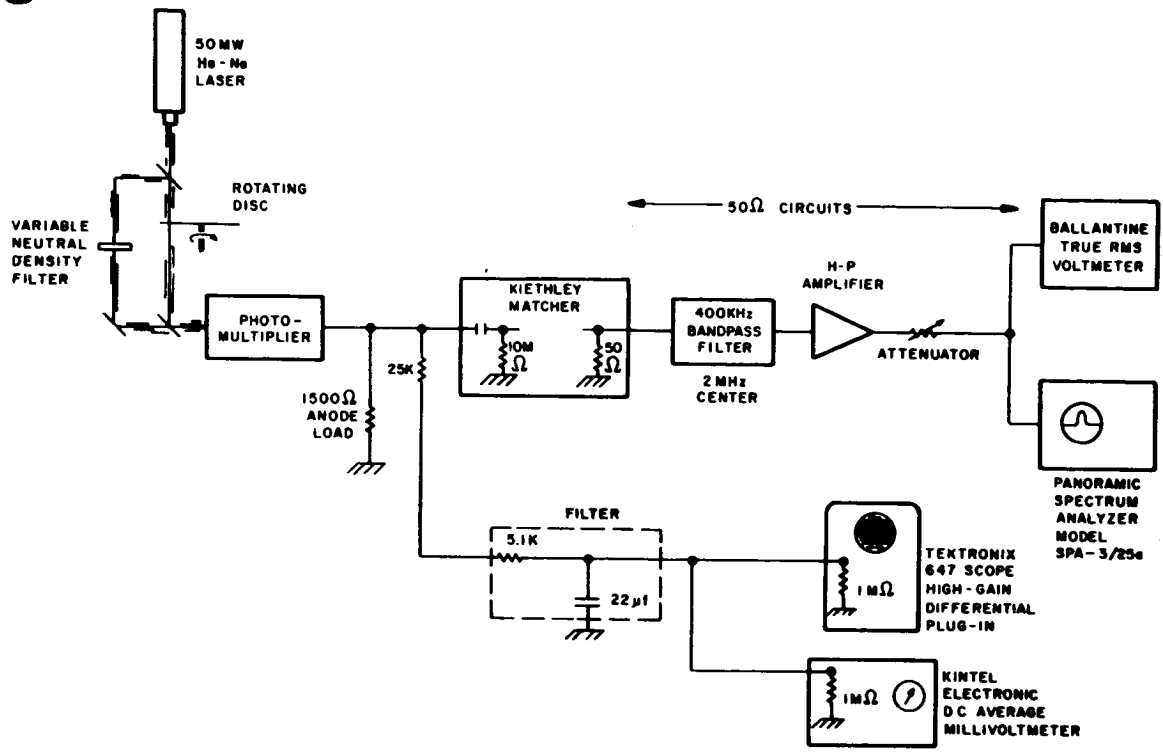


FIGURE 6. BLOCK DIAGRAM OF SIGNAL-TO-NOISE MEASUREMENT SYSTEM

Figure 7 shows a curve comparing many experimental data with the calculated signal-to-noise curve. The calculated curve has been adjusted for the heterodyning loss factor of the wheel. Bearing in mind that, using a 50 milliwatt laser, we are working at signal-to-noise ratios no greater than unity, the agreement appears to be excellent. Based on these measurements and Equation (4), a one-watt argon laser would give a signal-to-noise ratio using this wheel of 20 to 1, i. e., 30 db a very practical working figure for straightforward electronic system design.

As a further verification of the signal-to-noise equation, measurements were taken with a constant  $P_{LO}$ , set so that  $P_{LO}$  divided by  $P_{sc}$  was much greater than 1. Then the power  $P_{sc}$  was varied by placing a series of neutral

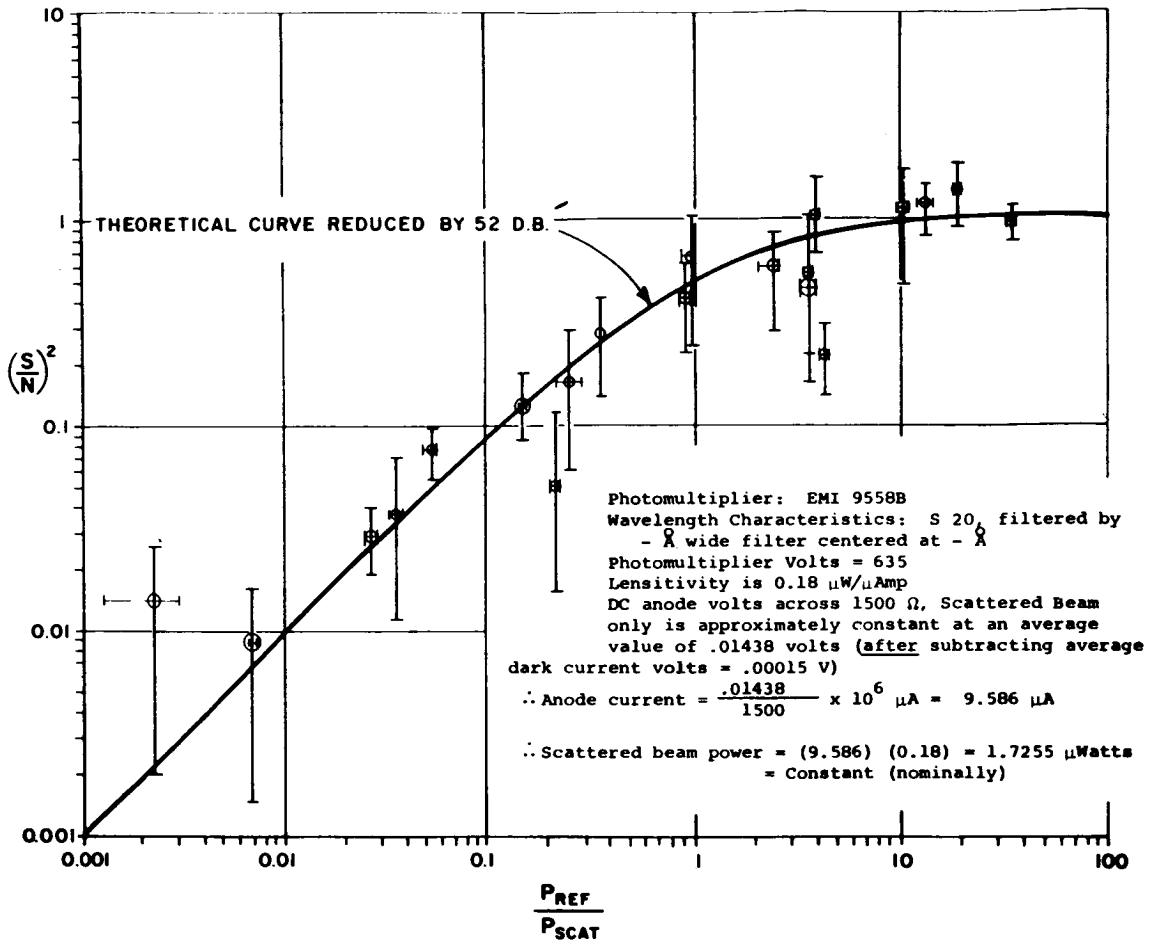


FIGURE 7. MEASURED VERSUS CALCULATED SIGNAL-TO-NOISE CURVE, USING 50 MILLIWATT LASER LIGHT SCATTERED BY ROTATING WHEEL

density filters in the scattered beam. Under these conditions, Equation (4) shows that the signal-to-noise ratio should be proportional to the scattered power. Figure 8 compares the calculated curve with many experimental points. Again the agreement of experimental with calculated data appears excellent. The final important factor in the signal-to-noise Equation (4), the inverse

dependence on system bandwidth, was verified by using a succession of narrow band filters. As expected, experimental data also were in complete agreement with Equation (4).

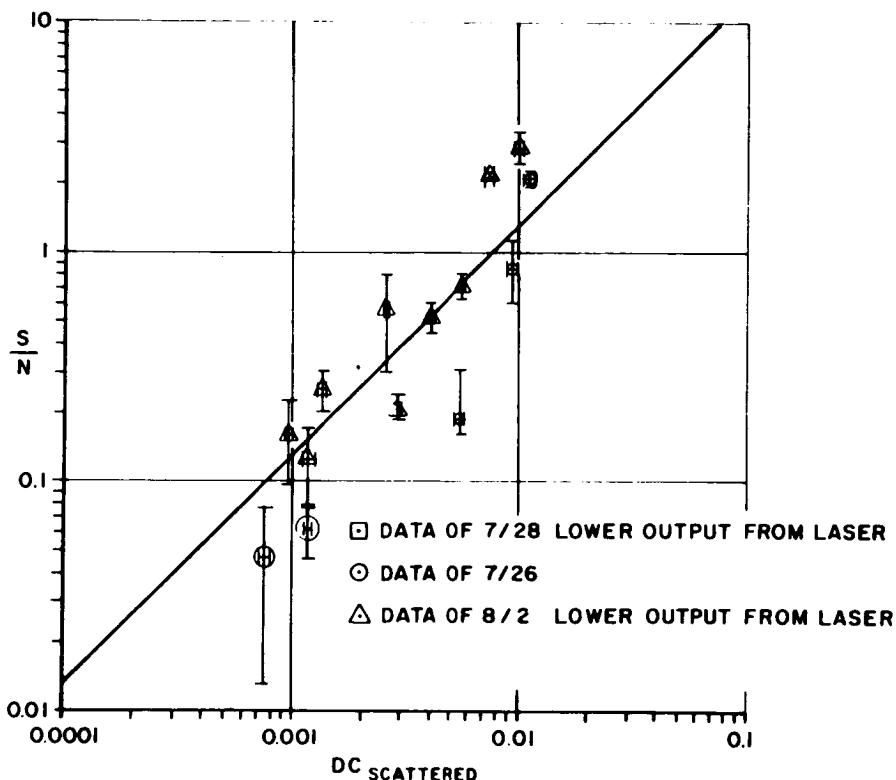


FIGURE 8. COMPARISON OF EXPERIMENTAL AND CALCULATED SIGNAL-TO-NOISE RATIO,  $P_{LO}$  MUCH GREATER THAN  $P_S$ , 50 MILLIWATT LASER SCATTERED BY ROTATING WHEEL

This means that we are now in a position to specify, quite precisely, the key laser Doppler velocity instrument system design parameters in terms of laser power, injectant particle size and concentration in the flow stream, and range of turbulent and mean velocities to be measured. The only unknown in the equation is  $\mu_T$ , the heterodyning loss factor. This includes a factor for loss of coherence in the scattering medium and imperfections in geometrical alignment. The biggest unknown is the loss of coherence in the scattering medium. This must be determined for a particular injectant by experimental measurement, preferably supported by calculation from the physical constants of the injectant material. Both experimental and analytical efforts on this problem are now in process.

Figure 9 shows a schematic diagram of a system for determining the vector velocity of the flow stream. One laser is used to provide both scattered light and the reference beams for three separate channels. These channels receive scattered light at three different angles, from which the velocity vector, in magnitude and angle, can be reconstructed. Notice that the vector information is instantaneous, and, after suitable recording as discussed earlier, can be reconstructed as a continuous function of time. By further data reduction, either by computer or in real time, turbulence intensity, scale and power spectrum, etc. , can readily be derived.

In the electronic system being designed for this instrument, in order to minimize the system bandwidth, a frequency tracking discriminator is to be used. In brief, this instrument, always operating at an effective narrow bandwidth, tracks the moving Doppler shift which is received after scattering from turbulent fluctuations. This Doppler shift is the mean velocity of the gas within the scattering volume defined above. Because this volume is finite, and also because the receiving lens receives scattered light over a continuous range of scattering angles corresponding to the solid angle of reception, the actual frequency signal received is slightly broadened. This broadening is termed instrumental broadening, since it is determined completely by the instrument design parameters. However, the tracking frequency discriminator effectively removes this broadening because it is a "continuum" broadening. That is, all frequencies within the broadened waveband are present at the same time, so that the only effect is to require that the frequency tracking loop be capable of remaining locked onto the center frequency of the spread.

The three-dimensional (3-D) instrument (see Fig. 10) has been designed in two parts: and optical receiver system and a movable mount. The mount has adjustments which insure that the laser beam is focused at all times on the same scattering volume as the receiving 3-D optics. The photograph shows the receiving optics, consisting of a reference beam tube, and three angularly spaced scattered beam tubes. Now in the final stages of assembly and alignment, this instrument will be used first in laboratory measurements on subsonic flows, and then at the Arnold Engineering Development Center for the measurement of rocket engine base flow on a model of the Saturn rocket engine cluster. Eventually, it is expected that it will be used in measurements on the Saturn engine.

It is important to note that, with reference to real engine measurements, because the scattering is measured from relatively massive particles, temperature effects are negligible, so that the instrument measures true velocity.

**KEY** BS = BEAM SPLITTER  
 L = LENS  
 CF = IMPEDANCE MATCHING AMPLIFIER  
 PM = PHOTOMULTIPLIER  
 ND = NEUTRAL DENSITY FILTER  
 M = FRONT SURFACE MIRROR  
 BA = BORESIGHT APERTURE

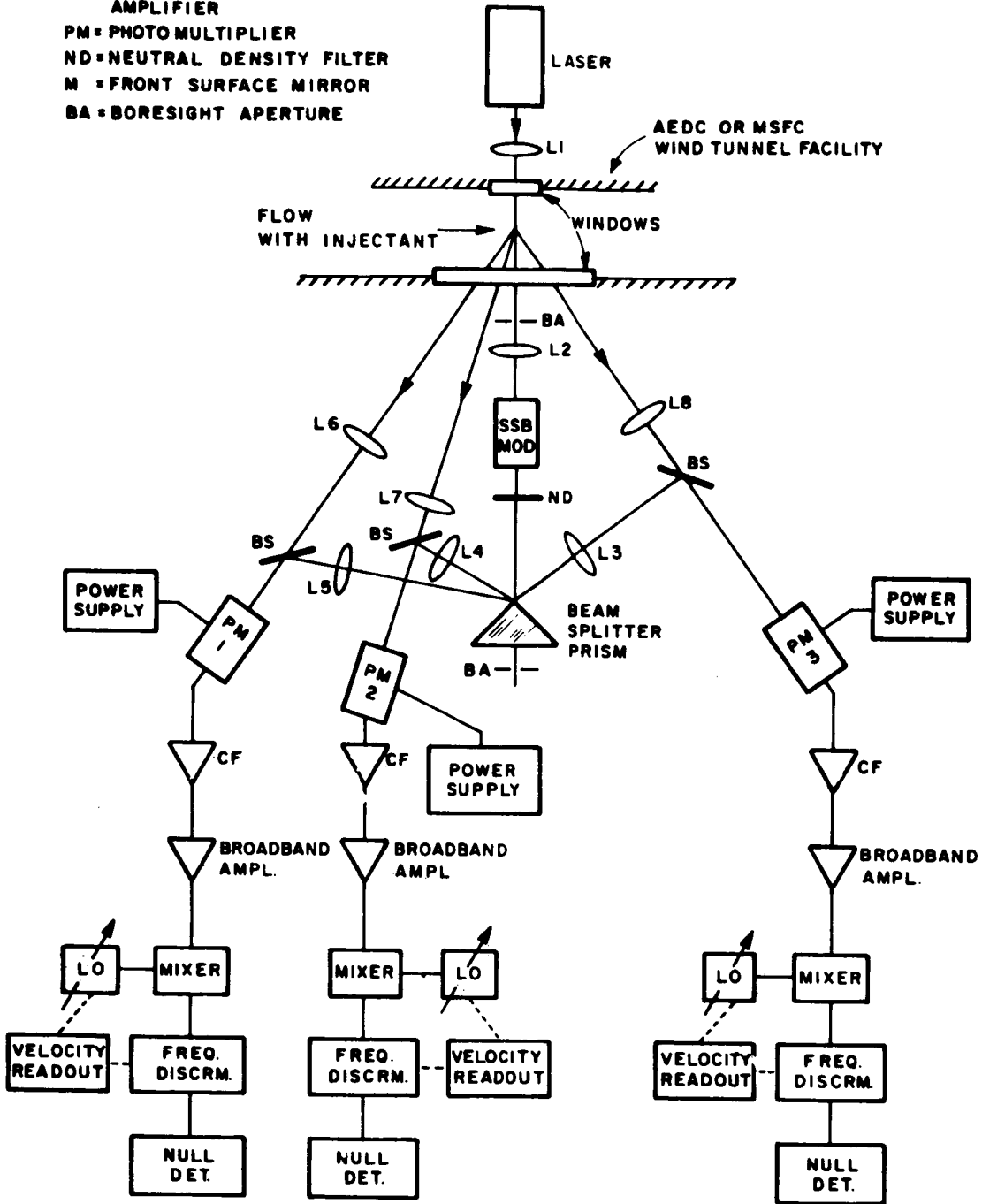


FIGURE 9. SCHEMATIC DIAGRAM OF 3-D SYSTEM FOR VECTOR VELOCITY MEASUREMENT

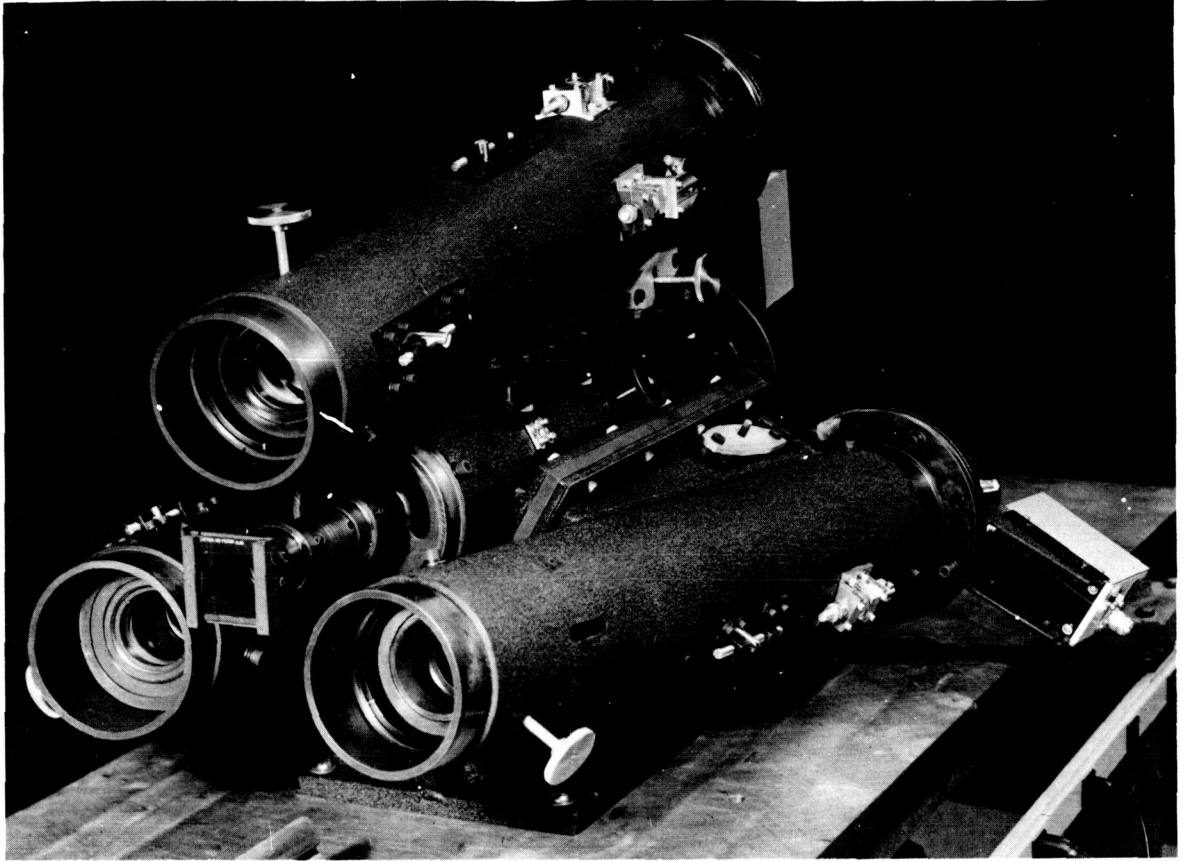
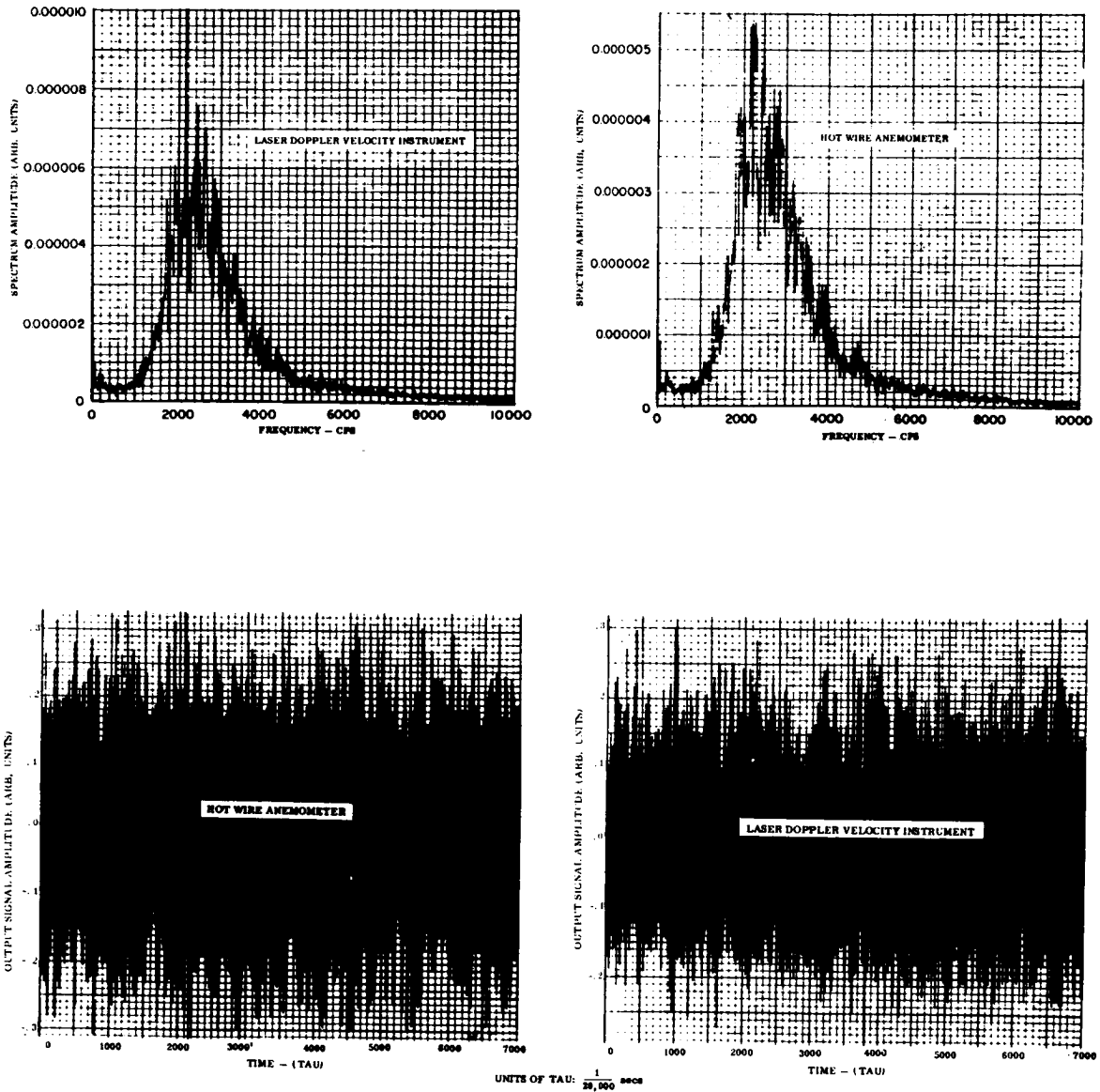


FIGURE 10. PHOTOGRAPH OF ASSEMBLED OPTICAL RECEIVER SYSTEM OF THE 3-D INSTRUMENT

In an experiment with the Marshall Space Flight Center personnel, measurements were made of subsonic turbulent flow from a nozzle, both by hot-wire anemometer and by a laser Doppler velocity laboratory instrument. The received signal from the latter was passed through a frequency discriminator, and the output of the discriminator was recorded. At the same time, the output of the hot-wire anemometer was recorded. The two recordings were passed through analog-to-digital conversion equipment, and subjected to statistical analysis, using MSFC computer programs, to determine the power spectra of each of the turbulence recordings. Figure 11 shows samples of the time display of the signals as recorded, and the power spectra after computer analysis. The similarity between the two could be described as remarkably good.

# Laser Doppler Velocity Instrumentation Spectral Density Curves Measured at George C. Marshall Space Flight Center



**FIGURE 11. COMPARISON OF TURBULENCE POWER SPECTRA  
MEASURED BY LASER DOPPLER VELOCITY INSTRUMENT  
AND BY HOT WIRE ANEMOMETER**



## CONCLUSION

We have shown conclusively the feasibility of accurate measurements of turbulence and velocity by a laser-Doppler velocity instrument. The instrument is capable of measuring mean velocity to the same or better precision than conventional gas velocity measuring instruments, and is capable of measuring turbulence to determine the identical parameters as those determined by hot-wire anemometer. However, the advantages of such an instrument over the hot-wire or other turbulence measuring instruments is evident: (1) It has no apparent limitation on upper velocity so far as practicable flow streams are concerned; (2) It can measure both subsonic velocity and high Mach numbers; (3) It does not disturb the flow in any way; (4) The resolution is very high since the scattering volume can be made very small; (5) Since no flow disturbances occur, precise longitudinal correlation measurements can be made; and (6) It is completely independent of the gas temperature so that no corrections are required on its measured and recorded data.

One disadvantage perhaps is that it does depend on scattering from solid particles and not from molecules or electrons. This means that there must be sufficient concentration of Mie scattering particles in the flow stream for adequate scattering. In a Saturn or similar rocket engine, this is expected to present no problem since there is a relatively high concentration of carbon macromolecules. In clean wind tunnels, either some injectant or ambient impurities, such as condensed water vapor, must be used in connection with the latter; it may be noted that, while a smoke injectant was used for experiments described above, nevertheless, signals could be seen to continue long after the smoke had disappeared so far as the eye could see. Developments are now in progress to improve the signal-to-noise ratio capability of the instrument, and there is good expectation that eventually no artificial injectants will be required.

## REFERENCE

1. Rolfe, E., et al., Raytheon Report no. R67-4450, November 1967.

# PART II. LASER DOPPLER TECHNIQUES FOR REMOTE WIND VELOCITY MEASUREMENTS

By

Albert V. Jelalian\* and R. M. Huffaker

## INTRODUCTION

The overall goal of this program is the verification of the feasibility of measuring atmospheric wind velocity using the laser Doppler heterodyne techniques previously developed by the George C. Marshall Space Flight Center and Raytheon for gas flows in wind tunnels. The present program efforts involve both analytical studies and experimentation. The studies are required to determine the optimum configurations for the present experimental system and systems for longer range applications. As a part of the experimental effort, the parameters that affect the measurement of wind velocities and their fluctuations are being investigated.

As a result of preliminary studies, a CO<sub>2</sub> gas laser operating at a wavelength of 10.6 microns is being used in the experimental system. The reasons for this choice are as follows:

- a. Lower spatial coherence losses as compared to available lasers operating at visible or near IR wavelengths.
- b. Less bandwidth required to cover the same range of velocities.
- c. A greater number of photons per watt of transmitted power.
- d. A highly efficient laser with greater average power output than any other available type of CW laser.
- e. Reduced alignment tolerances because of the laser wavelength.

---

\*Raytheon Company, Sudbury, Massachusetts

## PARAMETRIC ANALYSIS

The feasibility of an optical Doppler system to remotely measure the return signal from atmospheric particles centers around the S/N equation. The S/N power at the output of the receiver for a monochromatic source is

$$S/N = \frac{Q P_R P_{L.O.}}{B h f P_{L.O.} + P_N + P_{AMP}}, \quad (1)$$

where

$Q$  = Detector quantum efficiency

$P_R$  = Received signal power

$P_{L.O.}$  = Local oscillator signal power

$P_N$  = Equivalent optical noise power

$P_{AMP}$  = Equivalent noise figure power of post detection amplifier

$B$  = Electronic bandwidth

$h$  = Planck's constant

$f$  = Transmission frequency.

Typically, in a coherent detection process, one may increase the local oscillator power to outweigh the effects of the additional noise contributing term. As a result of this, the S/N equation becomes equal to the product of the detector quantum efficiency and the received signal power and inversely related to the electronic bandwidth, transmission frequency and Planck's constant.

Replacing the received signal power expression ( $P_R$ ) with its equivalent expression for an extended target, we may observe the S/N equation to be a function of

$$S/N = \frac{Q P_T D_R^2 \times \beta \times L}{16 h f R^2 B} , \quad (2)$$

where

Q = Quantum efficiency

P<sub>T</sub> = Transmitter power

D<sub>R</sub> = Receiver optics diameter

β<sub>ρ</sub> = Aerosol scattering coefficient

L = Length of scattering volume

h = Planck's constant

f = Transmission frequency

R = System range

B = Electronic bandwidth.

Of particular note are four parameters: (1) transmitter power, P<sub>T</sub>, (2) electronic bandwidth, B, (3) the aerosol scattering coefficient, β, and (4) the length of the scattering volume, L. Typical system analyses usually revolve around determining the amount of transmitter energy required to perform a chosen task. However, for remote wind measurements at large distances, typically we are transmitter power limited. Referring to the electronic bandwidth and the length of the scattering volume, we now see that the interface between the turbulence and the turbulence detection system manifests itself in the interaction between the particulate matter velocity with the laser beam. Doppler shift occurs when there is a relative motion between the laser beam and a target.

The equation for the Doppler frequency shift, F<sub>d</sub>, may be expressed as

$$F_d = \frac{2V}{\lambda} \cos \theta, \quad (3)$$

where

$V$  = Relative velocity

$\lambda$  = Transmission wavelength

$\theta$  = Pointing angle between relative velocity vectors.

Correspondingly, the Doppler spectral bandwidth,  $\Delta f_d$ , caused by the uncertainty of wind velocity,  $\Delta V$ , over the sampled volume is similarly related:

$$\Delta f_d = \frac{2\Delta V}{\lambda} \cos \theta. \quad (4)$$

The processing bandwidth may then be determined by the instantaneous velocity spread,  $\Delta V$ , expected within the target volume. If a differential velocity spread of one meter per second occurred over the sampled volume, then a 200 kHz processing bandwidth would be required at a 10.6 micron operating wavelength. Correspondingly, for a 15 M/sec differential velocity, a three-megacycle bandwidth requirement would exist.

In most ordinary Doppler systems, the bandwidth of the returned Doppler spectrum is relatively small compared with that required in a pulse system using ideal matched filter concepts. Therefore, significant power savings may be made by narrow banding to the relatively narrow Doppler spectrum.

The Doppler bandwidth requirement for a differential wind velocity of one meter/second is of the order of 200 kHz, which is identical to that required for a matched filter where the pulse width is five microseconds. One must conclude, therefore, that for the situation discussed, the average power required for a CW system would be substantially greater than the average required in a pulsed system. The use of a CW Doppler technique, therefore, appears inefficient for use in a long range system.

Because of the spectrum broadening caused by the turbulent wind velocity, a pulse-type laser technique is indicated for a long range system having sufficient Doppler shift to make suitable measurements.

The choice of transmitter pulse width may be shown to directly affect (1) signal-to-noise ratio,  $S/N$ , (2) the sampling length,  $L$ , and (3) the velocity resolution,  $\Delta f$ . This indicates that the pulse width should be as large as possible consistent with the Doppler broadening anticipated over the incremented measurement length. As this length increases, the differential velocity expected would increase, and, therefore, larger bandwidths would be required. Theoretically, then, either a CW or a pulse heterodyne system could be used for Doppler detection of the velocity of particulate matter in the atmosphere.

At very short ranges, a pulse Doppler system might suffer T/R switch recovery time limitations and an insufficient Doppler shift, and, therefore, a CW system would be more practical. Correspondingly, at long ranges the use of CW Doppler systems would seem impractical from the standpoint of transmitter power requirements and a pulse Doppler system would be indicated.

## EXPERIMENTAL SYSTEM

A block diagram of the experimental system may be observed in Figure 1. Here we see that the 10.6 micron single mode CW laser transmitter is the source

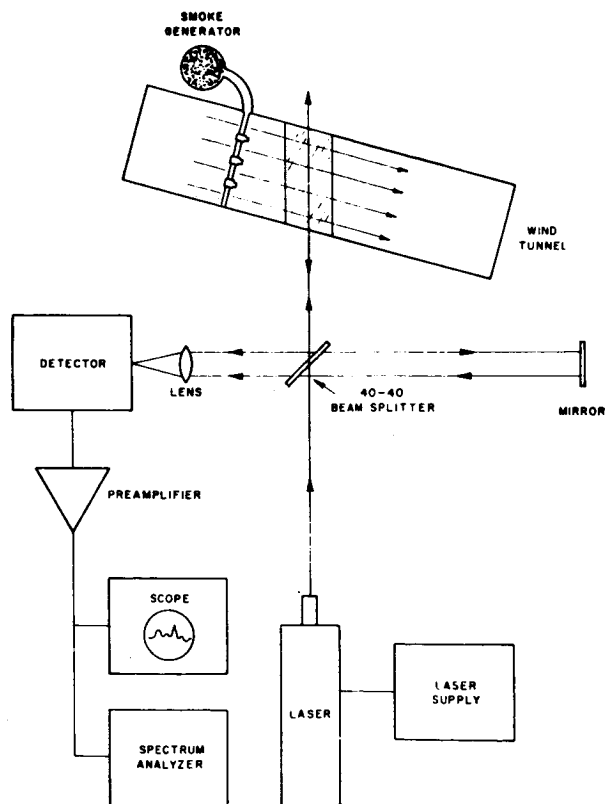


FIGURE 1. EXPERIMENTAL ARRANGEMENT FOR WIND TUNNEL TESTS

for a Michelson interferometer. The laser energy is directed via a 40 percent reflectance Irtran 2 beamsplitter to a 4 percent reflectance uncoated Irtran 2 mirror used in the local oscillator arm of the interferometer. An f/1.0 two-inch Irtran lens couples the reflected LO into the detector. The transmitted beam, after passing through the beamsplitter, is directed into a wind tunnel. Backscatter from the smoke particle concentration in the wind tunnel is then directed to the AR coated side of the beamsplitter and also directed via the f/1.0 lens to the copper-doped germanium detector. Here, the local oscillator beam and the Doppler shifted signal beam heterodyne. The resulting electronic signal, after passing through a low noise receiver is suitably displayed. Figure 2 is a photograph of the actual laboratory unit.

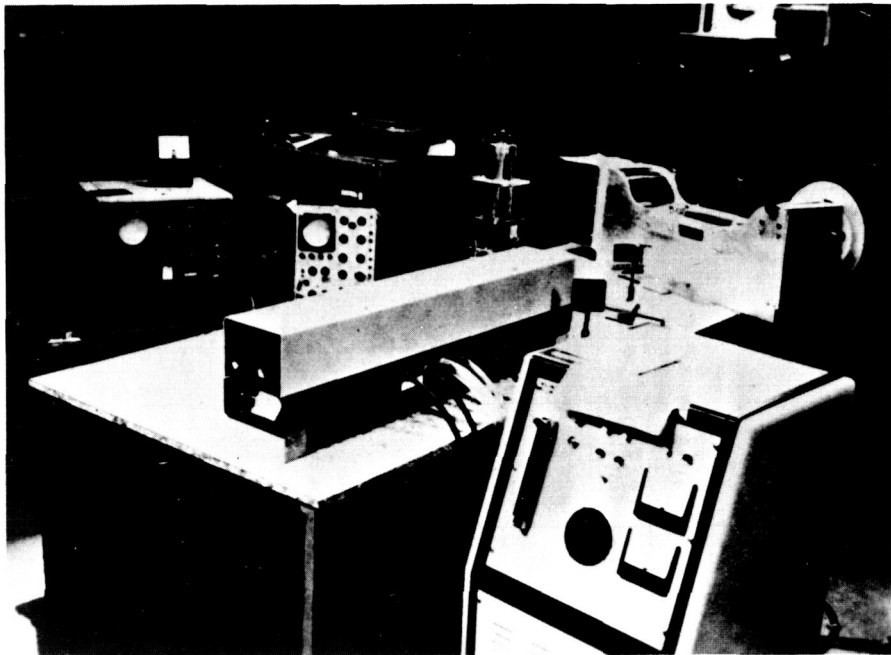


FIGURE 2

The series of pictures in Figures 3, 4, and 5 show Doppler returns from the wind tunnel as the velocity of the air was reduced in three steps: 0.5 m/sec, 0.43, and 0.3 m/sec. The amplitude does not remain constant because the smoke from the smoke generator was allowed to decay. In this case, the wind tunnel is at an angle of  $60^\circ$  to the signal beam. The width of the Doppler signal is about 50 kc, or the equivalent velocity spread of  $\pm 1$  m/sec, and is primarily due to turbulence in the wind tunnel.

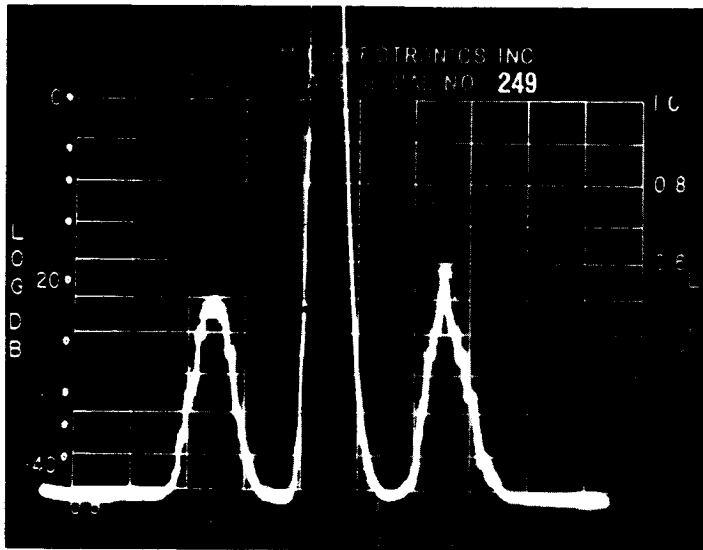


FIGURE 3. DOPPLER RETURNS FROM SMOKE IN WIND TUNNEL -  
 VELOCITY COMPONENT PARALLEL TO LASER BEAM = 0.5 METER/  
 SECOND -  $\theta = 60^\circ$

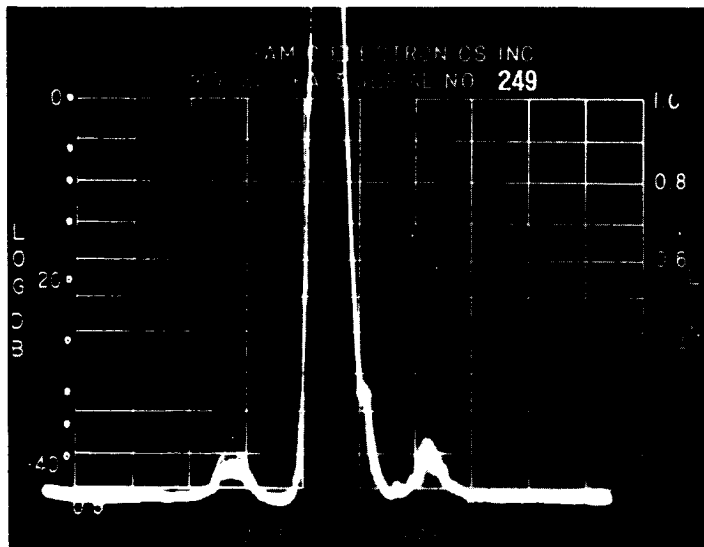


FIGURE 4. DOPPLER RETURNS FROM SMOKE IN WIND TUNNEL -  
 VELOCITY COMPONENT PARALLEL TO LASER BEAM = 0.43 METER/  
 SECOND -  $\theta = 60^\circ$



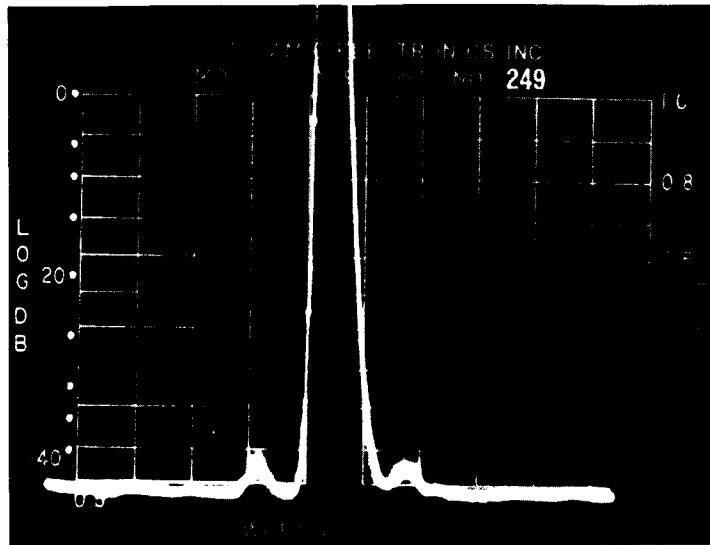


FIGURE 5. DOPPLER RETURNS FROM SMOKE IN WIND TUNNEL -  
 VELOCITY COMPONENT PARALLEL TO LASER BEAM = 0.31 METER/  
 SECOND -  $\theta = 60^\circ$

### Smoke Outdoors - Fifteen Feet

For the next experiment, the wind tunnel was removed and the signal beam was directed through the window of the laboratory by means of three plane, aluminized mirrors and passed four inches to one side of a rotron fan on top of a ladder. The Doppler from the turbulent, fan-blown smoke is very broad, as shown in Figure 6. The corresponding picture of the smoke is shown in Figure 7. The scale is 500 kHz or 2.5 m/sec full scale with zero at the left edge. The lower smooth curve represents the system noise level.

### Wind-Blown Smoke - Two Hundred Feet

The third experiment was to observe wind-blown smoke at a distance of 200 feet. A smoke bomb was ignited at the top of a ten-foot stepladder set up in

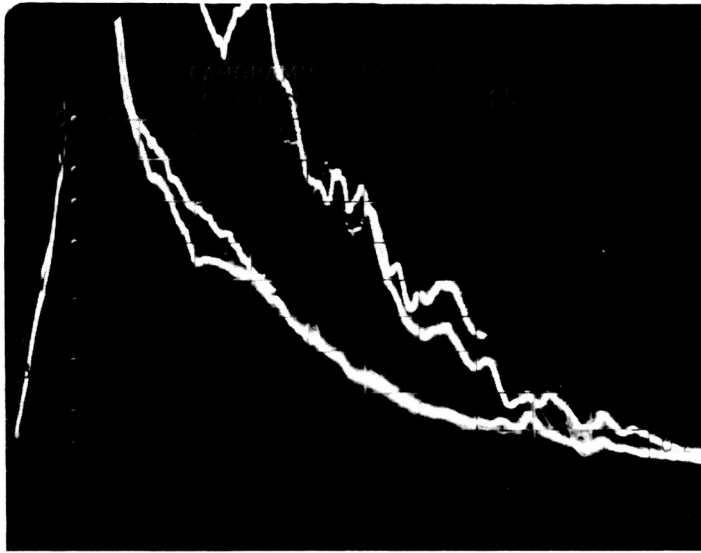


FIGURE 6. DOPPLER RETURNS FROM SMOKE AT 15-FOOT RANGE -  
VELOCITY DISPERSION - 0.25 METER/SECOND/DIVISION

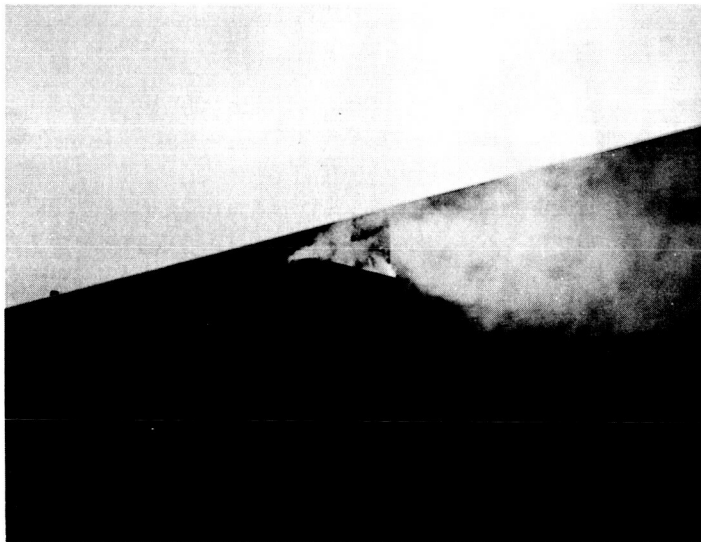


FIGURE 7. SMOKE GENERATOR SETUP AT 15-FOOT RANGE

the parking lot about 200 feet away. Because of the proximity to the ground, much turbulence occurs and can be seen in the actual picture of the smoke and in the Doppler signal (Figs. 8 and 9).



FIGURE 8. SMOKE GENERATOR AT 200-FOOT RANGE

Figure 10 illustrates the Doppler from the wind-blown smoke. There is a wide Doppler peak at about 3.0 m/sec with the wind coming at 30° to the signal beam. This corresponds to a wind speed of 3.6 m/sec or about 10 mph. Correspondingly, Figure 11 shows a similar Doppler spectrum at 5 mph. The anemometer located on the building was reading 5 to 10 mph at these times.

Presently, the experimentation is continuing and measurements are being made to substantiate the theoretical predictions and improve system performance.



FIGURE 9. SMOKE GENERATOR AT 200-FOOT RANGE

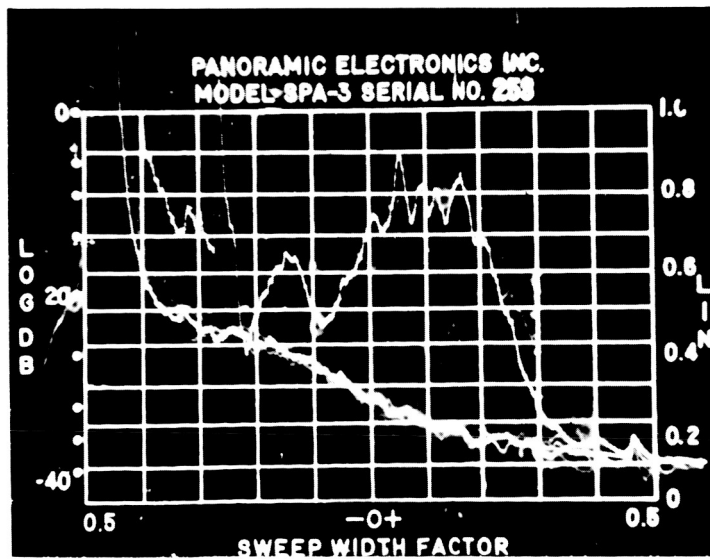


FIGURE 10. DOPPLER RETURNS FROM WIND-BLOWN SMOKE AT 200-FOOT RANGE - VELOCITY DISPERSION = 0.5 METER/SECOND/DIVISION

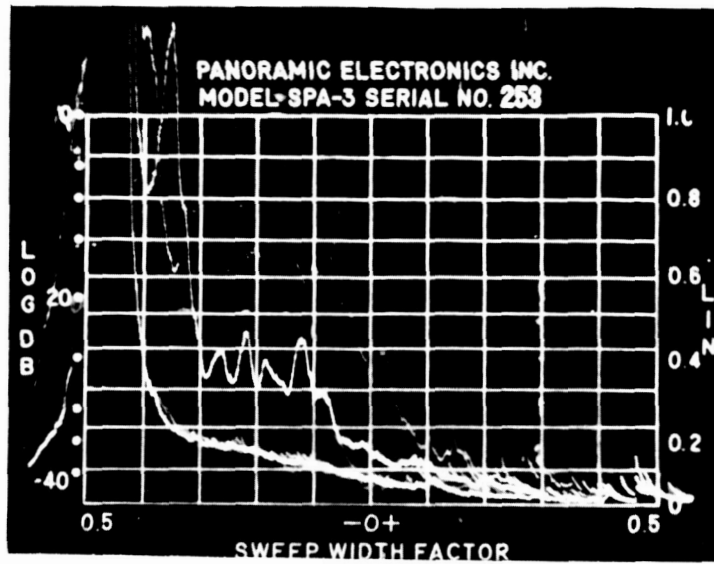


FIGURE 11. DOPPLER RETURNS FROM WIND-BLOWN SMOKE AT  
200-FOOT RANGE - VELOCITY DISPERSION = 0.5  
METER/SECOND/DIVISION

---

## DISCUSSION

F. R. Krause, NASA/MSFC: Mr. Jelalian, in your signal-to-noise analysis, have you included the possible effect of any optical wave front distortions which could come from turbulence or wave phenomena along the optical path?

A. Jelalian: Atmospheric effects are included ordinarily in the signal-to-noise equations that we use. Some of the losses consist of diffuse target losses, atmospheric absorption and transmission losses, and atmospheric turbulence losses. The signal-to-noise equation presented does not include these functions at present, because the main point of the analysis was to compare CW against pulse-type heterodyne operations. The losses previously noted are similar regardless of the choice of system operation, whether it be CW or pulse-type. They are not presented at this point as they would tend to complicate the discussion.

S. C. Traugott, Cornell: Mr. Rolfe, do you mean that you could measure turbulent velocities not only in the mean flow direction, but transversely in the other two directions, as well? If one had a steady but complicated three-dimensional flow field without a priori knowledge of velocity direction, could one map out this field with the laser?

E. Rolfe: Yes, you can, because you are measuring the magnitude of three vectors, which are the three components of the velocity vector. These measurements can then be interpreted to obtain the velocity vector.

S. C. Traugott: Another tool used in turbulence measurements is the hot wire. It can be used both subsonically and supersonically to measure temperature as well as velocity fluctuation; but it is bothersome to unravel which is which (one of the reasons why one gets into trouble supersonically). But, somehow, one can infer how much of the signal is a velocity fluctuation and how much is a density or temperature fluctuation. What happens, however, if you look with your laser probe at a high speed rocket plume? How do you make out the turbulence in the sense of velocity fluctuations from that which represents the temperature fluctuations?

E. Rolfe: If we were looking at Rayleigh scattering or Thomson scattering, we would have some thermal broadening which we could extract from the actual velocity broadening. But we are looking here at scattering from much more massive particles in which their "thermal" broadening is quite negligible compared with any broadening caused by flow velocity.

A. Thomson, IDA: Mr. Jelalian, have you been able to obtain returns from natural aerosols or clouds?

A. Jelalian: We are presently using smoke bombs to determine atmospheric effects because the system we presented does not have a range measurement capability. As a result, we have set up a smoke bomb at a given distance from the instrument to avoid the necessity of establishing the range. I would not venture to say at this point that the turbulence effects which we note in the absence of smoke are returns from aerosols or fogs, but we do get returns. Our measurements indicate returns from rain, clouds, and other interesting soft targets.

---

# TEMPERATURE AND CONCENTRATION MEASUREMENTS IN MODEL EXHAUST PLUMES USING INVERSION TECHNIQUES

By

N 68-18100

William Herget

Rocketdyne Division  
North American Rockwell Corporation  
Canoga Park, California

---

## ABSTRACT

The experimental determination of temperature and pressure distribution in the high velocity gas stream encountered in a rocket engine exhaust plume is of value in gaining greater insight into the actual combustion processes occurring in the engine. The study of injector and nozzle processes is also aided by such measurement. In addition, knowledge of temperature and pressure distribution is essential for the calculation of the radiation emanating from the exhaust plume.

In the technique described herein the spectral radiance and spectral transmittance of infrared active exhaust species are measured along a series of coplanar, chordal lines of sight spanning the exhaust. The data thus obtained allow equations describing the radiant energy transferred through the exhaust to be solved either directly or by inversion methods of the radial distributions of spectral radiance and spectral emissivity. From these latter two quantities the radial distributions of temperature and partial pressure are calculated. This technique has been used to map a portion of the exhaust plume of a 1000 pound thrust rocket motor for the propellants liquid oxygen/kerosene and liquid oxygen/alcohol.

---



## INTRODUCTION

Spectroscopic studies of the radiation produced by the combustion of rocket propellants have been made with three particular goals in mind: detection of an in-flight missile and identification of propellants from emitted electromagnetic radiation; formation of an exhaust plume model that allows calculation of emitted radiation; and determination of rocket engine performance characteristics.

The first goal requires the data obtainable from emission spectroscopy; i. e. , ultraviolet, visible, and infrared emission intensities are measured as functions of wavelength for various propellants and engine sizes, and the emitting species are identified. Once sufficient information of this type is available, it should be possible to deduce the propellant and engine size from observation of the exhaust plume spectra.

The second and third goals each require the same spectroscopic techniques since the quantities to be determined in each case are temperature and species partial pressure distributions in the exhaust. It has been shown that meaningful data cannot be obtained from a single line-of-sight measurement when significant gradients exist in the exhaust. To determine the requisite quantities properly, the spectral radiance and spectral transmittance of the exhaust must be measured spectroscopically along a set of predetermined coplanar lines of sight. This measurement technique has been termed "zone radiometry" at Rocketdyne, and the work done to date is described in references 1, 2, and 3. With this type of data, the equations for radiant energy transfer through the exhaust for each line of sight may be solved simultaneously for the local values of spectral radiance and spectral emissivity. From these latter two quantities, the local values of temperature and species partial pressure may be calculated.

Temperature and pressure distributions can be obtained in this manner across various planes in an exhaust and can serve as checks on various phases of plume model calculations. Such distributions determined at the nozzle exit plane can be compared with theoretical predictions of exhaust temperatures and constituents. The mixing characteristics of various injector patterns may also be studied by zone radiometry techniques.

The prime advantage of optical spectroscopic techniques over other diagnostic techniques is that no physical contact with the hot gas stream is required. The disadvantage is that temperature and partial pressures can both be determined only for combustion products (such as CO<sub>2</sub>, HF, H<sub>2</sub>O, carbon particles, HCl, etc.) that possess suitable absorptive and emissive properties. It is possible to determine relative concentration distributions for "nonequilibrium" species such as OH, CH, NB, etc.

This document explains the spectroscopic technique of zone radiometry as it has been developed at Rocketdyne. Methods of calculating partial pressure and temperature distributions from line-of-sight measurements of spectral radiance and transmittance are discussed first. Experimental techniques are discussed, and finally, some typical results are presented and possible applications mentioned.

## THEORY OF ZONE RADIOMETRY

From the absorptive properties of a gaseous medium, the partial pressures of the absorbing species may be determined. If the medium is at elevated temperatures, then measurement of both the radiative properties and absorptive properties allows the temperature and partial pressure to be determined. The required techniques are best understood by first considering media homogeneous in temperature and pressure, and then extending the technique to heterogeneous media.

### Absorption of Radiation by Homogeneous Gaseous Media

The extent to which a gaseous medium absorbs incident radiation depends principally upon the wavelength,  $\lambda$ , of the radiation, the density and identity of the molecular species in the gas, and the optical path length,  $L$ , in the medium. These parameters are related by the equation

$$\tau(\lambda) = e^{-K(\lambda, T)PL} = 1 - \alpha(\lambda) = 1 - \epsilon(\lambda), \quad (1)$$

where  $P$  is the partial pressure of the absorbing gas. The quantity  $K(\lambda, T)$  is called the spectral absorption coefficient and, for a given wavelength and temperature, is a unique property of the absorbing gas. The temperature

dependence is small compared to the wavelength dependence. The quantity  $\tau(\lambda)$  is the spectral transmissivity (fractional transmittance),  $\alpha(\lambda)$  is the spectral absorptivity, and  $\epsilon(\lambda)$  is the spectral emissivity;  $\alpha(\lambda) = \epsilon(\lambda)$  for a medium in thermodynamic equilibrium.

In a laboratory absorption experiment the gas to be studied is contained in an absorption cell at known temperature and pressure. Radiation from a continuum source,  $I_0(\lambda)$ , is sent through the cell by suitable optics.

The radiation transmitted by the gas and the cell windows,  $I(\lambda)$ , is detected and recorded. By making the same measurement with the cell evacuated, the background spectrum,  $I_0(\lambda)$ , may be recorded. The absorption spectrum (percent transmission as a function of wavelength) is obtained from the simple relation  $\tau(\lambda) = I(\lambda)/I_0(\lambda)$ . In this type of experiment,  $P$  and  $L$  are known, and  $K(\lambda, T)$  can be calculated from Equation (1). By performing this experiment over a range of temperatures,  $K(\lambda, T)$  can be completely determined for a particular species.

The effect of any variation in  $K(\lambda, T)$  over the wavelength interval encompassed by the spectral band pass of the instrument must be considered in these experiments. This effect will be discussed later.

The spectroscopic method of pressure determination makes use of the fact that once  $K(\lambda, T)$  has been determined for various species by the method outlined above, then the pressure of an unknown gas concentration can be determined from Equation (1) by measurement of  $\tau(\lambda)$ ,  $T$ , and  $L$ . The identity of the gas is determined from its absorption spectrum. When the medium under study contains a mixture of gases, then measurements at a particular wavelength yield the partial pressure of a particular species.

This technique of pressure determination is restricted to gases which do possess an absorption spectrum. Generally, any gas whose molecules contain at least two dissimilar atoms will have an absorption spectrum. For a gas in thermodynamic equilibrium, absorption and emission of radiation occur in identical wavelength regions, so that the above restriction will also apply to the spectral radiance measurements discussed below. Generally, different species absorb (and emit) in different wavelength regions, although some overlap may occur.

Spectral Radiance. The intensity of radiation emanating from a gaseous medium is most conveniently measured in terms of the amount of energy per unit wavelength interval leaving a unit area of the gas surface and filling a given solid angle. This quantity is called "spectral radiance" and may be expressed in units of watts  $\text{cm}^{-2}$  steradian $^{-1}$  micron $^{-1}$ .

Spectral radiance is most simply measured by comparing the brightness of the hot gas with the brightness of a standard source at known temperature, such as a blackbody. The optical system and the monochromator serve to ensure that the detector is viewing the same solid angle, area of the source, and wavelength interval, whether viewing the hot gas or the blackbody. In this manner, the spectral radiance of the hot gas will be equal to that of the blackbody if the detector produces the same output signal whether viewing one source or the other. In this situation, the gas and the blackbody have the same "brightness temperature" but not the same true temperature. (Any emission from the cell windows must be taken into account.)

The spectral radiance of a blackbody  $N_{\text{BB}}(\lambda, T)$  is a unique function of wavelength and temperature, and is given by the expression

$$N_{\text{BB}}(\lambda, T) = \frac{C_1}{\lambda^5} (\epsilon^{-C_2/\lambda T} - 1), \quad (2)$$

where  $C_1$  and  $C_2$  are known constants. The blackbody source itself must periodically be temperature-calibrated with an optical pyrometer.

Temperature. The spectral radiance of the gas,  $N(\lambda)$ , is related to the spectral radiance produced by a blackbody which is at the same temperature,  $T_g$ , as the gas, by the expression

$$N(\lambda) = N_{\text{BB}}(\lambda, T_g) / \epsilon(\lambda), \quad (3)$$

where  $\epsilon(\lambda)$  is the spectral emissivity as determined by Equation (1). Thus, once  $N(\lambda)$  and  $\epsilon(\lambda)$  have been measured, the quantity  $N_{\text{BB}}(\lambda, T_g)$  can be calculated from Equation (3), and the gas temperature is then uniquely determined from Equation (2), since  $T_g$  is now the only unknown quantity in that expression.

## MEDIA CONTAINING CONCENTRATION AND TEMPERATURE GRADIENTS

The spectroscopic technique of pressure determination described above is of particular value in analyzing a system consisting of several gases that are intermixing while traveling at high velocity. If the gases are high-temperature combustion products, then their temperature also must be determined spectroscopically. For a medium which contains concentration and temperature gradients, the expressions for the transmissivity and the radiance along a particular line of sight must be written in terms of integrals along that line of sight. With reference to Figure 1, consider a particular plane passing through the medium and perpendicular to the gas-flow axis. It must be assumed that conditions across this plane are fixed in time for the duration of the measurements. The fraction of incident radiation transmitted along a line of sight parallel to the  $y$  axis would be given by

$$\tau_{\lambda, x} = \epsilon \int_{y_1}^{y_2} K_{\lambda, T} P(x, y) dy. \quad (4)$$

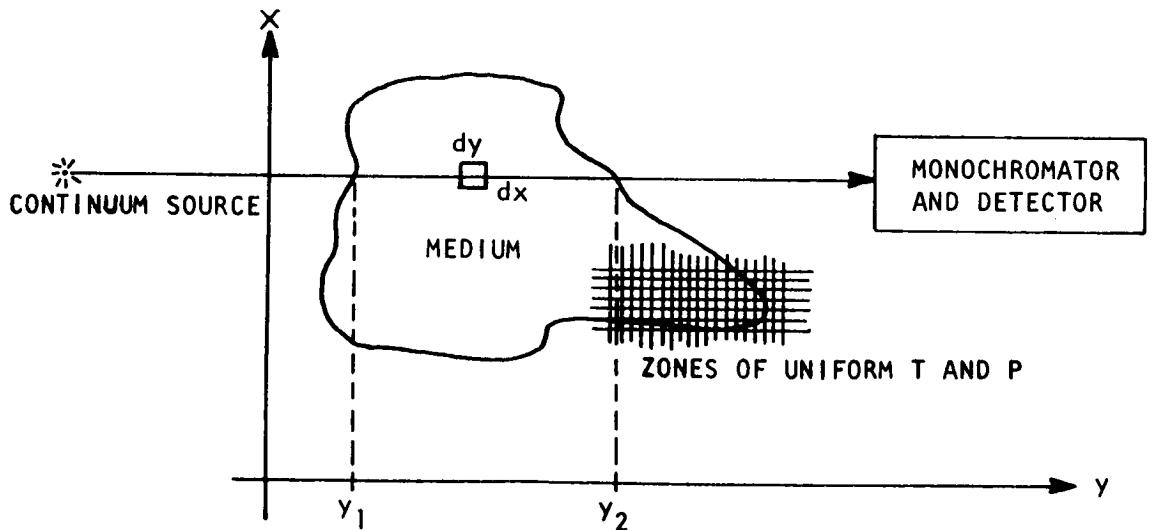


FIGURE 1. CROSS SECTION OF MEDIUM CONTAINING CONCENTRATION AND TEMPERATURE GRADIENTS

If  $N_\lambda(x, y)$  is a local value of the radiance per unit path length, then  $N_\lambda(x, y)dy$  is the amount of radiance leaving a small-volume element parallel to the x axis. This radiance will be attenuated by the gas between the volume element and  $y_2$ . Thus, the actual amount of radiance from a single-volume element that escapes the medium is given by

$$N_\lambda(x, y)dy \epsilon^{-\int_y^{y_2} K_{\lambda, T} P(x, y) dy}.$$

The value of spectral radiance that would actually be measured for a particular line of sight is thus given by

$$N_{\lambda, x} = \int_{y_1}^{y_2} N_\lambda(x, y) \left[ \epsilon^{-\int_y^{y_2} K_{\lambda, T} P(x, y) dy} \right] dy. \quad (5)$$

Equations (4) and (5) express quantities which may be measured,  $\tau_{\lambda, x}$  and  $N_{\lambda, x}$ , in terms of the unknown quantities  $[K_{\lambda T} P(x, y)]$  and  $N_\lambda(x, y)$ . It should be understood that any attempt to calculate a temperature and pressure from values of  $\tau_{\lambda, x}$  and  $N_{\lambda, x}$  obtained at a single line of sight and wavelength for a heterogeneous medium would yield "some sort of average" temperature and pressure, and these average values would be essentially meaningless.

In the most general case, Equations (4) and (5) would be solved in the following manner. A particular plane of the medium is assumed to be divided into a matrix of M zones (hence, the term "zone radiometry") of uniform size. The zones are small enough so that the temperature and pressure in each zone may be assumed to be uniform, and the variation between adjacent zones is small. Equations (4) and (5) may then be replaced by the appropriate summation expressions. The line-of-sight quantities  $\tau_\lambda$  and  $N_\lambda$  must each be measured at the same wavelength along M different lines of sight, with each zone being traversed at least once. A number equal to the  $\sqrt{M}$  line of sight can be made parallel to the y axis, an equal number parallel to the x axis, and the remaining number can be at various angles to the y axis. These measurements of M values of  $\tau_\lambda$  furnish a set of M simultaneous equations of the form of Equation (4) which can be solved for M values of the product  $[K_{\lambda, T} P(x, y)]$  for each of the M zones. The M values of  $[K_{\lambda, T} P(x, y)]$  obtained from the

transmission measurements are used with the  $M$  measured values of  $N_\lambda$  in a set of simultaneous equations of the form of Equation (5). These equations can be solved for  $N_\lambda(x, y)$ .

The value of the emissivity for each zone is calculated from the expression

$$\epsilon_\lambda(x, y) = 1 - e^{-K_{\lambda, T} P(x, y) a},$$

where  $a$  is the zone width along the line of sight. As discussed previously, the temperature of each zone is defined by the equation

$$N_{BB}[\lambda, T_g(x, y)] = \frac{N_\lambda(x, y)}{\epsilon_\lambda(x, y)}. \quad (7)$$

Once the zonal temperature has been determined, a value of  $K_{\lambda, T}$  can be assigned to each zone, and the zonal partial pressure can be calculated as before.

One set of absorption and emission measurements, as described above, allows the temperature and pressure distribution to be determined across a single plane in the medium. By performing the measurements across a series of planes, temperature and pressure profiles for the entire flow field can be obtained.

Effect of Symmetry. If the flow field under study possesses symmetry, then the number of lines of sight required to determine the temperature and pressure distributions can be considerably reduced. Since as many as 100 zones might be required to describe a particular flow field properly, it is of value to recognize any symmetry that is present. For example, if two symmetry planes are present, then 25 lines of sight would be sufficient to obtain the data necessary for solving a 100-zone flow field problem. Radially symmetric flow fields which are often encountered, are the most convenient to analyze and handle experimentally. In the work done at Rocketdyne [1, 2, and 3], the rocket exhausts studied all possessed radial symmetry. In this case, the zones of uniform temperature and pressure and corresponding lines of sight are chosen as shown in Figure 2, and Equations (4) and (5) become

$$\tau_{\lambda, x} = e^{-\int_{-y_0}^{y_0} K_{\lambda, T} P_r dy} \quad (8)$$

$$N_{\lambda, x} = \int_{-y_0}^{y_0} N_r e^{-\int_{-y_0}^{y_0} K_{\lambda, T} P_r dy} dy \quad (9)$$

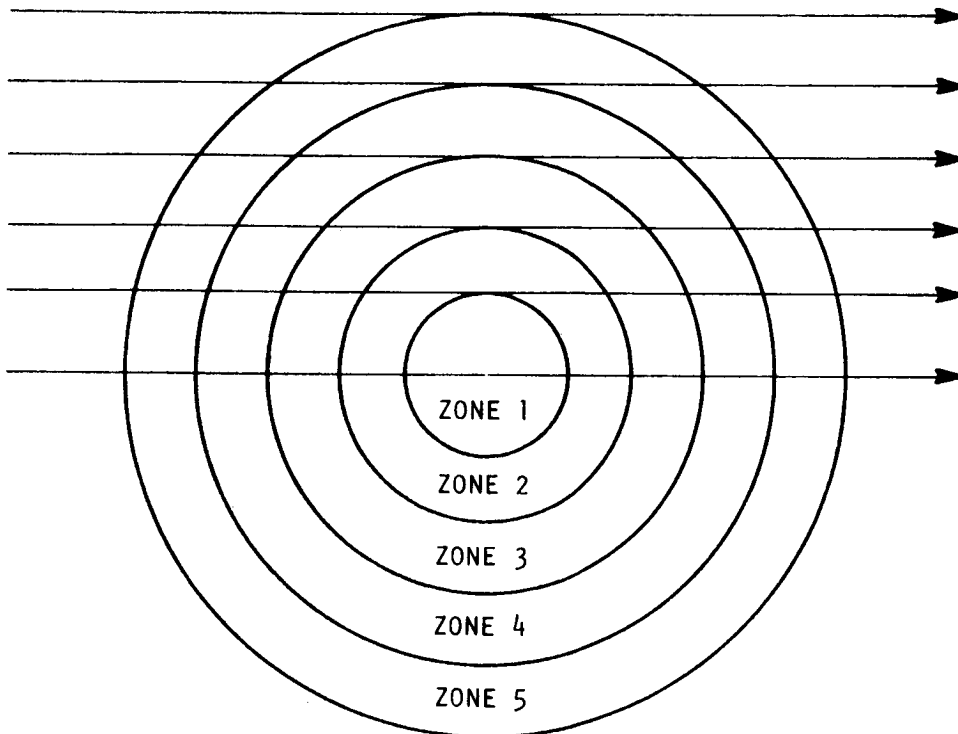


FIGURE 2. LINES OF SIGHT FOR RADIALLY SYMMETRIC FLOW FIELD

Two methods have been used to solve these equations. The first follows the method outlined by Freeman and Katz [4] and makes use of the Abel integral equation. This equation is

$$F(x) = 2 \int_x^{r_0} G(r) (r^2 - x^2)^{-\frac{1}{2}} r dr, \quad (10)$$

and has its solution



$$G(r) = -\frac{1}{\pi} \int_r^{r_0} \frac{dF(x)}{dx} (x^2 - r^2)^{-\frac{1}{2}} dx. \quad (11)$$

Freeman and Katz [4] show how to place Equations (8) and (9) in the form of Equation (10). Their technique requires the expansion of the exponential in Equation (9) and the retention of only certain terms. This approximation limits the use of this method to the study of flows which have a maximum absorption along any one line of sight of about 30 percent. Equation (11) has been treated in numerous ways. In Nestor and Olsen's treatment [5], the resulting expressions are

$$[K_{\lambda, T^P}]_K = -\frac{2}{\pi a} \sum_{n=K}^N \left( \ln \frac{1}{\tau_n} \right) B_{Kn} \quad (12)$$

$$N_K = -\frac{2}{\pi a} \sum_{n=K}^N \frac{2N_n}{1 + \tau_n} B_{Kn} \quad (13)$$

for the solutions of Equations (8) and (9). The subscript  $n$  refers to the  $n$ th line of sight and  $K$  refers to the  $K$ th zone;  $a$  is the zone width. The elements in the matrix  $B_{Kn}$  are tabulated in reference 5.

The above method was used in the program described in reference 3 in which the rocket motors were operated at simulated altitude and the maximum absorption along any line of sight was less than 35 percent.

A second method was used to solve Equations (8) and (9) for the work described in reference 2, where the motors were operated at sea level and the exhaust plume was optically thick in various wavelength regions. This method is simply to solve the set of equations of the form of Equation (8) simultaneously by back substitution. The radial values of the product  $K_{\lambda, T^P r}$  thus obtained are then used in the set of equations of the form of Equation (9) which are also solved by back substitution. Back substitution means that  $K_{\lambda, T^P N}$  and  $N_N$  for the outermost zone are obtained directly from data taken along the line of sight through that zone ( $N$ th line-of-sight).

These results are then used with the data taken along the (N-1)th line of sight to obtain  $K_{\lambda, T} P_{N-1}$  and  $N_{N-1}$ . In this manner the complete problem may be solved.

The methods of obtaining the line-of-sight radiance and transmittance values are independent of the method of solution of the resulting equations. These experimental details are covered in the next section. It should be remembered that in order to use zone radiometry for a complete temperature and partial pressure determination, it is necessary that the species under study be in local thermodynamic equilibrium. This requirement has the effect of limiting the complete zone radiometry treatment to species which are active in the infrared spectral region. It is, however, possible to obtain relative concentration distributions for species that radiate in the ultraviolet and visible spectral regions but absorb little or none of this radiation.

## EXPERIMENTAL DETAILS

### Measurements

To provide the required line-of-sight radiance and transmittance data, the ideal infrared instrumentation system must be able to allow performance of the following experiments:

1. Measure plume spectral radiance by comparing plume intensity with blackbody intensity; radiation is optically chopped between the plume and the detector.
2. Measure plume spectral transmittance by locating a greybody source on the opposite side of the plume from the spectrometer; greybody radiation is optically chopped between the greybody and the plume (preferably) so that the plume transmittance may be directly determined.
3. Provide for variation of line of sight by spatially scanning the images of the plume, greybody, or blackbody that are formed at the entrance slit of the spectroradiometer.

4. Obtain both radiance and absorptance measurements at several different, but accurately reproducible, wavelengths during each individual motor firing.

The method for carrying out these experiments would depend on engine test duration and engine size. For the programs described in references 1, 2, and 3 the nozzle exit diameter ranged from 4 to 8 inches and the test duration was normally 20 seconds.

Figure 3 shows the emission-absorption experimental arrangement. The greybody (absorption source) consists of an electrically heated carbon rod six inches in length mounted in an airtight, argon-purged housing. The greybody is mounted inside a 400 cps cylindrical "squirrel cage" optical chopper. Calcium fluoride windows 0.375 inch thick and 6.5 inches in diameter isolate various portions of the optical path. The three gate valves in the optical path which act as safety shutters are sequenced to open just after motor ignition and to close just before motor cutoff. The entire system may be purged with nitrogen to minimize atmospheric absorption. The diffuser was not used in the work described in reference 2.

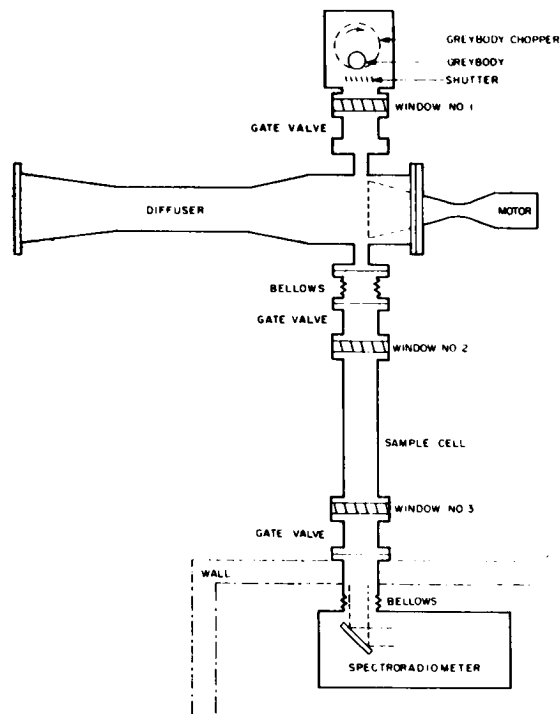


FIGURE 3. EXPERIMENTAL ARRANGEMENT FOR ABSORPTION-EMISSION MEASUREMENTS

The images of the blackbody, greybody and/or plume that are formed at the monochromator entrance slit are spatially scanned in the following manner. A cam which is rotated at constant angular velocity drives a rod at constant linear velocity up and down in front of, and in a plane parallel to, the entrance slit. This rod, called the zone ranger, contains a small aperture (subtending approximately 0.1 the plume image diameter) which limits the field of view at the plume to 1 cm x 0.2 cm (the smaller dimension depends on the slit width). Thus, this device is essentially a travelling field stop. The size of this aperture is adjustable.

During zone radiometry experiments, a filter wheel, in conjunction with a diffraction grating blazed at 30 microns, provides for wavelength selection and accurate reproducibility. A grating with a blaze wavelength of 30 microns was chosen because radiation diffracted by this grating at the blaze angle in high orders falls into spectral regions suitable for the required radiance and emissivity determinations. For instance, at the blaze angle, this grating will diffract  $4.29 \mu$  energy in seventh order to the detector, thus allowing a determination of the  $\text{CO}_2$  (gas) radial temperature distribution; similarly, in the nineteenth order,  $1.58 \mu$  energy will be diffracted to the detector, thus allowing a determination of carbon particle radial temperature distribution. In this method each desired spectral order is isolated by a narrow band pass spectral filter, while the 30  $\mu$  blaze grating is held fixed at the blaze angle. Four filters are used in each motor firing, and the fact that the grating remains fixed insures an extremely accurate wavelength reproducibility for the absorption and emission measurements. The grating is used at the blaze angle to insure that sufficient energy is diffracted into the desired spectral orders.

Operation of the zone ranger and filter wheel, as well as the change from tuning fork chopper to greybody chopper, is automatic. A schematic of the control system is shown in Figure 5. The shaft of the zone ranger cam holds three electrical cams. One electrical cam produces a signal on the recorder event pen to key the zone ranger position. The second electrical cam momentarily disengages the filter wheel positive stop mechanism as the third activates the filter wheel stepping motor. The four-position filter wheel also produces an electrical signal on the recorder during its motion for positive filter identification. The filter wheel is activated after each zone ranger cycle. The filter wheel 30-degree stepping motor drives the filter wheel through a 3:1 gear reduction. Thus, the filter wheel makes three revolutions while the stepping motor makes one revolution. After the filter wheel has made one revolution, the wafer switch activates relays which in turn remove power from the tuning fork chopper, switch the 400 cps reference signal from the tuning fork chopper to the greybody chopper, and then open the greybody optical shutter.

Figure 4 shows schematically the infrared spectroradiometer. A Perkin Elmer Model 98G grating monochromator is used with either an uncooled PbS detector or a liquid nitrogen cooled PbSe detector, or a photomultiplier tube. The internal optical chopper used to chop plume emission is located just inside the monochromator exit slit. This chopper is basically a tuning fork with chopper blades attached to the tines. The tuning fork is electrically driven at the desired chopping frequency (400 cps) when plume spectral radiance is being measured. When plume absorptance is to be measured power is removed from the tuning fork driving mechanism, the tines stop in an open position in approximately one second, and the greybody optical shutter is opened to allow the chopped greybody radiation to pass through the plume.

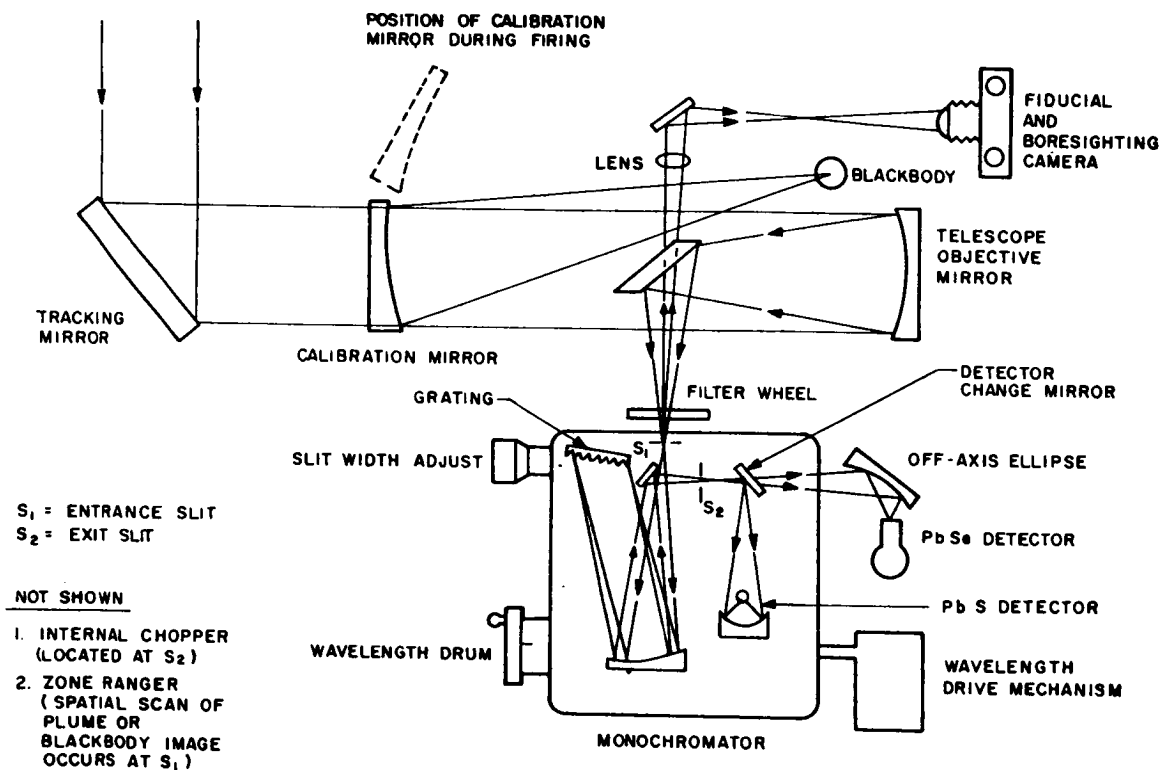


FIGURE 4. OPTICAL DIAGRAM OF INFRARED SPECTRORADIOMETER

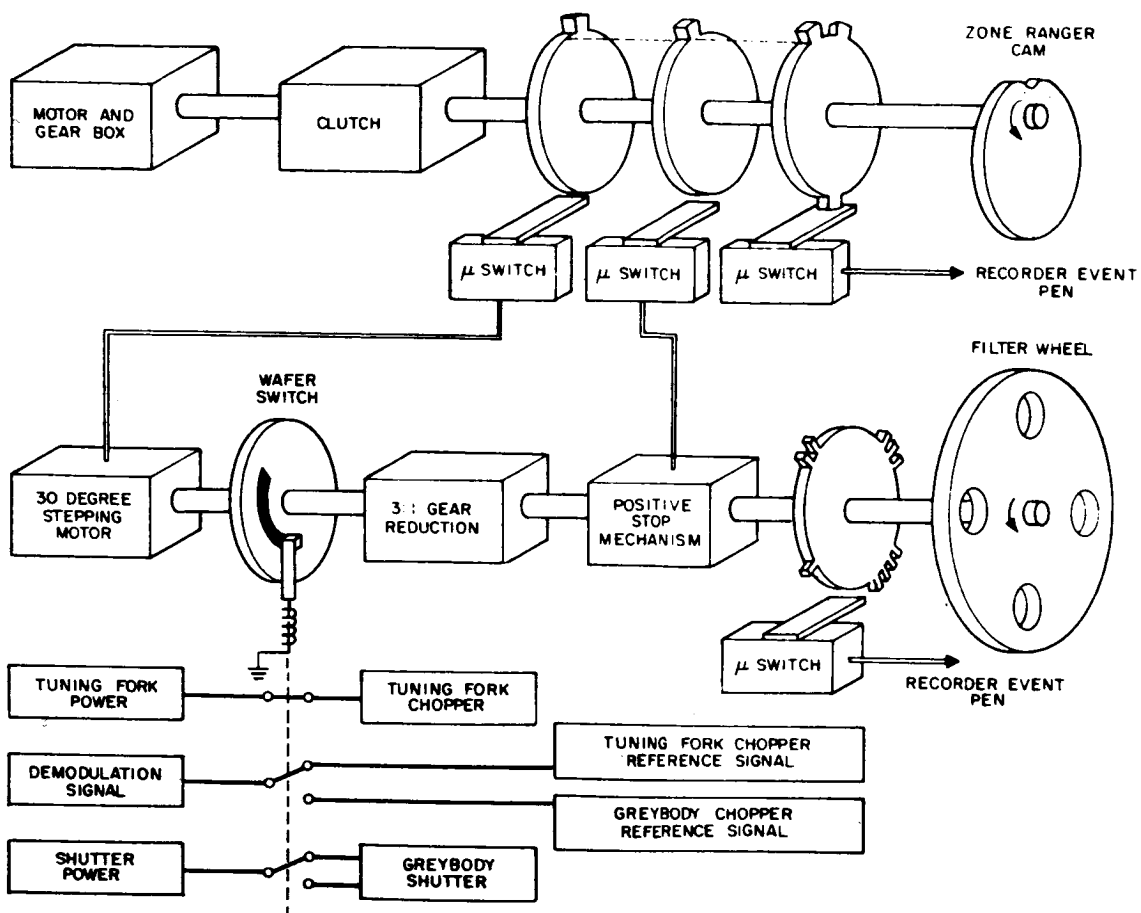


FIGURE 5. SCHEMATIC OF ZONE RANGER CONTROL SYSTEM

Approximately 20 seconds were available for the gathering of data during each motor firing. Spatial scans of the plume in emission and absorption were obtained in the following manner:

1. Before motor firing, the internal and greybody choppers are activated, the greybody is set at a desired brightness temperature, and the filter wheel is positioned so that filter No. 1 is in the optical train and so that the wafer switch relays have closed the greybody shutter, supply power to the tuning fork chopper, and allow the tuning fork 400 cps reference signal to reach amplifiers.

2. After motor ignition, the zone ranger mechanism is activated manually (all following operations then occur automatically). The zone ranger scans the plume image radius in one direction in one second. After the zone ranger makes a complete cycle (scans the plume image radius twice) the electrical cams activate the filter wheel stepping mechanism; the filter wheel makes one-quarter of a revolution, allowing energy at a second wavelength to reach the detector. The zone ranger continues to run at a half cycle per second.
3. After the filter wheel has made a complete revolution (plume radiance will have been measured at four wavelengths), the wafer switch activates relays as described above, and the zone ranger now scans at four identical wavelengths the chopped greybody radiation that is transmitted by the plume.
4. For intensity calibration purposes, the greybody and blackbody images are similarly scanned before and after each firing.

For much of the work described in reference 2, two pairs of identical filters were used in the filter wheel so that two complete sets of data were obtained at each of two wavelengths during a single firing.

Conventional spectral scans of plume emission or absorption can also be made. In this case the zone ranger device and the filter wheel are removed from the instrument. For the 1 to 2  $\mu$  range, a grating blazed at 1.6  $\mu$  is used in first order, and higher orders are eliminated by a silicon window. A grating blazed at 4  $\mu$  is used in the 2-6  $\mu$  spectral region in first order. Below 3.5  $\mu$ , higher orders are eliminated by a germanium window and above 3.5  $\mu$  by an indium arsenide window. Ultraviolet-visible spectra were obtained in the 2500 to 5000 Angstrom range using an RCA 7200 photomultiplier and grating blazed at 3000 Angstroms.

## Data Reduction

Zone radiometry data were recorded on a strip chart recorder. Line-of-sight values (corresponding to pen deflection) of unattenuated greybody radiation, greybody radiation attenuated by the plume, blackbody radiation and plume radiation (all for the same line of sight) were read from the strip charts and served as input data for the computerized data reduction procedures. The

computer calculated the radial values of spectral radiance, spectral emissivity, temperature, and the product  $K_{\lambda, T} P_K$ . For the species  $\text{CO}_2$ , values of  $K_{\lambda, T}$  were taken from the work of Malkmus [6]. The product  $K_{\lambda, T} P_K$  for each zone is divided by the value of  $K_{\lambda, T}$  (based on the temperature of each zone) to determine the  $\text{CO}_2$  partial pressure,  $P_K$ , for each zone.

The carbon particle density was determined in the following manner. As described in reference 2, samples of carbon particles were extracted from various portions of a  $\text{LO}_2/\text{RP-1}$  exhaust, and the particle size distribution was determined from photomicrographs of the samples. The size distribution, along with the local values of spectral emissivity determined from zone radiometry, allowed computation of the local density of carbon particles from the theoretical curves of Stull and Plass [7] which plot spectral emissivity as a function of density for various size distributions.

## RESULTS AND DISCUSSION

Figures 6, 7, and 8 are taken from reference 2. The results in these figures were obtained from data taken during ten 20-second-duration  $\text{LO}_2/\text{RP-1}$  firings of a 1000-pound-thrust, 1000 psi chamber pressure, model of the F-1 rocket engine. The exhaust plume was assumed to be divided into concentric rings of width 0.45 cm.

Figure 6 shows that the species  $\text{CO}_2$  is fairly evenly distributed across the exhaust plume at the nozzle exit plane and 2 inches downstream. However, 8 inches downstream the  $\text{CO}_2$  partial pressure has risen considerably; this pressure rise is expected since this latter station is approximately 2 inches behind the first shock. Figure 7 shows the carbon particles to be concentrated within a ring at the outer edges of the plume. Presumably the carbon particles are formed in the cooler, fuel-rich combustion region along the chamber walls, and remain so distributed until they are several inches downstream. Figure 8 shows a cool central plume core at the nozzle exit plane (attributed to the injector pattern) and a sharp rise in temperature behind the first shock. The apparent existence of  $\text{CO}_2$  and carbon particles at the nozzle exit plane a distance of several zones outside the nozzle edge is attributed to the field of view of the zone radiometer at the plume (about 1.5 cm in height). This effect, which is identical to that arising when a spectrometer scans a narrow spectral line, causes the carbon particle distribution to be considerably broader and less sharp than the true distribution. No attempt was made to correct for this broadening effect, although it would not be difficult to do so.



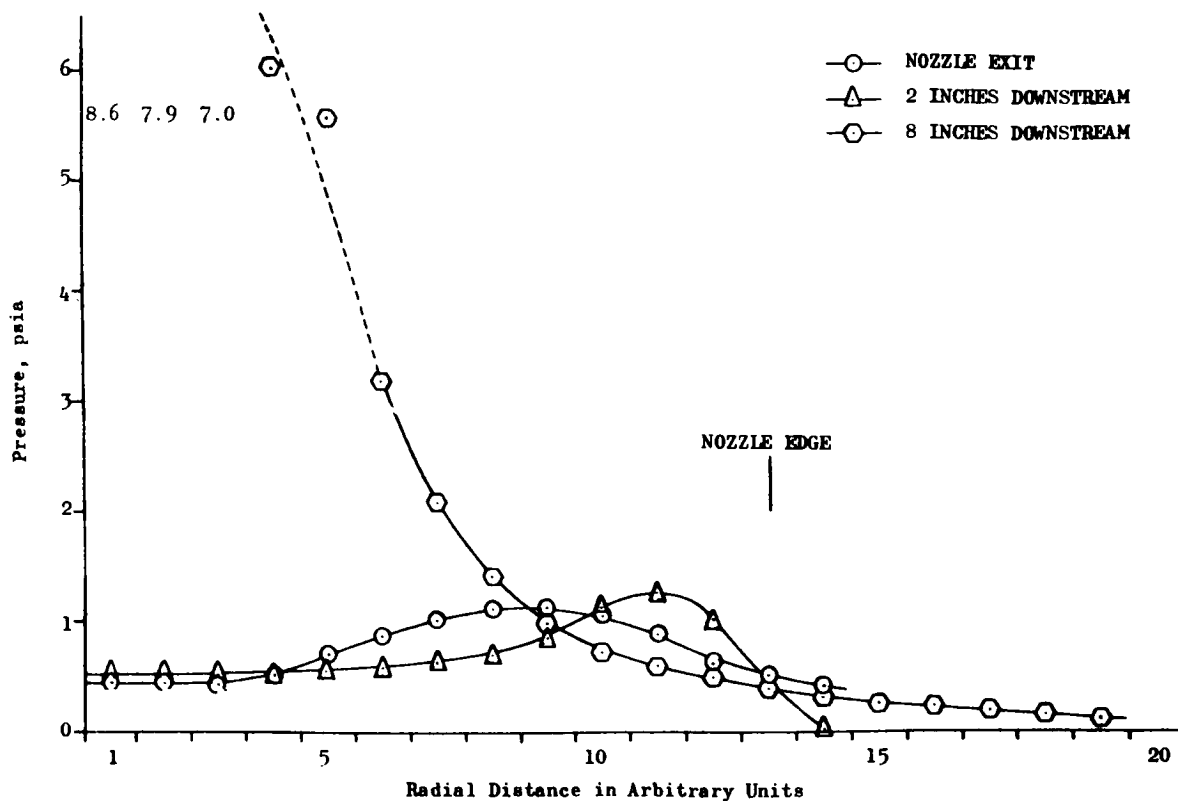


FIGURE 6. RADIAL DISTRIBUTION OF CO<sub>2</sub> PARTIAL PRESSURE, MODEL F-1, LO<sub>2</sub>/RP-1

It is difficult to determine the absolute accuracy of the zone radiometry technique since there is no independent, more accurate technique of measuring the temperature or pressure in the exhaust. However, it can be said that the values obtained are reasonable; the measured CO<sub>2</sub> partial pressures at the nozzle exit are bounded by the theoretically predicted values of frozen and shifting equilibrium; there is fair agreement between CO<sub>2</sub> and carbon particle densities as measured spectroscopically and by sampling techniques. Temperature determinations made during different portions of a single run or during different runs with the same motor operating parameters showed reproducible results to within 100 degrees Kelvin.

As long as the assumption that gradients are small within individual zones is valid, the method of equation solution (inversion or simultaneous) introduces no errors into the data. In fact, one set of data with maximum line-of-sight transmittance of about thirty percent were reduced using both methods; the results were essentially identical.

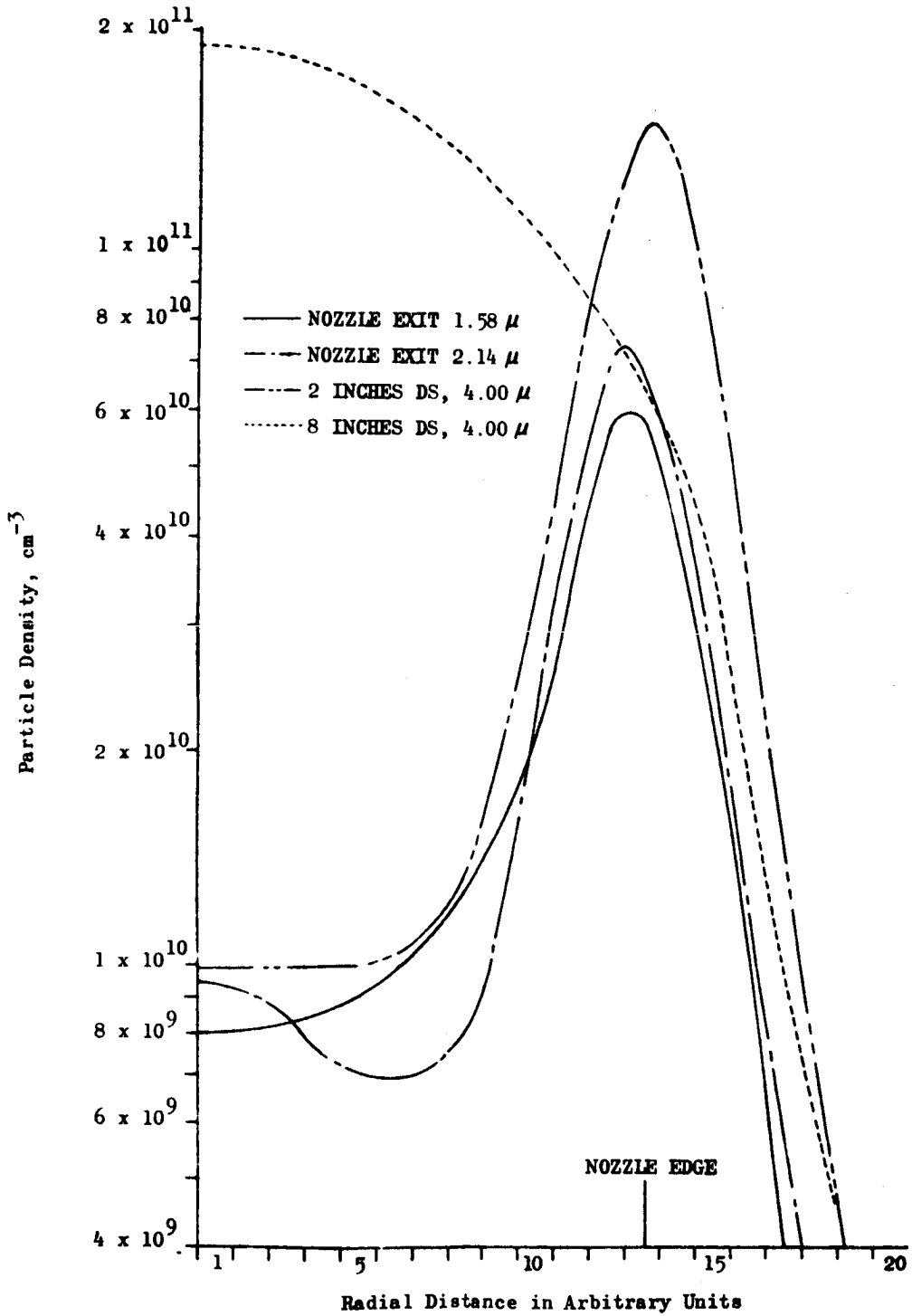


FIGURE 7. RADIAL DISTRIBUTION OF CARBON PARTICLE DENSITY, MODEL F-1,  $\text{LO}_2/\text{RP-1}$

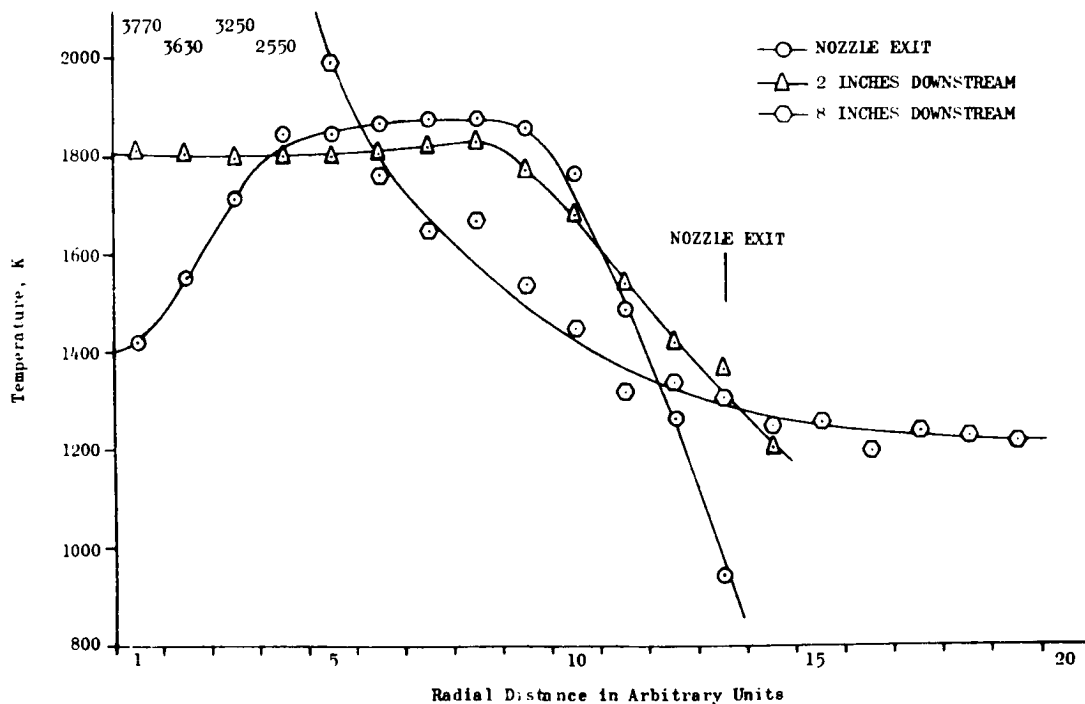


FIGURE 8. RADIAL DISTRIBUTION OF CO<sub>2</sub> TEMPERATURE, MODEL F-1, LO<sub>2</sub>/RP-1

In the work to date, it has been possible to make temperature and pressure calculations only for the species CO<sub>2</sub> and carbon particles. The primary reason for this is that radiation from these species can be treated as continuum radiation over the spectral band pass of the spectrometer. In addition, there is considerable experimental and theoretical data available on these species. With the large amount of data that are now becoming available on H<sub>2</sub>O and with the use of band model techniques, there should be no great problem in determining water partial pressures and concentrations.

Zone radiometry techniques are applicable to the study of any gas system. To study large rocket engine exhausts, an instrument is being developed (Contract NAS8-21144) that will use multiple absorption sources and a rotating mirror to achieve spatial scanning of the exhaust. Another instrument that is planned for the study of millisecond duration tests at Cornell Aeronautical Laboratory will image a plane in the flow field onto a detector array to achieve spatial resolution. One particular experiment that Rocketdyne hopes to carry out in the

future is of interest because it will afford a check on the absolute accuracy of zone radiometry. In this experiment, partial pressures would be determined for a cold flow of premixed non-reacting gases exhausted to the atmosphere at ambient pressure. Since the concentration and total pressure of the species are known, an absolute check on absorption zone radiometry will be obtained.

## REFERENCES

1. Herget, W. F.; Schumacher, P. E.; Enloe, J. D.; Levin, B. P.; and Suarez-Alfonso, E.: An Instrumentation System to Study Rocket Exhaust Plume Radiative Processes. Rpt. R-6288. Rocketdyne, a Division of North American Rockwell Corporation, Canoga Park, California, Contract No. NAS8-11261, August 27, 1965.
2. Herget, W. F.; Schumacher, P. E.; Cline, G. L.; and Ford, W. M.: Radiative and Structural Characteristics of Rocket Engine Exhaust Plumes. Rpt. R-6742. Rocketdyne, a Division of North American Rockwell Corporation, Canoga Park, California, September 29, 1966.
3. Herget, W. F.; Schumacher, P. E.; and Enloe, J. E.: Radiative Properties of Rocket Exhausts at Simulated Altitudes. Rpt. R-6347. Rocketdyne, a Division of North American Rockwell Corporation, Canoga Park, California, Contract AF08 (635)-4385, October 1966, SECRET.
4. Freeman, M. P.; and Katz, S.: J. Opt. Soc. Am., vol. 50, 1960, p. 826.
5. Nestor, O. H.; and Olsen, H. N.: SIAM Review, vol. 2, 1960, p. 200.
6. Malkmus, W.: J. Opt. Soc. Am., vol. 53, 1963, p. 951.
7. Stull, R.; and Plass, G.: J. Opt. Soc. Am., vol. 50, 1960, p. 121.

# THE INVERSION PROBLEM IN STELLAR ATMOSPHERES

By

N 68-18101

Oran R. White

Sacramento Peak Observatory  
Sunspot, New Mexico

---

## ABSTRACT

Because of the large distances and extreme physical conditions involved, the radiation from stars is our only source of information on stellar constitution. The analysis of this radiation necessarily requires inversion of the intensity integral if we are to estimate the run of physical conditions with depth. As an example of the stellar atmospheres problem, the basic data and analytic techniques for analysis of solar limb darkening data are given. The analytic approach will be general enough to allow for departures from thermodynamic equilibrium.

---

## INTRODUCTION

Since the sun and stars are remote by definition, any estimates of temperature, density, and motion of the stellar material must come from remote sensing techniques. The desire to know physical conditions in stellar atmospheres has led to analytic methods based primarily on interpretation of spectral lines and free-bound continua. The astrophysics problem most pertinent to the discussions here is the analysis of line profiles and limb-darkening curves obtained by measurement of the solar radiation. Although astrophysicists have worked on the analytical problem for many years, they do not yet have a truly satisfactory method; and in particular, the methods for inverting the emergent intensity integral are suspect.

## THE TYPE OF DATA AVAILABLE

The solar disk spectrum above  $2000 \text{ \AA}$  consists of absorption lines superposed on a background continuum, but at shorter wavelengths the continuum weakens to leave only an emission line spectrum. Here we will discuss only the absorption spectrum and its variation across the solar disk. Figure 1 shows the solar disk at two different times as seen in the center of the  $H\alpha$  line at  $6563 \text{ \AA}$ . A typical observing program requires measurement of a line profile in many positions in the quiet regions as well as measurements in the active centers. However, only the spectra of quiet regions are amenable to simple inversion techniques. Figures 2 and 3 show mean line profiles of the two D lines of Na I and two of the Mg I triplet lines as measured at the center of the quiet solar disk. The non-gaussian shapes of these lines show that the entire profile cannot be explained in terms of a simple absorption coefficient and source function, but the profile does, in principle, contain information on the depth variation of these quantities since the center of the line originates from a higher layer than the wings.

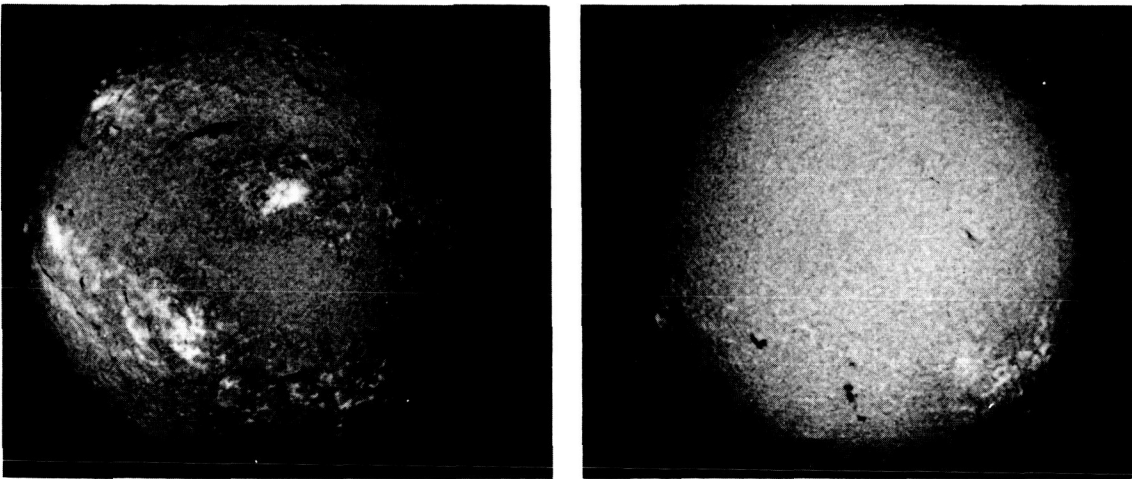


FIGURE 1. TWO  $H\alpha$  FILTERGRAMS MADE FEBRUARY 1966 AND FEBRUARY 1967 TO SHOW THE DIFFERENCE IN THE QUIET AND ACTIVE SOLAR DISK

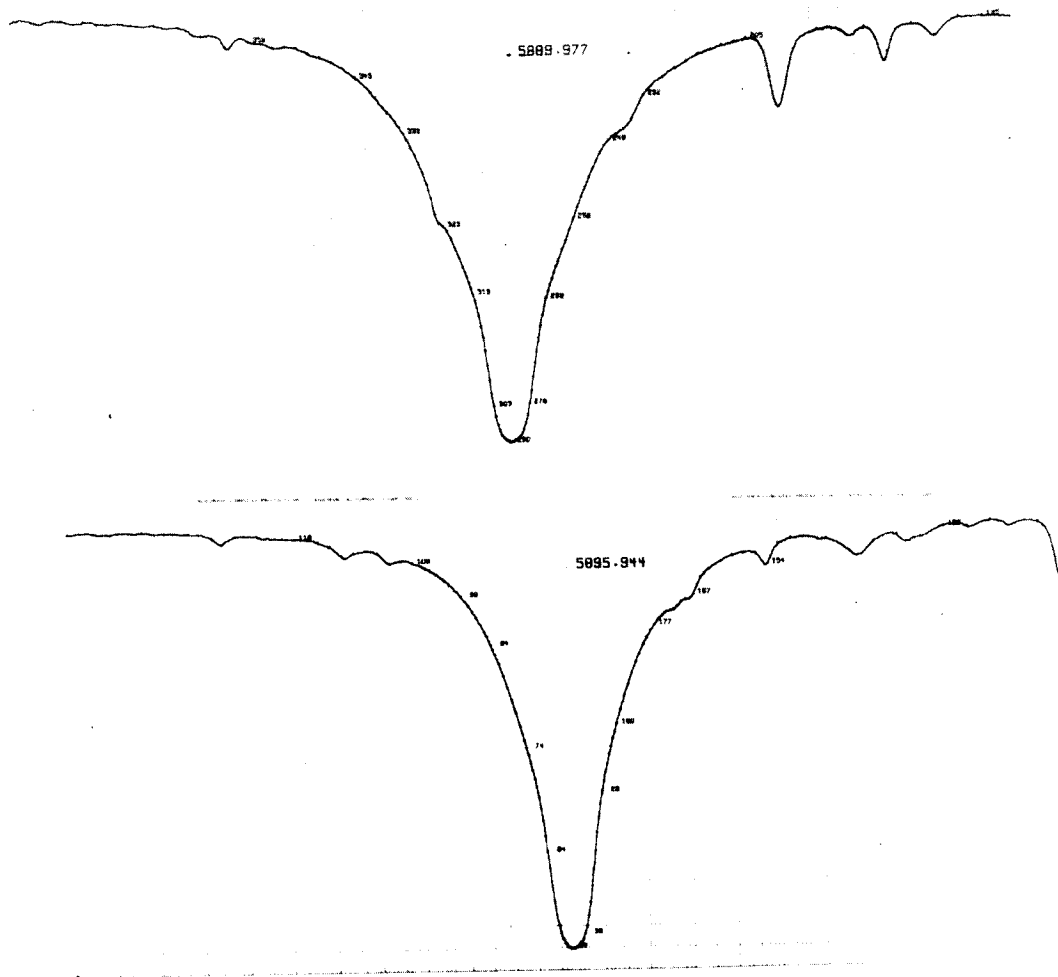


FIGURE 2. PROFILES OF THE Na D LINES AS OBSERVED FOR AN AVERAGE, QUIET REGION NEAR THE CENTER OF THE SOLAR DISK

The second direct evidence of depth variations is shown by the intensity variations from the sun's center to its edge. Figure 4 shows three such limb-darkening curves at wavelengths in the  $D_1$  line of Na I. Note that the abscissa is the coordinate in the plane of the solar disk,  $\sin \theta$ . Figure 5 shows two of the previous curves plotted on the more convenient  $\cos \theta$  scale. The different shapes of the curves at various wavelengths indicate the differences in the regions sampled by the emergent radiation. The inversion of such curves does, in principle, give us the run of the source function over a depth range of  $\mu_{\min} \leq \tau_{\lambda} \leq 1.0$  only at the observed wavelength. The smearing of the limb-darkening curve by instrumental and atmospheric effects limits the usable data to  $\mu \geq .2$ .

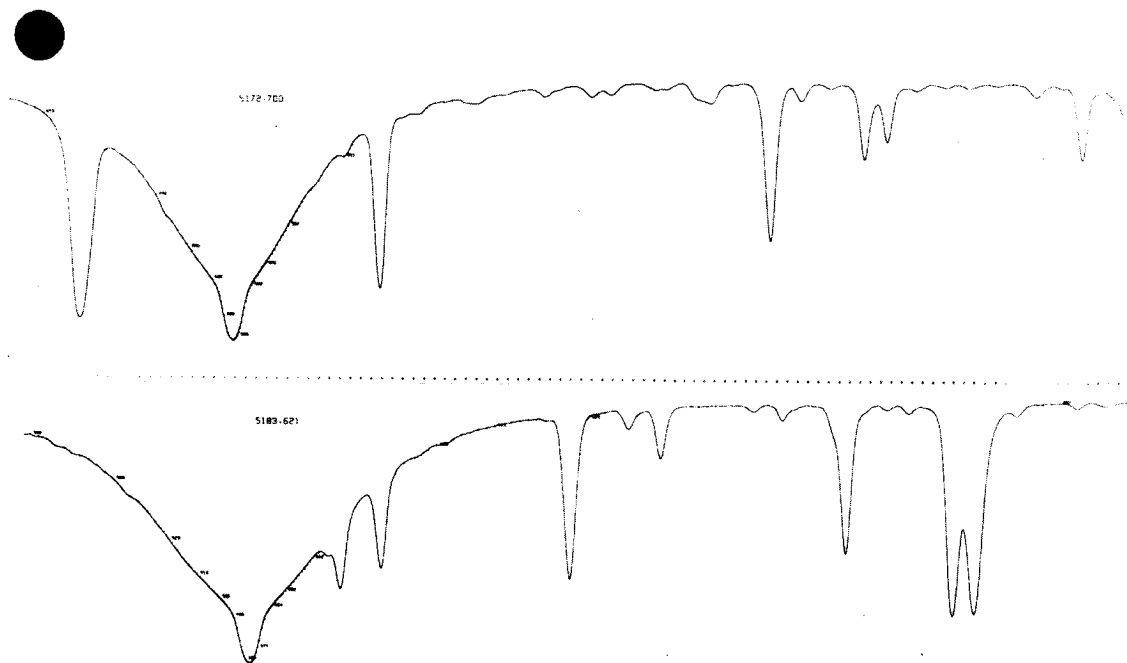


FIGURE 3. PROFILES OF THE  $b_1$  AND  $b_2$  LINES OF Mg I AS OBSERVED FOR AN AVERAGE, QUIET REGION AT THE CENTER OF THE SOLAR DISK

In the case of stellar spectra, the situation is worse because the star's disk is not resolved. As a result, no limb-darkening data can be obtained; only the wavelength variation of the intensities is available.

### THE MATHEMATICAL MODEL AND THE INVERSION OF LIMB-DARKENING CURVES

Since the visible solar layer is very thin relative to the solar radius — .005 of the radius — the plane parallel approximation is good out to  $\cos \theta \sim .03$ , which is usually the range of reliable observations. As the mathematical model we adopt a semi-infinite, plane-parallel atmosphere. The emergent intensity is then described by the usual solution to the equation of transfer:

$$I_{\lambda}(\mu) = \int_0^{\infty} S_{\lambda}(\tau_{\lambda}) \exp(-\tau_{\lambda}/\mu) d\tau_{\lambda}/\mu. \quad (1)$$



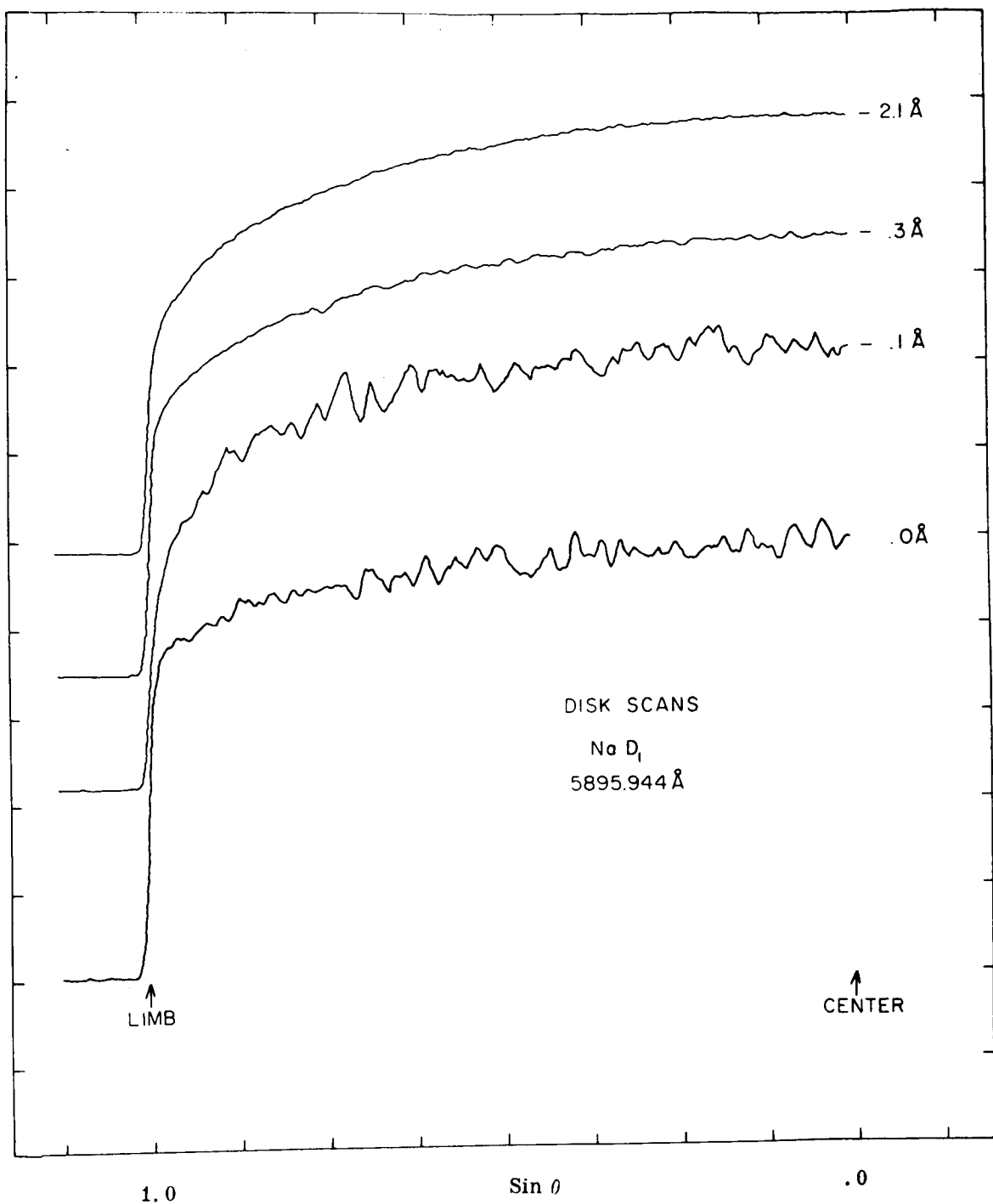


FIGURE 4. THREE NORMALIZED LIMB DARKENING CURVES MADE AT WAVELENGTHS IN THE D<sub>1</sub> LINE OF Na I. THE CURVES ARE TRACED FROM ORIGINAL DATA WHERE THE x COORDINATE IS SIN  $\theta$  ( $\theta$  IS THE ANGLE BETWEEN THE LINE-OF-SIGHT AND THE NORMAL TO THE SOLAR SURFACE)

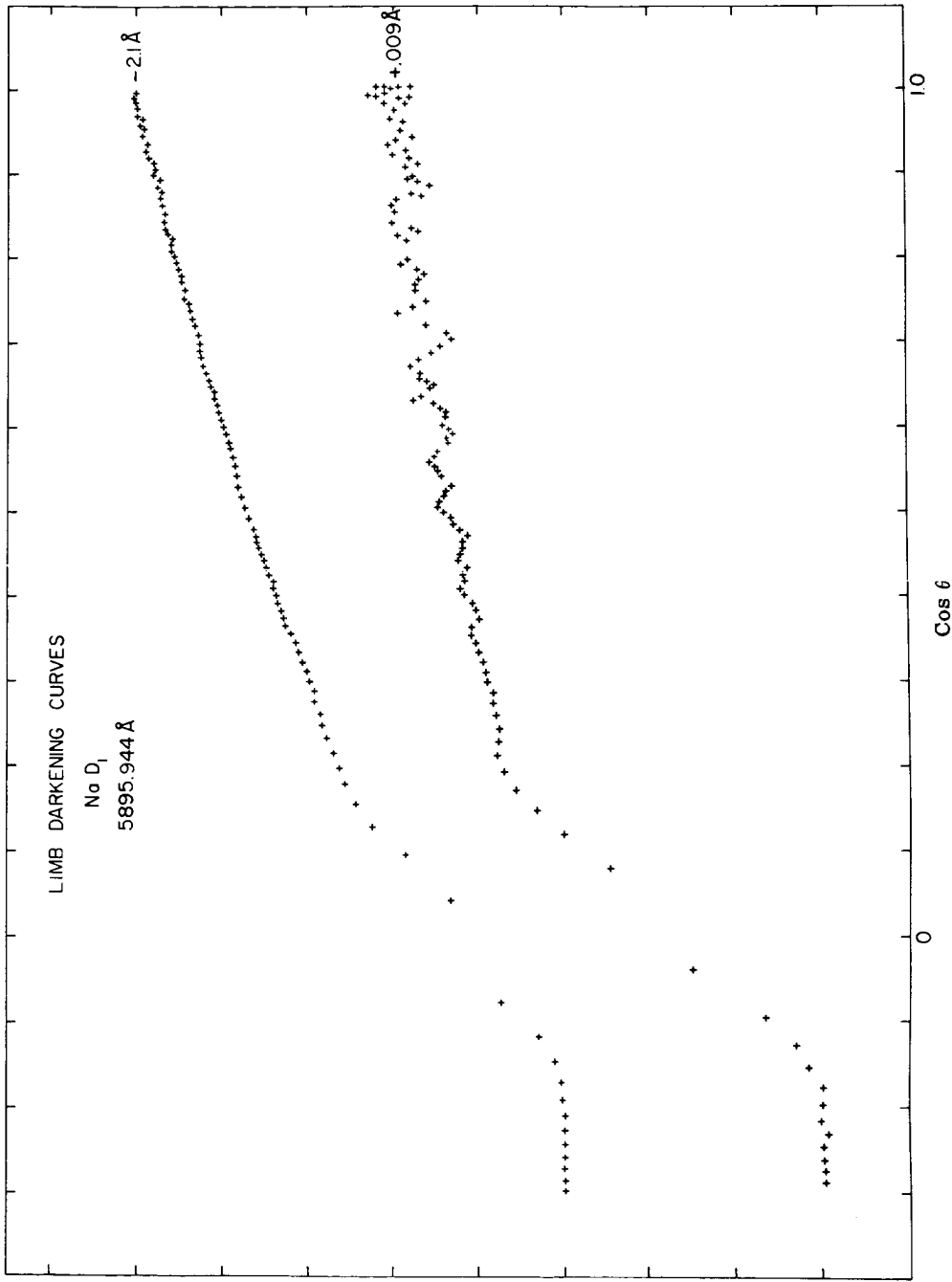


FIGURE 5: TWO OF THE LIMB-DARKENING CURVES FROM FIGURE 4 PLOTTED AS A FUNCTION OF  $\cos \theta$ . THE SHAPES OF THESE CURVES GIVE SOME IDEA AS TO THE FORM OF SOURCE FUNCTIONS THAT WOULD BE OBTAINED BY INVERSION

Given the observed values of  $I_\lambda(\mu)$ , the inversion of Equation (1) is commonly performed by adopting integrable forms for  $S_\lambda(\tau_\lambda)$ . Also, in many cases,  $S_\lambda(\tau_\lambda)$  is chosen so that  $I_\lambda(\mu)$  is linear in a set of unknown coefficients, in which case the inversion is conveniently performed by least-squares fitting. Table I shows a list of linear inversions often used to analyze solar data.

TABLE I

#	$S(\tau_\lambda)$	$I(\mu)$
1.	$a + b\tau$	$a + b\mu$
2.	$a + b\tau + c\tau^2$	$a + b\mu + 2\mu^2$
3.	$a + b\tau + c E_2(\tau)$	$a + b + c [1 - \mu \ln(1+1/\mu)]$
4.	$a + b \ln \gamma \tau + c (\ln^2 \gamma \tau - \pi^2/6)$	$a + b \ln \mu + c \ln^2 \mu$

Inversion Equation (1) has some physical justification since the form linear in  $\tau$  corresponds to the solution for the grey atmosphere under the Eddington approximation. Similarly, Kourganoff [1] found that in form 3 the addition of exponential integral terms to the linear form gave a close approximation to the solution of the Milne problem. The quadratic forms 2 and 4 are only expansion formulae chosen for convenience. The source functions obtained from these functional forms are usually taken to be valid only in the range  $\mu_{\min} \leq \tau \leq 1.0$ . Figure 6 shows empirical excitation temperature distributions derived from limb-darkening data in the  $H\alpha$  line of neutral hydrogen. Note that the line source functions and the excitation temperature are related by

$$S_\ell = B_\lambda(T_{\text{ex}}).$$

However, since we observe real atmospheres that do not necessarily have the textbook solutions, the use of the functional forms in Table I is not completely satisfactory. So, more general inversion methods have been sought, and two methods of interest have been discussed by Jefferies [2] and King [3]. Jefferies' method is the least-squares fit of the data to a quadrature of the integral (1), but a smoothness condition has been included in the function to be minimized. The function to be minimized is

$$\sum_{i=1}^n (I_i - \sum_{j=1}^m c_{ij} S_j)^2 + \lambda \sum_{j=1}^m a_j S_j^2, \quad (2)$$

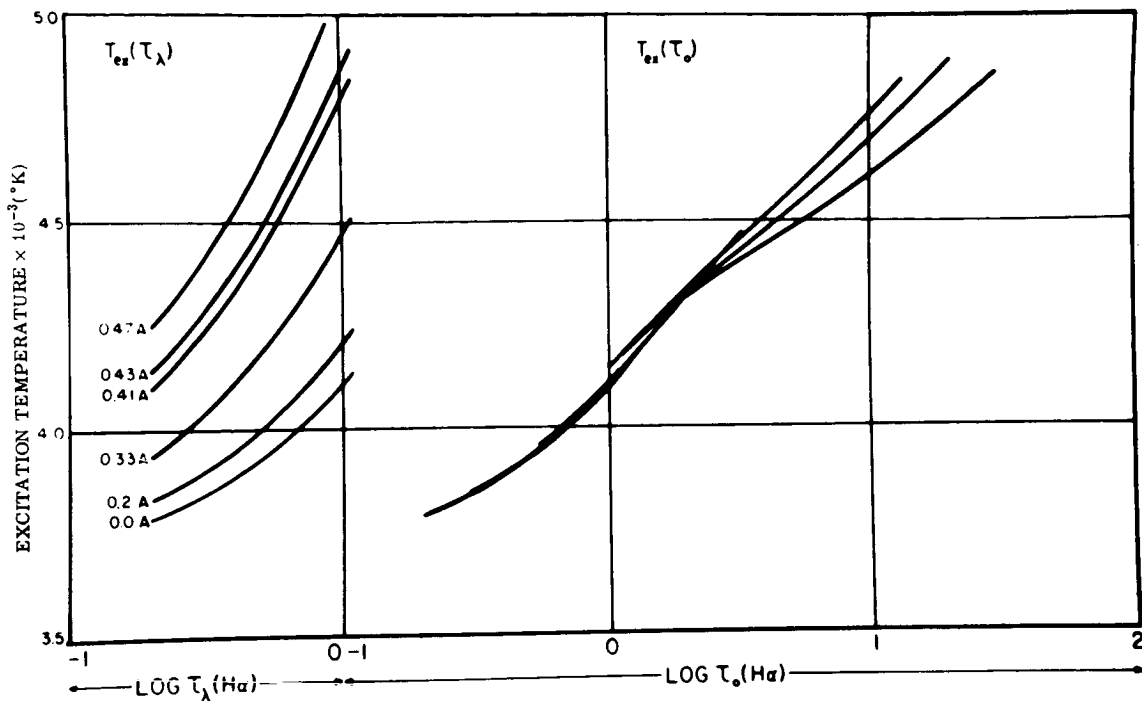


FIGURE 6. EXAMPLES OF EXCITATION TEMPERATURE DISTRIBUTIONS OBTAINED BY INVERSION OF  $H\alpha$  LIMB DARKENING DATA WITH A QUADRATIC IN  $\cos \theta$ . THE LEFT SIDE SHOWS THE INFERRED EXCITATION TEMPERATURE CURVES ON THE  $\log \tau$  SCALE FOR THE INDICATED WAVELENGTHS AND THE RIGHT SIDE SHOWS THE  $T_{ex}$  DISTRIBUTION AFTER MAPPING TO A COMMON OPTICAL DEPTH.

where  $\lambda$  is an arbitrary parameter chosen by trial for best fit to the data, and the  $a_j$  are values of a weighting function that vanishes at each end of the optical depth range. The inclusion of the additional  $\sum_j a_j S_j^2$  term reduces the ill conditioning encountered in least-squares inversions.

King's [3] approach employs the Prony algorithm commonly used in fitting data with a sum of exponentials. In its application to the inversion problem, the Prony solution defines a slab model atmosphere where both the slab heights and thickness are given by the solution. In addition, the values of  $\cos \theta$  for observation are specified, and the complexity of the solution

automatically reduces as the noise in the data increases. The Prony method has been modified by White [4] to treat both line profiles and limb-darkening curves and to estimate the smooth run of the source function with depth. Although neither the Jefferies nor the King approach has been used extensively yet, they appear to be superior to other methods in that the solutions extend reasonably to depths below  $\tau = 1$ .

## THE PHYSICAL BASIS FOR AN ANALYSIS

Given that the emergent intensity integral can be inverted with sufficient confidence, how can we proceed to obtain temperature and density estimates from the inferred source function  $S_{\lambda}(\tau_{\lambda})$  in Equation (1)? Notice that we have not identified this function with the Planck function so that the question of departures from thermodynamic equilibrium can be examined in the analysis. Let us consider a general case where both line and continuum processes are present, but we limit the wavelength range to the neighborhood of the line so that the continuum emission and absorption may be considered as independent of wavelength. Using the definition of the source function as the ratio of the emissivity to the absorptivity, we find the total source function to be

$$S_{\lambda}(\tau_{\lambda}) = \frac{S_{\ell} + r_{\lambda} S_c}{1 + r_{\lambda}}, \quad (3)$$

where  $S_{\ell}$  = line source function =  $f_1(\lambda, \tau)$

$S_c$  = continuum source function =  $f_2(\tau)$

$r_o$  = ratio of continuous and line absorption coefficients

=  $r_{\lambda} \phi_{\lambda} = f_3(\tau)$

$\phi_{\lambda}$  = normalized wavelength profile of line absorption coefficient

=  $f_4(\lambda, \tau)$ .

The functional dependences are indicated at the right. These four quantities are the spectroscopic functions necessary to describe the radiation field in the spectral neighborhood of the line under study (see Jefferies and White [5]), and an objective analysis must attempt to infer these functions from the data.

However, simple considerations show that the number of unknowns far exceeds the observables, in which case we must call upon all reasonable assumptions if an empirical solution is to be found. For example, a set of intensities at  $m$  positions across the disk and at  $n$  wavelengths in a line will allow at most only  $mn$  inferred parameters. However, the desired spectroscopic description requires values of  $S_\ell$ ,  $S_c$ ,  $r_o$ , and  $\phi_\lambda$  at  $m$  depths and, in addition, values of  $S_\ell$  and  $\phi_\lambda$  at  $n$  frequencies or a total of  $m(2n+1)^*$  parameters from  $mn$  observations. One justifiable assumption that may be used is that the line source function is independent of wavelength (see Hummer [6]). In this case, we have  $m(n+2)$  unknowns, which is still too many. Resort to thermodynamic equilibrium, where  $S_\ell = S_c = B_\lambda(T)$ , does not solve the problem since the number of unknowns is still  $m(n+1)$ . We conclude that an analysis of limb-darkening observations in a single line is not possible, even under the LTE assumption, unless additional assumptions are made such as specifying the wavelength dependence of  $\phi_\lambda$ . In the cores of strong lines, it is reasonable to assume that  $\phi_\lambda$  has the form given by Doppler broadening, but rarely will this assumption be valid for the analysis of the entire profile.

A more general solution is possible when we have two close-lying multiplet lines that share a common wavelength-independent source function. Such lines are the Na D lines and Mg b lines shown earlier. In this case, we have  $2mn$  observations and  $m(n+2)$  unknowns so that data at two or more wavelengths in each line will, in principle, give all of the spectroscopic variables in Equation (3). See Jefferies and White [5] for a more detailed discussion of the method of solution.

---

\* Only  $m(n-1)$  values of  $\phi_\lambda$  are required in the solar case since we take  $\phi_{\lambda_0} = 1$  at some reference wavelength.

## THE PHYSICAL MEANING OF THE INFERRED SPECTROSCOPIC QUANTITIES

Usually the continuum source function is taken to be the Planck function so that its value defines a local temperature as a function of depth. Similarly, in the line cores  $\phi_\lambda$  may yield a Doppler width that, in turn, can be used to compute a kinetic temperature and a microturbulent velocity. In the line wings the wavelength variation of  $\phi_\lambda$  may give the collisional broadening parameter that depends on the local density of perturbing particles. The continuous absorption parameter  $r_0$  is essentially the ratio of the number of particles absorbing in the continuum to the number of particles absorbing in the line, and in this case, the interpretation of  $r_0$  is not simple unless one knows the excitation in both sets of particles. In the sun where the  $H^-$  ion contributes most of the continuous opacity in the visible spectrum, the empirical values of  $r_0$  have been used to estimate the abundance of the element producing the line (see Jefferies and Curtis [7]).

The inferred value of the line source function  $S_\ell$  will give the first indication of departures from thermodynamic equilibrium. If  $S_\ell \neq S_c$ , then one suspects that non-LTE effects are present. In most cases, the first order non-LTE effects are produced by the presence of an atmospheric boundary through which the system loses radiation. The result of this leak is that near the boundary the contribution of scattering to  $S_\ell$  decreases, and the line source function tends to be smaller than  $S_c$ . In such cases, the identification of the total source function  $S_\lambda(\tau_\lambda)$  with  $B_\lambda(\tau_\lambda)$  results in an underestimate of the local temperature.

More quantitative interpretations of the line source function require extensive calculation since its value depends on the local value of the radiation field, the local collision rate, and the interlocking with other lines. If the local radiation field is the controlling factor, the value of  $S_\ell$  may be determined by long range transfer effects, and as such its value may not reflect local temperature values at all. In contrast, if the collisions predominate, then the line source function will indeed reflect a local temperature, and we have an LTE situation. Each atomic model and atmospheric geometry must be examined before we can draw any conclusions on the interpretation of the line source function.

## RESUME

The goal of the analysis of a real stellar atmosphere is to contrast empirically the run of  $S_\ell$ ,  $S_c$ ,  $r_o$ , and  $\phi_\lambda$  with optical depth over as large a depth range as possible. The interpretation of these spectroscopic parameters, in turn, gives temperature and excitation models. However, this general inversion problem—the conversion of measured intensities to temperatures, densities, etc.—rests squarely on the mathematical problem of inverting the Laplace transform of the total source function. Hopefully, this need will result in more accurate inversion techniques, as well as methods for estimating their reliability.

## REFERENCES

1. Kourganoff, V.: *Basic Methods in Transfer Problems*, Oxford, 1952.
2. Jefferies, J. T. and Hummer, D. G.: *JILA Report*, 1966.
3. King, J. I. F.: *J. Atmos. Sci.*, vol. 21, 1964, p. 324.
4. White, O. R.: *Inversion of the Limb Darkening Equation Using the Prony Algorithm*. *Ap. J.* (in press), 1967.
5. Jefferies, J. T. and White, O. R.: *Ap. J.* (in press), 1967.
6. Hummer, D. G.: *Proceedings, Second Harvard-Smithsonian Conference on Stellar Atmospheres*, 1965, p. 13.
7. Jefferies, J. T. and Curtis, G. W.: *Proceedings, Second Harvard Smithsonian Conference on Stellar Atmospheres*, 1965, p. 297.



---

## DISCUSSION

T. L. Altshuler, NASA Electronics Research Center: Dr. White, were you able to determine your source function by superimposing, say, 4 ramps, 3 ramps, 2 ramps?

O. R. White: The solutions that I have shown are obtained from the usual linear approach. From the data that I used for testing the Prony algorithm, I have taken solutions for different numbers of slabs and then superposed them to see whether we get a single distribution and whether they fall on the same curve.

T. L. Altshuler: I have used the same kind of experimental curve, but I have changed the spacing between the data points. This change altered the spacing between the joints in the ramps; I then combined these, which gave a much more accurate representation. Furthermore, if you change your initial data point, you can shift the whole scale over. In this fashion, you can get many multiple ramps.

O. R. White: I think we are talking about the same procedure. I changed the Prony formulation to allow scaling in order to make the sampling grid fit the observable range in cosine  $\theta$ . From several solutions for different scaling parameters, one can build up a smooth source function distribution.

S. A. Golden: Dr. White, have you made any comparison of the local temperatures you obtain by performing the spatial inversion with  $2n$  lines of sight and the results you would get by using only one line of sight through the center of the sun with a very high resolution in the individual lines and then obtaining the required  $2n$  equations by looking at  $2n$  different frequencies in that line?

O. R. White: We take many disk scans at different wavelengths in the line; but we have to put together all of this data (both line profiles and limb darkening curves) to get out the 4 parameters  $S_l$ ,  $S_c$ ,  $\phi_\lambda$ , and  $r_o$ .

S. A. Golden: In principle, if you require, let us say,  $2n$  equations to get  $2n$  local temperatures, couldn't you use either  $2n$  lines of sight or  $2n$  frequencies?

O. R. White: In our problem, there are more unknown parameters than the local temperature. You cannot keep observing more and more frequencies, because each frequency adds another undetermined value of the absorption coefficient and another value of the line source function, if it is frequency-dependent.

The problem gets away from you, unless you start putting in new information; for instance, you could try to find lines that have a common source function. What you are suggesting could be done, for example, if we had three lines sharing a common source function. The three lines could be analyzed in pairs and the results compared for consistency. This procedure has not been done yet, but we hope to do it when the observations are available.

---

PRECEDING PAGE BLANK NOT FILMED.

SESSION IV  
SHORT COMMUNICATIONS

# SOME THEORETICAL FREQUENCY AVERAGES FOR THE EMITTANCE OF A HOMOGENEOUS GAS-PARTICLE CLOUD\*

By

N 68-18102

Charlotte Decker Bartky  
Applied Research Laboratory  
Aeronutronic Division of Philco-Ford Corporation  
Newport Beach, California

---

## ABSTRACT

Frequency averages, assuming an Elsasser band model, have been obtained for the one-dimensional beam emittance of a thick cloud composed of a radiating gas and non-absorptive particles in the two limits, absorption or scattering predominant. These expressions, together with the trivial thin cloud and smeared line emittance, provide a means of calculating the radiance of a finite slab.

---

## INTRODUCTION

We have used the one-dimensional beam approximation to calculate the radiance of an inhomogeneous cloud of scattering and absorbing particles [1]. The general solution of the beam equations, containing two constants, is written for each finite "homogeneous" slab in the inhomogeneous cloud. The desired result is obtained by computer solution of a matrix equation derived from the boundary conditions. The advantages of this method are that an analytic expression exists for the single slab, and that multiple scattering and anisotropy are taken into account. The worst error, ~ 45 percent, in the monochromatic emittance is in the thick, isotropic scattering, scattering predominant ( $\epsilon_{\infty} \ll 1$ ) case. The agreement between the beam approximation for the emittance and the

---

\*This work was supported by Air Force Contract F 33615-67-C-1784, sponsored by Air Force Avionics Laboratory (RTD), Wright-Patterson Air Force Base, Ohio 45433.

exact emittance must improve as scattering in the vicinity of  $\pi/2$  decreases, i. e., as the scattering becomes peaked in the forward (and/or backward) directions.

On a strictly monochromatic basis, there is no difficulty in including gas radiation in the total absorption coefficient. However, the observed emittance suffers the same problem as the observed emittance of a purely gaseous medium; the behavior is not as expected, and for the same reason: the rapid variation of the absorption coefficient. The correct behavior in both cases is obtained by calculating the average emittance:

$$\epsilon(\ell) = \frac{1}{\Delta_\nu} \int_{\Delta_\nu} \epsilon_\nu(\ell) d\nu. \quad (1)$$

In the gas-only case,  $\epsilon(\ell)$  is

$$\epsilon(\ell) = \frac{1}{\Delta_\nu} \int_{\Delta_\nu} \left[ 1 - e^{-k_\nu \ell} \right] d\nu, \quad (2)$$

where  $k_\nu$  is the linear absorption coefficient at the existing radiating gas density, and  $\ell$  the ordinary thickness. Equations (1) and (2) are quite general, and the only problem is to find a "band model" to describe the line shape, intensity, and distribution for which a solution exists, at least for certain ranges of the parameters.

There is no need to go into detail in describing the presently well-known solutions for Equation (2). Some of the functional behavior is as follows:

Arbitrary line shape, distribution

$$\epsilon(\ell \rightarrow 0) = \tau = k\ell = \beta x$$

$$\epsilon_\infty = 1$$

Smearred line shape, large  $\beta$

$$\epsilon(\ell) = 1 - e^{-k\ell} = 1 - e^{-\beta x}, \text{ any } x \text{ or } \ell$$

Sharp line shape, small  $\beta$

$$\epsilon(x) = \beta f(x), \text{ small } x \text{ ("non-overlapping lines")}$$

$$\epsilon(x) = \epsilon \left[ (\beta^2 x)^{\frac{1}{2}} \right], \text{ large } x \text{ ("strong line")}$$

The equations are commonly plotted as functions of two nondimensional parameters,

$$x = S\ell/2\pi\alpha \tag{3}$$

$$\beta = 2\pi\alpha/d, \tag{4}$$

where  $S$  is the line strength,  $\alpha$  the half-width of the lines, and  $d$  the average line spacing. This paper gives the results, approximately to date, of a search for integrals of Equation (1) when scattering is present, given the analytical one-dimensional beam monochromatic emittance. Both a single Lorentz line and an Elsasser band, with equidistant, equal-intensity lines, were assumed.

## THE EMITTANCE OF A HOMOGENEOUS CLOUD

The equations for the monochromatic emittance of a homogeneous cloud of arbitrary optical depth  $\tau$  in the one-dimensional beam approximation are [2]\*

---

\*Reference 2 refers to early work using this method. The paper contains plots of Equation (5) and compares them with several exact calculations.

$$\epsilon_{\nu}(\tau) = 2k \left[ e^{K\tau} (K+\eta) + e^{-K\tau} (K-\eta) - 2K \right] / D(\tau) \quad (5)$$

$$D_{\nu}(\tau) = (K+\eta)^2 e^{K\tau} - (K-\eta)^2 e^{-K\tau} \quad (6)$$

$$K_{\nu} = \left\{ \eta \left[ 2(1-\eta)\beta_s + \eta \right] \right\}^{\frac{1}{2}} \quad (7)$$

$$\eta_{\nu} = \left( \sum_i n_i \sigma_{ai} + \sum_j k_{\nu j} \right) / \left[ (\leftarrow) + \sum_i n_i \sigma_{si} \right] \quad (8)$$

$$\tau_{\nu} = \left( \sum_i n_i (\sigma_{ai} + \sigma_{si}) + \sum_j k_{\nu j} \right) \ell, \quad (9)$$

where  $\beta_s$  is the fraction of a collimated beam scattered into the backward hemisphere ( $\pi/2 \leq$  scattering angle  $\leq \pi$ ),  $n$  is the number density of particles, and  $\sigma_a$  and  $\sigma_s$  their absorption and scattering cross sections. The  $\nu$ -dependence on the RHS of Equations (5) through (7) has been omitted. The scattering and absorption properties averaged over a distribution of particle sizes are a slowly varying function of frequency, and will be treated as constants. Equation (3) is still more difficult to average over frequency than is Beer's law, so that the somewhat simpler limiting regions of the parameters  $\tau$ ,  $\beta_s$ ,  $\beta$  and  $\eta$  have been considered, namely,

$$\lim_{\tau \rightarrow 0} \epsilon_{\nu}(\tau) = \eta_{\nu} \tau_{\nu} = \left( \sum_i n_i \sigma_{ai} + \sum_j k_{\nu j} \right) \ell \quad (10)$$

$$\lim_{\tau \rightarrow \infty} \epsilon_{\nu}(\tau) = \epsilon_{\nu\infty} = 2\eta_{\nu} / (K_{\nu} + \eta_{\nu}) \quad (11)$$

$$\lim_{\eta_{\nu}/\beta_s \rightarrow 0} \epsilon_{\nu\infty} = \left[ 2\eta_{\nu}/\beta_s \right]^{\frac{1}{2}} = \left[ \frac{\sum_i n_i \sigma_{ai} + \sum_j k_{\nu j}}{\sum_i n_i \beta_s \sigma_{si}} \right]^{\frac{1}{2}} \quad (12)$$

$$\lim_{\eta_{\nu} \rightarrow 1} \epsilon_{\nu\infty} = 1 - \beta_s (1-\eta_{\nu})/2 = 1 - \beta_s \frac{\sum_i n_i \sigma_{si}}{\sum_i n_i (\sigma_{ai} + \sigma_{si}) + \sum_j k_{\nu j}} \quad (13)$$

$$\lim_{\beta_s/2\eta_{\nu} \rightarrow 0} \epsilon_{\nu\infty} = 1 - \beta_s (1-\eta_{\nu})/2\eta_{\nu} \quad (14)$$

Equations (14), (23) and (24) demonstrate that a highly forward-peaked scattering function has the effect of reducing the effective scattering cross section.

When the spectral lines are crowded together or extremely broadened by high pressure (large  $\beta$ ), the spectral coefficient becomes a constant in  $\Delta_\nu$ , with the result that Equations (5) through (14) are trivially identical on the average. This will be called the "smeared line" case, in contrast to the "sharp line" case (small  $\beta$ ).

Equation (1) is integrated very simply using any of the band models or real distribution for  $k_j$ :

$$\epsilon(\ell) = \left( \sum_i n_i \sigma_{ai} + \sum_j k_j \right) \ell = \sum_i n_i \sigma_{ai} \ell + \sum_j (\beta x)_j \quad (15)$$

$$k_j = S_j / d_j \quad (16)$$

Equation (11) is not integrable, nor are Equations (12) through (14), in general, since  $\left[ \sum_i f_i(\nu) \right]^{\frac{1}{2}}$  is not separable into a sum or product of independent functions. In contrast, when there is no scattering, the transmission  $\exp \left[ -\sum_i f_i(\nu) \right]$  can be written  $\prod_i \exp \left[ -f_i(\nu) \right]$ ; the average transmission of several species with uncorrelated spectra is the product of their individual transmissions. Equation (12) has been integrated in the sharp line case when the absorption is due to a single Lorentz line,

$$k_{\nu SL} = (S\alpha/\pi) (\nu^2 + \alpha^2)^{-1}, \quad (17)$$

or to an Elsasser band. Both give the same emittance in the limit  $\beta \rightarrow 0$ . Integration of  $(k_{\nu SL})^{\frac{1}{2}}$  between the limits  $\pm d/2$  leads to a function of the form  $-\beta \ell n\beta \rightarrow \beta$ ,  $\beta \ll 1$ . The Elsasser band absorption coefficient is

$$k_{\nu E} = (\beta x/\ell) \sinh \beta \left[ \cosh \beta - \cos z \right]^{-1}, \quad z = 2\pi\nu/d. \quad (18)$$



The quantity  $(x/l)$  is a molecular constant,  $S/2\pi\alpha$ . When  $\beta$  is small, Equation (18) is approximately

$$k_{\nu E} = (\beta^2 x/l) (1 + \beta^2/2 - \cos z)^{-1}, \beta \ll 1. \quad (19)$$

The  $\beta^2/2$  term in the expansion of  $\cosh \beta$  must be retained to prevent  $k_{\nu E}$  from becoming infinite for  $\cos z = 1$ . Equation (1) was evaluated by the following steps: (1) transformation into a complete elliptic integral of the first kind, (2) transformation from the very large argument  $(4/\beta^2)$  to a very small one, and (3) retention of the largest term, which has the form  $-\beta l n \beta$  in the series expansion of the elliptic integral. We obtain finally

$$\lim_{\beta \rightarrow 0} \langle k_{\nu SL}^2 \rangle = \lim_{\beta \rightarrow 0} \langle k_{\nu E}^2 \rangle = \frac{1}{\pi} (2\beta^2 x/l)^{1/2}. \quad (20)$$

It appears that the average Equation (1) depends only on the shape of the total spectral absorption coefficient, as long as  $\eta_{\nu}/\beta_s \ll 1$  for all  $\nu$  in  $\Delta_{\nu}$ . The scattering coefficient is then so much larger than the absorption coefficient at any frequency that the emittance approaches the limit at nearly the same rate for all frequencies. This is analogous to the nonoverlapping line approximation for pure gases, which fails to hold for large enough  $\tau$ . You cannot see far enough into the gas-particle medium in this case for overlapping to become important.

Equations (13) and (14) can also be averaged for a single Lorentz line and for an Elsasser band, for small  $\beta$  with

$$\epsilon_{\infty SL} = 1 - \frac{n\beta_s \sigma_s}{2} \cdot \frac{\pi^2}{6} \left( \frac{l}{\beta^2 x} \right) = 1 - \frac{\pi^2 \beta_s}{12\beta} (1 - \eta), \quad (21)$$

$\beta$  small  
 $1 - \eta \ll 1$

$$\epsilon_{\infty E} = 1 - \frac{n\beta_s \sigma_s}{2} \cdot \frac{l}{\beta^2 x} = 1 - \frac{\beta_s}{2\beta} (1 - \eta) \quad (22)$$

$$\epsilon_{\infty SL} = 1 - \frac{n\beta_s \sigma_s}{2} \cdot \frac{\pi^2 \ell}{6\beta^2 x} = 1 - \frac{\pi^2 \beta_s}{12 \beta \eta} \quad (23)$$

$$\epsilon_{\infty E} = 1 - \frac{n\beta_s \sigma_s}{2} \cdot \frac{\ell}{\beta^2 x} = 1 - \beta_s / 2\beta \eta \quad (24)$$

As we would expect, the results are sensitive to the absorption coefficient of the tails or troughs. This is analogous to the strong-line case in the pure gas, where the shape of the absorption curve for small  $\beta$  and large  $x$  is sensitive to the band model assumed (See Figure 1).

---

FREQUENCY AVERAGED BEAM EMITTANCES FOR HOMOGENEOUS GAS-PARTICLE CLOUDS

---

THIN, $\tau \ll 1$	$\epsilon = \kappa \tau$
THICK, $\tau \rightarrow \infty$	
HIGHLY ABSORBING, $1 - \kappa \ll 1$	
SMEARED LINE	$\epsilon_{\infty} = 1 - \beta_s (1 - \kappa) / 2$
SHARP LORENTZ LINE*	$\epsilon_{\infty SL} = 1 - \pi^2 \beta_s (1 - \kappa) / 12 \beta$
SHARP ELSASSER BAND*	$\epsilon_{\infty E} = 1 - \beta_s (1 - \kappa) / 2 \beta$
LITTLE ABSORPTION, $\kappa / 2 \beta_s \ll 1$	
SMEARED	$\epsilon_{\infty} = [2 \kappa / \beta_s]^{1/2}$
SHARP LORENTZ, ELSASSER*	$\epsilon_{\infty SL} = \epsilon_{\infty E} = \frac{2}{\pi} [\beta \kappa / \beta_s]^{1/2}$
HIGHLY FORWARD SCATTERING, $\beta_s / 2 \kappa \ll 1$	
SMEARED, ANY $\kappa$	$\epsilon_{\infty} = 1 - \beta_s (1 - \kappa) / 2 \kappa$
SHARP LORENTZ LINE, $\kappa \ll 1$	$\epsilon_{\infty SL} = 1 - \pi^2 \beta_s / 12 \beta \kappa$
SHARP ELSASSER, $\kappa \ll 1$	$\epsilon_{\infty E} = 1 - \beta_s / 2 \beta \kappa$

---

\* IN THESE CASES, THE PARTICLES ARE ASSUMED NONABSORBING.

FIGURE 1

# CALCULATIONS FOR ELSASSER-BAND GAS AND NON-ABSORBING PARTICLE CLOUD. COMPARISON WITH THE GAS-ONLY CASE.

The results of the preceding section have been used to plot the average emittance as a function of  $\tau$  in Figure 2. The shape of the extrapolated curves is influenced by physical arguments. The uppermost curve for the pure gas is

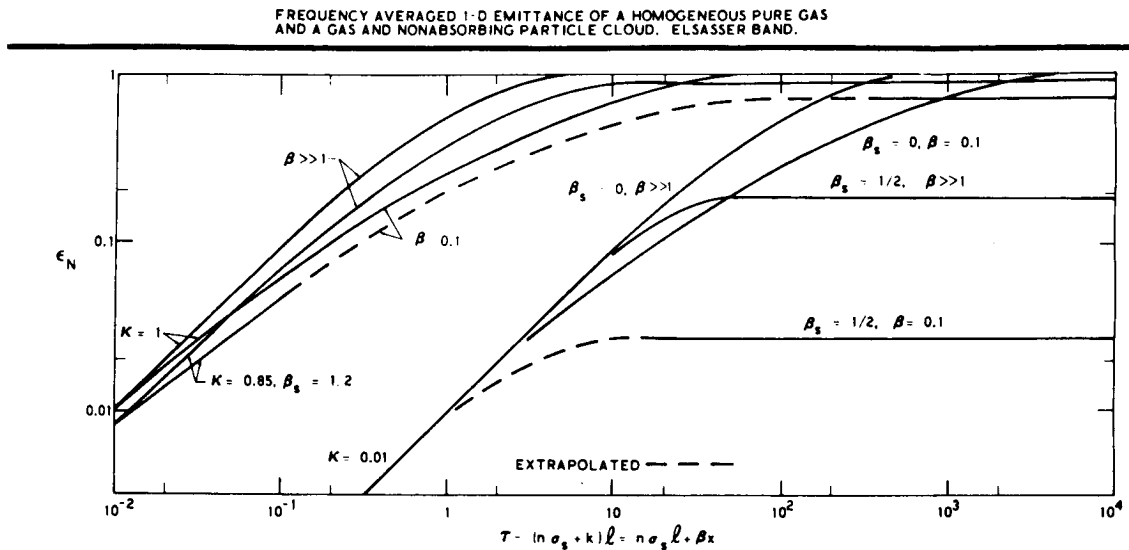


FIGURE 2

merely a plot of Beer's law. The curve for the Elsasser band,  $\beta = 0.1$ , was taken from Figure 6 shown in one of the several papers by Plass [3] for Elsasser band absorption. The four curves with  $\eta = 0.01$  are of four types: large and small  $\beta$  combined with isotropic and highly forward-directed scattering. The hypothetical extreme of forward scattering is a delta function of zero scattering angle for which  $\beta_s = 0$ . Since light is undeviated in this

"scattering," the radiation properties of a medium with optical depth  $\tau$ , including the ineffective particles, are identical on a monochromatic basis to those of a pure-gas medium with optical depth  $\tau' = \eta\tau$ . The curves with  $\beta_s = 0$ ,  $\eta = 0.01$  are therefore the same shape as those for  $\eta = 1$ , and are merely

shifted on the log  $\tau$  scale. These curves represent the upper limit of the emittance, for any scattering function, for those particular values of  $\tau$ ,  $\eta$  and  $\beta$ . The two curves with  $\eta = 0.01$  and  $\beta_s = 0.5$  must have approximately the same curvature at the knee, since as mentioned earlier, the limit is approached almost uniformly for all frequencies in  $\Delta_\nu$ . The limits of the two curves with  $\eta = 0.85$  are given in Equations (13) and (22). For  $\beta_s/2\eta \ll 1$ , the emittance would follow the  $\beta_s = 0$  curves closely and taper off to the limits Equations (14) or (24) according to whether  $\beta$  is large or small. From a practical view, the conditions  $\eta \ll 1$  and  $\beta_s/2\eta \ll 1$  may never simultaneously be met in a typical solid propellant exhaust.

## FUTURE EFFORTS

Some thought is being given to the possibility of further analytic results for the homogeneous slab. It is hoped that a computer parameter analysis will establish the behavior that so far has only been reasoned in the connecting regions. For the inhomogeneous cloud, probably one of two empirical methods will be used to calculate the radiance. The general monochromatic equations [1] for the radiance at any point  $\tau_r$  within or on the surface of the  $r$ -th slab are

$$\begin{aligned}
 N_r^+(\tau_r) &= c_{1r} (K_r - \eta_r) e^{K_r \tau_r} + c_{2r} (K_r + \eta_r) e^{-K_r \tau_r} + B(T_{\text{eff}, r}) \\
 N_r^-(\tau_r) &= c_{1r} (K_r + \eta_r) e^{K_r \tau_r} + c_{2r} (K_r - \eta_r) e^{-K_r \tau_r} + B(T_{\text{eff}, r}),
 \end{aligned}
 \tag{25}$$

where  $N^+(\tau)$  is the radiance in the direction of increasing  $\tau$ , the  $N^-$  the radiance in the opposite direction. The effective temperature in the  $r$ -th slab, by inspection of Equations (25) and the original radiative transfer equations, is defined by

$$B(T_{\text{eff},r}) = \left[ \sum_i n_{i,r} \sigma_{a,i,r} (T_{i,r}) B(T_{i,r}) + \sum_j k_{j,r} (T_{j,r}) B(T_{j,r}) \right] \cdot \left[ \sum_i n_{i,r} \sigma_{a,i,r} (T_{i,r}) + \sum_j k_{j,r} (T_{i,r}) \right]^{-1}. \quad (26)$$

The simpler method to apply Equations (25) would be to follow the smeared line values unless  $\tau$  is so large that the emittance of this slab would be better approximated by one of the indicated limits. In this case, the emittance and reflectance of the closest thick slab would be a boundary condition on the radiation of thinner layers between it and the observer. The final step will be to solve the matrix, derived from the boundary conditions, for the observed radiance. This method will probably over-estimate the radiance of the cloud surface. The second method would be to use an absorption coefficient for each slab which is a continuous synthetic function of the various parameters, and substitute these in Equations (25) through Equations (7) through (9). Neither of these methods requires a fixed increment size in the cloud, so that the size can be based on the gradient of the effective blackbody radiance [1].

## REFERENCES

1. Laderman, A. L., et al: Study of Thermal Radiation, Particle Impingement, Heating, and Flow Field Analysis of Solid Propellant Rocket Exhausts. Applied Research Laboratories, Philco-Ford Corporation, Aeronutronic Division Publication No. U-4045, April 19, 1967.
2. Bartky, C. D.; and Bauer, Ernest: J. Spacecraft, vol. 3, 1966, p. 1523.
3. Plass, G. N.: J. Opt. Soc. Am., vol. 50, 1960, p. 868.

# DETERMINATION OF ATMOSPHERIC TEMPERATURE PROFILES FROM SATELLITE RADIANCE MEASUREMENTS AT THE LIMB OF THE EARTH

By

N 68-18103

James W. Burn

Lockheed Missiles and Space Company  
Sunnyvale, California

---

## ABSTRACT

Some preliminary results we have achieved at LMSC on the problem of inferring atmospheric temperature profiles from satellites are very briefly discussed. This work, although not part of Project PROFILE, has grown out of the horizon definition studies performed at Lockheed Missiles and Space Company for the Massachusetts Institute of Technology, Instrumentation Laboratory, on Project PROFILE as part of Air Force Program 681D.

---

It can be shown that the following relations are valid for isothermal atmospheres:

$$\ln a + b\left(\frac{z}{T}\right) = -\ln \left[ -\frac{1}{T^{\frac{1}{2}}} \ln \left( -\frac{N(z)}{N(o)} \right) \right] \quad (1)$$

$$\ln a' + b\left(\frac{z}{T}\right) = -\ln \left[ \frac{1}{T^{\frac{1}{4}}} \operatorname{erf}^{-1} \left( \frac{N(z)}{N(o)} \right) \right], \quad (2)$$

where  $a$  and  $a'$  are absorption constants of the atmosphere,  $b$  is a constant equal to  $mg/k$ , the product of the mass of a molecule of air and gravity divided by Boltzman's constant,  $z$  is the tangent altitude,  $T$  the temperature, and  $n(z)$  the radiance at altitude  $z$ . The first equation is a restatement of an expression for limb radiance derived by King [1] for gray isothermal atmospheres. The second equation is the restated expression for limb radiance by Uplinger [2] for isothermal atmospheres with an error function transmissivity model.

In reality, of course, the atmosphere is neither gray nor isothermal, and the spectral bandwidths of interest are sufficiently broad that Equation (2) is not valid. Unfortunately, a closed form solution of Equation (2) integrated over wavelength does not exist. An integral of the form

$$\int_a^b \frac{\text{erf}(y)}{y} dy$$

is involved and has only been solved numerically. However, Equations (1) and (2) indicate that a semi-isothermal model of the form

$$\ln a + b \left( \frac{z}{T} \right) = f \left( T, \frac{N(z)}{N(o)} \right) \quad (3)$$

may be valid where the constants  $a$  and  $b$  are modified by the temperature lapse rates which exist in the atmosphere. This expression can be solved to yield temperature at altitude  $z$ .

$$T = \frac{bz}{f \left( T, \frac{N(z)}{N(o)} \right) - \ln a} \quad (4)$$

Because of the weak dependence of  $f(T, N(z)/N(o))$  on  $T$ , Equation (4) can be solved iteratively with only one or two iterations required.

The function  $f(T, N(z)/N(o))$  is not understood at this time, and it would be preferable to wait until a future time when the proper theoretical understanding has been obtained to discuss this function. The constant  $b$  has been found to exceed  $\text{mg/k}$  for positive lapse rates and be less than  $\text{mg/k}$  for negative lapse rates. An example of applying Equation (3) to three different mean atmospheres, Jan. 70° N and Feb. and Mar. 60° N [3] is shown in Figure 1. Although there is considerable difference between these atmospheres, they are very similar here (except at high altitudes, which are not of concern because of low signal-to-noise ratios) and much of the apparent difference is believed to be caused by the incorrect function  $f(T, N(z)/N(o))$ . Shown also is the curve for an isothermal atmosphere.

These results were applied to computer radiance data (14-16 microns) for the mean atmospheric parameters for Jan 40° N, 80° W [3] and the Project Scanner experimental data (14-16.25 microns) [4]. Experimental limb radiance

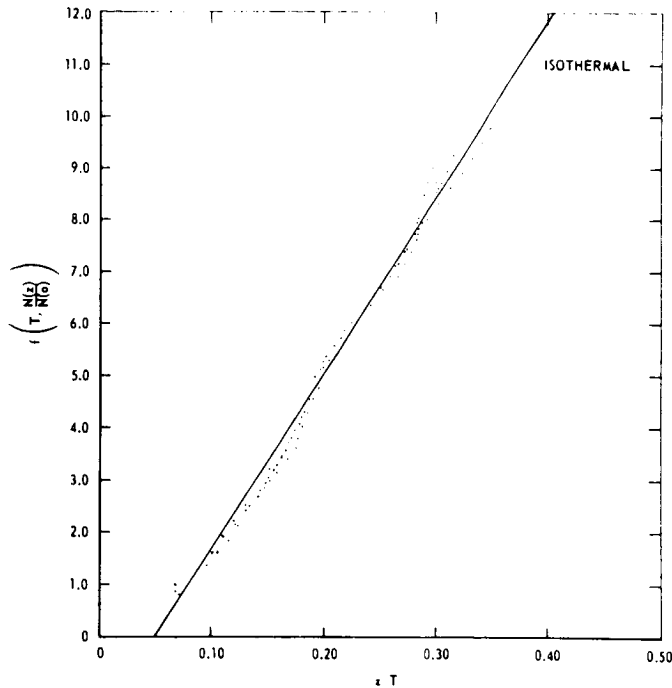


FIGURE 1. GRAPH OF EQUATION 3 FOR ISOTHERMAL ATMOSPHERES AND FOR THE THREE MEAN ATMOSPHERES, JAN. 70° N AND FEB. AND MAR. 60° N

profiles and temperature profiles were given for Goose Bay, Labrador (53° N) and Antigua (11° N). These data were taken on August 16, 1966. The results for Jan. 40° N are shown in Figure 2. The solid curve is the actual temperature-altitude profile. The dash-dot curve is the inferred temperature profile. The agreement is seen to be quite good except in the vicinity of the stratopause. The dashed curve was obtained by an iteration technique. A second iteration should produce a very accurate reproduction of the actual temperature profile. The results for Project Scanner experimental data from Goose Bay are shown in Figure 3. The differences are remarkably small considering the poor signal-to-noise ratio at the higher altitudes. The maximum difference is 8.5 degrees with a S/N of about 4.

Although this work is in a very preliminary state, it is clear that stratospheric and mesospheric temperatures can be determined with the following advantages over other methods.



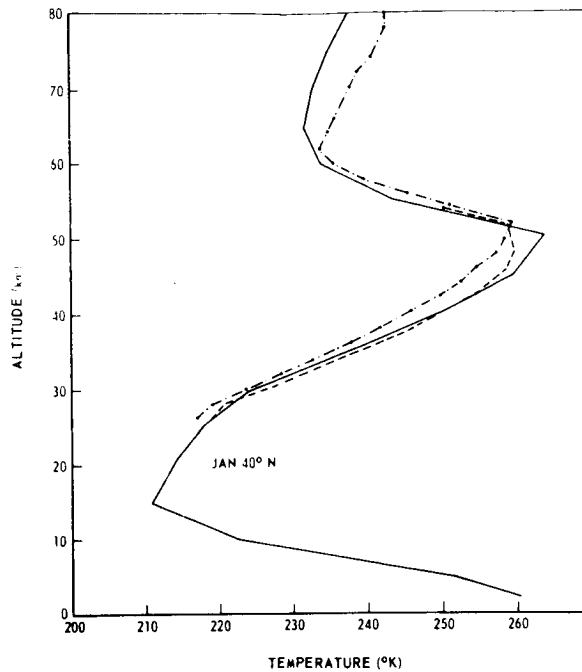


FIGURE 2. COMPARISON BETWEEN THE INFERRED TEMPERATURE PROFILE (— · —) (— — —) AND THE MEAN TEMPERATURE PROFILE (—) FOR JAN. 40° N LATITUDE FROM WHICH THE LIMB RADIANCE PROFILE WAS CALCULATED

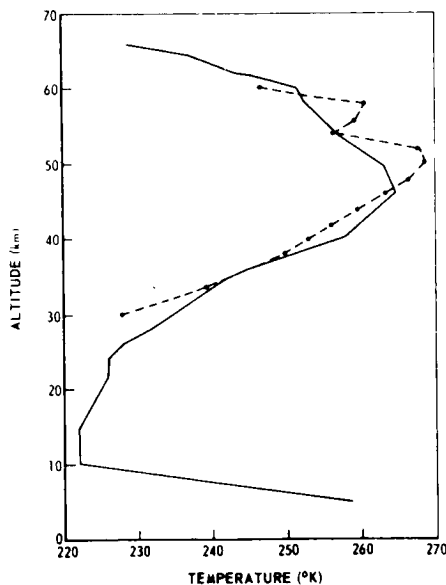


FIGURE 3. COMPARISON BETWEEN THE INFERRED TEMPERATURE PROFILE (— · —) DERIVED FROM THE MEASURED LIMB RADIANCE PROFILE AND THE TEMPERATURE PROFILE FOR GOOSE BAY, LABRADOR AS ESTIMATED FROM MRN DATA OBTAINED AT FORT CHURCHILL AND WALLOPS ISLAND

- Temperatures can be determined with a single spectral channel radiometer.
- The spatial resolution is about 2.8 km.
- Wide spectral bandwidths of approximately 2 microns within the 15 micron CO<sub>2</sub> band can be used.
- S/N ratios required for temperature determination at stratospheric and mesospheric altitudes can be obtained.
- Temperature is computed directly from radiance ratios rather than radiance differences, eliminating the severe matrix mathematics problem.

## REFERENCES

1. King, J. I. F. : Theoretical Radiance Profiles for the 15 Micron Carbon Dioxide Band. Presented at the Second Symposium on Infrared Sensors for Spacecraft Guidance and Control.
2. Uplinger, W. G. : Theoretical Planetary Limb Radiance Profiles for Isothermal Atmospheres. In preparation.
3. Burn, J. W. ; Uplinger, W. G. ; and Morris, P. P. : Earth Limb Radiance Profiles for the 15-Micron Carbon Dioxide Absorption Band. Lockheed Missiles and Space Co. , LMSC-677318, March 10, 1967.
4. Dodgen, J. A. ; McKee, T. B. ; and Jalink, A. : NASA Program for Definition of the Earth's Horizon. Presented at the Second Symposium on Infrared Sensors for Spacecraft Guidance and Control.

# ESTIMATING DIURNAL TEMPERATURE VARIATION AT THE STRATOPAUSE FROM HORIZON RADIANCE MEASUREMENTS\*

By

N 68-18104

John C. Gille  
Department of Meteorology  
Florida State University  
Tallahassee

---

## ABSTRACT

Calculations indicate that information about the size and phase of the diurnal temperature variation between 40-60 km may be obtained from the size and phase of the diurnal horizon radiance variation. In particular, horizon radiance measurements should indicate whether the rocket temperature measurements or theoretically calculated temperature variations are in error.

---

The atmosphere between 40-60 km is heated by absorption of solar radiation during daylight, and continuously cooled by infrared radiation. Leovy [1] calculated the magnitude of the heating and cooling and the size of the daily temperature range on the assumption that there were no atmospheric motions. This direct radiative control led to values typically about 4°C. However, heating and cooling lead to motions. Using the same heating rates, Lindzen [2] calculated the variations of motion and temperature from his complete solutions of the tidal equations. Variations, from the tidal calculations, are typically 3°C. Measurements, notably by Beyers et al. [3] at White Sands, show variations typically two to three times greater than the theoretical values. These measurements have been subjected to considerable criticism, however. The purpose of this study was to determine whether satellite measurements of the horizon at 15  $\mu$  (where opacity is due to CO<sub>2</sub>) would yield an independent determination of

---

\* This work was partially completed while the author was a visitor at the National Center for Atmospheric Research, Boulder, Colorado.

the size of the diurnal temperature variation above 30 km and information on its phase.

Models of temperature variation as a function of altitude based on tidal theory, radiative control, and the White Sands observations were used. Each model was superposed on the June-July mean vertical temperature distribution at White Sands, and temperature profiles calculated at 3-hour intervals. The horizon radiance was calculated in a manner similar to that of Wark et al. [4]. The calculations included refractive effects, and corrected the transmission for temperature and pressure variations along the path. From the three-hourly radiance profiles, the size and phase of the diurnal radiance variation as a function of height were found for each of the three models.

The results show that the "observed" temperature variation leads to radiance variations at 45 km tangent height of  $0.35 \text{ W/m}^2 \text{ ster}$ , compared to  $0.10 \text{ W/m}^2 \text{ ster}$  for the tidal model.

Because of the steep slope of the horizon radiance versus tangent height curve, the resolution is limited by the pointing accuracy of the radiometer. It is located within 15 arc seconds, resolution is  $0.03 \text{ W/m}^2 \text{ ster}$ . Thus, separation of these two models is measurable with a signal-to-noise ratio of 8. The time of radiance maximum at 45 km tangent height is predicted to be about 2:00 PM local time for the "observed" temperature, and about 5:00 PM for the tidal temperatures.

It is clear that measuring the horizon radiance three or more times a day over a particular location will give considerable information about the 40-60 km temperature variation there. It should suffice to locate the source of the discrepancy between the rocket measurements and theoretically calculated temperature variations.

A more complete account of this work has been submitted for publication elsewhere.

The computations were supported by the computer centers of the Florida State University under NSF Grant GP 5114, and the National Center for Atmospheric Research.

## REFERENCES

1. Leovy, C.: J. Atmos. Sci., vol. 21, 1964, pp. 238-248.
2. Lindzen, R. S.: Quart. J. Roy. Meteor. Soc., vol. 93, 1967, pp. 18-42.
3. Beyers, N. J.; Miers, B. T.; and Reed, R. J.: J. Atmos. Sci., vol. 23, 1966, pp. 325-333.
4. Wark, D. Q.; Alishouse; and Yamamoto, G.: Appl. Opt., vol. 3, 1964, pp. 221-227.

---

## DISCUSSION

S. A. Golden, Rocketdyne: Dr. Gille, how were the temperatures measured?

J. C. Gille: The temperatures that I showed were measured mostly with thermistors on rockets. They are subject to very large corrections.

J. W. Burn, Lockheed: I have made the same calculations which Dr. Gille has discussed, for the purpose of determining the effect of diurnal variations on horizon stability. They show approximately the same results.

---

# MOLECULAR TEMPERATURE DETERMINATIONS\* IN FLOW FIELDS OF RE-ENTERING BODIES

N 68-18105

By

W. G. Planet, R. Watson, and C. C. Pitts

Heliodyne Corporation  
Data Services and Analyses  
Norton Air Force Base, California

---

## ABSTRACT

Molecular temperature determinations represent a technique for the diagnosis of the flow fields of re-entering bodies. During a typical re-entry test, remote spectrographic systems acquire large quantities of optical data. With appropriate data reduction and analysis procedures, standard spectroscopic techniques can be applied to these large stores of data to yield estimates of the flow-field gas temperatures. This paper discusses the important features of a procedure which uses radiation from the CN  $A^2\Sigma \rightarrow X^2\Sigma$  (violet) band system to determine the temperature.

---

## INTRODUCTION

Some of the data reduction and analysis techniques established during a study to determine spectroscopic temperatures of the flow field of a re-entering body are discussed. The spectral radiation from the CN violet system ( $A^2\Sigma \rightarrow X^2\Sigma$ ) is used to determine gas temperatures by comparing the test data to spectra generated from theoretical considerations of the instrument system (the cinespectrograph-film-microdensitometer combination). The study uses film records which were obtained with a 70mm cinespectrograph and subsequently digitized at the Holloman Air Force Base Data Reduction Center. The data were obtained by Aerojet-General Corporation (Astrionics Division) as part of the checkout phase of the TRAP 7 aircraft program under the direction of the Air Force SAMSO TRAP Office.

---

\* This work was supported by the Air Force Space and Missile Systems Organization under Contract No. F04694-67-C-0148.

The procedures discussed here are specifically applicable only to the CN violet molecular system and the cinespectrograph used to collect the data. However, applications to other systems are straightforward by using the appropriate spectroscopic relations and instrument response functions.

## DATA RECORDING AND REDUCTION

The cinespectrograph used to record the data used in this study has the characteristics shown in Table I.

TABLE I.

Cinespectrograph Characteristics

Type	Maksutov
Format	29mm × 57mm on 70mm film
Focal Length	300mm
f/number	f/2.7
Field of View	4.7° vertical × 5.6° horizontal
Resolution	0.1 m $\mu$
Dispersion	90 Å/mm (nominal) at film plane
Grating	360 line/mm blazed at 3200 Å
Framing Rate	100 fps (typical)
Exposure Time	33 ms at 10 fps

For the observation and recording conditions of this test, the spectral resolution was 3–5 Å, the spatial resolution was about 10 m, and the viewing was approximately broadside to the wake trail. The cinespectrograph was calibrated as closely as possible in time to the actual recording of data. Spectral calibration was performed using an Hg–Cd lamp and intensity calibration with an NBS-calibrated tungsten strip lamp attenuated by a series of neutral density filters. Both calibration sources were used in conjunction with a reflecting collimator.



## Data Sampling Rate

A single frame of data is shown in Figure 1. The reference wavelength,  $\lambda_R$ , is the location in the wavelength scale of the reference image which is obtained by a periscope device in the camera optics and is equivalent to the undispersed zero order image common to all grating instruments. In-frame motion of the image is manifested as a smearing of the spectral lines in a direction of the wake.

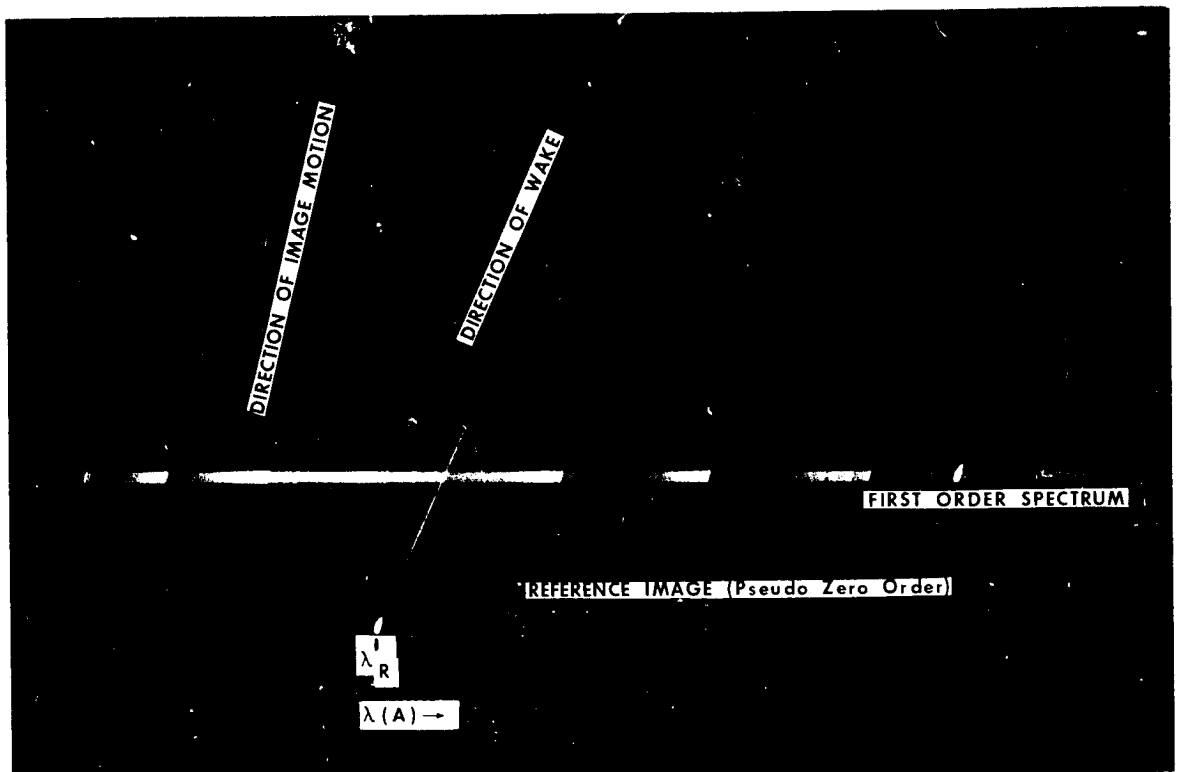


FIGURE 1. TYPICAL RE-ENTRY SPECTRUM

Densitometry of the film images is done in the manner illustrated in Figure 2. The dimensions of the scanning densitometer aperture are chosen as a compromise in order to preserve the spatial and spectral resolution of the film record, and yet not suffer too severely from grain effects. Spectra such as those shown in Figure 1 do not have the quality of the laboratory spectra typically used for spectroscopic temperature determinations. The nature of re-entry observations, the environment in which the instruments operate, and the overall objectives of the particular tests preclude the use of laboratory

instruments. Nevertheless, re-entry spectra are invaluable and, inherently, have a large information content which is becoming more and more useful as a diagnostic tool.

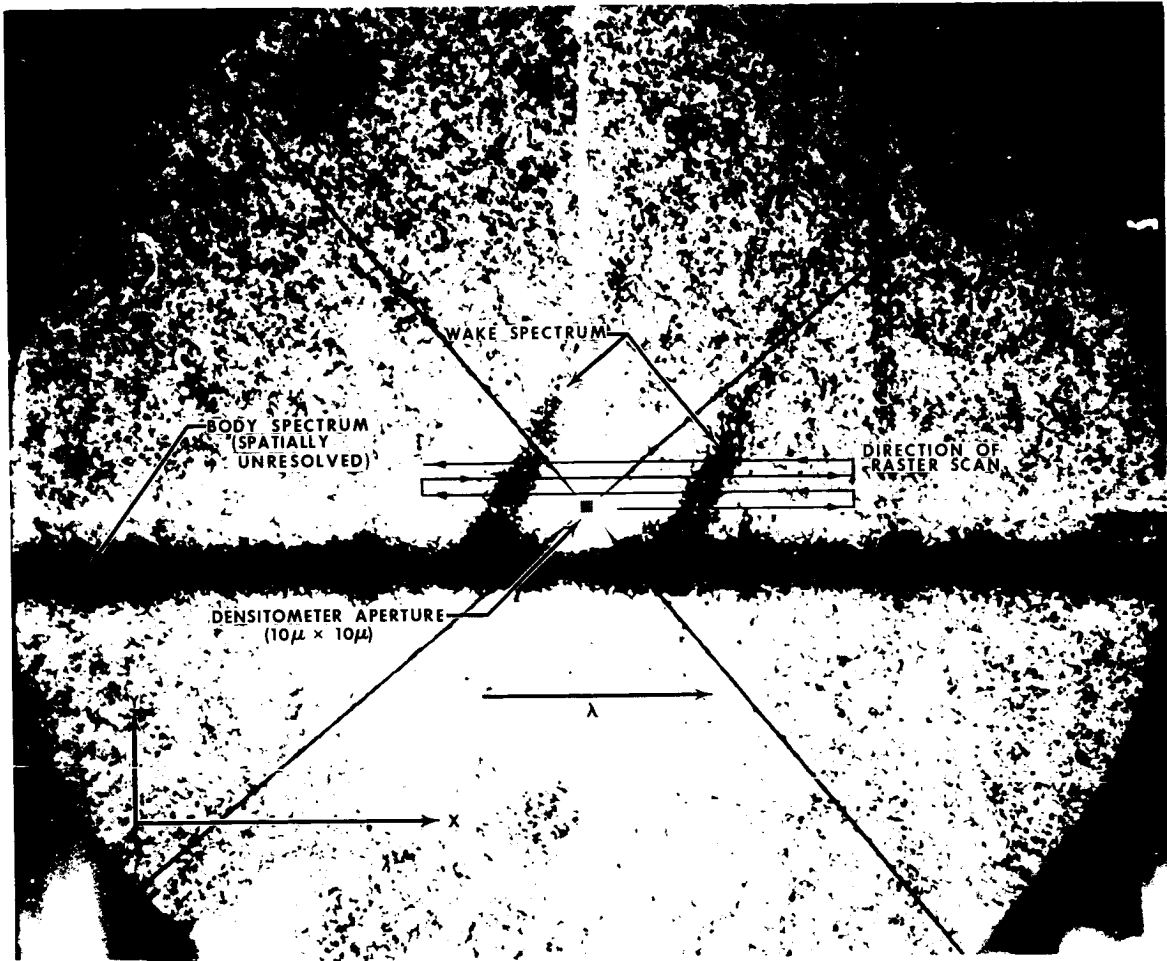


FIGURE 2. ENLARGEMENT OF TYPICAL SPECTRUM SHOWING DETAILS OF RASTER SCAN OF SPECTRAL IMAGES BY DENSITOMETER APERTURE

Under the conditions given above, one scan of the densitometer slit in the X (spectral) direction throughout the spectral region of the data yields about 6000 data points (i. e. , 6000 distinct values of spectral intensity). For a detailed scanning of the spectral features of the wake (the Y direction), this number becomes typically of the order of  $10^5$  data points. If analysis of the wake is desired throughout the whole luminous re-entry period, the number can

become of the order of  $10^7$  data points. Such a quantity of data is capable of negating any meaningful analysis within a reasonable time period, and therefore considerable editing must precede the analysis phase. In the present study, the analysis has been restricted to the CN violet system at selected altitude intervals, thereby reducing the number of data points to about  $10^5$ . All frames of the test data are normally densitometered, however, and the results stored on digital computer tape for future extraction and analysis.

## Data Reduction Procedures

The raw films were densitometered at the Data Reduction Center, Holloman AFB. The images were scanned in the manner shown in Figure 2, which the X-Y coordinates referenced to the reference image. Here, the X-coordinate is the wavelength and the Y-coordinate is distance. The output of the densitometer is put on digital tape in the form of density (actually densitometer output in counts) versus X at all values of Y at which images are detectable above background. Following standard wavelength and densitometric calibration procedures, the data are transformed to relative irradiance versus wavelength. These latter data are machine-plotted for comparison with temperature-dependent theoretical spectra calculated as described later in this report. A sample flight spectrum is shown in Figure 3 with the appropriate CN spectral features annotated. No corrections are made for atmospheric attenuation, since the method for temperature determination (see page 424) is based essentially on the spectral features of individual  $\Delta v$  sequences which cover wavelength intervals of only 100-200 Å.

## THEORETICAL SPECTRUM

Temperature determinations are made by comparing various features of the reduced test data to theoretical temperature-dependent spectra which are generated to match the features of the non-resolved spectra on the film as seen by the densitometer.

The images of individual spectral lines are approximated by a rectangle with width  $\Delta\lambda_I$  of about 3-5 (see Figure 4). Depending on the densitometer slit width ( $\Delta\lambda_D$ ) chosen, the output of the densitometer is the result of the slit observing all or part of the wider images of a number of spectral lines. The

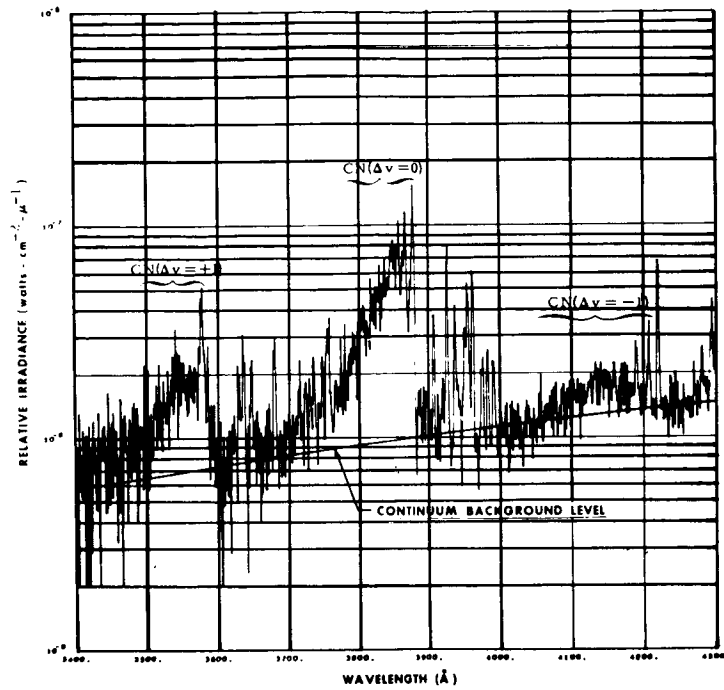


FIGURE 3. RELATIVE INTENSITY PLOT OF MISSION DATA IN THE CN VIOLET REGION

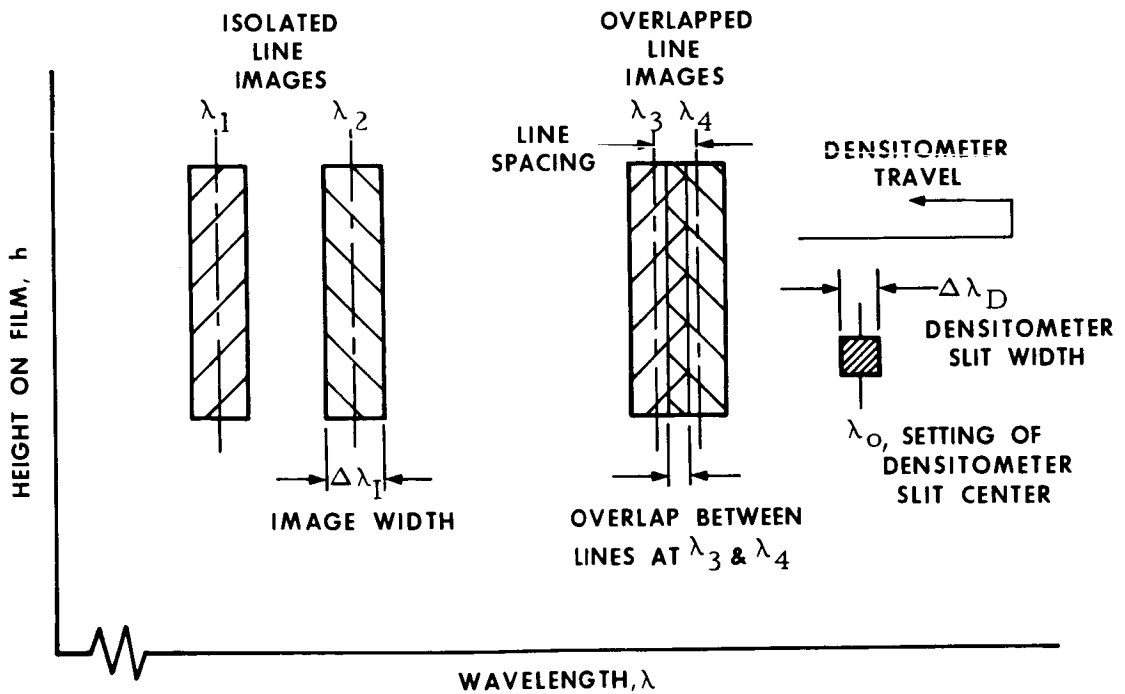


FIGURE 4. GRAPHICAL ILLUSTRATION OF NON-RESOLVED SPECTRAL LINE IMAGES ON CINESPECTROGRAPH FILM

images of the lines overlap because the rotational line spacings are smaller than the image width. The choice of an appropriate slit function can be coupled with straightforward relationships to generate the proper theoretical spectra.

## Spectroscopic Relationships

The relative intensities of the various lines in the CN spectrum are calculated in the usual manner following the procedures outlined in reference 1. The result for a transition between the states  $n$  and  $m$  at the wavenumber  $\nu_{nm}$  is given by

$$I_{nm, \text{rel}} = \nu_{nm}^4 q_{v'v''} S_{K''} e^{-hc(G' + F')/kT} \quad (1)$$

where  $q_{v'v''}$  and  $S_{K''}$ , respectively, are the Franck-Condon factor and the rotational line strength for the particular vibrational sequence and rotational transition being observed, and  $G'$  and  $F'$  are the energy levels for the vibrational and rotational states involved (see reference 1 for details). Equation (1) has the numerical constants, the absolute CN population, and the partition function removed since only the relative intensity is required for the spectroscopic temperature analysis. The Franck-Condon factors are available from calculations involving the vibrational wave functions, as in reference 2, while the rotational line strengths may be calculated from relationships given in reference 1.

## The System Slit Function

As discussed previously, the relative intensity for each line is spread out over the finite width,  $\Delta\lambda_I$ , of the image of that line on the cinespectrograph film. These spread-out images must be coupled with the known characteristics of the densitometer in order to finally obtain a non-resolved intensity profile which corresponds to that generated by the densitometer as it scans the actual flight data.

The appropriate slit function for the cinespectrograph-densitometer instrument combination can be obtained by inspection of Figure 4. It is seen that with the densitometer slit centered at  $\lambda_0$ , spectral lines that lie outside the

interval,  $\lambda_o \pm \frac{1}{2} (\Delta\lambda_I + \Delta\lambda_D)$ , do not lie within the densitometer slit opening and, hence, do not contribute to the densitometer signal. Lines lying within the interval,  $\lambda_o \pm \frac{1}{2} (\Delta\lambda_I - \Delta\lambda_D)$ , lie entirely within the densitometer slit and, hence, contribute 100 percent to the densitometer signal. Lines lying within these two intervals contribute less than 100 percent to the densitometer signal, and the resultant, or effective, slit function for the instrument combination is trapezoidal in shape with a slit function base of  $2\Delta\lambda^* = \Delta\lambda_I + \Delta\lambda_D$ . The slit function response is  $g(\lambda)$  and is normalized to a maximum value of 1.0 for lines whose images are fully within the densitometer slit width.

Although the value of  $\Delta\lambda_D$  is known exactly from the densitometer characteristics and the cinespectrograph plate factor,  $\Delta\lambda_I$  depends on the slant range (between the re-entry body and the cinespectrograph) and also on in-frame motion of the instrument during tracking. This means that  $\Delta\lambda_I$  must be treated as a parameter, adjusted to give best agreement between the calculated spectrum and the flight data.

## Resultant Theoretical Non-Resolved Intensity Profile

The intensity profile that a densitometer generates in scanning cinespectrograph film with relatively wide line images is thus a nonresolved contour of the bands. The equivalent theoretical model is given by coupling the trapezoidal slit function to the spectroscopic relationships of reference 1. The resultant theoretical intensity profile is then calculated at each densitometer location,  $\lambda_o$ , as

$$I(\lambda_o) = \sum_{2\Delta\lambda^*} I_{nm}(\lambda) g(|\lambda - \lambda_o|), \quad (2)$$

where the summation extends over all lines in all branches within the slit function base,  $2\Delta^*$ . Equation (2) has been adapted to a computer solution, allowing theoretical profiles for various temperatures to be calculated and plotted on scales equivalent to the data processed from flight films. A background continuum is added to the CN radiation and normalized appropriately to match the calculated theoretical spectrum to the level of the observed flight data.

In the following section, the theoretical spectrum is plotted for a comparison to the mission spectrum (see Figures 5 and 6).

## TEMPERATURE DETERMINATION

The theoretical intensity profiles are temperature-dependent only (with no self-absorption) for a given set of instrument conditions,  $\Delta\lambda_I$ ,  $\Delta\lambda_D$ , etc.

Therefore, a number of features of the theoretical spectrum could be used to establish pyrometric curves from which the gas temperature may be determined.

The most accurate method of determining the spectroscopic temperature is to use the complete CN spectrum since the overall shape contains the most information. Thus, the calculated spectrum which fits the main features of the CN violet radiation in the flight data yields the best estimate of the gas temperature. Certain portions of the CN mission spectrum are less susceptible to problems, primarily self-absorption and noise (film graininess) plus uncertainties in the assumed line image width,  $\Delta\lambda_I$ , and should therefore be given more credence when fitting the overall spectrum. The most important "error free" spectral region for matching the main features of the flight data with theoretical spectra appears to be the tail of the  $\Delta v = 0$  sequence. Therefore, this region should be given the most weight when actually analyzing the flight data.

Depending on the amount of noise in the reduced flight data (the noise being a function of the ratio of the area of the densitometer slit to the average grain size on the film), ratios of peak intensities or ratios of integrated areas of individual bands within a particular sequence may serve as a temperature calibration. The temperatures reported in reference 3 are based on peak intensity ratios of the  $\Delta v = -1$  sequence. Reference 4 gives results for measurements of non-resolved CN spectra of a laboratory carbon-arc operated in air, using both peak intensity ratios and band-area ratios. Because these methods depend only on the CN radiation from relatively narrow wavelength intervals, however, errors due to self-absorption and noise tend to make them inherently less accurate than those techniques mentioned previously in this section. This is particularly true when these techniques are applied to flight data which are obtained under noncontrolled laboratory conditions and inherently contain a large amount of noise due to use of fast film.

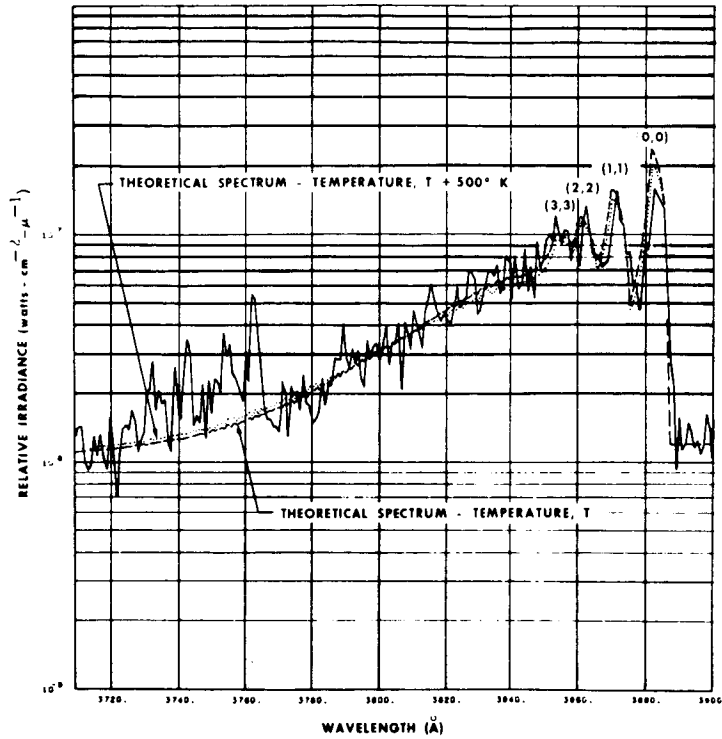


FIGURE 5. COMPARISON OF MISSION DATA AND THEORETICAL SPECTRUM FOR THE CN VIOLET  $\Delta v = 0$  SEQUENCE

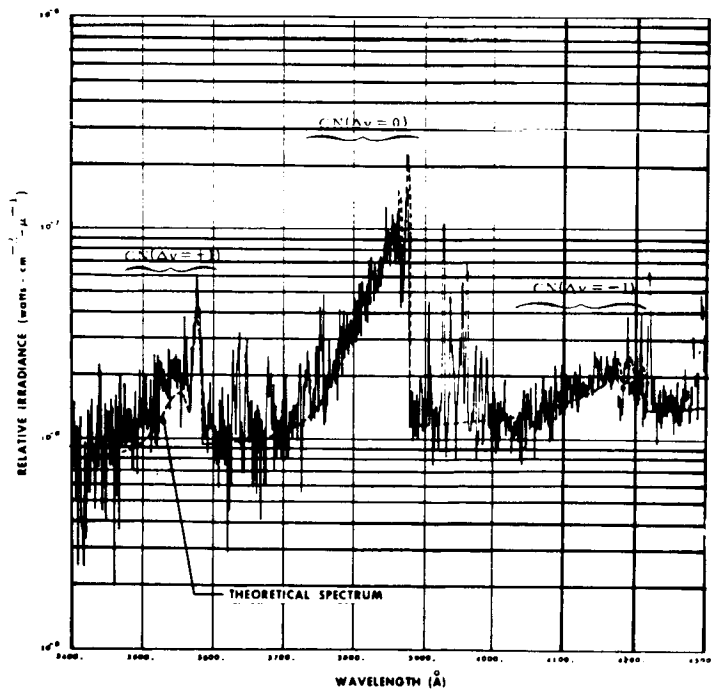


FIGURE 6. COMPARISON OF MISSION DATA AND THEORETICAL SPECTRUM FOR THE CN VIOLET  $\Delta v = 0$  AND  $\pm 1$  SEQUENCES



## Examples of Temperature Determinations

Test data to the overall best-fit theoretical spectrum are compared in Figures 5 and 6. In Figure 5, over the  $\Delta v = 0$  sequence for the calculated spectrum labeled T, excellent agreement is evident from 3700-3870 Å in the region of the tail of the sequence and all bands except the (0, 0). Also shown on Figure 5 is a calculated spectrum for  $T + 500^\circ\text{K}$ , which is evidently a poorer fit in the 3700-3860 Å region and which fits the (1, 1)-, (2, 2)-, and (3, 3)-bands no better than the curve for the temperature, T. Hence, the temperature, T, can be deduced with an estimated accuracy of about  $\pm 300 - 400^\circ\text{K}$ . Figure 6 shows the same comparison extended to the  $\Delta v = \pm 1$  sequence. In Figure 6, the fit to the  $\Delta v = +1$  sequence is not as good as for the other sequences, but only as far as absolute level is concerned; the relative shape of the tail of the  $\Delta v = +1$  sequence shows agreement comparable with that in the  $\Delta v = 0$  sequence. Because the intensity levels of the  $\Delta v = \pm 1$  sequences are about the same order of magnitude as the background, they are not as useful as the  $\Delta v = 0$  sequence for establishing the spectroscopic temperature. However, the fact that the overall fit to all three of the CN violet  $\Delta v$ -sequences is quite good lends support to the theoretical intensity model and gives greater confidence to the temperature determined from the fit to the  $\Delta v = 0$  sequence.

## Effects of Self-Absorption

As mentioned previously, the effects of self-absorption will be generally to degrade the accuracy of temperatures determined by ratios of peak or integrated intensities of individual bands within a sequence if the amount of self-absorption is not known. The method used in this study (i. e., a comparison of the overall features of a particular  $\Delta v$ -sequence with greatest weighting given to the tail of the sequence) does not rely on knowing the amount of self-absorption nor is it greatly affected by unknown self-absorption. In fact, this method allows the temperature and the amount of self-absorption to be deduced simultaneously. This is seen in Figure 5 where the  $\Delta v = 0$  sequence of flight data is shown along with the theoretical spectrum determined to be the best fit to the tail of the flight spectrum. The intensities of the individual bands are below those of the theoretical bands while the tail regions of both show agreement over a spectral region of about 150 Å. The ratios of the band intensities of flight data to theoretical calculations yield the amount of self-absorption. Values of self-absorption in optically thick regions (e. g., boundary layers) of CN re-entry spectra may be

as high as 35-40 percent for the (0, 0)-band, with appropriately lower values for bands not having highly populated lower states.

## CONCLUDING REMARKS

The elementary analysis presented here is applicable only to an isothermal, uniformly radiating species. A number of factors (beyond control of the data observer) make the spectra from an actual re-entry situation deviate considerably from such an ideal problem. Foremost among these are temperature gradients and chemical reactions in the flow field from which the radiation is recorded, particularly in the vehicle boundary layer. Applying an isothermal, uniform model to a non-uniform radiation field yields, at best, only an effective temperature for the radiating volume observed.

Because of the complex nature of the flow field and because of the more practical limitations of instrument resolution, it is quite difficult to refine re-entry temperature measurements to the degree possible in such situations as laboratory flames, shock tubes, etc. One should be aware of the limitations involved in analysis of re-entry data and treat the result with appropriate caution.

## REFERENCES

1. Herzberg, G.: Spectra of Diatomic Molecules. Second ed., D. Van Nostrand Company, Princeton, N. J., 1950.
2. Spindler, R. J.: J. Quant. Spectry. Radiative Transfer, vol. 5, . 1965, p. 165.
3. Bauer, J. R.: Measurements of the Temperature and Self-Absorption of the CN Molecule from the Emission Spectrum of a Re-entry Vehicle. AMRAC Proc., Institute of Science and Technology, University of Michigan, vol. XVI, part II, April 1967 (SECRET).
4. Spier, J. L.; and Smit-Miessen, M. M.: Physica IX, vol. 422, 1942.

# THE RELEVANCE OF FREQUENCY-AVERAGED PROPERTIES

N 68-18106

By

S. C. Traugott

Sibley School of Mech. Engineering  
Cornell University  
Ithaca, New York 14850

The problem of radiative heat transfer is distinguished from that of detection or temperature inversion by the fact that the rate of heat transfer is an integral over all frequencies. This means that spectral characteristics are not of primary interest; rather, they could be regarded as an obstacle to simple and rapid heating estimates. From this point of view it is understandable that a considerable portion of the radiative transfer community would attempt to overcome this obstacle with gross spectral simplifications. At this conference devoted to molecular radiation and diagnostics, there are very few, if any, representatives of this group. Nevertheless, we know that it exists and that it has produced a large body of literature of what one may call non-spectral calculations. It can be agreed that calculations based on crude assumptions about the spectral characteristics of a radiating gas are at best irrelevant to real life and at worst in bad taste. By this argument one ignores, by definition, all non-spectral calculations and replaces them with new ones. This is, of course, done at a price which can be, as we have heard, up to forty hours of digital computer time. Therefore, it may not be inappropriate to adopt an attitude with which one first asks, in a given real situation, whether one might not find some relation to non-spectral calculations and thereby possibly save some labor. The point of these remarks is to illustrate the idea by an example. The example involves a homogeneous real gas and the most crude non-spectral model of them all, the grey gas.

Suppose a one-dimensional gas slab in local thermodynamic equilibrium, is bounded on either side by either a vacuum or a cold black wall. The physical thickness of the slab is  $\Delta$ . The properties of the gas are taken to be invariant with respect to distance measured into the gas from the surface. The emergent spectral heat flux at either surface is

$$I_{1\nu}(\Delta) = \pi B_{\nu} [1 - 2 E_3(\kappa_{\nu}\Delta)] .$$

The integrated heat flux is

$$I_1(\Delta) = \pi B - 2\pi \int_0^\infty B_\nu E_3(\kappa_\nu \Delta) d\nu.$$

The rate of change of the emergent flux at the surface with respect to the thickness of the gas sample behind is

$$\frac{dI_1}{d\Delta} = 2\pi \int_0^\infty \kappa_\nu B_\nu E_2(\kappa_\nu \Delta) d\nu.$$

An optical depth based on a frequency-averaged absorption coefficient may be introduced as follows:

$$\frac{dI_1}{d\tau_1} = \frac{dI_1}{\kappa_1 d\Delta} = \int_0^\infty \frac{dI_{1\nu}}{\kappa_\nu d\Delta} d\nu.$$

From this definition,  $\tau_1 = \int \kappa_1 d\Delta$ , with

$$\kappa_1(\Delta) = \frac{\int_0^\infty \kappa_\nu B_\nu E_2(\kappa_\nu \Delta) d\nu}{\int_0^\infty B_\nu E_2(\kappa_\nu \Delta) d\nu}.$$

The radiative heat flux is only one of many directional averages (moments) that can be defined. Similar reasoning as that above, but based on other directional moments of the spectral intensity, results in various optical depths based on various frequency-averaged absorption coefficients as follows:

If 
$$I_{n\nu} = 2\pi \int_{-1}^1 I_\nu \mu^n d\mu$$

$$I_n = \int_0^\infty I_{n\nu} d\nu$$

$$\frac{dI_n}{d\tau_n} = \frac{dI_n}{\kappa_n d\Delta} = \int_0^\infty \frac{dI_{n\nu}}{\kappa_\nu d\Delta} d\nu$$

$$\kappa_n(\Delta) = \frac{\int_0^\infty \kappa_\nu B_\nu E_{n+1}(\kappa_\nu \Delta) d\nu}{\int_0^\infty B_\nu E_{n+1}(\kappa_\nu \Delta) d\nu}$$

The various  $\kappa_n$ 's are not identical. Any differences are reflected in differences in the rate of growth of the corresponding moments of the emerging radiation with increasing slab thickness. However, one might suspect, from the way the exponential integrals appear in both numerator and denominator in the expression for  $\kappa_n$ , that these average absorption coefficients are not too different from each other. This suspicion has been supported by a number of sample calculations [1]. One can, in fact, show that it is a reasonable approximation to substitute an exponential for the exponential integrals, and with this approximation, there is then a single optical depth based on a single average absorption coefficient

$$\kappa(\Delta) = \frac{\int_0^\infty \kappa_\nu B_\nu e^{-\beta \kappa_\nu \Delta} d\nu}{\int_0^\infty B_\nu e^{-\beta \kappa_\nu \Delta} d\nu}$$

$$\tau = \int \kappa d\Delta = \frac{1}{\beta} \ln \left[ \frac{\int_0^\infty B_\nu d\nu}{\int_0^\infty B_\nu e^{-\beta \kappa_\nu \Delta} d\nu} \right]$$

Here  $\beta$  is an adjustable parameter available to fit the exponential integral. A reasonable value lies between  $\sqrt{3}$  and 2.0.

Considered as a function of  $\tau$ , defined above, the various moments vary just as they would in a grey gas. For instance, the emerging heat flux at the surface of two slabs, with identical  $\tau$  but composed of different gases, will be nearly the same. Furthermore, other moments, such as the integrated mean intensity or the radiation pressure, can be obtained directly from the corresponding grey results.

Thus, the grey gas has indeed a relevance for this simple example. It must not be thought that the problem has been completely reduced to a grey problem. The determination of  $\tau$  involves a frequency integration over the spectrum, and this varies from one case to the next. But it should be noticed that for a given situation only one such integration is necessary. Integration along many lines of sight is not involved once directional moments are used.

## REFERENCE

1. Traugott, S. C.: On Grey Absorption Coefficients in Radiative Transfer. RIAS Technical Report 67-9C, Martin-Marietta Corp., August 1967.

# GAS EMISSIVITY MODEL FOR RADIATIVE TRANSFER CALCULATIONS

N 68-18107

By

A. F. Sarofim, Associate Professor

Chemical Engineering Department, M. I. T.  
Cambridge, Massachusetts

The model used to describe radiation from gases is to a large extent determined by the problem of interest. Three applications that illustrate the need for different models are the evaluations of

- (1) the detailed spectral transmission through an isothermal gas layer,
- (2) the total radiative flux from a nonisothermal gas volume for a prescribed temperature and concentration distribution, and
- (3) the temperature and flux distribution in a gas volume, given the boundary conditions and flow field.

A number of papers in this conference have described models which can provide solutions to the first two problems. These models are, however, too complex for use in calculations of temperature and flux fields when allowance must be made for interaction of radiation with convection and/or other energy terms. A model of gas emissivity which provides an accurate description of total emissivity and yet retains a functional form simple enough for calculations in which interaction is important has been proposed by Professor Hottel [1, 2]. The model, sometimes referred to as the mixed gray gas approximation, represents the dependence on path length  $l$  of the total emissivity  $\epsilon_G$  of an isothermal gas of fixed partial pressure  $p$ , by a series of the form

$$\epsilon_G = \sum_n a_n (l - e^{-k_n p l})$$

where the number of terms  $n$  in the series is determined by the accuracy with which the emissivity needs to be fitted. This representation has the special merit that it permits the expression of radiative flux in different configurations as a weighted sum of geometrical factors which have been evaluated and tabulated for gray gas exchange. For example, the flux in a unidimensional temperature field can be expressed as a weighted sum of terms involving the exponential integrals. Another advantage of this gas emissivity model is that the number of constants needed adequately to describe total emissivity is far smaller than that required for a description of the spectral emissivity. Figure 1 shows an approximation of total emissivities for water vapor, calculated [3] from the spectral data reported by Ludwig et al. [4], by a three-term exponential series. The inadequacy of a gray gas approximation fitted at one point, also shown on the diagram, demonstrates that the use of a single mean absorption coefficient such as the Rosseland and Planck mean has validity only over a narrow path length range.

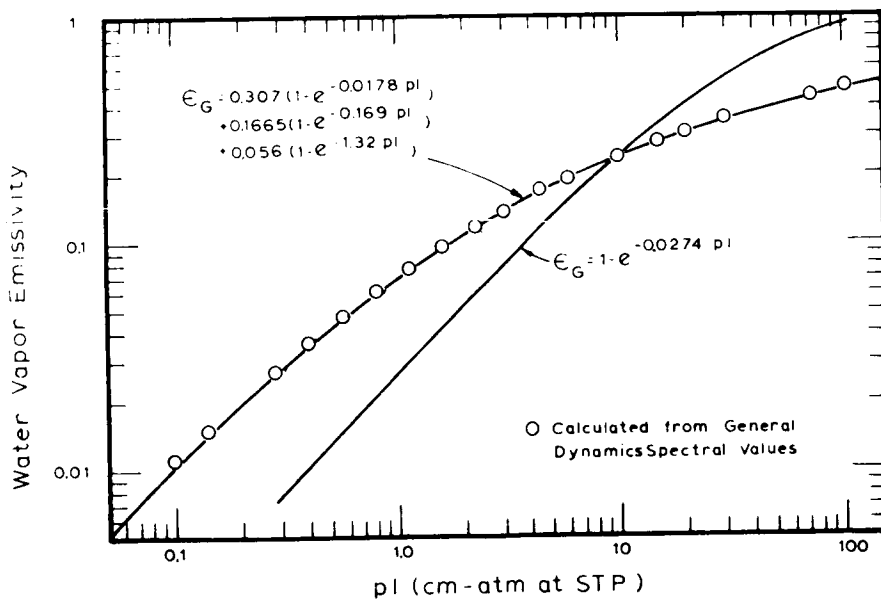


FIGURE 1. MIXED GRAY GAS APPROXIMATION OF WATER VAPOR EMISSIVITY:  $T = 1575^\circ\text{K}$   $P = 1 \text{ ATM}$   $P_W = 0.185 \text{ ATM}$



Application of the model to calculations of heat transfer in nonisothermal gases is approximate to the extent that only partial allowance is made for the changes with temperature of the spectral absorption coefficient. The errors introduced by such an approximate treatment are small because the flux calculations include the correct treatment of the much greater dependence of emissive power on temperature and because partial compensation of errors occurs in the solution of the governing integral equations. Limited testing of the model by comparison of measured radiant intensity distributions across a flame with those calculated using the mixed gray gas approximation has provided encouraging results [5]. More extensive testing, in which fluxes calculated using the mixed gray approximation are compared with those obtained with the more rigorous Curtis-Godson model, is in progress [3].

## REFERENCES

1. Hottel, H. C.: Chapter IV in McAdams, Heat Transmission, Third ed, McGraw-Hill, 1954.
2. Hottel, H. C.; and Sarofim, A. F.: Radiative Transfer. McGraw-Hill, 1967.
3. Reed, D. W.: Sc.D. thesis, M. I. T., in preparation.
4. Study of an Exhaust Plume Radiation Predictions. Convair, Space Science Laboratory, San Diego, California.
5. Hemsath, K.: Sc.D. thesis, Stuttgart, in preparation.

---

## DISCUSSION

J. I. F. King: I am sure that you could take any four experimental points among those shown on Figure 1 and then use a Prony algorithm for two values of  $a_n$  and two values of  $k_n$ . In other words, you could fit that curve with just two piecewise grey gases probably better than you did with three.

A. F. Sarofim: It depends on how many decades of data you wish to fit and how good a fit you wish to have. We have used one, two, or three terms and one term is quite good for many applications. If you are interested, for instance, in the emissivity from a furnace with pL values between one and five foot-atmospheres, then you can be a little casual with the lower values of pL.

J. I. F. King: This is an inversion problem and you are treating it synthetically. How can you ever be sure that you have made the right choice?

A. F. Sarofim: We are getting a least mean square fit. We could make a two grey gas model fit four points exactly. The question is: How good a fit would it be in the intermediate regions? I contend that, if you use just four points, then your ability to fit the correct emissivity in these intermediate regions would not be as good as if you use six or more.

---

# THE DOPPLER ANALOG OF AN ELSASSER BAND MODEL

N 68-18108

By

S. A. Golden

Rocketdyne, A Division of North American Rockwell Corporation

The properties of the spectral absorption coefficient and integrated emissivity (i. e., the equivalent width) of the Doppler analog of an Elsasser band have been investigated and the results reported in two papers, the abstracts of which appear below.

## I. Spectral Absorption Coefficient of the Doppler Analog [1]

An expression has been obtained for the spectral absorption coefficient of a distribution of  $2N + 1$  equally intense, equally spaced Doppler-broadened spectral lines of equal half-width in the limit of large  $N$ , i. e., the Doppler analog of an Elsasser band. The expression is

$$P_{\omega} = P_o \exp\left(\frac{\alpha^2}{4\beta^2}\right) \theta_3\left(\frac{\pi\alpha}{2\beta^2} \middle| \frac{\pi i}{\beta^2}\right) = \frac{S}{d} \theta_3\left(\frac{\alpha}{2i} \middle| -\frac{\beta^2}{\pi i}\right),$$

where

$$P_o \equiv \left(\frac{\ln 2}{\pi}\right)^{\frac{1}{2}} \frac{S}{\gamma}, \quad \alpha \equiv \frac{2\pi i(\omega - \omega_o)}{d}, \quad \beta = \frac{\pi\gamma}{d} \left(\frac{\ln 2}{\pi}\right)^{\frac{1}{2}}$$

and the function  $\theta_3(u|\tau)$  is the third Jacobi theta function. Several interesting properties of the distribution have been obtained, namely,

$$(1) \quad P_{\omega \pm d} = P_{\omega},$$

$$(2) \quad P_{\omega_o \pm nd} = P_o \theta_3\left(0 \middle| \frac{\pi i}{\beta^2}\right) \text{ is a maximum,}$$

$$(3) \quad P_{\omega_{\pm(n+\frac{1}{2})d}} = P_o \theta_2 \left( 0 \left| \frac{\pi i}{\beta^2} \right. \right) \text{ is a minimum,}$$

and (4) the ratio of the minimum to maximum values of the absorption coefficient is  $k^{\frac{1}{2}}$ , where  $k$  is the modulus of the complete elliptic integral of the first kind,  $K(k)$ . This last result may be used to establish conditions for the validity of limiting cases. For example, for values of  $k^{\frac{1}{2}} < 0.01$  (corresponding to  $\gamma/d < 0.18$ ), the band may be considered to consist of isolated lines; conversely, for values of  $k^{\frac{1}{2}} < 0.99$  (corresponding to  $\gamma/d > 0.65$ ) the lines are so highly overlapped that the absorption coefficient may be considered constant with a value

$$\overline{P}_{\omega} = P_o \left[ \frac{K(k)}{2\pi} \right]^{\frac{1}{2}} (1 + k^{\frac{1}{2}}) = \frac{S}{d} \left[ \frac{K'(k)}{2\pi} \right]^{\frac{1}{2}} (1 + k^{\frac{1}{2}}).$$

## II. The Integrated Emissivity [2]

The integrated emissivity of the Doppler analog of an Elsasser band has been investigated by both analytical and numerical methods. Values of the integrated emissivity have been calculated for values of  $SX/d$  between 0 and 1000 and  $\gamma/d = 0.10, (0.01), 0.69$ . Various limiting cases have been investigated and, in particular, the expression

$$\frac{\epsilon}{d} = 1 - I_o \left( \frac{SX\alpha}{d} \right) \exp \left( - \frac{SX}{d} \right),$$

where

$$\alpha = \frac{1}{2} \left[ \theta_3 \left( 0, e^{-\beta^2} \right) - \theta_3 \left( \frac{1}{2}\pi, e^{-\beta^2} \right) \right], \quad \beta^2 = (\pi^2/\ln 2) (\gamma/d)^2$$

can be used for any value of  $SX/d$  and  $\gamma/d > 0.27$  with an error of less than 0.5 percent. Conversely, for values of  $\gamma/d \leq 0.18$  and any value of  $SX/d$ , and isolated line expression,

$$\frac{\epsilon}{d} = \frac{SX}{d} \sum_{n=0}^{\infty} \frac{(-1)^n}{(n+1)!(n+1)^{\frac{1}{2}}} \left( \frac{\pi^{\frac{1}{2}}}{\beta} \frac{SX}{d} \right)^n,$$

can be used with comparable accuracy. Some of the properties of the integrals appearing as coefficients in the Taylor series expansion of the integrated emissivity have been studied and numerical values have been determined.

## REFERENCES

1. Golden, S. A.: Spectral Absorption Coefficient of the Doppler Analog. JQSRT, vol. 7, 1967, p. 453.
2. Golden, S. A.: The Integrated Emissivity. JQSRT, vol. 8, in press.

# TEMPERATURE SOUNDING WITH THE 4.3 MICRON CO<sub>2</sub> BAND

By

R. A. McClatchey  
Avco Space Systems Division  
Lowell Industrial Park  
Lowell, Massachusetts 01851

N68-18109

This paper briefly describes an experiment which is under development at the Jet Propulsion Laboratory for determining the vertical temperature structure, as well as several other parameters of meteorological importance, by making measurements in the vicinity of the 4.3 micron CO<sub>2</sub> band. Many people have spoken of measurements in the 15 micron band and attempts to invert the equation of radiative transfer to determine the temperature profile. We think it is not too well known that attempts are being made to do a similar type of thing in the 4.3 micron region. The instrument being developed for this purpose, a grating spectrometer having 35 individual channels, has been flown on a balloon and has been recommended for earth orbital flight as part of the Apollo applications program.

The spectral location of the 4.3 micron CO<sub>2</sub> band with respect to the solar radiation curve is indicated in Figure 1. This figure represents the energy/cm<sup>2</sup>/sec/steradian/wavenumber that would be received by a satellite-borne instrument assuming a mean earth albedo of 0.40 and assuming a surface brightness temperature of 275°K. This figure demonstrates that at 4.3 microns we are operating near the cross-over region where thermal emission dominates at longer wavelengths and reflected solar radiation dominates at shorter wavelengths. We intend to take advantage of this situation and place some detectors in the 2.0μ and 2.7μ absorption bands of CO<sub>2</sub> as well as in the 7600Å oxygen band. In addition we plan to make measurements at longer wavelengths up to and including the short wavelength wing of the 6.3μ H<sub>2</sub>O band. We expect to be able to determine the heights of clouds by means of the shorter wavelength measurements of the absorption of solar radiation by a uniformly mixed atmospheric constituent (i.e., CO<sub>2</sub> and O<sub>2</sub>). The measurement in the 6.3μ H<sub>2</sub>O band together with the temperature sounding information obtained in the 4.3μ CO<sub>2</sub> band should be sufficient to determine the vertical mixing ratio of water vapor above the surface or cloud top.

We plan to determine the temperature structure of the atmosphere in six atmospheric layers skewed so that we have more information about both the lower layers of the atmosphere and the stratosphere. We are working toward an accuracy of  $\pm 1^\circ\text{K}$ . Measurements will also be made near  $5\mu$  where the atmosphere is nearly transparent in order to determine the surface brightness temperature. This is required in the mathematical inversion technique applied to data obtained in the  $4.3\mu$   $\text{CO}_2$  band.

Measurements just short of  $2\mu$  will be examined in order to determine whether the spectral response can be interpreted in terms of the composition of cloud tops in the field of view. A shift of the characteristic water feature can be used for the identification of water or ice clouds.

A final general objective of this experiment is to determine methods of analysis of our results in the presence of partial cloud cover. As a direct result of the strong temperature dependence of the Planck function in this spectral region, we feel that up to 20 percent cloud cover can be tolerated in the temperature sounding experiment with only slight effect on the resulting temperature profiles. Additional studies of this problem will be made, both theoretical and experimental, by virtue of the analysis of the results of future balloon flights of this spectrometer.

Various mathematical inversion techniques have been applied to the radiative transfer equation. The best test of the method is whether or not it gets the correct answer. A test of the method developed by McClatchey [1] was recently made in the most objective manner we could devise. Dr. Farmer at JPL computed the spectral distribution of radiance in the  $4.3\mu$  region from a particular atmospheric model which he devised. He mailed me the radiance distribution, but withheld all information concerning the atmospheric model. After application of the method outlined in reference 1 (with slight modifications), the result presented in Figure 2 was obtained. The vertical lines in Figure 2 represent the mean temperature over atmospheric layers having a thickness indicated by the length of the lines. The continuous temperature profile is the initial temperature profile used by Dr. Farmer in his calculations. We feel that we should run many more such tests in order to establish that our first test was not a mere coincidence. If subsequent results are as good or better, we would gain confidence in the mathematical technique, and we would concentrate on other theoretical aspects of the problem (e.g., the computation of transmittance) and on the accuracy of the experimental measurements.

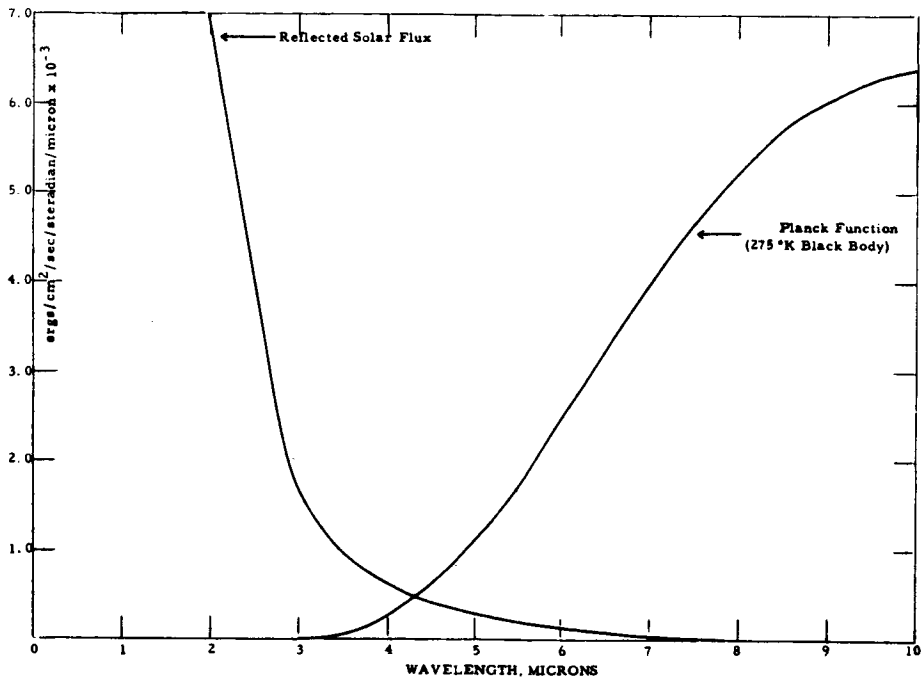


FIGURE 1

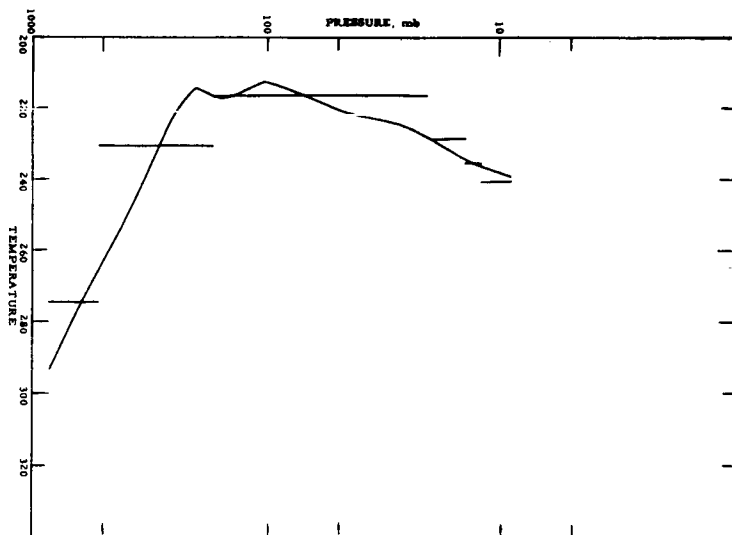


FIGURE 2



## REFERENCES

1. McClatchey, R. A.: The Use of the 4.3 CO<sub>2</sub> Band to Sound Planetary Atmospheres. Proceedings of the Symposium on Electromagnetic Sensing of the Earth from Satellites, Ed. Ralph Zirkind, Published by the Polytechnic Press of the Polytechnic Institute of Brooklyn, 1967.

# NUMERICAL STUDY OF NONLINEAR INVERSION\*

By

E. T. Florance

GCA Corporation  
Bedford, Massachusetts 01730

N 68-18110

---

## ABSTRACT

This paper presents some preliminary results obtained in a numerical study of nonlinear inversion applied to the inference of atmospheric temperature profiles from satellite radiometric measurements in the 15 micron absorption band of CO<sub>2</sub>. Previous work [1] on nonlinear inversion techniques employed the Prony algorithm, which was first suggested for profile inference by King [2]. To circumvent certain restrictive assumptions which had to be made in the earlier study [1], we developed a generalized nonlinear inversion method applicable to a wide class of band absorption spectra.

---

The generalized inversion method has been used to invert synthetic radiance data which are generated by computer from a set of model temperature profiles. The spectral intervals chosen for this study correspond to the channels used on previous versions of the SIRS instrument [3]; namely, 669, 677.5, 691, 697, 703, and 709 cm<sup>-1</sup>. An additional channel at 747.5 cm<sup>-1</sup> has also been considered in order to better define the temperature structure in the lower troposphere. Transmittance data for the six SIRS channels have been kindly supplied by H. E. Fleming of ESSA/NESC.

A number of assumptions concerning the inferred profile must be made:

1. For heights greater than the level corresponding to a fixed pressure  $p_s$ , the temperature profile is assumed known a priori. Climatological information can be used for this purpose. In the results reported here,  $p_s$  has been rather arbitrarily set at about 16 mb.

---

\* This work was supported by NASA Goddard Space Flight Center under Contract NAS5-10393.

2. The pressure at the ground level is assumed known, and the associated temperature  $T_g$  is obtained from a window channel observation. Only clear model atmospheres are being studied because the consideration of partly cloudy and overcast conditions would lead to additional complications.

3. If one uses the height parameter  $t = \ell \ln p$ , then a comparison profile  $T_o(t)$  is calculated as follows:

- a.  $T_o(t)$  equals the assumed profile for  $t \leq \ell \ln p_s$ ;
- b.  $T_o = T_g$  at ground level;
- c.  $T_o(t)$  is a linear function of  $t$  elsewhere.

The purpose of these assumptions is to anchor the inferred profiles at heights for which the contribution of the profile to the upwelling radiance is sufficiently small to render the profile noninferable. The difficulties encountered in trying to determine freely variable endpoints are indicated in reference [1].

By referring all radiances to a standard wave number  $\nu_s$  (taken as  $703 \text{ cm}^{-1}$  for the above channels), we generate the radiance differences:

$$\Delta I(i, \nu_s) = \int_{\tau_g(i)}^{\tau_s(i)} \{B[T(t), \nu_s] - B[T_o(t), \nu_s]\} d\tau(\nu_i, t), \quad (1)$$

where  $i$  denotes the  $i$ th channel with wave number  $\nu_i$ ,  $B[T, \nu]$  is the Planck function at temperature  $T$  and wave number  $\nu$ , and

$$\tau_g(i) = \tau(\nu_i, \ell \ln p_g) \text{ and } \tau_s(i) = \tau(\nu_i, \ell \ln p_s)$$

are, respectively, the transmissivities of channel  $i$  at the ground and fixed upper levels. The radiance differences in Equation (1) are considered as measured data to which random error may be added to simulate instrumental noise.

The generalized nonlinear inversion method is applied, first, by approximating the Planck function difference under the integral in Equation (1) by a spline function of order 2. An order 2 spline function is simply a continuous

piecewise-linear function of  $t$ . The positions of the spline joints (points of slope discontinuity)  $t_1 \dots t_n$  and the gradient jump magnitudes  $\Delta B'_1 \dots \Delta B'_n$  constitute  $2n$  parameters to be determined by minimizing the summed square "error" in the inferred radiance difference  $\Delta I(i; \{t_j\}, \{\Delta B'_j\})$ :

$$F(\{t_j\}, \{\Delta B'_j\}) = \sum_{i=1}^M \left[ \Delta I(i, \nu_s) - \Delta I(i, \{t_j\}, \{\Delta B'_j\}) \right]^2 \quad (2)$$

An initial guess for the set  $\{t_j\}$  is made and the set  $\{\Delta B'_j\}$  is calculated so as to minimize  $F$  [i. e., from the linear regression equations based on Equation (2)]. Improved estimates of  $\{t_j\}$  and  $\{\Delta B'_j\}$  are obtained by using the Davidson-Fletcher-Powell iteration method for minimizing a general nonlinear function.

A computer program has been prepared to apply the method described above to a large variety of atmospheric temperature profiles. A few preliminary results are illustrated in Figures 1-4 for typical climatological mean profiles. The dots indicate the original profile, while the solid curves show three-joint inferred profiles obtained by inverting noise-free synthetic data. The black triangular arrowheads have been placed at the pressure levels used as a first guess in the iteration procedure. The variation in joint position caused by reduction of the mean square radiance error  $F/M$  is particularly evident in Figures 3 and 4. The rms error between the original and inferred temperatures is noted on each profile.

The effects of different amounts of instrumental noise in the data on the temperature inference error are of great current interest. Since the present inversion technique is nonlinear, the effects of noise must be studied case by case. Results with realistic amounts of noise should be available shortly.

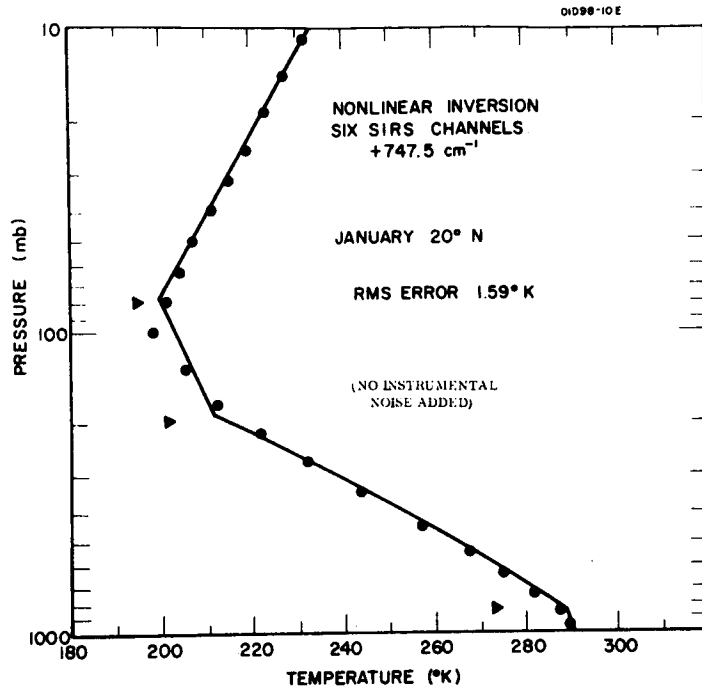


FIGURE 1. THREE-JOINT INFERRED PROFILE (SOLID LINE) COMPARED TO CLIMATOLOGICAL MEAN PROFILE (DOTS) FOR JANUARY (20° N, 100° W)

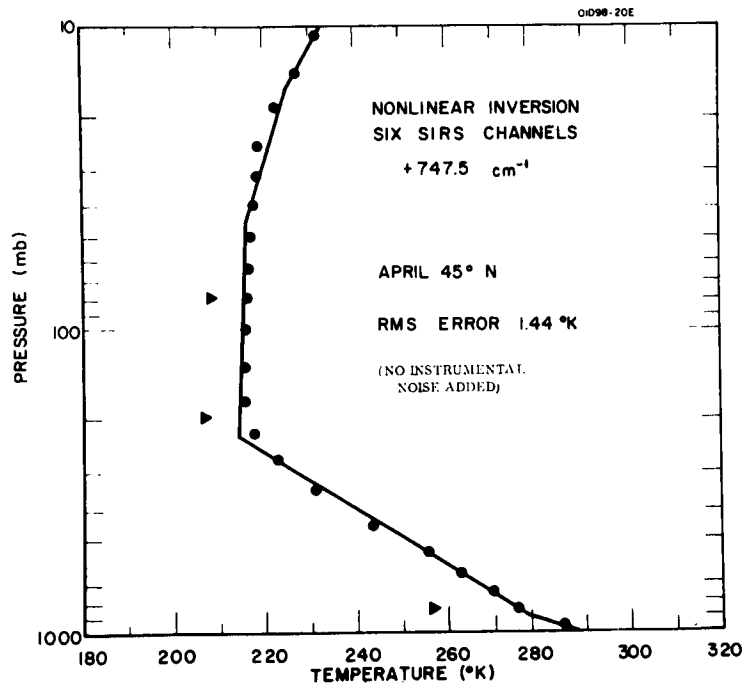


FIGURE 2. THREE-JOINT INFERRED PROFILE (SOLID LINE) COMPARED TO CLIMATOLOGICAL MEAN PROFILE (DOTS) FOR APRIL (45° N, 100° W)

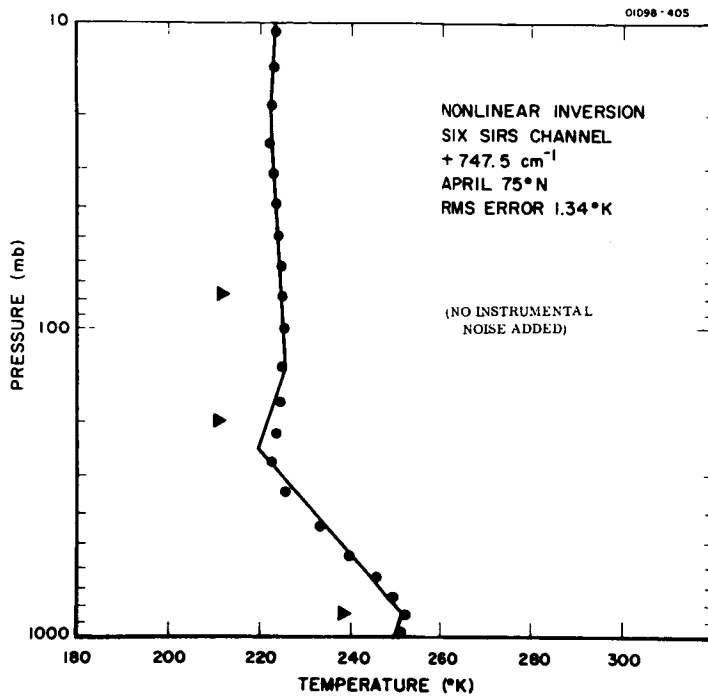


FIGURE 3. THREE-JOINT INFERRED PROFILE (SOLID LINE) COMPARED TO CLIMATOLOGICAL MEAN PROFILE (DOTS) FOR APRIL (75° N, 100° W)

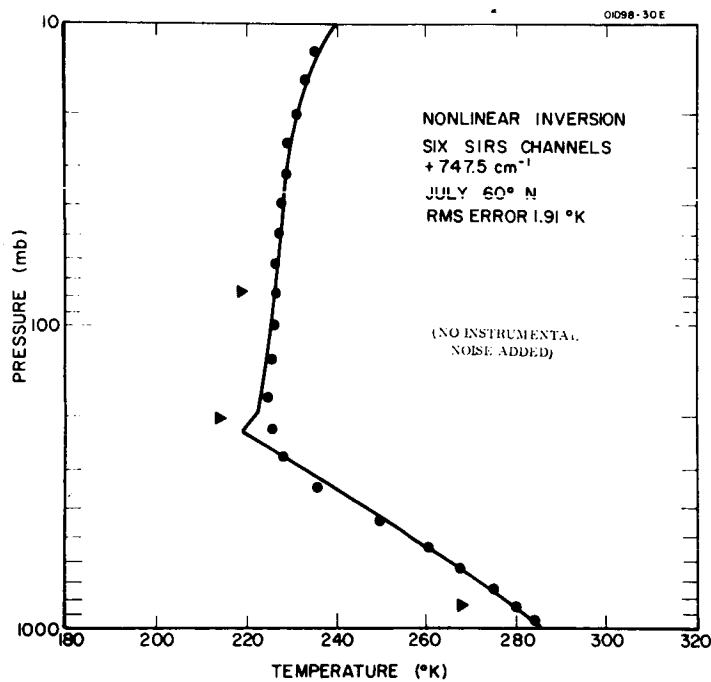


FIGURE 4. THREE-JOINT INFERRED PROFILE (SOLID LINE) COMPARED TO CLIMATOLOGICAL MEAN PROFILE (DOTS) FOR JULY (60° N, 100° W)

## REFERENCES

1. Florance, E. T.: Error Analysis of Inversion Techniques. GCA-TR-67-8-N, GCA Technology Division, GCA Corp., June, 1967.
2. King, Jean I. F.: Inversion by Slabs of Varying Thickness. J. Atmos. Sciences, vol. 21, 1964, pp. 324-326.
3. Wark, D. Q.; and Fleming, H. E.: Indirect Measurements of Atmospheric Temperature Profiles from Satellites: I. Introduction. Monthly Weather Review, vol. 94, 1966, pp. 351-362.

FORUM

Chairman: R. Goulard,  
Purdue University



## QUESTION I

N 68-18111

## HEAT TRANSFER AND FLOW FIELD SOLUTIONS

Introductory Remarks: Milton Huffaker, NASA/MSFC

M. Huffaker: The accuracy of the radiation heat transfer solutions in rocket plume calculations depends on how well we can calculate the contributions along lines of sight. For example, consider the dashed line on the attached Figure 1 which is borrowed from Mr. Reardon's talk and which represents the temperature field of a Saturn S-II rocket plume. It goes first through a region at 2400° K, then at 3000° K, 4000° K, and afterwards through decreasing temperatures: 1800° K, 1200° K, etc. The physical path length is of the order of 30 feet.

I would like to ask three questions regarding the existing calculations concerning this kind of radiating source:

1. Assuming that the flow field is completely known, what is the absolute level of confidence in the heat transfer results?
2. What are the largest uncertainties besides gas properties?
3. What further work should be done to improve over what I believe is the current 25 percent accuracy in liquid and solid propellant plume radiation?

S. A. Golden, Rocketdyne: The line of sight illustrated on Figure 1 presents large temperature ratios (up to 3) and pressure ratios (up to 2). If one goes back to Dr. Thomson's paper, it would seem that the reliability of the Curtis-Godson model cannot be expected to be terribly great in the plume of the Saturn S-II rocket.

R. Goulard, Purdue: Since computers have a finite capacity, it seems that sophistication in the radiation properties is acquired at the expense of accuracy in the flow properties and vice versa. Could it be that more accuracy would be obtained for the flow field if the radiation models used by Mr. Reardon (#3 or #3A) were replaced by a simple grey gas? [Ed. note: Traugott's and Sarofim's short papers (Session IV) were introduced at this point of the discussion.]

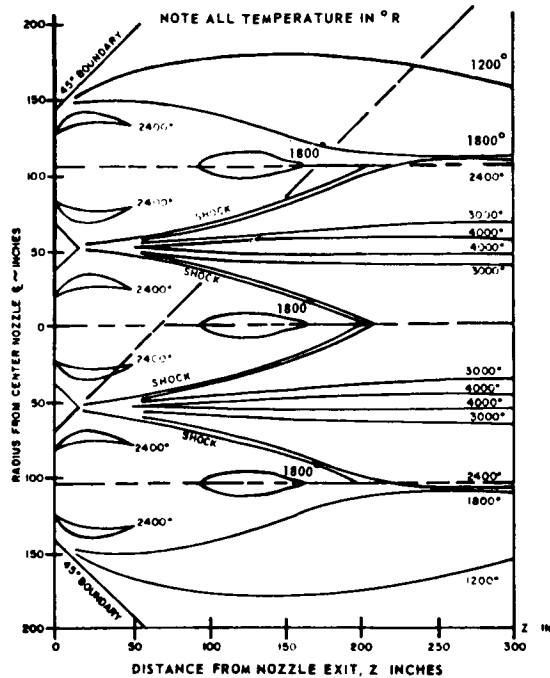


FIGURE 1. ISOTHERMAL CONTOURS FOR THE X-Z PLANE OF THE S-II FLOW FIELD APPROXIMATION

J. Reardon, Hayes: I am not sure about the accuracy of the band models, but as long as you use a simplified band model (model 3A for instance) I do not believe that the calculation time is excessive.

R. Goulard: You feel satisfied that you can do better than with a grey gas model and still produce a detailed and accurate flow field?

J. Reardon: Yes. Of course, we had originally to make estimates for the Saturn stages before the band model data were available. Because of the uncertainties in these estimates, they were necessarily quite conservative. The increased accuracy expected with the more precise band model methods is certainly worth the computer time required.

A. Sarofim, MIT: Could you still retain your relatively complex band model if the radiation losses were large enough to cool and appreciably modify the flow field (the "coupled" case)?

A. Thompson, IDA: It is fair to assume that in traditional coupled problems where molecular radiation plays a role (cool stellar atmospheres, nuclear blasts), there is a limit to the sophistication of the band models one can use. We heard yesterday (Dr. Auman's paper) that an exact line-by-line method necessitated 40 hours on an IBM 7094 computer for the calculation of one flux value in a simple isothermal non-coupled case. Such lengthy computational times do not fit easily into the iterative methods inherent to coupled problems.

On the other hand, the accuracy of the models such as Curtis-Godson's cannot be tested in a given configuration unless one can produce such line-by-line calculations and suitable laboratory experiments for comparison. This is why, as more powerful computers become available, there is a noticeable tendency towards more and more detailed models, which will eventually lead to essentially exact calculations if the line strengths and widths are known.

A. Laderman, Philco/Ford: I would like to comment on solid propellant plumes and address myself to the first two questions posed by Mr. Huffaker. Based on our current knowledge, I would say that we cannot expect to calculate radiation from the particles within the plume better than within a factor of two. I think the main question to answer here is whether or not there is a relatively significant amount of radiation at wavelengths beyond 4 or 5  $\mu$ . If there is, then what we lack for more precise radiation calculations is data on the optical properties of alumina in this spectral region. If there is not, then the trouble must be associated with uncertainties in the existing optical data. I suggest that under these circumstances some sort of measurement is necessary to resolve the issue; either a spectral measurement of a typical plume at wavelengths beyond 5  $\mu$ , or measurement of the particle optical properties at these wavelengths. As I mentioned yesterday in my talk, there also are uncertainties in particle size data which contribute to the present dilemma. However, I think that these uncertainties are less important than those in the optical data. This is supported by the calculations we have made for the S-II ullage motor, where the change in particle radiation produced by changing the number and mass mean diameters by a factor of two was considerably less than that caused by using the alternate extrapolations for the refractive index of alumina which were described yesterday.

1 N 68-18112

## QUESTION II

# REQUIREMENTS, POSSIBILITIES AND PROMISES OF INVERSION TECHNIQUES FOR ROCKET EXHAUST PLUME TECHNOLOGY

Introductory Remarks: J. I. F. King, GCA

J. I. F. King: Over the past two days we have heard about two main groups of inversion methods: the linear and the nonlinear techniques. Dr. Conrath has worked extensively with both, and I wonder if he would care to comment on the advantages and disadvantages pertaining to each.

B. Conrath, NASA Goddard: I have not done what could be called a very critical study of these methods; I am, perhaps, more familiar with the linear techniques than with the nonlinear techniques.

We have tried doing some work with the empirical orthogonal function approach which involves essentially a linear technique. It incorporates a lot of a priori information into the solution, and works rather well as long as you do not have a statistically anomalous case; but it seems to be unable to pick out the unusual meteorological situations.

The nonlinear method, particularly the Prony algorithm method, is the most objective of the methods involved, in that you do not predetermine the shape of the solutions. But it has two disadvantages. First, at least in the original Prony algorithm form, an exponential type kernel is required, so that the true atmospheric transmission functions cannot be represented exactly in the formulation; it is a severe limitation. Second, there seems to be limitations on the extent to which it can fit a temperature profile with an arbitrary degree of complexity. This usually infers two ramps, sometimes three at the very most.

In my opinion, we have not arrived yet at a completely satisfactory method of temperature inversion. The large amount of global data that will be retrieved from the forthcoming Nimbus satellite will be very useful in testing on real data the various methods that have been proposed, and we are planning to do these comparisons as soon as the data become available.

J. I. F. King: We still do not have a routine program that could be applied to data given by a satellite for temperature inversions?

B. Conrath: I do not think that we have anything approaching a routine program at the moment.

R. A. McClatchey, AVCO: I would like to comment briefly on what seems to me an important aspect of the determination of vertical temperature profiles: who wants to know it, and to what accuracy? I think the answer is that in the meteorological community, the numerical weather forecasters, want this information in order to use it in their calculations. As for the accuracy they need, I might just quote from a recent COSPAR meeting:

"For the vertical resolution of the hydrostatic motion, it should be sufficient to use about 10 levels, not uniformly distributed, but skewed, to give more resolution with respect to pressure near the ground and in the stratosphere."

This is, in general, a slightly higher resolution than we can obtain with our experiments at this point. It gives us something that we should strive toward, but also points out that probably we should not attempt to obtain every little detail in the temperature profile. We should be striving toward some sort of mean temperature over atmospheric layers of reasonable thickness which is what the numerical weather forecasters need.

Dr. Drayson pointed out to me that, in the course of an inversion of some measured data in the  $15 \mu$  region, he chose as a first guess in his procedure the climatological mean for the particular latitude and month in question. He found that the temperature profile that existed on the day of their measurement was almost identical to the mean, so that very little correction was required. I think it should be established how different the climatological mean temperatures are from what the numerical weather forecasters really need. It would be embarrassing to find that they really do not need anything better than exists in the climatological mean.

J. I. F. King: I concur completely. It seems to me that inversion is in danger of being oversold. I think that we have also to be wary of what you might call the "inversion fallacy" on which Dr. White briefly commented this morning: "If you indefinitely sample more and more points, you cannot indefinitely improve your knowledge of the system you observe." The limits on what you can infer are set fundamentally by the inaccuracy of your data; this is a very stringent limitation.

To infer, say, 10 valid bits of information for 10 levels (the forecast requirement which was indicated), an instrumental accuracy of 6 decimals or so might be required. I think, therefore, that one should always keep in mind the connection between the noise in the data and the number of new pieces of information that are retrievable.

S. Hales, General Electric: I would like to respond to Dr. McClatchey's comments about the atmospheric profiles being close to the climatological average and the implied suggestion that we do not really need the inversion. We all recognize that the reason that the climatological average exists is that it does, in fact, occur a great deal of the time. Nevertheless, the reason that we need the inversion techniques is to catch the deviations from this average. It is a matter of rule by exception. For instance, a particular type of temperature sounding which is two standard deviations warmer than the average would be very important to catch, even though it may occur only 5 percent of the time.

I think that we do have an assignment to probe the atmosphere and to produce reasonably accurate temperature soundings, so that the numerical weather prediction can be upgraded by world-wide meaningful weather observations of temperature and humidity. Eventually, the meteorologist will also want wind measurements, which we are really not getting from the satellites. We are just beginning to probe the atmosphere from satellites.

R. Goulard, Purdue: I am quite anxious to know whether some of the experience acquired in the meteorological satellite measurements could be transferred to the probing of rocket plumes.

R. Drayson, Univ. of Michigan: I was hoping to bring the discussion around somewhat more in the direction Dr. Goulard just proposed. In the earth's atmosphere, where you already have a very good idea of what the temperature profile is like, we are really only putting the finishing touches on the atmospheric structure. As far as water vapor and ozone are concerned, we have a fairly good idea of their distributions; but the deviations are much larger.

As to rocket exhausts and some of the other planetary atmospheres, there may be quite a number of surprises in store for us, and we do not really have a very good idea of what conditions are like. We cannot use either climatology or empirical orthogonal functions because nobody has observed them. The idea is to look from the outside assuming that you know nothing of

what is happening on the inside. The problem of obtaining a solution seems to be the same as reducing the temperature profile in the earth's atmosphere and many of the mathematical ideas are the same, but the details of how you go about solving it will be completely different.

J. I. F. King: . . . and should be conditioned by the problem.

R. Drayson: That is right.

F. Krause, NASA/MSFC: I would like to comment on the combination of the inversion techniques with the crossed-beam methods. The same instrumentation is used in both methods. The only thing that differs is the data reduction. Our group at NASA/MSFC has proposed to develop a moving cross-beam system consisting of two telescopes on the same airplane or satellite for measuring winds and turbulence profiles. If you add the spectroscopic techniques I have discussed this morning, the system could also give you temperature as well as composition information. Cross-beam spectroscopy and inversion techniques seem to be complementary since the crossed-beam method works best for inhomogeneous and time-varying distributions of radiation sources, whereas inversion techniques work best for smooth distributions.

J. I. F. King: I would like to ask Dr. Herget why he assumed what appeared to be a transparent plume in the inversion paper he gave in Session III.

W. Herget, Rocketdyne: We did not make a transparent (negligible absorption) plume assumption. In order to make use of the Abel integral equation, however, one must write the equations for radiative transfer through the plume in the particular form shown in our paper. The equations for the line-of-sight transmittance of radiation from an external source through the plume may be put in the required form using no approximations whatsoever. The equations for the line-of-sight radiance emanating from the plume require the approximation  $e^{-kpL} \approx 1 - kpL$  in order to put them in the desired form. In practice, this approximation introduces no errors into the data as long as the maximum absorption (along a diametrical line of sight) does not exceed 30 percent.

J. I. F. King: Why did you resort to this approximation? Was the exact formulation too difficult to handle?

W. Herget: The exhaust plumes which we studied first were produced by motors operated at simulated altitudes, and, because of the resulting low pressures, the maximum line of sight absorption did not exceed 30 percent. Thus, the approximation was valid.

On succeeding programs, where rocket motors were operated at sea level conditions, we could no longer use the Abel method. We then solved the radiative transfer equations simultaneously by back substitution. In this method, just as in any absorption experiment, one obtains good results until maximum absorption along a particular line of sight exceeds 90 percent. If the absorption for a particular line of sight reaches 100 percent, then no information can be learned about zones inside that line of sight; temperatures and pressures can still be determined for the outer zones, though.

It does seem that the inversion techniques used by atmospheric investigators are much more complicated than those used in studying rocket exhausts. Perhaps this is because it is possible to study the rocket exhaust along a wide variety of lines of sight encompassing widely different path lengths.

J. I. F. King: Your comment really surprises me, because I would think that a cylindrical geometry would certainly be more complicated than the plane parallel atmosphere meteorologists usually work with.

E. T. Florance, GCA: I think the difference is in the kernels of the integral equations. In the Abel case, the kernels are not nearly so overlapping as they are in the atmospheric case. If the kernels are severely overlapping, you have the problems of ill-conditioning, and of sensitivity to noise. But, if the kernels are not as overlapping, as is fairly obvious in the cylindrical geometry since the beams near the edge do not penetrate the middle, the kernels are much less singular and the integral equations are not as unstable to noise.

J. C. Burns, GE: I found no sensitivity to noise in using limb-radiance profiles for temperature inversions for exactly the reason Dr. Florance just gave. The weighting function (the kernel) is really very narrow for the horizon (roughly 2.8 km), while if you are looking straight down, the weighting functions become very broad and are coupled.



RELEVANCE OF LABORATORY EXPERIMENTS TO ACTUAL  
RADIATING FLOWS

Introductory Remarks: Werner K. Dahm, NASA/MSFC

One can give a variety of interpretations to this title. I choose to take the parochial approach, and look at it with the eyes of an engineer who is concerned with the design of base heat shields of rocket vehicles. So for me this theme asks in essence: "What can we do with the radiation characteristics and the radiative heating component that we measure in our base heating model tests?"

As I mentioned in a previous presentation [1], base heating model tests have become a standard practice in the design of rocket vehicles, despite the tough questions of scaling.\* Up until the late 1950's, we have used for these model tests actual small scale rocket engines (see references 2 and 3). Figure 1 shows the engine cluster of a typical model of this type. It simulates the eight-engine cluster of the first stage of the Saturn I vehicle, using eight model engines of 500 pounds thrust each. The model engines burn liquid oxygen and kerosene, and are water-cooled. Engines sizes below about 500 pounds thrust are inopportune, since cooling difficulties increase rapidly with decreasing size. The model of Figure 1 is a plumber's nightmare. The cluster contains 56 individual pipes carrying water, liquid oxygen, kerosene, and a hypergolic igniter fluid. All of these pipes have to be tuned for uniform flow. Models of this type cost about 50,000 to 150,000 dollars. They require a countdown of several hours, comparable to that of, e. g., the Redstone rocket, and are fairly inflexible with respect to model geometry and test conditions.

---

\* The word "scaling" is used here in the sense of determining emission characteristics of a full scale rocket jet plume from the experimentally determined emission of a geometrically and thermodynamically similar small scale plume without knowing the details of their structure.

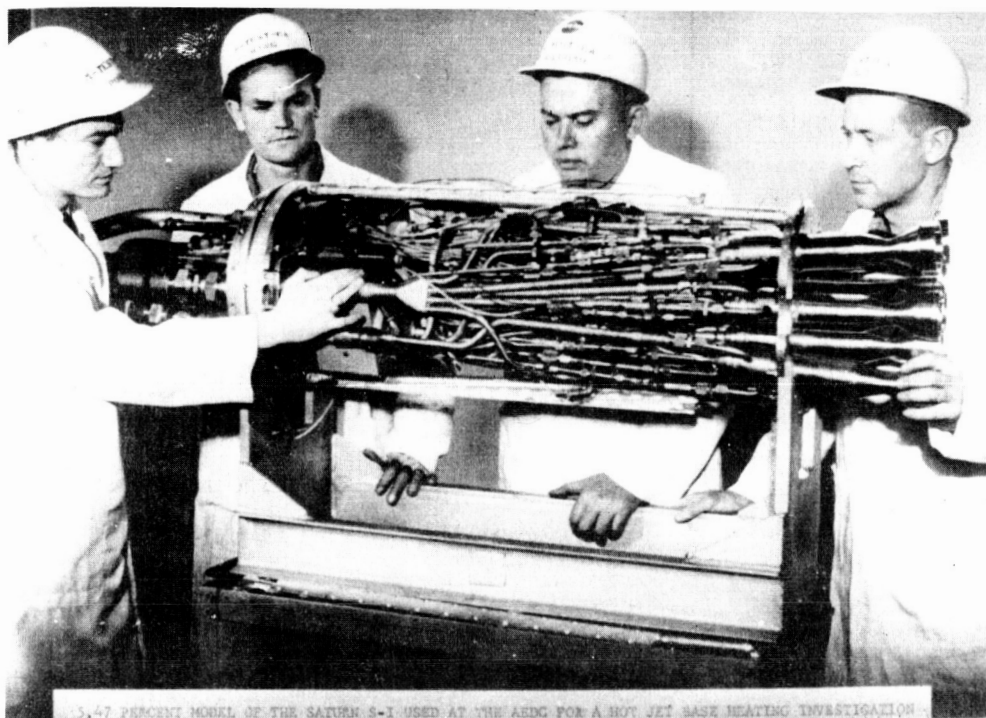


FIGURE 1

In order to escape the drawbacks of the "Long Duration" approach described above, a so-called "Short Duration" technique was subsequently developed by the Cornell Aeronautical Laboratory in cooperation with MSFC (see references 4 through 6). The principle of this shock-tube-type technique is sketched on Figure 2. Two supply tubes, closed by diaphragms, are filled with compressed gaseous fuel and oxidizer, selected to yield the same combustion products as the desired liquid propellants. When the diaphragms are cut, the propellants flow into the combustion chamber, are ignited, and discharge through the exhaust nozzle(s). The wave diagram on the upper part of Figure 2 explains the flow process. When the diaphragms open at time  $t = 0$ , a fan of expansion waves runs toward the lefthand side into the supply tubes, and a set of compression waves runs toward the right through the combustion chamber and nozzles. After a short buildup period, the flow out of the nozzles becomes stationary, and remains so until the expansion fan, reflected from the closed end of the tubes, has returned to the combustion chamber, bringing the message that the tubes are of finite length. Steady flow times of 5 to 10 milliseconds are obtained with supply tubes of moderate length, and the meaningful part of our measurements is taken during this period. The models are simple and uncooled. The method has cut our costs to less than 10 percent of our previous expense level. For testing at high altitude conditions, where the ambient flow has

# CONSTANT PRESSURE COMBUSTOR, SHORT DURATION FLOW GENERATOR

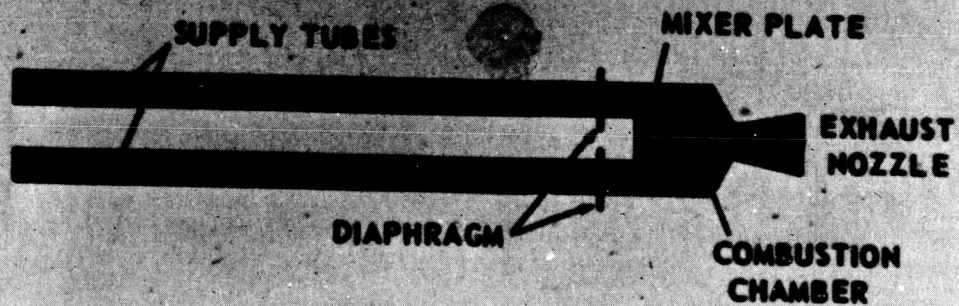
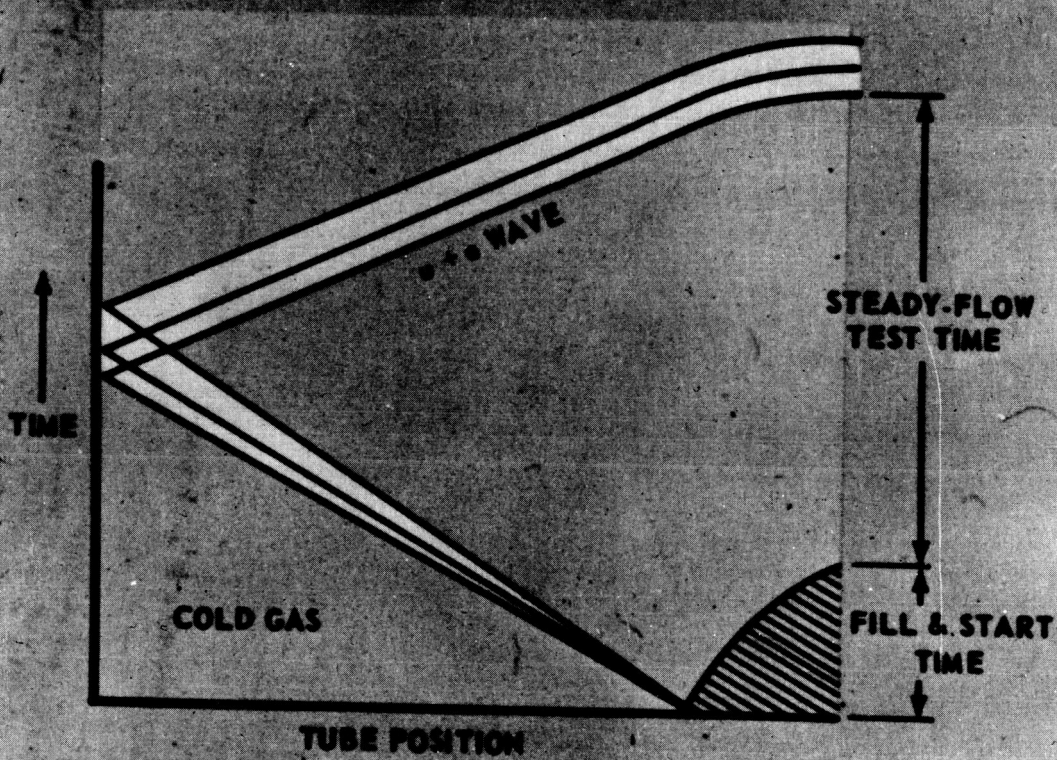


FIGURE 2

normally no effect in the neighborhood of the base, the exhaust of the model is simply discharged into a large vacuum tank. Figure 3 shows a typical tank of this type. The supply tube on the left side of the figure is of a single-tube concept used in an early phase of the development. Figure 4 shows the business end of a model of the S-IV stage, i. e., the second stage of the Saturn I vehicle. A row of heat transfer gages runs from the center of the model through the gap between two of its six nozzles. Instrumentation techniques used are identical to those used in shock tubes and shock tunnels. Figure 5 shows a typical heat transfer gage. A thin resistance thermometer strip is deposited on the surface of a quartz slug, and measures the surface temperature. The temperature/time trace during the steady flow period yields the heat flux rate; the latter must be independent of time for the duration of the steady period. Due to the short duration, only a very thin layer of the quartz slug takes part in the temperature

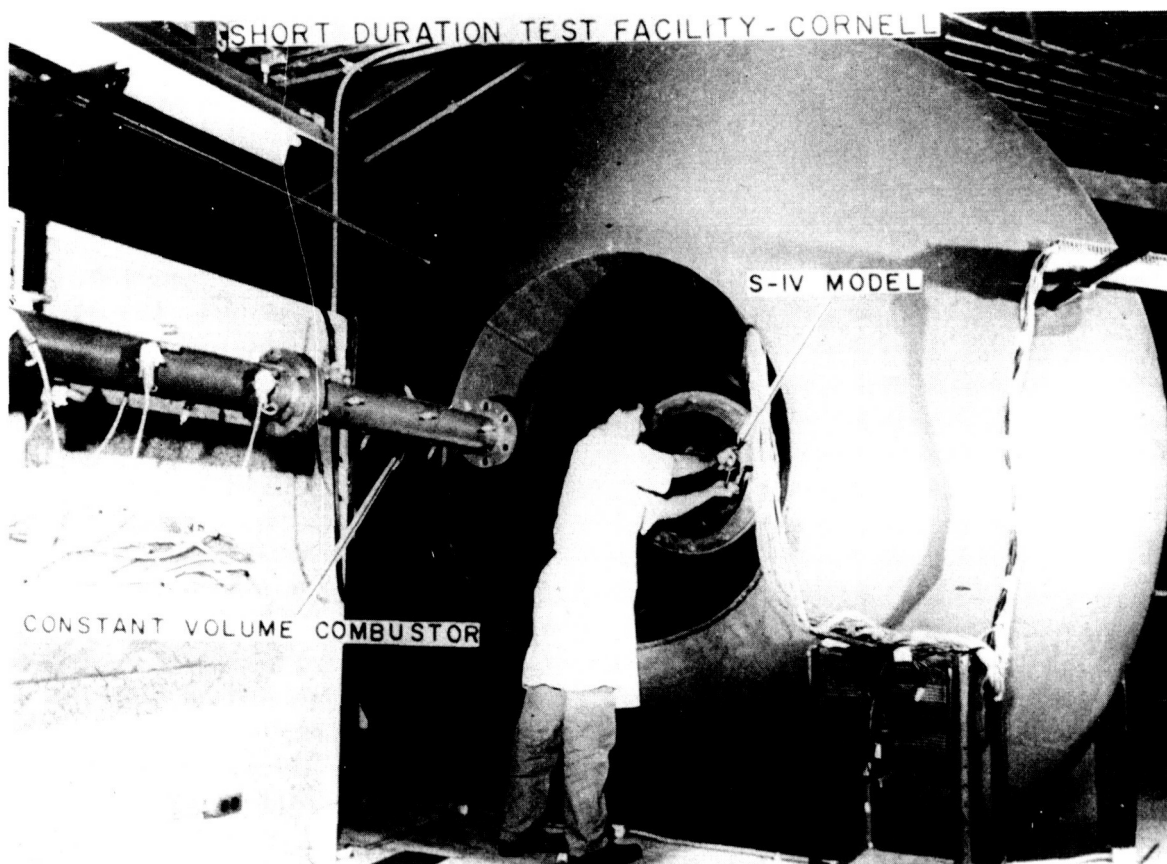


FIGURE 3

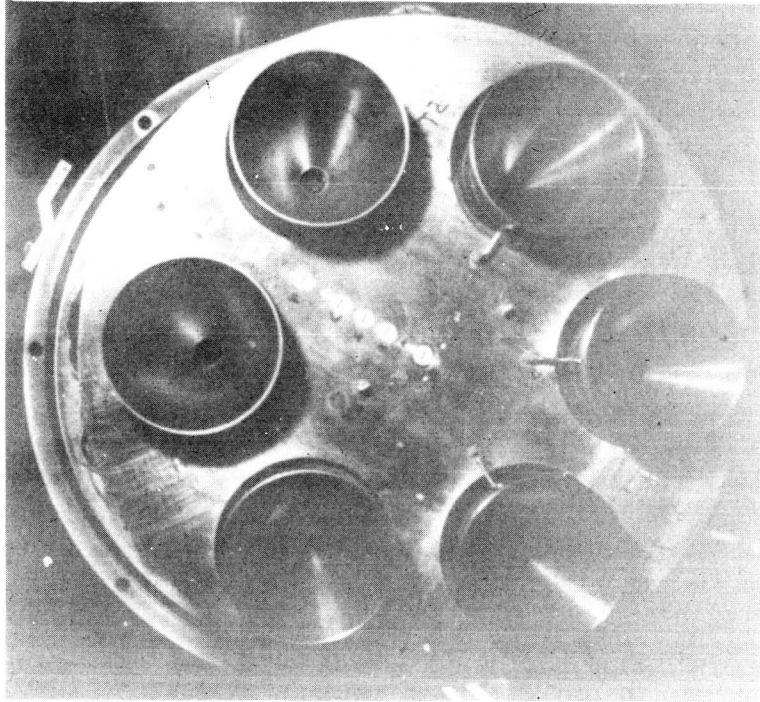


FIGURE 4

CORNELL HEAT TRANSFER GAUGE

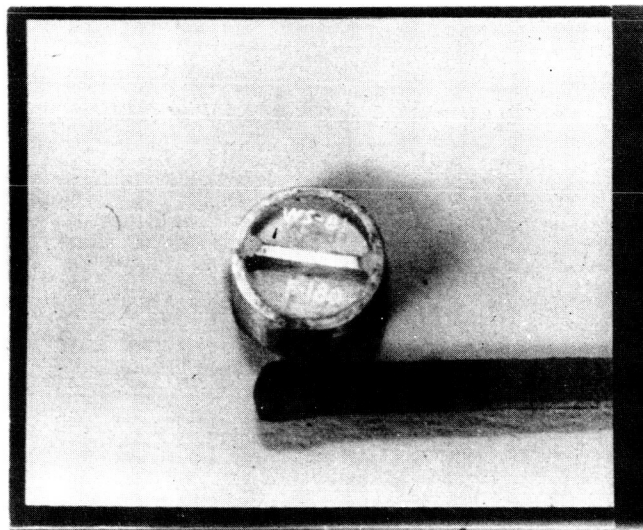


FIGURE 5



rise. When the thermometer strip faces outward, the gage measures the sum of convective and radiative heat flux; with the slug turned over, only the radiative component is measured. The short duration method can also be used in wind tunnels. It is then preferable to replace the diaphragms by quick-acting valves, in order to avoid having to shut down the tunnel after each shot to replace the diaphragms. Figure 6 shows the rear end of a model of a Saturn I/Block II vehicle in a wind tunnel. Figure 7 shows a similar Saturn I/Block I model firing into a transonic wind tunnel. Figure 8 shows an upstream view of the same shot. Figure 10 of reference 1 shows a typical picture of a twin-engine shot in a vacuum tank. The size of the models used in these experiments is normally between 5 and 10 percent of full scale. The preceding description may suffice to give you an idea of the procedures used in our model tests of rocket base heating.

When the engineer performs model tests, he prefers to have similarity laws that permit him to directly convert his model test results into full scale design numbers, without any investigation of the details of his problem. Quite frequently, this experimental approach is his only chance to obtain his design information. Ordinary wind tunnel testing is a typical example of this approach. All the experimenter has to do is assure geometric similarity, and watch some similarity numbers, mainly the Mach number and the Reynolds number (and

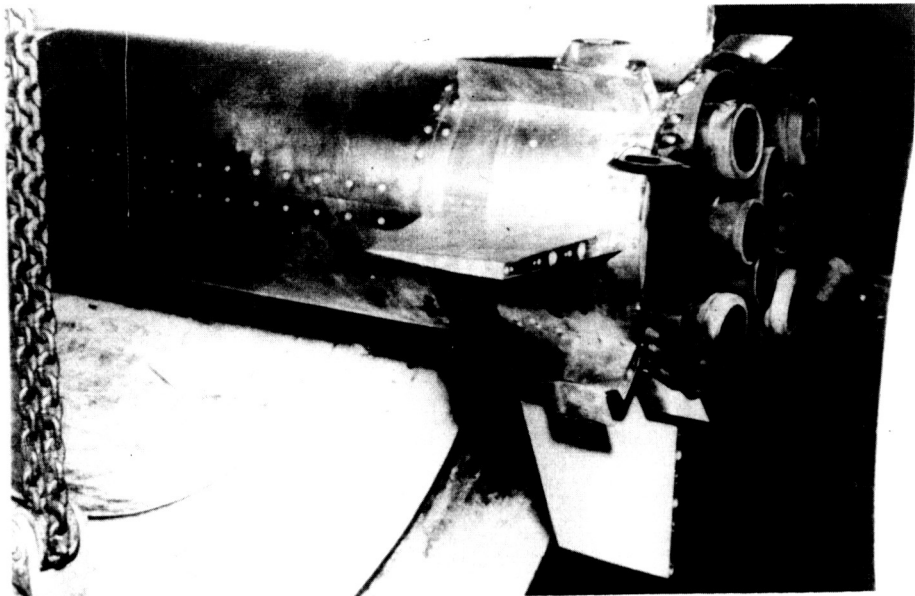


FIGURE 6

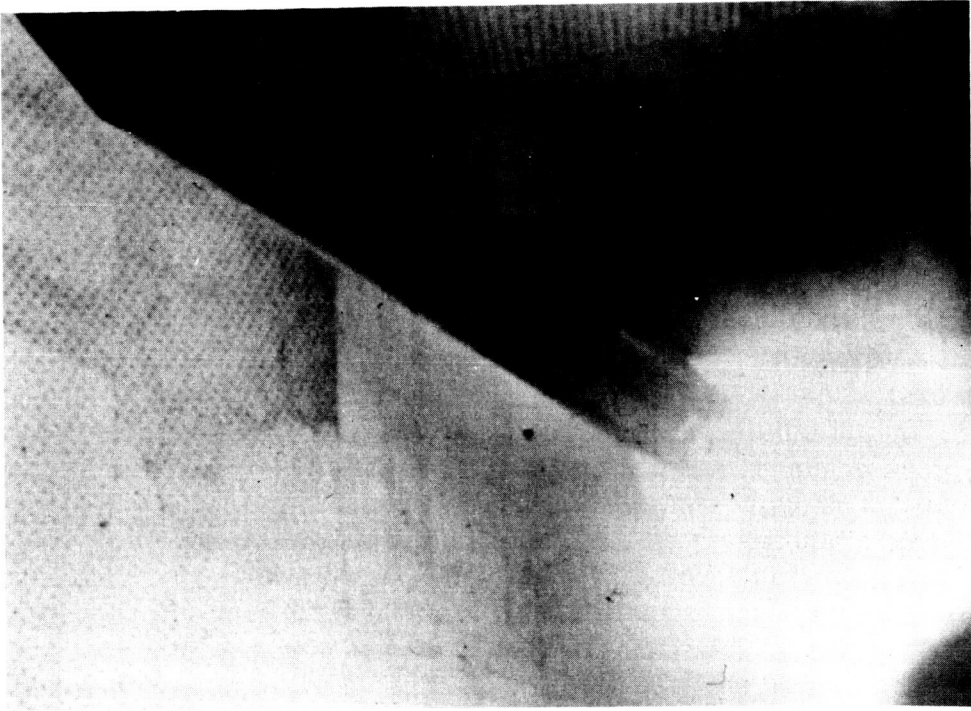


FIGURE 7

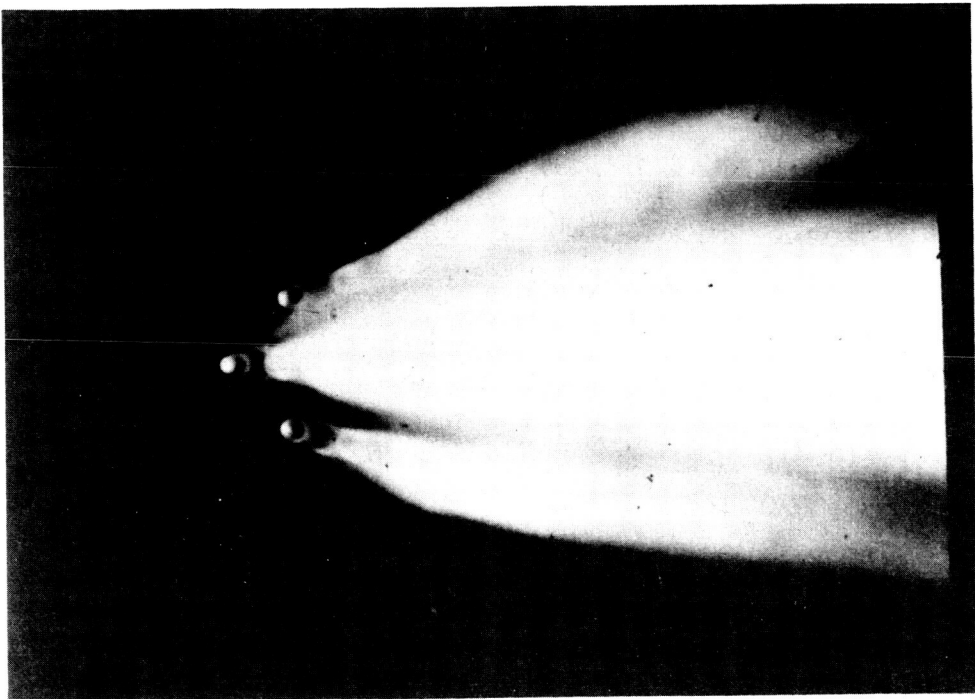


FIGURE 8

considerable liberties can be taken with the latter). A simple similarity transformation then converts his measured pressures, forces, or velocities into the desired full scale numbers.

When we investigate our chance of using this scaling approach with our rocket model radiation measurements, we find that our chance is very slim indeed. We are faced with two combined problems, namely, a fluid mechanics problem which determines the shape of the plume and its temperature, density, and composition distributions, and the radiative transfer problem of emission and absorption in this inhomogeneous volume. For the scaling approach to be valid, similarity laws must exist for both of these problems, and we must be able to simultaneously meet their prescribed similarity conditions.

On the fluid mechanics side we find that the chemical reactions which take place in our jet plumes tend to spoil similarity between small and full scale plumes. Looking for instance at the plumes of a small scale and a full scale version of a liquid oxygen-kerosene engine at sea level conditions, we see immediately that the geometry of the secondary burning, which has a controlling influence on the plume radiation [1], is anything but similar. To a first approximation the ignition delay length [1] is about constant, independent of model size. As a consequence, the secondary combustion on the model engine is shifted way downstream as measured in terms of exit diameters. Evidently the jet plume flow does not "scale" under these conditions. There does exist a so-called "pL-scaling" technique of combustion modeling, which is frequently used in problems like the development of airbreathing engines, the correlation of chemically reacting entry body wakes, etc. [7]. This technique postulates that global combustion similarity is obtained, if velocities and temperatures are maintained at full scale magnitudes, and the products  $pL$  of pressure  $p$  and length scale  $L$  of both model and full scale version are kept at the same value. If one assumes this technique valid for our scale factors of 10 to 20, which is open to question, it would require model combustion chamber pressures in the order of 1000 to 1500 atm. Our small scale engines could not survive pressures of this level, not even with the Short Duration approach.

At high altitudes, where the secondary combustion reactions are sufficiently slow to be negligible for our purposes, there still remain the recombination reactions that go on in the expanding jet flows. The gases that leave the combustion chamber are usually in a state of equilibrium dissociation. In the subsequent expansion some of the dissociated species recombine, freeing their heats of dissociation. As temperature and pressure decrease, the speed of these recombination reactions slows until they can finally no more keep



pace with the expansion rate. Thus, the chemical composition becomes essentially "frozen" downstream of some point that is usually within the nozzle. For a small scale engine model this "frozen" state will be more dissociated than for a full scale engine, tending to falsify somewhat temperatures and compositions. Whether or not this falsification is significant has to be determined from case to case. Shocks within the jet plume are likely to "unfreeze" the chemistry again for some distance.

Two-phase flow as represented by the soot carried in luminous jets, or the metal additives in solid propellant jets can also spoil the fluid mechanic similarity. The effects are negligible when the particles are minute and light and the gas phase is dense, but turn significant under the opposite condition.

On the radiative transfer side the picture also looks unpromising. The band models discussed during this conference permit us to calculate with acceptable accuracy the radiation from given similar gas plumes for an arbitrary range of plume sizes. While we have not yet performed such systematic calculations, we can nevertheless not expect them to reflect a general similarity law, since obviously such a general law does not exist. There are two special cases, though, where similarity does exist. One is the regime of gas plumes that are optically thin at least in their significant bands. In this regime the radiation intensity would grow proportional to the scale size  $L$ , and a single measurement would consequently represent a whole family of sizes. The plumes of our hydrogen-oxygen engines at high altitudes may have a chance to fall sufficiently into this regime. Systematic investigations are required to clarify this point. The other case where radiative similarity can be expected is the case of a gas that obeys Beer's law. Here, the similarity condition would be that  $pL$  would be identical for both small and full scale versions, a condition we had met before with respect to combustion scaling. The catch is, however, that our exhaust gases do not obey Beer's law, and that furthermore the previously mentioned engineering difficulties make  $pL$ -scaling virtually impossible.

The radiation properties of carbon particles do obey Beer's law. Our LOX-kerosene plumes may, therefore, at first glance appear as likely candidates for  $pL$ -scaling. However, besides the previously named difficulties, this approach would also require the assumption that particle size and mass fraction would be independent of pressure, combustion chamber size, and residence time, an assumption that is hardly realistic. An enterprising soul may instead consider controlling the particle density by seeding a clear plume model of moderate pressure level with an appropriate dust. True radiation scaling could be obtained this way, but the task would by no means be an easy one.

In summation, we may conclude that it is in general not possible to obtain design numbers of full scale plume radiation by direct scaling of scale model test results. This is caused by the absence of suitable similarity laws on both the fluid-mechanics and the radiative transfer side, and/or insurmountable engineering difficulties in meeting the apparent similarity requirements. There is a chance that in some special cases, like the high altitude plumes of hydrogen-oxygen engines below some upper size limit, such scaling can be done, but this must first be verified by some systematic investigations.

Our actual practice reflects this situation. In our usual testing we use the experimental radiative component only to extract the convective heating component from the measured total heat flux rate. The full scale radiation intensity is estimated analytically, and our band model studies and computer programs reported in some of the previous papers were aimed at developing an improved capability for such estimates. In addition, we do some model testing to compare measured spectral and total radiation data with calculated results of the same jet plume in order to test the accuracy of our analytical procedures, as reflected in some of the previous papers.

There is still another aspect under which one can look at our question of "scaling." We have acceptable scale model and full scale flight results for the first stage of the Saturn I vehicle. It is natural to inquire how these two compare. Figure 9 compares these data. The drawing on the upper right sketches a rear-end view of the vehicle, with the eight engines, the four-lobed tail cross section of the Block I vehicles, and the location of the total radiation gage. The point symbols represent the model tests. The solid circles mark tests by the "Long Duration Method" with the model of Figure 1, and the other symbols represent "Short Duration" tests. The curve represents the flight results of the fourth Saturn I vehicle. The sudden drop of the curve at 48-km altitude was caused by an intentional shutting off of one engine to test the vehicle's engine-out capability. The surprising result is that flight data and model test results virtually coincide over the whole range of altitudes, despite all the above mentioned reasons why no simple relationship should exist between them, and especially despite the very obvious differences in the geometry of the secondary burning. The secondary burning is responsible for the intensity spike on the left-hand side of the graph. The scale model data of Figure 9 could have been used to generate much needed design numbers, had we been able to predict this coincidence. On the basis of available knowledge, though, I can consider this coincidence only as accidental, without being able to explain its puzzling aspects. It will be interesting to see whether the Saturn V flights will reveal a similar or dissimilar result.\*

\* See note at end of this text.

**COMPARISON OF RADIATIVE HEATING RATES  
FROM MODEL AND FLIGHT TEST  
ON SATURN I VEHICLES**

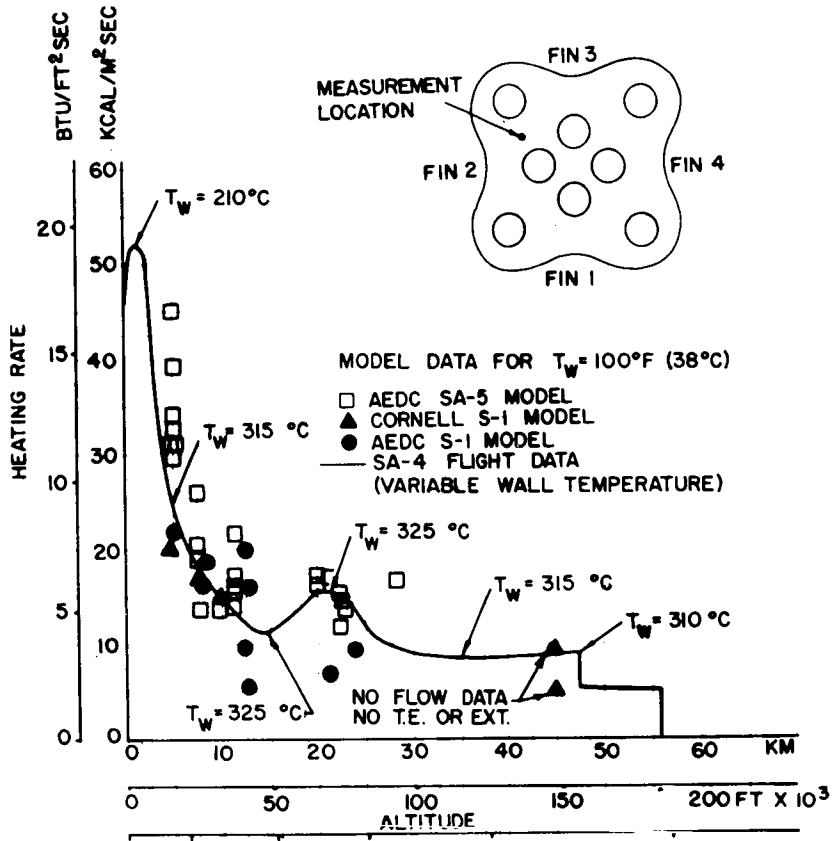


FIGURE 9

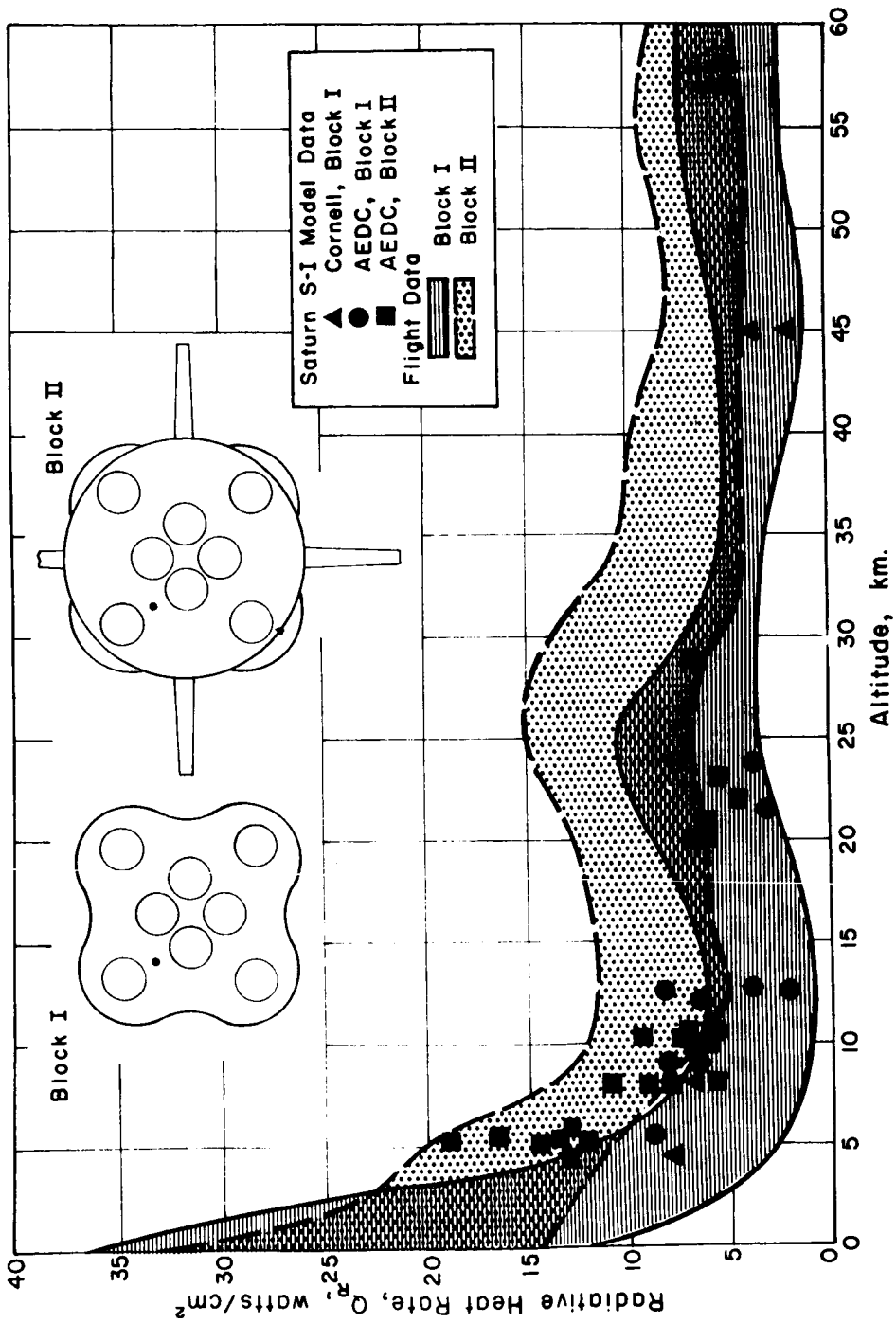
I must now confess to a certain bit of cheating with respect to Figure 9. The cheating consisted in comparing the scale model results with the results of only one single flight, using an old slide that was readily at hand. We have actually obtained acceptable sets of radiation measurements from two of the four Block I flights, and from all six Block II flights. Block II had replaced the four-lobed tail barrel of Block I (see Fig. 7) by a cylindrical one, and was equipped with fins (see Fig. 6); one would expect that both modifications have no significant effect on the plume radiation. Due to a variety of reasons the

results of a set of flight tests do not fall on a single curve, but scatter rather within a certain envelope. Figure 10 shows one such envelope each for the Block I and Block II flights, together with the scale model test points of Figure 9. The use of envelopes tends to overemphasize the true scatter, while Figure 9 underemphasizes it. The truth lies between these two representations, and does not materially change the previous conclusions.\*

---

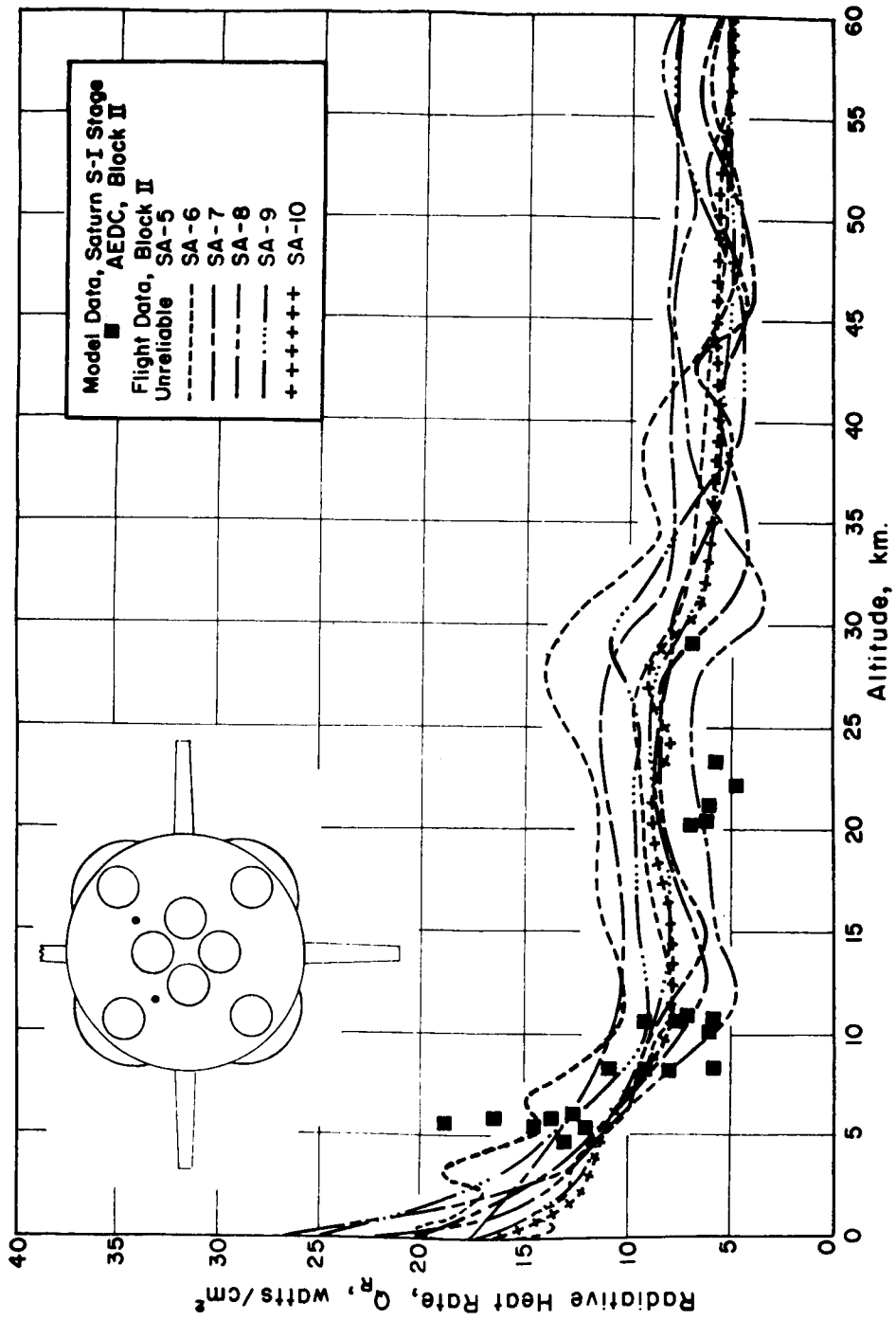
\* A graph showing individual radiometer curves for the Block II flights has meanwhile become available, and is added as Figure 11. For some flights the graph shows two curves, representing two total-intensity gages in similar locations with respect to the engine pattern. Differences between these two curves are partly caused by random scatter, and partly by angle of attack. The Block II-envelope of Figure 10 included another radiometer, and is therefore wider than Figure 11 warrants.

Note: The evaluation of results of the first Saturn V flight has meanwhile shown that this virtual coincidence between model test and full scale radiation intensities was not repeated. The 2.22 percent scale model intensities were considerably below the full scale intensities. This confirms the accidental and capricious nature of the Saturn I results discussed above.



COMPARISON OF RADIATIVE HEAT RATES ON MODEL AND FLIGHT TESTS OF S-I STAGE OF SATURN VEHICLES

FIGURE 10



COMPARISON OF RADIATIVE HEAT RATES ON MODEL AND FLIGHT TESTS OF S-I STAGE OF SATURN, BLOCK II, VEHICLES

FIGURE 11

## REFERENCES

1. Dahm, W. K.: Introduction to the Problem of Rocket Base Heating, and to the Behavior of Liquid Propellant Rocket Jet Plumes. Proceedings of the present conference.
2. Rocket Testing in Simulated Space and High Altitude Environments. Symposium Proceedings, June 28-29, 1961, vols. I and II, AEDC-TR-61-14, October 1961.
3. Beheim, M. A.; and Obery, L. J.: Wind Tunnel Studies of Booster Base Heating. IAS Paper 62-166; also Aeronaut and Astrospce Engin. , 1963.
4. Bird, K. D.; Matthis, C. L.; and Reece, J. W.: The Application of Short-Duration Techniques for the Experimental Study of Base Heating. Part I: High Altitude Testing Technique and Experimental Results for a Four-Engine Rocket Configuration. Cornell Aeron. Lab. Rep. HM-1510-Y-1 (I), April 1962.
5. Sergeant, R. J.: The Application of Short-Duration Techniques to the Experimental Study of Base Heating. Part II: A Study of Reynolds Number and Temperature Effects on Base Heating for a Four-Engine Hot Rocket Configuration Operating at High Altitude. Cornell Aeron. Lab. Rep. HM-1510-Y-1 (II), April 1965.
6. Hendershot, K. C.: The Application of Short-Duration Techniques to the Experimental Study of Base Heating. Cornell Aeron. Lab. Rep. HM-1510-Y-18, May 1965.
7. Spalding, D. B.: The Art of Partial Modeling. Ninth Intern. Symp. on Combustion, Colloquium on Modeling Principles, 1963, pp. 833-843.

F. S. Simmons, Univ. of Michigan: It is a little difficult to compare heating rates from the model engines to those for the full size engines because most of the radiation is due to the carbon content of the exhaust. This carbon, as someone mentioned earlier, is a nonequilibrium product, and the mechanism of its formation is not too well understood. One thing we had observed some years ago at Rocketdyne is that, in a vernier engine, which burned at a ratio of oxygen to fuel of 1.8, the carbon concentration was considerably greater than in the Atlas booster engine, which burned at a ratio of about 2.4. I think the Saturn I engines are close to the Atlas engines in their configuration and operating mixture ratio. The carbon production in the smaller engines was relatively greater, and the plume size and radiation were correspondingly more. This might have something to do with the discrepancies you have noted.

S. C. Traugott, Cornell: Figures 9 and 10 show a second maximum in the radiative flux around 25 km. Can this effect be explained?

W. K. Dahm: No, we cannot give any well-founded explanation for this bump. You may perhaps hear talk about shock wave formations and so on, but in the end it all boils down to pure conjecture. Our ability to understand and predict first stage plume radiation is still in a very unsatisfactory state, predominantly because we cannot yet solve the fluid mechanics side of the problem. We can make, at the present, only a rough estimate of the radiation intensity at sea level altitude, using shell models [1]. Mr. Reardon showed such a shell model on one of his slides. From the sea level radiation intensities thus obtained, we make an extrapolation versus altitude based on trends found empirically in previous flights. This extrapolation is inaccurate, since these trends are not identical for different types of vehicles, but it is about all we can presently do. We cannot make analytical estimates, because we cannot as yet, sufficiently treat the secondary combustion which dominates the low altitude radiation; and we cannot trust any extrapolation of our scale model test results, for the reasons described before. This coincidence of scale model experiments and flight results may tempt one to use the model results directly, but I would not dare to go this route. Efforts are being made to obtain an acceptable analytical solution for the secondary combustion.

R. Goulard, Purdue: I was thinking of the analogy with the situation some years ago in the analysis of reentry shock layers. Some forms of overall scaling were shown to exist in some limited flight ranges, but in general the flow field techniques and the chemical/radiation properties were studied independently; then they were put together. In this manner, there was a good degree of confidence in the results, but no overall scaling was expected nor obtained.



W. K. Dahm: The analytical approach you point to seems to be our only solution, but it meets in our case with much greater difficulties than it does in the entry body problem. In the controlling part of the flow fields of jet clusters at high altitudes, we find a complicated criss-cross pattern of interference shocks, and zones of mixed subsonic-supersonic flow. As we step down to lower altitudes, we get rid of the mixed subsonic-supersonic zones and some of the shocks, but find unsteady turbulent shear layers and secondary combustion in a controlling position. For neither of these problems do we, at present, have a satisfactory solution, and any solution we can expect in the future is bound to be laborious. In contrast, the direct scaling of model test results, be it in a spectral or total sense, is attractively simple and all-encompassing, if it could only be proved workable.

W. Herget, Rocketdyne: The Cornell Aeronautical Laboratory tests do not reproduce the cool carbon-rich shroud generated by the turbines of the outboard H-1 engines. Should this contribution be taken into consideration or not?

W. K. Dahm: As I see it, this turbine exhaust may either cut down or increase the radiation. It puts an additional absorbent shroud around the initial part of the jet and increases somewhat the ignition delay of the secondary combustion, but it also adds fuel to that combustion. I would estimate that, to a first approximation, the effect of this turbine exhaust is negligible.

F. K. Moore, Cornell: I do not think that a direct agreement between these laboratory tests and the flight tests was sought after, but it would seem to me that such a possibility would depend on the variation of optical thickness with scale. If both the small scale models and the large Saturn plumes are optically thick, a coincidence of heating rates might not be too surprising.

W. K. Dahm: On the basis of measurements of Simmons, DeBell, and others, we know that the jet plumes of the Saturn I first stage are optically thick and impenetrable in a wide range of wavelengths, even right at the nozzle exit. Our scale model engine plumes are in an intermediate range. You can "see" through them, but absorption is not negligible.

F. K. Moore: I suspect, then, that opacity considerations do tend to explain why the results were nearly the same; one does not have to look too deep into the flow field, in either case, to find the effective temperature radiating from the surface.

W. K. Dahm: I would argue as follows: The effect of finite optical thickness tends to hide the interior of a plume, and to emphasize the outer layers. It does this more on the full-scale than on the small-scale version, because the ratio of the "optical free path" to the plume diameter is smaller. Whether this fact enhances or decreases the output of the small scale plume relative to the large scale one depends on the temperature profile of the plumes, and is difficult to estimate offhand. I see the puzzle of Figure 9, etc., in the fact that the small-scale and full-scale data strips seem virtually to coincide over the whole range of altitudes, i.e., over a very wide range of plume conditions. If the two strips would just cross at some altitude, one would coolly discard the coincidence at this point as accidental. As things are, however, this discarding comes harder, though I can see no other acceptable choice.

F. Krause, NASA/MSFC: I have another comment on scaling. In our systematic cross-beam measurements of turbulence in supersonic jets, we found out that the spreading of the supersonic shear layer is very much dependent on the disturbances on the supersonic edge. If you have sound wave or turbulence produced at the supersonic edge, the shear layer spread, i.e., the turbulent exchange, is as high as in subsonic cases. The entrainment of secondary combustibles is to a large extent given by the turbulent mixing through the adjacent jet shear layers. Whether combustible mixtures and flames ultimately develop in the base area may thus depend to a large extent on the disturbances in the adjacent jets. These disturbances depend on the model surroundings. You have no way of knowing or scaling them.

S. Golden, Rocketdyne: It seems to me that with the carbon-producing exhaust, most of the radiation will come from the boundary layers. So whether the inside of the plume is optically thick or not is really not important since all the radiation is confined to the outside shell. On that basis, I would not be particularly surprised at the similarities which have been shown here.

W. K. Dahm: I believe you tend at the moment to oversimplify the shell model. The temperature profile of a typical plume cross section starts with ambient temperature at what we may define as the plume surface, rises to a maximum of some 2000° K caused by secondary combustion, and drops again to, say, 1500° K at the jet axis. The effective temperature of our shell model is determined by how deeply we can "look" into this profile, which in turn depends on the ratio of optical free path to plume size. There exists no plume surface temperature that we could assign to the shell model. The "plume boundary layer" is not thin; it grows to a considerable thickness and fills the whole jet downstream of a point some 5 to 10 diameters from the nozzle exit.

## QUESTION IV

N 68-18114

### BAND MODELS AND NON-MODELS

Introductory Remarks: Alex Thomson, IDA

A. Thomson: I would like to come back to the question that was raised during Dr. Auman's talk yesterday concerning the possibility of carrying out detailed calculations for water vapor at high temperature and at pressures between one-tenth atmosphere and one atmosphere. The question has two parts. The first concerns the feasibility of carrying out the computation in terms of time and cost. The second is does the present state of knowledge of line strengths, line widths, and line position warrant such a calculation? Would Dr. Auman care to comment on that?

J. Auman, Princeton: The main problem (and I have really no opinion on it because I have not looked into it) is the determination of the line profiles when you have pressure broadening. I suppose that there are experimental determinations for  $N_2$  and  $O_2$  in the atmosphere, but I do not know how well it can be determined in a rocket exhaust. There are some free electrons there which will broaden the lines; also, there may be all sorts of weird molecules depending upon what the rocket fuels are. It will take detailed calculations for all the constituents to determine correctly the profiles.

Conceivably one could assume a Lorentz profile, pick arbitrarily three or four values for  $\gamma$  and then calculate the distribution of the opacities with these different values. I am not at all sure how accurately a person would be able to do it at this time. I would expect that when pressure broadening is important the number of lines that would have to be considered would be considerably reduced due to the wings which the strong lines would have.

Regarding computation times, the results I presented earlier took forty hours on an IBM 7094; this included the calculations that were needed for determining the molecular constants and the debugging of the necessary programs. I treated seven band systems for four temperatures, and three assumed line profiles. If you had to worry about only one band, then of course the time necessary to make the calculation would also be less.

A. Thomson: Maybe some of the people who have had this problem and dealt with it in the earth's atmosphere could comment.

R. F. Calfee, ESSA: I do not care to make a comment on the virtues of bands versus nonbands. I merely wish to state that certain government agencies have become very much interested in making available the line parameters for the atmospheric gases. I happen to be one of those persons who has been commissioned to make this information available within the next year. With the assistance of Dr. William Benedict, we will be publishing practically all of the line strengths, half-widths, and other information that is necessary on the water vapor bands and the carbon dioxide bands and the nitrous oxide. Methane and ozone are being treated similarly by other people, so that for those who do want this information, it will become available. In many cases, it is not necessary to treat the entire band, but only to pick out some outstanding feature of a band which is relatively narrow in spectral width and then to treat this narrow spectral interval as you have been treating bands. It works very well using the line-by-line calculation. This narrow spectral interval can be treated in a layered situation; and, depending on the amount of money one wants to spend, one can make 20, 30, 40 layers, or one or two. It works quite well and gives you good answers,

R. Drayson, Univ. of Michigan: I would like to make one or two comments on the applicability of band models and the direct integration methods. Personally, I think that we really do not have a dispute here. The choice of the method you are going to use depends on the application you have in mind and on the sort of accuracy and spectral resolution you need. If you cannot be satisfied with anything but high accuracy, direct integration has advantages. One application where high accuracy is necessary is remote sensing of temperatures in the earth's atmosphere. It has been shown that it is important to calculate transmissivity very accurately.

On the other hand, from the examples that we have been shown in the last couple of days on the hot gases, it seems that the Elsasser and the random band model produce solutions that are not very different from one another. The positions and distributions of the lines do not seem to be very important for these applications. In hot gases there are many more lines to deal with than in the atmosphere. The overtone bands or hot bands come into prominence, and you cannot possibly at the moment deal with these by direct integration methods, even if you wanted to.

Some of the advantages of direct integration are that you can also use them to compare some of the band models and see whether the models give you the sort of accuracy that you are looking for. You can test for small parts of the bands. Which method is used depends on the requirements each individual user wants to meet.

A. Thomson: Band model techniques have not yet been applied to the evaluation of the heat transfer from a strongly scattering exhaust of a solid propellant rocket engine. Charlotte Bartky has made a start in doing such a mixed problem of molecular emission and absorption with scattering. I wonder if this problem has been dealt with in connection with planetary atmospheres. For instance, is the reflectance of a cloud in the  $4.3 \mu$   $\text{CO}_2$  band a case where scattering and molecular emission are simultaneously important?

R. A. McClatchey, AVCO: I would like to comment briefly on that question. In the  $4.3 \mu$   $\text{CO}_2$  band temperature sounding experiment, scattering is probably not important unless we have significant aerosol layers at high levels in the atmosphere. As soon as a cloud forms (even a thin cloud), it emits as a block body at the local temperature. Any scattering of importance would have to be scattering of the incoming solar radiation by aerosols at a height at which solar radiation is only slightly attenuated.

However, at shorter wavelengths, for example, in the  $2 \mu$   $\text{CO}_2$ ,  $2.7 \mu$   $\text{CO}_2$ , and in the  $7600 \text{ \AA}$  oxygen band, the attempts to make cloud height determinations by measuring the absorption of the gas above the cloud result in rather large errors. The Weather Bureau group who did this experiment found that scattering is important. Therefore, they had to consider multiple scattering inside the cloud and its effect on the radiation flux and then to correct appropriately their cloud height estimates. Hence, scattering is a problem in near infrared measurements.

A. Thomson: In the treatments that have been attempted with multiple scattering, where the molecular absorption is important, has any kind of grey gas assumption been made?

R. A. McClatchey: No. Detailed calculations have been made including Mie scattering theory for the non-grey situation. Some of this work has been done by the Weather Bureau, and I personally have done some work of this sort in connection with both the  $2 \mu$  experiment that we have contemplated and in connection with some work related to the atmosphere of Venus, where one has a simultaneous scattering and absorption problem. There, we have done line-by-line calculations, point by point across a whole band, considering both scattering and absorption.

A. Thomson: Monochromatically?

R. A. McClatchey: Right. It is very difficult to do a problem like that based on any kind of band model; I would not know how to do it.

T. L. Altshuler, NASA/ERC: If you are going to do line-by-line integration, I do not see that it needs to be done more than once; with this information, you can certainly develop theoretical growth curves. Those growth curves can be compared with laboratory data to find out whether you are using the correct line shape. The growth curves are all the information you need. If you wish then to expand on these growth curves, you can invert them and thereby get a probability distribution, as I showed earlier. The beauty of the probability distribution is that, by using it together with Beer's law, you can integrate and determine the transmission for any optical thickness.

A. Thomson: But don't you have to evaluate the probability distribution for each condition, for every different pressure? It is not obvious what the pressure dependence is.

T. Altshuler: You are quite correct. You would have to develop these growth curves for different pressure conditions and find out whether there is any significant difference or not.

S. A. Golden, Rocketdyne: But that has been the whole bone of contention, whether or not you can do the frequency integration before doing any spatial integration. The advocates of the band model approach say you can, and the advocates of the line-by-line approach say it is inherently wrong because we do not know what the errors are.

**ATTENDEES AT RADIATION CONFERENCE**

Walter G. Planet  
Heliodyne Corporation  
SAMSO/BMRS Data Services & Analysis  
P. O. Box 4097  
Norton AFB, California 92409

Robert O. Platz  
General Electric Company  
Space Sciences Laboratory  
Room M7223  
P. O. Box 8555  
Philadelphia, 1, Pennsylvania 19101

J. von Puttkamer  
R-AERO-AT, NASA/MSFC  
Huntsville, Alabama

Dr. R. D. Rawcliffe  
Aerospace Corporation  
Box 95085  
Los Angeles, California 90045

John E. Reardon  
Hayes International Corporation  
P. O. Box 2287  
Birmingham, Alabama 35201

Dr. T. R. Reithof  
General Electric Company  
Valley Forge, Pennsylvania

Roger Russin  
R-AERO-AT, NASA/MSFC  
Huntsville, Alabama

Adel F. Sarofim  
12-188  
Massachusetts Institute of Technology  
Cambridge, Massachusetts 02139

Dr. F. S. Simmons  
University of Michigan  
P. O. Box 618  
Ann Arbor, Michigan 48107

J. G. Skifstad  
Jet Propulsion Center  
School of Mechanical Engineering  
Purdue University  
Lafayette, Indiana 47906

J. B. Stephens  
R-AERO-AF, NASA/MSFC  
Huntsville, Alabama

Dr. V. R. Stull  
General Research Corporation  
(Formerly: Defense Research Corporation)  
P. O. Box 3587  
Santa Barbara, California 93105

Ming Yang Su  
Northrop Space Laboratory  
Huntsville, Alabama

Donald Takewchi  
R-AERO-AT, NASA/MSFC  
Huntsville, Alabama

Dr. Jose Tamagona  
General Applied Sciences Laboratory  
Merrick and Steward Avenues  
Westbury, Long Island, New York 11590

Robert Taylor  
Chrysler Corporation Space Division  
P. O. Box 29200  
New Orleans, Louisiana 70129

Devron Thibodeaux  
Chrysler Corporation Space Division  
Department 2782  
P. O. 29200  
New Orleans, Louisiana 70129

Dr. J. A. L. Thomson  
General Dynamics/Convair  
5001 Kearny Villa Road  
San Diego, California 92112

S. C. Traugott  
210 Upson Hall  
Cornell University  
Ithaca, New York 14850

John Tucker  
Chrysler Corporation Space Division  
Department 2782  
P. O. Box 29200  
New Orleans, Louisiana 70129



Prasad Varanasi  
Department of Mechanics  
State University of New York  
Stony Brook, Long Island, New York 11790

Bill Walker  
U. S. Army Missile Command  
Research and Development Directorate  
ATTN: Advanced Systems Lab., AMSMI-RDK  
Redstone Arsenal, Alabama 35809

Oran R. White  
Sacramento Peak Observatory  
Air Force Cambridge Research Laboratory  
Sunspot, New Mexico 88349

Homer B. Wilson, Jr.  
R-AERO-AT, Chief, Thermo Environment Branch  
NASA/MSFC  
Huntsville, Alabama

Dr. S. T. Wu  
University of Alabama in Huntsville  
P. O. Box 1247  
Huntsville, Alabama 35807

Dr. W. Wurster  
Cornell Aeronautical Laboratory  
Buffalo, New York 14221

Harold Yates  
Environmental Science Services Administration  
National Environmental Satellite Center  
FOB #4  
Suitland, Maryland 20233

Wallace W. Youngblood  
Northrop Space Lab.  
Huntsville, Alabama

Dr. G. J. Zissis  
University of Michigan  
P. O. Box 618  
Ann Arbor, Michigan 48107

J. J. Brainerd  
University of Alabama in Huntsville  
P. O. Box 1247  
Huntsville, Alabama 35807

M. A. Britt  
The Boeing Company  
Huntsville, Alabama

Terry F. Greenwood  
R-AERO-AT, NASA/MSFC  
Huntsville, Alabama

B. K. Hodge  
Thiokol Chemical Corp.  
Huntsville, Alabama

O. C. Holderer  
R-AERO-A, NASA/MSFC  
Huntsville, Alabama

A. V. Jelalian  
Box 205  
Raytheon Company  
Sudbury, Massachusetts 01776

Ira P. Jones  
R-AERO-AT, NASA/MSFC  
Huntsville, Alabama

Mrs. Beverly A. Lavender  
Mail Stop 32  
Brown Engineering Co.  
Research Park  
Huntsville, Alabama 35807

W. K. McGregor  
ARO, Inc.  
RTF - Research Branch  
Arnold Air Force Station, Tennessee 37389

C. R. Mullen  
The Boeing Company, M/S #48  
2819 Newby Road, SW  
Huntsville, Alabama

G. D. Reny  
Lockheed Missiles & Space Co., D54-20  
Huntsville Research and Engineering Center  
P. O. Box 1103, West Station  
Huntsville, Alabama 35807

R. P. Rhodes  
ARO, Inc.  
RTF - Research Branch  
Arnold Air Force Station, Tennessee 37389

Carl D. Engel  
Lockheed Missiles & Space Co.  
Huntsville, Alabama

Harold C. Euler  
NASA/MSFC  
Huntsville, Alabama

Vincent J. Falcone, Jr.  
AFCL (CRDIO)  
L. G. Hanscom Field  
Bedford, Massachusetts 01730

Dr. Edwin T. Florance  
GCA Technology Division, GCA Corp.  
Burlington Road  
Bedford, Massachusetts 01730

Phyllis Forbush  
R-AERO-AT, NASA/MSFC  
Huntsville, Alabama

Edward P. French  
NAR North American-Rockwell  
Downey, California

Dr. Ernst D. Geissler  
Director, Aero-Astrodynamics Laboratory  
NASA/MSFC  
Huntsville, Alabama

Professor John C. Gille  
Department of Meteorology  
Florida State University  
Tallahassee, Florida 32306

Dr. Leonard Glatt  
TRW Systems  
One Space Park  
Redondo Beach, California 90278

Dr. Dieter Goetze  
Honeywell, Inc.  
Systems and Research Division  
2700 Ridgeway Road  
Minneapolis, Minnesota 55413

S. A. Golden  
Rocketdyne, A Division of North American Aviation  
6633 Canoga Ave.  
Canoga Park, California 91304

Dr. Robert Goulard  
Purdue University  
School of Engineering & Aeronautical Sciences  
Lafayette, Indiana 47907

Dr. L. D. Gray  
Dr. A. T. Young  
Jet Propulsion Laboratory  
4800 Oak Grove Drive  
Pasadena, California 91103

B. C. Hablutzel  
R-AERO-AF, NASA/MSFC  
Huntsville, Alabama

J. Vern Hales  
General Electric Company  
Philadelphia, Pennsylvania

Dr. Kenneth E. Harwell  
Aerospace Engineering Department  
Auburn University  
Auburn, Alabama 35830

Ewell R. Heatherly  
R-AERO-AT, NASA/MSFC  
Huntsville, Alabama

Dr. William Herget  
North American Rockwell  
Rocketdyne Division  
6633 Canoga Park  
Canoga Park, California 91304

Dr. R. Hermann  
University of Alabama in Huntsville  
P. O. Box 1247  
Huntsville, Alabama 35807

Steve S. Hu  
Northrop Space Lab.  
Huntsville, Alabama

Robert M. Huffaker  
R-AERO-AT, NASA/MSFC  
Huntsville, Alabama

R. R. Jayroe  
R-AERO-AF, NASA/MSFC  
Huntsville, Alabama

Gilbert H. Kelley  
Thermodynamics Section, Plant 35  
Grumman Aircraft Engineering Corporation  
Bethpage, Long Island, New York 11714

E. Rolfe  
Box 205  
Raytheon Company  
Sudbury, Massachusetts 01776

L. M. Seale  
GCA Corporation  
Bedford, Massachusetts

W. H. Seiber  
R-TEST-I, NASA/MSFC  
Huntsville, Alabama

Ed. R. Westwater  
Environmental Sciences Services Administration  
ITSA  
Suitland, Maryland 20233


## APPROVAL

# MOLECULAR RADIATION AND ITS APPLICATION TO DIAGNOSTIC TECHNIQUES

Edited by R. Goulard

The information in this report has been reviewed for security classification. Review of any information concerning Department of Defense or Atomic Energy Commission programs has been made by the MSFC Security Classification Officer. This report, in its entirety, has been determined to be unclassified.

This document has also been reviewed and approved for technical accuracy.



---

WERNER K. DAHM  
Chief, Aerophysics Division, NASA/MSFC



---

E. D. GEISSLER  
Director, Aero-Astroynamics